



HAL
open science

Iterative self-assembly of nanostructured block copolymer thin films, toward the development of functional three-dimensional structures with nanometric periodicity

Nils Demazy

► **To cite this version:**

Nils Demazy. Iterative self-assembly of nanostructured block copolymer thin films, toward the development of functional three-dimensional structures with nanometric periodicity. *Polymers*. Université de Bordeaux, 2022. English. NNT : 2022BORD0067 . tel-03663690

HAL Id: tel-03663690

<https://theses.hal.science/tel-03663690v1>

Submitted on 10 May 2022

HAL is a multi-disciplinary open access archive for the deposit and dissemination of scientific research documents, whether they are published or not. The documents may come from teaching and research institutions in France or abroad, or from public or private research centers.

L'archive ouverte pluridisciplinaire **HAL**, est destinée au dépôt et à la diffusion de documents scientifiques de niveau recherche, publiés ou non, émanant des établissements d'enseignement et de recherche français ou étrangers, des laboratoires publics ou privés.

THÈSE PRÉSENTÉE

POUR OBTENIR LE GRADE DE

DOCTEUR DE

L'UNIVERSITÉ DE BORDEAUX

ÉCOLE DOCTORALE des Sciences Chimiques

SPÉCIALITÉ : Polymères

Par Nils DEMAZY

**ITERATIVE SELF-ASSEMBLY OF NANOSTRUCTURED BLOCK
COPOLYMER THIN FILMS**

*TOWARD THE DEVELOPMENT OF FUNCTIONAL THREE-DIMENSIONAL STRUCTURES WITH
NANOMETRIC PERIOD*

Sous la direction de Guillaume FLEURY

Soutenue le 17/03/2022

Membres du jury :

Mme RESSIER Laurence, Professeure, LCPNO – *Université de Toulouse*
M. ZELSMANN Marc, Chargé de recherche, LTM – *Université Grenoble Alpes*
M. RAVAINÉ Serge, Professeur, CRPP – *Université de Bordeaux*
M. SOPPERA Olivier, Directeur de recherche, IS2M – *Université Haute-Alsace*
M. HADZIIOANNOU Georges, Professeur, LCPO – *Université de Bordeaux*
M. FLEURY Guillaume, Professeur, LCPO – *Université de Bordeaux*

Rapportrice
Rapporteur
Président du jury
Examineur
Invité
Directeur de thèse

REMERCIEMENTS

Cette thèse a été réalisée dans le laboratoire de chimie de polymères organiques (LCPO) au sein de l'équipe 4, « Polymer materials for electronic, energy, information and communication technologies ». Je tenais en premier lieu remercier Sébastien LECOMMANDOUX, directeur du LCPO, et Georges HADZIIOANNOU, directeur de l'équipe 4, de m'avoir accueilli dans leur laboratoire. Je voudrais surtout remercier mon directeur de thèse, Guillaume FLEURY, qui m'a épaulé et dirigé pendant ces 3 ans et demi de thèse, tout en me laissant la liberté et l'autonomie dont j'avais besoin. Je suis convaincu que le bon déroulement de ma thèse tient en grande partie de lui notamment par la qualité de son accompagnement, tant sur le plan scientifique que relationnel. Je voudrais ensuite remercier mon jury de thèse, Laurence RESSIER, Marc ZELSMANN, Serge RAVAINES Serge, et Olivier SOPPERA d'avoir pris le temps d'étudier ce présent manuscrit, et pour l'échange très intéressant et enrichissant après la soutenance.

Je tenais ensuite à remercier toutes les personnes qui ont contribué au bon déroulement technique de cette thèse, en particulier pour les produits chimiques, la formation sur les équipements et la partie administrative. Je remercie donc ARKEMA, et plus précisément Xavier CHEVALIER et Christophe NAVARRO, pour m'avoir fourni des polymères et des conseils bien avisés sur le PS-*b*-PMMA. Ensuite un grand merci à toute l'équipe de la plateforme ELORPrintTec, qui m'a permis de travailler en toute autonomie sur plusieurs machines, notamment le plasma, l'ALD et le SEM, et plus particulièrement à Sokha KIEV qui est responsable de ces trois machines et qui m'a formé et conseillé tout au long de la thèse. Je tenais aussi à remercier tout particulièrement Gilles PECASTAINGS qui gère la salle blanche du LCPO et notamment le bon fonctionnement de l'AFM. Je le remercie pour tout ce qu'il a pu m'apprendre sur l'AFM, et pour la confiance qu'il m'a accordé pour le gérer conjointement. Merci aussi à toutes les discussions plus ou moins scientifiques qu'on a pu avoir ensemble. Je remercie aussi Mélanie BOUSQUET, qui gère toute la partie sécurité du labo, et donc notre sécurité, mais aussi la SEC, en m'aidant pour l'analyse d'un bon nombre de mes polymères. Finalement je remercie tous les permanents du laboratoire, et particulièrement Aude MANSON et Ellena STEFFY KARNEZIS qui s'occupent de toute la partie administrative.

Je voulais maintenant remercier toutes les personnes qui ont passé une partie ou toute la thèse à mes côtés dans le labo, le fameux groupe des B8ers. Vous avez réussi à me faire passer des moments géniaux durant ces quelques années de thèse, que ce soit d'un point de vue scientifique

au labo, mais aussi personnel, avec de nombreux moments de partage et de soirées. Merci à tous ceux qui ont partagé le bureau avec moi, Kosta, Cindy, Alizée, Naser, Lorenzo, Nico, Yanid, Emin, Xiaojiao et Kaili. Mention spéciale pour Pablo, qui m'a directement aidé sur le projet, et avec qui j'ai pu passer des dizaines d'heures à préparer des films pour aller faire les mesures GISAXS au Synchrotron. Merci aussi à Estelle pour ton aide durant ton stage. Merci à tous les autres membres du B8 : Solène, Ben, Micah, Ari, Cian, Alberto, Lauriane, Florian, Alexander, Rim, Shekhar, Sasikumar, Milutin, Tommaso, Federico, Silvia, Eunkyung, Camille, Geoffrey, Pane, Florent, Antoine, Pedro, J-D, Joulia, Raymond, Emile, Alexia, Quentin, Jérémy et Julien. Un grand merci tout spécial à mon ami Pino, avec qui j'ai passé le plus clair de mon temps au labo mais aussi en dehors.

Je voulais aussi remercier tous mes amis qui ne sont pas à Bordeaux mais qui ont suivi l'avancée de ma thèse de loin : le 100 et la meute, vous vous reconnaitrez. Merci aussi à Zellner, pour tous les coups de fil à discuter de tout et de rien, comme on sait le faire depuis nos 2 ans ! Un énorme merci aussi à tous ceux qui sont venus nous aider à rénover (ou construire ?) notre maison pendant cette dernière année de thèse, je pense particulièrement à Pino, Solène, Claire & Mathieu, Chachou et mon bibi, Mathieu.

Je remercie ma famille, qui m'a soutenu durant toute la thèse ! Merci à mes trois frères, Axel, Jonathan et Noé, ainsi qu'à leur moitié, Aurore, Cindy et Aglaé. Petite dédicace à mes neveux et nièce : Eythan, Charlie, Albane et Wyatt. Merci à mes parents qui sont aussi venu nous aider pour la maison. Merci aussi à ma belle-famille, et surtout à Valérie pour son soutien moral et son aide pour la maison. Finalement merci à la personne la plus importante à mes yeux, celle qui partage ma vie, celle avec qui je me suis lancé dans le projet fou de rénover entièrement une maison : Pauline. Merci à toi de m'avoir supporté et aidé durant ces 3 ans et demi, et sans qui cette thèse n'aurait pas été si agréable.

RESUME EN FRANÇAIS

ASSEMBLAGE ITERATIF DE FILMS NANOSTRUCTURES DE COPOLYMERES A BLOCS

VERS LE DEVELOPPEMENT DE STRUCTURES TRIDIMENSIONNELLES FONCTIONNELLES A PERIODICITE NANOMETRIQUE

Les copolymères à blocs (BCPs) sont des polymères composés de deux blocs ou plus, ayant une composition chimique différente, et connectés ensemble par une ou plusieurs liaisons covalentes. La structure la plus simple est composée de deux blocs reliés par une liaison, appelée copolymères di-blocs. Ces macromolécules ont tendance à produire une séparation de phase due à l'incompatibilité chimique entre les deux blocs, représentée par le paramètre de Flory-Huggins noté χ . Aussi, la liaison covalente entre ces deux blocs force cette séparation de phase à se produire à une échelle nanométrique, dont la taille dépend de la longueur de la chaîne de BCPs. Ce phénomène thermodynamique est appelé auto-assemblage, et permet de générer des structures périodiques complexes avec une périodicité de quelques nanomètres à des centaines de nanomètres. En particulier, les copolymères di-blocs peuvent s'auto-assembler dans des réseaux de sphères, cylindres, gyroïdes ou encore lamelles en fonction de la fraction volumique d'un bloc par rapport à l'autre. Habituellement, pour obtenir ces morphologies en film mince ou en volume, les chaînes polymères ont besoin d'un apport de mobilité permettant de l'auto-organisation, obtenue par recuit thermique ou par vapeurs de solvant.

Au vu de la taille et périodicité de ces nanostructures, les BCPs sont souvent utilisés pour les nanosciences et les nanotechnologies, sous forme de couches minces de l'ordre de quelques dizaines de nanomètres. Dans cette géométrie de film mince, il est important de contrôler l'orientation des structures par rapport au plan du substrat. Actuellement, les films nanostructurés obtenus par auto-assemblage de BCPs sont principalement utilisés pour la formation de masques lithographiques permettant de produire des formes géométriques bien définies, telles que des lignes avec des lamelles perpendiculaires au plan ou bien des motifs hexagonaux avec des sphères ou des cylindres perpendiculaires au plan. En effet, après auto-assemblage, un des deux blocs peut être sélectivement retiré avec un traitement plasma par exemple, permettant d'obtenir un masque ayant un motif nanométrique qui peut être utilisé pour graver le substrat. Cette technique possède un grand intérêt afin de compléter d'autres techniques permettant d'obtenir ces résolutions nanométriques, telle que la nanolithographie extrême UV, ou la nanolithographie par faisceau d'électron. Par contre, un désavantage inhérent

au phénomène d'auto-assemblage limite la production de motifs parfaitement définis sur de larges domaines : l'auto-assemblage de BCPs conduit à des structures polycristallines dont les grains possèdent une orientation aléatoire les uns par rapport aux autres. Ce type de structures polycristallines limite l'emploi des BCPs pour des applications en nano-électronique par exemple, qui requiert un ordonnancement parfait. Une solution a été développée pour résoudre ce problème, utilisant des méthodes dites d'auto-assemblage dirigé (DSA), consistant à former un motif géométrique sur le substrat avec des méthodes lithographiques classiques qui va permettre de contraindre l'auto-assemblage de BCPs pour former un unique grain. Ces motifs peuvent être topographiques ou chimiques, et doivent tenir compte de règles de commensurabilité avec la structure de BCPs.

L'application des BCPs en nanolithographie ne tire parti que de l'aspect géométrique de l'auto-assemblage, alors qu'il existe un autre avantage à cette technique : chaque bloc peut présenter des caractéristiques intéressantes directement liées à leur composition chimique. En effet, il est possible de choisir un bloc possédant des propriétés recherchées (thermiques, optiques, électriques, magnétiques, etc...) ou bien de le modifier sélectivement après auto-assemblage pour le transformer en métal, en oxyde métallique, ou en composite. Ainsi, des structures nanométriques fonctionnalisées peuvent être générées et tirent profit des corrélations entre la composition du BCP et la morphologie auto-assemblée. De plus, ces couches minces fonctionnalisées avec un contrôle à la fois de leur structure mais aussi de leur composition, peuvent être empilées pour produire des structures tridimensionnelles à la demande. Cela pourrait permettre de cibler des architectures complexes inhérentes aux applications visées et de produire des dispositifs fonctionnels à moindre coût.

Ce travail de doctorat a ainsi été consacré à la compréhension et au contrôle des configurations d'auto-assemblage relatives aux empilements de couches de BCPs.

Dans un premier chapitre expérimental, nous nous sommes concentrés sur des (co)polymères contenant des fonctions azobenzènes. Cette fonction peut subir une commutation réversible de sa conformation (cis/trans) par absorption de photons produisant un déplacement de matière à large échelle. Ainsi, un film mince composé d'un (co)polymère contenant ces fonctions peut voir sa topographie modifiée par stimulation lumineuse. L'utilisation de motifs interférentiels produit ainsi des motifs topographiques sinusoïdaux, appelés SRG pour « Surface Relief Grating ». Une première étude s'est intéressée à un système de BCPs dont un des blocs est porteur de telles fonctions azobenzènes. Nous avons démontré qu'une combinaison d'inscription de motifs SRG dans la couche de BCPs et d'auto-assemblage par vapeurs de solvant peut générer des structures parfaitement orientées par rapport aux motifs SRG (*Figures 1.a-c*). Cette approche

permet d'enrichir les méthodologies en ayant recours à un design macromoléculaire précis combinant séparation de phase et photo-stimulation.

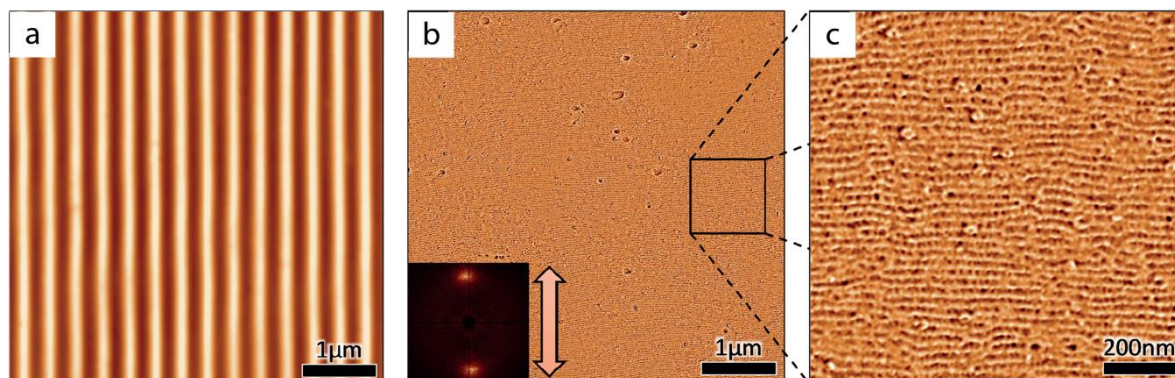


Figure 1. Images obtenues par microscopie à force atomique (a) des vagues produites par SRG dans la couche de BCP (image de topographie), et (b-c) de la structure obtenue après auto-assemblage par recuit de vapeurs de solvant (image de phase) démontrant la formation de cylindres dans le plan orientés perpendiculairement aux motifs SRG. L'insert de la figure (b) est la transformée de Fourier de l'image AFM.

Nous avons également tiré profit de la création de motifs SRG afin de développer plus en avant l'utilisation de ces motifs topographiques pour l'auto-assemblage dirigé (Figure 2). En effet, ces motifs géométriques obtenus par interférence optique peuvent être modifiés plus en avant afin d'augmenter leur rapport d'aspect, pour ensuite être transformés en matériau inorganique par la technique de « sequential infiltration synthesis » (SIS). Cela permet la formation de motifs topographiques en Al_2O_3 . Cette modification a pour objectif d'augmenter la résistance aux solvants et aux fortes températures afin de pouvoir les utiliser pour le guidage de l'auto-assemblage de BCPs.

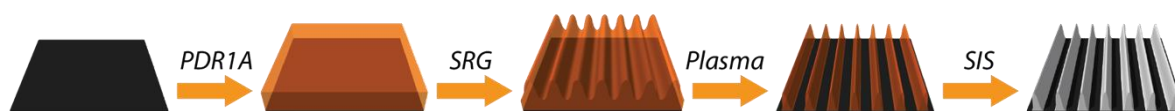


Figure 2. Représentation schématique du protocole pour la formation de motifs inorganiques utilisant un polymère contenant des fonctions azobenzènes. 1) Déposition d'un film de PDR1A ; 2) Formation du motif par interférence optique (SRG) ; 3) Gravure plasma afin d'augmenter le rapport d'aspect ; 4) Transformation du motif en matériau inorganique par SIS.

En modifiant les paramètres du procédé, de nombreuses structures géométriques ont été obtenues, avec entre autres des lignes parallèles (Figure 3.a), une grille carrée (Figure 3.b), une grille rectangulaire (Figure 3.c), un réseau carré de piliers (Figure 3.d), un réseau hexagonal de piliers (Figure 3.e) ou une grille formée de losanges (Figure 3.f)

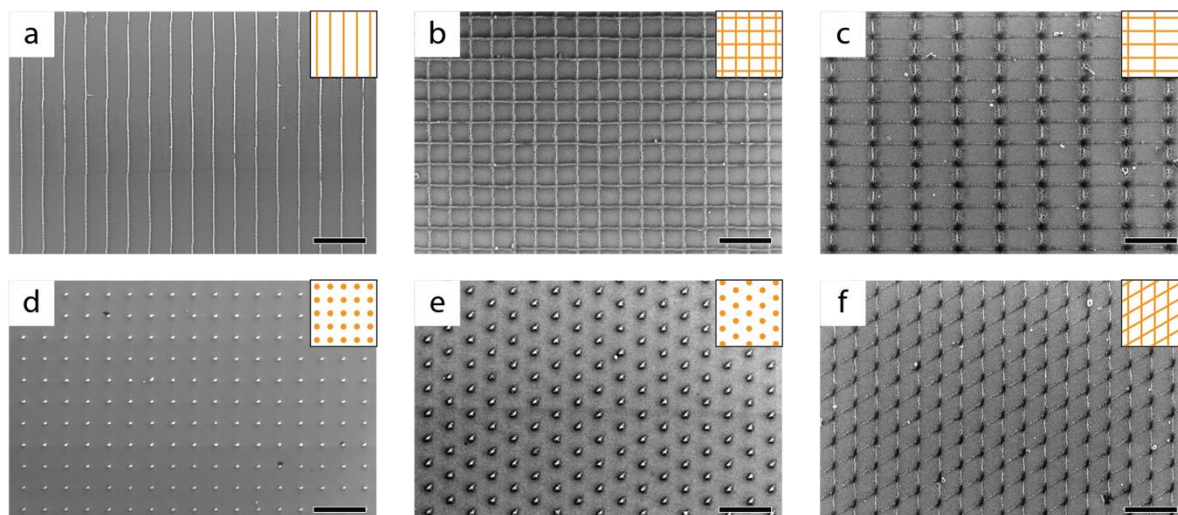


Figure 3. Caractérisation par microscopie électronique à balayage des motifs obtenus en utilisant un film polymère contenant des fonctions azobenzènes après SRG, gravure plasma et modification en alumine. Les barres d'échelle représentent 1 μm .

Ces différents motifs ont ensuite été utilisés avec succès pour diriger l'auto-assemblage de BCPs pour plusieurs types de morphologies et d'orientations, notamment des lamelles perpendiculaires au substrat (Figure 4.a), des cylindres perpendiculaires au substrat (Figure 4.b) ou des cylindres ayant les deux orientations selon leur position (Figure 4.c).

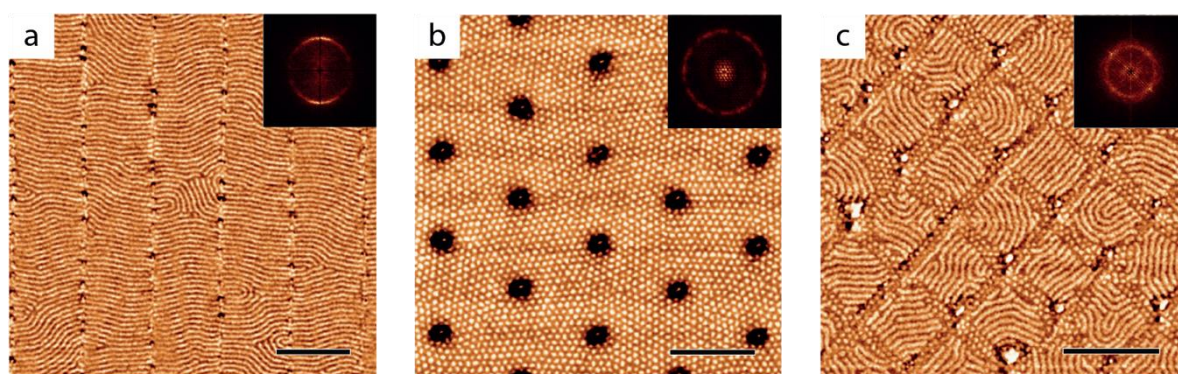


Figure 4. Images de phase obtenues par microscopie à force atomique (a) de lamelles perpendiculaires au substrat dirigées orthogonalement au motif linéaire obtenu par SRG, (b) de cylindres perpendiculaires au substrat formant des grains dépendant du réseau hexagonal de piliers obtenu par SRG, (c) de cylindres parallèles et perpendiculaires au plan en fonction de leurs positions respectives dans la grille carrée obtenue par SRG. Les inserts sont les transformées de Fourier des images. Les barres d'échelle représentent 400 nm.

Ainsi ce procédé permet de réaliser des motifs topographiques dont les dimensions (hauteur, période dans chaque direction) peuvent être finement réglées afin de diriger l'auto-assemblage de BCPs en film mince. De plus, cette méthode est peu coûteuse en comparaison aux techniques plus conventionnelles, et peut facilement être adaptée et optimisée en fonction du BCP, notamment de sa période et de sa morphologie.

Dans le deuxième chapitre expérimental, nous avons exploré le diagramme de phase du polystyrène-*bloc*-poly(méthyl méthacrylate), noté PS-*b*-PMMA (Figure 5), en faisant varier sa

composition, f_{PS} et sa masse molaire en nombre, M_n , afin de modifier la structure auto-assemblée et sa période.

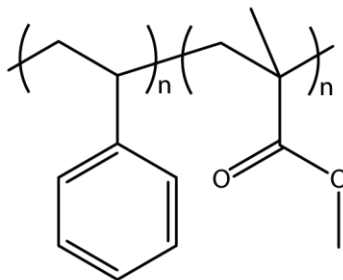


Figure 5. Structure chimique du PS-*b*-PMMA.

Ce BCP est particulièrement intéressant pour la suite de l'étude car son auto-assemblage se réalise simplement et son comportement est très proche des prédictions théoriques. Le procédé d'auto-assemblage est réalisé en deux étapes (Figure 6), avec en premier la modification de l'énergie de surface du substrat, en greffant un copolymère statistique (RCP) de PS et PMMA, dont la composition permet de contrôler l'orientation de la morphologie. Ensuite un film mince de PS-*b*-PMMA est déposé sur le substrat modifié, et est auto-assemblé par recuit thermique, c'est-à-dire en le chauffant à une température donnée (de 200 °C à 280 °C) pendant un temps donné (de 5 min à 15 min).



Figure 6. Représentation schématique du protocole de formation d'une structure auto-assemblée de PS-*b*-PMMA. 1) Modification de la surface du substrat en greffant un RCP ; 2) Déposition d'un film mince de BCP ; 3) Chauffage du film pour promouvoir l'auto-assemblage par déplacement des chaînes polymères.

Ce chapitre a donc consisté en l'optimisation des protocoles expérimentaux permettant l'obtention pour chacune des structures de BCPs un ordre à longue distance important. Plus précisément, cinq structures différentes ont été obtenues, qui sont dans l'ordre croissant de f_{PS} , des sphères de PS, des cylindres de PS, des lamelles, des cylindres de PMMA et des sphères de PMMA. Trois de ces structures ont été retenues pour l'étude sur les empilements du fait du contrôle poussé de leur auto-assemblage : des cylindres de PS (Figure 7.a), des lamelles (Figure 7.b) et des cylindres de PMMA (Figure 7.c).

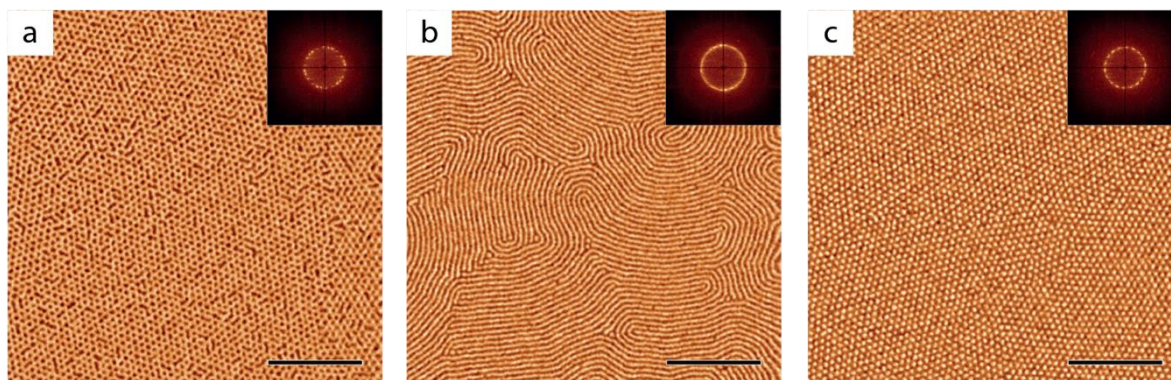


Figure 7. Images de phase obtenues par microscopie à force atomique de PS-*b*-PMMA auto-assemblé perpendiculairement au substrat formant (a) des cylindres de PS, (b) des lamelles et (c) des cylindres de PMMA. Les inserts sont les transformées de Fourier des images. Les barres d'échelle représentent 400 nm.

Ces structures ont été modifiées par infiltration sélective du bloc de PMMA en alumine par SIS, suivi d'une gravure plasma pour enlever partiellement le bloc PS, permettant d'obtenir les répliques inorganiques des structures auto-assemblées (Figure 8) dont les topographies effectives sont contrôlées par la gravure du bloc PS.



Figure 8. Représentation schématique du protocole de la modification d'une structure auto-assemblée pour l'empilement. 1) Infiltration du PMMA avec de l'alumine par SIS ; 2) Gravure du PS par plasma.

Il est ainsi possible de former un réseau de lignes parallèles par des lamelles, noté L pour « line & space », un réseau hexagonal de piliers par des cylindres de PMMA, noté D pour « dot », et un réseau hexagonal de trous par des cylindres de PS, aussi appelé nid d'abeille, noté H pour « hole ». De plus, en utilisant des BCPs ayant la même f_{PS} mais des M_n différentes, ces structures ont pu être déclinées en plusieurs périodes de 24 nm à 64 nm selon les morphologies. La Figure 9 présente les images de microscopie électronique à balayage de toutes les structures 2D obtenues, montrant clairement une diminution de la qualité de l'auto-assemblage pour les plus grandes périodicités (due notamment à la diminution de la mobilité des chaînes polymères).

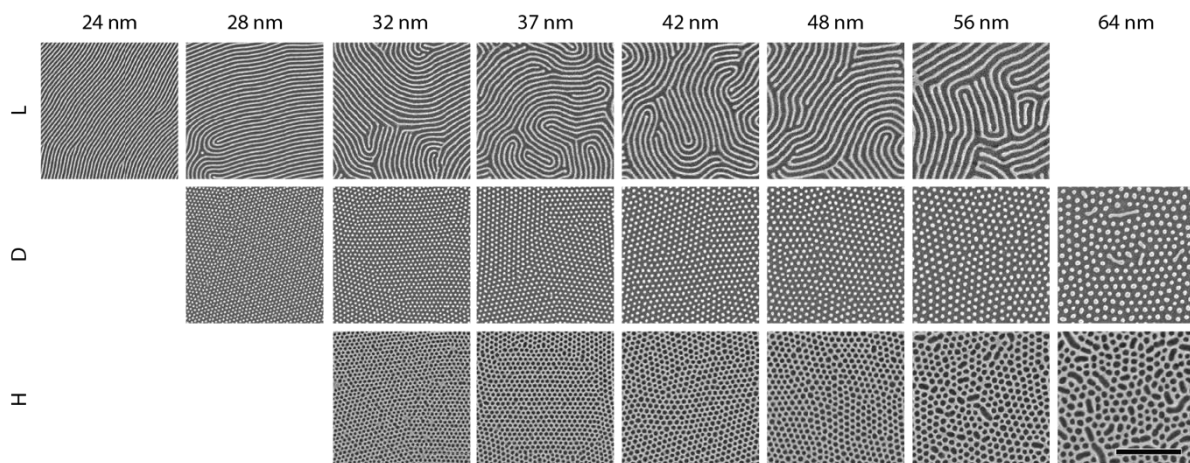


Figure 9. Caractérisation par microscopie électronique à balayage des différentes structures 2D en alumine (L, D et H) dérivées de BCPs de PS-*b*-PMMA auto-assemblés en lamelles, cylindres de PMMA et cylindres de PS, orientés perpendiculairement au substrat. Différentes périodicités sont obtenues par mélange de BCPs de longueurs différentes mais de composition similaire. Les zones sans images représentent les structures non obtenues expérimentalement. La barre d'échelle représente 500 nm.

Le troisième chapitre expérimental se concentre sur l'étude de structures composées de deux couches auto-assemblées. Trois objectifs sont visés : premièrement réussir à obtenir des structures empilées bien définies pour pouvoir être observées et étudiées, ensuite comprendre l'organisation et l'orientation relatives entre les couches, et finalement contrôler ces dernières.

Ainsi, un procédé d'empilement a été développé, comptant trois étapes distinctes (Figure 10) : la préparation de la surface de la première couche, ensuite l'ajout de la seconde couche et finalement la modification de la seconde couche soit pour observer la structure, soit pour préparer la seconde couche pour un nouveau cycle d'empilement.

La première étape est similaire au greffage d'un RCP sur le substrat comme décrit précédemment, à la différence que la surface de la première couche doit être précédemment passivée par un dépôt d'une couche très fine d'alumine (environ 1 nm). Afin de mieux comprendre les mécanismes d'empilement, le RCP utilisé peut être choisi parfaitement neutre, mais aussi légèrement sélectif envers le PS ou le PMMA. La seconde étape est parfaitement similaire au procédé décrit dans le chapitre précédent. Ces deux étapes peuvent être répétées autant de fois que nécessaire. La dernière étape consiste soit à graver entièrement le PS, pour pouvoir observer la structure résultante par microscope électronique à balayage, soit à enlever partiellement le PS pour pouvoir recommencer le cycle. L'étape de gravure est cruciale car elle permet l'étude systématique de l'orientation relative obtenue par l'empilement de deux couches.

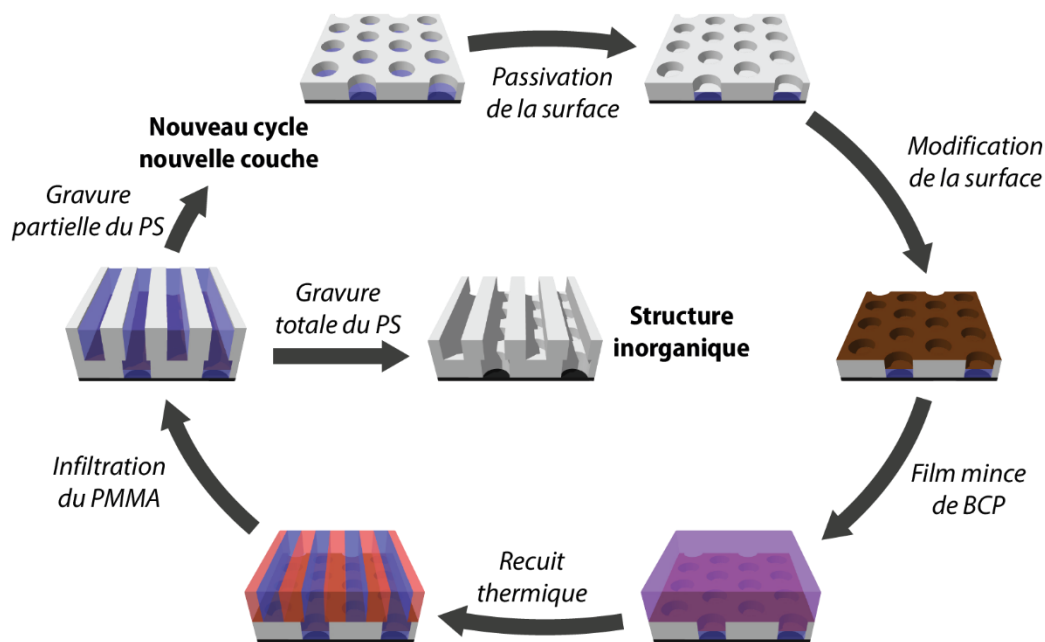


Figure 10. Représentation schématique du protocole de l'empilement de couches 1) Passivation de la surface d'une première couche préparée pour l'empilement ; 2) Modification de la surface de la structure en greffant un RCP ; 3) Déposition d'un film mince de BCP ; 4) Chauffage du film pour promouvoir l'auto-assemblage ; 5) Infiltration du PMMA avec de l'alumine par SIS ; 6) Gravure du PS par plasma soit de façon totale pour obtenir une structure entièrement inorganique, soit partielle pour déposer une nouvelle couche.

Ainsi, une observation systématique des structures bicouches a été réalisée en faisant varier 3 paramètres :

- Le type de structure de chaque couche qui peut être L, D ou H ;
- La période de chaque couche, comprise entre 24 nm et 64 nm ;
- La modification énergétique réalisée entre les deux couches, qui peut être neutre, sélectif envers le PS ou sélectif envers le PMMA.

Cette large étude a permis d'observer l'orientation relative des couches en fonction de ces trois paramètres, et de proposer un mécanisme expliquant les résultats, corroboré par des simulations. Ces résultats peuvent être classés par rapport au type de structure des deux couches empilées, résultant en 6 différentes catégories : D-D, L-L, H-H, L-D, H-D et H-L.

Le cas L-L est celui qui a servi de base pour comprendre le mécanisme d'orientation des structures, avec peu de structures possibles puisque la symétrie est linéaire. Ainsi, pour deux couches de lignes de même période, 3 orientations ont été observées en fonction du RCP utilisé : soit les lignes sont orthogonales (Figure 11.a), soit elles sont colinéaires et superposées (Figure 11.b), soit elles sont colinéaires et en quinconce (Figure 11.c).

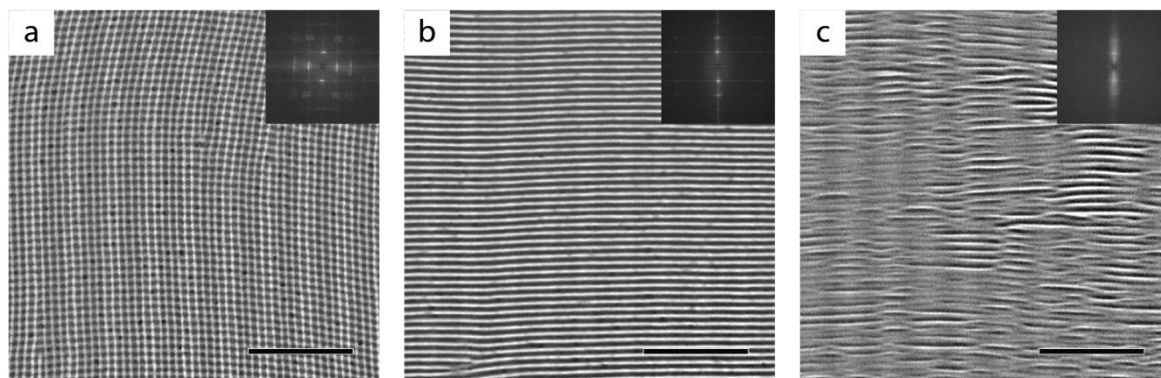


Figure 11 . Caractérisation par microscopie électronique à balayage de la superposition de deux couches formant des lignes de même période avec une interface (a) neutre, (b) sélective au PMMA et (c) sélective au PS. L'insert montre la transformée de Fourier de l'image. Les barres d'échelle représentent 500 nm.

En utilisant un modèle prenant en compte l'énergie de courbure des chaînes polymères et les interactions interfaciales, il est possible de rationaliser ces trois orientations en fonction du RCP :

- Si la surface est neutre, les chaînes polymères seront peu courbées. Ainsi la structure la plus stable est celle où les deux réseaux de lignes sont orthogonaux ;
- Si la surface est sélective envers le PS (PMMA), le bloc préférentiellement placé au-dessus des lignes d'alumine sera le PS (PMMA), afin d'augmenter l'interface affine et donc de diminuer l'énergie totale du système.

La suite de l'étude systématique a permis d'observer de très nombreuses structures qui ne pourraient pas être nativement obtenues avec le PS-*b*-PMMA. Les *Figures 12.a-f* montrent une structure remarquable pour chaque couple de structures possibles, avec les périodes et les modifications d'interfaces adéquates.

En outre, le modèle développé dans ce chapitre permet de prédire toutes les orientations obtenues selon deux règles simples : l'orientation relative entre les couches tend à former la structure finale la plus symétrique possible, c'est-à-dire ayant la maille primitive la plus petite, et dans le cas d'interfaces non neutres, le bloc affine aura tendance à se placer majoritairement au-dessus des structures en alumine, c'est-à-dire au-dessus du bloc de PMMA de la couche précédente.

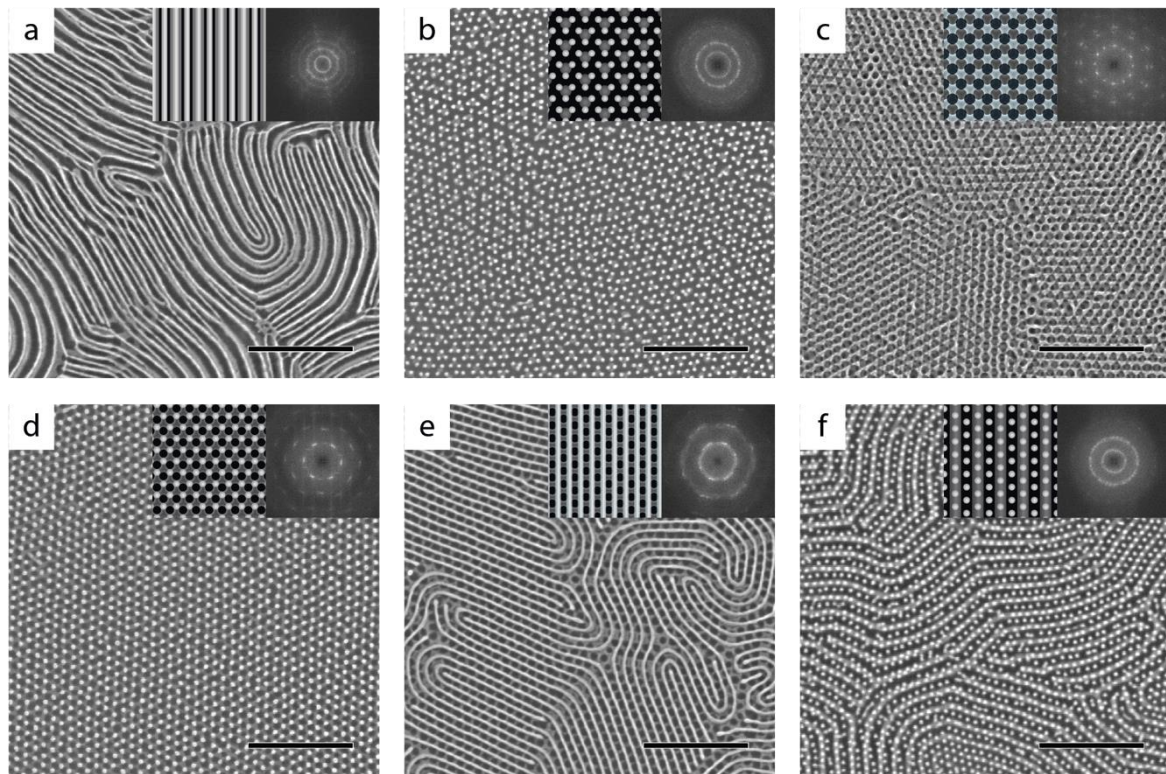


Figure 12. Caractérisation par microscopie électronique à balayage de la superposition de (a) L-L, (b) D-D (c) H-H, (d) H-D, (e) H-L et (f) L-D. Les inserts montrent la structure théorique prédite ainsi que la transformée de Fourier de l'image. Les barres d'échelle représentent 500 nm.

Le quatrième et dernier chapitre de ce manuscrit est une ouverture aux applications possibles de ce procédé d'empilement pour former des structures 3D fonctionnalisées. Ainsi, deux dispositifs ont été imaginés :

- Une nano-grille 3D formée par un empilement répétitif de lignes orthogonales fonctionnalisées en matériel conducteur le tout dans une matrice isolante. Ce type de structure conducteur/isolant pourrait conduire à l'obtention de propriétés plasmoniques intéressantes du fait de sa périodicité plus faible que les longueurs d'onde de la lumière visible ;
- Un réseau hexagonal de colonnes formées de 8 couches de matériau multiferroïque séparés par des électrodes. Cette structure permettrait de stocker 8 informations binaires dans chacune des colonnes, ce qui permettrait de multiplier la capacité de stockage par 8 comparé à un simple réseau hexagonal de piliers obtenue par l'auto-assemblage d'un BCP.

Bien entendu, de nombreux challenges restent à relever pour réussir à produire ces structures, le procédé d'empilement couche par couche du PS-*b*-PMMA n'est que la première brique pour pouvoir imaginer la formation de ces dernières.

LIST OF ABBREVIATIONS

General

AFM.....Atomic Force Microscopy
ALD.....Atomic Layer Deposition
BCB.....Benzocyclobutene
BCC.....Body-Centered Cubic
BCP.....Block Copolymer
BFO.....Bismuth Ferrite Oxide
CSRG.....Cross Surface Relief Gratings
CVD.....Chemical Vapor Deposition
CZA-SS.....Cold Zone Annealing Soft Shear
DEZ.....Diethylzinc
DPD.....Dissipative Particles Dynamics
DSA.....Directed Self-Assembly
FFT.....Fast Fourier Transform
GBSH.....Gentle Beam Super High Resolution
GISAXS.....Grazing Incidence Small Angle X-Rays Scattering
HCP.....Hexagonally Close Packing
ICP.....Inductively Coupled Plasma
MPI.....Multiple Pulsed Infiltration
NP.....Nanoparticle
ODT.....Order Disorder Transition
PGMEA.....Propylene Glycol Methyl Ether Acetate
PPD.....Peak-to-Peak Distance
PSD.....Power Spectral Density
PVD.....Physical Vapor Deposition
RCP.....Random Copolymer
RIE.....Reactive Ion Etching
RTA.....Rapid Thermal Annealing
RTP.....Rapid Thermal Processing
SAM.....Self-Assembled Monolayers
SAXS.....Small Angle X-Rays Scattering
SCFT.....Self-Consistent Field Theory
SEM.....Scanning Electron Microscope
SIS.....Sequential Infiltration Synthesis
SRG.....Surface Relief Gratings
SS-LZA.....Soft Shear Laser Zone Annealing
SVA.....Solvent Vapor Annealing
SVI.....Sequential Vapor Infiltration
TEM.....Transmission Electron Microscope
TFEMA.....Trifluoroethyl Methacrylate
THF.....Tetrahydrofuran
TMA.....Trimethyl Aluminum
TPMS.....Triply-Periodic Minimal Surface
TPS.....tris(tert-pentoxy) silanol
UV.....Ultra Violet

Polymers

azoPMA.....Polymethacrylate containing azobenzene moieties
P2VP.....Poly(2-vinylpyridine)
P2FEMA.....Poly(2-fluoroethylmethacrylate)
P4VP.....Poly(2-vinylpyridine)
PA-6.....Polyamine-6
PAA.....Polyacrylic Acid
PB.....Polybutadiene
PBMA.....Polybutyl Methacrylate
PBT.....Polybutylene Terephthalate
PC.....Polycarbonate
PDLLA.....Poly(D,L-lactide)
PDMS.....Polydimethylsiloxane
PDMSB.....Polydimethyl silacyclobutane
PDR1A.....Poly(disperse red 1 acrylate)
PEMA.....Polyethyl methacrylate
PEO.....Polyethylene oxide
PEP.....Poly(ethylene-alt-propylene)
PET.....Polyethylene terephthalate
PFMS.....Polyferrocenyldimethylsilane
PFS.....Poly(4-fluorostyrene)
PI.....Polyisoprene
PIO.....Polyepoxyisoprene
PMMA.....Polymethyl Methacrylate
PPMA.....Polypropyl Methacrylate
PS.....Polystyrene
PTFEMA.....Polytrifluoroethyl Methacrylate
PTMSS.....Poly(4-trimethylsilylstyrene)
PVA.....Polyvinyl Alcohol
PVP.....Polyvinyl Pyridine

LIST OF SYMBOLS

<i>Symbol</i>	<i>Symbol name</i>	<i>Units</i>
a	Statistical segment length	nm
C	Concentration	mol.L ⁻¹
d or d_{hkl}	Interplanar distance	nm
f or f_i	Volume fraction	-
K	Correlation length	nm
k_B	Boltzmann constant	J.K ⁻¹
\vec{k}_i	Wave vector	nm ⁻¹
L_0	Domain spacing	nm
l_k	Kuhn length	nm
M_n	Number averaged molecular weight	g.mol ⁻¹
N or N_i	Degree of polymerization	-
\mathcal{N}_a	Avogadro number	mol ⁻¹
\vec{q} or q_{hkl}	Scattering vector	nm ⁻¹
R_g	Radius of gyration	nm
t	Film thickness	nm
T	Temperature	°C or K
T_g	Glass transition temperature	°C or K
T_{ODT}	Order disorder transition temperature	°C or K
Z	Number of nearest neighbors	-
γ	Interfacial energy	J.m ⁻²
ΔG_m	Mixing free energy	J
ϵ_{ij}	Interaction energy	J
θ	Angle	°
λ	Wavelength	nm
ρ	Density	g.cm ⁻³
χ_{AB}	Flory-Huggins parameter	-
ω	Rotation speed	rpm

TABLE OF CONTENTS

Remerciements.....	i
Résumé en Français.....	iii
List of Abbreviations.....	xiii
List of Symbols.....	xiv
General Introduction.....	1
Chapter I: State-of-the-art.....	5
I.1/ Block copolymer self-assembly.....	6
I.1.A/ Phase separation.....	7
I.1.B/ Thin film self-assembly of BCPs.....	12
I.1.C/ Directed self-assembly.....	18
I.1.D/ PS- <i>b</i> -PMMA phase diagram.....	22
I.2/ Functionalization and hybridization of BCP thin films.....	26
I.2.A/ Chemical modification.....	26
I.2.B/ Selective swelling of BCP domains.....	27
I.2.C/ Etching processes for the selective removal of a BCP domain.....	28
I.2.D/ Infiltration of a selective BCP domain.....	30
I.2.E/ BCP pattern as template for further oxide or metal addition.....	34
I.3/ Iterative stacking of BCP layers.....	37
I.3.A/ Literature review.....	37
I.3.B/ Discussion.....	49
I.4/ Azobenzene-containing polymers.....	51
I.4.A/ Cis-Trans photoisomerization.....	51
I.4.B/ Surface Relief Gratings.....	51
I.4.C/ BCP self-assembly induced by SRG.....	53
I.5/ Conclusions and Ph.D. objectives.....	56
I.6/ References.....	58
Chapter II: Azobenzene-Containing Polymers.....	75
II.1/ Introduction.....	76
II.2/ Directed Self-Assembly enabled by Surface Relief Gratings.....	77
II.2.A/ Optical alignment of azobenzene containing BCP thin films induced by SRG.....	77
II.2.B/ Discussion.....	89
II.3/ Substrate nanotexturing with SRG.....	90
II.3.A/ Pattern formation via SRG.....	90
II.3.B/ A large diversity of tunable nanostructures.....	96
II.3.C/ “Low cost” graphoepitaxy.....	97
II.4/ Conclusions.....	103
II.5/ References.....	104
Chapter III: A rich variety of 2D-nanostructures obtained by PS-<i>b</i>-PMMA self-assembly	107
III.1/ Introduction.....	108
III.2/ Formation of 2D nanostructures from PS-<i>b</i>-PMMA.....	110

III.2.A/ PS- <i>b</i> -PMMA self-assembly.....	110
III.2.B/ Structure hybridization	121
III.3/ Phase diagram exploration.....	124
III.3.A/ Different morphologies by changing the BCP composition	124
III.3.B/ Tuning the structure periodicities	131
III.4/ Preparation for iterative stacking	136
III.4.A/ Geometrical considerations.....	136
III.4.B/ Resulting 2D-structures	137
III.5/ Conclusions.....	142
III.6/ References	143
Chapter IV: 3D-structures formed by iterative self-assembly of PS-<i>b</i>-PMMA films.....	147
IV.1/ Introduction	148
IV.2/ General process for the formation of stacked nanostructures from BCP films ...	150
IV.2.A/ Formation of an immobilized BCP layer.....	150
IV.2.B/ Surface energy modification of the immobilized BCP layer via RCP grafting	150
IV.2.C/ Deposition of the 2 nd BCP layer and immobilization of the stacked structure.....	151
IV.2.D/ Structural characterization of the stacked BCP layers	152
IV.2.D/ The concept of responsive layering.....	153
IV.3/ Stacking of two layers with lamellar symmetry (L-L).....	155
IV.3.A/ Stacked structures formed from lamellar PS- <i>b</i> -PMMA BCPs with the same periodicity	155
IV.3.B/ Rationalization of the mechanisms involved in the “responsive layering”	161
IV.3.C/ Stacking of two lamellar BCP layers with different periodicities	168
IV.4/ Hierarchical nanostructures by stacking two layers with a hexagonal symmetry	173
IV.4.A/ Expected configurations between the two stacked hexagonal patterns	173
IV.4.B/ Stacking of two dot patterns (D-D).....	175
IV.4.C/ Stacking of two hole patterns (H-H).....	181
IV.4.D/ Stacking of a dot pattern on top of hole pattern (H-D)	185
IV.5/ Stacking of two layers with different symmetry	188
IV.5.A/ Expected configurations between two stacked patterns of different symmetry.....	188
IV.5.B/ Stacking of a dot pattern on top of a line & space pattern (L-D).....	190
IV.5.C/ Stacking of a line & space pattern on top of a hole pattern (H-L).....	194
IV.6/ Conclusions.....	197
IV.7/ References.....	198
Chapter V: outlook for BCP iterative self-assembly	201
V.1/ Introduction.....	202
V.2/ Beyond the stacking of two layers	203
V.3/ Optically active structures from BCP self-assembly	205
V.3.A/ Bibliographical study	205
V.3.B/ Tailored 3D-nanogrid targeting optics	209
V.3.C/ Experimental challenges.....	210
V.4/ Electronic devices from BCP self-assembly.....	212
V.4.A/ Bibliographical study	212
V.4.B/ 3D-nanopillars memory device.....	214
V.4.C/ Experimental challenges.....	215
V.5/ Conclusions	218

V.6/ References	219
General conclusions	225
Annex.....	229
1/ Thin film process.....	230
1.A/ Self-assembly.....	230
1.B/ Hybridization.....	231
2/ Thin film characterization.....	235
2.A/ Atomic Force Microscopy (AFM)	235
2.B/ Scanning Electron Microscopy (SEM)	236
2.C/ Grazing Incidence Small Angle X-ray Scattering (GISAXS).....	237
3/ Matlab programs & simulations.....	239
3.A/ Plasma etching waves simulation.....	239
3.B/ Hexagonally packed dots image analysis.....	241
3.C/ Di-block copolymers theoretical pitch and phase diagram position calculation.....	243
3.D/ SAXS intensity plot fitting to determine χ parameter	244
3.E/ Triply-Periodic Minimal Surface 3D modelling and 2D-slicing.....	256
3.F/ Lamellae stacking orientation	266
3.G/ NanoScope AFM image viewer and processing	271
4/ 2D-structures large SEM images	276
5/ References.....	289

GENERAL INTRODUCTION

Invisible to the eyes and yet surrounding us, nanoscience has become a major research field in the past decades and has driven many potent technological advances. By definition, an object is considered as a nanomaterial if at least one of its dimensions is lower than 100 nm. Such structural characteristic leads to unique physical and chemical properties due to quantum and/or surface effects, which are used in diverse scientific fields such as catalyst, optics, magnetic, electric or biology.

Nanomaterials require very precise manufacturing processes, and Nature excels at the generation of exquisite nanostructures such as the ones found in butterfly wings or lotus leaves. Nanomaterials are also produced artificially by using for instance nanolithography or nanoparticle synthesis. Another concept of interest for the formation of nanostructured materials is related to the thermodynamical processes found in Soft Matter which can yield to the formation of a panoply of morphologies. Among the Soft Matter processes, block copolymers (BCPs) self-assembly enables nanostructuring while taking profit on the physical-chemical properties of polymers. Indeed, these materials hold the property to self-assemble into different periodic structures (in one, two or three dimensions), with a periodicity that can vary from few nanometers to hundreds of nanometers. This self-assembly process is related to microphase separation due to chemical incompatibility which arises from the block copolymer structure: two or more different polymeric chains linked together by a covalent bond. Thus, BCPs based nanomaterials are artificial materials taking advantage of a thermodynamic process to generate nanomaterials, i.e. a statistical process that naturally occurs in order to reduce the overall energy of the system.

Over the past decades, innovative polymerization methods have been developed to generate on-demand BCPs with the adequate architecture in order to produce a targeted nanostructure. This was also consolidated with the development of the self-consistent field theory (SCFT), which permitted to understand and predict the BCP behavior for simple architectures. With such foundation spanning from macromolecular engineering to thermodynamics, it is not surprising that many researches focused on methods to transpose these periodical nanostructures in nanotechnologies.

As today, one of the main applications of this technology is the nano-manufacturing of masks for lithography, as BCP self-assembly produces very small features at a low budget. However, this application restricts the BCP self-assembly to the formation of patterns in thin film,

subsequently used to transfer the features in a substrate of interest. A more ambitious paradigm would be to functionalize these nanostructures into practical devices. Unfortunately, only a scarce number of devices based on BCP manufacturing is yet described in literature, due to the difficulty to produce complex and precise technological architectures that are required for cutting-edge nanotechnologies.

This Ph.D. is dedicated to the understanding and the control of the formation of complex functional nanostructures using an iterative layering approach of self-assembled BCP thin films. Such an exploration was performed using the polystyrene-*block*-polymethyl methacrylate (PS-*b*-PMMA) system, for which an in-depth understanding of the self-assembly behavior in thin films has been reported over the past ten years. The manuscript is organized as follow:

The first chapter is a description of the general context of the study. A first part is dedicated to the BCP self-assembly theory and experimental processes, with a strong focus on PS-*b*-PMMA. Then a second part referenced most of the methods to functionalize BCP nanostructures, and is followed by a literature survey on the different stacking methods in order to produce layered structures. Finally, a last part is related to azobenzene-containing (co)polymers and the opportunities inherent to their use in nano-manufacturing.

The second chapter is a two-fold study on the use of azobenzene-containing (co)polymers to direct BCP self-assembly. In a first study, the interplay between the azobenzene photo-stimulation and BCP self-assembly is reported for a BCP engineered with a block containing azobenzene moieties. The second part dealt with the development of a reliable method to perform substrate texturing of an azobenzene-containing polymer thin film with interferential light patterns.

The third chapter presents a large study of PS-*b*-PMMA self-assembly with the description of the nanostructures achievable in thin film geometry, i.e. for a film thickness around few tens of nanometers. The experimental phase diagram was explored, leading to a panoply of high-quality nanostructured patterns obtained from BCP self-assembly with periodicities varying from around 20 nm to 60 nm. Also, a hybridization process, immobilizing the BCP pattern, was developed to allow the subsequent thin film layering.

The fourth chapter is the systematic study of the layering of two BCP thin films in order to understand the registration mechanisms of the two layers. Interestingly, a methodology to control the registration behavior is proposed and rationalized by energetical considerations as well as by simulations. Several configurations obtained through this stacking method are novel structures and thus widen the versatility of BCP self-assembly for nano-manufacturing. Furthermore, the

developed stacking process is shown to be compatible for the stacking of more than two layers, which further opens avenues for the production of complex 3D layered nanostructures.

The last chapter of the Ph.D., which can be also considered as a “conclusion and perspectives” part, is devoted to the application of the iterative process for the generation of functional devices. In particular, the design of two prospective device architectures is proposed, and the methodologies and challenges related to the fabrication of such structures are discussed.

Finally, an annex with the description of the techniques used in this study, the Matlab programs and functions developed during the Ph.D., and several large SEM images of the nanostructures is provided at the end of the manuscript.

CHAPTER I: STATE-OF-THE-ART

I.1/ Block copolymer self-assembly.....	6
I.1.A/ Phase separation.....	7
I.1.B/ Thin film self-assembly of BCPs.....	12
I.1.C/ Directed self-assembly.....	18
I.1.D/ PS- <i>b</i> -PMMA phase diagram.....	22
I.2/ Functionalization and hybridization of BCP thin films	26
I.2.A/ Chemical modification.....	26
I.2.B/ Selective swelling of BCP domains.....	27
I.2.C/ Etching processes for the selective removal of a BCP domain	28
I.2.D/ Infiltration of a selective BCP domain	30
I.2.E/ BCP pattern as template for further oxide or metal addition	34
I.3/ Iterative stacking of BCP layers	37
I.3.A/ Literature review	37
I.3.B/ Discussion	49
I.4/ Azobenzene-containing polymers.....	51
I.4.A/ Cis-Trans photoisomerization.....	51
I.4.B/ Surface Relief Gratings	51
I.4.C/ BCP self-assembly induced by SRG.....	53
I.5/ Conclusions and Ph.D. objectives	56
I.6/ References.....	58

In this first chapter, the general context of this Ph.D. thesis is described by highlighting the recent advances in nano-manufacturing using polymer materials. After a theoretical background on block copolymer (BCP) self-assembly and directed self-assembly (DSA) methods, an exhaustive survey of the studies on the polystyrene-*block*-poly(methyl methacrylate) (PS-*b*-PMMA) BCP system is conducted. Indeed, this particular BCP system is the workhorse for the formation of nanostructures via BCP self-assembly due to the fine control of the associated synthetic and self-assembly procedures. Besides, PS-*b*-PMMA nanostructures can further yield to functional arrangements of features as it is possible to selectively hybridize one of the BCP domains by various techniques. This is of particular interest for applications, as functional properties can arise from both the spatial arrangement and the constitutive material composition. Thus, the functionalization processes to selectively hybridize self-assembled BCP thin films is reviewed with a highlight on processes compatible with PS-*b*-PMMA. Then, the four different approaches referenced in literature to achieve iterative stacking will be described with an emphasis on the advantages and bottlenecks of each methodology. Finally, a quick review on azobenzene-containing polymers is presented as they allow combining stimuli-responsive materials to BCP self-assembly.

I.1/ Block copolymer self-assembly

Block copolymers (BCPs) are macromolecules formed from two or more chemically different polymer chains linked by covalent bonds. *Figure 13* shows different macromolecular architectures that can be synthetically obtained by varying the number of blocks - diblock, triblock or more - and their connectivity - linear, star-shaped, branched among others. The chemical difference between each block can induce a phase separation process leading to the formation of segregated domains. Nonetheless, the covalent bond between the chemically distinct chains prevents a macroscopic phase separation. Accordingly, the phase separation is limited to a length scale comparable to the radius of gyration of the polymer chain and leads to geometrically remarkable periodic structures with features on the nanometer length scale [1], [2].

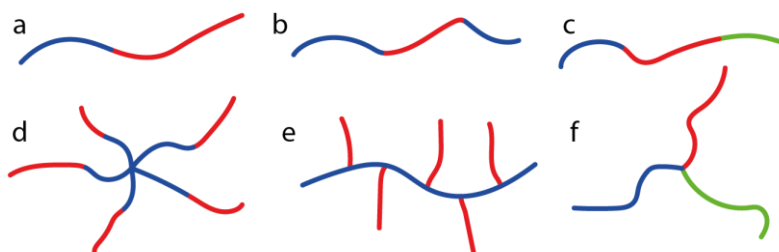


Figure 13. Schematic representations of different architectures of BCPs: (a) linear AB diblock, (b) linear ABA triblock, (c) linear ABC triblock, (d) star-shaped AB diblock (e) branched AB diblock and (f) star-shaped ABC triblock.

One specific use of such microphase separation process is linked to the formation of nanostructured thin films which can be further used for nanofabrication purposes, such as lithographic masks, photonic crystals, surface coatings, membranes, etc. [3], [4]. To obtain these nanostructured thin films, multiple processing steps are required and a panoply of parameters needs to be controlled in order to promote the formation of well-defined BCP structures as shown in *Figure 14*.

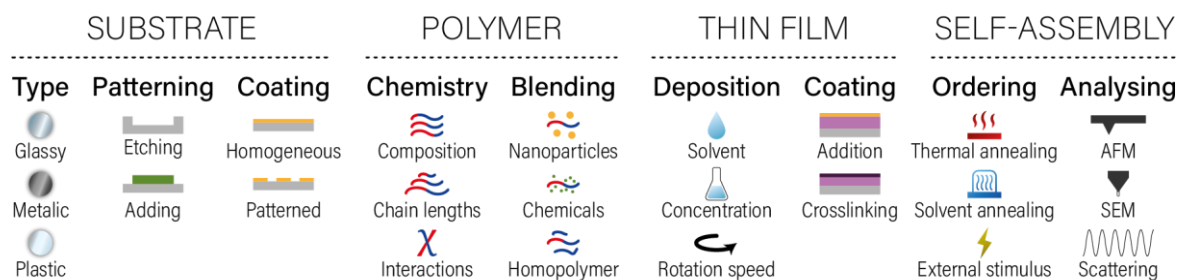


Figure 14. Summary of parameters affecting the formation of a self-assembled BCP structure, from the substrate type and modification, BCP type and blending, thin film and self-assembly processing.

I.1.A/ Phase separation

I.1.A.i/ Driving force for microphase separation

In 1942, a lattice model was developed separately by Flory [5] and Huggins [6], [7] to describe a simple binary mixture of two different polymers, here labelled A and B. In this model, segregation occurs when the mixing free energy (ΔG_m) becomes unfavorable, which can be rewritten using thermodynamic principles and Stirling's approximation as *Equation (1)* where f_A and f_B are the volume fractions of A and B, N_A and N_B the polymerization indexes of A and B, k_B the Boltzmann constant, T the absolute temperature, and χ_{AB} the so-called Flory-Huggins parameter.

$$\frac{\Delta G_m}{k_B T} = \frac{f_A}{N_A} \ln(f_A) + \frac{f_B}{N_B} \ln(f_B) + \chi_{AB} f_A f_B \quad (1)$$

The Flory-Huggins parameter quantifies the degree of incompatibility between the A and B segments, and is expressed as *Equation (2)* where Z is the number of nearest neighbor monomers for a lattice site, and ε_{ij} are the interaction energies between i and j monomers.

$$\chi_{AB} = \frac{Z}{k_B T} \times \left(\varepsilon_{AB} - \frac{\varepsilon_{AA} + \varepsilon_{BB}}{2} \right) \quad (2)$$

Experimentally, it has been noticed that the variation of χ_{AB} with respect to the temperature is more complex than *Equation (2)* [8], and the parameter is usually modeled as *Equation (3)* where α and β are empiric parameters for entropy and enthalpy contributions, respectively.

$$\chi_{AB} = \chi_H + \chi_S = \alpha + \frac{\beta}{T} \quad (3)$$

I.1.A.ii/ Phase diagram: experiments versus theory

The Flory-Huggins model, developed for homopolymer mixture, is not suitable to predict BCP microphase separation because of the covalent bond between each block. In 1980, Leibler [9] investigated the order-disorder transition (ODT) of AB diblock copolymers containing N repeating units in the weak segregation limit using a Landau expansion of the free energy to the fourth order, giving microscopic expressions for the coefficients as functions of two key parameters: an incompatibility parameter expressed as the product χN , and the BCP volume fraction f . With this model, for a symmetric di-BCP architecture, i.e. perfectly symmetrical and monodisperse distribution of chain lengths, the ODT is predicted for $\chi N \cong 10.5$, with ordered phases above this value and disordered phases below. *Figure 15.a* shows Leibler's theoretical phase diagram, which predicts three stable nanostructures according to the BCP composition: lamellae, hexagonally

packed cylinders or body-centered cubic spheres, for which the respective unit cells are represented in *Figure 15.e*.

A decade later, using self-consistent field theory (SCFT), Matsen [10], [11] predicted a more consistent phase diagram, also valid for higher χN values (*Figure 15.b*). It enlightens a stable gyroid phase (*Figure 15.e*) between cylinders and lamellae, that have been experimentally observed [12]–[15] and proven to be stable [16]. Later, they generalized their approach for asymmetric copolymers (i.e. with blocks composed of repeating units having different statistical segment lengths, a) leading to a distortion of the phase diagram [17], [18] (*Figure 15.c*). Indeed, by increasing a_A/a_B ratio, it is easier to stretch the A block than the B block, resulting in an extended curvature of the domain interface towards the A domains.

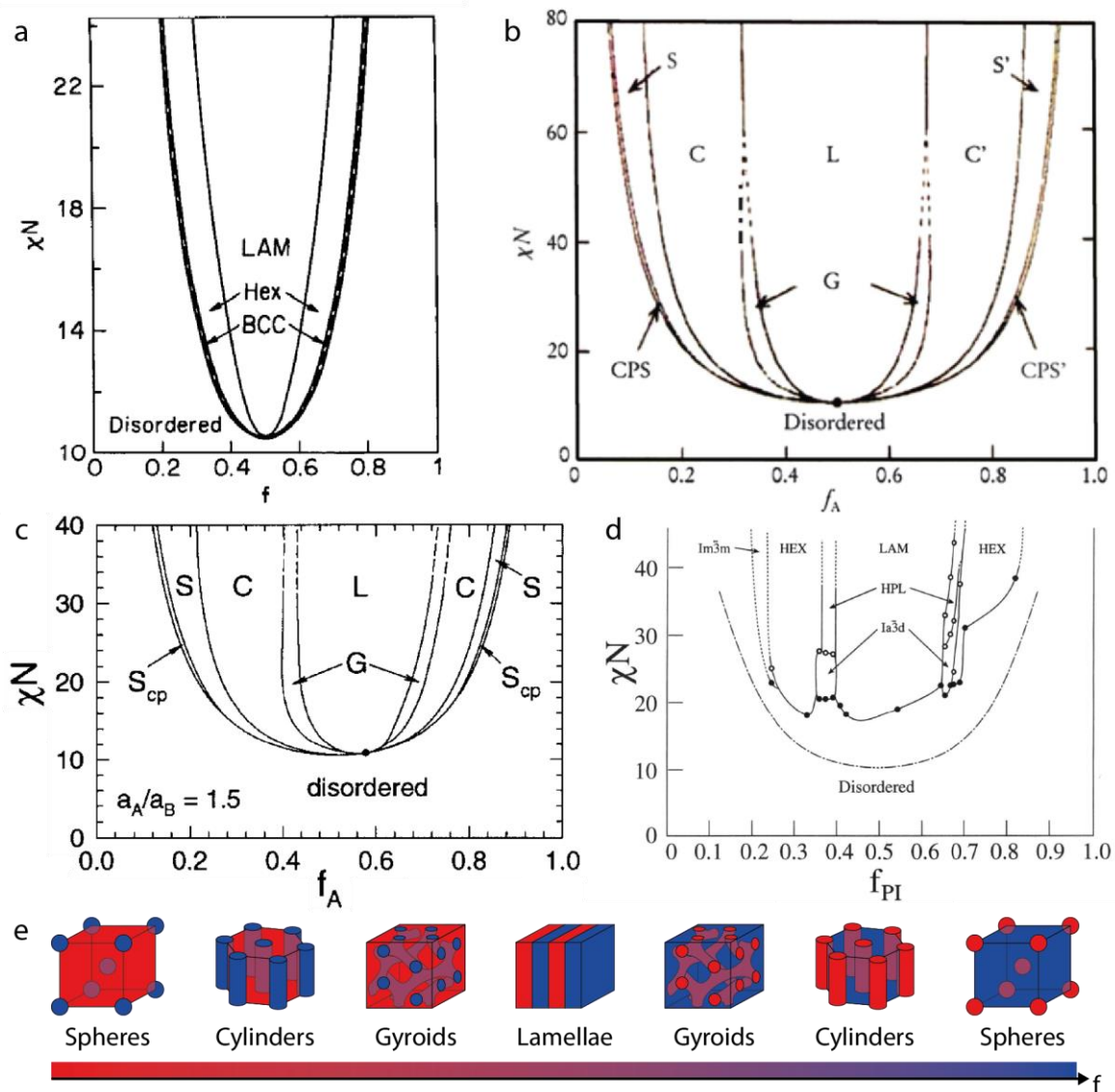


Figure 15. Theoretical phase diagrams for (a) diblock copolymers obtained from a Landau expansion of the free energy [19], (b) diblock copolymers obtained from SCFT [11] and (c) diblock copolymers with conformational asymmetry obtained from SCFT [18]. (d) Experimental phase diagram obtained for the PS-b-PI system [20]. (e) Diblock copolymer stable morphologies according to the composition.

Further theoretical developments were proposed in 1987 by Fredrickson and Helfand with the investigation of the effect of composition fluctuations close to the ODT. These effects are not taken into account by the SCFT theory even if they greatly impact self-assembly for BCPs of low degree of polymerization. Indeed, they predicted, and experimentally observed an ODT for symmetrical BCPs at $\chi N \cong 10.5 + 41N^{-1/3}$ [19], [21]. Very recently, the Morse group revisited the effect of composition fluctuations and found out that a third term appears, leading to an even higher ODT for short BCPs: $\chi N \cong 10.5 + 41N^{-1/3} + 123N^{-0.56}$ [22].

Experimental phase diagrams have been reported for some BCP systems [20], [23], [24]. For instance, Khandpur *et al.* explored the polystyrene-*b*-polyisoprene (PS-*b*-PI) phase diagram (*Figure 15.d*) using ten different compositions near the phase separation threshold, modifying χ_{AB} by changing the temperature. They showed that predictions from simulations are in agreement with their experimental results with two notable differences: a higher experimental ODT and a perforated lamellae structure which have been proven to be a long-lived metastable precursor to the gyroid structure [25]. It highlights that theoretical phase diagrams are often derived from ideal cases (mean-field approximation of interactions, symmetric conformational characteristics of both blocks), which do not take in account every parameter, such as dispersity, sample thermal history, end-chains, among others.

Obviously, with the increase of the BCP structure complexity (such as triblock or non-linear copolymers), a panoply of morphologies are accessible, with for instance “three-color” lamellae, core-shell cylinders or spheres in lamellae [26].

I.1.A.iii/ Domain spacing of BCP structures

In a given nanostructured phase, one key value is the domain spacing, named here L_0 , which quantifies the typical periodicity of the segregated structure. In the strong segregation limit, i.e. for high $\chi_{AB}N$, the periodicity of the lamellar, cylindrical and spherical phases can be predicted from the characteristics of the BCP system, i.e. f , χ , N and a the averaged statistical segment length of each blocks [18]. These general equations are not presented here, but for perfectly symmetric block copolymer, i.e. $f_A = f_B = 0.5$ and $a_A = a_B = a$, the results of this treatment can be simplified, and the domain spacing of a lamellar phase can be written as *Equation (4)*.

$$L_0 \approx 1.1aN^{\frac{2}{3}}\chi^{\frac{1}{6}} \quad (4)$$

Experimentally, one of the main interests of BCP self-assembly in nanofabrication is the definition of extremely small objects formed from one of the BCP domains. The related dimension, which is called the pitch, is $L_0/2$ for a lamellar phase. Thus, an important part of recent studies on BCPs focused on the generation of these small features. Using *Equation (4)* and respecting $\chi N \geq$

10.5 in order to drive phase separation, smaller domain spacing can be obtained for a high value of χ and a small value of N , as recently demonstrated by several groups with the formation of sub-10 nm features using BCP self-assembly [27].

In the bulk regime, Small Angle X-ray Scattering (SAXS) enables the structural characterization of self-assembled BCP morphologies. With the small X-ray wavelengths, from 0.1 to 10 nm, it is possible to monitor interactions of atomic electron clouds, by looking at the X-ray beam scattering due to electron density fluctuations (as light would scatter with refractive index fluctuations). For this purpose, let's consider an incident wave vector \vec{k}_i with a $2\pi/\lambda$ magnitude, and a λ wavelength. This incident wave vector will be scattered by electron density gap, which occurs at BCP interfaces, into a scattered wave vector, denoted \vec{k}_s , at a θ angle, as depicted in

Figure 16.

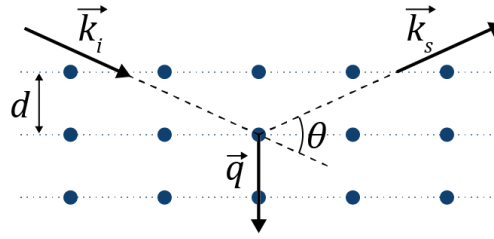


Figure 16. Schematic of an elastic scattering event. \vec{k}_i and \vec{k}_s represent incident and scattered wave vectors, θ the scattering angle and q the scattering vector. Blue dots represent scattering objects (which are domain interfaces for BCPs). d represent interplanar spacing distance between these objects.

In the case of an elastic scattering event, \vec{k}_i and \vec{k}_s are of equal magnitudes, and the scattering vector, defined as $\vec{q} = \vec{k}_i - \vec{k}_s$, which represents the amount of momentum that have to be transferred into the medium along the direction of \vec{q} . By trigonometry, it is possible to calculate the magnitude of \vec{q} , given by Equation (5).

$$|\vec{q}| = q = \frac{4\pi}{\lambda} \sin\left(\frac{\theta}{2}\right) \quad (5)$$

In the case of BCPs in bulk, the scattering objects are the domain interfaces linked to the overall self-assembled structure. This periodically ordered structure possesses scattering plans yielding to the superimposition of scattering waves. Then, a unique diffraction pattern is created, which is directly linked to the arrangement of the domain interfaces. Geometrically, this constructive superposition occurs when the Bragg's law (Equation (6)) is respected, with n an integer and d the interplanar spacing between parallel plans.

$$n\lambda = 2d \sin\left(\frac{\theta}{2}\right) \quad (6)$$

Thus, by combining *Equations (5) and (6)* and rewriting d using Miller indices h , k and l (defined according to the periodic rules of the unit cell), it is possible to relate the scattered peak positions to the structural periodicity of the studied object by *Equation (7)*.

$$q_{hkl} = \frac{2\pi}{d_{hkl}} \quad (7)$$

Consequently, it is possible to analyze the SAXS spectra of BCP self-assembled structures to precisely determine the morphology: the four standard morphologies of di-BCPs – lamellae, cylinders, gyroids and spheres – have precise peak position sequences. It is also possible to evaluate the domains spacing, L_0 , from the first scattered peak which represents the smallest periodicity of the structure. All these information are summarized in *Table 1* [25].

Morphology	Space group	q_{hkl}	L_0	q/q^*
Lamellae	$\bar{1}$	$\frac{2\pi}{d} h$	$2\pi \frac{1}{q^*}$	1, 2, 3, 4, 5, 6 ...
Cylinders	$P6mm (2D)$	$\frac{2\pi}{d} \sqrt{h^2 + k^2 + hk}$	$\frac{4\pi}{\sqrt{3}} \frac{1}{q^*}$	$1, \sqrt{3}, \sqrt{4}, \sqrt{7}, \sqrt{9}, \sqrt{12} \dots$
Gyroid	$Ia\bar{3}d$	$\frac{2\pi}{d} \sqrt{h^2 + k^2 + l^2}$	$2\pi\sqrt{6} \frac{1}{q^*}$	$\sqrt{6}, \sqrt{8}, \sqrt{14}, \sqrt{16}, \sqrt{20} \dots$
Spheres	$Im\bar{3}m$	$\frac{2\pi}{d} \sqrt{h^2 + k^2 + l^2}$	$\pi\sqrt{6} \frac{1}{q^*}$	$1, \sqrt{2}, \sqrt{3}, \sqrt{4}, \sqrt{5}, \sqrt{6} \dots$

Table 1. Domains spacing and sequence of peak positions for the different BCP morphologies.

It is also possible to determine the domain spacing by direct measurement from any imaging technique that has a suitable resolution, such as Atomic Force Microscope (AFM), Scanning Electron Microscope (SEM) or Transmission Electron Microscope (TEM). With AFM and SEM, only the surface of the sample is probed, while TEM requires to cut the sample in thin slices in order to visualize by transmission the morphological features. In any case, the sample processing and history have an impact of each type of measurements and slightly different results can be obtained depending of the type of characterization.

I.1.A.iv/ Determination of the Flory-Huggins parameter

Ultimately, to understand and predict BCP phase behavior in term of self-assembly, it is crucial to estimate the χ_{AB} value, and several methods have been developed to estimate the enthalpic and entropic parameters from *Equation (3)*. It is noteworthy that the values reported in the literature for a particular system are highly dependent from the methodology used to estimate the χ_{AB} value, inherently to uncertainties from experimental data [28].

A first technique consists in measuring the complex viscosity or dynamic moduli in function of the temperature for BCPs with different N (keeping the composition constant) to determine the order-disorder transition temperature (T_{ODT}) between the ordered and disordered

phases [29], [30], and then estimate χ using the mean-field theory (i.e. at the T_{ODT} $\chi N \cong 10.5$ for a symmetric di-BCP). A second method consists to estimate χ from *Equation (4)* by measuring domain spacing for BCPs of different degree of polymerization (keeping the composition constant) with direct imaging or scattering techniques [31].

Another method is the SAXS analysis of BCP melt in the disordered state at different temperatures while still presenting some fluctuations of density. Leibler [9] and Sakurai [32] demonstrated that the scattering peak intensity of such state is linked to χ , and can be precisely fitted from the macromolecular parameters of the studied BCP [33]. This method leads to a more accurate estimation of χ since it takes in account the macromolecular properties of the BCP, such as molecular weight, density and dispersity of each block. This method is the most commonly used for di-BCP.

A last method, called the critical molecular weight method, consists in finding the threshold of miscibility of a blend of two homopolymers, and then using the Flory Huggins theory and the binary interaction model, to estimate χ [34]. This method is not widely used because of its imprecision.

I.1.B/ Thin film self-assembly of BCPs

In the thin film regime – for thicknesses below ≈ 100 nm – BCP chains exhibit different behaviors than in the bulk regime due to the importance of interfacial fields. The resulting morphologies can thus be tuned by the processing parameters, such as film thickness, substrate energy, atmosphere composition, or film annealing.

I.1.B.i/ Thickness of the BCP layer

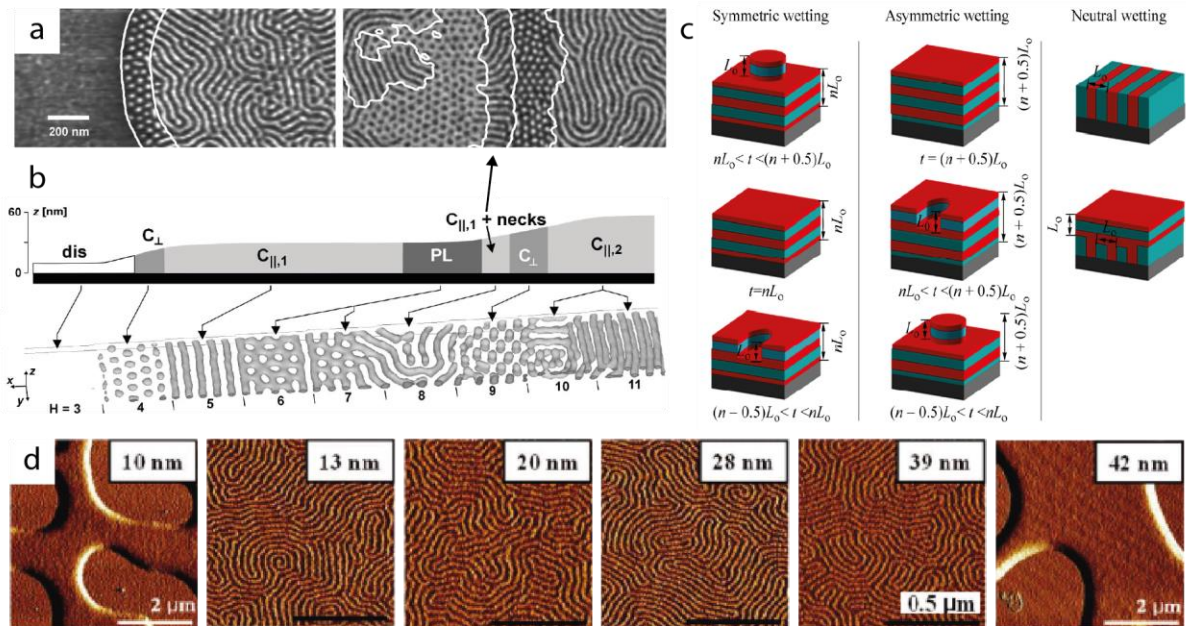
In contrast to bulk, a thin film configuration creates a chain confinement for which thickness is a crucial parameter leading to several morphologies and/or orientations for the same BCP system [35]–[38]. To understand the impact of thickness on self-assembly, the key parameter is the ratio between thickness, denoted t here, and domain spacing, denoted L_0 here, called the commensurability ratio.

For instance, Knoll *et al.* showed that out-of-plane cylinders, in-plane monolayer or bilayer of cylinders and perforated lamellae can be obtained using the same polystyrene-*b*-polybutadiene (PS-*b*-PB) sample for different film thicknesses (*Figures 17.a-b*) [35]. Using simulations, they further demonstrated that the commensurability ratio dictates the resulting self-assembled structure. For instance, it requires $t = 0.75L_0$ to place one layer of unconstrained laying cylinders, and $t = 1.5L_0$ for two layers (here L_0 represents the cylinder-to-cylinder distance).

For lamellae, the behavior is slightly different because the structure adapts differently to the modification of film thickness through the formation of terraces, often called “islands and holes”, in order to overcome chain stretching. *Figure 17.c* shows several theoretical rules that have been erected to predict the formation of terraces in function of the thickness and the wetting behavior at interfaces (see *I.1.B.ii/*):

- For symmetrical wetting, i.e. the same block wets the substrate and the air, terraces are observed if $t \neq nL_0$.
- For asymmetrical wetting, i.e. a block wets the substrate and the other the air, terraces are observed if $t \neq (n + 0.5)L_0$.
- For neutral wetting, i.e. both blocks wet the substrate, an out-of-plane orientation of the lamellae is the most energetically stable if both blocks are neutral toward air, and mixed structures are obtained if one block preferentially wets the air interface.

Interestingly, Ham *et al.* showed for the neutral wetting case that the formation of terraces for PS-*b*-PMMA lamellae can be obtained for very low thickness, i.e. $t < 1.5L_0$, or when the thickness is perfectly incommensurate, i.e. $t = (n + 0.5)L_0$ (*Figure 17.d*) [39], [40]. More recently, Kim *et al.* also enlightened the formation of more exotic half terraces, when only one interface is neutral (as for the mixed structure case described before) with $t = (n \pm 0.25)L_0$ [37].



*Figure 17. (a) SEM pictures of a PS-*b*-PB self-assembly (cylindrical in bulk) with different morphologies and orientations depending on the film thickness as shown in (b) with the schematic height profile and 3D structures obtained by simulation showing a perfect correlation with the experiments [35]. (c) Rules for the formation of terraces according to the wetting behavior and thickness of lamellar BCP films [38]. (d) AFM phase images of PS-*b*-PMMA lamellae with a 29 nm domain spacing for different thicknesses after thermal annealing [39].*

The most common method to deposit a BCP thin film is by spin coating, which consists of spinning a droplet of a BCP solution at a certain concentration C into a solvent with a rotation speed ω until complete evaporation of the solvent. Several models have been developed to predict the thickness of the deposited film [41], [42], which vary with C , ω , but also temperature, solvent viscosity, density, evaporation rate, etc. Nonetheless, for a given solvent at a given temperature, the thickness t can be approached by *Equation (8)* where α is a constant depending on the solvent and atmospheric parameters.

$$t = \alpha \frac{C}{\sqrt{\omega}} \quad (8)$$

In a controlled environment, it is thus simple to control the film thickness by changing the concentration of the BCP solution or the rotation speed. This aspect leads to a fine control of the commensurability ratio between the film thickness and the domain spacing of the BCP structure.

I.1.B.ii/ Surface energy

In the thin film regime, the two boundary interfaces, i.e. substrate-film and film-air, are creating constraints that cannot be neglected with respect to bulk self-assembly. Accordingly, in order to control the thin film BCP self-assembly, these interfaces have to be modulated, as observed in the previous paragraph for lamellae.

For the substrate-film interface, the main approach is to tune the substrate energy by grafting random copolymers brushes (RCP) with different compositions [43]–[48]. *Figure 18.a* shows the typical grafting process which is induced by heating up a RCP thin film long enough to provide covalent bonding between the RCP chains and SiO₂ substrate. The use of an adequate RCP composition enables the control of the wetting of the BCP domains by balancing (or not) the surface energies between the BCP domains and the substrate. Accordingly, such methodology affords an exquisite control of the morphology orientation.[47] (*Figure 18.b*). Indeed, a neutral surface can induce a perpendicular orientation while a non-neutral surface favors a parallel orientation of the BCP structure [39], [47]–[49].

A second method similar to the grafting of RCPs is based on the use of self-assembled monolayers (SAM) which constituent molecules are grafted through their chlorosilane function on the SiO₂ substrate [50]. Such treatment yields as well to a modification of the surface energy.

It is noteworthy that blending RCPs or SAMs with different (macro)molecular characteristics [51] can enable a modification of the grafting density and the surface properties [52], [53].

The “free surface” behavior, i.e. the film-air interfacial properties, is inherent to the surface energy of BCP domains. For thermodynamical reasons, this free interface will be preferentially wet by the block with the lower surface energy. To overcome this phenomenon (particularly pronounced for the so-called high- χ BCPs), the most common method consists in adding a sacrificial top coat [54]–[56] that will transform the “free surface” into a film-film interface for which the interactions can be controlled by the top coat composition (*Figure 18.c*). A recent study showed a slightly different method, consisting in the amorphization of the top surface of an as-casted BCP thin film by a gentle plasma. This process is conceptually similar to a grafted brush layer of statistical copolymers and could be used as an universal neutral top coating since the top-coat composition necessarily balances the interfacial energy of the segregated BCP domains [57] (*Figure 18.d*).

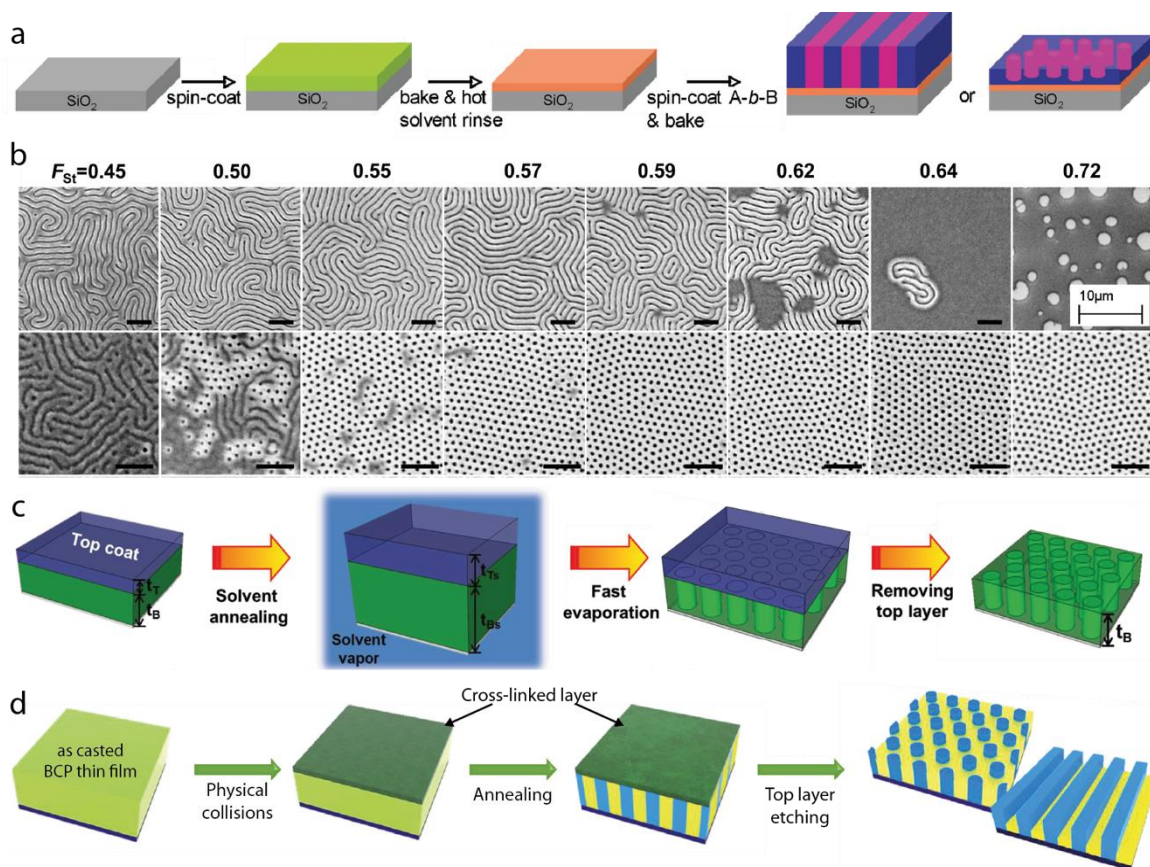


Figure 18. (a) Schematics of the substrate coating process by a RCP grafted layer [58] and (b) SEM images of PS-b-PMMA lamellar (top) and cylinders (bottom) self-assembled on substrate coated with different PS-r-PMMA RCPs (F_{St} is the volume fraction of styrene in the RCP) [47]. Schematics of (c) standard top coat process enabling the control of the orientation of BCP structure having components of drastically different interfacial energies [54] and (d) universal top coat process by the top-surface amorphization of BCP layer in its disordered state [57].

The top coat approach has two major drawbacks, which are the increased process complexity, and the constraint that the topcoat deposition should not dissolve or deteriorate the BCP thin film underneath.

Without resorting to a top coat approach, two other methods can have an impact on the “free surface” energy and yields to a controlled orientation of BCP structures:

- Heating BCP thin films which will modify the surface tensions of each block in a different way. This method is used for PS-*b*-PMMA, for which both blocks will have the same interfacial energies for a temperature around 225°C under vacuum [59];
- Modifying the atmosphere by adding solvent vapors [60], [61].

These methods are called thermal and solvent annealing, respectively. They will have other uses and impacts on BCP thin film, which will be the subject of the following part.

I.1.B.iii/ Annealing of BCP layer

The spin-coating process usually traps the BCP chains in an unstable state because of the fast solvent evaporation leading to a drastic decrease of the BCP chain mobility. In order to promote the self-assembly of BCPs, two main processes are described in literature: thermal annealing in which the BCP thin film is heated above the glass transition temperature of the blocks, and solvent vapor annealing in which solvent vapors swell the BCP thin film and screen unfavorable contacts.

Thermal annealing is industrially interesting because it does not require the use of hazardous solvents and it can be easily tuned and optimized with duration and temperature (*Figure 19.a*). During thermal annealing, the mobility of BCP chains is increased to promote self-assembly. Ultimately, the film is quenched at room temperature to freeze the ordered structure (i.e. below the glass transition temperature of one of the blocks) [62]. This technique is often used for PS-*b*-PMMA to organize thin films into lamellae, cylinders or spheres using RCP or SAM with an adequate composition [63]. Unfortunately, for some BCP systems, this annealing technique has a limitation since it requires a thermal budget inducing chemical modifications or decomposition of the BCPs [64].

Alternatively, solvent vapor annealing (SVA) is a more versatile technique that have been developed to overcome the thermal annealing limitations. Plenty of parameters can be modified during the promotion of self-assembly by SVA, such as solvent nature (tuning solvent quality by the use of mixture), annealing chamber volume and shape, temperature, duration, etc. As compared to thermal annealing, the mobility of the BCP chains are induced by a (selective or not) swelling of the BCP domains, thus promoting self-assembly [65]. Interestingly, this type of annealing has also an impact on the effective composition of the BCP since each block can have a different swelling ratio over the solvent, leading to a possible tuning of the phase behavior. For instance, Bai *et al.* demonstrated that a bulk-gyroid polystyrene-*b*-polydimethylsiloxane (PS-*b*-

PDMS) can self-assemble in spheres, cylinders or perforated lamellae in thin films by using different solvent mixtures for SVA [66] (*Figure 19.b*).

Moreover, there is no experimental standard setup for SVA, and each research team has their own self-made setup. Nevertheless, the various set-ups reported in the literature can be separated in two distinct techniques (*Figure 19.c*):

- Static SVA, where the sample is held in a closed jar with solvent vapors [65], [66];
- Dynamic SVA, where the sample is exposed to a continuous gas flow containing solvent vapors [67]–[69].

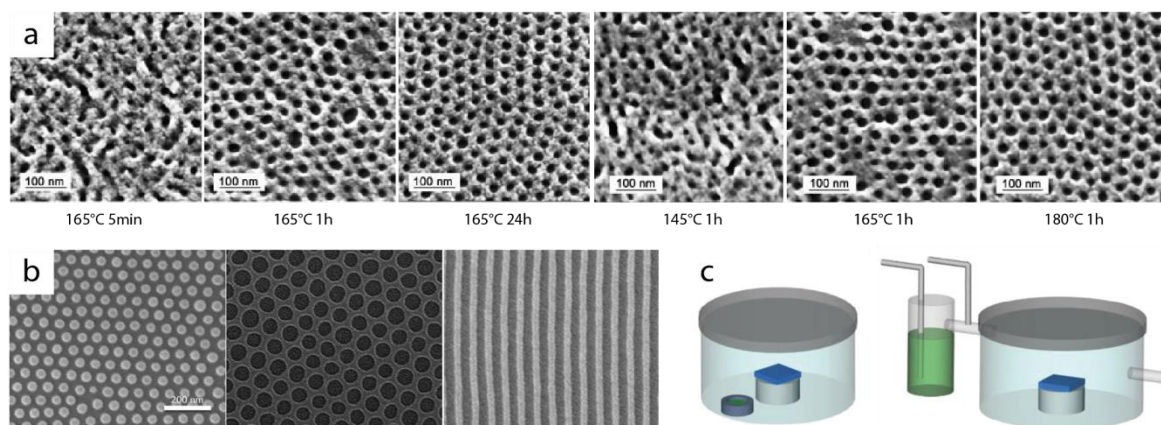


Figure 19. (a) SEM images of cylindrical PS-b-PMMA thin films thermally annealed at different temperatures and durations after the removal of PMMA domains [62]. (b) SEM images showing three different morphologies obtained by solvent vapor annealing of the same PS-b-PDMS using toluene/heptane mixtures with different ratios (left: 3:1, middle: 5:1 and right 10:1) [66]. (c) Solvent vapor annealing standard set-ups with (left) static and (right) dynamic solvent vapor flows [70].

Other annealing methods have been developed to improve the quality of the self-organization of BCPs, such as rapid thermal annealing (RTA) also called rapid thermal processing (RTP) which might prevent polymers from degrading during thermal annealing at higher temperature than classical thermal annealing [71]–[73], or solvothermal annealing that combines both thermal and solvent annealing [74].

There is no unified theory establishing rules for enabling self-assembly by annealing, but some guidelines can be erected from the overall literature about BCP self-assembly:

- Thermal annealing is efficient to drive out-of-plane orientation of BCP structures if the two blocks have similar surface energy. Otherwise, wetting layers will form at the interfaces which will promote an in-plane orientation. To overcome this, the use of both surface energy modifiers (grafted RCPs or top coats) and annealing under nitrogen or vacuum has been proposed.
- The quality of the solvents used for SVA with respect to the blocks is highly important. Usually, the solvents should have a good affinity with both blocks (theta or good solvents) in order to

provide sufficient swelling to the BCP chains. Additionally, one should choose solvents with balanced affinity for both blocks if order-order transitions due to selective swelling are not sought. Besides, thin films are prone to dewetting phenomena which can be accelerated if the solvent quality is too high.

- Volatile solvents are preferred because a high vapor pressure can be reached leading to enhanced chain mobility.

I.1.C/ Directed self-assembly

For many applications, such as nanolithography applied for microelectronics, the BCP patterns resulting from self-assembly should exhibit a perfect long-range order, i.e. extremely low defect density. Unfortunately, the self-assembly is a thermodynamical process involving driving forces of weak intensity, that creates ordered structures with their inherent low energy defects. For instance, common defects observed in thin films are dislocations and disclinations for line & space pattern, e.g. out-of-plane lamellar structure or in-plane cylinders, and dislocations located at grain boundaries for hexagonal pattern, e.g. out-of-plane cylinders or spheres [75].

Thus, several methods have been developed to achieve long-range order, called directed self-assembly (DSA) [76]–[78], that can be sorted in three categories: graphoepitaxy, chemical epitaxy and annealing under external stimuli.

I.1.C.i/ Graphoepitaxy

Graphoepitaxy consists in combining the bottom-up BCP self-assembly technique with a top-down method used to engrave a substrate with a guiding pattern (*Figure 20.a*) [78]–[81]. The patterning methods used to generate the directing pattern should have high enough resolution ($\approx 10L_0$) to define topographical fields which constrain the BCP self-assembly. Additionally, commensurability rules depending of the surface energy of the patterns have to be ensured to obtain long-range ordering. Plenty of nanoscale top-down patterning methods can be used, such as interference lithography, UV photolithography, ion beam lithography or nano-imprint. Then, the patterned substrate will create uneven boundary constraints, that can induce a preferential alignment of BCP structures called translational or lateral ordering [82], [83].

As introduced above, one key parameter for DSA by graphoepitaxy is the ratio between the substrate pattern size and the BCP domain spacing in order to avoid chain distortion (stretching or compression). Thus, this ratio should be carefully chosen according to the wetting configuration [83], [84], for instance an integer for a symmetric wetting configuration at the walls (pink affinity toward both walls) as highlighted in *Figure 20.b*, and its magnitude is a compromise:

it should be small enough for creating a topographic field strong enough to induce ordering, but high enough to be in the resolution range of substrate patterning method.

In addition, the pattern height is also an important parameter since it can influence the final BCP configuration in the topographical pattern. There are two possibilities:

- the substrate pattern is high enough and the BCP film is confined inside the trenches, creating disjointed areas that self-assemble independently (*Figure 20.c*) [85],
- the BCP film is thick enough as compared to the pattern height. Consequently, the BCP thin film overlays it, creating thus two distinct zones with different thickness. Such configuration can induce either two different orientations of the BCP structures (*Figure 20.d*) [86], or a single BCP grain due to the propagation of the topographical fields (*Figure 20.e*) [87].

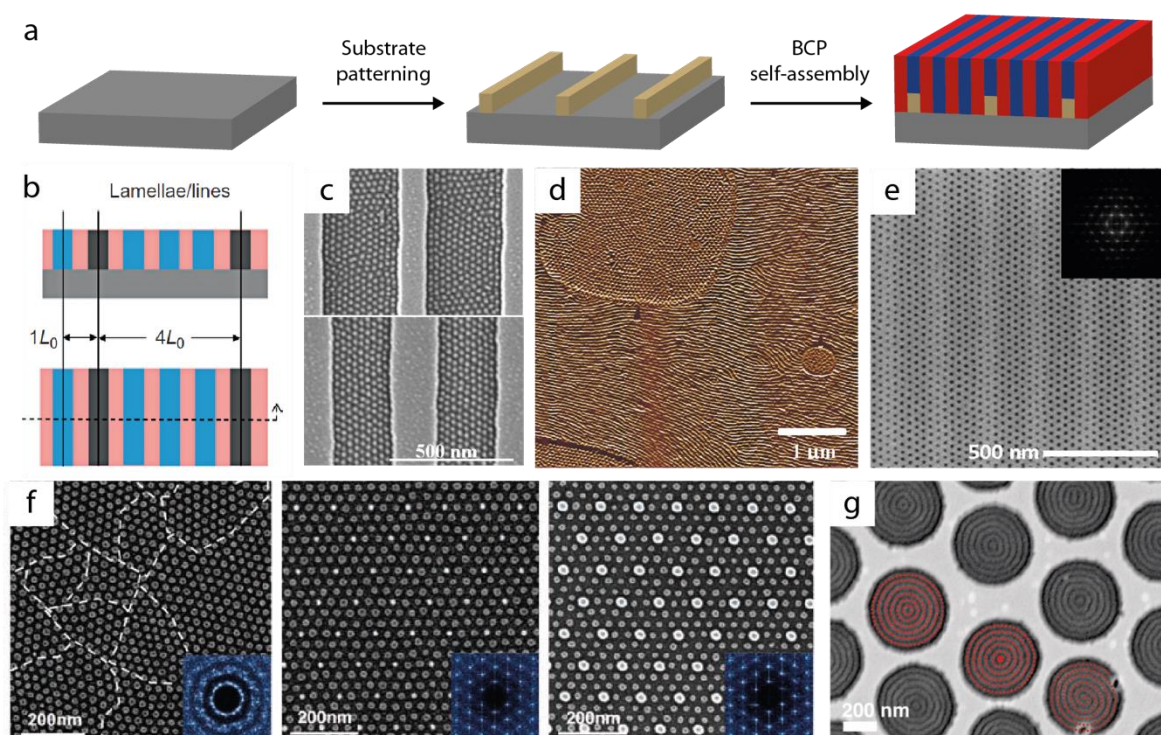


Figure 20. Schematics of (a) typical graphoepitaxy process and (b) an example of respected commensurability conditions for out-of-plane lamellae with an affinity of the red domains with the pattern walls [side-view at the top, top-view at the bottom] [83]. (c) SEM images of PS-b-polyferrocenyldimethylsilane (PS-b-PFDMS) spheres into 320 nm (top) and 240 nm (bottom) wide trenches [85]. (d) AFM image of PS-b-PI cylinders on a pre-patterned substrate showing in-plane orientation in thick regions (50 nm) and out-of-plane orientation in thin regions (20 nm) [86]. (e) SEM image of highly-ordered PS-b-PMMA cylinders deposited on grooved substrate [87]. (f) SEM images of PS-b-PDMS spheres assembled on (left) a flat substrate or a hexagonally patterned substrate functionalized with (middle) PDMS brushes or (right) PS brushes [88] and (g) PS-b-PMMA cylinders confined in nanoholes creating nanorings and spirals due to confinement [36].

This method unlocks the long-range ordering of BCP nanostructures by confinement and enables density multiplication [84], [85], [87]–[90] (*Figures 20.e-f*), which are two of the main limitations for application of BCPs in microelectronics. Graphoepitaxy also unlocks novel non-native morphologies such as spirals [36] (*Figure 20.g*) or ladders [91] due to confinement effects.

I.1.C.ii/ Chemical epitaxy

Chemical epitaxy consists in modifying the surface energy of the substrate with a spatially defined pattern to guide the self-assembly process (*Figure 21.a*). The most common technique to create this chemical pattern is coating either an RCP or a SAM layer on the substrate, followed by the deposition of a chemical resist that is used to pattern the aforementioned layer. After development of the resist pattern, a second grafting procedure with a chemically distinct RCP or SAM layer is applied in the exposed regions [79], [92]. This methodology leads to the generation of a chemical pattern having selective affinities with the BCP domains, and thus enables the long-range ordering of BCP structures.

As graphoepitaxy, chemical epitaxy is enabled by top-down techniques in order to create a well-defined chemical pattern on the substrate, which further leads to a lower defect density of BCP structure and/or a directed alignment. Experimentally, two parameters are important to implement DSA of BCPs with this technique:

- The chemical modification pattern shape and size, requiring a commensurable ratio with the BCP domain spacing.
- The surface energies of modified and unmodified areas, requiring an adequate contrast to provide different affinity with respect to the BCP domains.

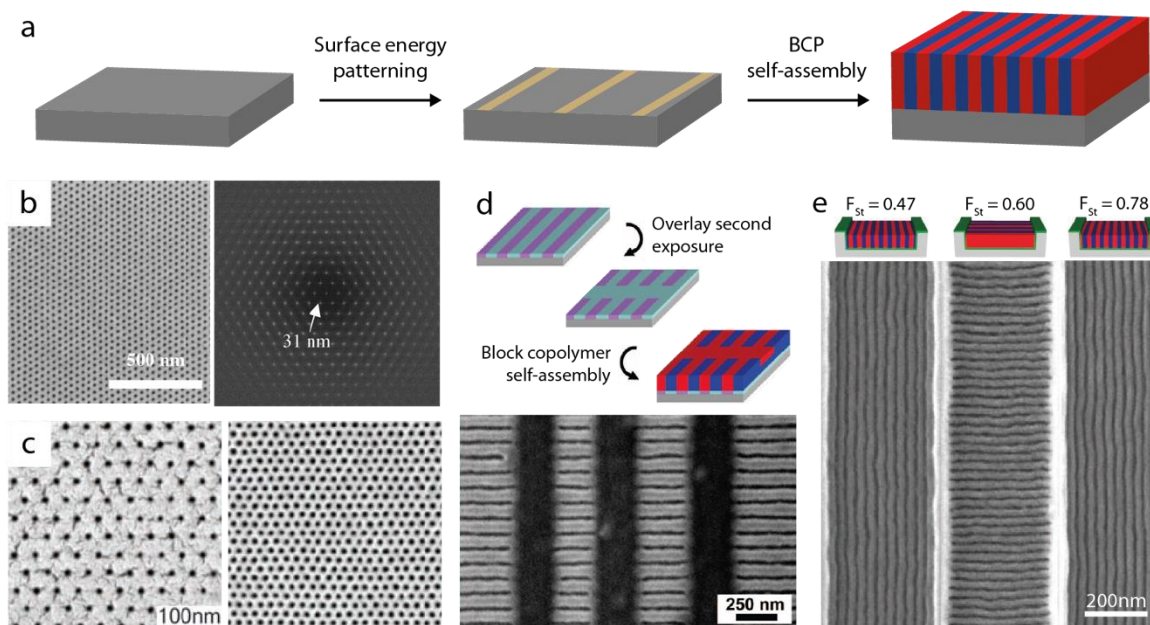


Figure 21. Schematics of (a) typical chemical epitaxy process. (b) SEM image and corresponding FFT of PS-b-PMMA cylinders assembled on a hexagonally grafted PS nanodot layer patterned by e-beam lithography [93].

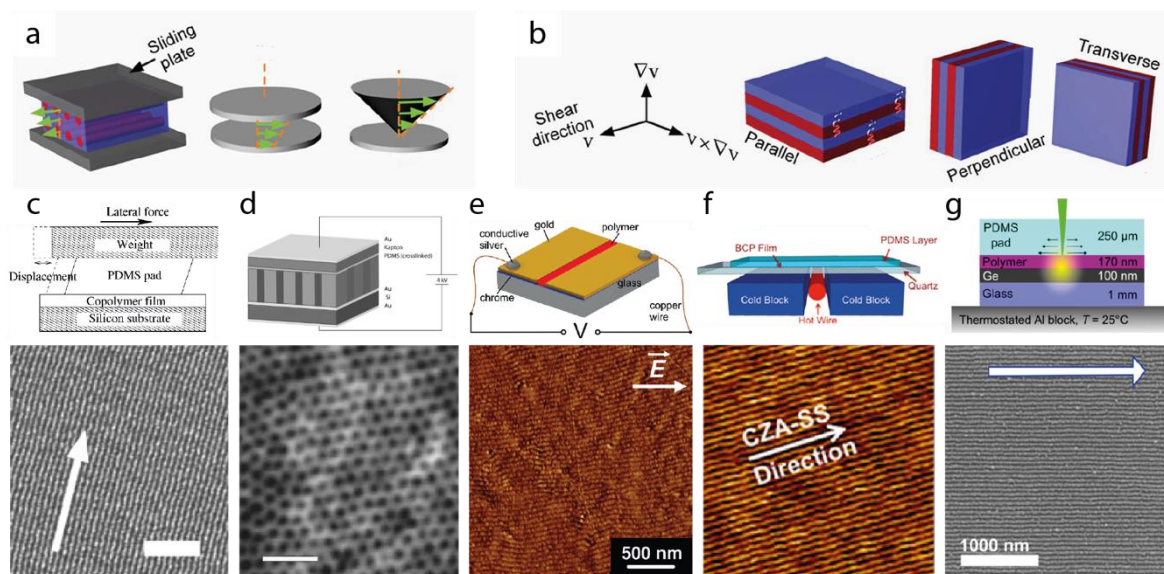
(c) SEM images of a hexagonal pattern (right) of PS-b-PMMA cylinders self-assembled on top of a surface modified substrate (left) with a pattern having twice the BCP period [94]. (d) Schematics and SEM image of PS-b-PMMA assembled on a chemical pattern fabricated using a two-step exposure process [95]. (e) Directed self-assembly of a lamellar PS-b-PMMA in trenches with different substrate coating composition [96].

This method unlocks long-range ordering and/or density multiplication [84], [92]–[94], [97], [98] (*Figures 21.b-c*), but also the possibility to create non-classical patterns by spatially controlling the orientation of a BCP structure as demonstrated by Stoykovich *et al.* (*Figure 21.d*) [95], [99]. Other groups have also developed processes that use both graphoepitaxy and chemical tuning of interfaces to induce long-range order with a precise orientation of the BCP structure (*Figure 21.e*) [96], [100].

I.1.C.iii/ External Stimuli for DSA

Different external stimuli can be used for promoting the BCP self-assembly process or for guiding the self-assembled BCP structure in a specific direction [77].

A first type of stimuli is based on shear alignment through the application of a mechanical stress in a particular direction during annealing. Several shear geometries are presented in *Figure 22.a*. This external shearing solicitation induces the long-range alignment of the BCP structure (either alongside, perpendicularly or transversally to the flow direction depending of the solicitation parameters) (*Figure 22.b*) [77]. In the specific case of thin films, a good adhesion between the moving part and the BCP film is required to efficiently transfer the mechanical stress. For instance, Angelescu *et al.* used a PDMS pad between a PS-*b*-poly(ethylene-*alt*-propylene) (PS-*b*-PEP) thin film and a moving plate, leading to in-plane cylinders aligned along the shear direction (*Figure 22.c*) [101].



*Figure 22. Schematics of (a) three standard shear alignment geometries and (b) three possible alignments of lamellae under shear alignment [77]. (c-g) Set-up schematics (top) and AFM or SEM images of directed self-assembled BCP thin films. (c) Shear alignment of PS-*b*-PEP cylinders [101]. Electric field alignment of (d) poly(4-fluorostyrene)-*b*-poly(D,L-lactide) (PFS-*b*-PDLLA) cylinders sandwiched between two electrodes [102] and (e) PS-*b*-PMMA cylinders in a side-by-side electrode configuration [103]. Zone annealing of PS-*b*-PMMA cylinders by (f) CZA-SS [104] and (g) SS-LZA [105].*

Self-assembly can also be directed using electrical or magnetic fields during an annealing process above the T_g of both blocks. The driving force is the minimization of electrostatic or magnetostatic energy by orientating the chains along the applied field [77]. Obviously, this method requires a high enough dielectric permittivity or magnetic susceptibility contrast between the BCP domains to be efficient. For an electrical field alignment, two set-ups have been reported in the literature: either by sandwiching the BCP thin film between two electrodes (*Figure 22.d*) [102], or by depositing a BCP thin film between two electrodes previously deposited on a substrate with a thin gap (*Figure 22.e*) [103]. Then a voltage is applied between both electrodes during solvent or thermal annealing to promote self-assembly along the electrical field direction. Magnetic field alignment shares the same procedure, with magnetic field instead of electrical field [106].

A last type of directing stimuli is called zone annealing and consists in applying a thermal gradient field to a BCP thin film that is confined between a solid substrate interface and a soft pad, usually in PDMS. This process creates a gradient soft-shear field, which will further direct the self-assembly along this thermal gradient direction. In order to be efficient, thermal gradient has to be sharp enough, to induce sharp fields at the nanometric scale. A first method, named Cold Zone Annealing Soft Shear (CZA-SS), consists in moving the sample by pushing the PDMS pad through a hot and a cold zone (*Figure 22.f*) [104]. A second one relies on a “sweeping” thermal annealing using a focused laser, named Soft Shear Laser Zone Annealing (SS-LZA) (*Figure 22.g*) [105]. An interesting feature of this technique is the possibility to use a patterned PDMS pad, which can spatially define zones with long-range ordering on the BCP thin film.

I.1.D/ PS-*b*-PMMA phase diagram

PS-*b*-PMMA is one of the most studied diblock copolymers in literature. Indeed, the sequential anionic polymerization of PS-*b*-PMMA offers a fine control of the macromolecular architecture, while the conditions of self-assembly via thermal annealing are well-mastered. Besides, the molar weight of the repeating units, the surface energies γ , the glass transition temperatures T_g , the statistical segment lengths a as well as the densities ρ of each block are very similar (*Table 2*), which is an asset to predict accurately the phase separation behavior. Furthermore, most of the DSA processes, discussed in the I.1.C/ Directed self-assembly part, have been established using this particular system.

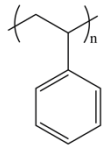
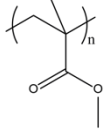
Polymer	Structure	M_n (g/mol)	γ (mN/m)	T_g (°C)	a (nm)	ρ (g/cm ³)
PS		104	$40.7 - 0.072(T - 20)$ [107]	100 [108]	0.68 [109]	1.05 at 25°C [110]
PMMA		100	$41.1 - 0.076(T - 20)$ [107]	105 [111]	0.74 [109]	1.19 at 25°C [110]

Table 2. PS and PMMA physical and chemical characteristics. For γ , the temperature is in Celsius degree

Usually, PS-*b*-PMMA BCPs are synthesized by a living anionic polymerization [112] in tetrahydrofuran (THF) at -78 °C under vacuum in dry conditions, using a strong base such as *sec*-Butyllithium (*sec*-BuLi) as initiator. Firstly, a PS block is polymerized, then it is end-capped by 1,1-diphenylethylene (DPE) or a derivative of DPE, followed by the polymerization of the PMMA block.

This system exhibits a low χ value, between 0.03 and 0.04 at 100 °C according to the literature, and the temperature dependences are listed in Table 3. For a symmetrical composition, using $\chi = 0.038$ at 100 °C as the median value from literature, the $\chi N > 10.5$ condition is obtained for $N = 276$. Using Equation (4), a theoretical minimum domain spacing at 19 nm is found, which is experimentally observed in literature [113], [114].

Method	χ_{AB}	T range (°C)	$\chi_{AB}@100^\circ\text{C}$	Comment	Ref
SAXS	$0.035 + \frac{8.8}{T}$	130-210	0.059		[115]
SANS	$0.0284 + \frac{3.902}{T}$	120-180	0.039	dPS- <i>b</i> -PMMA	[116]
SANS	$0.0292 + \frac{3.188}{T}$	170-190	0.038	PS- <i>b</i> -dPMMA	[117]
SANS	$0.0251 + \frac{3.199}{T}$	135-195	0.034	dPS- <i>b</i> -dPMMA	[117]
SAXS	$0.0282 + \frac{4.46}{T}$	120-220	0.040		[118]
Critical Molecular Weight	$0.021 + \frac{3.2}{T}$	190-260	0.030	PS PMMA blends	[34]

Table 3. PS-*b*-PMMA Flory-Huggins parameters measured with different methods and the corresponding probed temperature ranges (dPS / dPMMA: deuterated PS / PMMA).

Table 4 references a summary of self-assembled thin film studies using PS-*b*-PMMA from the literature. Using $\chi = 0.038$, it is also possible to calculate the theoretical domain spacing [18] which is referenced in Table 4.

M_n (kg/mol)	f_{PS}	Morphology	Measured L_0 (nm)	Calculated L_0 (nm)	Comments	Ref.
80	0.7	PMMA Cylinders	30 ^a	29.6		[119]
65	0.3	PS Cylinders	35 ^a	34.8		[119]
237	0.19	PS Cylinders	37.2 ^a	73.3		[120]
89	0.51	Lamellae	38.1 ^a	41.2	Poor self-assembly	[120]
55.5	0.81	PMMA Spheres	25.9 ^a	29.1		[120]
67	0.69	PMMA Cylinders	38.7 ^b	36.1		[63]
74	0.5	Lamellae	38.6 ^b	36.5		[63]
84	0.86	PMMA Spheres	41.2 ^b	34.4		[63]
88	0.72	PMMA Cylinders	40.9 ^c	41.8	Domain spacing rescaled	[121]
86	0.76	PMMA Cylinders	40.3 ^c	39.3	Domain spacing rescaled	[121]
87	0.8	PMMA Cylinders	39.3 ^c	37.6	Domain spacing rescaled	[121]
39	0.69	PMMA Cylinders	24 ^b , 23.5 ^c	25.1		[122]
53.8	0.69	PMMA Cylinders	28.8 ^b , 28.3 ^c	31.1		[122]
67.1	0.69	PMMA Cylinders	35 ^b , 34.4 ^c	36.1		[122]
82	0.7	PMMA Cylinders	42.9 ^b , 43.9 ^c	40.9		[122]
101.5	0.67	PMMA Cylinders	47 ^b , 48.7 ^c	48.3		[122]
132	0.73	PMMA Cylinders	59 ^b , 62.1 ^c	54.3		[122]
205	0.68	PMMA Cylinders	73 ^b , 74 ^c	76.3		[122]
29.4	0.73	Disordered	-	-		[122]
278	0.66	Gyroid	-	-		[123]
88	0.72	PMMA Cylinders	41 ^c	41.8	Domain spacing rescaled	[39]
50	0.5	Lamellae	29.4 ^c	28.1		[39]
28	0.56	Lamellae	20.6 ^c	19		[118]
25.7	0.53	Disordered	-	-		[118]
28	0.54	Lamellae	20 ^a , 21.2 ^c	19		[114]
36	0.5	Lamellae	28.6 ^a , 30.3 ^c	22.54		[114]
51	0.49	Lamellae	31.3 ^a , 33.8 ^c	28.5		[114]
75	0.51	Lamellae	36.7 ^a	36.7		[114]
83	0.45	Lamellae	40.2 ^a	39.5		[114]
104	0.48	Lamellae	43.5 ^a	45.8		[114]
141	0.5	Lamellae	63 ^a	56		[114]
176	0.48	Lamellae	74.7 ^a , 75.6 ^c	65		[114]
205	0.52	Lamellae	98.2 ^a	71.8		[114]
338	0.5	Lamellae	137 ^a	100.3		[114]
39	0.69	PMMA Cylinders	24 ^b , 23.5 ^c	25		[124]
89	0.83	PMMA Spheres	42 ^b	38.1	Measured by SEM analysis	[125]
66.5	0.66	Perf. Lamellae	-	-	28.7nm cylinders in bulk	[126]
67	0.69	PMMA Cylinders	43 ^b	36	Infiltrated BCP structure	[127]
70.7	0.29	PS Cylinders	39 ^b	36.4	Infiltrated BCP structure	[127]
104	0.5	Lamellae	48 ^b	45.7	Infiltrated BCP structure	[127]
51	0.49	Lamellae	35 ^b	28.5	Infiltrated BCP structure	[127]

Table 4. Macromolecular characteristics of different PS-*b*-PMMA from literature with the corresponding phase and domain spacing (measured by AFM^a, SEM^b, SAXS^c), and the calculated theoretical domain spacing [18].

The experimental data extracted from this survey can be compared with the theoretical phase diagram (*Figure 23.a*), as well as with the expected dependency of domain spacing with the degree of polymerization (*Figure 23.b*). As shown below, a very good agreement was obtained

between the experimental and theoretical data, clearly demonstrating the robustness of the BCP phase behavior theory when applied to this particular system.

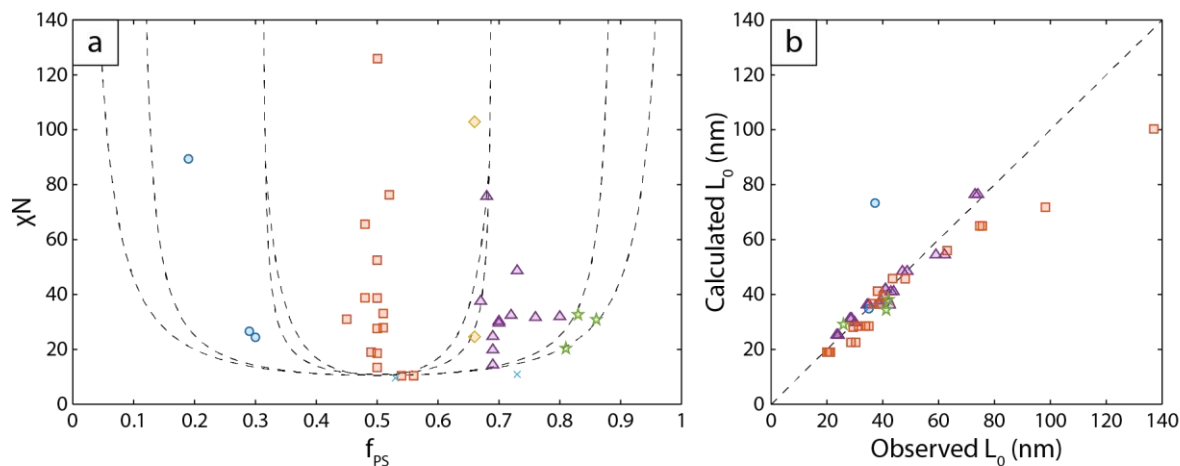


Figure 23. Survey of self-assembled PS-*b*-PMMA thin films from literature. (a) observed phase behavior as compared to the theoretical phase diagram (dashed lines) [11]. (b) observed domain spacing compared to the calculated one using the theory developed by Matsen et al. [18]. Circles, squares, lozenges, triangles, stars and crosses are PS cylinders, lamellae, gyroid or perforated lamellae, PMMA cylinders, PMMA spheres and disordered phase, respectively.

Finally, self-assembled thin films made from PS-*b*-PMMA are also interesting because of the possibility to subsequently hybridize the nanostructures. Indeed, the PMMA domains can be selectively removed using the appropriate wet or dry etch treatments or swelled (the so-called surface reconstruction) for further chemical loadings. Recently, the sequential infiltration synthesis (SIS) method has also been demonstrated for PS-*b*-PMMA BCPs. These various hybridization processes are discussed in the next part.

I.2/ Functionalization and hybridization of BCP thin films

Polymers intrinsically display interesting properties due to their chemical composition, such as optical, electrical, or mechanical properties [128]. Nevertheless, a path forward to enhance functionality in (nanostructured) polymers is related to the hybridization of the segregated domains [129]. Consequently, various chemical or physical-chemical processes have been developed in order to enhance the breath of functionalities of BCP thin films (*Figure 24*).

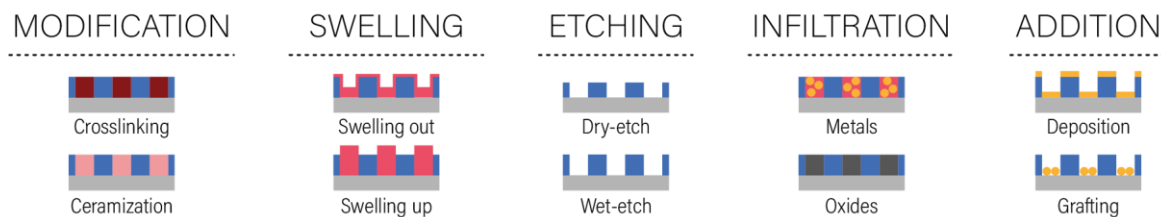


Figure 24. Schematics of functionalization processes used for self-assembled BCP thin films.

I.2.A/ Chemical modification

Depending on the chemical moieties of each block, it is possible to modify the chemical nature of a specific block to afford specific physical-chemical responses.

An interesting chemical modification with applications to the control of the self-assembly behavior of BCPs is cross-linking (i.e. the formation of covalent or physical bonds between individual chains), which leads to a drastic change in the polymer physical properties (e.g. toughening, solvent insolubility, etc.). Several processes can initiate cross-linking in polymers, such as radical formation via thermal annealing or irradiations, or the incorporation of crosslinking agents. For BCP systems, the privileged process is exposure to UV radiations, since thermal annealing or the addition of crosslinking agents can strongly impact the self-assembly behavior. Crosslinking can be used to “lock” a metastable morphology [130], to modify the domain spacing of a BCP structure [131] (*Figure 25.a*), to render insoluble a BCP thin film for further layering [131]–[134] (*Figure 25.a*), to selectively crosslink one BCP domain for improved contrast etching [133], [135] (*Figure 25.b*). In most of the cases, the crosslinking process involves a PS block as it can be cross-linked via UV exposure [135], or through post-modification [134]. It is noteworthy that a particular block can be also copolymerized with a reactive co-monomer in order to improve the crosslinking efficiency [131].

Heteroatom-containing BCPs can also undergo an interesting chemical modification by an oxidation process. The most popular are silicon containing BCPs, such as PS-*b*-PDMS, that can be oxidized in SiO₂ by an oxygen plasma treatment [136]–[138]. This treatment usually removes as well the other block(s) (*Figure 25.c*) leading to a “hard mask” for further transfer in a substrate of

interest [139]. It is also possible to selectively ceramize a BCP domain by adding a sol-gel precursor during the formation of the BCP thin film [140].

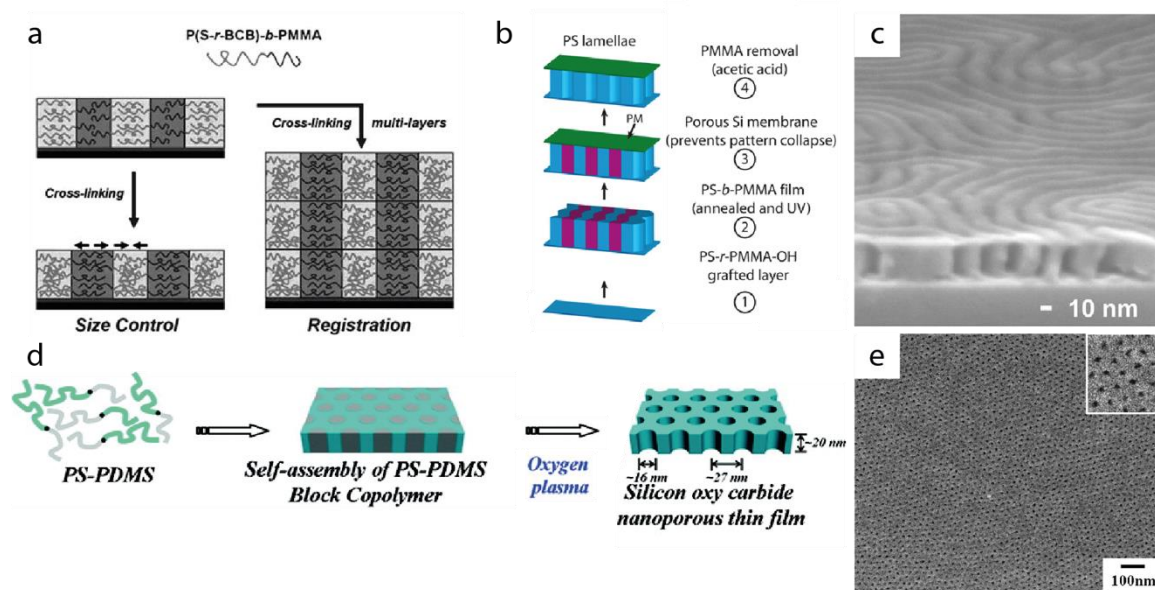


Figure 25. (a) Crosslinking of PS-*b*-PMMA thin films containing benzocyclobutene (BCB) units copolymerized in the PS block in order to tune the domain spacing or to render the film insoluble for further layering [131]. (b) Process flow and (c) SEM image of PS-*b*-PMMA lamellae treated by UV to crosslink the PS domains and remove the PMMA domains via a subsequent acetic acid bath [133]. (d) Schematics and (e) SEM image of PS-*b*-PDMS cylinders treated by oxygen plasma to ceramize the PDMS domains in SiC_xO_y and remove the PS domains [137].

I.2.B/ Selective swelling of BCP domains

The selective swelling of a particular BCP domain in a nanostructured thin film can also be used to obtain morphologies or patterns that are not achievable otherwise. For instance, surface reconstruction has been first employed by Mori *et al.* in 1994 [141] and popularized by the Matsen group in 2003 [142]. This term indicates a selective swelling of one particular BCP domain until it expands out of its registered position. The mechanism is often reversible by heating above T_g (Figure 26.a). This reversibility demonstrates that the BCP chains are not damaged during the process, especially the covalent bond between the two blocks. Typically, surface reconstruction is used to create protuberances from cylindrical morphology by plunging a BCP film into a solvent bath.

This process has been widely used to create nanopores [142], [143] (Figure 26.b) or mushroom-type structures [144] (Figures 26.c-d) depending on swelling conditions. Alternatively, Son *et al.* [145] used this method on PS-*b*-PMMA lamellar or cylindrical morphologies to selectively swell either the PS or the PMMA domains with cyclohexane or acetic acid solvent vapors, respectively. This process generates a high topographic contrast between the domains (Figures 26.e-h).

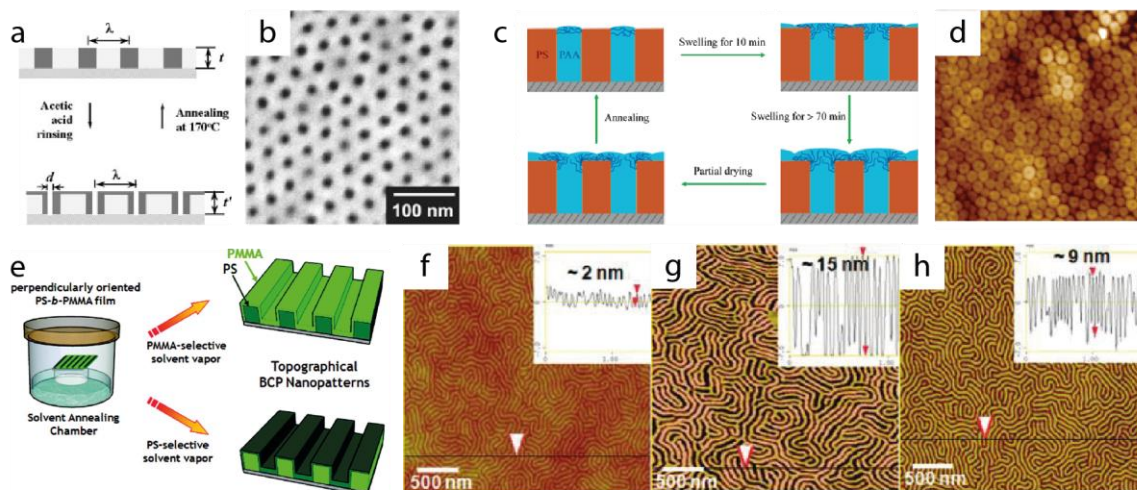


Figure 26. (a) Surface reconstruction process leading to the formation of nanopores and (b) SEM picture of the pores obtained for a PS-*b*-PMMA system [142]. (c) Schematics of the mushroom-like morphology obtained from the selective swelling of PS-*b*-PAA thin films and (d) the corresponding AFM image [144]. (e) Schematics of the selective swelling process applied to a lamellar PS-*b*-PMMA thin film and the corresponding AFM images: (f) before swelling, (g) after acetic acid swelling (PMMA thickening), (h) after cyclohexane swelling (PS thickening) [145].

I.2.C/ Etching processes for the selective removal of a BCP domain

The two major types of etching processes used in BCP nanofabrication are wet etching, using liquid chemicals or liquid etchants to dissolve material, and dry etching, using plasma or etchant gases to remove the material. For both processes, the selectivity and etching rate are related to the BCP chemical composition [146]. This etching step is crucial for lithographic applications in order to transform a nanostructured BCP thin film into a mask [147]. Figures 27.a-b show typical processes of wet and dry etching for PS-*b*-PMMA applied to pattern transfer.

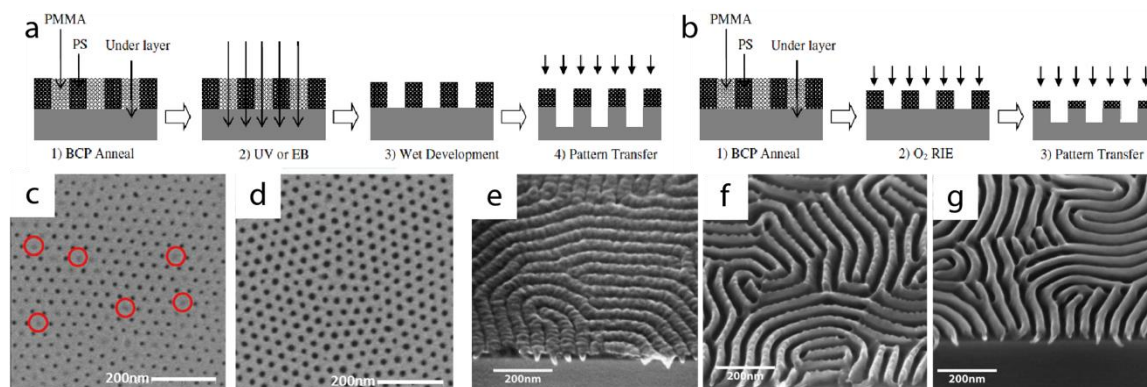


Figure 27. Typical PMMA removal step for a PS-*b*-PMMA BCP layer by (a) wet etching and (b) dry etching followed by a pattern transfer step [146]. SEM images of PS-*b*-PMMA cylinders (c) after an acetic acid rinse showing a surface reconstruction and (d) after UV exposure followed by an acetic acid rinse showing wet etching [148]. Dry etching of PMMA domains from PS-*b*-PMMA lamellae by (e) Ar plasma, (f) O₂ plasma and (g) Ar:O₂ 10:1 plasma.

For wet etching processes, a solvent that solubilizes one specific block is obviously a good candidate for selective etching. However, the covalent bond between the blocks will prevent the

solubilized block to be completely removed from the BCP layer, and a surface reconstruction will commonly occur instead of etching (*Figure 27.c*). Thus, a pretreatment (e.g. a short UV exposure [146], [148]–[150], a short e-beam exposure [146], [148], a ion implantation [148]) is needed to partially degrade one block or at least “break” some covalent bonds of the BCP chains. Then, a rinsing step by dipping the BCP film into a well-chosen solvent bath is enough to perform the wet development (*Figure 27.d*). One of the main solvents used for PS-*b*-PMMA surface reconstruction is acetic acid, which solubilizes PMMA but not PS. It is noteworthy that a too long UV pretreatment can be counterproductive as it promotes polymer crosslinking and degradation [149].

For dry etching processes, the etching rates are highly dependent on the material chemistry but also on the plasma composition. Many studies have focused on this topic with the aim to find the most selective plasma toward a chosen BCP system. Indeed, this selectivity enables a proper development of a BCP mask, i.e. keeping the highest thickness of the resulting pattern. *Table 5* references studies on plasma selectivity for PS-*b*-PMMA dry etching, enlightening the effect of gas composition and processing parameters on selectivity (defined as the ratio between PMMA and PS etching rates). It is also important to evaluate the impact of the plasma on the non-etched domains of the BCP structure. For instance, Ting *et al.* compared different plasma chemistries in order to etch PS-*b*-PMMA [151]. They showed that an Ar plasma chemistry has a very high selectivity toward PMMA, but the remaining PS domains are very rough and deformed (*Figure 27.e*). Such behavior is highly detrimental for the fidelity of the pattern transfer into a substrate of interest. As opposed, an O₂ plasma chemistry preserved the PS domains at the cost of a reduced selectivity (*Figure 27.f*). The best compromise was found to be an Ar plasma with some O₂ impurities giving a good development as shown in *Figure 27.g*.

Gas	Flow (sccm)	P (mTorr)	Power (W)	Plasma type	Selectivity	Ref.
Ar	50	-	700	helicon	3.63	[151]
Ar	-	15	100	ICP	3.9	[152]
Ar/O ₂	50/5	10	300	helicon	2.4	[151]
CF ₄	30	-	500	helicon	1.85	[151]
O ₂	50	-	700	helicon	1.5	[151]
O ₂	-	15	100	ICP	1.7	[152]
O ₂	50	10	50	RIE	2.1	[153]
O ₂	50	10	60	RIE	1.4	[153]
O ₂	70	10	70	RIE	1.3	[153]
O ₂ /CHF ₃	10/20	-	700	helicon	1.82	[151]
O ₂ /CHF ₃	5/40	10	150	RIE	2.4	[153]
O ₂ /CHF ₃	25/20	10	150	RIE	2.4	[153]
O ₂ /CHF ₃	10/40	10	100	RIE	2.1	[153]
O ₂ /CHF ₃	5/40	10	100	RIE	3.5	[153]

*Table 5. Plasma etching chemistries used for PS-*b*-PMMA selective etch and selectivity toward PMMA for different plasma compositions, plasma machines and operating settings. (ICP for Inductively Coupled Plasma, and RIE for Reactive Ion Etching)*

I.2.D/ Infiltration of a selective BCP domain

In thin film configuration, polymers have the ability to be infiltrated by diffusion of species. Such behavior is a strong asset to functionalize BCP thin films with various oxide or metallic precursors. Furthermore, the chemical differences between the blocks can lead to a selective incorporation of the infiltrated materials in a particular BCP domain [154]. These chemicals can be loaded in thin films from gaseous or liquid phases, resulting to the formation of metals or oxides after specific post-treatments.

I.2.D.i/ Vapor phase infiltration

Among the different chemical vapor deposition (CVD) processes, atomic layer deposition (ALD) shows very interesting performance due to a high control of the chemical reactions based on self-limiting mechanisms. Briefly, ALD consists in repetitive cycles, which deposit each time a monolayer of the two precursors needed to form the chemical of interest on top of a substrate placed in a vacuum chamber [155]. Each cycle is composed of several steps, which are summed up in *Figure 28.a*:

- The vapor phase precursor A is pulsed in excess in the chamber;
- The precursor A is adsorbed / reacting at the substrate surface creating a homogeneous layer;
- The excess of precursor A (and potential by-products) are removed by an inert gas carrier, usually N₂;
- The vapor phase precursor B is pulsed in excess in the chamber;
- The precursors A and B react together, usually by an oxidation reaction;
- The excess of precursor B and the reaction by-products are removed by the same carrier gas.

This process was transposed to BCP infiltration by increasing the duration of precursor pulses, allowing the absorption and diffusion of chemical species into a selective block. According to the sequence of pulses, three different processes have been developed, sequential infiltration synthesis (SIS), multiple pulsed infiltration (MPI) and sequential vapor infiltration (SVI) (*Figure 28.b*). In literature, these processes are usually not differentiated, and indifferently called SIS. The selectivity is enabled by a selective bonding between a precursor molecule and a reactive functional group of a specific block. It allows the trapping of the precursor molecules during the purge (*Figure 28.c*), while the excess of precursors is removed (*Figure 28.d*).

However, two limiting parameters of this method remain: *i*) the reaction temperature to perform the diffusion and the reaction between the precursors has to be low enough in order to not modify the self-assembly or degrade the BCP layer; *ii*) and the precursors molecules should be small enough to diffuse into the polymer matrix. Knowing these constraints, the process have

been optimized for the selective growth of different metal oxides into four different BCPs: PS-*b*-PMMA, PS-*b*-polyepoxyisoprene (PS-*b*-PIO), PS-*b*-poly(2-vinylpyridine) (PS-*b*-P2VP) and PS-*b*-poly(4-vinylpyridine) (PS-*b*-P4VP) [156]. Other polymers have been successfully infiltrated by this method, such as polyethyl methacrylate (PEMA), polypropyl methacrylate (PPMA), polybutyl methacrylate (PBMA), polyvinyl alcohol (PVA), polyvinyl pyridine (PVP), polyacrylic acid (PAA), polyamide-6 (PA-6), polybutylene terephthalate (PBT), polylactic acid (PLA), polycarbonate (PC), polyethylene oxide (PEO) and polyethylene terephthalate (PET). These polymers could probably be used as a selective block of a BCP architecture, but no literature have been referenced on such developments.

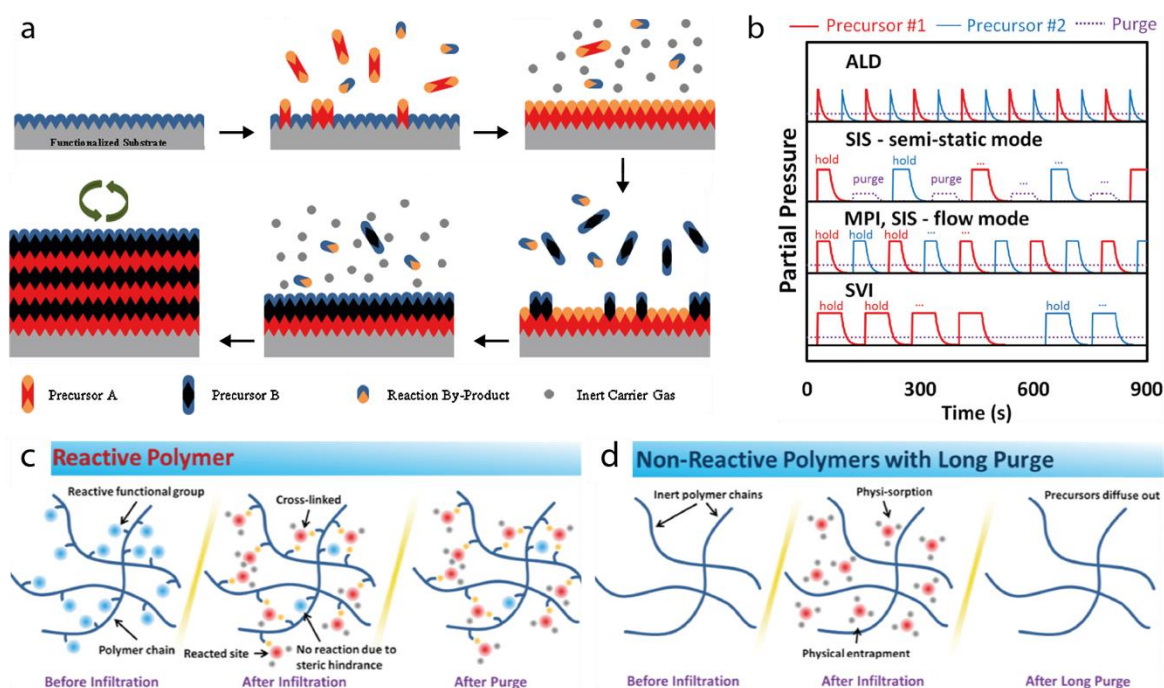


Figure 28. (a) Schematics of the ALD process [155], (b) Typical partial pressure profiles for ALD, SIS, MPI and SVI. (c) Precursor entrapment mechanism in a polymer with functional groups, and (d) complete removal after purge in a polymer without functional groups [157].

PS-*b*-PMMA is a good candidate for SIS because of the carbonyl function of PMMA, which was demonstrated to trap ALD precursors, even if the mechanism is not fully understood yet [157], [158]. Table 6 references metal oxides infiltrated into PS-*b*-PMMA with the associated couple of precursors and the processing temperature. Plenty of other precursors may be used for infiltration, with two major constraints: *i*) the precursor should be able to diffuse into the PMMA matrix and *ii*) the reaction between the two precursors should be efficient at a low temperature (with respect to polymer degradation or self-assembly capability).

Metal oxide	Precursor A	Precursor B	T (°C)	Ref.
Al ₂ O ₃	Al(CH ₃) ₃ Trimethyl aluminium (TMA)	H ₂ O	80°C – 135°C	[159]–[166]
		O ₃	90°C	[167]
TiO ₂	TiCl ₄ Titanium tetrachloride	H ₂ O	135°C	[160], [165], [168]
In ₂ O ₃	In(CH ₃) ₃ Trimethyl indium (TMIn)	H ₂ O	80°C	[169]
ZnO	Zn(C ₂ H ₅) ₂ Diethylzinc (DEZ)	H ₂ O	85°C – 90°C	[159], [162], [166]
W/WO _x	WF ₆ Tungsten hexafluoride	Si ₂ H ₆	80 - 85°C	[159], [163]
SiO ₂	Si(OC ₅ H ₁₁) ₃ OH tris(tert-pentoxy)silanol (TPS)	TMA	125°C	[159]

Table 6. Various metal oxides infiltrated in PS-*b*-PMMA by SIS, with the associated couple of precursors and the operating temperature range referenced.

For a given couple of precursors and a BCP system, many operating parameters can be optimized to modify the infiltration process, such as the type of SIS, the number and duration of each cycle (precursor A, B and purge), the chamber temperature, etc. [163], [170], [171]. This variety of processing parameters leads to different resulting structures as shown in *Figure 29.a* for “structure consistency” or in *Figure 29.b* for pore size.

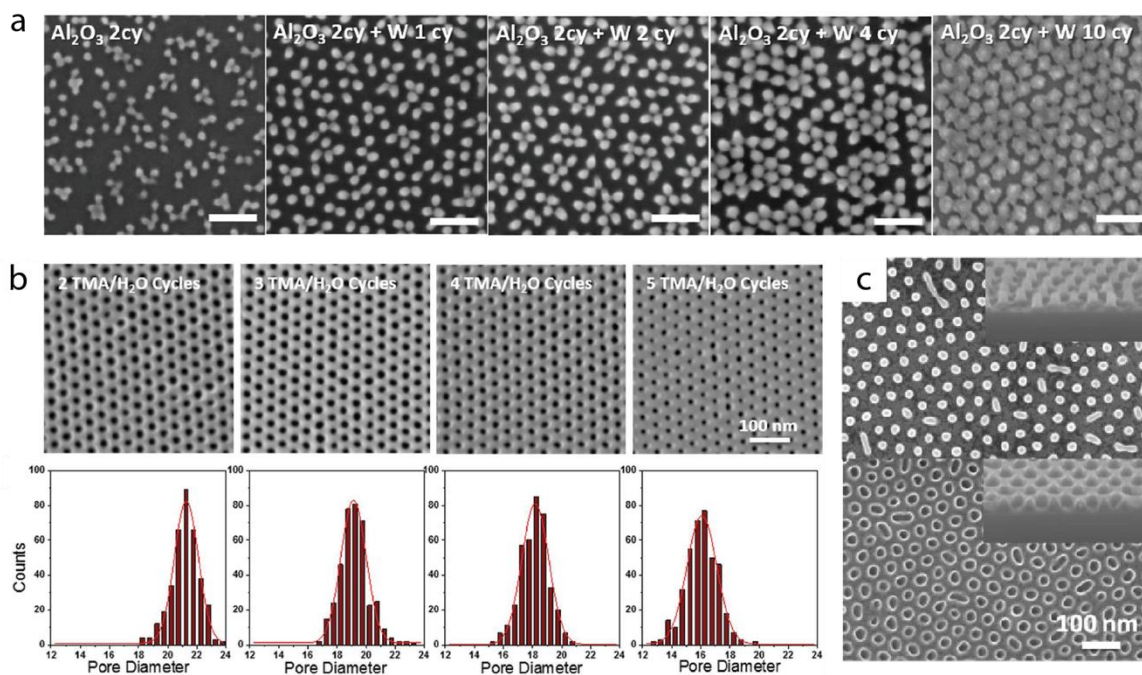


Figure 29. SEM images of (a) a cylindrical PS-*b*-PMMA layer infiltrated by Al₂O₃ and W with different number of SIS cycles [163]. (b) PMMA honeycomb patterns formed from PS-*b*-PMMA transformed into Al₂O₃ by SIS which exhibit a reduction of the pore diameter with the number of SIS cycles [170]. (c) A cylindrical PS-*b*-PMMA layer infiltrated by Al₂O₃ (top) without any pretreatment and (bottom) with UV exposure treatment leading to a opposite block selectivity [166]. Every SIS treatment has been followed by an O₂ plasma step to remove organic remaining materials.

This infiltration process can also be used to toughen a BCP mask for further pattern transfer [164], or to generate well-defined metal oxide nanostructures [162]. Interestingly,

Kamcev *et al.* have demonstrated that a UV pretreatment on a PS-*b*-PMMA thin film leads to a switch in the precursor selectivity by creating oxygen containing Lewis basic groups within the PS domains [166] (*Figure 29.c*).

Otherwise, the most common physical vapor deposition (PVD) processes are sputtering and evaporation, which does not usually show chemical selectivity to a particular BCP domain since they are based on physical processes. However, Lopes and Jeager [172] showed that thermal evaporation of metals can be used to selectively decorate PS-*b*-PMMA thin films. Indeed, for low metal thickness - less than 0.6 nm - the thermal evaporation process on top of a BCP layer is not homogeneous, and a “selective” deposition occurs on top of a specific domain. For Au and Ag, the PS domains are preferred, while for In, Pb, Sn and Bi, the PMMA domains are selectively covered by the metals. Thus, metal nanowires, nanochains or nanoparticles can be selectively grown onto PS or PMMA domains.

I.2.D.ii/ Liquid phase infiltration

Another route to modify a specific domain of a BCP nanostructure with metallic precursors is called metal impregnation. It consists in dipping a BCP thin film in a solution containing metallic ions in order to initiate the diffusion of the species into a specific BCP domain. Indeed, the ions can be selectively complexed through macromolecular engineering of the BCP architecture, i.e. using the appropriate functional groups. The most common BCPs for metal impregnation is PS-*b*-P_xVP ($x=2$ or 4) in association to $[MCl_4]^n$ - metal ions from salts such as H₂AuCl₄, Na₂PdCl₄ or Na₂PtCl₄ [173]–[175]. Different loadings can be obtained by tuning the bath duration and the precursor concentration (*Figure 30.a*). Typically, metal ions are first dissolved in a diluted HCl aqueous solution leading to the protonation of the nitrogen atoms of P_xVP. This yields to the complexation of the anionic metal precursor. Interestingly, this impregnation also induces swelling of the P_xVP domains, and it unlocks novel nanostructures through surface reconstruction, such as a nanoring array or a double nanowire array [175] (*Figure 30.b*).

Unfortunately, metal impregnation for PS-*b*-PMMA has not been reported since this system does not provide the required functionality to strongly interact with metallic salts. However, several demonstrations of the formation of gold nanoparticles in a PMMA matrix have been referenced in the literature [176], [177]. Besides, PS-*b*-PEO has been successfully impregnated with metal salts, such as Fe(NO₃)₃, Ce(NO₃)₃ or Cu(NO₃)₂ by “activating” the PEO domains with ethanol through a surface reconstruction process (i.e. generation of a porous structure), which allows a subsequent salt impregnation by capillary forces and coordination [178].

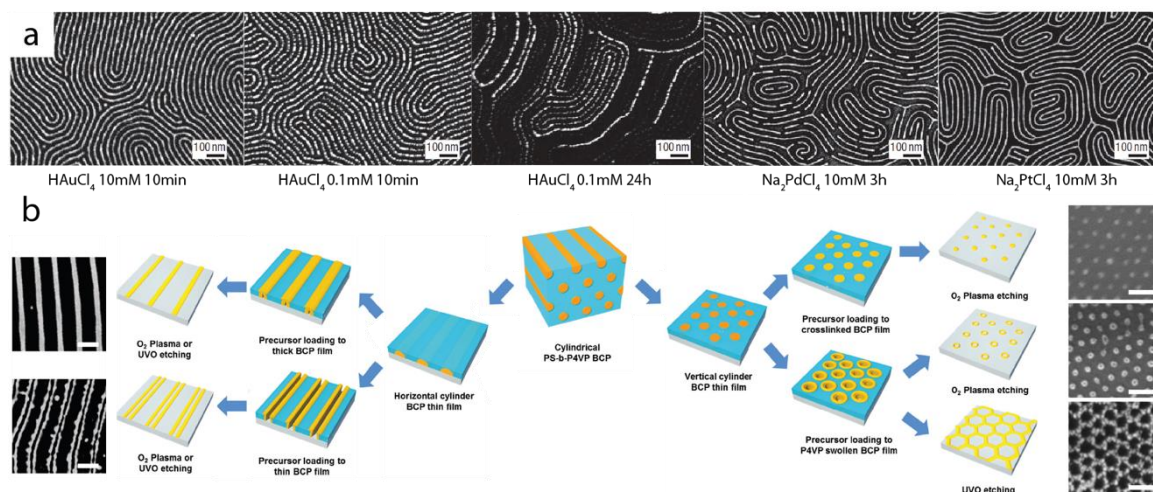


Figure 30. (a) SEM pictures of gold, palladium and platinum lines formed from in-plane PS-*b*-P2VP cylinders impregnated with metallic salts with different concentration and duration, followed by a plasma treatment [173]. (b) Schematics of PS-*b*-P4VP cylinders infiltration process with H₂AuCl₄ for different structure orientation and processing, and the corresponding SEM images of the gold nanostructures [175].

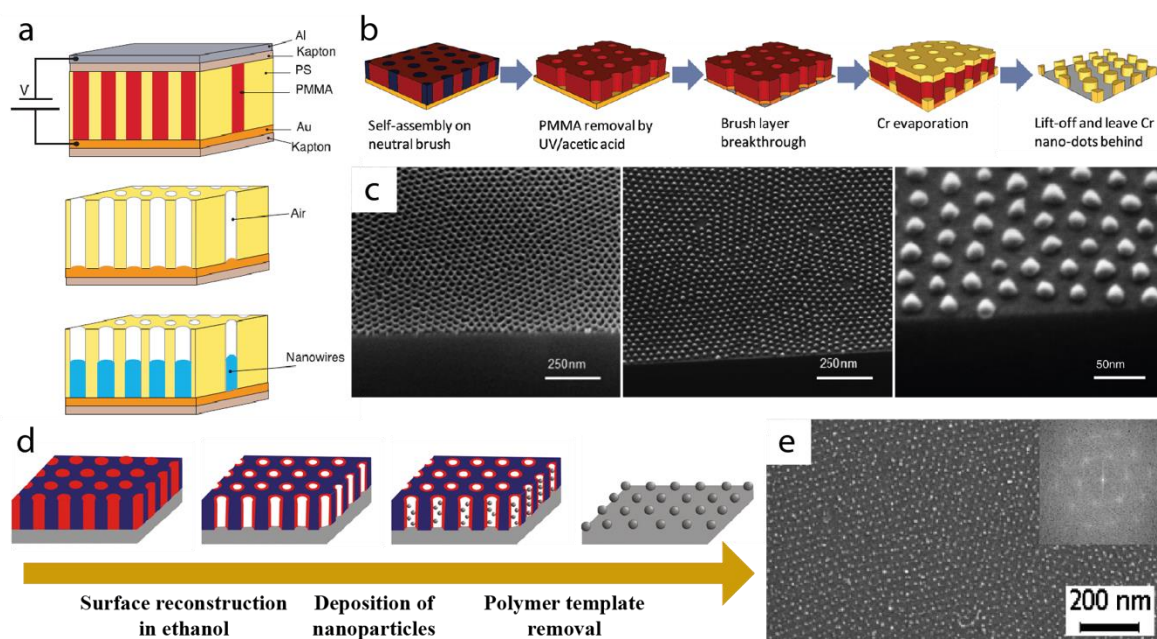
It is noteworthy that a final treatment, usually an oxygen plasma or an UV/ozone exposure, is performed to oxidize or reduce the metallic salts into its most stable form and conjointly remove surrounding polymer matrix. Noble metals resist oxidation and are conversely reduced into Au(0), Pt(0) and Pd(0) by oxygen plasma [173], while other metals are oxidized into CuO, CeO₂ and Fe₃O₄ by UV/O₃ treatment [178].

I.2.E/ BCP pattern as template for further oxide or metal addition

It is also possible to “add” metals or oxides in a specific domain using the BCP pattern as a template. The first step of such process consists in a selective etching or in a surface reconstruction of a BCP nanostructure. The resulting pattern is further used as a scaffold for electrodeposition, gaseous deposition or nanoparticle grafting.

In 2000, the Russell group [179] transposed the electrodeposition process from inorganic porous to organic porous templates (*Figure 31.a*). They used an out-of-plane PMMA cylindrical structure deposited on a gold-coated silicon substrate as a template for the growth of metal nanowires by electrodeposition. The PMMA domains were removed by an UV treatment followed by rinsing with acetic acid, leading to a cylindrical nanoporous PS template. Using this process, they were able to form Co and Cu nanowire arrays through electrodeposition from the gold bottom electrode. Another interesting use of electrodeposition in combination to BCP templating was demonstrated for the gyroid morphology. Indeed, such co-continuous structure can be fully impregnated by electrodeposition after removal of one of the domains. This allows the generation of metallic 3D nanostructures with interesting optical properties [180], [181].

A different process allowing the formation of oxide or metallic structures from a BCP template is based on the deposition of materials by thermal evaporation, sputtering or ALD [154]. Then a subsequent stripping of the BCP template leads to the removal of the coated materials in no direct contact with the substrate. This method have been widely used to create metallic lines or arrays of dots and anti-dots, using lamellar [182], cylindrical [119], [183], [184] or spherical [185] scaffolds, respectively. *Figures 31.b-c* show a typical process flow for the generation of chromium dots by thermal evaporation using a PS-*b*-PMMA nanostructured layer [183]. A constraint arises from the inherent anisotropy of this process, that limits its use to 2D BCP scaffolds. However, it has been used by Park *et al.* [184] to create nano-rings thanks to a 5° glancing angle evaporation on top of cylindrical hole pattern preventing a coating inside the pores. In addition, ALD is also a suitable method to create a coating on a BCP template, allowing the deposition of metal oxides, but also the formation of more complex structures such as nanotubes [186].



*Figure 31. (a) Schematics of electrodeposition growth in a PS scaffold made from a cylindrical PS-*b*-PMMA layer self-assembled under electrical field [179]. (b) Schematic process for the fabrication of chromium dots using a PS-*b*-PMMA layer and a lift-off process. (c) SEM images of the different steps: (left) the BCP template before evaporation and (middle and right) after lift-off [183]. (d) Schematics of Pd nanoparticle selective deposition in a PS-*b*-P4VP surface reconstructed template and (e) resulting SEM image after template removal [187].*

Finally, it is also possible to infiltrate nanoparticles (NPs) on a BCP template. Obviously, the size of the NPs should be smaller than the characteristic size of the BCP features. Additionally, preferential interactions between one of the BCP domains and the NPs are mandatory to promote the selective aggregation of NPs [188]. *Figures 31.d-e* show the typical process of NP inclusion in a PS-*b*-P4VP surface reconstructed cylindrical pattern [187]. To achieve this selectivity, Gowd *et al.* used Pd NPs stabilized by citrate molecules which strongly interact with P4VP. Accordingly, the

surface modification of the NPs is often necessary to promote the selective registration of NPs onto a BCP pattern [145], [188].

I.3/ Iterative stacking of BCP layers

The stacking of BCP layers has the potential to add further complexity and functionality to nanostructured BCP thin films. The individual layers can also be hybridized with the various processes described in the previous section, thus expanding the scope of designs for targeted applications in optics, biology or microelectronics. Such methodology, called iterative (directed) self-assembly, affords the generation of 3D nanostructures beyond native BCP morphologies.

I.3.A/ Literature review

The state-of-the-art concerning iterative self-assembly of BCPs is presented via a progress report published in *Advanced Materials Interfaces* describing the “ins and outs” of the various iterative self-assembly processes referenced in literature [132]. Four categories of iterative self-assembly processes were identified and the “table-of-content” (see *Figure 32*) schematically highlights the details of each process:

- A protective layer is inserted between the individual BCP layers to ensure the integrity of the first layer at the time of the deposition of the second BCP layer;
- A direct stacking method in which each individual layer is “immobilized” by a hybridization process (by SIS for instance);
- A method taking advantage of the first layer crosslinking before the second layer spin-coating;
- A process using a transfer mold technique to deposit the second layer on top of the first one.

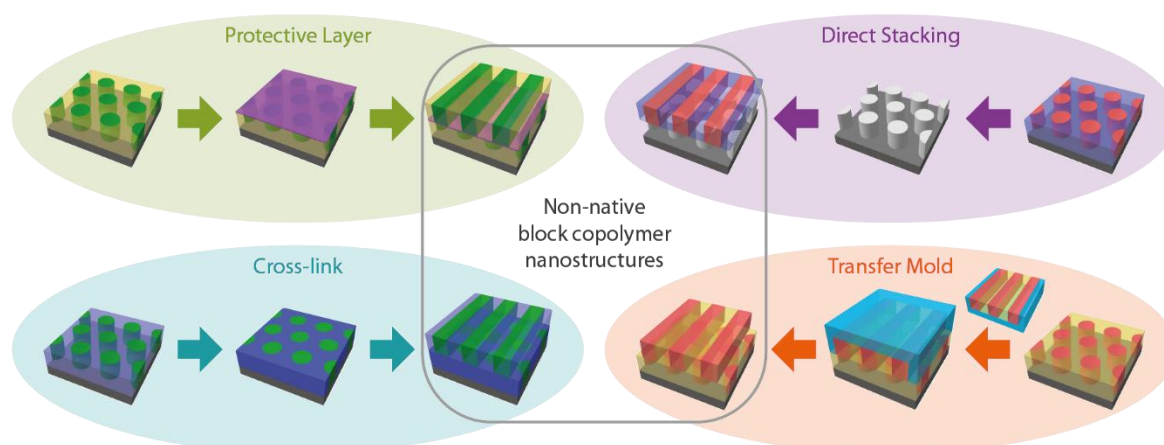


Figure 32. Schematics of four different processes identified for iterative stacking of nanostructured BCP thin films [132].

The bibliographic details of the published manuscript are:

N. Demazy, C. Cummins, K. Aissou, and G. Fleury, “Non-Native Block Copolymer Thin Film Nanostructures Derived from Iterative Self-Assembly Processes” *Advanced Materials Interfaces*, vol. 1901747, pp. 1–11, 2019.

<https://doi.org/10.1002/admi.201901747>

Non-Native Block Copolymer Thin Film Nanostructures Derived from Iterative Self-Assembly Processes

Nils Demazy, Cian Cummins, Karim Aissou, and Guillaume Fleury*

Nanostructured block copolymer (BCP) thin films constitute an elegant tool to generate complex periodic patterns with periodicities ranging from a few nanometers to hundreds of nanometers. Such well-organized nanostructures are foreseen to enable next-generation nanofabrication research with potent applications in the design of functional materials in biology, optics or microelectronics. This valuable platform is, however, limited by the geometric features attainable from diblock copolymer architectures considering the thermodynamic driving force leaning toward the formation of structures minimizing the interface between the blocks. Therefore, strategies to enrich the variety of structures obtained by BCP self-assembly processes are gaining momentum and this progress report reviews the opportunities inherent to iterative BCP self-assembly by considering the emerging strategies for the generation of “non-native” morphologies.

hexagonally packed cylinders, double gyroid, to lamellae.^[1,4–6] As virtually any combination of chemistry and sequencing is attainable by macromolecular design,^[3] BCPs offer tremendous opportunities for the design of functional materials with applications in biology, separation process and nanotechnologies among others.^[7–9]

Further opportunities in the development of BCP nanotechnologies are linked to the formation of well-ordered periodic nanoscale patterns in thin film configuration with nanolithography as the “flagship” application. Indeed, the chemical dissimilarities between the domains allow selective removal by plasma or wet etching of one of the BCP domains leading to a mask that can be further used to define features in microelectronic applications. The formation of self-assembled patterns in thin film can also be combined with hybridization methods,^[10] thus converting the BCP patterns into functional structured surfaces such as bit-patterned media,^[11–13] field effect transistors,^[14,15] optical metamaterials,^[16–18] or photonic structures.^[19–21] This can be performed by using the nanostructured BCP scaffold as a template for a subsequent deposition of functional materials (via sequential infiltration synthesis,^[22,23] electro-deposition or replication,^[17,24–26] lift-off process,^[27,28] aqueous metal reduction,^[29,30] inclusion of nanoparticles,^[31,32] sol-gel process,^[33] etc.). Alternatively, coassembly strategies can be employed in which the BCP self-assembly process acts as a structure directing agent for nano-objects^[34–37] or metal-oxide precursors.^[16,38–40] Most of the aforementioned applications require the precise positioning or registration of the BCP nanostructure arranged within a highly ordered nanoscale array. However, even if the equilibrium energy state of a BCP morphology would be reached for a uniform array of single-grain BCP features, a polygrain BCP structure is generally observed in thin film due to the prevalence of slow coarsening kinetics over the thermodynamic driving force. This weak thermodynamic driving force pushed scientists to develop directed self-assembly (DSA) methods providing means to control the domain alignment and orientation occurring through defect annihilation at grain boundaries. Methods to dictate self-assembly in this regard include solvent vapor annealing (SVA),^[41] unidirectional solution casting,^[42] graded thermal annealing via laser writing,^[43] the application of external mechanical,^[44,45] electrical,^[46,47] or magnetic^[48,49] fields, the use of surface energy modifiers^[50,51] and guiding patterns.^[52,53] For instance, further progresses were achieved in DSA lithography by the synergistic combination of the

1. Introduction

Block copolymer (BCP) self-assembly is an elegant tool to generate complex periodic structures with exquisite symmetries. The driving force inherent to BCP phase behavior is related to the thermodynamic incompatibility between the two or more chemically distinct building blocks allowing BCP chains to microphase-separate into a panoply of well-ordered nanostructures with periodicities ranging from a few nanometers to hundreds of nanometers.^[1–3] Innovative polymerization methods capable of generating on-demand BCP architectures associated with the conceptual framework of self-consistent field theory (SCFT) enable the rationalization of the rich bulk phase behavior of BCPs over the last decades, with, for the most simple di-BCP phase diagram, a progression of morphologies from spheres arranged into a body-centered cubic (BCC) lattice,

hexagonally packed cylinders, double gyroid, to lamellae.^[1,4–6] As virtually any combination of chemistry and sequencing is attainable by macromolecular design,^[3] BCPs offer tremendous opportunities for the design of functional materials with applications in biology, separation process and nanotechnologies among others.^[7–9]

Further opportunities in the development of BCP nanotechnologies are linked to the formation of well-ordered periodic nanoscale patterns in thin film configuration with nanolithography as the “flagship” application. Indeed, the chemical dissimilarities between the domains allow selective removal by plasma or wet etching of one of the BCP domains leading to a mask that can be further used to define features in microelectronic applications. The formation of self-assembled patterns in thin film can also be combined with hybridization methods,^[10] thus converting the BCP patterns into functional structured surfaces such as bit-patterned media,^[11–13] field effect transistors,^[14,15] optical metamaterials,^[16–18] or photonic structures.^[19–21] This can be performed by using the nanostructured BCP scaffold as a template for a subsequent deposition of functional materials (via sequential infiltration synthesis,^[22,23] electro-deposition or replication,^[17,24–26] lift-off process,^[27,28] aqueous metal reduction,^[29,30] inclusion of nanoparticles,^[31,32] sol-gel process,^[33] etc.). Alternatively, coassembly strategies can be employed in which the BCP self-assembly process acts as a structure directing agent for nano-objects^[34–37] or metal-oxide precursors.^[16,38–40] Most of the aforementioned applications require the precise positioning or registration of the BCP nanostructure arranged within a highly ordered nanoscale array. However, even if the equilibrium energy state of a BCP morphology would be reached for a uniform array of single-grain BCP features, a polygrain BCP structure is generally observed in thin film due to the prevalence of slow coarsening kinetics over the thermodynamic driving force. This weak thermodynamic driving force pushed scientists to develop directed self-assembly (DSA) methods providing means to control the domain alignment and orientation occurring through defect annihilation at grain boundaries. Methods to dictate self-assembly in this regard include solvent vapor annealing (SVA),^[41] unidirectional solution casting,^[42] graded thermal annealing via laser writing,^[43] the application of external mechanical,^[44,45] electrical,^[46,47] or magnetic^[48,49] fields, the use of surface energy modifiers^[50,51] and guiding patterns.^[52,53] For instance, further progresses were achieved in DSA lithography by the synergistic combination of the

N. Demazy, Dr. C. Cummins, Dr. G. Fleury
 Univ. Bordeaux
 CNRS
 Bordeaux INP
 LCPO
 UMR 5629, F-33600 Pessac, France
 E-mail: gffleury@enscbp.fr

Dr. K. Aissou
 Institut Européen des Membranes
 Université de Montpellier – CNRS – ENSCM
 300 Avenue du Professeur Emile Jeanbrau
 F-34090 Montpellier, France

 The ORCID identification number(s) for the author(s) of this article can be found under <https://doi.org/10.1002/admi.201901747>.

DOI: 10.1002/admi.201901747

“bottom-up” BCP self-assembly with the “top-down” fabrication of guiding patterned templates relying on chemoepitaxy^[54,55] and graphoepitaxy.^[56,57] The interested reader is referred to comprehensive reviews detailing these DSA methodologies and their implementation.^[58–62]

Nevertheless, the geometric features attainable from di-BCP architectures are limited considering the thermodynamic driving force leaning toward the formation of structures minimizing the interface between the blocks, even if deviations from the bulk equilibrium structure have been observed in thin films due to boundary or commensurability effects.^[63–67] Therefore, strategies to enrich the variety of structures obtained by BCP self-assembly processes are gaining momentum in the BCP community.^[3,68–70] A first strategy builds on macromolecular engineering by incorporating additional chemical blocks in complex architectures (from linear to star, brush, H-shaped or supramolecular) in order to bring morphological variety and advanced functional properties.^[71–76] Another strategy is to design novel 3D nanostructures with unique structural motifs and symmetries by a layering process derived from the iterative self-assembly of BCP layers. This layer-by-layer stacking of BCP patterns comes in a variety of multifaceted processes as shown in **Figure 1**: application of a protective layer, direct deposition of a BCP layer on top of an immobilized one, cross-linking of the underlying pattern and transfer of a nanostructured film on top of an underlying one. The breadth of methods to generate these complex structures is directly linked to the advances in the control of BCP self-assembly in thin films through DSA and hybridization methods.

Here, we review the opportunities inherent to the iterative BCP self-assembly by considering the emerging strategies for the generation of “non-native” morphologies (i.e., BCP nanostructures deviating from the bulk equilibrium phase behavior). We will particularly focus on the methods allowing fine control of 3D structures resulting from iterative self-assembly approaches. The emergence of 3D nanoelectronic devices^[77,78] highlights the importance of advancing nanofabrication methods to precisely position material stack layers. In this regard, there is a clear motivation to assess the potential of BCP materials that can be patterned to form “non-native” morphologies.^[69] This progress report therefore centers on the most recent techniques disclosed in the BCP field that show promise to benefit a range of device applications. Finally, we highlight that such nontrivial structures could find applications in critical technological fields where precise 3D placement is imperative including nanoelectronics (for integrated logic and memory features),^[79,80] membranes (for high active surface areas),^[81] batteries (for ion transport),^[82] and nanophotonics (for metamaterials).^[21]

2. Layering of Block Copolymer Patterns

Pioneering works by Osuji and co-workers demonstrated how the deposition of BCP layers by electrospray deposition suggests an ability for the formation of complex morphologies, only by selecting the sequence of BCP materials deposition.^[83] Indeed, the deposition of sub-micron droplets formed by electrospray fluid atomization allows the continuous growth of BCP



Nils Demazy is currently a Ph.D. candidate in Material Science at Laboratoire de Chimie des Polymères Organiques (LCPO, University of Bordeaux), with Dr. Guillaume Fleury. He received his engineering degree in materials science at "Ecole Supérieure de Physique et de Chimie Industrielle" (ESPCI, Paris) in 2017, and a master degree in chemistry at "Université Pierre et Marie Curie" (UPMC, Paris) in 2018. His current research focuses on the fabrication of multilayered block-copolymer thin films to create 3D nanostructures for novel nanodevice applications.



Cian Cummins is currently a postdoctoral researcher at the University of Bordeaux studying block copolymer thin films for photonic applications with Dr. Guillaume Fleury and Dr. Virginie Ponsinet. His other research interests focus on developing new methods for modifying nanoscale polymer templates for semiconductor, sensing, and energy applications. He completed his Ph.D. on inorganic block copolymer nanolithography in 2015 (University College Cork, Ireland) with Prof. Mick Morris.



Guillaume Fleury is an associate professor at Laboratoire de Chimie des Polymères Organiques (LCPO, University of Bordeaux) and focuses his research on the macromolecular engineering and physical chemistry of complex polymer systems with an emphasis on nanostructured materials for emerging nanotechnologies. Guillaume received a Ph.D. in materials science from the University of Strasbourg in 2005 working on supramolecular polymeric materials. Following his Ph.D., he completed a postdoctoral fellowship at the University of Minnesota working on block copolymer self-assembly.

thin films providing a versatile approach to build composite layered BCP nanostructures. An exquisite demonstration was provided a few years later by Choo et al. with the production

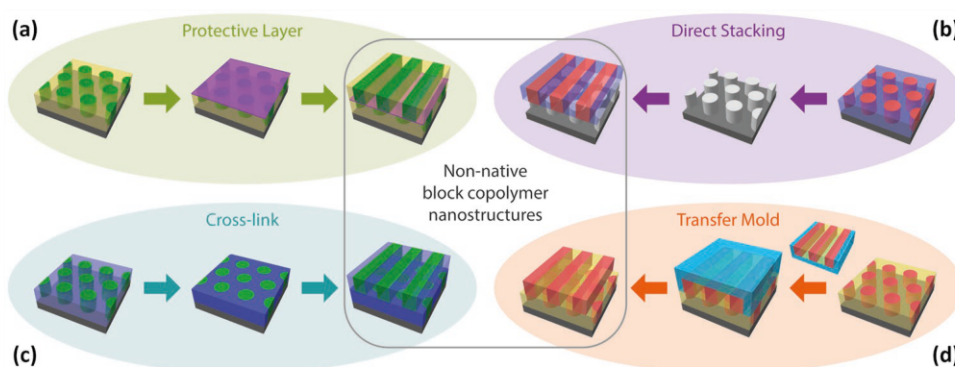


Figure 1. Schematic illustration of various iterative self-assembly methods for the generation of 3D structures beyond the native BCP morphologies. a) deposition of a nanostructured BCP thin film onto a protective layer, b) direct stacking of layered BCP structures via an immobilization method, c) stacking of cross-linked BCP patterns, and d) BCP film transfer method on top of a nanostructured BCP layer.

of lamellar heterolattices (i.e., lamellar stacks of varying periodicity) by sequential electrospray deposition of dilute solutions of poly(styrene)-*block*-poly(4-vinylpyridine) (PS-*b*-P4VP) chains having different molecular weights.^[84] Interestingly, depending on the substrate temperature, distinct layers (sharp interface profiles) or graded layers (smooth interface profile) were produced by altering the inter-diffusion of BCP chains, although orientation control and respective alignment of the BCP layers were not demonstrated.

A step forward for the formation of customized 3D layered BCP structures was demonstrated via the definition of complex mesh patterns for which the control of the crossing angle allows the realization of all possible 2D Bravais lattice symmetries as shown in **Figure 2**.^[85–88] Indeed, the orientation of different superposed layers of cylinders issued from BCP self-assembly can be directly controlled by topography to produce nonequilibrium morphologies in thin films. Tavakkoli et al. pioneered the fabrication of 3D multilevel structures of cylinder arrays with controllable angles, bends and junctions whose geometries were dictated by periodic arrays of posts obtained by electron-beam lithography (see **Figure 2a,b**).^[85,89] In particular, they demonstrated how a periodic array of posts could independently control the orientation of individual layers of cylinders in BCP bilayers through the control of the chemical affinity between the posts and the BCP domains. An exceptional combinatorial control over the final structure was achieved by fine tuning of postarray geometrical features allowing the fabrication of various aperiodic mesh arrays. As a result, 3D cross-point structures, highly attractive for the fabrication of memory arrays, were formed through the connection between cylinders of different layers.^[85]

Several other processes have been described in the literature to obtain these multilayered mesh patterns using either film transfer methods or iterative self-assembly of BCP layers. Nanotransfer printing of BCP layers, allowing a long range ordering of the BCP structure through the use of nanopatterned poly(dimethyl siloxane) (PDMS) mold have been demonstrated by Jeong et al. on various types of conformable substrates (indium tin oxide (ITO), Kapton, poly(3,4-ethylenedioxythiophene):poly(styrene sulfonate) (PEDOT:PSS)).^[86] This method allows the sequential printing of BCP layers on patterned substrates while selecting the crossing angle through the transfer

process of the second layer (**Figure 2c,d**). Another demonstration of film transfer process was proposed by Abate et al. who deposited a free-standing cylinder-forming BCP monolayer on top of a shear-aligned one.^[90] The underlying cylinder layer acts then as a seed site to control the ordering of the final assembly during a subsequent thermal annealing step, highlighting the strong orientation coupling induced by the bottom layer.

BCP layers can also be independently stacked through the use of intercalated silicon or graphene separation layers (see **Figure 2e,f**).^[87,91] Likewise, both chemoepitaxy and graphoeptitaxy which provide long range ordering of the BCP structure have proven to be compatible with such processes, to direct the orientation of mesh arrays. In particular, Kim et al. demonstrated how a chemically modified graphene layer can be used to screen the topographical and surface energy modulations induced by an underlying gold pattern obtained from nanostructured BCP thin film. The overlay of a second nanostructured BCP thin film on top of the separation layer generates a double layer gold mesh pattern without epitaxial registration between the layered structures. Interestingly, by combining such a method with DSA, square array of dots, widely required for microelectronic device architecture, could be fabricated from mesh arrays via double steps of orthogonal etching.^[87]

3. Cross-Linking for Sequential Deposition of BCP Patterns

Alternatively, BCPs can be designed to incorporate cross-linkable moieties into their architecture in order to immobilize the underlying BCP layers for a subsequent deposition process.^[92–95] Pioneering works by Kim et al. using cylinder-forming poly(styrene)-*block*-poly(methyl methacrylate) (PS-*b*-PMMA) with reactive benzocyclobutene functionality inserted in the PS block have demonstrated how the stacking of cross-linked BCP patterns can be utilized to register the cylindrical domains of overlying layers formed on top of the underlying one (see **Figure 3a,b**).^[92] In an attempt to control the sidewall profile of nanostructures obtained from lamellar-forming PS-*b*-PMMA BCPs, He et al. reported vertically graded structures for which the domain size was tuned by the addition of cross-linkable PS or PMMA homopolymers while keeping

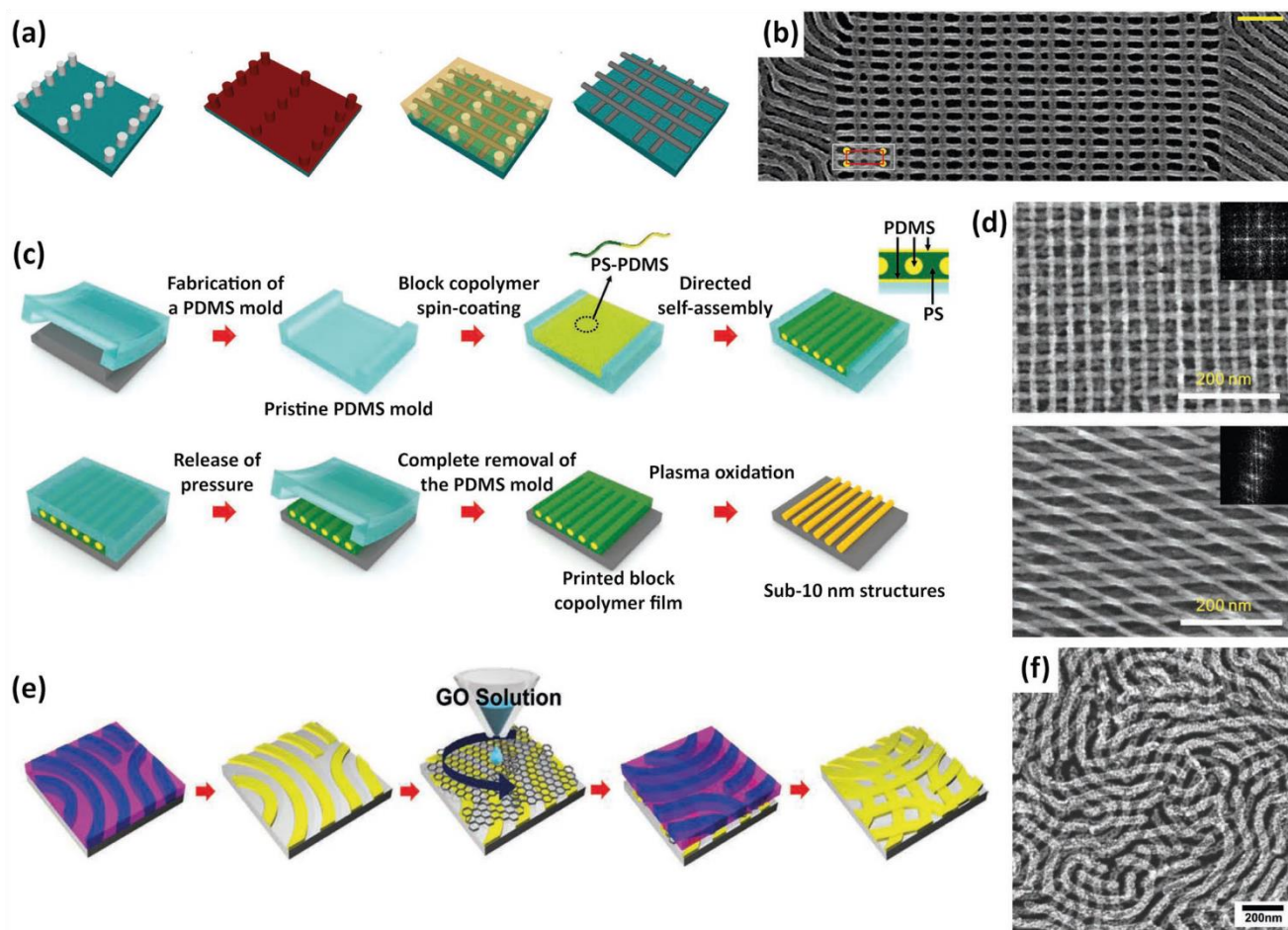


Figure 2. a,b) Schematic process flow for the fabrication of a bilayer BCP array using the post-templating method and SEM image of the multilevel structure (scale bar: 100 nm): a cylindrical PS-*b*-PDMS bilayer is templated by an array of functionalized posts to form oxidized PDMS mesh structures after plasma treatment. Reproduced with permission.^[89] Copyright 2014, Wiley-VCH. c,d) Process flow for nanotransfer printing of BCP patterns and SEM images of two double-layer mesh structures with different crossing angles: a patterned PDMS mold is used to guide the self-assembly of a PS-*b*-PDMS BCP followed by its transfer on a substrate. The sequential printing of BCP structures leads to mesh patterns with controllable crossing angle. Reproduced with permission.^[86] Copyright 2012, Wiley-VCH. e,f) Gold mesh array fabrication procedure: a protective chemically modified graphene layer is deposited on top of a gold nanowire pattern formed from BCP self-assembly which allows the deposition of a second nanostructured BCP layer. Reproduced with permission.^[87] Copyright 2013, Wiley-VCH.

the registration between the stacked layers.^[94] The non-native undercut (i.e., negative sidewall) profiles of the PS lamellar nanostructure resulting from the selective removal of the PMMA domains were proven to facilitate subsequent lift-off process for the formation of gold nanowires.

More sophisticated stacks obtained from cross-linkable BCPs were also reported by combining BCP layers with different morphologies. For instance, Jung et al. have demonstrated how lamellae-on-cylinders can be obtained from stacking a cross-linkable cylinder-forming PS-*b*-PMMA BCP layer with a lamellar-forming PS-*b*-PMMA BCP layer (Figure 3c,d).^[93,96] The study of the epitaxial relationships between both layers showed that the PMMA lamellae were remarkably registered to the underlying PMMA cylinders due to a favorable minimization of the interfacial free energies of the two BCP layers facilitated by the commensurability between their interdomain spacings.

Another simple method to create nanoscale cross-patterns (square, rectangular, and rhombic) over macroscopic areas was

proposed by Kim et al. via shear-alignment of distinct layers of cylinder-forming polystyrene-*block*-poly(ferrocenylisopropylmethylsilane) (PS-*b*-PFiPMS) layers BCPs, immobilized through cross-linking using ultraviolet light (Figure 3e,f).^[97] The pattern symmetry could be adjusted through the variation of the cylinder-forming PS-*b*-PFiPMS pitches (i.e., rectangular vs square) and through the independently set shear directions for the two layers (square vs rhombic). This double-layered cross-bar pattern further serves as template for the definition of four-fold symmetry lattices of various features (nanowells, nanoposts, nanodots) using various etching and lift-off techniques.

Recently, Oh et al. have demonstrated how a cross-linked layer can also be applied to the fabrication of orientation-controlled 3D multilayer structures.^[98] Through filtered plasma treatment of BCP thin films, a thin cross-linked layer was formed by the physical collisions of neutral species and retains the original chemical BCP composition, thus acting as a neutral top-coat for the underlying BCP layer or as neutral underlayer

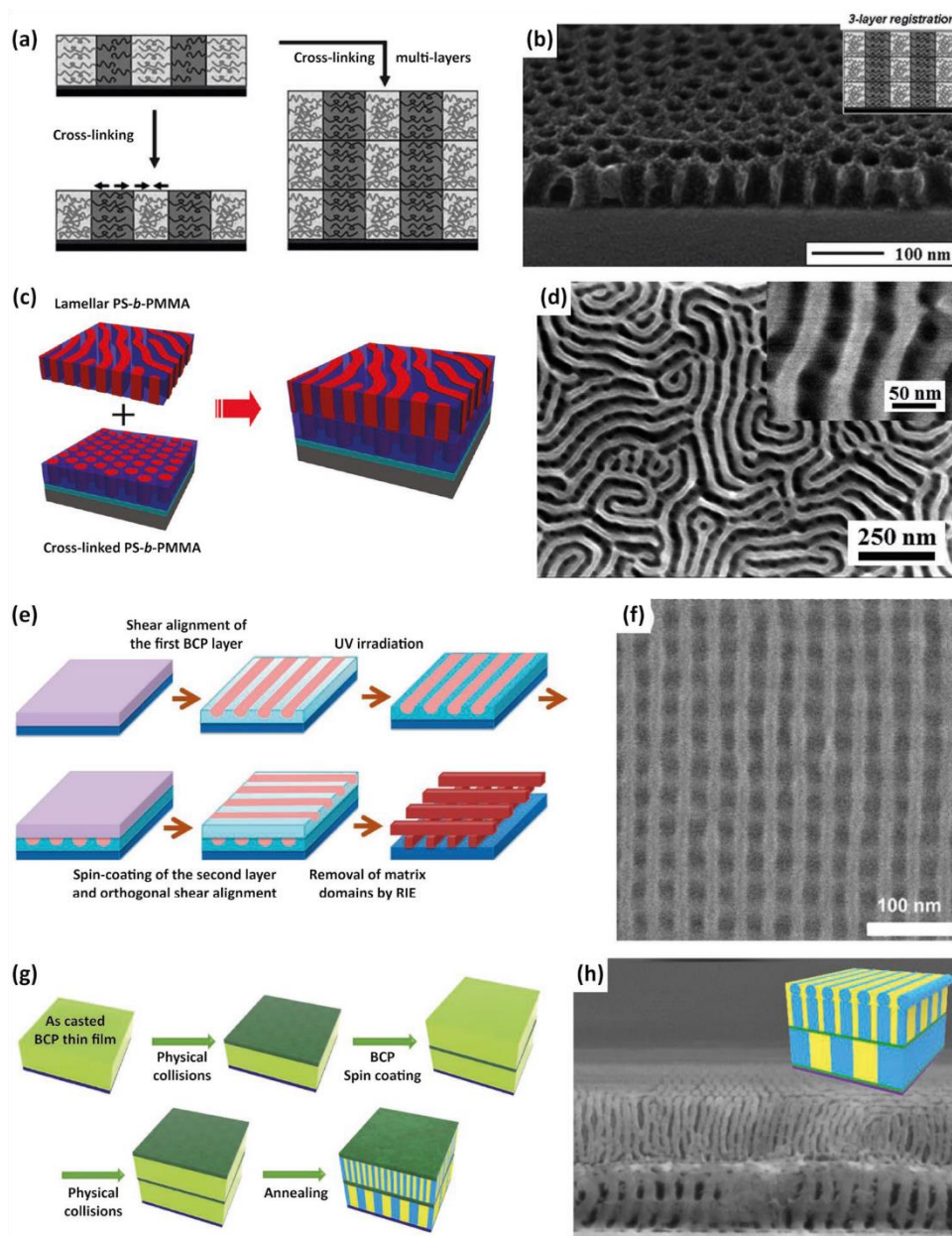


Figure 3. a,b) Schematics of the cross-linking and registration processes for stacked cylinder-forming PS-*b*-PMMA layers bearing reactive benzocyclobutene functionalities within the PS block and cross-sectional SEM image of a three layered BCP film in which the PMMA domains were etched by UV-exposure and acetic acid treatment. Reproduced with permission.^[92] Copyright 2008, Royal Society of Chemistry. c,d) Process flow for the formation of multilayered BCP nanostructures with controlled domain orientation produced from cross-linkable BCP thin films and SEM image of a double-layer BCP structure consisting of an upper lamellar layer formed on an underlying cylindrical layer. Reproduced with permission.^[93] Copyright 2011, American Chemical Society. e,f) Fabrication of nanoscale square patterns using cross-linked cylinder-forming BCP layers aligned by shear in a cross-pattern and SEM image of a double-layered cross-bar pattern obtained after RIE treatment. Adapted with permission.^[97] Copyright 2014, American Chemical Society. g,h) Schematic process flow for the fabrication of orientation-controlled 3D multilayer structure and cross-sectional SEM image of a hierarchical templated structure consisting of a stack of out-of-plane lamellae, out-of-plane cylinders, and a monolayer of in-plane cylinders: through filtered plasma treatment of an as-casted BCP thin film, a thin cross-linked layer is formed at the top surface while retaining the original chemical BCP composition. Such cross-linked layer can further act as a neutral top-coat for the underlying BCP layer or as neutral underlayer for a BCP layer deposited on top of it. Reproduced under the terms of the Creative Commons Attribution 4.0 International License.^[98] Copyright 2019, the Authors. Published by Springer Nature.

for a BCP layer deposited on top of it. The filtered plasma treated cross-linked layer is conceptually similar to a grafted brush layer of random copolymers correcting the mismatch of surface energy between the BCP domains.^[50] This approach

combined with chemoepitaxy was applied to create hierarchical structures of chemically different BCP patterns with the notable generation of arbitrary sequences of in-plane and out-of-plane features as shown in Figure 3g,h. As a demonstration,

Oh et al. fabricated a BCP stack similar to a fin field-effect transistor (FinFET) structure with sequential layering of out-of-plane lamellae and cylinders covered by a monolayer of in-plane cylinders connecting the apices of the vertical cylinders.

4. Immobilization of BCP Pattern via Hybridization Methods for Subsequent Deposition of BCP Structure

Advances in the formation of complex BCP structures from iterative self-assembly are related to the advent of various hybridization methods^[10] leading to the immobilization of BCP structures. Indeed, the selective transformation of one of the BCP domains into oxides or metals combined with the removal of the BCP scaffold by wet or dry chemistries constitutes an original pathway for the production of non-native morphologies. For instance, Majewski et al. demonstrated fine control over the mesh pattern and symmetry through the conversion of polystyrene-*block*-poly(2-vinylpyridine) (PS-*b*-P2VP) patterns into metallic replicas, enabling the formation of non-native BCP thin film structures by successive layering of PS-*b*-P2VP thin films.^[88] Photo-thermal annealing (i.e., laser-zone annealing) combined with soft-shear effects induced by an elastomeric pad was used to iteratively align the BCP structures, thus producing arbitrary lattice symmetries (Figure 4a,b).

Further progress in the manipulation of iterative BCP self-assembly in thin films were demonstrated by exploiting a “responsive layering” approach^[99] in which subsequent BCP layers order as function of the underlying layers to generate complex 3D structures. This method exquisitely exploits the natural propensity of BCP materials to respond to chemical or topographical fields. This intermediate “responsive layering” approach allows one to manipulate BCP self-assembly toward non-native 3D morphologies as each self-assembled BCP film acts as both a component of the final functional structure and a guiding pattern for the subsequent nanostructured layers. Consequently, immobilized BCP patterns can be used as a topographic or chemical template^[100–102] for a subsequent BCP layer and complex 3D structures can be obtained by iterative self-assembly of layers of BCPs with different molecular weights or compositions.^[103–105] Tavakkoli et al. explored this particular facet for the formation of cross-point structures derived from self-assembly of BCPs with different periodicities.^[104] A first PS-*b*-PDMS layer was self-assembled on a substrate leading to a topographic pattern of oxidized-PDMS cylinders after reactive ion etching (RIE) treatment. This grating pattern was subsequently used as a template to self-assemble a novel BCP layer which orthogonally aligned as regards to the previous layer due to weak chemical interactions between the oxidized-PDMS pattern and the BCP domains. Combining this orthogonal self-assembly process with circular or Y-junction lithographic patterns led to the fabrication of complex nanomesh structures as shown in Figure 4c,d.

Another example of hierarchical nanostructures in which an immobilized BCP pattern acts as a guiding template for the self-assembly of a second BCP layer was provided by Son et al.^[103] Using top-down methods to pattern a PS-*b*-PDMS BCP

of large periodicity, they demonstrated how smaller period BCP patterns are registered on the larger BCP template. Following this methodology, line-on-line, dots-on-line, and dots-in-hole hierarchical structures were produced depending on solvent annealing conditions as shown in Figure 4e–g.

Interestingly, the spherical BCP morphology has attracted particular attention for the realization of hierarchical structures from iterative self-assembly. For instance, density multiplication of single layer hexagonal silica dot pattern was demonstrated by Jin et al. through the stacking of plasma treated sphere-forming PS-*b*-PDMS monolayers.^[106] A first monolayer of hexagonally close-packed dots was formed by spin-coating a highly asymmetric PS-*b*-PDMS BCP blended with PS homopolymer chains. The subsequent deposition of the BCP on top of this first plasma treated layer results in the formation of a dot pattern exhibiting a honeycomb lattice, since the dots of the second layer position themselves in the triangular interstitial positions of the first hexagonal pattern, as shown in Figure 5a,b. The dots formed by spin coating a third BCP monolayer on top of the oxidized honeycomb lattice registered to the hexagonal lattice positions resulting in a three-fold increase in dot density. The driving force governing the spatial positioning of the second and third layers of dots was linked to the topological constraints induced by the former dot layers. It is noteworthy that the addition of PS homopolymer chains was crucial to limit the dot overlap between layers, which is a primary concern for enabling density multiplication methodologies. Recently Jung et al. proposed a more direct approach to form dense dot layers from sphere-forming BCP thin films.^[107] A double layer of PDMS spherical domains was formed by spin-coating a concentrated sphere-forming PS-*b*-PDMS solution in toluene. After plasma treatment, a distinct double pattern of hexagonally packed silica dots was revealed through top-view SEM observation even if the two layers of dots were positioned at their respective sphere layer height (denoted as “pondering” pattern by the authors). Buriak’s group pushed forward their studies on the sequential deposition of dot arrays formed by microphase-separated PS-*b*-PDMS thin films. Using BCPs having different periodicity, they studied the interrelationships between (in)commensurability and epitaxial alignment between different dot layers formed by following the same iterative deposition method of sphere-forming PS-*b*-PDMS layers. The sequential self-assembly of dot layers having different array pitches resulted in the formation of Moiré superstructures with preferential dot lattice orientation derived from the epitaxial registration of the top layer (see Figure 5c,d).^[108]

Rahman et al. progressed further these methodologies by showing how “responsive layering” self-assembly allows access to a huge diversity of morphologies not native to the equilibrium BCP phase diagram, including square and rectangular mesh patterns, dots localized between nanopores, dots bridging lines. Their approach also relies on sequential deposition and immobilization of 2D nanostructured BCP thin films but takes further advantage of a secondary registration field induced through the BCP chain stretching/compression (i.e., the second-layer morphology orients and registers so as to accommodate the underlying height variation by overlapping the interblock interface atop of it). As shown in Figure 6a, the detailed process flow is based on the selective infiltration

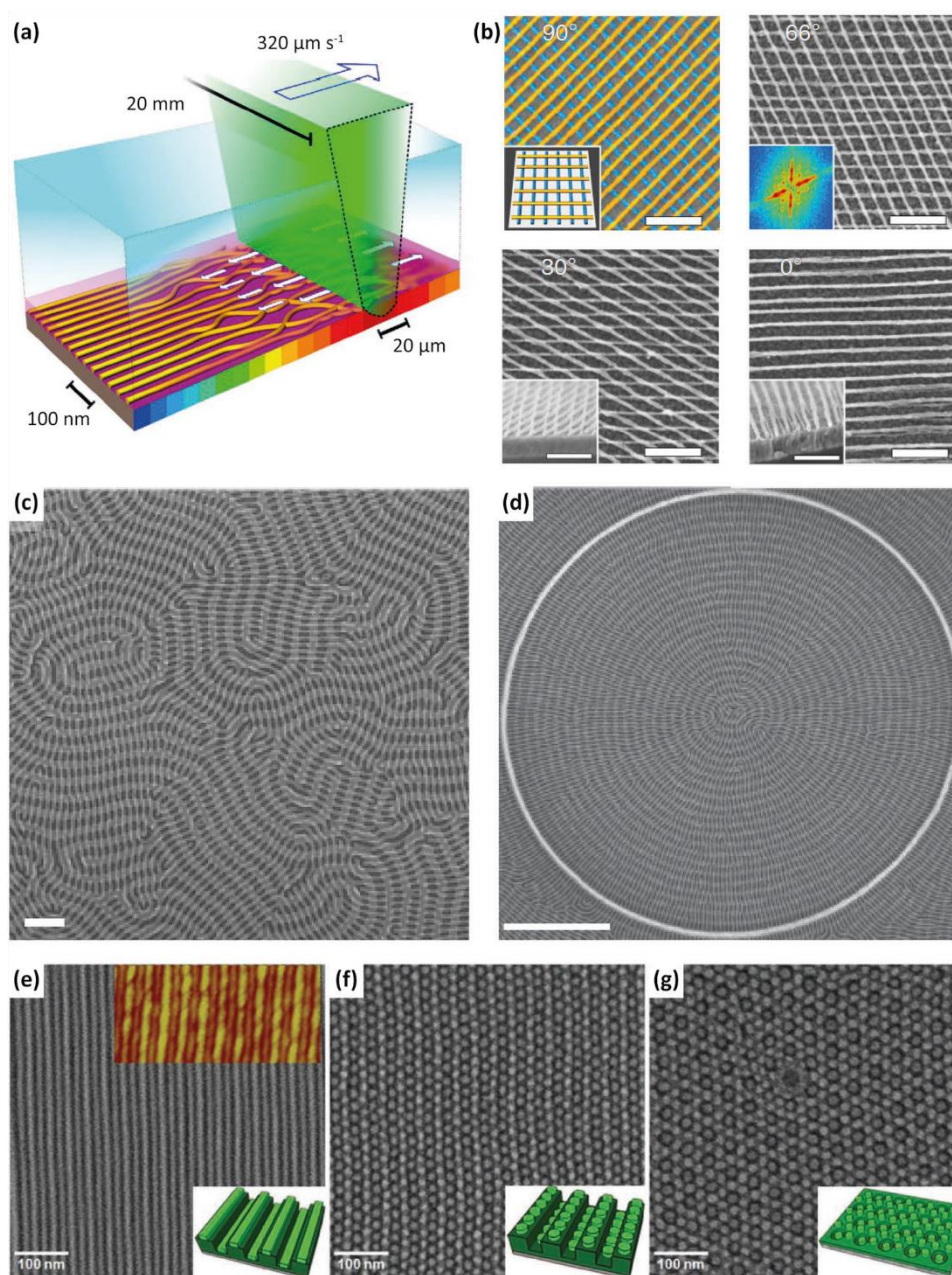


Figure 4. a,b) Schematics of photo-thermal annealing set-up combined with soft-shear effects (soft shear-laser zone annealing (SS-LZA)) for the alignment of BCP structures and SEM images of double-layered Pt mesh patterns obtained using various angles between the SS-LZA sweeps (scale bars: 200 nm). Reproduced under the terms of the Creative Commons Attribution 4.0 International License.^[88] Copyright 2015, the Authors. Published by Springer Nature. c,d) Nanomesh pattern obtained via orthogonal self-assembly of PS-*b*-PDMS BCPs of different molecular weights on bare Si (scale bars: 100 nm) and on a circular template obtained by electron beam lithography from a hydrogen silsesquioxane resist (scale bars: 500 nm), respectively. Adapted under the terms of the Creative Commons Attribution 4.0 International License^[104] Copyright 2016, the Authors. Published by Springer Nature. Hierarchical structures including e) line-on-line, f) dots-on-line, and g) dot-in-hole made from a small period PS-*b*-PDMS BCP templated by a larger period PS-*b*-PDMS BCP. The different hierarchical structures were obtained by tuning the SVA conditions. Reproduced with permission.^[103] Copyright 2011, Wiley-VCH.

synthesis of nanostructured PS-*b*-PMMA thin films which generates a topographical pattern reproducing the BCP morphological features. After neutralization of the immobilized layer by a random copolymer brush to prevent chemoepitaxial replication, a second PS-*b*-PMMA layer is deposited on top of the underlying BCP pattern which self-assembles in response to

the aforementioned topographical field. A striking demonstration was given by combinatorially stacking the three different classical 2D BCP morphologies using PS-*b*-PMMA of different compositions and molecular weights resulting in a cornucopia of multilayered structures with a high level of spatial control (see Figure 6b,c).

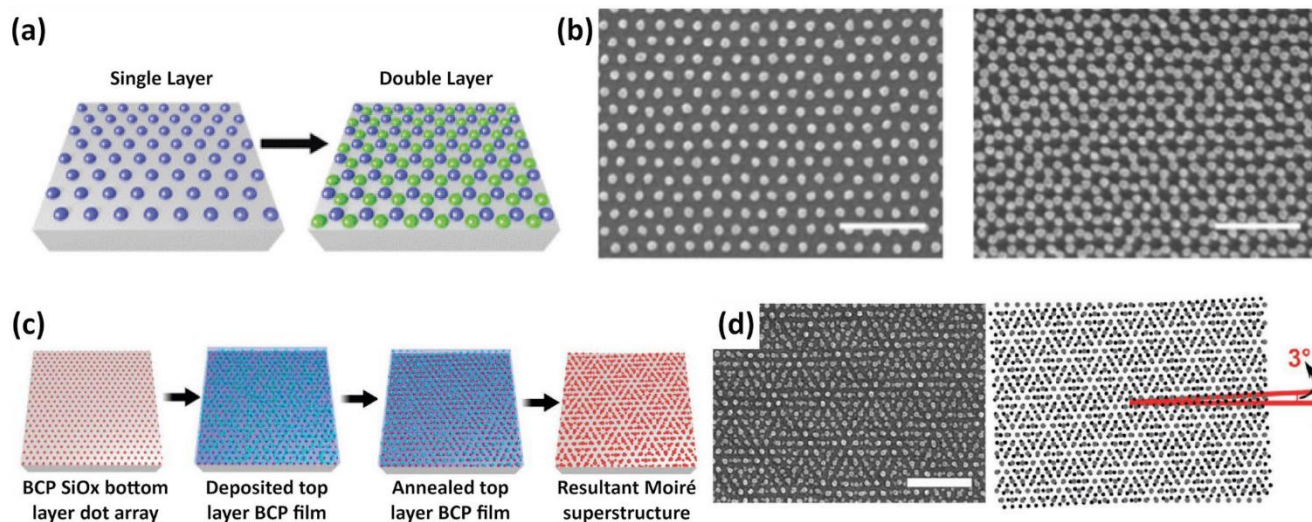


Figure 5. a,b) Sequential self-assembly process for the formation of density-doubled dot patterns from sphere-forming PS-*b*-PDMS BCP and SEM images of the single layer hexagonal and double layer honeycomb dot patterns (scale bars: 200 nm). Reproduced with permission.^[106] Copyright 2016, American Chemical Society. c,d) Process flow for the fabrication of dot-array-based Moiré superstructures from sphere-forming PS-*b*-PDMS BCPs with different molecular weights and SEM image of a resulting structure with a relative rotation angle of 3° between the two layers (scale bar: 250 nm). Adapted with permission.^[108] Copyright 2017, American Chemical Society.

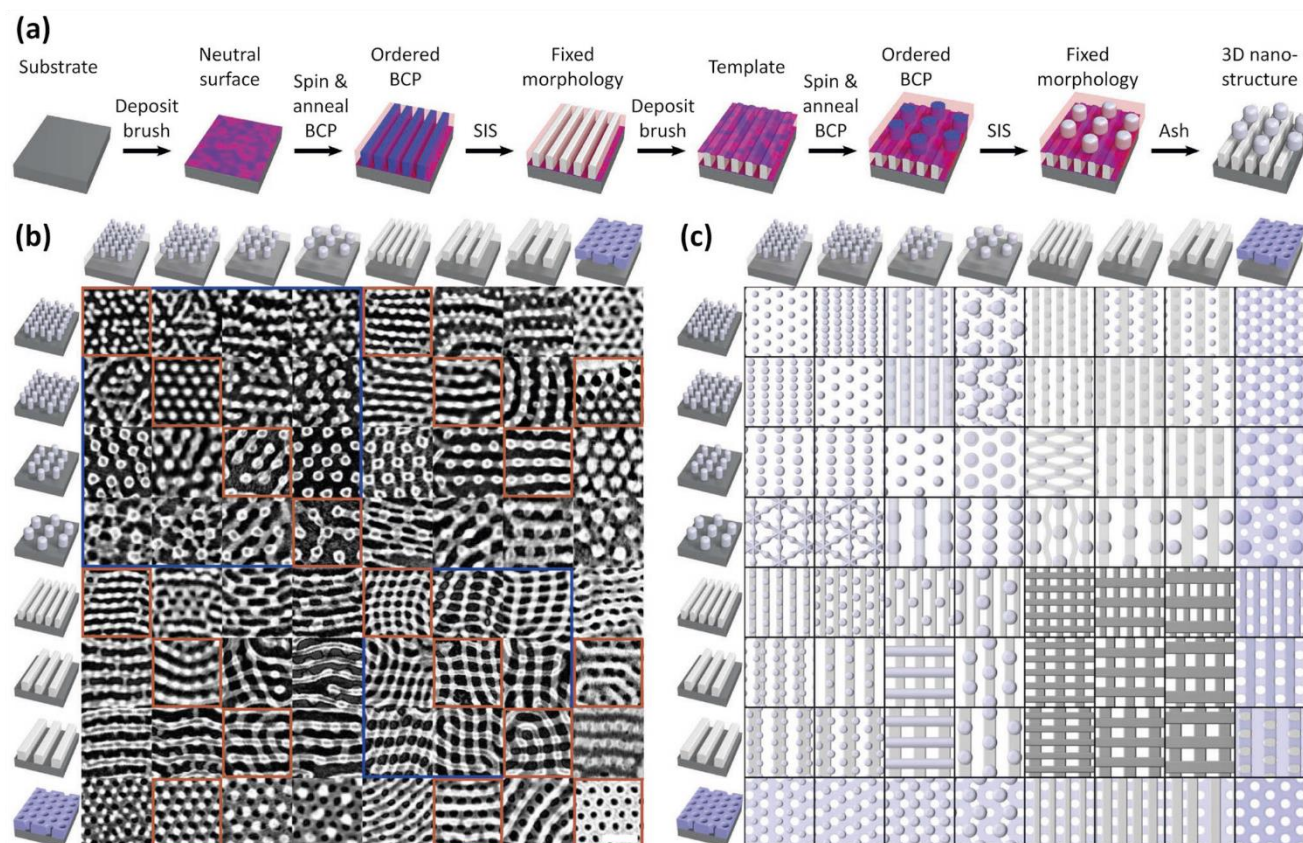


Figure 6. a) Process flow for the formation of 3D nanostructures obtained from the “responsive layering” approach. b) SEM images showing the considerable diversity of two-layer nanostructures formed by the iterative self-assembly of BCP thin films using the “responsive layering” approach (scale bar: 100 nm). c) Schematics of the idealized 3D nanostructures. Adapted under the terms of the Creative Commons Attribution 4.0 International License.^[99] Copyright 2016, the Authors. Published by Springer Nature.

5. Conclusion and Outlook

During the last decades, BCP self-assembly in thin film has enabled researchers in their quest to design ordered microstructures with nanometrically defined periodicity. Tremendous opportunities have emerged from these studies enabling the fabrication of functional materials from nanostructured BCP thin films; the most striking example being nanopatterning applications for semiconductor and memory uses. While directed self-assembly methods allow the generation of 2D perfect ordered patterns, the intrinsic BCP phase behavior limits the variability of structures and symmetries achievable through BCP self-assembly. We have highlighted that iterative self-assembly in the form of stacking BCP layers allows access to an enormous diversity of non-native morphologies beyond the classical bulk equilibrium di-BCP phase diagram. Such great progress in the design of multilayered hierarchical structures was enabled by both a deep understanding of the underlying mechanisms controlling the BCP self-assembly in thin film and the development of hybridization methods for the immobilization of the BCP patterns. It is noteworthy that theoretical and modeling efforts have provided guidance to expand the landscape of complex structures by assessing the critical parameters and design rules allowing the fine control of the multilayered BCP structures, and therefore is viewed as pivotal in future multilayer designs of non-native BCP morphologies. As a result, the BCP community faces up to a challenge in translating these novel complex structures into potent applicative advances with smart functionalities, as only a scarce number of the multilayered structures described herein has been transitioned to device manufacturing. For instance, 3D nanostructures formed by directed self-assembly of BCP multilayers could be valuable in cutting-edge technologies such as optical metamaterials or metasurfaces,^[21,109,110] graphene nanoribbon or fin field effect transistors,^[98,111,112] filtration membranes with improved permeability-selectivity tradeoff,^[113–115] cross-point memories,^[85] or optoelectronic devices.^[26,116] Additionally, the conversion of the BCP scaffolds into functional inorganic materials^[10] broadens the scope of applications by adding specific optical, electronic, or magnetic properties to the 3D nanostructures.^[21,70,117] Nevertheless, several challenges still need to be addressed for the advent of multilayered BCP structures in nanotechnology. Powerful DSA methods effective in the 3D space are required for the precise registration of the BCP features, as such approaches will thus enable a high scalability of self-assembly processes. Understanding defect annihilation mechanisms in the formation of these complex structures is also mandatory, as most of the applications require specific and intricate device architectures with a very low level of defectivity. Another challenge is to extend iterative self-assembly to ultralow dimensions by using “high χ ” BCPs as building blocks while creative macromolecular engineering could enrich the pool of starting morphologies. In summary, this progress report has overviewed exquisite demonstrations of multiple BCP layer self-assembly strategies, however, we also point to the need to define a better understanding of key influencing factors governing precise stack placement. For example, future research and development exploring the surfaces and interfaces of 3D BCP features will further allow us to not only advance

morphology intricacy, but will also enable us to define limitations of particular systems and approaches. Moreover, given that the “non-native” BCP field is in its infancy, there are many important learnings that will be established in the coming years that will progress the transition to new devices. In particular, we suggest further exploration researching the influence of surface chemistry between stack layers, the effect of using different BCP chemistries and resulting orientation control, and advanced 3D characterization studies (e.g., GISAXS and TEM tomography) will help in the realization of novel device concepts. Such milestones on non-native BCP control coupled with the opportunities inherent to sophisticated functionalization methods will further enhance the viability of multilayered BCP structures for nanotechnologies.

Acknowledgements

N.D. and C.C. are grateful for financial support from the University of Bordeaux and the LabEx AMADEus (ANR-10-LABEX-0042-AMADEUS), respectively. This work was supported by the European Union Horizon 2020 research and innovation program under grant agreement #760915 (SUN-PILOT project) and the French National Research Agency under grant agreement ANR-16-CE24-0007 (Dirac-III-V project).

Conflict of Interest

The authors declare no conflict of interest.

Keywords

3D nanostructures, block copolymers, iterative self-assembly, nanopatterning, registration

Received: October 15, 2019

Revised: November 21, 2019

Published online: December 29, 2019

- [1] F. S. Bates, G. H. Fredrickson, *Annu. Rev. Phys. Chem.* **1990**, *41*, 525.
- [2] A. J. Meuler, M. a. Hillmyer, F. S. Bates, *Macromolecules* **2009**, *42*, 7221.
- [3] F. S. Bates, M. a. Hillmyer, T. P. Lodge, C. M. Bates, K. T. Delaney, G. H. Fredrickson, *Science* **2012**, *336*, 434.
- [4] L. Leibler, *Macromolecules* **1980**, *13*, 1602.
- [5] M. W. Matsen, M. Schick, *Phys. Rev. Lett.* **1994**, *72*, 2660.
- [6] M. W. Matsen, *Macromolecules* **2012**, *45*, 2161.
- [7] C. Park, J. Yoon, E. L. Thomas, *Polymer* **2003**, *44*, 6725.
- [8] *Block Copolymers in Nanoscience* (Eds: M. Lazzari, G. Liu, S. Lecommandoux), Wiley-VCH, Weinheim, Germany **2006**.
- [9] I. W. Hamley, *Angew. Chem., Int. Ed.* **2003**, *42*, 1692.
- [10] C. Cummins, T. Ghoshal, J. D. Holmes, M. A. Morris, *Adv. Mater.* **2016**, *28*, 5586.
- [11] K. Aissou, T. Alnasser, G. Pecastaings, G. Goglio, O. Toulemonde, S. Mornet, G. Fleury, G. Hadziioannou, *J. Mater. Chem. C* **2013**, *1*, 1317.
- [12] Y. S. Jung, W. Jung, C. A. Ross, *Nano Lett.* **2008**, *8*, 2975.
- [13] J. Y. Cheng, C. A. Ross, V. Z.-H. Chan, E. L. Thomas, R. G. H. Lammertink, G. J. Vancso, *Adv. Mater.* **2001**, *13*, 1174.

- [14] C. T. Black, *Appl. Phys. Lett.* **2005**, *87*, 163116.
- [15] J. G. Son, M. Son, K. J. Moon, B. H. Lee, J. M. Myoung, M. S. Strano, M. H. Ham, C. A. Ross, *Adv. Mater.* **2013**, *25*, 4723.
- [16] M. C. Orilall, U. Wiesner, J. Lee, F. J. DiSalvo, U. Wiesner, S. M. Gruner, A. Baiker, U. Wiesner, F. J. DiSalvo, U. Steiner, H. J. Snaith, U. Steiner, H. J. Snaith, *Chem. Soc. Rev.* **2011**, *40*, 520.
- [17] S. Vignolini, N. A. Yufa, P. S. Cunha, S. Guldin, I. Rushkin, M. Stefik, K. Hur, U. Wiesner, J. J. Baumberg, U. Steiner, *Adv. Mater.* **2012**, *24*, OP23.
- [18] J. A. Dolan, B. D. Wilts, S. Vignolini, J. J. Baumberg, U. Steiner, T. D. Wilkinson, *Adv. Opt. Mater.* **2015**, *3*, 12.
- [19] Y. Kang, J. J. Walsh, T. Gorishnyy, E. L. Thomas, *Nat. Mater.* **2007**, *6*, 957.
- [20] H. S. Lim, J. H. Lee, J. J. Walsh, E. L. Thomas, *ACS Nano* **2012**, *6*, 8933.
- [21] M. Stefik, S. Guldin, S. Vignolini, U. Wiesner, U. Steiner, *Chem. Soc. Rev.* **2015**, *44*, 5076.
- [22] Q. Peng, Y.-C. C. Tseng, S. B. Darling, J. W. Elam, *Adv. Mater.* **2010**, *22*, 5129.
- [23] Q. Peng, Y. C. Tseng, S. B. Darling, J. W. Elam, *ACS Nano* **2011**.
- [24] T. Thurn-Albrecht, J. Schotter, G. A. Kastle, N. Emley, T. Shibauchi, L. Krusin-Elbaum, K. Guarini, C. T. Black, M. T. Tuominen, T. P. Russell, *Science* **2000**, *290*, 2126.
- [25] V. N. Urade, T. C. Wei, M. P. Tate, J. D. Kowalski, H. W. Hillhouse, *Chem. Mater.* **2007**, *19*, 768.
- [26] E. J. W. Crossland, M. Kamperman, M. Nedelcu, C. Ducati, U. Wiesner, D.-M. Smilgies, G. E. S. Toombes, M. A. Hillmyer, S. Ludwigs, U. Steiner, H. J. Snaith, *Nano Lett.* **2009**, *9*, 2807.
- [27] M. Park, P. M. Chaikin, R. A. Register, D. H. Adamson, *Appl. Phys. Lett.* **2001**, *79*, 257.
- [28] K. W. Guarini, C. T. Black, K. R. Milkove, R. L. Sandstrom, *J. Vac. Sci. Technol., B: Microelectron. Nanometer Struct.–Process., Meas., Phenom.* **2001**, *19*, 2784.
- [29] J. Chai, D. Wang, X. Fan, J. M. Buriak, *Nat. Nanotechnol.* **2007**, *2*, 500.
- [30] J. Chai, J. M. Buriak, *ACS Nano* **2008**, *2*, 489.
- [31] S. B. Darling, N. A. Yufa, A. L. Cisse, S. D. Bader, S. J. Sibener, *Adv. Mater.* **2005**, *17*, 2446.
- [32] N. C. Bigall, B. Nandan, E. B. Gowd, A. Horechyy, A. Eychmüller, *ACS Appl. Mater. Interfaces* **2015**, *7*, 12559.
- [33] H.-Y. Y. Hsueh, H.-Y. Y. Chen, M.-S. S. She, C.-K. K. Chen, R.-M. M. Ho, S. Gwo, H. Hasegawa, E. L. Thomas, *Nano Lett.* **2010**, *10*, 4994.
- [34] A. Haryono, W. H. Binder, *Small* **2006**, *2*, 600.
- [35] Q. Zhang, S. Gupta, T. Emrick, T. P. Russell, *J. Am. Chem. Soc.* **2006**, *128*, 3898.
- [36] K. Thorkelsson, A. J. Mastroianni, P. Ercius, T. Xu, *Nano Lett.* **2012**, *12*, 498.
- [37] K. Aissou, G. Fleury, G. Pecastaings, T. Alnasser, S. Mornet, G. Goglio, G. Hadziioannou, *Langmuir* **2011**, *27*, 14481.
- [38] E. L. Crepaldi, G. J. d. A. A. Soler-Illia, D. Grosso, F. Cagnol, F. Ribot, C. Sanchez, *J. Am. Chem. Soc.* **2003**, *125*, 9770.
- [39] G. J. Galo, E. L. Crepaldi, D. Grosso, C. Sanchez, *Curr. Opin. Colloid Interface Sci.* **2003**, *8*, 109.
- [40] J. Lee, M. Christopher Orilall, S. C. Warren, M. Kamperman, F. J. DiSalvo, U. Wiesner, *Nat. Mater.* **2008**, *7*, 222.
- [41] C. Sinturel, M. Vayer, M. Morris, M. A. Hillmyer, *Macromolecules* **2013**, *46*, 5399.
- [42] C. Tang, W. Wu, D.-M. M. Smilgies, K. Matyjaszewski, T. Kowalewski, *J. Am. Chem. Soc.* **2011**, *133*, 11802.
- [43] P. W. Majewski, K. G. Yager, *ACS Nano* **2015**, *9*, 3896.
- [44] D. E. Angelescu, J. H. Waller, D. H. Adamson, P. Deshpande, S. Y. Chou, R. A. Register, P. M. Chaikin, *Adv. Mater.* **2004**, *16*, 1736.
- [45] D. E. Angelescu, J. H. Waller, R. A. Register, P. M. Chaikin, *Adv. Mater.* **2005**, *17*, 1878.
- [46] T. L. Morkved, M. Lu, A. M. Urbas, E. E. Ehrichs, H. M. Jaeger, P. Mansky, T. P. Russell, *Science* **1996**, *273*, 931.
- [47] H. U. Jeon, H. M. Jin, J. Y. Kim, S. K. Cha, J. H. Mun, K. E. Lee, J. J. Oh, T. Yun, J. S. Kim, S. O. Kim, *Mol. Syst. Des. Eng.* **2017**, *2*, 560.
- [48] P. W. Majewski, M. Gopinadhan, C. O. Osuji, *J. Polym. Sci., Part B: Polym. Phys.* **2012**, *50*, 2.
- [49] M. Gopinadhan, Y. Choo, L. H. Mahajan, D. Ndaya, G. Kaufman, Y. Rokhlenko, R. M. Kasi, C. O. Osuji, *Mol. Syst. Des. Eng.* **2017**, *2*, 549.
- [50] P. Mansky, Y. Lui, E. Huang, T. P. Russell, C. J. Hawker, *Science* **1997**, *275*, 1458.
- [51] C. M. Bates, T. Seshimo, M. J. Maher, W. J. Durand, J. D. Cushen, L. M. Dean, G. Blachut, C. J. Ellison, C. G. Willson, *Science* **2012**, *338*, 775.
- [52] S. Park, D. H. Lee, J. Xu, B. Kim, S. W. Hong, U. Jeong, T. Xu, T. P. Russell, *Science* **2009**, *323*, 1030.
- [53] K. Aissou, J. Shaver, G. Fleury, G. Pécastaings, C. Brochon, C. Navarro, S. Grauby, J.-M. Ramponoux, S. Dilhaire, G. Hadziioannou, *Adv. Mater.* **2013**, *25*, 213.
- [54] S. O. Kim, H. H. Solak, M. P. Stoykovich, N. J. Ferrier, J. J. De Pablo, P. F. Nealey, *Nature* **2003**, *424*, 411.
- [55] C.-C. Liu, E. Han, M. S. Onses, C. J. Thode, S. Ji, P. Gopalan, P. F. Nealey, *Macromolecules* **2011**, *44*, 1876.
- [56] R. A. Segalman, H. Yokoyama, E. J. Kramer, *Adv. Mater.* **2001**, *13*, 1152.
- [57] J. Y. Cheng, C. a. Ross, E. L. Thomas, H. I. Smith, G. J. Vancso, *Appl. Phys. Lett.* **2002**, *81*, 3657.
- [58] S. B. Darling, *Prog. Polym. Sci.* **2007**, *32*, 1152.
- [59] *Directed Self-Assembly of Block Co-Polymers for Nano-Manufacturing* (Eds: R. Gronheid, P. Nealey), Woodhead Publishing, Cambridge, England **2015**.
- [60] H. Hu, M. Gopinadhan, C. O. Osuji, *Soft Matter* **2014**, *10*, 3867.
- [61] W. Li, M. Müller, *Prog. Polym. Sci.* **2016**, *54–55*, 47.
- [62] *Functional Organic and Hybrid Nanostructured Materials* (Ed: Q. Li), Wiley-VCH Verlag GmbH & Co. KGaA: Weinheim, Germany **2018**.
- [63] A. Karim, N. Singh, M. Sikka, F. S. Bates, W. D. Dozier, G. P. Felcher, *J. Chem. Phys.* **1994**, *100*, 1620.
- [64] L. H. Radzilowski, B. L. Carvalho, E. L. Thomas, *J. Polym. Sci., Part B: Polym. Phys.* **1996**, *34*, 3081.
- [65] M. W. Matsen, *Curr. Opin. Colloid Interface Sci.* **1998**, *3*, 40.
- [66] A. Knoll, A. Horvat, K. S. Lyakhova, G. Krausch, G. J. A. Sevink, A. V. Zvelindovsky, R. Magerle, *Phys. Rev. Lett.* **2002**, *89*, 035501.
- [67] G. E. Stein, E. J. Kramer, X. Li, J. Wang, *Macromolecules* **2007**, *40*, 2453.
- [68] W. Bai, C. A. Ross, *MRS Bull.* **2016**, *41*, 100.
- [69] G. S. Doerk, K. G. Yager, *Mol. Syst. Des. Eng.* **2017**, *2*, 518.
- [70] J. H. Kim, H. M. Jin, G. G. Yang, K. H. Han, T. Yun, J. Y. Shin, S. Jeong, S. O. Kim, *Adv. Funct. Mater.* **2019**, 1902049.
- [71] K. Hayashida, A. Takano, S. Arai, Y. Shinohara, Y. Amemiya, Y. Matsushita, *Macromolecules* **2006**, *39*, 9402.
- [72] Y. Matsushita, *Macromolecules* **2007**, *40*, 771.
- [73] B. R. Sveinbjörnsson, R. a Weitekamp, G. M. Miyake, Y. Xia, H. a Atwater, R. H. Grubbs, *Proc. Natl. Acad. Sci. USA* **2012**, *109*, 14332.
- [74] W. Gu, J. Huh, S. W. Hong, B. R. Sveinbjörnsson, C. Park, R. H. Grubbs, T. P. Russell, *ACS Nano* **2013**, *7*, 2551.
- [75] K. Aissou, W. Kwon, M. Mumtaz, S. Antoine, M. Maret, G. Portale, G. Fleury, G. Hadziioannou, *ACS Nano* **2016**, *10*, 4055.
- [76] S. Antoine, K. Aissou, M. Mumtaz, G. Pécastaings, T. Buffeteau, G. Fleury, G. Hadziioannou, *Macromol. Rapid Commun.* **2019**, *40*, 1800860.

- [77] S. Salahuddin, K. Ni, S. Datta, *Nat. Electron.* **2018**, *1*, 442.
- [78] R. Clark, K. Tapily, K. H. Yu, T. Hakamata, S. Consiglio, D. O'Meara, C. Wajda, J. Smith, G. Leusink, *APL Mater.* **2018**, *6*, 058203.
- [79] T. N. Theis, H. S. Philip Wong, *Comput. Sci. Eng.* **2017**, *19*, 41.
- [80] C. Cummins, M. A. Morris, *Microelectron. Eng.* **2018**, *195*, 74.
- [81] H.-Y. Y. Hsueh, C.-T. T. Yao, R.-M. M. Ho, *Chem. Soc. Rev.* **2015**, *44*, 1974.
- [82] T. Ito, G. Ghimire, *ChemElectroChem* **2018**, *5*, 2937.
- [83] H. Hu, S. Rangou, M. Kim, P. Gopalan, V. Filiz, A. Avgeropoulos, C. O. Osuji, *ACS Nano* **2013**, *7*, 2960.
- [84] Y. Choo, H. Hu, K. Toth, C. O. Osuji, *J. Polym. Sci., Part B: Polym. Phys.* **2016**, *54*, 247.
- [85] A. Tavakkoli K. G., K. W. Gotrik, A. F. Hannon, A. Alexander-Katz, C. A. Ross, K. K. Berggren, *Science* **2012**, *336*, 1294.
- [86] J. W. Jeong, W. I. Park, L.-M. M. Do, J.-H. H. Park, T.-H. H. Kim, G. Chae, Y. S. Jung, *Adv. Mater.* **2012**, *24*, 3526.
- [87] J. Y. Kim, B. H. Kim, J. O. Hwang, S. J. Jeong, D. O. Shin, J. H. Mun, Y. J. Choi, H. M. Jin, S. O. Kim, *Adv. Mater.* **2013**, *25*, 1331.
- [88] P. W. Majewski, A. Rahman, C. T. Black, K. G. Yager, *Nat. Commun.* **2015**, *6*, 7448.
- [89] A. Tavakkoli K. G., S. M. Nicaise, A. F. Hannon, K. W. Gotrik, A. Alexander-Katz, C. A. Ross, K. K. Berggren, *Small* **2014**, *10*, 493.
- [90] A. A. Abate, G. T. Vu, A. D. Pezzutti, N. A. García, R. L. Davis, F. Schmid, R. A. Register, D. A. Vega, *Macromolecules* **2016**, *49*, 7588.
- [91] F. Rose, J. K. Bosworth, E. A. Dobisz, R. Ruiz, *Nanotechnology* **2011**, *22*, 035603.
- [92] E. Kim, C. Shin, H. Ahn, D. Y. Ryu, J. Bang, C. J. Hawker, T. P. Russell, *Soft Matter* **2008**, *4*, 475.
- [93] H. Jung, D. Hwang, E. Kim, B.-J. Kim, W. B. Lee, J. E. Poelma, J. Kim, C. J. Hawker, J. Huh, D. Y. Ryu, J. Bang, *ACS Nano* **2011**, *5*, 6164.
- [94] C. He, M. P. Stoykovich, *Adv. Funct. Mater.* **2014**, *24*, 7078.
- [95] Y. J. Choi, J. Y. Kim, J. E. Kim, J. H. Mun, S. K. Cha, S. O. Kim, *Adv. Funct. Mater.* **2016**, *26*, 6462.
- [96] H. Jung, S. Woo, S. Park, S. Lee, M. Kang, Y. Choe, J. G. Son, D. Y. Ryu, J. Huh, J. Bang, *Soft Matter* **2015**, *11*, 4242.
- [97] S. Y. Kim, A. Nunns, J. Gwyther, R. L. Davis, I. Manners, P. M. Chaikin, R. A. Register, *Nano Lett.* **2014**, *14*, 5698.
- [98] J. Oh, H. S. Suh, Y. Ko, Y. Nah, J. C. Lee, B. Yeom, K. Char, C. A. Ross, J. G. Son, *Nat. Commun.* **2019**, *10*, 2912.
- [99] A. Rahman, P. W. Majewski, G. Doerk, C. T. Black, K. G. Yager, *Nat. Commun.* **2016**, *7*, 13988.
- [100] R. Ruiz, R. L. Sandstrom, C. T. Black, *Adv. Mater.* **2007**, *19*, 587.
- [101] S. M. Park, P. Ravindran, Y. H. La, G. S. W. Craig, N. J. Ferrier, P. F. Nealey, *Langmuir* **2007**, *23*, 9037.
- [102] Y. S. Jung, J. B. Chang, E. Verploegen, K. K. Berggren, C. A. Ross, *Nano Lett.* **2010**, *10*, 1000.
- [103] J. G. Son, A. F. Hannon, K. W. Gotrik, A. Alexander-Katz, C. A. Ross, *Adv. Mater.* **2011**, *23*, 634.
- [104] A. Tavakkoli K. G., S. M. Nicaise, K. R. Gadelrab, A. Alexander-Katz, C. A. Ross, K. K. Berggren, *Nat. Commun.* **2016**, *7*, 10518.
- [105] D. O. Shin, J. H. Mun, G.-T. Hwang, J. M. Yoon, J. Y. Kim, J. M. Yun, Y. Yang, Y. Oh, J. Y. Lee, J. Shin, K. J. Lee, S. Park, J. U. Kim, S. O. Kim, *ACS Nano* **2013**, *7*, 8899.
- [106] C. Jin, B. C. Olsen, N. L. Y. Wu, E. J. Lubber, J. M. Buriak, *Langmuir* **2016**, *32*, 5890.
- [107] H. Jung, W. H. Shin, T. W. Park, Y. J. Choi, Y. J. Yoon, S. H. Park, J. H. Lim, J. D. Kwon, J. W. Lee, S. H. Kwon, G. H. Seong, K. H. Kim, W. I. Park, *Nanoscale* **2019**, *11*, 8433.
- [108] C. Jin, B. C. Olsen, E. J. Lubber, J. M. Buriak, *ACS Nano* **2017**, *11*, 3237.
- [109] J. Y. Kim, H. Kim, B. H. Kim, T. Chang, J. Lim, H. M. Jin, J. H. Mun, Y. J. Choi, K. Chung, J. Shin, S. Fan, S. O. Kim, *Nat. Commun.* **2016**, *7*, 12911.
- [110] A. Alvarez-Fernandez, K. Aissou, G. Pécastaings, G. Hadziioannou, G. Fleury, V. Ponsinet, *Nanoscale Adv.* **2019**, *1*, 849.
- [111] S. J. Jeong, S. Jo, J. Lee, K. Yang, H. Lee, C. S. Lee, H. Park, S. Park, *Nano Lett.* **2016**, *16*, 5378.
- [112] J. Arias-Zapata, J. D. Garnier, H. Al Mehedi, A. Legrain, B. Salem, G. Cunge, M. Zelsmann, *Chem. Mater.* **2019**, *31*, 3154.
- [113] K. V. Peinemann, V. Abetz, P. F. W. Simon, *Nat. Mater.* **2007**, *6*, 992.
- [114] C. Zhou, T. Segal-Peretz, M. E. Oruc, H. S. Suh, G. Wu, P. F. Nealey, *Adv. Funct. Mater.* **2017**, *27*, 1701756.
- [115] K. Aissou, M. Mumtaz, H. Bouzit, G. Pécastaings, G. Portale, G. Fleury, G. Hadziioannou, *Macromolecules* **2019**, *52*, 4413.
- [116] S. B. Darling, *Energy Environ. Sci.* **2009**, *2*, 1266.
- [117] S. W. Robbins, P. A. Beaucage, H. Sai, K. W. Tan, J. G. Werner, J. P. Sethna, F. J. DiSalvo, S. M. Gruner, R. B. Van Dover, U. Wiesner, *Sci. Adv.* **2016**, *2*, e1501119.

I.3.B/ Discussion

This article details four stacking methods that have their pros and cons with respect to the final applications. One of the main objectives of this Ph.D. is to generate 3D nanostructures which are controlled through epitaxial relationships, meaning that the orientation and translational order of each layer is dependent of the previous one. This correlation between layers is called registration, and is required for creating complex nanostructures with enhanced functionality.

Within the four techniques, two of them allow a “native” registration, meaning that the stacked layer ordering is dictated by the underneath layer: the direct stacking method with a topographic registration, and the crosslinking method with a chemical registration. The transfer mold method shows a potential for ex-situ registration through the chosen orientation of the mold with respect to the underneath layer. The last method does not lead to a registration since a protective layer decorrelates the epitaxial ordering between layers. However, in-situ registration shows a major drawback which is the defect propagation between layers. Nevertheless, this limitation can be overcome by using directed self-assembly methods.

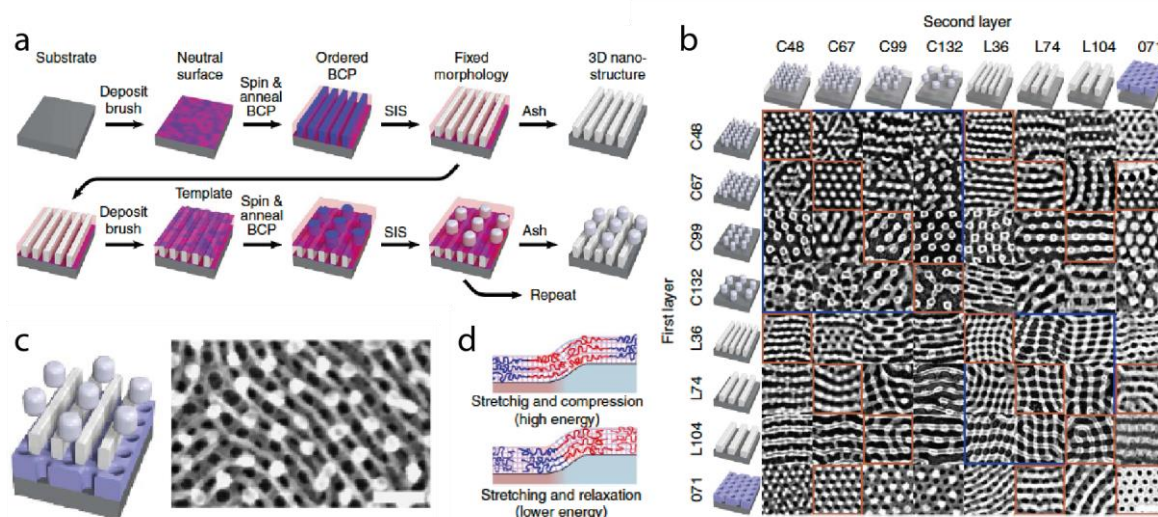


Figure 33. (a) Schematics of the stacking process and SEM images of (b) bi-layers and (c) tri-layers formed using a direct stacking method. (d) Schematics of the two possible stacking configurations with different energy costs depending of the BCP chain position with respect to the first BCP layer. [189]

Our choice for this Ph.D. fell on the direct stacking method as a promising demonstration of registration between stacked BCP nanostructures was obtained in 2016 by Rahman *et al.* [189]. More precisely, they showed the formation of a panoply of non-native nanostructures made by stacking two layers of PS-*b*-PMMA with various morphology and domain spacing. The immobilization of the layers through the conversion in Al₂O₃ were performed using a SIS process. (Figures 33.a-b). They also showed that this process can be used for the tri-layers (Figure 33.c). In their study, it is the topographic field created by the underneath infiltrated layer that induces the registration of the top layer by minimizing the energy related to the stretching and compression

of the BCP chains (*Figure 33.d*). Nevertheless, the long-range ordering and the registration rules enabling the control of such complex self-assembly process were not deeply tackled in this report and will consequently be the outline of this Ph.D. study. Besides, further tuning of the direct stacking method is envisioned by the control of the interfacial energy between the BCP layers, providing thus a dual registration field (i.e. topographical and chemical).

I.4/ Azobenzene-containing polymers

Polymers bearing azobenzene moieties in their structure have been synthesized over the past few decades for their interesting photochemical properties [190]–[193]. In the field of BCP self-assembly, such materials can be used to generate topographical fields for the long-range ordering of BCP thin films.

I.4.A/ Cis-Trans photoisomerization

The azobenzene molecule and its derivatives have a chemical structure including a N=N double bond sandwiched between two benzene π -systems that can undergo an isomerization from the stable *trans* configuration to a less stable *cis* configuration under photo-irradiation (around 400nm depending on the side groups) (Figure 34). This unstable conformation quickly relaxes - within a few seconds - to the stable *trans* configuration at room temperature since the energy gap is a few kcal [193]–[196].

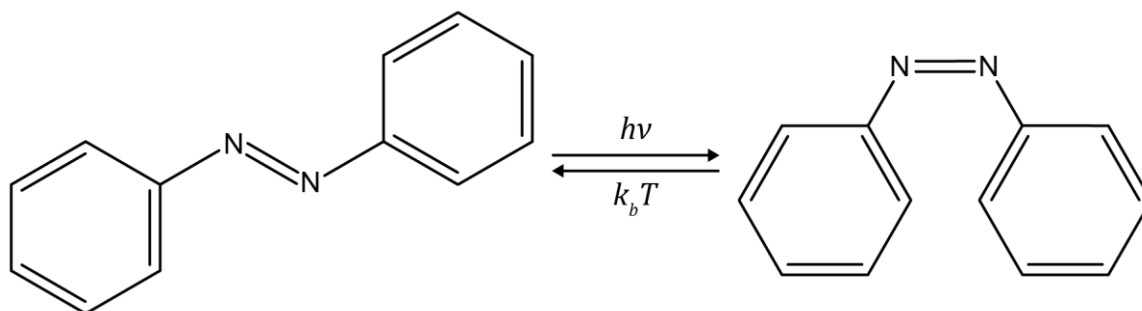


Figure 34 – Cis-trans photo-isomerization of an azobenzene molecule, from *trans* to *cis* with a light stimulus, and back to *trans* with temperature.

These molecules have demonstrated a strong potential for applications as dye in optoelectronics [197], [198] or as photo-regulators for biology purposes [199], [200]. It can also be associated to polymers to form photo-responsive polymers for which stimuli-responsiveness is triggered by irradiation [193].

I.4.B/ Surface Relief Gratings

In 1995, Kim *et al.* performed the first photo-isomerization on an azobenzene-containing polymer thin film in order to induce a surface corrugation called surface relief gratings (SRG) [201]. Experimentally, the generation of SRG into an azobenzene-containing polymer layer requires to apply illumination with a controlled pattern. Since it is possible to use visible light, the most simple and common setup is a Lloyd's mirror interferometer with a laser to form perfectly defined parallel interference fringes, leading to the formation of a wavy pattern (Figures 35.a-c).

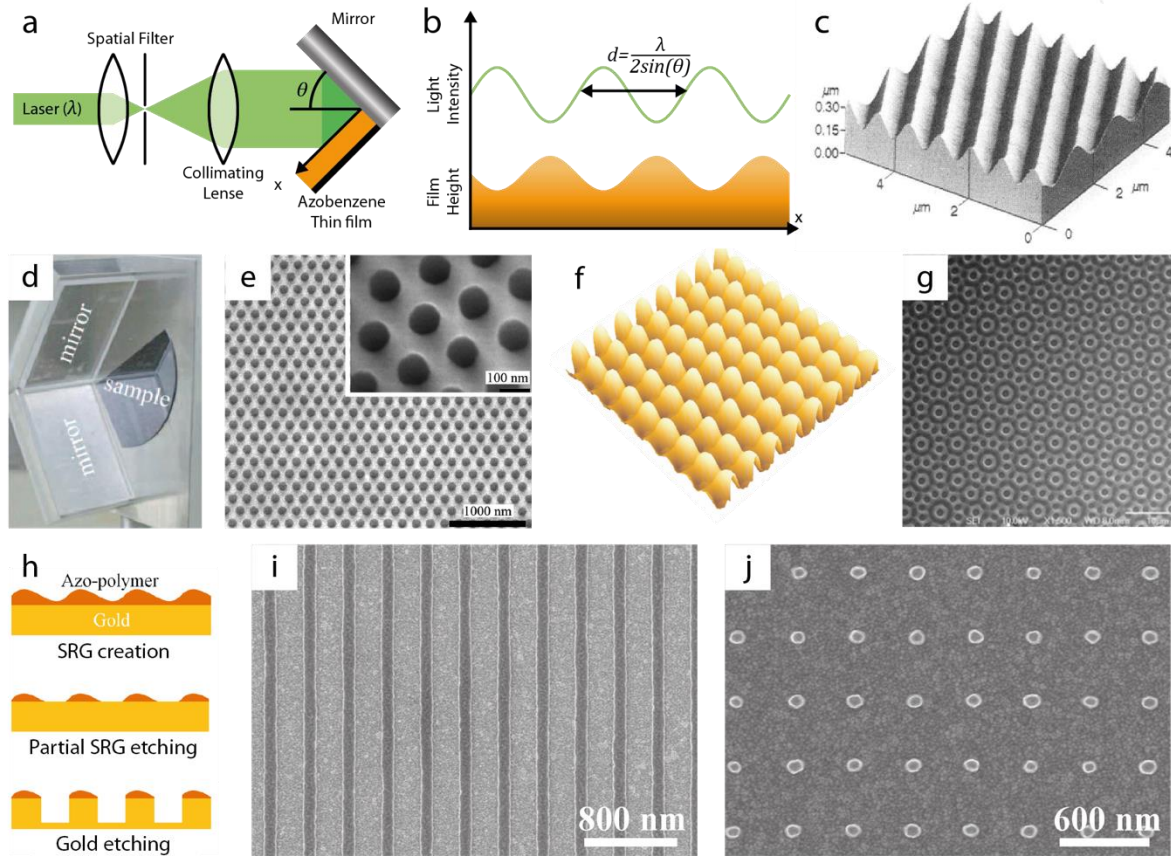


Figure 35. Schematics of (a) Lloyd's mirror interferometer applied to the formation of a SRG pattern into an azobenzene thin film and (b) light intensity profile and SRG induced to the film. (c) AFM three dimensional view of SRG on an azobenzene-containing polymer [201] (d) Experimental two mirror Lloyd's interferometer and (e) hexagonal pattern created with it on a photoresist thin film [202]. (f) AFM image of the SRG pattern formed after two orthogonal exposures on an azobenzene-containing thin film [203]. (g) SEM image of a quasicrystal made by the SRG patterning of a photoresist through a process composed of six exposures with different angles (0° , 30° , 60° , 90° , 120° and 150°) [204]. (h) Schematics of the formation of gold pattern using a SRG mask and SEM images of (i) strips made with one exposure and (j) squared dots made with two orthogonal exposures [205].

This technique is very convenient because it is possible to tune the periodicity of the pattern d by changing the incident angle θ or the light source wavelength λ (Equation (9)). Also, the grating amplitude can be easily tuned by controlling the exposure time, the film thickness, the light source power and its polarization [206]

$$d = \frac{\lambda}{2\sin(\theta)} \quad (9)$$

It is also possible to create hexagonal interference pattern using a two mirrors Lloyd's interferometer (Figures 35.d-e), or by doing two standard SRG inscription with an angle of 60° between them [202]. Such type of procedures has been used for the formation of a squared matrix of dots into azobenzene-containing thin film via two orthogonal exposures, called crossed surface relief gratings (CSRG) [203], [206], [207] (Figure 35.f). Interestingly, such kind of multiple exposures by rotating the sample have also been theoretically and experimentally studied to form quasicrystals [204], [208], [209] (Figure 35.g). These SRG patterns can be further exposed to a

controlled plasma etching in order to create a mask for the patterning of a metallic layer [205], [210] (*Figures 35.h-j*). Another route for creating metallic features from SRG patterns have been developed by Moerland *et al.* [211], and it consists in sputtering a gold layer above a SRG pattern followed by an ion milling step to etch the thinnest areas.

Several theories on the formation of SRG patterns have been developed to explain this non-trivial phenomenon. Indeed, the generation of the patterns occurs at room temperature which is often below the T_g of the polymer layer [212].

A first theory, proposed by Rochon *et al.* in 1995, is based on a thermo-physical process that induces mass diffusion by a local photo-thermal heating above T_g [213]. A second theory have been proposed by Barrett *et al.* in 1996, suggesting that an internal pressure arises from the regions where the cyclic isomerization occurs, leading to a gradient pressure that displaces the matter [214]. Both of these theories are not enough to fully apprehend SRG as completely different behaviors between *s*-polarization and *p*-polarization (not taken into account in both theoretical frameworks) have been experimentally observed. In fact, SRG is only possible with a *p*-polarized light [215]. A third theory developed by Lefin *et al.* in 1998 explains that SRG is driven by the chromophore displacement along the excitation direction which generates a flow of matter in the volume of the SRG layer [216]. Nonetheless, the SRG mechanism has been demonstrated to be initiated on the layer surface [217], disproving this particular theory. Then, Kumar *et al.* proposed in 1998 a theory based on a matter displacement induced by interactions between the dipoles of the azobenzene moieties and light. These interactions would generate an electrical field leading to a gradient force [218]. More recently, in 2014, Hurduc *et al.* proposed an athermal photo-fluidization mechanism to explain SRG [219].

Obviously, a consolidated theory on the formation of SRG has not been reached yet, but the two mechanisms that seem to be the most probable are the mechanical stress and the photo-fluidization [220], [221].

I.4.C/ BCP self-assembly induced by SRG

Since the emergence of azobenzene-containing polymers, synergies with BCPs have been studied to improve the control of the self-assembly behavior. There are mostly two routes: using the SRG property to generate guiding patterns for BCP directed self-assembly, or using the response of azobenzene moieties (usually grafted on the backbone of a BCP chain) to a polarized illumination to trigger directional ordering of BCP structure during the self-assembly process.

I.4.C.i/ SRG patterns for directed self-assembly

As explained before, azobenzene-containing layers can produce perfectly defined patterns through SRG with a periodicity of several hundreds of nanometers (*Equation (9)*). These patterns can be further used to generate topographical fields (as in graphoepitaxy) with tunable amplitude and width. Aissou *et al.* developed a process using SRG patterns as guiding pattern through a subsequent cross-linking step after the SRG inscription. The SRG pattern was employed for the directed self-assembly of cylindrical PS-*b*-PEO or PDMSB-*b*-PMMA. Long-range ordering is achieved thanks to the directional guidance stress induced by the pattern, which favors a lateral ordering of hexagonally packed cylinders, thus reducing isolated dislocations [222], [223] (*Figures 36.a-c*).

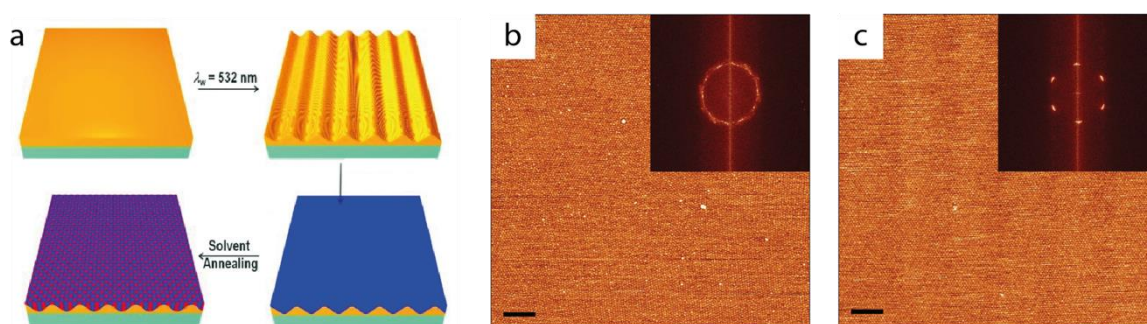


Figure 36. (a) Schematics of a PDMSB-*b*-PMMA cylindrical structure obtained by directed self-assembly on a sinusoidal pattern made by a crosslinked azobenzene SRG layer, and AFM images (scale bars: 200 nm) of these cylinders (b) without and (c) with the SRG pattern [222], [223].

This method seems to be interesting since it requires a simple setup compared to conventional lithography and the pattern periodicity and amplitude can be easily tuned with respect to the BCP system. The main drawbacks are that only few pattern symmetries are achievable, with a minimal size of $\lambda/2$ that physically cannot be overcome.

I.4.C.ii/ Azobenzene-containing block copolymers

Another route to take advantage of the peculiar property of azobenzene moieties in BCP self-assembly is to incorporate them in a BCP architecture. The azobenzene moiety is often located on a poly(methacrylate) block, unlocking a light trigger during self-assembly process. These azobenzene moieties are attached to a long alkyl chain, which can further produce a liquid-crystal behavior that can be orientated according to the light polarization direction [191], [224].

For instance, Morikawa *et al.* used this effect to induce the orientation of PS cylinders into a matrix of a polymethacrylate containing azobenzene moieties (azoPMA) with polarized light followed by an annealing step at 130°C (*Figure 37.a*) [225]. Interestingly, it is possible to successively order the cylindrical structure following different directions by repeating this

process. Furthermore, by adding a mask during irradiation, it is possible to control the cylinder orientation over selected areas.

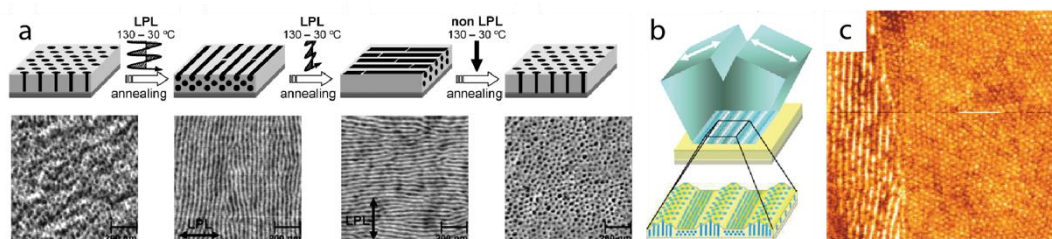


Figure 37. (a) Schematics of successive ordering direction of a PS-*b*-azoPMA cylindrical structure by using different polarization and direction of light followed by an annealing and the corresponding SEM images [225]. (b) Schematics of the orientation of PEO-azoPMA cylinders within a SRG pattern made with a p-polarized light source showing two orientation depending on the thickness and (c) AFM image at the interface between the two orientations [226].

More recently, the same group improved the method with a Lloyd's mirror interference setup able to directly control the orientation of PEO-*b*-azoPMA cylinders within the SRG pattern. They obtained the same type of result as before with a mask, i.e. two different side-by-side orientations within the same thin film, but without using a mask. In this case, they achieved in-plane cylinders in the thin regions and out-of-plane cylinders in the thick regions (Figures 37.b-c) [226].

This route to control the orientation of BCP structure has a great advantage since it uses polarized light which is easy to produce and manipulate. However, the incorporation of an azobenzene moiety in a polymer backbone is highly challenging from a synthetic point-of-view. This could explain why the use of azobenzene-containing BCPs is not a common method for DSA in the literature.

I.5/ Conclusions and Ph.D. objectives

In this chapter, BCP self-assembly have been introduced with an emphasis on this use to spontaneously generate various structures at a nanometric length scale. We also highlighted the versatility offered by the panoply of block chemistries in order to add functional properties to a BCP structure. Furthermore, it was demonstrated that BCP thin films are also compatible with layer stacking processes for the production of novel non-native nanostructures, which expand the interest of BCP self-assembly for nano-manufacturing. In particular, further opportunities could be envisioned for specific applications in many technological fields; e.g. for electronics (lithographic mask, storage media, microelectronics), optics (photonic, absorption, photovoltaic), biology (membrane, sensor) and chemistry (catalyst, nanoparticle synthesis) [227]–[231].

Accordingly, the core objectives of this work range from the implementation of robust self-assembly processes for BCP iterative self-assembly to an in-depth understanding of the registration mechanisms between the different layers. To achieve these ambitious objectives, we chose the PS-*b*-PMMA system as it allows leveraging the well-mastered microphase separation behavior of this system to a more complex iterative layering method.

In the first experimental chapter of this Ph.D., a complementary study on the use of azobenzene-containing (co)polymers in the field of DSA is proposed as it is expected to enrich the methodologies to obtain long-range ordering of BCP structures. Such methods could be further used for iterative layering for the production of BCP structures of low defectivity and would allow an easier deciphering of the complex registration processes between BCP layers.

The second experimental chapter is devoted to the production of the various building bricks with a focus on the optimization of the self-assembly processes. The three structural “patterns” targeted during this work are a line & space pattern, a hexagonal dot pattern and a honeycomb pattern, each produced from a different self-assembled monolayer. The study presented in this chapter was performed in order to provide a solid foundation for the following study on iterative layering.

Then, we tackled in the third experimental chapter the core objective of this Ph.D. by implementing the staking of the different patterns previously studied. An important aspect of this chapter is the attention devoted to the understanding of the stacking rules determining the final assembly. This was done by quantifying the importance of topographical and chemical fields as well as commensurability between the building bricks on the registration (alignment and orientation) between the different PS-*b*-PMMA self-assembled layers. A mapping of the non-native

structures obtained by the direct stacking methodology is thus presented as a function of the initial building bricks.

Finally, the last chapter of this thesis is a prospective description of the use of iterative self-assembly for targeted applications with some preliminary experimental results. In particular, applications of iterative self-assembly for data storage and advanced optics are the focus of the study. It is noteworthy that this study was done by “imagining” an ideal nanostructure for a given application, and then demonstrating the ability of iterative self-assembly and hybridization methods to generate it.

I.6/ References

- [1] F. S. Bates and G. H. Fredrickson, "Block Copolymer Thermodynamics: Theory and Experiment," *Annu. Rev. Phys. Chem.*, vol. 41, no. 1, pp. 525–557, 1990, doi: 10.1146/annurev.pc.41.100190.002521.
- [2] F. S. Bates and G. H. Fredrickson, "Block copolymers-designer soft materials," *Phys. Today*, vol. 52, no. 2, pp. 32–38, 1999, doi: 10.1063/1.882522.
- [3] M. W. Matsen, "Self-assembly of block copolymers in thin films," *Curr. Opin. Colloid Interface Sci.*, vol. 3, no. 1, pp. 40–47, 1998, doi: 10.1016/S1359-0294(98)80040-X.
- [4] M. J. Fasolka and A. M. Mayes, "Block Copolymer Thin Films: Physics and Applications," *Annu. Rev. Mater. Res.*, vol. 31, no. 1, pp. 323–355, Aug. 2001, doi: 10.1146/annurev.matsci.31.1.323.
- [5] P. J. Flory, "Thermodynamics of High Polymer Solutions," *J. Chem. Phys.*, vol. 10, no. 1, pp. 51–61, Jan. 1942, doi: 10.1063/1.1723621.
- [6] M. L. Huggins, "Theory of Solutions of High Polymers," *J. Am. Chem. Soc.*, vol. 64, no. 7, pp. 1712–1719, 1942, doi: 10.1021/ja01259a068.
- [7] M. L. Huggins, "Some properties of solutions of long-chain compounds," *J. Phys. Chem.*, vol. 46, no. 1, pp. 151–158, 1942, doi: 10.1021/j150415a018.
- [8] F. S. Bates, M. A. Hillmyer, T. P. Lodge, C. M. Bates, K. T. Delaney, and G. H. Fredrickson, "Multiblock polymers: Panacea or Dandora's box?," *Science (80-.)*, vol. 336, no. 6080, pp. 434–440, 2012, doi: 10.1126/science.1215368.
- [9] L. Leibler, "Theory of Microphase Separation in Block Copolymers," *Macromolecules*, vol. 13, no. 6, pp. 1602–1617, 1980, doi: 10.1021/ma60078a047.
- [10] M. W. Matsen and M. Schick, "Stable and unstable phases of a diblock copolymer melt," *Phys. Rev. Lett.*, vol. 72, no. 16, pp. 2660–2663, 1994, doi: 10.1103/PhysRevLett.72.2660.
- [11] M. W. Matsen and F. S. Bates, "Unifying weak- and strong-segregation block copolymer theories," *Macromolecules*, vol. 29, no. 4, pp. 1091–1098, 1996, doi: 10.1021/ma951138i.
- [12] D. A. Hajduk *et al.*, "The Gyroid: A New Equilibrium Morphology in Weakly Segregated Diblock Copolymers," *Macromolecules*, vol. 27, no. 15, pp. 4063–4075, 1994, doi: 10.1021/ma00093a006.
- [13] M. E. Vigild, K. Almdal, K. Mortensen, I. W. Hamley, J. P. A. Fairclough, and A. J. Ryan, "Transformations to and from the gyroid phase in a diblock copolymer," *Macromolecules*, vol. 31, no. 17, pp. 5702–5716, 1998, doi: 10.1021/ma9716746.
- [14] C. Y. Wang and T. P. Lodge, "Kinetics and mechanisms for the cylinder-to-gyroid transition in a block copolymer solution," *Macromolecules*, vol. 35, no. 18, pp. 6997–7006, 2002, doi: 10.1021/ma0205212.
- [15] I. Vukovic *et al.*, "Double gyroid network morphology in supramolecular diblock copolymer complexes," *Macromolecules*, vol. 45, no. 8, pp. 3503–3512, 2012, doi: 10.1021/ma300273f.
- [16] E. W. Cochran, C. J. Garcia-Cervera, and G. H. Fredrickson, "Stability of the gyroid phase in diblock copolymers at strong segregation," *Macromolecules*, vol. 39, no. 7, pp. 2449–2451, 2006, doi: 10.1021/ma0527707.
- [17] M. W. Matsen and M. Schick, "Stable and Unstable Phases of a Linear Multiblock Copolymer Melt," *Macromolecules*, vol. 27, no. 24, pp. 7157–7163, 1994, doi: 10.1021/ma00102a025.
- [18] M. W. Matsen and F. S. Bates, "Conformationally asymmetric block copolymers," *J. Polym. Sci. Part B Polym. Phys.*, vol. 35, no. 6, pp. 945–952, Apr. 1997, doi: 10.1002/(SICI)1099-

- 0488(19970430)35:6<945::AID-POLB9>3.0.CO;2-G.
- [19] F. S. Bates, J. H. Rosedale, and G. H. Fredrickson, "Fluctuation effects in a symmetric diblock copolymer near the order-disorder transition," *J. Chem. Phys.*, vol. 92, no. 10, pp. 6255–6270, 1990, doi: 10.1063/1.458350.
- [20] A. K. Khandpur *et al.*, "Polyisoprene-Polystyrene Diblock Copolymer Phase Diagram near the Order-Disorder Transition," *Macromolecules*, vol. 28, no. 26, pp. 8796–8806, 1995, doi: 10.1021/ma00130a012.
- [21] G. H. Fredrickson and E. Helfand, "Fluctuation effects in the theory of microphase separation in block copolymers," *J. Chem. Phys.*, vol. 87, no. 1, pp. 697–705, 1987, doi: 10.1063/1.453566.
- [22] T. M. Gillard, P. Medapuram, D. C. Morse, and F. S. Bates, "Fluctuations, phase transitions, and latent heat in short diblock copolymers: Comparison of experiment, simulation, and theory," *Macromolecules*, vol. 48, no. 8, pp. 2801–2811, 2015, doi: 10.1021/acs.macromol.5b00277.
- [23] M. F. Schulz *et al.*, "Phase behavior of polystyrene-poly(2-vinylpyridine) diblock copolymers," *Macromolecules*, vol. 29, no. 8, pp. 2857–2867, 1996, doi: 10.1021/ma951714a.
- [24] J. Zhao *et al.*, "Phase behavior of pure diblocks and binary diblock blends of poly(ethylene)-poly(ethylene)," *Macromolecules*, vol. 29, no. 4, pp. 1204–1215, 1996, doi: 10.1021/ma9507251.
- [25] I. Hamley and V. Castelletto, "Small-Angle Scattering of Block Copolymers," in *Soft Matter Characterization*, vol. 58, no. 12, Dordrecht: Springer Netherlands, 2008, pp. 1021–1081.
- [26] P. Tang, F. Qiu, H. Zhang, and Y. Yang, "Morphology and phase diagram of complex block copolymers: ABC linear triblock copolymers," *Phys. Rev. E - Stat. Nonlinear, Soft Matter Phys.*, vol. 69, no. 3 1, pp. 1–8, 2004, doi: 10.1103/PhysRevE.69.031803.
- [27] C. Sinturel, F. S. Bates, and M. A. Hillmyer, "High χ -Low N Block Polymers: How Far Can We Go?," *ACS Macro Lett.*, vol. 4, no. 9, pp. 1044–1050, 2015, doi: 10.1021/acsmacrolett.5b00472.
- [28] G. Miquelard-Garnier and S. Roland, "Beware of the Flory parameter to characterize polymer-polymer interactions: A critical reexamination of the experimental literature," *Eur. Polym. J.*, vol. 84, pp. 111–124, 2016, doi: 10.1016/j.eurpolymj.2016.09.009.
- [29] M. W. Schulze, C. Sinturel, and M. A. Hillmyer, "Poly(cyclohexylethylene)-block-poly(ethylene oxide) Block Polymers for Metal Oxide Templating," *ACS Macro Lett.*, vol. 4, no. 9, pp. 1027–1032, 2015, doi: 10.1021/acsmacrolett.5b00458.
- [30] J. G. Kennemur, L. Yao, F. S. Bates, and M. A. Hillmyer, "Sub-5 nm domains in ordered poly(cyclohexylethylene)- block -poly(methyl methacrylate) block polymers for lithography," *Macromolecules*, vol. 47, no. 4, pp. 1411–1418, 2014, doi: 10.1021/ma4020164.
- [31] M. D. Rodwogin, C. S. Spanjers, C. Leighton, and M. A. Hillmyer, "Polylactide-poly(dimethylsiloxane)-polylactide triblock copolymers as multifunctional materials for nanolithographic applications," *ACS Nano*, vol. 4, no. 2, pp. 725–732, 2010, doi: 10.1021/nn901190a.
- [32] S. Sakurai, K. Mori, A. Okawara, K. Kimishima, and T. Hashimoto, "Evaluation of Segmental Interaction by Small-Angle X-ray Scattering Based on the Random-Phase Approximation for Asymmetric, Polydisperse Triblock Copolymers," *Macromolecules*, vol. 25, no. 10, pp. 2679–2691, 1992, doi: 10.1021/ma00036a019.
- [33] W. J. Durand *et al.*, "Design of high- χ block copolymers for lithography," *J. Polym. Sci. Part A*

- Polym. Chem.*, vol. 53, no. 2, pp. 344–352, 2015, doi: 10.1002/pola.27370.
- [34] T. A. Callaghan and D. R. Paul, “Interaction Energies for Blends of Poly(methyl methacrylate), Polystyrene, and Poly(α -methylstyrene) by the Critical Molecular Weight Method,” *Macromolecules*, vol. 26, no. 10, pp. 2439–2450, 1993, doi: 10.1021/ma00062a008.
- [35] A. Knoll *et al.*, “Phase behavior in thin films of cylinder-forming block copolymers,” *Phys. Rev. Lett.*, vol. 89, no. 3, pp. 355011–355014, 2002, doi: 10.1103/PhysRevLett.89.035501.
- [36] K. Brassat, D. Kool, C. G. A. Nallet, and J. K. N. Lindner, “Understanding Film Thickness-Dependent Block Copolymer Self-Assembly by Controlled Polymer Dewetting on Prepatterned Surfaces,” *Adv. Mater. Interfaces*, vol. 7, no. 1, pp. 1–10, 2020, doi: 10.1002/admi.201901605.
- [37] S. Kim *et al.*, “Consequences of surface neutralization in diblock copolymer thin films,” *ACS Nano*, vol. 7, no. 11, pp. 9905–9919, 2013, doi: 10.1021/nn403616r.
- [38] X. sa Jin, Y. yuan Pang, and S. xiang Ji, “From self-assembled monolayers to chemically patterned brushes: Controlling the orientation of block copolymer domains in films by substrate modification,” *Chinese J. Polym. Sci. (English Ed.)*, vol. 34, no. 6, pp. 659–678, 2016, doi: 10.1007/s10118-016-1800-x.
- [39] S. Ham *et al.*, “Microdomain orientation of PS-b-PMMA by controlled interfacial interactions,” *Macromolecules*, vol. 41, no. 17, pp. 6431–6437, 2008, doi: 10.1021/ma8007338.
- [40] D. G. Walton, G. J. Kellogg, A. M. Mayes, P. Lambooy, and T. P. Russell, “A Free Energy Model for Confined Diblock Copolymers,” *Macromolecules*, vol. 27, no. 21, pp. 6225–6228, Oct. 1994, doi: 10.1021/ma00099a045.
- [41] A. G. Emslie, F. T. Bonner, and L. G. Peck, “Flow of a viscous liquid on a rotating disk,” *J. Appl. Phys.*, vol. 29, no. 5, pp. 858–862, 1958, doi: 10.1063/1.1723300.
- [42] D. Meyerhofer, “Characteristics of resist films produced by spinning,” *J. Appl. Phys.*, vol. 49, no. 7, pp. 3993–3997, 1978, doi: 10.1063/1.325357.
- [43] S. Ji *et al.*, “Generalization of the Use of Random Copolymers To Control the Wetting Behavior of Block Copolymer Films,” *Macromolecules*, vol. 41, no. 23, pp. 9098–9103, 2008, doi: 10.1021/ma801861h.
- [44] E. Han, K. O. Stuen, M. Leolukman, C. C. Liu, P. F. Nealey, and P. Gopalan, “Perpendicular orientation of domains in cylinder-forming block copolymer thick films by controlled interfacial interactions,” *Macromolecules*, vol. 42, no. 13, pp. 4896–4901, 2009, doi: 10.1021/ma9002903.
- [45] E. Han and P. Gopalan, “Cross-linked random copolymer mats as ultrathin nonpreferential layers for block copolymer self-assembly,” *Langmuir*, vol. 26, no. 2, pp. 1311–1315, 2010, doi: 10.1021/la902483m.
- [46] P. Mansky *et al.*, “Controlling Polymer-Surface Interactions with Random Copolymer Brushes,” *Science (80-.)*, vol. 275, no. March, pp. 1458–1461, 1997, doi: 10.1126/science.275.5305.1458.
- [47] E. Han, K. O. Stuen, Y. H. La, P. F. Nealey, and P. Gopalan, “Effect of composition of substrate-modifying random copolymers on the orientation of symmetric and asymmetric diblock copolymer domains,” *Macromolecules*, vol. 41, no. 23, pp. 9090–9097, 2008, doi: 10.1021/ma8018393.
- [48] I. In, Y. H. La, S. M. Park, P. F. Nealey, and P. Gopalan, “Side-chain-grafted random copolymer brushes as neutral surfaces for controlling the orientation of block copolymer microdomains in thin films,” *Langmuir*, vol. 22, no. 18, pp. 7855–7860, 2006, doi:

- 10.1021/la060748g.
- [49] E. Huang, L. Rockford, T. P. Russell, and C. J. Hawker, "Nanodomain control in copolymer thin films," *Nature*, vol. 395, no. 6704, pp. 757–758, Oct. 1998, doi: 10.1038/27358.
- [50] D. H. Park, "The fabrication of thin films with nanopores and nanogrooves from block copolymer thin films on the neutral surface of self-assembled monolayers," *Nanotechnology*, vol. 18, no. 35, 2007, doi: 10.1088/0957-4484/18/35/355304.
- [51] J. N. L. Albert, M. J. Baney, C. M. Stafford, J. Y. Kelly, and T. H. Epps, "Generation of monolayer gradients in surface energy and surface chemistry for block copolymer thin film studies," *ACS Nano*, vol. 3, no. 12, pp. 3977–3986, 2009, doi: 10.1021/nn900750w.
- [52] A. Niemz, K. Bandyopadhyay, E. Tan, K. Cha, and S. M. Baker, "Fabrication of nanoporous templates from diblock copolymer thin films on alkylchlorosilane-neutralized surfaces," *Langmuir*, vol. 22, no. 26, pp. 11092–11096, 2006, doi: 10.1021/la062594a.
- [53] R. D. Peters, X. M. Yang, T. K. Kim, and P. F. Nealey, "Wetting behavior of block copolymers on self-assembled films of alkylchlorosiloxanes: Effect of grafting density," *Langmuir*, vol. 16, no. 24, pp. 9620–9626, 2000, doi: 10.1021/la000822+.
- [54] E. Kim, W. Kim, K. H. Lee, C. A. Ross, and J. G. Son, "A top coat with solvent annealing enables perpendicular orientation of sub-10 nm microdomains in Si-containing block copolymer thin films," *Adv. Funct. Mater.*, vol. 24, no. 44, pp. 6981–6988, 2014, doi: 10.1002/adfm.201401678.
- [55] H. S. Suh *et al.*, "Sub-10-nm patterning via directed self-assembly of block copolymer films with a vapour-phase deposited topcoat," *Nat. Nanotechnol.*, vol. 12, no. 6, pp. 575–581, 2017, doi: 10.1038/nnano.2017.34.
- [56] H. Yoshida *et al.*, "Topcoat Approaches for Directed Self-Assembly of Strongly Segregating Block Copolymer Thin Films," *J. Photopolym. Sci. Technol.*, vol. 26, no. 1, pp. 55–58, 2013, doi: 10.2494/photopolymer.26.55.
- [57] J. Oh *et al.*, "Universal perpendicular orientation of block copolymer microdomains using a filtered plasma," *Nat. Commun.*, vol. 10, no. 1, 2019, doi: 10.1038/s41467-019-10907-5.
- [58] S. Ji, G. Liu, F. Zheng, G. S. W. Craig, F. J. Himpsel, and P. F. Nealey, "Preparation of neutral wetting brushes for block copolymer films from homopolymer blends," *Adv. Mater.*, vol. 20, no. 16, pp. 3054–3060, 2008, doi: 10.1002/adma.200800048.
- [59] P. Mansky, T. P. Russell, C. J. Hawker, J. Mays, D. C. Cook, and S. K. Satija, "Interfacial segregation in disordered block copolymers: Effect of tunable surface potentials," *Phys. Rev. Lett.*, vol. 79, no. 2, pp. 237–240, 1997, doi: 10.1103/PhysRevLett.79.237.
- [60] X. Yu, J. Peng, L. Cui, H. Wang, B. Li, and Y. Han, "Morphology development of ultrathin symmetric diblock copolymer film via solvent vapor treatment," *Macromolecules*, vol. 37, no. 19, pp. 7301–7307, 2004, doi: 10.1021/ma0497761.
- [61] K. A. Cavicchi, K. J. Berthiaume, and T. P. Russell, "Solvent annealing thin films of poly(isoprene-*b*-lactide)," *Polymer (Guildf.)*, vol. 46, no. 25, pp. 11635–11639, 2005, doi: 10.1016/j.polymer.2005.09.072.
- [62] K. W. Guarini, C. T. Black, and S. H. I. Yeung, "Optimization of diblock copolymer thin film self assembly," *Adv. Mater.*, vol. 14, no. 18, pp. 1290–1294, 2002, doi: 10.1002/1521-4095(20020916)14:18<1290::AID-ADMA1290>3.0.CO;2-N.
- [63] T. Segal-Peretz *et al.*, "Characterizing the three-dimensional structure of block copolymers via sequential infiltration synthesis and scanning transmission electron tomography," *ACS Nano*, vol. 9, no. 5, pp. 5333–5347, 2015, doi: 10.1021/acs.nano.5b01013.
- [64] J. Y. Kelly *et al.*, "Investigation of thermally responsive block copolymer thin film

- morphologies using gradients," *ACS Appl. Mater. Interfaces*, vol. 2, no. 11, pp. 3241–3248, 2010, doi: 10.1021/am100695m.
- [65] C. Sinturel, M. Vayer, M. Morris, and M. A. Hillmyer, "Solvent vapor annealing of block polymer thin films," *Macromolecules*, vol. 46, no. 14, pp. 5399–5415, 2013, doi: 10.1021/ma400735a.
- [66] W. Bai *et al.*, "Thin film morphologies of bulk-gyroid polystyrene-block-polydimethylsiloxane under solvent vapor annealing," *Macromolecules*, vol. 47, no. 17, pp. 6000–6008, 2014, doi: 10.1021/ma501293n.
- [67] K. W. Gotrik, A. F. Hannon, J. G. Son, B. Keller, A. Alexander-Katz, and C. A. Ross, "Morphology control in block copolymer films using mixed solvent vapors," *ACS Nano*, vol. 6, no. 9, pp. 8052–8059, 2012, doi: 10.1021/nn302641z.
- [68] S. Park, B. Kim, J. Xu, T. Hofmann, B. M. Ocko, and T. P. Russell, "Lateral ordering of cylindrical microdomains under solvent vapor," *Macromolecules*, vol. 42, no. 4, pp. 1278–1284, 2009, doi: 10.1021/ma802480s.
- [69] R. Lundy *et al.*, "Controlled solvent vapor annealing of a high: χ block copolymer thin film," *Phys. Chem. Chem. Phys.*, vol. 19, no. 4, pp. 2805–2815, 2017, doi: 10.1039/c6cp07633e.
- [70] G. Nelson, C. S. Drapes, M. A. Grant, R. Gnabasik, J. Wong, and A. Baruth, "High-precision solvent vapor annealing for block copolymer thin films," *Micromachines*, vol. 9, no. 6, 2018, doi: 10.3390/mi9060271.
- [71] F. F. Lupi *et al.*, "Rapid thermal processing of self-assembling block copolymer thin films," *Nanotechnology*, vol. 24, no. 31, pp. 1–14, 2013, doi: 10.1088/0957-4484/24/31/315601.
- [72] M. Perego *et al.*, "Ordering dynamics in symmetric PS-*b*-PMMA diblock copolymer thin films during rapid thermal processing," *J. Mater. Chem. C*, vol. 2, no. 32, pp. 6655–6664, 2014, doi: 10.1039/c4tc00756e.
- [73] M. Ceresoli *et al.*, "Evolution of lateral ordering in symmetric block copolymer thin films upon rapid thermal processing," *Nanotechnology*, vol. 25, no. 27, 2014, doi: 10.1088/0957-4484/25/27/275601.
- [74] K. W. Gotrik and C. A. Ross, "Solvothermal annealing of block copolymer thin films," *Nano Lett.*, vol. 13, no. 11, pp. 5117–5122, 2013, doi: 10.1021/nl4021683.
- [75] W. Li and M. Müller, "Defects in the Self-Assembly of Block Copolymers and Their Relevance for Directed Self-Assembly," *Annu. Rev. Chem. Biomol. Eng.*, vol. 6, no. April, pp. 187–216, 2015, doi: 10.1146/annurev-chembioeng-061114-123209.
- [76] S. B. Darling, "Directing the self-assembly of block copolymers," *Prog. Polym. Sci.*, vol. 32, no. 10, pp. 1152–1204, 2007, doi: 10.1016/j.progpolymsci.2007.05.004.
- [77] H. Hu, M. Gopinadhan, and C. O. Osuji, "Directed self-Assembly of block copolymers: A tutorial review of strategies for enabling nanotechnology with soft matter," *Soft Matter*, vol. 10, no. 22, pp. 3867–3889, 2014, doi: 10.1039/c3sm52607k.
- [78] S. J. Jeong, J. Y. Kim, B. H. Kim, H. S. Moon, and S. O. Kim, "Directed self-assembly of block copolymers for next generation nanolithography," *Mater. Today*, vol. 16, no. 12, pp. 468–476, 2013, doi: 10.1016/j.mattod.2013.11.002.
- [79] I. Gunkel, "Directing Block Copolymer Self-Assembly on Patterned Substrates," *Small*, vol. 14, no. 46, pp. 1–8, 2018, doi: 10.1002/sml.201802872.
- [80] C.-C. Liu *et al.*, "Integration of block copolymer directed assembly with 193 immersion lithography," *J. Vac. Sci. Technol. B, Nanotechnol. Microelectron. Mater. Process. Meas. Phenom.*, vol. 28, no. 6, p. C6B30-C6B34, 2010, doi: 10.1116/1.3501348.
- [81] C. Park, J. Yoon, and E. L. Thomas, "Enabling nanotechnology with self assembled block

- copolymer patterns," *Polymer (Guildf.)*, vol. 44, no. 22, pp. 6725–6760, 2003, doi: 10.1016/j.polymer.2003.08.011.
- [82] Y. Zhu, K. Aissou, D. Andelman, and X. Man, "Effect of Sinusoidal Surface Roughness and Energy on the Orientation of Cylinder-Forming Block Copolymer Thin Films," pp. 1–10, 2018, [Online]. Available: <http://arxiv.org/abs/1811.01539>.
- [83] S. M. Nicaise, K. G. Amir Tavakkoli, and K. K. Berggren, "Self-assembly of block copolymers by graphoepitaxy," in *Directed Self-assembly of Block Co-polymers for Nano-manufacturing*, Elsevier, 2015, pp. 199–232.
- [84] M. J. Maher *et al.*, "Directed self-assembly of silicon-containing block copolymer thin films," *ACS Appl. Mater. Interfaces*, vol. 7, no. 5, pp. 3323–3328, 2015, doi: 10.1021/am508197k.
- [85] J. Y. Cheng, C. A. Ross, E. L. Thomas, H. I. Smith, and G. J. Vancso, "Fabrication of nanostructures with long-range order using block copolymer lithography," *Appl. Phys. Lett.*, vol. 81, no. 19, pp. 3657–3659, 2002, doi: 10.1063/1.1519356.
- [86] C. Park *et al.*, "Double textured cylindrical block copolymer domains via directional solidification on a topographically patterned substrate solidification on a topographically patterned substrate," vol. 848, no. April 2001, pp. 1999–2002, 2016, doi: 10.1063/1.1389766.
- [87] R. Tiron *et al.*, "Optimization of block copolymer self-assembly through graphoepitaxy: A defectivity study," *J. Vac. Sci. Technol. B, Nanotechnol. Microelectron. Mater. Process. Meas. Phenom.*, vol. 29, no. 6, p. 06F206, 2011, doi: 10.1116/1.3659714.
- [88] I. Bitá, J. K. W. Yang, Y. S. Jung, C. A. Ross, E. L. Thomas, and K. K. Berggren, "Graphoepitaxy of Self-Assembled Block Copolymers on Two-Dimensional Periodic Patterned Templates," *Science (80-.)*, vol. 321, no. 5891, pp. 939–943, Aug. 2008, doi: 10.1126/science.1159352.
- [89] S. Kim *et al.*, "Graphoepitaxy of block-copolymer self-assembly integrated with single-step ZnO nanoimprinting," *Small*, vol. 8, no. 10, pp. 1563–1569, 2012, doi: 10.1002/smll.201101960.
- [90] C. Cummins *et al.*, "Parallel Arrays of Sub-10 nm Aligned Germanium Nanofins from an in Situ Metal Oxide Hardmask using Directed Self-Assembly of Block Copolymers," *Chem. Mater.*, vol. 27, no. 17, pp. 6091–6096, 2015, doi: 10.1021/acs.chemmater.5b02608.
- [91] H. W. Do *et al.*, "Directed self-assembly of a two-state block copolymer system," *Nano Converg.*, vol. 5, no. 1, 2018, doi: 10.1186/s40580-018-0156-z.
- [92] S. O. Kim, H. Solak, M. P. Stoykovich, N. J. Ferrier, J. J. de Pablo, and P. F. Nealey, "Epitaxial self-assembly of block copolymers on lithographically defined nanopatterned substrates," *Nature*, vol. 424, pp. 411–414, 2003.
- [93] Y. Tada *et al.*, "Directed Self-Assembly of Diblock Copolymer Thin Films on Chemically-Patterned Substrates for Defect-Free Nano-Patterning Directed Self-Assembly of Diblock Copolymer Thin Films on Chemically-Patterned Substrates for Defect-Free Nano-Patterning," pp. 9267–9276, 2008, doi: 10.1021/ma801542y.
- [94] R. Ruiz, H. Kang, F. A. Detcheverry, and E. Dobisz, "Density Multiplication and Improved Lithography by Directed Block Copolymer Assembly," vol. 936, no. 2008, pp. 936–940, 2014, doi: 10.1126/science.1157626.
- [95] M. P. Stoykovich *et al.*, "Directed Self-Assembly of Block Copolymers for Nanolithography: Fabrication of Isolated Features and Essential Integrated Circuit Geometries," *ACS Nano*, vol. 1, no. 3, pp. 168–175, Oct. 2007, doi: 10.1021/nn700164p.
- [96] E. Han, H. Kang, C. C. Liu, P. F. Nealey, and P. Gopalan, "Graphoepitaxial assembly of symmetric block copolymers on weakly preferential substrates," *Adv. Mater.*, vol. 22, no. 38, pp. 4325–4329, 2010, doi: 10.1002/adma.201001669.

- [97] J. K. Cheng, C. T. Rettner, D. P. Sanders, H. C. Kim, and W. D. Hinsberg, "Dense self-assembly on sparse chemical patterns: Rectifying and multiplying lithographic patterns using block copolymers," *Adv. Mater.*, vol. 20, no. 16, pp. 3155–3158, 2008, doi: 10.1002/adma.200800826.
- [98] C. C. Liu *et al.*, "Chemical patterns for directed self-assembly of lamellae-forming block copolymers with density multiplication of features," *Macromolecules*, vol. 46, no. 4, pp. 1415–1424, 2013, doi: 10.1021/ma302464n.
- [99] M. P. Stoykovich, "Directed Assembly of Block Copolymer Blends into Nonregular Device-Oriented Structures," *Science (80-.)*, vol. 308, no. 5727, pp. 1442–1446, Jun. 2005, doi: 10.1126/science.1111041.
- [100] S.-M. Park, M. P. Stoykovich, R. Ruiz, Y. Zhang, C. T. Black, and P. F. Nealey, "Directed Assembly of Lamellae-Forming Block Copolymers by Using Chemically and Topographically Patterned Substrates," *Adv. Mater.*, vol. 19, no. 4, pp. 607–611, 2007, doi: 10.1002/adma.200601421.
- [101] D. E. Angelescu *et al.*, "Macroscopic orientation of block copolymer cylinders in single-layer films by shearing," *Adv. Mater.*, vol. 16, no. 19, pp. 1736–1740, 2004, doi: 10.1002/adma.200400643.
- [102] E. J. W. Crossland, S. Ludwigs, M. A. Hillmyer, and U. Steiner, "Freestanding nanowire arrays from soft-etch block copolymer templates," *Soft Matter*, vol. 3, no. 1, pp. 94–98, 2007, doi: 10.1039/b609780d.
- [103] V. Olszowka, M. Hund, V. Kuntermann, S. Scherdel, L. Tsarkova, and A. Böker, "Electric field alignment of a block copolymer nanopattern: direct observation of the microscopic mechanism," *ACS Nano*, vol. 3, no. 5, pp. 1091–1096, 2009, doi: 10.1021/nn900081u.
- [104] G. Singh, K. G. Yager, B. Berry, H. C. Kim, and A. Karim, "Dynamic thermal field-induced gradient soft-shear for highly oriented block copolymer thin films," *ACS Nano*, vol. 6, no. 11, pp. 10335–10342, 2012, doi: 10.1021/nn304266f.
- [105] P. W. Majewski and K. G. Yager, "Millisecond Ordering of Block Copolymer Films via Photothermal Gradients," *ACS Nano*, vol. 9, no. 4, pp. 3896–3906, Apr. 2015, doi: 10.1021/nn5071827.
- [106] M. Gopinadhan *et al.*, "Thermally switchable aligned nanopores by magnetic-field directed self-assembly of block copolymers," *Adv. Mater.*, vol. 26, no. 30, pp. 5148–5154, 2014, doi: 10.1002/adma.201401569.
- [107] S. Wu, "Surface and interfacial tensions of polymer melts," *J. Colloid Interface Sci.*, vol. 31, no. 2, pp. 153–161, 1969, doi: 10.1016/0021-9797(69)90321-x.
- [108] U. Gaur and B. Wunderlich, "Heat Capacity and Other Thermodynamic Properties of Linear Macromolecules. V. Polystyrene," *J. Phys. Chem. Ref. Data*, vol. 11, no. 2, pp. 313–325, Apr. 1982, doi: 10.1063/1.555663.
- [109] J. D. Ferry and H. S. Myers, "Viscoelastic Properties of Polymers," *J. Electrochem. Soc.*, vol. 108, no. 7, p. 142C, 1961, doi: 10.1149/1.2428174.
- [110] B. Hartmann and J. Jarzynski, "Immersion apparatus for ultrasonic measurements in polymers," *J. Acoust. Soc. Am.*, vol. 56, no. 5, pp. 1469–1477, 1974, doi: 10.1121/1.1903466.
- [111] U. Gaur, S. Lau, B. B. Wunderlich, and B. Wunderlich, "Heat Capacity and Other Thermodynamic Properties of Linear Macromolecules VI. Acrylic Polymers," *J. Phys. Chem. Ref. Data*, vol. 11, no. 4, pp. 1065–1089, Oct. 1982, doi: 10.1063/1.555671.
- [112] J. Jagur-Grodzinski, "Functional polymers by living anionic polymerization," *J. Polym. Sci. Part A Polym. Chem.*, vol. 40, no. 13, pp. 2116–2133, Jul. 2002, doi: 10.1002/pola.10291.

- [113] X. Chevalier *et al.*, "Scaling-down lithographic dimensions with block-copolymer materials: 10-nm-sized features with poly(styrene)- block -poly(methylmethacrylate)," *J. Micro/Nanolithography, MEMS, MOEMS*, vol. 12, no. 3, p. 031102, Aug. 2013, doi: 10.1117/1.jmm.12.3.031102.
- [114] E. Sivaniah *et al.*, "Symmetric diblock copolymer thin films on rough substrates: Microdomain periodicity in pure and blended films," *Macromolecules*, vol. 41, no. 7, pp. 2584–2592, 2008, doi: 10.1021/ma702465t.
- [115] B. Stühn, "The relation between the microphase separation transition and the glass transition in diblock copolymers," *J. Polym. Sci. Part B Polym. Phys.*, vol. 30, no. 9, pp. 1013–1019, 1992, doi: 10.1002/polb.1992.090300909.
- [116] T. P. Russell, R. P. Hjelm, and P. A. Seeger, "Temperature Dependence of the Interaction Parameter of Polystyrene and Poly(methyl methacrylate)," *Macromolecules*, vol. 23, no. 3, pp. 890–893, May 1990, doi: 10.1021/ma00205a033.
- [117] T. P. Russell, "Changes in Polystyrene and Poly(methyl methacrylate) Interactions with Isotopic Substitution," *Macromolecules*, vol. 26, no. 21, p. 5819, 1993, doi: 10.1021/ma00073a044.
- [118] Z. Yue, E. Sivaniah, and T. Hashimoto, "SAXS analysis of the Order-disorder transition and the interaction parameter of Polystyrene-block-poly(methyl methacrylate)," *Macromolecules*, vol. 41, no. 24, pp. 9948–9951, 2008, doi: 10.1021/ma8013004.
- [119] K. Shin *et al.*, "A Simple Route to Metal Nanodots and Nanoporous Metal Films," *Nano Lett.*, vol. 2, no. 9, pp. 933–936, Sep. 2002, doi: 10.1021/nl0256560.
- [120] M. Ma and Y. Guo, "Accelerated Aging of PS Blocks in PS- b-PMMA Diblock Copolymer under Hard Confinement," *J. Phys. Chem. B*, vol. 123, no. 10, pp. 2448–2453, 2019, doi: 10.1021/acs.jpcc.8b12565.
- [121] D. Y. Ryu, S. Ham, E. Kim, U. Jeong, C. J. Hawker, and T. P. Russell, "Cylindrical microdomain orientation of PS-b-PMMA on the balanced interfacial interactions: Composition effect of block copolymers," *Macromolecules*, vol. 42, no. 13, pp. 4902–4906, 2009, doi: 10.1021/ma900110w.
- [122] F. Ferrarese Lupi *et al.*, "Fine tuning of lithographic masks through thin films of PS-b-PMMA with different molar mass by rapid thermal processing," *ACS Appl. Mater. Interfaces*, vol. 6, no. 10, pp. 7180–7188, 2014, doi: 10.1021/am5003074.
- [123] S. Park, Y. Kim, W. Lee, S. M. Hur, and D. Y. Ryu, "Gyroid Structures in Solvent Annealed PS-b-PMMA Films: Controlled Orientation by Substrate Interactions," *Macromolecules*, vol. 50, no. 13, pp. 5033–5041, 2017, doi: 10.1021/acs.macromol.7b00898.
- [124] G. Seguini *et al.*, "Thermally induced self-assembly of cylindrical nanodomains in low molecular weight PS-b-PMMA thin films," *Nanotechnology*, vol. 25, no. 4, 2014, doi: 10.1088/0957-4484/25/4/045301.
- [125] S. Ji, U. Nagpal, W. Liao, C. C. Liu, J. J. De Pablo, and P. F. Nealey, "Three-dimensional directed assembly of block copolymers together with two-dimensional square and rectangular nanolithography," *Adv. Mater.*, vol. 23, no. 32, pp. 3692–3697, 2011, doi: 10.1002/adma.201101813.
- [126] I. Park, S. Park, H. W. Park, T. Chang, H. Yang, and C. Y. Ryu, "Unexpected hexagonally perforated layer morphology of PS-b-PMMA block copolymer in supported thin film," *Macromolecules*, vol. 39, no. 1, pp. 315–318, 2006, doi: 10.1021/ma0515937.
- [127] S. J. Jeong *et al.*, "Universal block copolymer lithography for metals, semiconductors, ceramics, and polymers," *Adv. Mater.*, vol. 20, no. 10, pp. 1898–1904, 2008, doi: 10.1002/adma.200702930.

- [128] “[Plastics Engineering] Jozef Bicerano - Prediction of polymer properties (2002, Dekker) - libgen.lc.pdf.”
- [129] M. Lazzari and M. Arturo López-Quintela, “Block Copolymers as a Tool for Nanomaterial Fabrication,” *Adv. Mater.*, vol. 15, no. 19, pp. 1583–1594, 2003, doi: 10.1002/adma.200300382.
- [130] K. Tietz, S. Finkhäuser, K. Samwer, and P. Vana, “Stabilizing the microphase separation of block copolymers by controlled photo-crosslinking,” *Macromol. Chem. Phys.*, vol. 215, no. 16, pp. 1563–1572, 2014, doi: 10.1002/macp.201400214.
- [131] E. Kim *et al.*, “Size control and registration of nano-structured thin films by cross-linkable units,” *Soft Matter*, vol. 4, no. 3, pp. 475–479, 2008, doi: 10.1039/b717903k.
- [132] N. Demazy, C. Cummins, K. Aissou, and G. Fleury, “Non-Native Block Copolymer Thin Film Nanostructures Derived from Iterative Self-Assembly Processes,” *Adv. Mater. Interfaces*, vol. 1901747, pp. 1–11, 2019, doi: 10.1002/admi.201901747.
- [133] F. Rose, J. K. Bosworth, E. A. Dobisz, and R. Ruiz, “Three-dimensional mesoporous structures fabricated by independent stacking of self-assembled films on suspended membranes,” *Nanotechnology*, vol. 22, no. 3, p. 035603, Jan. 2011, doi: 10.1088/0957-4484/22/3/035603.
- [134] H. Jung *et al.*, “Three-dimensional multilayered nanostructures with controlled orientation of microdomains from cross-linkable block copolymers,” *ACS Nano*, vol. 5, no. 8, pp. 6164–6173, 2011, doi: 10.1021/nn2006943.
- [135] L. Li *et al.*, “Fabrication of robust honeycomb polymer films: A facile photochemical cross-linking process,” *J. Colloid Interface Sci.*, vol. 331, no. 2, pp. 446–452, 2009, doi: 10.1016/j.jcis.2008.11.053.
- [136] I. J. Chen and E. Lindner, “The stability of radio-frequency plasma-treated polydimethylsiloxane surfaces,” *Langmuir*, vol. 23, no. 6, pp. 3118–3122, 2007, doi: 10.1021/la0627720.
- [137] C. C. Chao, T. C. Wang, R. M. Ho, P. Georgopoulos, A. Avgeropoulos, and E. L. Thomas, “Robust block copolymer mask for nanopatterning polymer films,” *ACS Nano*, vol. 4, no. 4, pp. 2088–2094, 2010, doi: 10.1021/nn901370g.
- [138] T. Hirai *et al.*, “One-step direct-patterning template utilizing self-assembly of POSS-containing block copolymers,” *Adv. Mater.*, vol. 21, no. 43, pp. 4334–4338, 2009, doi: 10.1002/adma.200900518.
- [139] T. Y. Lo, M. R. Krishnan, K. Y. Lu, and R. M. Ho, “Silicon-containing block copolymers for lithographic applications,” *Prog. Polym. Sci.*, vol. 77, pp. 19–68, 2018, doi: 10.1016/j.progpolymsci.2017.10.002.
- [140] J. Wan, A. Alizadeh, S. T. Taylor, P. R. L. Malenfant, M. Manoharan, and S. M. Loureiro, “Nanostructured non-oxide ceramics templated via block copolymer self-assembly,” *Chem. Mater.*, vol. 17, no. 23, pp. 5613–5617, 2005, doi: 10.1021/cm051124j.
- [141] H. Mori, A. Hirao, S. Nakahama, and K. Senuki, “Synthesis and Surface Characterization of Hydrophilic-Hydrophobic Block Copolymers Containing Poly(2,3-dihydroxypropyl methacrylate),” *Macromolecules*, vol. 27, no. 15, pp. 4093–4100, Jul. 1994, doi: 10.1021/ma00093a010.
- [142] T. Xu *et al.*, “Block copolymer surface reconstruction: A reversible route to nanoporous films,” *Adv. Funct. Mater.*, vol. 13, no. 9, pp. 698–702, 2003, doi: 10.1002/adfm.200304374.
- [143] Y. Wang and F. Li, “An emerging pore-making strategy: Confined swelling-induced pore generation in block copolymer materials,” *Adv. Mater.*, vol. 23, no. 19, pp. 2134–2148, 2011, doi: 10.1002/adma.201004022.

- [144] C. Xu *et al.*, "Reversible Stimuli-Responsive Nanostructures Assembled from Amphiphilic Block Copolymers," *Nano Lett.*, vol. 6, no. 2, pp. 282–287, Feb. 2006, doi: 10.1021/nl052332d.
- [145] J. G. Son, W. K. Bae, H. Kang, P. F. Nealey, and K. Char, "Placement Control of Nanomaterial Arrays on the Surface-Reconstructed Block Copolymer Thin Films," *ACS Nano*, vol. 3, no. 12, pp. 3927–3934, Dec. 2009, doi: 10.1021/nn900914q.
- [146] M. Muramatsu, "Nanopatterning of diblock copolymer directed self-assembly lithography with wet development," *J. Micro/Nanolithography, MEMS, MOEMS*, vol. 11, no. 3, p. 031305, 2012, doi: 10.1117/1.JMM.11.3.031305.
- [147] B. Rathsack *et al.*, "Pattern scaling with directed self assembly through lithography and etch process integration," *Proc. SPIE*, vol. 8323, pp. 83230B–83230B–14, 2012, doi: 10.1117/12.916311.
- [148] A. Gharbi *et al.*, "PMMA removal options by wet development in PS- b -PMMA block copolymer for nanolithographic mask fabrication," *J. Vac. Sci. Technol. B, Nanotechnol. Microelectron. Mater. Process. Meas. Phenom.*, vol. 33, no. 5, p. 051602, 2015, doi: 10.1116/1.4929548.
- [149] G. Freychet *et al.*, "Removal of poly(methyl methacrylate) in diblock copolymers films studied by grazing incidence small-angle X-ray scattering," *J. Polym. Sci. Part B Polym. Phys.*, vol. 54, no. 12, pp. 1137–1144, 2016, doi: 10.1002/polb.24017.
- [150] D. H. Lee, D. O. Shin, W. J. Lee, and S. O. Kim, "Hierarchically organized carbon nanotube arrays from self-assembled block copolymer nanotemplates," *Adv. Mater.*, vol. 20, no. 13, pp. 2480–2485, 2008, doi: 10.1002/adma.200702712.
- [151] Y. Ting *et al.*, "Plasma etch removal of poly(methyl methacrylate) in block copolymer lithography," *J. Vac. Sci. Technol. B Microelectron. Nanom. Struct.*, vol. 26, no. 5, p. 1684, 2008, doi: 10.1116/1.2966433.
- [152] M. Satake, T. Iwase, M. Kurihara, N. Negishi, Y. Tada, and H. Yoshida, "Effect of oxygen addition to an argon plasma on etching selectivity of poly(methyl methacrylate) to polystyrene," *J. Micro/Nanolithography, MEMS, MOEMS*, vol. 12, no. 4, p. 041309, 2013, doi: 10.1117/1.jmm.12.4.041309.
- [153] R. A. Farrell, N. Petkov, M. T. Shaw, V. Djara, J. D. Holmes, and M. A. Morris, "Monitoring PMMA elimination by reactive ion etching from a lamellar PS-b-PMMA thin film by ex situ TEM methods," *Macromolecules*, vol. 43, no. 20, pp. 8651–8655, 2010, doi: 10.1021/ma101827u.
- [154] C. Cummins, T. Ghoshal, J. D. Holmes, and M. A. Morris, "Strategies for Inorganic Incorporation using Neat Block Copolymer Thin Films for Etch Mask Function and Nanotechnological Application," *Adv. Mater.*, pp. 5586–5618, 2016, doi: 10.1002/adma.201503432.
- [155] R. W. Johnson, A. Hultqvist, and S. F. Bent, "A brief review of atomic layer deposition: From fundamentals to applications," *Mater. Today*, vol. 17, no. 5, pp. 236–246, 2014, doi: 10.1016/j.mattod.2014.04.026.
- [156] R. Z. Waldman, D. J. Mandia, A. Yanguas-Gil, A. B. F. Martinson, J. W. Elam, and S. B. Darling, "The chemical physics of sequential infiltration synthesis - A thermodynamic and kinetic perspective," *J. Chem. Phys.*, vol. 151, no. 19, 2019, doi: 10.1063/1.5128108.
- [157] C. Z. Leng and M. D. Losego, "Vapor phase infiltration (VPI) for transforming polymers into organic-inorganic hybrid materials: A critical review of current progress and future challenges," *Mater. Horizons*, vol. 4, no. 5, pp. 747–771, 2017, doi: 10.1039/c7mh00196g.
- [158] E. C. Dandley, C. D. Needham, P. S. Williams, A. H. Brozena, C. J. Oldham, and G. N. Parsons,

- “Temperature-dependent reaction between trimethylaluminum and poly(methyl methacrylate) during sequential vapor infiltration: experimental and ab initio analysis,” *J. Mater. Chem. C*, vol. 2, no. 44, pp. 9416–9424, 2014, doi: 10.1039/C4TC01293C.
- [159] Q. Peng, Y. C. Tseng, S. B. Darling, and J. W. Elam, “A route to nanoscopic materials via sequential infiltration synthesis on block copolymer templates,” *ACS Nano*, vol. 5, no. 6, pp. 4600–4606, 2011, doi: 10.1021/nn2003234.
- [160] J. W. Elam *et al.*, “New Insights into Sequential Infiltration Synthesis,” *ECS Trans.*, vol. 69, no. 7, pp. 147–157, 2015, doi: 10.1149/06907.0147ecst.
- [161] M. Lorenzoni, L. Evangelio, M. Fernández-Regúlez, C. Nicolet, C. Navarro, and F. Pérez-Murano, “Sequential Infiltration of Self-Assembled Block Copolymers: A Study by Atomic Force Microscopy,” *J. Phys. Chem. C*, vol. 121, no. 5, pp. 3078–3086, 2017, doi: 10.1021/acs.jpcc.6b11233.
- [162] R. Azoulay, N. Shomrat, I. Weisbord, G. Atiya, and T. Segal-Peretz, “Metal Oxide Heterostructure Array via Spatially Controlled-Growth within Block Copolymer Templates,” *Small*, vol. 15, no. 51, pp. 1–7, 2019, doi: 10.1002/sml.201904657.
- [163] J. J. Kim *et al.*, “Mechanistic understanding of tungsten oxide in-plane nanostructure growth: Via sequential infiltration synthesis,” *Nanoscale*, vol. 10, no. 7, pp. 3469–3479, 2018, doi: 10.1039/c7nr07642h.
- [164] Y. C. Tseng, Q. Peng, L. E. Ocola, J. W. Elam, and S. B. Darling, “Enhanced block copolymer lithography using sequential infiltration synthesis,” *J. Phys. Chem. C*, vol. 115, no. 36, pp. 17725–17729, 2011, doi: 10.1021/jp205532e.
- [165] Q. Peng, Y. C. Tseng, S. B. Darling, and J. W. Elam, “Nanoscopic patterned materials with tunable dimensions via atomic layer deposition on block copolymers,” *Adv. Mater.*, vol. 22, no. 45, pp. 5129–5133, 2010, doi: 10.1002/adma.201002465.
- [166] J. Kamcev, D. S. Germack, D. Nykypanchuk, R. B. Grubbs, C. Y. Nam, and C. T. Black, “Chemically enhancing block copolymers for block-selective synthesis of self-assembled metal oxide nanostructures,” *ACS Nano*, vol. 7, no. 1, pp. 339–346, 2013, doi: 10.1021/nn304122b.
- [167] J. Frascaroli, E. Cianci, S. Spiga, G. Seguni, and M. Perego, “Ozone-Based Sequential Infiltration Synthesis of Al₂O₃ Nanostructures in Symmetric Block Copolymer,” *ACS Appl. Mater. Interfaces*, vol. 8, no. 49, pp. 33933–33942, 2016, doi: 10.1021/acsami.6b11340.
- [168] Q. Peng *et al.*, “Effect of Nanostructured Domains in Self-Assembled Block Copolymer Films on Sequential Infiltration Synthesis,” *Langmuir*, vol. 33, no. 46, pp. 13214–13223, 2017, doi: 10.1021/acs.langmuir.7b02922.
- [169] R. Z. Waldman, N. Jeon, D. J. Mandia, O. Heinonen, S. B. Darling, and A. B. F. Martinson, “Sequential Infiltration Synthesis of Electronic Materials: Group 13 Oxides via Metal Alkyl Precursors,” *Chem. Mater.*, vol. 31, no. 14, pp. 5274–5285, 2019, doi: 10.1021/acs.chemmater.9b01714.
- [170] C. Zhou, T. Segal-peretz, M. E. Oruc, H. S. Suh, G. Wu, and P. F. Nealey, “Fabrication of Nanoporous Alumina Ultrafiltration Membrane with Tunable Pore Size Using Block Copolymer Templates,” vol. 1701756, pp. 19–22, 2017, doi: 10.1002/adfm.201701756.
- [171] J. Yin, Q. Xu, Z. Wang, X. Yao, and Y. Wang, “Highly ordered TiO₂ nanostructures by sequential vapour infiltration of block copolymer micellar films in an atomic layer deposition reactor,” *J. Mater. Chem. C*, vol. 1, no. 5, pp. 1029–1036, 2013, doi: 10.1039/C2TC00306F.
- [172] W. A. Lopes and H. M. Jaeger, “Hierarchical self-assembly of metal nanostructures on diblock copolymer scaffolds,” vol. 414, no. December, pp. 735–738, 2001.

- [173] J. Chai, D. Wang, X. Fan, and J. M. Buriak, "Assembly of aligned linear metallic patterns on silicon," *Nat. Nanotechnol.*, vol. 2, no. 8, pp. 500–506, 2007, doi: 10.1038/nnano.2007.227.
- [174] J. Chai and J. M. Buriak, "Using Cylindrical Domains of Block Copolymers To Self-Assemble and Align Metallic Nanowires," *ACS Nano*, vol. 2, no. 3, pp. 489–501, Mar. 2008, doi: 10.1021/nn700341s.
- [175] J. H. Mun *et al.*, "Nanodomain swelling block copolymer lithography for morphology tunable metal nanopatterning," *Small*, vol. 10, no. 18, pp. 3742–3749, 2014, doi: 10.1002/smll.201400600.
- [176] M. K. Abyaneh, D. Paramanik, S. Varma, S. W. Gosavi, and S. K. Kulkarni, "Formation of gold nanoparticles in polymethylmethacrylate by UV irradiation," *J. Phys. D. Appl. Phys.*, vol. 40, no. 12, pp. 3771–3779, 2007, doi: 10.1088/0022-3727/40/12/032.
- [177] A. Alexandrov, L. Smirnova, N. Yakimovich, and N. Sapogova, "UV-initiated growth of gold nanoparticles in PMMA matrix," vol. 248, pp. 181–184, 2005, doi: 10.1016/j.apsusc.2005.03.002.
- [178] T. Ghoshal, M. T. Shaw, C. T. Bolger, J. D. Holmes, and M. A. Morris, "A general method for controlled nanopatterning of oxide dots: A microphase separated block copolymer platform," *J. Mater. Chem.*, vol. 22, no. 24, pp. 12083–12089, 2012, doi: 10.1039/c2jm30468f.
- [179] T. Thurn-Albrecht *et al.*, "Ultrahigh-density nanowire arrays grown in self-assembled diblock copolymer templates," *Science (80-.)*, vol. 290, no. 5499, pp. 2126–2129, 2000, doi: 10.1126/science.290.5499.2126.
- [180] S. Vignolini *et al.*, "A 3D optical metamaterial made by self-assembly," *Adv. Mater.*, vol. 24, no. 10, pp. 23–27, 2012, doi: 10.1002/adma.201103610.
- [181] S. Salvatore *et al.*, "A high transmission wave-guide wire network made by self-assembly," *Nanoscale*, vol. 7, no. 3, pp. 1032–1036, 2015, doi: 10.1039/c4nr04485a.
- [182] Y. S. Jung, J. H. Lee, J. Y. Lee, and C. A. Ross, "Fabrication of diverse metallic nanowire arrays based on block copolymer self-assembly," *Nano Lett.*, vol. 10, no. 9, pp. 3722–3726, 2010, doi: 10.1021/nl1023518.
- [183] A. J. Hong *et al.*, "Metal nanodot memory by self-assembled block copolymer lift-off," *Nano Lett.*, vol. 10, no. 1, pp. 224–229, 2010, doi: 10.1021/nl903340a.
- [184] S. Park, J. Y. Wang, B. Kim, and T. P. Russell, "From nanorings to nanodots by patterning with block copolymers," *Nano Lett.*, vol. 8, no. 6, pp. 1667–1672, 2008, doi: 10.1021/nl0805110.
- [185] Y. S. Jung and C. A. Ross, "Well-ordered thin-film nanopore arrays formed using a block-copolymer template," *Small*, vol. 5, no. 14, pp. 1654–1659, 2009, doi: 10.1002/smll.200900053.
- [186] S. J. Ku *et al.*, "Highly ordered freestanding titanium oxide nanotube arrays using Si-containing block copolymer lithography and atomic layer deposition," *Nanotechnology*, vol. 24, no. 8, 2013, doi: 10.1088/0957-4484/24/8/085301.
- [187] E. Bhoje Gowd *et al.*, "Highly ordered palladium nanodots and nanowires from switchable block copolymer thin films," *Nanotechnology*, vol. 20, no. 41, 2009, doi: 10.1088/0957-4484/20/41/415302.
- [188] J. J. Chiu, B. J. Kim, E. J. Kramer, and D. J. Pine, "Control of nanoparticle location in block copolymers," *J. Am. Chem. Soc.*, vol. 127, no. 14, pp. 5036–5037, 2005, doi: 10.1021/ja050376i.
- [189] A. Rahman, P. W. Majewski, G. Doerk, C. T. Black, and K. G. Yager, "Non-native three-

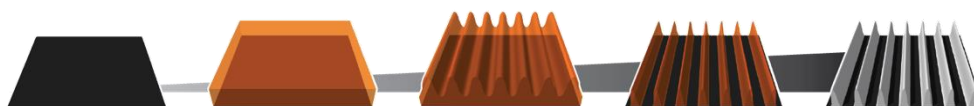
- dimensional block copolymer morphologies," *Nat. Commun.*, vol. 7, no. 1, p. 13988, Dec. 2016, doi: 10.1038/ncomms13988.
- [190] H. Yu and T. Kobayashi, *Photoresponsive block copolymers containing azobenzenes and other chromophores*, vol. 15, no. 1. 2010.
- [191] Y. Zhao and J. He, "Azobenzene-containing block copolymers: The interplay of light and morphology enables new functions," *Soft Matter*, vol. 5, no. 14, pp. 2686–2693, 2009, doi: 10.1039/b821589h.
- [192] T. Seki, "Meso- and microscopic motions in photoresponsive liquid crystalline polymer films," *Macromol. Rapid Commun.*, vol. 35, no. 3, pp. 271–290, 2014, doi: 10.1002/marc.201300763.
- [193] G. Sudesh, T. B. Road, P. Sciences, B. Green, G. S. Kumar, and D. C. Neckers, "Photochemistry of azobenzene-containing polymers," *Chem. Rev.*, vol. 89, no. 8, pp. 1915–1925, Dec. 1989, doi: 10.1021/cr00098a012.
- [194] T. Ishikawa, T. Noro, and T. Shoda, "Theoretical study on the photoisomerization of azobenzene," *J. Chem. Phys.*, vol. 115, no. 16, pp. 7503–7512, 2001, doi: 10.1063/1.1406975.
- [195] J. Henzl, M. Mehlhorn, H. Gawronski, K. H. Rieder, and K. Morgenstern, "Reversible cis-trans isomerization of a single azobenzene molecule," *Angew. Chemie - Int. Ed.*, vol. 45, no. 4, pp. 603–606, 2006, doi: 10.1002/anie.200502229.
- [196] E. Fischer, "Temperature Dependence of Photoisomerization Equilibria. Part I. Azobenzene and the Azonaphthalenes," *J. Am. Chem. Soc.*, vol. 82, no. 13, pp. 3249–3252, 1960, doi: 10.1021/ja01498a005.
- [197] T. Ikeda and O. Tsutsumi, "Optical switching and image storage by means of azobenzene liquid-crystal films," *Science (80-.)*, vol. 268, no. 5219, pp. 1873–1875, 1995, doi: 10.1126/science.268.5219.1873.
- [198] N. Tamai and H. Miyasaka, "Ultrafast Dynamics of Photochromic Systems," *Chem. Rev.*, vol. 100, no. 5, pp. 1875–1890, 2000, doi: 10.1021/cr9800816.
- [199] H. Asanuma, T. Takarada, T. Yoshida, D. Tamaru, X. Liang, and M. Komiyama, "Enantioselective incorporation of azobenzenes into oligodeoxyribonucleotide for effective photoregulation of duplex formation," *Angew. Chemie - Int. Ed.*, vol. 40, no. 14, pp. 2671–2673, 2001, doi: 10.1002/1521-3773(20010716)40:14<2671::AID-ANIE2671>3.0.CO;2-Z.
- [200] H. Asanuma, T. Ito, T. Yoshida, X. Liang, and M. Komiyama, "Photoregulation of the formation and dissociation of a DNA duplex by using the cis-trans isomerization of azobenzene," *Angew. Chemie - Int. Ed.*, vol. 38, no. 16, pp. 2393–2395, 1999, doi: 10.1002/(SICI)1521-3773(19990816)38:16<2393::AID-ANIE2393>3.0.CO;2-7.
- [201] D. Y. Kim, L. Li, X. L. Jiang, V. Shivshankar, J. Kumar, and S. K. Tripathy, "Polarized Laser Induced Holographic Surface Relief Gratings on Polymer Films," *Macromolecules*, vol. 28, no. 26, pp. 8835–8839, Dec. 1995, doi: 10.1021/ma00130a017.
- [202] J. de Boor, N. Geyer, U. Gösele, and V. Schmidt, "Three-beam interference lithography: upgrading a Lloyd's interferometer for single-exposure hexagonal patterning," *Opt. Lett.*, vol. 34, no. 12, p. 1783, 2009, doi: 10.1364/OL.34.001783.
- [203] R. G. Sabat, N. Rochon, and P. Rochon, "Dependence of surface plasmon polarization conversion on the grating pitch," *J. Opt. Soc. Am. A*, vol. 27, no. 3, p. 518, Mar. 2010, doi: 10.1364/JOSAA.27.000518.
- [204] J.-B. Yeo, S.-D. Yun, N.-H. Kim, and H.-Y. Lee, "Fabrication of Si-based two-dimensional photonic quasicrystals by using multiple-exposure holographic lithography," *J. Vac. Sci. Technol. B Microelectron. Nanom. Struct.*, vol. 27, no. 4, p. 1886, 2009, doi:

- 10.1116/1.3159782.
- [205] A. Kravchenko, A. Shevchenko, P. Grahn, V. Ovchinnikov, and M. Kaivola, "Photolithographic periodic patterning of gold using azobenzene- functionalized polymers," *Thin Solid Films*, vol. 540, pp. 162–167, 2013, doi: 10.1016/j.tsf.2013.05.156.
- [206] O. Sakhno, L. M. Goldenberg, M. Wegener, and J. Stumpe, "Deep surface relief grating in azobenzene-containing materials using a low-intensity 532 nm laser," *Opt. Mater. X*, vol. 1, no. October 2018, p. 100006, 2019, doi: 10.1016/j.omx.2019.100006.
- [207] S. Nair, C. Escobedo, and R. G. Sabat, "Crossed Surface Relief Gratings as Nanoplasmonic Biosensors," *ACS Sensors*, vol. 2, no. 3, pp. 379–385, 2017, doi: 10.1021/acssensors.6b00696.
- [208] A. Hassanzadeh, M. Mohammadnezhad, and S. Mittler, "Multiexposure laser interference lithography," *J. Nanophotonics*, vol. 9, no. 1, p. 093067, 2015, doi: 10.1117/1.jnp.9.093067.
- [209] L. Jia, I. Bitá, and E. L. Thomas, "Level set photonic quasicrystals with phase parameters," *Adv. Funct. Mater.*, vol. 22, no. 6, pp. 1150–1157, 2012, doi: 10.1002/adfm.201101804.
- [210] C. Kauppinen *et al.*, "A technique for large-area position-controlled growth of GaAs nanowire arrays," *Nanotechnology*, vol. 27, no. 13, 2016, doi: 10.1088/0957-4484/27/13/135601.
- [211] R. J. Moerland *et al.*, "Large-area arrays of three-dimensional plasmonic subwavelength-sized structures from azopolymer surface-relief gratings," *Mater. Horizons*, vol. 1, no. 1, pp. 74–80, 2014, doi: 10.1039/c3mh00008g.
- [212] T. Fukuda *et al.*, "Photofabrication of surface relief grating on films of azobenzene polymer with different dye functionalization," *Macromolecules*, vol. 33, no. 11, pp. 4220–4225, 2000, doi: 10.1021/ma991803d.
- [213] P. Rochon, E. Batalla, and A. Natansohn, "Optically induced surface gratings on azoaromatic polymer films," *Appl. Phys. Lett.*, vol. 136, no. November 1994, p. 136, 1995, doi: 10.1063/1.113541.
- [214] C. J. Barrett, A. L. Natansohn, and P. L. Rochon, "Mechanism of optically inscribed high-efficiency diffraction gratings in azo polymer films," *J. Phys. Chem.*, vol. 100, no. 21, pp. 8836–8842, 1996, doi: 10.1021/jp953300p.
- [215] X. L. Jiang, L. Li, J. Kumar, D. Y. Kim, and S. K. Tripathy, "Unusual polarization dependent optical erasure of surface relief gratings on azobenzene polymer films," *Appl. Phys. Lett.*, vol. 72, no. 20, pp. 2502–2504, 1998, doi: 10.1063/1.121400.
- [216] P. Lefin, C. Fiorini, and J. M. Nunzi, "Anisotropy of the photoinduced translation diffusion of azo-dyes," *Opt. Mater. (Amst.)*, vol. 9, no. 1–4, pp. 323–328, 1998, doi: 10.1016/S0925-3467(97)00100-6.
- [217] N. K. Viswanathan, S. Balasubramanian, L. Li, J. Kumar, and S. K. Tripathy, "Surface-initiated mechanism for the formation of relief gratings on azo-polymer films," *J. Phys. Chem. B*, vol. 102, no. 31, pp. 6064–6070, 1998, doi: 10.1021/jp981425z.
- [218] J. Kumar, L. Li, X. L. Jiang, D. Y. Kim, T. S. Lee, and S. Tripathy, "Gradient force: The mechanism for surface relief grating formation in azobenzene functionalized polymers," *Appl. Phys. Lett.*, vol. 72, no. 17, pp. 2096–2098, 1998, doi: 10.1063/1.121287.
- [219] N. Hurduc *et al.*, "Direct observation of athermal photofluidisation in azo-polymer films," *Soft Matter*, vol. 10, no. 26, pp. 4640–4647, 2014, doi: 10.1039/c4sm00397g.
- [220] N. S. Yadavalli, S. Loebner, T. Papke, E. Sava, N. Hurduc, and S. Santer, "A comparative study of photoinduced deformation in azobenzene containing polymer films," *Soft Matter*, vol. 12, no. 9, pp. 2593–2603, 2016, doi: 10.1039/c6sm00029k.

- [221] P. Weis, W. Tian, and S. Wu, "Photoinduced Liquefaction of Azobenzene-Containing Polymers," *Chem. - A Eur. J.*, vol. 24, no. 25, pp. 6494–6505, 2018, doi: 10.1002/chem.201704162.
- [222] K. Aissou *et al.*, "Nanoscale block copolymer ordering induced by visible interferometric micropatterning: A route towards large scale block copolymer 2D crystals," *Adv. Mater.*, vol. 25, no. 2, pp. 213–217, 2013, doi: 10.1002/adma.201203254.
- [223] Y. Rho *et al.*, "Laterally Ordered Sub-10 nm Features Obtained from Directed Self-Assembly of Si-Containing Block Copolymer Thin Films," *Small*, vol. 11, no. 48, pp. 6377–6383, 2015, doi: 10.1002/smll.201500439.
- [224] H. Yu, A. Shishido, T. Iyoda, and T. Ikeda, "Photoinduced alignment of nanocylinders in an amphiphilic diblock liquid-crystalline copolymer by supramolecular cooperative motions," *Polym. Prepr. Japan*, vol. 55, no. 2, p. 3996, 2006.
- [225] Y. Morikawa, T. Kondo, S. Nagano, and T. Seki, "Photoinduced 3D ordering and patterning of microphase-separated nanostructure in polystyrene-based block copolymer," *Chem. Mater.*, vol. 19, no. 7, pp. 1540–1542, 2007, doi: 10.1021/cm0630845.
- [226] Y. Morikawa, S. Nagano, K. Watanabe, K. Kamata, T. Iyoda, and T. Seki, "Optical alignment and patterning of nanoscale microdomains in a block copolymer thin film," *Adv. Mater.*, vol. 18, no. 7, pp. 883–886, 2006, doi: 10.1002/adma.200502573.
- [227] C. Cummins, R. Lundy, J. J. Walsh, V. Ponsinet, G. Fleury, and M. A. Morris, "Enabling future nanomanufacturing through block copolymer self-assembly: A review," *Nano Today*, vol. 35, p. 100936, 2020, doi: 10.1016/j.nantod.2020.100936.
- [228] I. W. Hamley, "Nanostructure fabrication using block copolymers," *Nanotechnology*, vol. 14, no. 10, 2003, doi: 10.1088/0957-4484/14/10/201.
- [229] F. H. Schacher, P. A. Rugar, and I. Manners, "Functional block copolymers: Nanostructured materials with emerging applications," *Angew. Chemie - Int. Ed.*, vol. 51, no. 32, pp. 7898–7921, 2012, doi: 10.1002/anie.201200310.
- [230] Y. C. Tseng and S. B. Darling, "Block copolymer nanostructures for technology," *Polymers (Basel)*, vol. 2, no. 4, pp. 470–489, 2010, doi: 10.3390/polym2040470.
- [231] H.-C. C. Kim, S.-M. M. Park, W. D. Hinsberg, and I. R. Division, "Block Copolymer Based Nanostructures: Materials, Processes, and Applications to Electronics," *Chem. Rev.*, vol. 110, no. 1, pp. 146–177, 2010, doi: 10.1021/cr900159v.

CHAPTER II: AZOBENZENE-CONTAINING POLYMERS

II.1/ Introduction.....	76
II.2/ Directed Self-Assembly enabled by Surface Relief Gratings.....	77
II.2.A/ Optical alignment of azobenzene containing BCP thin films induced by SRG.....	77
II.2.B/ Discussion.....	89
II.3/ Substrate nanotexturing with SRG	90
II.3.A/ Pattern formation via SRG.....	90
II.3.B/ A large diversity of tunable nanostructures	96
II.3.C/ “Low cost” graphoepitaxy	97
II.4/ Conclusions	103
II.5/ References	104



In this second chapter, two functional uses of azobenzene-containing (co)polymers will be discussed. Firstly, several azobenzene-containing BCPs were studied to observe the potential interplay between BCP phase separation and the photoisomerization from azobenzene moieties. Another use of azobenzene-containing (co)polymers is related to the formation of topographical patterns from such photoisomerization. Accordingly, a process using azobenzene-containing polymer have been developed to generate fully inorganic periodical patterns with a wide variety of shapes and sizes, that can be further used for directed self-assembly based on topographical fields (i.e. graphoepitaxy).

II.1/ Introduction

Azobenzene-containing (co)polymers present interesting functional properties that can be harnessed for the control of BCP self-assembly among other applications. Indeed, azobenzene moieties undergo a cis-trans isomerization under light stimulus, which produces a mass displacement. By coupling such property with interferential patterning, it is possible to produce a topographical pattern, called surface relief gratings (SRG). Even if a consolidated theory about the formation of SRG patterns has not been yet established (see *Chapter 1.4.B/*), many research groups have been interested by this peculiar property, with about 2000 publications on Google Scholar with “surface relief grating” and “azobenzene” keywords.

In a first part of this chapter, a series of BCPs with azobenzene moieties grafted on one block have been studied to decipher the interplay between self-assembly and SRG. Indeed, literature reports have shown that photo-stimulation coupled with liquid-crystalline phase behavior could trigger the controlled self-assembly of BCPs in thin film configuration. We were interested to transpose this methodology to fully amorphous azobenzene-containing BCPs in order to generate DSA fields by coupling SRG and BCP self-assembly.

In a second part, another strategy taking advantage of the azobenzene photoisomerization for DSA has been developed with the manufacturing of processes able to generate periodical inorganic patterns from SRG. Interestingly, this process does not require advanced lithographic tools, and can be performed in a laboratory environment, producing on-demand patterns with a wide variety of achievable structures and periodicities. Also, some of these patterns were integrated in a DSA flow for the formation of highly ordered PS-*b*-PMMA patterns in thin films.

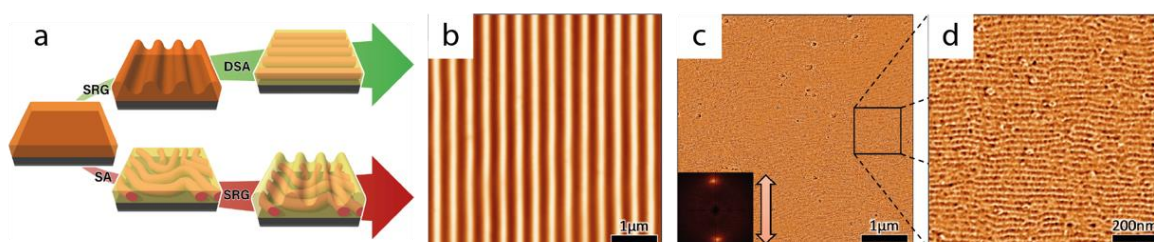
II.2/ Directed Self-Assembly enabled by Surface Relief Gratings

As described in *Chapter I.1/*, several research groups have demonstrated that azobenzene moieties grafted onto a BCP backbone can enable DSA via a polarized light stimulus. In this case, the azobenzene groups are used to trigger the BCP organization according to the light polarization axis taking advantage of the liquid-crystal behavior. This behavior has been shown to provide long-range ordering for nanostructured liquid-crystalline BCP films [1], [2].

However, (co)polymers bearing azobenzene moieties have also the ability to produce SRG through the exposure of a thin layer to light interferences generated by an interferometer setup. The resulting topographical structure is a sinusoidal pattern with a wavelength of several hundreds of nanometers. Our group have previously shown that a SRG layer enables the DSA of BCP thin films due to confinement effects [3], [4]. Nevertheless, this approach requires the design and processing of two different polymeric layers (the SRG and BCP layers). Alternatively, both functionalities could be gathered into a single BCP architecture in which one of the block also comprises azobenzene moieties. Such methodology was explored in the following article.

II.2.A/ Optical alignment of azobenzene containing BCP thin films induced by SRG

A novel approach has been presented in *Macromolecules* [5], describing first the synthesis of a fully amorphous BCP containing azobenzene moieties, and then the optimization of the self-assembly process leading to DSA promoted by SRG as schematically described in *Figure 37.a*. In this work, the synthetic part was performed by M. Spiridon, while the study and the optimization of the self-assembly were done during this Ph.D.



*Figure 38. (a) Schematics of the formation of PDMS-*b*-azoPMA in-plane cylinders via (green arrow) a first step of SRG patterning followed by a solvent annealing leading to cylinders orthogonal to the SRG waves or via (red arrow) the inverse pathway leading to randomly orientated cylinders. (b) AFM height image of the SRG pattern. (c) AFM phase image of in-plane cylinders orientated orthogonally to the SRG pattern as attested by the FFT inset. (d) Zoom of (c) showing the translational ordering of the in-plane cylinders [5].*

The bibliographic details of the published manuscript are:

M. Spiridon, N. Demazy, C. Brochon, E. Cloutet, G. Hadziioannou, K. Aissou and G. Fleury, "Optical Alignment of Si-Containing Nanodomains Formed by Photoresponsive Amorphous Block Copolymer Thin Films" *Macromolecules*, vol. 53, no. 1, pp. 68–77, 2020.

<https://doi.org/10.1021/acs.macromol.9b01551>

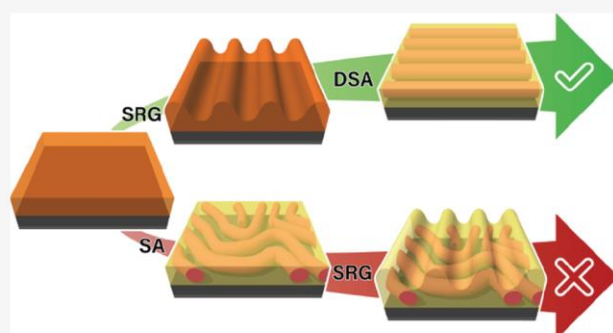
Optical Alignment of Si-Containing Nanodomains Formed by Photoresponsive Amorphous Block Copolymer Thin Films

Mitica Cezar Spiridon,[†] Nils Demazy,[†] Cyril Brochon,[‡] Eric Cloutet,[‡] Georges Hadziioannou,[‡] Karim Aissou,^{*,†,‡} and Guillaume Fleury^{*,‡}

Univ. Bordeaux, CNRS, Bordeaux INP, LCPO, UMR 5629, F-33600 Pessac, France

Supporting Information

ABSTRACT: A series of amorphous block copolymers (BCPs), consisting of a low-glass-transition polydimethylsiloxane (PDMS) block associated with a photoresponsive azobenzene-containing poly(disperse red 1 methacrylate-*co*-alkyl methacrylate) (P(DR1MA-*co*-RMA)) block, were prepared from a PDMS macro-chain transfer agent used for the reversible addition–fragmentation chain-transfer (RAFT) copolymerization of binary mixtures of methacrylate monomers of various compositions. The resulting BCPs containing up to 40 wt % of azo dye exhibited low dispersity demonstrating a good control of the RAFT polymerization through the copolymerization of the DR1MA and RMA units. Long-range-ordered in-plane PDMS cylinders were produced by exposing the (as-cast) disordered BCP thin films to a *p*-polarized laser beam, to orthogonally align the azo groups with the polarization direction, prior to promoting the microphase separation of the BCP domains with a solvent vapor annealing treatment. Conversely, the photoinduced alignment of the azo chromophores was not effective within microphase-separated BCP thin films since randomly oriented PDMS features were observed after exposure to a *p*-polarized laser light.



INTRODUCTION

Block copolymers (BCPs) bearing azobenzene (azo) moieties constitute an attractive class of advanced materials since multifunctional surfaces comprising laterally ordered nanoscale features on a periodic surface corrugation pattern, called surface relief grating (SRG), can be created due to an efficient photoalignment and mass transfer of BCP chains, triggered by azobenzene *cis*–*trans* isomerization.^{1–4} For instance, pioneer works by Ikeda and Seki groups have demonstrated that the optical alignment of cylinder-forming liquid-crystalline (LC) BCP thin films was achievable using a linearly polarized light to directionally orient the azo mesogens.^{5,6} SRG formed as a result of the mass transport induced by the photoisomerization of azo moieties is another interesting property of microphase-separated LC BCP thin films that was also explored by Seki and co-workers.^{7,8} In these studies, a thickness-dependent orientation of the cylindrical nanodomains incorporated into the micrometer-scale corrugated relief was demonstrated since the in-plane and out-of-plane orientations of the BCP features were precisely observed on the thin and thick regions of the SRG, respectively.

Besides, directed self-assembly (DSA) of laterally ordered BCP patterns on a large scale has been achieved from thickness-gradient BCP films induced by dewetting⁹ as well as from microphase-separated BCP thin films deposited onto sinusoidally shaped SRG formed by amorphous azo-containing polymer layers,^{10,11} wrinkled graphene layer surfaces,^{12–14} or

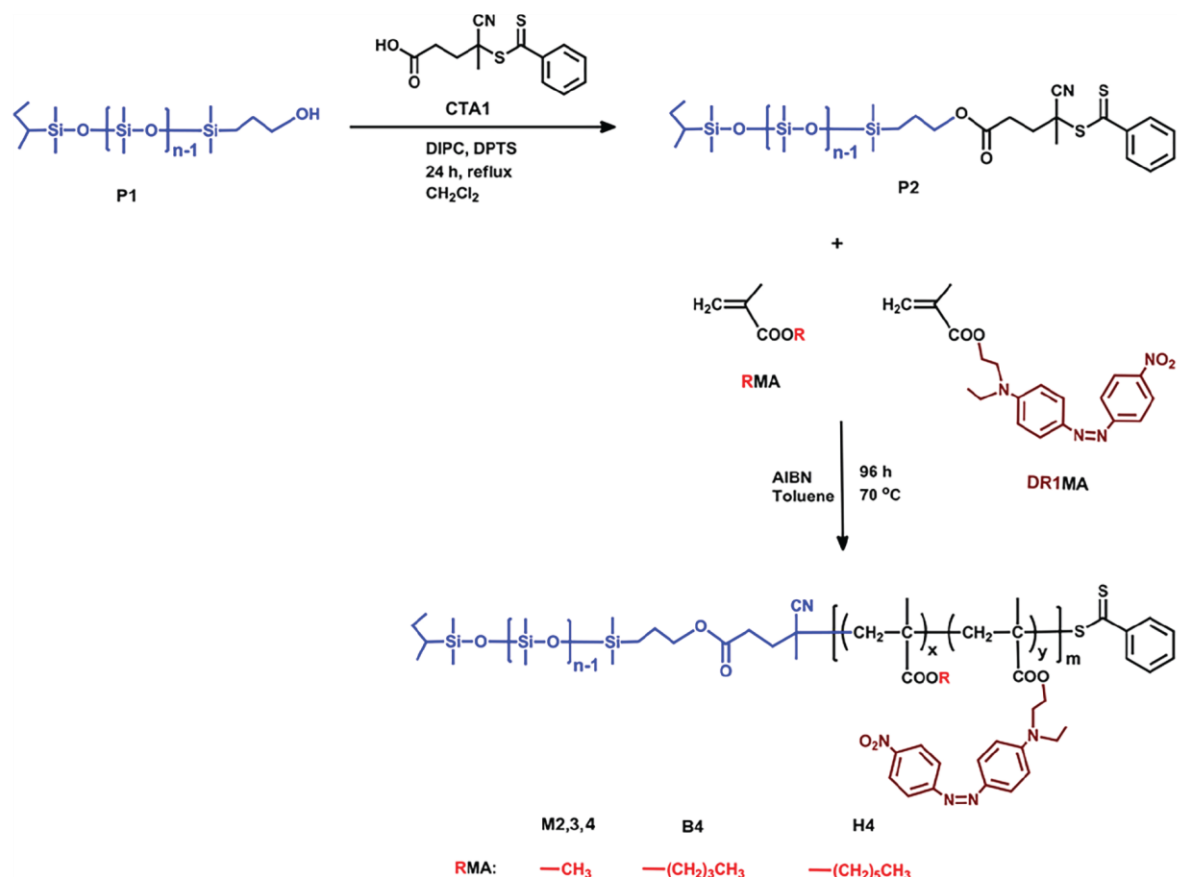
faceted surfaces.^{15,16} In particular, the relative stability of a BCP nanostructure deposited onto sinusoidally shaped SRG was recently investigated within the framework of the self-consistent field theory to better apprehend the combined effect of substrate corrugation and its surface energy.¹⁷ Conversely, the perfect photoalignment of microphase-separated BCP features formed by amorphous azo-based BCP thin films has never been demonstrated. In this regard, we designed a series of amorphous poly(dimethylsiloxane)-*block*-poly(disperse red 1 methacrylate-*co*-alkyl methacrylate) (PDMS-*b*-P(DR1MA-*co*-RMA)) BCPs as photoactive materials to explore the combinations of different treatment processes for the formation of long-range-ordered in-plane PDMS cylinders oriented along an arbitrary direction.

The synthesis of the PDMS-based BCPs seldom follows a straightforward pathway.¹⁸ Usually, a telechelic PDMS is first designed by anionic polymerization followed by a modification of the chain end group for its further use as a macro-initiator or macro-chain transfer agent (CTA) in controlled radical polymerization.^{19–23} Such multistep approaches allow access to well-defined functional PDMS-based BCPs. On the other hand, disperse red 1 (DR1)-containing polymers are usually synthesized by a polymer analogous reaction route rather than

Received: July 25, 2019

Revised: November 15, 2019

Published: January 3, 2020

Scheme 1. Synthetic Pathway Used for the Synthesis of the PDMS-*b*-P(DR1MA-*co*-RMA) BCPs

by azo-monomer polymerization.^{24,25} Indeed, the success of the direct polymerization of the azo monomers strongly depends on the reactivity of the azo monomers with the growing chain active centers, challenging its control as the dye loading increases. As a result, the polymerization of the DR1 monomers is often hindered by the inherent low reactivity caused by the bulkiness and the inhibition effect of this particular functional group.^{26,27} Therefore, a functional group-tolerant polymerization method has to be considered in combination with the use of suitable comonomers for an improved polymerization control. Reversible addition-fragmentation chain-transfer (RAFT) polymerization has been successfully used in the synthesis of azo-BCPs, i.e. amphiphilic, liquid-crystalline, and stimuli-responsive polymers.^{28–31} Most of the azo-BCPs obtained by RAFT were designed with “reactive” azo monomers, i.e. monomers with a long and flexible spacer between the azo moiety and the polymerizable fragment and without strong activating and/or deactivating groups substituted on the aromatic ring (electronic “push-pull” system as in DR1). However, such a design is rather destined for liquid-crystalline azo-BCPs⁴ than for SRG-forming materials, i.e. amorphous DR1-containing polymers, which are known as the gold standard for SRG applications.^{32,33} Only a few reports describe the RAFT polymerization of azo monomers containing short spacers and a pseudo-stilbene-type azo moiety, as this monomer design decreases its reactivity toward polymerization.^{34,35} To the best of our knowledge, DR1MA RAFT copolymerization with two different methacrylate derivatives was solely reported by Hoogen-

boom and co-workers, and the corresponding azo polymers designed for sensing application embedded only 3–5 wt % DR1MA.^{31,35} Hence, to date, there has been no information available on azo polymers embedding higher amounts of DR1MA via RAFT (co)polymerization, which are required for an effective SRG formation (i.e. dye content higher than ca. 30 wt %) to eventually produce laterally ordered BCP features.

In this work, a series of amorphous PDMS-*b*-P(DR1MA-*co*-RMA) BCPs containing up to 40 wt % azo dye were prepared via a well-controlled RAFT polymerization. By using an original method, combining the SRG photoinscription into the PDMS-*b*-P(DR1MA-*co*-RMA) layers and the microphase separation of the BCP features by solvent vapor annealing (SVA), laterally ordered in-plane PDMS cylinders over a large area were demonstrated broadening the toolset inherent to the manipulation of the self-assembly of BCP features. Indeed, such long-range-ordered Si-containing cylinders aligned along an arbitrary direction can eventually be oxidized under an oxygen plasma to produce line and space patterns for directed self-assembly lithography.^{36–38}

RESULTS AND DISCUSSION

Synthesis of Amorphous Azo-Containing Block Copolymers. Herein, a straightforward approach employing a combination of the anionic and RAFT polymerizations has been successfully used for the synthesis of various well-defined amorphous DR1-containing BCPs, as presented in Scheme 1.

First, a macro-chain transfer agent (CTA) was devised through the esterification reaction of a commercially available

Table 1. Macromolecular Characteristics of the Synthesized Polymers

code	feed composition (wt %)			polymer composition ^b (wt %)			M _n (kg/mol)			Đ ^c	T _g ^d (°C)
	DMS	RMA ^a	DR1MA	DMS	RMA	DR1MA	theo.	NMR ^b	SEC ^c		
P1	n/a	n/a	n/a	100	n/a	n/a	11.6	10.0	9.7	1.08	n.d.
P2	n/a	n/a	n/a	100	n/a	n/a	10.0	11.3	9.5	1.08	n.d.
M1	20	80	0	17	83	0	51.7	57.7	40.2	1.13	123
M2	20	72	8	27	63	10	51.7	37.5	34.3	1.07	122
M3	20	60	20	30	49	21	51.7	33.8	29.8	1.08	123
M4	20	40	40	38	22	40	51.7	26.0	19.9	1.10	125
B4	20	40	40	32	32	36	51.7	31.4	20.2	1.13	84
H4	20	40	40	31	34	35	51.7	31.8	17.7	1.18	60

^aRMA: methyl methacrylate (MMA), *n*-butyl methacrylate (*n*-BMA), or *n*-hexyl methacrylate (*n*-HMA). ^bDetermined by ¹H NMR. ^cSEC in tetrahydrofuran (THF) (40 °C, PS calibration) for BCPs and in toluene for P1 and P2 (40 °C, PDMS calibration). ^dT_g value for the P(DR1MA-*co*-RMA) block as determined by differential scanning calorimetry (DSC) (n/a: not applicable and n.d.: not determined).

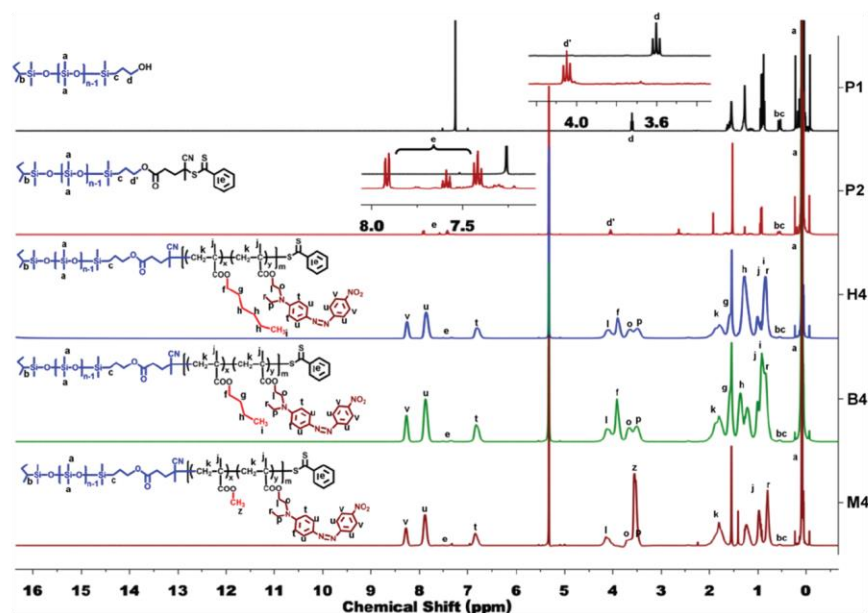


Figure 1. Overlaid ¹H NMR spectra corresponding to the monocarbinol PDMS (P1) in CDCl₃, the PDMS macro-CTA (P2), and typical BCPs in CD₂Cl₂.

carboxylic-acid-functionalized CTA with a monocarbinol PDMS. The anionic polymerization of hexamethylcyclotrisiloxane (D3) using *sec*-butyllithium as the initiator and chlorodimethylsilane as the terminating agent was first performed for the synthesis of a monohydride-terminated PDMS. The resulting homopolymer has a molecular weight close to 10 kg/mol according to the end-group analysis given by the proton nuclear magnetic resonance (¹H NMR) spectrum shown in Figure S1. The $-(\text{CH}_3)_2\text{SiH}$ chain-end functionality of this precursor is close to unity, as determined by comparing the integration value for the methine proton from the *sec*-butyl groups (1H_a) at 0.5–0.6 ppm and for the hydrosilyl proton (1H_e) at 4.7 ppm. The hydrosilylation of the monohydride-terminated PDMS with allyl alcohol employing a Pt catalyst leads to the monocarbinol PDMS. The $-\text{CH}_2\text{OH}$ chain-end functionality was determined to be around 95% from the comparison between the integration value for the methine proton of the *sec*-butyl groups overlapped with $-\text{Si}-\text{CH}_2-$ protons ($1\text{H}_c + 2\text{H}_e$) at 0.5–0.6 ppm and the integration value for the $-\text{CH}_2-$ protons next to $-\text{OH}$ at 3.6 ppm (2H_d) (see Figure S2). A dithiobenzoate CTA was chosen for the polymerization of DR1MA due to its success in

the RAFT polymerization of azo methacrylates.^{30,31,39,40} The corresponding PDMS macro-CTA (P2) was synthesized by esterification with a commercially available carboxylic-acid-functionalized dithiobenzoate CTA, as shown in Scheme 1. A modified Steglich esterification method, which employs *N,N'*-diisopropylcarbodiimide (DIPC) and 4-(dimethylamino)pyridinium *p*-toluenesulfonate (DPTS) as catalysts, was used to attain a quantitative conversion as noted by the downfield shift of the peak at 3.6 ppm attributed to $-\text{CH}_2-$ vicinal to $-\text{OH}$ (2H_d) in P1 to 4.05 ppm ($2\text{H}_d'$) in P2.⁴¹ A high degree of functionalization for P2 of ~84% was shown by end-group analysis using ¹H NMR (see Figure S3). This homopolymer has a molecular weight close to 10 kg/mol with a dispersity of 1.08, according to the size exclusion chromatography (SEC) trace performed in toluene using PDMS standards (see Figure S4).

The RAFT copolymerization of DR1MA and RMA was performed in toluene at 70 °C using various monomer feed compositions (see Table 1) and a constant molar ratio $[\text{PDMS-CTA}]/[\text{AIBN}] = 1:0.25$. Considering the high tendency of DR1MA and RMA toward copolymerization and homopolymerization, respectively,^{42,43} the monomer feeds

were adjusted as regards to the targeted BCP compositions, while the PDMS macro-CTA was kept constant at 20 wt % in the total feed mixture. The chemical structure of the obtained BCPs was confirmed by the characteristic resonance signals in the ^1H NMR spectra, and the assignment for some representative BCPs is given in Figure 1 (see Experimental Section for details). The molecular weight of the obtained BCPs was determined by ^1H NMR using the PDMS block as reference, while the DR1 content embedded in the side chain of the BCPs was obtained using the integration values for the aromatic protons at 6.9–8.3 ppm (2H_v , 4H_w , and 2H_t from Figure 1) (see the Supporting Information for details). The macromolecular characteristics of the synthesized BCPs as determined by SEC and ^1H NMR analyses are summarized in Table 1 (see also Figures S5–S11). It is noteworthy that the SEC traces obtained by UV detection give similar chromatograms to the ones acquired from the RI detector, confirming a PDMS chain extension with a UV-absorbing DR1MA block.

The BCPs were also characterized by differential scanning calorimetry (DSC) to study their thermal behaviors, and the DSC traces are presented in Figure S12. The glass transition (T_g) of the P(DR1MA-*co*-RMA) block is noticed at around 122 °C for P(DR1MA-*co*-MMA), 84 °C for P(DR1MA-*co*-*n*-BMA), and 60 °C for P(DR1MA-*co*-*n*-HMA), confirming the plasticizing effect of the *n*-butyl and *n*-hexyl moieties in B4 and H4. Interestingly, the characteristic melting temperature, T_m , of the PDMS block of –48 °C was only noticed for M4, as it contains enough PDMS to undergo a cold crystallization. The embedment of the ultraviolet–visible (UV–vis)-absorbing DR1 moieties in the BCP architecture was also confirmed by UV–vis absorption spectroscopy in THF at 25 °C (see Figure S13) with the characteristic absorptions of the DR1 moieties, i.e. a strong absorption band at 285 nm attributed to the π – π^* transitions of the aromatic rings and the maximum at 470 nm corresponding to the n – π^* transitions of nitrogen lone pairs.²⁷

Phase Behavior of Amorphous Azo-Containing Block Copolymers in the Bulk and Thin Films. Synchrotron small-angle X-ray scattering (SAXS) profiles are presented in Figure 2 for typical PDMS-*b*-P(DR1MA-*co*-RMA) BCPs. By increasing the PDMS weight fraction from 0.17 to 0.38, the usual sequence of morphologies occurring for microphase-separated diblock copolymers in the bulk is retrieved. The SAXS reflections for M1 could be tentatively assigned to

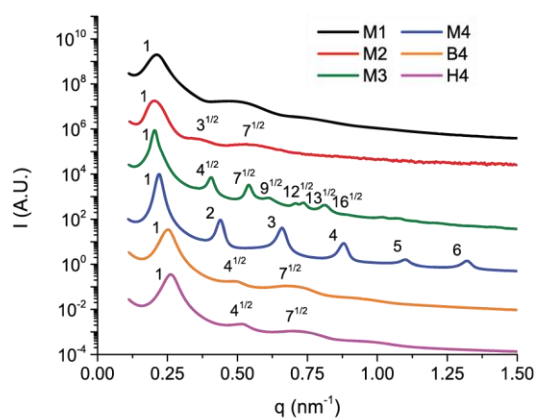


Figure 2. Synchrotron SAXS profiles of different PDMS-*b*-P(DR1MA-*co*-RMA) samples obtained at 180 °C. Curves have been shifted vertically for clarity.

PDMS spheres arranged in a body-centered cubic (BCC) lattice having a period, p , of ~ 36.4 nm since the first-order peak, q^* , is located at 0.21 nm^{-1} ($p = (2\pi/q^*)(3/2)^{1/2}$). The SAXS profile also shows two broad maxima located at 0.5 and 0.78 nm^{-1} due to the intraparticle interference of the single spherical domains. From the peak position, $q_{i\text{th}}$ of the i th maximum form factor, the average sphere radius, R_{sph} , is calculated to be ~ 11.6 nm (according to $q_i R_{\text{sph}} = 5.765, 9.111, \dots$ for $i = 1, 2, \dots$). It should be noted, however, that the BCC lattice should have a considerable distortion, as evident from the SAXS profile exhibiting only a first-order scattering from the lattice. Increasing the PDMS weight fraction within the M2 and M3 BCPs leads to hexagonal close-packed (HCP) cylindrical nanostructures. This is particularly unambiguous for M3, as the higher order peaks appear at $q/q^* = 1, 4^{1/2}, 7^{1/2}, 9^{1/2}, 12^{1/2}, 13^{1/2}, 16^{1/2}$ in accordance with a hexagonal array ($p6mm$ symmetry) having a period of 35.4 nm ($p = (2\pi/q^*)(4/3)^{1/2}$, where $q^* = 0.205 \text{ nm}^{-1}$). The second-order scattering extinction observed on the M3 SAXS profile is related to the cylinder form factor for a cylinder radius, R_{cyl} , of ~ 11 nm, which confirm that the PDMS composition, ϕ_{PDMS} , is about 0.3 ($R_{\text{cyl}} = p((\phi_{\text{PDMS}}\sqrt{3})/2\pi)^{1/2}$). For $\phi_{\text{PDMS}} \sim 0.38$, the SAXS profile shows a first-order peak at 0.22 nm^{-1} and higher order peaks located at $q/q^* = 1, 2, 3, 4, 5, 6$, which indicates that M4 is arranged into a lamellar structure having a period of ~ 28.6 nm ($p = 2\pi/q^*$). By varying the chemical nature of the comonomer in the P(DR1MA-*co*-RMA) block, SAXS reflections for both B4 and H4 samples are consistent with a HCP cylinder morphology ($p_{\text{B4}} = 28.6$ nm and $p_{\text{H4}} = 27.6$ nm).

Nanostructures formed by microphase-separated BCP thin films were also studied using solvent vapor annealing (SVA).⁴⁴ For that purpose, 170 nm thick PDMS-*b*-P(DR1MA-*co*-RMA) films, deposited on silicon substrates from 3 wt % solutions (tetrahydrofuran/propylene glycol monomethyl ether acetate, THF/PGMEA: 70/30), were exposed to chloroform (CHCl_3) vapor to promote the self-assembly (SA) of the BCP chains. The atomic force microscopy (AFM) image contrast was enhanced by treating the PDMS-*b*-P(DR1MA-*co*-RMA) thin films with a CF_4/O_2 reactive ion etch (RIE) plasma (plasma conditions are 40 W, 17 sccm CF_4 and 3 sccm O_2 , 45 s) to remove the PDMS surface wetting layer having a typical thickness of ~ 7 nm. Figure 3 shows AFM phase images for selected materials (M1, M2, and M3) having different P(DR1MA-*co*-MMA) compositions. The AFM phase image presented in Figure 3a shows a solvent-annealed M1 thin film in which a HCP arrangement of PDMS spheres having a period of 29.8 nm, extracted from the AFM fast Fourier transform (FFT), can be observed, which differs from the BCC phase observed in the bulk (see Figure 2). Such behavior is in accordance with previous studies demonstrating for spherical BCP features that the BCC phase is preferred in the bulk, while a HCP arrangement with the close-packed planes oriented parallel to the substrate are energetically more stable in thin films.^{45,46} An in-plane cylindrical structure is produced from both solvent-annealed (3 h, CHCl_3) M2 and M3 thin films, as shown in the AFM phase images presented in Figure 3b,c. Cylindrical repeat periods of ~ 26.7 and ~ 28.8 nm are measured from the M2 and M3 thin films, respectively, in agreement with the bulk periodicity obtained by SAXS.

Interestingly, the lamellar structure revealed by SAXS for M4 is not retrieved in the thin-film configuration as the AFM phase image presented in Figure 4a is rather consistent with an in-plane cylindrical structure having a period of ~ 24.9 nm. This is

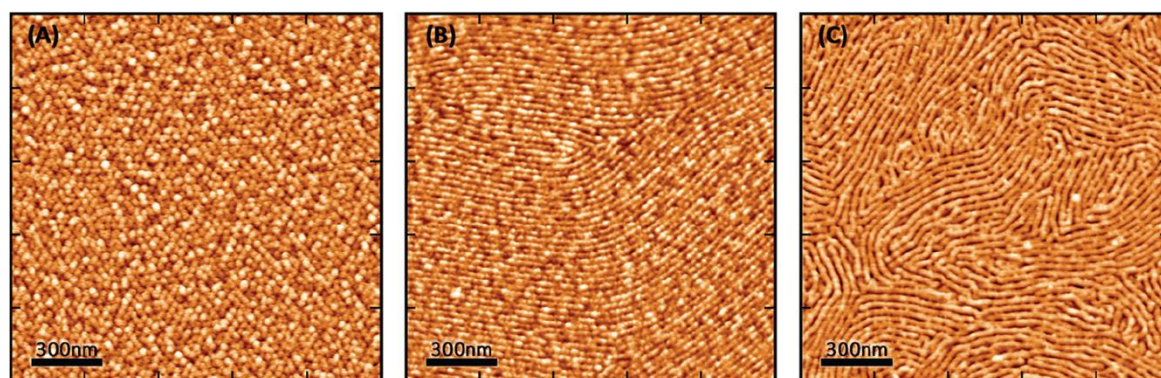


Figure 3. AFM phase views ($1.5 \times 1.5 \mu\text{m}$) of solvent-annealed (3 h, CHCl_3) PDMS-*b*-P(DR1MA-*co*-MMA) thin films with different PDMS compositions treated by a CF_4/O_2 RIE plasma: (A) 0.17 for M1, (B) 0.27 for M2, and (C) 0.3 for M3. An HCP array of PDMS spheres is produced from M1 ($p_{\text{M1}} = 29.8 \text{ nm}$), while an in-plane cylindrical structure is observed for both M2 ($p_2 = 26.7 \text{ nm}$) and M3 ($p_{\text{M3}} = 28.8 \text{ nm}$) thin films.

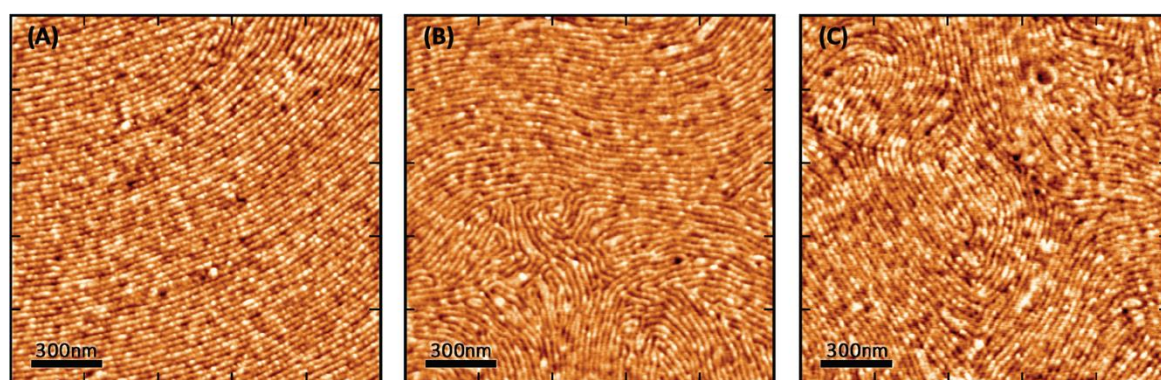


Figure 4. AFM phase views ($1.5 \times 1.5 \mu\text{m}$) of solvent-annealed (3 h, CHCl_3) PDMS-*b*-P(DR1MA-*co*-RMA) thin films with chemically distinct acrylate comonomers treated by a CF_4/O_2 RIE plasma: (A) MMA (M4), (B) *n*-BMA (B4), and (C) *n*-HMA (H4). An in-plane cylinder structure is observed for the M4 ($p_{\text{M4}} = 24.9 \text{ nm}$), B4 ($p_{\text{B4}} = 26.7 \text{ nm}$), and M3 ($p_{\text{H4}} = 25.8 \text{ nm}$) thin films.

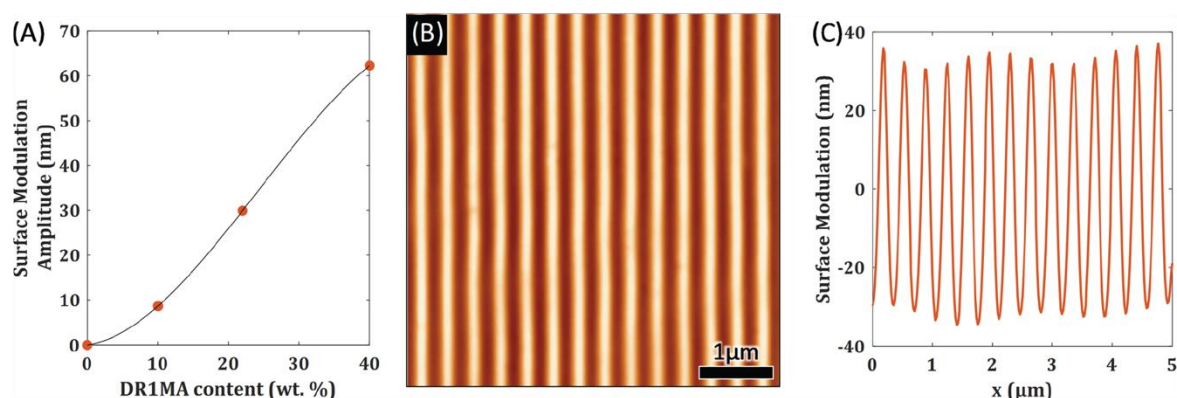


Figure 5. (A) SMA of different PDMS-*b*-P(DR1MA-*co*-MMA) layers as a function of their DR1MA content (wt %) measured after exposure to a *p*-polarized laser beam ($P = 250 \text{ mW}/\text{cm}^2$ and $\lambda_w = 532 \text{ nm}$) for 5 min (the continuous line is used to guide the eye). (B) AFM topographical view ($5 \times 5 \mu\text{m}$) of a photoinscribed sinusoidal SRG into a 170 nm thick M4 layer using a Lloyd's mirror interferometer setup. (C) Height profile extracted from the topographical AFM image presented in (B).

likely related to the high selectivity of CHCl_3 toward the methacrylate block (as suggested by the Hildebrand solubility parameter values: $\delta_{\text{PDMS}} = 14.9 \text{ MPa}^{1/2}$, $\delta_{\text{PMMA}} = 19 \text{ MPa}^{1/2}$, and $\delta_{\text{CHCl}_3} = 18.7 \text{ MPa}^{1/2}$),⁴⁷ which modified the overall BCP composition by selectively swelling the methacrylate domains during the SVA treatment. Additionally, the formation of a PDMS wetting layer at the air surface, which (i) artificially

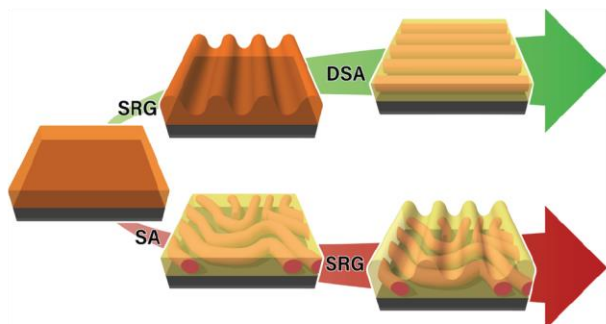
depletes the PDMS fraction in the self-assembled layer and (ii) imposes an in-plane orientation of the BCP features, should also be taken into account as a driving force that favors the microphase separation of the BCP chains into an in-plane cylindrical structure. To further probe the in-depth structure of the M4 BCP thin film, grazing-incidence small-angle X-ray scattering (GISAXS) experiments were performed and the

two-dimensional (2D) GISAXS pattern presented in Figure S14 supports the morphological assignment deduced from AFM, as the observed diffraction features are consistent with hexagonally structured domains aligned with their {10} planes parallel to the film surface.^{48–50} In contrast, similar morphologies are retrieved for the B4 and H4 samples since in-plane PDMS cylinders are formed within the solvent-annealed BCP thin films (see Figure 4b,c).

To know more about the effect of the azo-dye content on the photoinduced motion of azo-containing BCP chains, sinusoidal patterns were inscribed into several PDMS-*b*-P(DR1MA-*co*-MMA) layers having different amounts of DR1MA units (0–40 wt %) for the same exposure time. For that purpose, different 170 nm thick PDMS-*b*-P(DR1MA-*co*-MMA) layers, spin-coated from a 3 wt % solution (THF/PGEMA: 70/30), were exposed for 5 min to a *p*-polarized laser beam ($P = 250 \text{ mW/cm}^2$ and $\lambda_w = 532 \text{ nm}$, where λ_w is the writing wavelength) mounted on a Lloyd's mirror interferometer setup to generate the SRG inscription.¹⁰ Figure 5a shows that the dependence of the surface modulation amplitude (SMA), defined as the peak-to-valley distance, does not vary linearly with the number of DR1MA units since a threshold effect related to low azo-dye contents should be taken into account for the shape of the curve.⁵¹ For instance, the AFM topographic image presented in Figure 5b shows the sinusoidal pattern inscribed into a 170 nm thick M4 layer having a DR1MA content of 40 wt %. For such a sample, 5 min treatment enables producing a well-defined sinusoidal pattern over a large area having a period of $\sim 357 \text{ nm}$ and a SMA of $\sim 60 \text{ nm}$ (see Figure 5c).

The combination of the SRG and SVA processes was further investigated to better apprehend the potential synergy between the BCP self-assembly and the SRG photoinscription to manufacture long-range-ordered BCP features aligned along an arbitrary direction. In this regard, two experimental methodologies were applied to the BCP layers, as depicted in Scheme 2: (i) the BCP layer is self-assembled by SVA prior to the SRG inscription; or (ii) the sinusoidal SRG is inscribed into the as-

Scheme 2. Schematic Illustration of the Two Different Methods Used in This Work to Produce Laterally Aligned BCP Features from As-Cast (Disordered) DR1MA-Containing BCP Thin Films⁴⁴



“(Top panel) maximization of the orthogonal alignment of the DR1MA dyes during the SRG inscription into the disordered BCP layer, which subsequently induces the DSA of BCPs during the SVA process, and (bottom panel) SA of BCP chains by SVA followed by a SRG inscription, which lacks the preferential alignment of the PDMS cylinders.

cast (disordered) BCP layer prior to the nanodomain formation by SVA.

Both methods were applied to 170 nm thick M4 layers since well-defined in-plane PDMS cylinders have been produced by SVA (see Figure 4a), and also a large surface modulation amplitude was achieved thanks to the high content in DR1MA-dye moieties (see Figure 5). Importantly, the as-cast 170 nm thick M4 layers are disordered after their deposition by spin-coating, as shown in the AFM topographic image presented in Figure S15 where 2D-FFT is dominated by noise (no characteristic length scale). Therefore, the M4 layers have to be treated by SVA to realize the formation of the cylindrical nanodomains. The AFM topographic image presented in Figure 6 shows that, although a sinusoidal SRG was readily

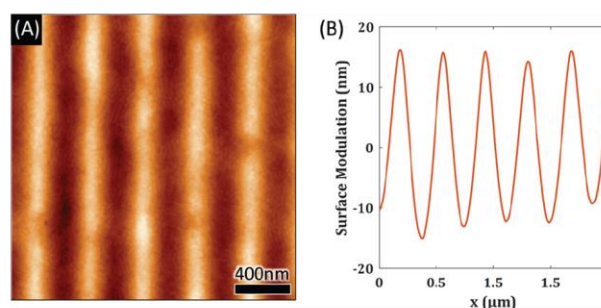


Figure 6. (A) AFM topographic view ($2 \times 2 \mu\text{m}$) of a solvent-annealed (3 h, CHCl_3) M4 layer exposed to a *p*-polarized laser beam ($\lambda_w = 532 \text{ nm}$, $P = 30 \text{ mW/cm}^2$) for 30 min. Poorly ordered PDMS cylinders are produced within the M4 layer having a periodic roughness induced by the SRG inscription. (B) AFM topographic profile reveals that the SRG pattern adopts a sinusoidal shape with a period of $\sim 357 \text{ nm}$ and a SMA of $\sim 30 \text{ nm}$.

inscribed into the solvent-annealed (3 h, CHCl_3) M4 layer (SMA $\sim 30 \text{ nm}$) after an exposure time of 30 min, an alignment of the PDMS cylinders along a preferential direction was not effective as previously reported for amorphous azo-containing BCP thin films.⁴¹

Conversely, laterally ordered in-plane cylinders aligned orthogonal to the polarization light plane were produced from as-cast photoinscribed (30 min) M4 layers treated by solvent vapor (3 h, CHCl_3) (see Figure 7). The AFM topographic and phase images presented in Figure 7a,b show long-range-ordered in-plane PDMS cylinders over $5 \times 5 \mu\text{m}^2$, as confirmed by the presence of two spots in 2D-FFT images (see the insets of Figure 7a,b). It is noteworthy that the periodic roughness profile (SMA $> 100 \text{ nm}$) observed after the SRG inscription into the disordered M4 layer vanished during the SVA process (see Figure S16). Indeed, a root-mean-square roughness, R_{rms} of $\sim 10 \text{ nm}$ was measured from the AFM topographical image presented in Figure 7a after exposing the M4 layer to a vapor treatment (3 h, CHCl_3). This phenomenon is obviously due to the enhanced diffusion of the BCP chains swelled by the CHCl_3 vapor during the SVA process, en route to form the in-plane PDMS cylinders (see also Figure 7c).

Overall, such results indicate that the alignment of the DR1MA dyes upon exposure to a *p*-polarized beam for 30 min is more effective within an as-cast (disordered) M4 layer than the one occurring within its microphase-separated homologue, as indirectly supported by the significant difference in the SMA values (SMA_{disordered,30 min} $> 100 \text{ nm}$ and SMA_{ordered,30 min} = 30

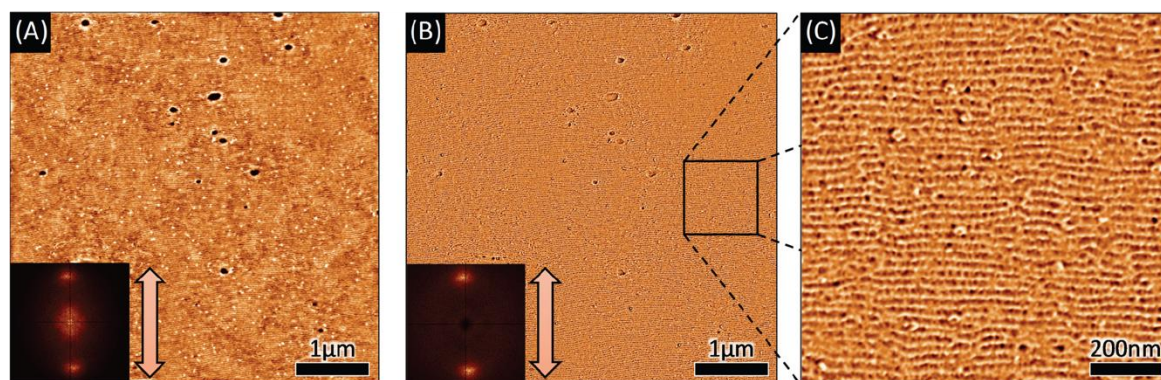


Figure 7. AFM ($5 \times 5 \mu\text{m}$) (A) topographical and (B) phase views of a solvent-annealed (3 h, CHCl_3) M4 layer in which a SRG pattern was previously inscribed (the arrows indicate the initial trench long axis). Under such conditions, in-plane cylindrical domains aligned orthogonal to the initial trench long axis are produced as confirmed by the sharp azimuthal distribution of the 2D-FFT spots (see insets). (C) Magnified AFM phase view of the cylindrical domains aligned orthogonal to the initial trench long axis.

nm). We believe that the effective pre-alignment of the DR1MA dyes within the disordered M4 layers directs the self-assembly of the BCP chains when exposed to CHCl_3 vapor to finally achieve laterally ordered in-plane PDMS cylinders oriented along an arbitrary direction.

CONCLUSIONS

In summary, a synthetic approach was developed to prepare well-defined DR1MA-based BCPs giving access to photo-responsive materials with a dye loading of up to 40 wt %. By varying the weight fraction of the azo-containing block, various self-assembled structures were identified both in the bulk and in thin films, while SRG inscription into these BCP layers led to a typical sinusoidal surface modulation pattern. The combination of the SRG photoinscription with a SVA treatment was further investigated to better apprehend the potential synergy between these two processes toward the fabrication of long-range-ordered BCP features aligned along an arbitrary direction. Interestingly, laterally ordered in-plane Si-containing nanoscale cylinders were demonstrated from a specific process combination. Such surfaces having highly ordered silica precursor domain-forming line and space patterns can be used as guides for the long-range-ordered nanofabrication of features (e.g., dots, holes, and pillars) derived from the BCP self-assembly processes.^{36,38,52–54}

EXPERIMENTAL SECTION

Materials. Toluene (99.5%, Sigma-Aldrich) was distilled first from CaH_2 and then from living polystyrene. Dichloromethane (99.9%, Sigma-Aldrich) was used as is from a drying column system. *n*-Hexyl methacrylate (*n*-HMA, 97%, TCI), *n*-butyl methacrylate (*n*-BMA, 99%, Sigma-Aldrich), and methyl methacrylate (MMA, 99%, Acros Organics) were first distilled from CaH_2 and then distilled over triethylaluminum (25% solution in hexane, Sigma-Aldrich). 4-(Dimethylamino)pyridinium *p*-toluenesulfonate (DPTS) was in-house synthesized as previously reported.⁴¹ Azobis(isobutyronitrile) (AIBN, 98%, Acros Organics) was recrystallized from methanol and dried at room temperature under vacuum prior to use. Tetrahydrofuran (THF, 99.9%, Sigma-Aldrich), Disperse Red 1 methacrylate (DR1MA, 95%, Sigma-Aldrich), *N,N'*-diisopropylcarbodiimide (DIPC, 99%, Sigma-Aldrich), 2-propanol (99.5%, Sigma-Aldrich), acetonitrile (99%, Fisher), 4-dimethylaminopyridine (99%, Acros Organics), 4-toluenesulfonic acid (99%, Alfa Aesar), and 4-cyano-4-(phenylcarbonothioylthio)pentanoic acid (CTA, 97%, Sigma-Aldrich) were used as received.

Self-Assembly of PDMS-*b*-P(DR1MA-*co*-RMA) Thin Films.

PDMS-*b*-P(DR1MA-*co*-RMA) thin films were spin-coated (2 krpm) using a 3 wt % copolymer solution in THF/PGMEA (70:30). The self-assembly of PDMS-*b*-P(DR1MA-*co*-RMA) thin films was promoted by exposing samples for 3 h to a continuous stream of CHCl_3 vapor produced by bubbling nitrogen gas through the liquid solvent, so that the solvent vapor consisted of 32 sccm CHCl_3 and 8 sccm N_2 (total 40 sccm).⁵⁵ In situ measurements of the BCP layer thickness during the SVA treatment were performed through a quartz SVA chamber lid using a Filmetrics reflectometer apparatus, and the BCP layers reached a plateau for a thickness variation of $\sim 150\%$. The morphology of the solvent-annealed PDMS-*b*-P(DR1MA-*co*-RMA) thin films was frozen by quickly removing the lid of the chamber.

Characterization Methods. *Proton NMR (^1H NMR).* Proton NMR (^1H NMR) spectra were all recorded using a liquid-state 400 MHz NMR spectrometer (Bruker AVANCE I) with a 5 mm BBFO probe in the appropriate deuterated solvent.

Size Exclusion Chromatography (SEC). Size exclusion chromatography (SEC) traces were acquired on a PL-GPC 50 Plus (Agilent Technologies) integrated system with RI and UV detectors using a three-column set of TSK gel TOSOH (G4000 HXL, G3000 HXL, and G2000 HXL with pore sizes of 20, 75, and 200 Å, respectively, connected in series) at 40 °C. The calibration was performed with PS standards for SEC traces using THF as the eluent (1 mL/min), while PDMS standards were used for SEC traces using toluene as the eluent (0.8 mL/min). Trichlorobenzene was used in both cases as a flow marker.

Differential Scanning Calorimetry (DSC). Differential scanning calorimetry (DSC) measurements were performed using a Q100 apparatus from TA Instruments. DSC experiments were carried out in aluminum sealed pans containing 5 to 10 mg of the sample. Each sample was first heated up to 150 °C at 10 °C/min and then the heating was kept constant at this temperature for 10 min to delete the thermal history. Further, the sample was cooled down to -80 °C at 10 °C/min followed by heating up to 250 °C at 10 °C/min.

Ultraviolet–Visible Spectroscopy (UV–vis). Ultraviolet–visible spectroscopy (UV–vis) was performed on a UV-3600 spectrophotometer from Shimadzu.

Atomic Force Microscopy (AFM). Atomic force microscopy (AFM) characterization was performed on a Bruker Dimension FastScan setup in tapping mode to characterize the surface morphology of BCP thin films. Silicon cantilevers (FastScan-A) with a typical tip radius of ≈ 5 nm were used. The resonance frequency of the cantilevers was about 1.25 kHz. AFM phase contrast was enhanced by treating all PDMS-*b*-P(DR1MA-*co*-RMA) thin films with a CF_4/O_2 RIE plasma (plasma conditions are 40 W, 17 sccm CF_4 and 3 sccm O_2 , 45 s) in a PE-100 chamber (Plasma Etch) prior to imaging.

Photoinscription of SRG Patterns. Photoinscription of SRG patterns was performed using a Lloyd's mirror interferometer setup.^{10,56} A *p*-polarized laser beam ($\lambda_w = 532$ nm) with a fluence of 30 mW/cm² was split into two beams, one directly incident onto the BCP film and the other reflected by a mirror to which the polymeric layer was perpendicularly attached. The produced sinusoidal patterns have a 357 nm wave period, independently of the inscribed PDMS-*b*-P(RMA-*co*-DR1MA) layer.

Small-Angle X-ray Scattering (SAXS). Small-angle X-ray scattering (SAXS) measurements were performed on the CRG-BM02 beamline at the European Synchrotron Radiation Facilities (ESRF) in Grenoble using a photon energy of 10 keV. The SAXS patterns were recorded in the classical transmission mode as a function of the scattering vector, q , using a XPAD 2D pixel detector (960 × 560 pixels, 130 μm pixel size) placed at a distance of 2500 mm from the sample. The raw data were corrected for scattering due to background noise and the fluctuations of the intensity of the incident beam. Finally, the two-dimensional SAXS patterns were radially averaged to obtain the one-dimensional scattering profiles.

Grazing-Incidence Small-Angle X-ray Scattering (GISAXS). Grazing-incidence small-angle X-ray scattering (GISAXS) experiments were performed at the Centre de Recherche Paul Pascal (CRPP) in Bordeaux using a high-resolution X-ray spectrometer Xeuss 2.0 from Xenox operating at 8.04 keV. The incidence angle was set at 0.2°, which was between the critical angle of the BCP film and the silicon substrate. 2D scattering patterns were collected using a PILATUS 300 K Dectris detector with an exposure of 30 min. The beam center position and the angular range were calibrated using a silver behenate standard sample. GISAXS patterns were reduced using the GIXSGUI package,⁵⁷ where $q_y = 2\pi/\lambda[\sin(2\theta_f)\cos(\alpha_f)]$ and $q_z = 2\pi/\lambda[\sin(\alpha_f) + \sin(\alpha_i)]$ are the modulus of the scattering vectors in the direction parallel and perpendicular to the substrate plane and α_i , $2\theta_f$, and α_f are the incident and scattering angles in the horizontal and vertical directions, respectively.

Synthetic Procedures. Synthesis of Monocarbinol-Terminated Polydimethylsiloxane (P1). The synthesis of the monocarbinol-terminated PDMS was performed as in our previous report.⁴¹

¹H NMR (400 MHz, CDCl₃, δ) of P1: 3.6 (t, 2H, -CH₂- vicinal to -OH), 1.61 (m, 2H, -CH₂- vicinal to -CH₂-OH), 1.54 (br, 2H, -CH₂- of *sec*-butyl overlaps with 1H of -OH groups), 0.93 (m, 6H, -CH₃ of *sec*-butyl), 0.55 (m, 1H, *sec*-butyl methine overlaps with 2H of -Si-CH₂-), 0.071 (br, 6H, -CH₃ of the PDMS backbone) all in ppm, as presented in Figure S2.

Synthesis of the Macro-CTA Mono-4-cyano-4-(phenylcarbonothioylthio)pentanoate-Terminated PDMS (P2). Typically, 2.6 g (ca. 0.26 mmol, $M_n^{1H\text{NMR}} = 10030$ g/mol) of monocarbinol-terminated PDMS and 0.2 g (0.68 mmol) of DPTS were dissolved in 25 mL of dry dichloromethane. A solution of 0.35 g (1.25 mmol) of 4-cyano-4-(phenylcarbonothioylthio)pentanoic acid in 10 mL of dry methylene chloride was prepared and added to the PDMS/DPTS solution. Then, 3 mL (19.37 mmol) of DIPC were dissolved in 10 mL of dry methylene chloride and added to the reaction mixture at 25 °C. Upon complete addition, the temperature was gradually increased to ca. 45 °C (solvent reflux). The reagents were left to react for 24 h under argon and continuous stirring. Upon cooling, the solvent was removed by rotary evaporation. The polymer was further purified by four extractions with methanol, yielding after drying 2.5 g of macro-CTA PDMS as a pink oil.

¹H NMR (400 MHz, CD₂Cl₂, δ) of P2: 7.9 (d, 2H, *o*-ArH), 7.6 (t, 1H, *p*-ArH), 7.4 (t, 2H, *m*-ArH), 4.05 (t, 2H, -CH₂- vicinal to -COO-PDMS chain), 2.6 (m, 2H, vicinal to -(CH₃)C(CN)-S-), 2.4 (m, 2H, -CH₂- vicinal to -COO-CTA side), 1.9 (s, 3H, -CH₃ of -(CH₃)C(CN)-S-), 1.66 (m, 2H, -CH₂- vicinal to -CH₂-COO-CTA), 1.55 (s, 2H, -CH₂- of *sec*-butyl), 0.93 (m, 6H, -CH₃ of *sec*-butyl), 0.56 (m, 1H, *sec*-butyl methine overlaps with 2H, -Si-CH₂-), 0.08 (br, 6H, -CH₃ of the PDMS backbone) all in ppm, as presented in Figure S3.

Synthesis of the PDMS-Based Diblock Copolymers (M1 to M4, H4, and B4). The synthesized PDMS macro-RAFT agent was used for the homopolymerization of MMA and DR1MA and also for the

DR1MA copolymerization with methyl methacrylate, *n*-butyl methacrylate, or *n*-hexyl methacrylate. Different weight ratios of the DR1 monomer and alkyl methacrylates were employed, as presented in Table 1. A representative RAFT copolymerization was as follows, for M4: 0.06 g (6×10^{-3} mmol) of PDMS macro-CTA (M_n ca. 10 kg/mol), 0.125 g (0.327 mmol) of Disperse Red 1 methacrylate, 0.134 mL (1.253 mmol) of methyl methacrylate, 0.43 mL of toluene and 18 μL (1.09×10^{-3} mmol) of AIBN solution in toluene were added in a Schlenk tube. The reaction mixture was deoxygenated by five freeze–vacuum–thaw cycles and then placed under an argon atmosphere. The polymerization reaction was carried out at 70 °C for 96 h under continuous stirring. Then it was cooled in liquid nitrogen and exposed to air. The reaction mixture was diluted with THF. The resulting impure diblock copolymer was purified by precipitation in acetonitrile and then washed with acetonitrile until the nonsolvent remained colorless, removing completely the unreacted Disperse Red 1 methacrylate. Then it was precipitated twice in cold 2-propanol, removing any residual unfunctionalized PDMS homopolymer, and dried overnight at 55 °C under continuous vacuum.

¹H NMR (400 MHz, CD₂Cl₂, δ) for M4: 8.28 (br, 2H, *o*-ArH to -NO₂), 7.88 (br, 4H, *m*-ArH to -NO₂ and *m*-ArH to -NEt₂), 6.85 (br, 2H, *o*-ArH to -NEt₂), 4.14 (br, 2H, -CH₂- vicinal to -COO- from DR1MA), 3.76–3.42 (br, 7H, the two -CH₂- from -NEt₂ of DR1MA overlap with 3H of -COO-CH₃ from MMA), 2.0–1.6 (br, 4H, -CH₂- from the backbone of MMA and DR1MA), 1.3–0.88 (br, 6H, CH₃- from the backbone of MMA and DR1MA), 0.79 (br, 3H, CH₃- next to the -CH₂-N(-azo)-CH₂- from DR1MA), 0.11 (br, 6H, CH₃- of the PDMS backbone) all in ppm, see Figure S9.

¹H NMR (400 MHz, CD₂Cl₂, δ) for B4: 8.27 (br, 2H, *o*-ArH to -NO₂), 7.88 (br, 4H, *m*-ArH to -NO₂ and *m*-ArH to -NEt₂), 6.83 (br, 2H, *o*-ArH to -NEt₂), 4.12 (br, 2H, -CH₂- vicinal to -COO- from DR1MA units), 3.92 (br, 2H, -CH₂- vicinal to -COO- from *n*-BMA units), 3.66 (br, 2H, -CH₂- vicinal to -CH₂-COO- from DR1MA units), 3.51 (br, 2H, -CH₂- vicinal to -N(-azo)-CH₂- from DR1MA units), 2.0–1.67 (br, 4H, -CH₂- from the backbone of *n*-BMA and DR1MA), 1.66–1.08 (br, 4H, -CH₂- vicinal to -CH₂-COO- and the -CH₂- vicinal to CH₃- from the alkyl chain of *n*-BMA), 1.07–0.7 (br, 12H, CH₃- from the backbone of *n*-BMA and DR1MA, CH₃- from the alkyl chain of *n*-BMA and CH₃- next to -CH₂-N(-azo)-CH₂- from DR1MA), 0.11 (br, 6H, CH₃- of the PDMS backbone) all in ppm, see Figure S10.

¹H NMR (400 MHz, CD₂Cl₂, δ) for H4: 8.26 (br, 2H, *o*-ArH to -NO₂), 7.86 (br, 4H, *m*-ArH to -NO₂ and *m*-ArH to -NEt₂), 6.81 (br, 2H, *o*-ArH to -NEt₂), 4.11 (br, 2H, -CH₂- vicinal to -COO- from DR1MA units), 3.9 (br, 2H, -CH₂- vicinal to -COO- from *n*-HMA units), 3.66 (br, 2H, -CH₂- vicinal to -CH₂-COO- from DR1MA units), 3.5 (br, 2H, -CH₂- vicinal to -N(-azo)-CH₂- from DR1MA units), 2.04–1.67 (br, 4H, -CH₂- from the backbone of *n*-HMA and DR1MA), 1.58 (br, 2H, -CH₂- vicinal to -CH₂-COO- from the alkyl chain of *n*-HMA), 1.29 (br, 6H, three -CH₂- vicinal to -CH₂-CH₂-COO- and vicinal to CH₃- from the alkyl chain of *n*-HMA), 1.07–0.7 (br, 12H, CH₃- from the backbone of *n*-HMA and DR1MA, CH₃- from the alkyl chain of *n*-HMA and CH₃- next to the -CH₂-N(-azo)-CH₂- from DR1MA), 0.11 (br, 6H, CH₃- of the PDMS backbone) all in ppm, see Figure S11.

■ ASSOCIATED CONTENT

Supporting Information

The Supporting Information is available free of charge at <https://pubs.acs.org/doi/10.1021/acs.macromol.9b01551>.

¹H NMR spectra, SEC traces and DSC thermograms of the synthesized materials, 2D GISAXS pattern of the solvent-annealed PDMS-*b*-P(DR1MA-*co*-RMA) M4 BCP thin film (PDF)

■ AUTHOR INFORMATION

Corresponding Authors

*E-mail: karim.aissou@umontpellier.fr (K.A.).

*E-mail: gfleury@enscbp.fr (G.F.).

ORCID

Cyril Brochon: 0000-0003-3242-1574

Eric Cloutet: 0000-0002-5616-2979

Georges Hadziioannou: 0000-0002-7377-6040

Karim Aissou: 0000-0002-9236-464X

Guillaume Fleury: 0000-0003-0779-191X

Present Address

[‡]Institut Européen des Membranes, Université de Montpellier—CNRS—ENSCM, 300 Avenue du Professeur Emile Jeanbrau, F-34090 Montpellier, France (K.A.).

Author Contributions

[†]M.C.S. and N.D. contributed equally to the manuscript.

Notes

The authors declare no competing financial interest.

ACKNOWLEDGMENTS

The research leading to these results received partial funding from the PLACYD project (ENIAC Joint Undertaking program) under grant agreement #621277. The D2AM CRG Beamline is acknowledged for allocating beam time at ESRF for the SAXS experiments. Ahmed Bentaleb is gratefully acknowledged for his help with the GISAXS experiments. This work was performed within the framework of the Equipex ELORPrintTec ANR-10-EQPX-28-01 and the LabEx AMADEUS ANR-10-LABEX-0042-AMADEUS with the help of the French state Initiative d'Excellence IdEx ANR-10-IDEX-003-02.

REFERENCES

- (1) Yu, H.; Kobayashi, T. Photoresponsive Block Copolymers Containing Azobenzenes and Other Chromophores. *Molecules* **2010**, *15*, 570–603.
- (2) Zhao, Y.; He, J. Azobenzene-Containing Block Copolymers: The Interplay of Light and Morphology Enables New Functions. *Soft Matter* **2009**, *5*, 2686–2693.
- (3) Yu, H. Photoresponsive Liquid Crystalline Block Copolymers: From Photonics to Nanotechnology. In *Progress in Polymer Science*; Pergamon, 2014; pp 781–815.
- (4) Seki, T. Meso- and Microscopic Motions in Photoresponsive Liquid Crystalline Polymer Films. In *Macromolecular Rapid Communications*; John Wiley & Sons: Ltd, 2014; pp 271–290.
- (5) Yu, H.; Iyoda, T.; Ikeda, T. Photoinduced Alignment of Nanocylinders by Supramolecular Cooperative Motions. *J. Am. Chem. Soc.* **2006**, *128*, 11010–11011.
- (6) Morikawa, Y.; Kondo, T.; Nagano, S.; Seki, T. Photoinduced 3D Ordering and Patterning of Microphase-Separated Nanostructure in Polystyrene-Based Block Copolymer. *Chem. Mater.* **2007**, *19*, 1540–1542.
- (7) Morikawa, Y.; Nagano, S.; Watanabe, K.; Kamata, K.; Iyoda, T.; Seki, T. Optical Alignment and Patterning of Nanoscale Microdomains in a Block Copolymer Thin Film. *Adv. Mater.* **2006**, *18*, 883–886.
- (8) Sano, M.; Nakamura, S.; Hara, M.; Nagano, S.; Shinohara, Y.; Amemiya, Y.; Seki, T. Pathways toward Photoinduced Alignment Switching in Liquid Crystalline Block Copolymer Films. *Macromolecules* **2014**, *47*, 7178–7186.
- (9) Kim, B. H.; Lee, H. M.; Lee, J.-H.; Son, S.-W.; Jeong, S.-J.; Lee, S.; Lee, D.; Il; Kwak, S. U.; Jeong, H.; Shin, H.; et al. Spontaneous Lamellar Alignment in Thickness-Modulated Block Copolymer Films. *Adv. Funct. Mater.* **2009**, *19*, 2584–2591.
- (10) Aissou, K.; Shaver, J.; Fleury, G.; Pécastaings, G.; Brochon, C.; Navarro, C.; Grauby, S.; Rampnoux, J.-M.; Dilhaire, S.; Hadziioannou, G. Nanoscale Block Copolymer Ordering Induced by Visible

Interferometric Micropatterning: A Route towards Large Scale Block Copolymer 2D Crystals. *Adv. Mater.* **2013**, *25*, 213–217.

(11) Rho, Y.; Aissou, K.; Mumtaz, M.; Kwon, W.; Pécastaings, G.; Mocuta, C.; Stanecu, S.; Cloutet, E.; Brochon, C.; Fleury, G.; et al. Laterally Ordered Sub-10 Nm Features Obtained From Directed Self-Assembly of Si-Containing Block Copolymer Thin Films. *Small* **2015**, *11*, 6377–6383.

(12) Kim, B. H.; Choi, Y.; Kim, J. Y.; Shin, H.; Kim, S.; Son, S. W.; Kim, S. O.; Kim, P. Wrinkle-Directed Self-Assembly of Block Copolymers for Aligning of Nanowire Arrays. *Adv. Mater.* **2014**, *26*, 4665–4670.

(13) Jin, H. M.; Lee, S. H.; Kim, J. Y.; Son, S.-W.; Kim, B. H.; Lee, H. K.; Mun, J. H.; Cha, S. K.; Kim, J. S.; Nealey, P. F.; et al. Laser Writing Block Copolymer Self-Assembly on Graphene Light Absorbing Layer. *ACS Nano* **2016**, No. 3435.

(14) Jin, H. M.; Park, D. Y.; Jeong, S.-J.; Lee, G. Y.; Kim, J. Y. S. Y.; Mun, J. H.; Cha, S. K.; Lim, J.; Kim, J. Y. S. Y.; Kim, K. H.; et al. Flash Light Millisecond Self-Assembly of High χ Block Copolymers for Wafer-Scale Sub-10 Nm Nanopatterning. *Adv. Mater.* **2017**, *29*, No. 1700595.

(15) Park, S.; Lee, D. H.; Xu, J.; Kim, B.; Hong, S. W.; Jeong, U.; Xu, T.; Russell, T. P. Macroscopic 10-Terabit-per-Square-Inch Arrays from Block Copolymers with Lateral Order. *Science* **2009**, *323*, 1030–1033.

(16) Hong, S. W.; Huh, J.; Gu, X.; Lee, D. H.; Jo, W. H.; Park, S.; Xu, T.; Russell, T. P. Unidirectionally Aligned Line Patterns Driven by Entropic Effects on Faceted Surfaces. *Proc. Natl. Acad. Sci. U.S.A.* **2012**, *109*, 1402–1406.

(17) Zhu, Y.; Aissou, K.; Andelman, D.; Man, X. Orienting Cylinder-Forming Block Copolymer Thin Films: The Combined Effect of Substrate Corrugation and Its Surface Energy. *Macromolecules* **2019**, *52*, 1241–1248.

(18) Matsuo, Y.; Konno, R.; Ishizone, T.; Goseki, R.; Hirao, A. *Precise Synthesis of Block Polymers Composed of Three or More Blocks by Specially Designed Linking Methodologies in Conjunction with Living Anionic Polymerization System*; Multidisciplinary Digital Publishing Institute, 2013; Vol. 5, pp 1012–1040.

(19) Pitet, L. M.; Wuister, S. F.; Peeters, E.; Kramer, E. J.; Hawker, C. J.; Meijer, E. W. Well-Organized Dense Arrays of Nanodomains in Thin Films of Poly(Dimethylsiloxane)-*b*-Poly(Lactide) Diblock Copolymers. *Macromolecules* **2013**, *46*, 8289–8295.

(20) Wei, R.; He, Y.; Wang, X. Diblock Copolymers Composed of a Liquid Crystalline Azo Block and a Poly(Dimethylsiloxane) Block: Synthesis, Morphology and Photoresponsive Properties. *RSC Adv.* **2014**, *4*, 58386–58396.

(21) Lim, K. T.; Webber, S. E.; Johnston, K. P. Synthesis and Characterization of Poly(Dimethyl Siloxane)-Poly[Alkyl (Meth)Acrylic Acid] Block Copolymers. *Macromolecules* **1999**, *32*, 2811–2815.

(22) Morgan, A. M.; Pollack, S. K.; Beshah, K. Synthesis and Multidimensional NMR Characterization of PDMS-*b*-PS Prepared by Combined Anionic Ring-Opening and Nitroxide-Mediated Radical Polymerization. *Macromolecules* **2002**, *35*, 4238–4246.

(23) Qin, X.; Li, Y.; Zhou, F.; Ren, L.; Zhao, Y.; Yuan, X. Polydimethylsiloxane-Polymethacrylate Block Copolymers Tethering Quaternary Ammonium Salt Groups for Antimicrobial Coating. *Appl. Surf. Sci.* **2015**, *328*, 183–192.

(24) Scarpaci, A.; Cabanetos, C.; Blart, E.; Montembault, V.; Fontaine, L.; Rodriguez, V.; Odobel, F. Postfunctionalization of Poly(Propargyl Methacrylate) Using Copper Catalyzed 1,3-Dipolar Huisgen Cycloaddition: An Easy Route to Electro-Optic Materials. *J. Polym. Sci., Part A: Polym. Phys.* **2009**, *47*, 5652–5660.

(25) Faccini, M.; Balakrishnan, M.; Torosantucci, R.; Driessen, A.; Reinhoudt, D. N.; Verboom, W. Facile Attachment of Nonlinear Optical Chromophores to Polycarbonates. *Macromolecules* **2008**, *41*, 8320–8323.

(26) Bag, D. S.; Alam, S. Synthesis and Characterization of Photoactive Chiral Copolymers of (S)-N-(1-Phenyl Ethyl) Meth-

acrylamide and Disperse Red 1 Methacrylate. *J. Appl. Polym. Sci.* **2012**, *125*, 2595–2603.

(27) Ding, L.; Russell, T. P. A Photoactive Polymer with Azobenzene Chromophore in the Side Chains. *Macromolecules* **2007**, *40*, 2267–2270.

(28) Jie, X. U.; Wei, Z.; Nianchen, Z.; Jian, Z.; Zhenping, C.; Yan, X. U.; Xiulin, Z. Synthesis of Azobenzene-Containing Polymers via RAFT Polymerization and Investigation on Intense Fluorescence from Aggregates of Azobenzene-Containing Amphiphilic Diblock Copolymers. *J. Polym. Sci., Part A: Polym. Phys.* **2008**, *46*, 5652–5662.

(29) Zhao, Y.; Qi, B.; Tong, X.; Zhao, Y. Synthesis of Double Side-Chain Liquid Crystalline Block Copolymers Using RAFT Polymerization and the Orientational Cooperative Effect. *Macromolecules* **2008**, *41*, 3823–3831.

(30) Zenati, A.; Han, Y. K. Synthesis and Properties of Azo-Based ABC Triblock Copolymers Owning Interaction and Composition Parameters That Influence Their Phase Behaviors. *Macromolecules* **2018**, *51*, 101–114.

(31) Pietsch, C.; Hoogenboom, R.; Schubert, U. S. Soluble Polymeric Dual Sensor for Temperature and PH Value. *Angew. Chem., Int. Ed.* **2009**, *48*, 5653–5656.

(32) Kravchenko, A.; Shevchenko, A.; Ovchinnikov, V.; Priimagi, A.; Kaivola, M. Optical Interference Lithography Using Azobenzene-Functionalized Polymers for Micro- and Nanopatterning of Silicon. *Adv. Mater.* **2011**, *23*, 4174–4177.

(33) Goulet-Hanssens, A.; Corkery, T. C.; Priimagi, A.; Barrett, C. J. Effect of Head Group Size on the Photoswitching Applications of Azobenzene Disperse Red 1 Analogues. *J. Mater. Chem. C* **2014**, *2*, 7505–7512.

(34) Cao, H. Z.; Zhang, W.; Zhu, J.; Chen, X. R.; Cheng, Z. P.; Wu, J. H.; Zhu, X. L. Azo Polymers with Electronical Push and Pull Structures Prepared via RAFT Polymerization and Its Photoinduced Birefringence Behavior. *Express Polym. Lett.* **2008**, *2*, 589–601.

(35) Pietsch, C.; Hoogenboom, R.; Schubert, U. S. PMMA Based Soluble Polymeric Temperature Sensors Based on UCST Transition and Solvatochromic Dyes. *Polym. Chem.* **2010**, *1*, 1005–1008.

(36) Son, J. G.; Gotrik, K. W.; Ross, C. A. High-Aspect-Ratio Perpendicular Orientation of PS-*b*-PDMS Thin Films under Solvent Annealing. *ACS Macro Lett.* **2012**, *1*, 1279–1284.

(37) Bai, W.; Gadelrab, K.; Alexander-Katz, A.; Ross, C. A. Perpendicular Block Copolymer Microdomains in High Aspect Ratio Templates. *Nano Lett.* **2015**, *15*, 6901–6908.

(38) Girardot, C.; Böhme, S.; Archambault, S.; Salaün, M.; Latur-Romain, E.; Cunge, G.; Joubert, O.; Zelsmann, M. Pulsed Transfer Etching of PS–PDMS Block Copolymers Self-Assembled in 193 Nm Lithography Stacks. *ACS Appl. Mater. Interfaces* **2014**, *6*, 16276–16282.

(39) Zhu, Y.; Zhou, Y.; Chen, Z.; Lin, R.; Wang, X. Photoresponsive Diblock Copolymers Bearing Strong Push–Pull Azo Chromophores and Cholesteryl Groups. *Polymer* **2012**, *53*, 3566–3576.

(40) Yang, C. A.; Chen, L.; Huang, H.; Lu, Y.; Xiong, B.; Liu, Y.; Yi, J. Effects of Molecular Weight on Dual Light- and Thermo-Responsive Behaviors of Homopolymers with Azobenzene Units and Terminal Oligo(Ethylene Glycol) Units. *Polym. Int.* **2017**, *66*, 1819–1826.

(41) Spiridon, M. C.; Aissou, K.; Mumtaz, M.; Brochon, C.; Cloutet, E.; Fleury, G.; Hadziioannou, G. Surface Relief Gratings Formed by Microphase-Separated Disperse Red 1 Acrylate-Containing Diblock Copolymers. *Polymer* **2018**, *137*, 378–384.

(42) Natansohn, A.; Rochon, P.; Gosselin, J.; Xie, S. Azo Polymers for Reversible Optical Storage. 1. Poly[4'-[[2-(Acryloyloxy)Ethyl]-Ethylamino]-4-Nitroazobenzene]. *Macromolecules* **1992**, *25*, 2268–2273.

(43) Xie, S.; Natansohn, A.; Rochon, P. Microstructure of Copolymers Containing Disperse Red 1 and Methyl Methacrylate. *Macromolecules* **1994**, *27*, 1885–1890.

(44) Sinturel, C.; Vayer, M.; Morris, M.; Hillmyer, M. A. Solvent Vapor Annealing of Block Polymer Thin Films. *Macromolecules* **2013**, *46*, 5399–5415.

(45) Stein, G. E.; Kramer, E. J.; Li, X.; Wang, J. Layering Transitions in Thin Films of Spherical-Domain Block Copolymers. *Macromolecules* **2007**, *40*, 2453–2460.

(46) Aissou, K.; Fleury, G.; Pecastaings, G.; Alnasser, T.; Mornet, S.; Goglio, G.; Hadziioannou, G. Hexagonal-to-Cubic Phase Transformation in Composite Thin Films Induced by FePt Nanoparticles Located at PS/PEO Interfaces. *Langmuir* **2011**, *27*, 14481–14488.

(47) Barton, A. M. *Handbook of Polymer–Liquid Interaction Parameters and Solubility Parameters*; Routledge, 2018.

(48) Lee, B.; Park, I.; Yoon, J.; Park, S.; Kim, J.; Kim, K.-W.; Chang, T.; Ree, M. Structural Analysis of Block Copolymer Thin Films with Grazing Incidence Small-Angle X-Ray Scattering. *Macromolecules* **2005**, *38*, 4311–4323.

(49) Busch, P.; Rauscher, M.; Moulin, J. F.; Müller-Buschbaum, P. Debye-Scherrer Rings from Block Copolymer Films with Powder-like Order. *J. Appl. Crystallogr.* **2011**, *44*, 370–379.

(50) Saito, I.; Miyazaki, T.; Yamamoto, K. Depth-Resolved Structure Analysis of Cylindrical Microdomain in Block Copolymer Thin Film by Grazing-Incidence Small-Angle X-Ray Scattering Utilizing Low-Energy X-Rays. *Macromolecules* **2015**, *48*, 8190–8196.

(51) Fukuda, T.; Matsuda, H.; Shiraga, T.; Kimura, T.; Kato, M.; Viswanathan, N. K.; Kumar, J.; Tripathy, S. K. Photofabrication of Surface Relief Gratings on Films of Azobenzene Polymer with Different Dye Functionalization. *Macromolecules* **2000**, *33*, 4220–4225.

(52) Qiang, Z.; Wadley, M. L.; Vogt, B. D.; Cavicchi, K. A. Facile Non-Lithographic Route to Highly Aligned Silica Nanopatterns Using Unidirectionally Aligned Polystyrene-Block-Polydimethylsiloxane Films. *J. Polym. Sci., Part B: Polym. Phys.* **2015**, *53*, 1058–1064.

(53) Cummins, C.; Ghoshal, T.; Holmes, J. D.; Morris, M. A. Strategies for Inorganic Incorporation Using Neat Block Copolymer Thin Films for Etch Mask Function and Nanotechnological Application. *Adv. Mater.* **2016**, *28*, 5586–5618.

(54) Legrain, A.; Fleury, G.; Mumtaz, M.; Navarro, C.; Arias-Zapata, J.; Chevalier, X.; Cayrefourcq, I.; Zelsmann, M. Straightforward Integration Flow of a Silicon-Containing Block Copolymer for Line-Space Patterning. *ACS Appl. Mater. Interfaces* **2017**, *9*, 43043–43050.

(55) Gotrik, K. W.; Hannon, A. F.; Son, J. G.; Keller, B.; Alexander-Katz, A.; Ross, C. A. Morphology Control in Block Copolymer Films Using Mixed Solvent Vapors. *ACS Nano* **2012**, *6*, 8052–8059.

(56) Ubukata, T.; Isoshima, T.; Hara, M. Wavelength-Programmable Organic Distributed-Feedback Laser Based on a Photoassisted Polymer-Migration System. *Adv. Mater.* **2005**, *17*, 1630–1633.

(57) Jiang, Z. GIXSGUI: A MATLAB Toolbox for Grazing-Incidence X-Ray Scattering Data Visualization and Reduction, and Indexing of Buried Three-Dimensional Periodic Nanostructured Films. *J. Appl. Crystallogr.* **2015**, *48*, 917–926.

II.2.B/ Discussion

As demonstrated in this manuscript, the DSA of BCPs containing azobenzene moieties was only observed when SRG was firstly inscribed into the BCP layer. A subsequent solvent vapor annealing provides enough mobility to the BCP chains to gain long range translational order due to the previous alignment of the azobenzene dyes. It is noteworthy that the SVA treatment also flattens the BCP layer (i.e. disappearance of the inscribed SRG pattern) which concurrently induces a matter flow, potential helping the long-range ordering (local shearing). Conversely, no long-range translational order was observed with the inverted process (self-assembly followed by SRG). Indeed, the SRG inscription induces an in-plane directional macroscopic flow of the azobenzene containing chains, leading to an erasure of the self-assembled structure.

Even if this method is an “exotic” way to perform DSA as compared to a standard graphoepitaxy method, it does not require expensive lithographic tools. Besides, it could be coupled to “classic” DSA methodologies, i.e. graphoepitaxy and chemical epitaxy, to enhance the breath of DSA methods. However, a drawback of this approach is the chemical modification requirement of one block to add the azobenzene moieties. Indeed, the design of this type of BCPs represents a synthetic challenge, and also prevents the use of the well-studied BCP systems for which the physico-chemical parameters and annealing protocols are reported. Accordingly, the methods to promote the self-assembly have to be developed for these particular systems taking into account the drastic modifications of the physical-chemical properties induced by the insertion of the azobenzene moieties in the BCP architecture.

II.3/ Substrate nanotexturing with SRG

As observed in the previous section, SRG triggered by the incorporation of azobenzene moieties in a BCP architecture can be integrated in a DSA process. In the following part, we decided to take advantage of polymeric layers containing azobenzene to create complex patterns further used to promote DSA of BCPs.

Indeed, the photoisomerization of azobenzene functional groups allows the formation of perfectly defined patterns by the use of light interferometry, the so-called SRG. These patterns, usually lines with a sinusoidal profile, have a width of a few hundred nanometers (depending of the incident angle and wavelength of the incoming laser), which is one order of magnitude higher than the usual periodicity of self-assembled BCP structures. As described before, these patterns can act as topographical templates in order to guide BCP self-assembly in thin film. In the following part, we aimed at the further improvement of this method. Firstly, the profile of the guides is sinusoidal when solely using SRG of a layer containing azobenzene moieties, which drastically modify the confinement constraints of BCP thin films with respect to the typical trenches with sharp edges usually employed in graphoepitaxy [6]–[8]. Secondly, the current process based on a single exposure of the polymeric layer limits the range of pattern geometries to parallel lines. Accordingly, we devised novel strategies to expand the breath of applicability of SRG guiding patterns.

II.3.A/ Pattern formation via SRG

II.3.A.i/ Line & space topographical patterns made by a “unique SRG” process

The first process consists in creating a sinusoidal wave pattern which is then modified into inorganic lines strongly anchored on the silicon substrate to form a robust textured substrate (*Figure 39.a*). The wave pattern is inscribed onto an azobenzene thin film using light interference fringes created with a Lloyd interferometer (see *Chapter I/Figures 35* and *Chapter I.4.B/*). Then, the thin film is etched by a controlled plasma treatment until only thin small lines obtained from the thicker regions (top of the waves) remain on the substrate. Finally, those lines are transformed into alumina using a SIS process to form a line & space pattern onto a silicon substrate.

The poly(disperse red 1 acrylate) (PDR1A) of 20 kg/mol used for this study was synthesized in our laboratory following a previously reported procedure [3]. A 3 wt.% solution of this polymer was dissolved in tetrahydrofuran (THF) and spin-coated onto a silicon wafer carefully washed in THF. The spin-coating was done at room temperature with a speed of 2000

rpm, leading to a 130 nm thick film. A thermal annealing above T_g at 110 °C for 3 hours was performed to flatten the surface, thus reducing the roughness linked to the fast THF evaporation rate.

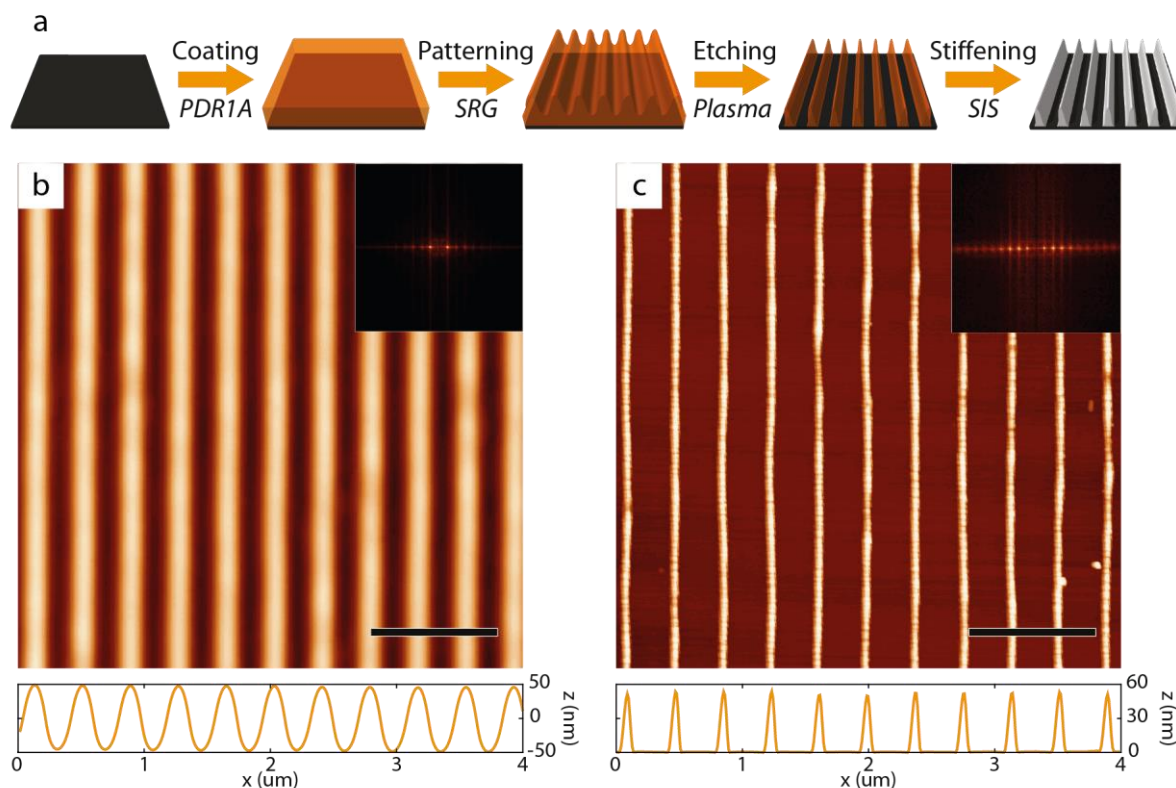


Figure 39. "Unique SRG" process. (a) Schematics of the patterning process. First a thin PDR1A film is deposited by spin-coating, then a wave pattern is created by Lloyd's mirror interferences (SRG), followed by a plasma etching, producing narrow lines, and finally the pattern is hybridized into alumina by a SIS process. AFM height images and height profiles of the produced wave pattern (b) after SRG (130 nm film - 10 min SRG - 45° incident angle) and (c) after RIE plasma (50 sec 20 sccm Ar 200 W). Insets are the corresponding FFTs. Scale bars: 1 μm .

Then, a SRG pattern is created using a Lloyd's mirror interferometer (Figure 39.b). The overall pattern can be defined by the wave size and inter-distance, which are controlled by the SRG inscription duration, the incident angle and the laser power [9].

The wave size is evaluated from the peak-to-valley height, also called amplitude, and increases with the duration and the laser power. Here, the laser power is constant (ca. 50 $\text{mW}\cdot\text{cm}^{-2}$), thus only the duration of the SRG inscription dictates the wave amplitude. It is noteworthy that the amplitude reaches a plateau after a prolonged exposure depending on exposure conditions [10], [11]. In our case, the maximal amplitude was obtained for an irradiation of 600 s and is around 100 nm.

The inter-distance between the waves was evaluated as the peak-to-peak distance (PPD), and is related to the incident angle θ by the Equation (1). The green laser used in this study has a wavelength of 532 nm, thus it is theoretically possible to reach pattern wavelength from 266 nm

to infinite. However, a sufficient light power is needed to induce SRG over a large area, which is geometrically maximized for $\theta = 45^\circ$, and reduces to 0 for angles at 0° and 90° .

$$PPD_\theta = \frac{\lambda_{laser}}{2\sin(\theta)} \quad (10)$$

Here, we choose to work with $\theta = 45^\circ$ in order to produce the largest patterned areas. This theoretically leads to a $PPD_{45^\circ} = 376$ nm. Experimentally, it has been observed $PPD_{45^\circ} = 384$ nm on a patterned area about 1 cm^2 . We also choose to work with $\theta = 21^\circ$ to reach $PPD_{21^\circ} = 742$ nm which is twice the PPD_{45} . Experimentally, such conditions produced a $PPD_{21^\circ} = 780$ nm on an area around half the 45° one.

After the formation of the sinusoidal pattern, a plasma step was used to etch the pattern until a complete removal of the polymer film in the valleys. By assuming that the plasma etching is isotropic, it is possible to simulate the pattern profile evolution over time (*Figure 40.a*, see Annex 3.A/ for the Matlab code). Interestingly, this simulation underlines the presence of a “working window”, i.e. between a film breakthrough (no polymer in the valley) and a full polymer removal (layer organic cleaning). Within this working window, it is possible to calculate an aspect ratio of the pattern, defined as the height divided by the full width at half maximum, which is an important for graphoepitaxy purpose. The simulation predicts an increase of the aspect ratio with the etching time. Accordingly, a compromise between the height of the pattern and its aspect ratio has to be targeted for specific commensurability conditions.

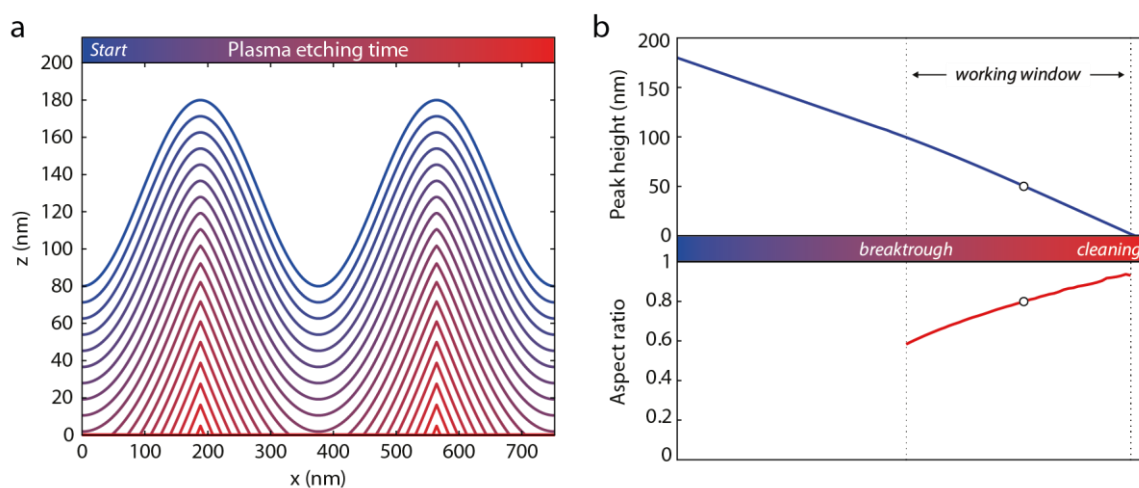


Figure 40. (a) Simulated isotropic etching profiles of a 130 nm thick film with 100 nm peak-to-valley SRG pattern inscribed on it. (b) Evolution of the peak height and pattern aspect ratio with plasma etching time. The dots indicate the predicted values for a 50 nm high pattern.

Experimentally, the best compromise was found for an argon reactive ion etching (RIE) plasma (20 sccm Ar, 200 W, 50 s) leading to a linear wave pattern with a height of around 50 nm and a width of 60 nm (*Figure 39.c*) (aspect ratio = 0.83). This value is coherent when compared to

the 0.8 aspect ratio estimated from the simulation, and is at the center of the working window (empty dots on *Figure 40.b*).

After the formation of such pattern, a SIS step was used to stiffen the PDR1A into alumina. Such transformation will preserve the integrity of the topographical pattern at the time of a subsequent BCP layer spin-coating while providing a higher thermal stability during the various annealing steps. Experimentally, the SIS was made following the standard recipe with a sequence of four infiltration cycles (see *Annex 1.B.i/*). This so-called “unique SRG” process allows the creation of perfectly aligned and spaced lines, which can have a controlled spacing by changing the incident angle during the SRG photo-inscription. Besides, it is rather simple to predict thus control the height and aspect ratio of the pattern.

II.3.A.ii/ Grid patterns made by the repetition of “unique SRG” process (“repeated SRG” process)

It is also possible to slightly modify this process to create more complex patterns. Indeed, the grooves obtained from the “unique SRG” process are especially interesting for the DSA of lamellar BCPs, but other optimized pattern configurations should be more adequate for hexagonal structures obtained from out-of-plane cylinders or hexagonally packed spheres. Additionally, nano-manufacturing often requires the design of complex shapes for targeted applications (e.g. circular bit patterned media for information storage).

A first alternative consists in repeating twice the previous process. Thus, a line & space pattern is firstly created, and then this patterned substrate is used as a standard substrate to perform again the same process. Interestingly, the second SRG photo-inscription is not disturbed by the first one which is in accordance with the large film thickness of 130 nm resulting from the deposition process with respect to the 50 nm pattern height. Then, by rotating the sample within the Lloyd’s mirror setup with a controlled angle between the first and second SRG photo-inscription, it is possible to create two line & space arrays with a desired angle between them.

Geometrically, hexagonal structures have a 6-fold symmetry. Thus, by rotating the substrate of 60° between each SRG, it is possible to create two arrays which generate lozenges. Besides, a 90° rotation angle will form squares which could have interesting applications for graphoepitaxy purposes (*Figure 41*). Moreover, it is possible to use different incident angles for each “unique SRG” process, i.e. changing the PPD of each pattern, which would transform squares into rectangles and lozenges into parallelograms.

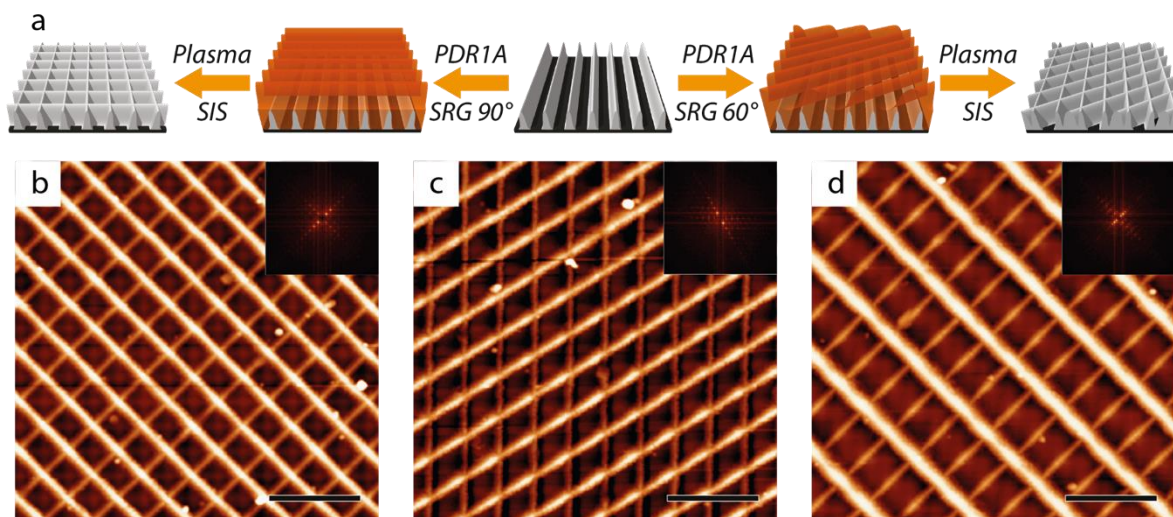


Figure 41. “Repeated SRG” process. (a) Schematics of the second SRG process leading to the formation of grids. Starting from the line & space pattern (created with the first “unique SRG” process), followed for the left (right) route by a second SRG at 90° (60°) angle from the first one, squares (lozenges) or rectangles (parallelograms) are generated depending of the SRG incident angles at each step. AFM height images of the produced (b) square (c) lozenge and (d) rectangle grid patterns created with this process. Insets are the corresponding FFTs. Scale bars: $1\ \mu\text{m}$.

Thus, the “Repeated SRG” process allows the formation of any 2D structures made with two arrays of line & space pattern for which the characteristic dimensions and shapes are dictated by the Equation (1) and the relative angle between them with for instance a perfectly squared grid matrix (Figure 41.b), 60° lozenge grid matrix (Figure 41.c) and a rectangle grid matrix (Figure 41.d). Interestingly, a 60° lozenge formation would match the 60° from the hexagonal symmetry of out-of-plane BCP cylinders.

II.3.A.iii/ Pillar patterns made by a “consecutive SRG” process

A third process called “consecutive SRG” process consists in performing a second SRG step directly on top of the first one before the RIE treatment. The sample is also rotated between the SRG photo-inscriptions for instance by 90° and 60° to create an orthogonal and hexagonal structures, respectively (Figure 42.a).

For this process, the most important parameter to control is the effective amplitude of the second SRG photo-inscription with respect to the first one. In this particular configuration, the SRG pattern created by the first photo-inscription has an impact on the second SRG photo-inscription. This means that different exposure times are required in order to obtain identical amplitude, thus symmetric geometrical features. Experimentally, it has been showed that isotropic features are formed when the duration of the first SRG is twice the duration of the second. Also, the cumulative duration of first and second SRGs should be equal to the optimal duration of the “unique SRG” process, i.e. 600 s. Otherwise, the saturation of the SRG effect is

reached during the second SRG. Thus, the duration of the first and second SRG were chosen to 400 s and 200 s, respectively. Then, the following steps (RIE treatment and SIS) were identical to the “unique SRG” process. Interestingly, this process leads to higher amplitude (around 60 nm). As a note, the pattern height and aspect ratio can be modified by modifying the film thickness, the duration of the SRG photo-inscription and the plasma duration, even if not deeply investigated during this work.

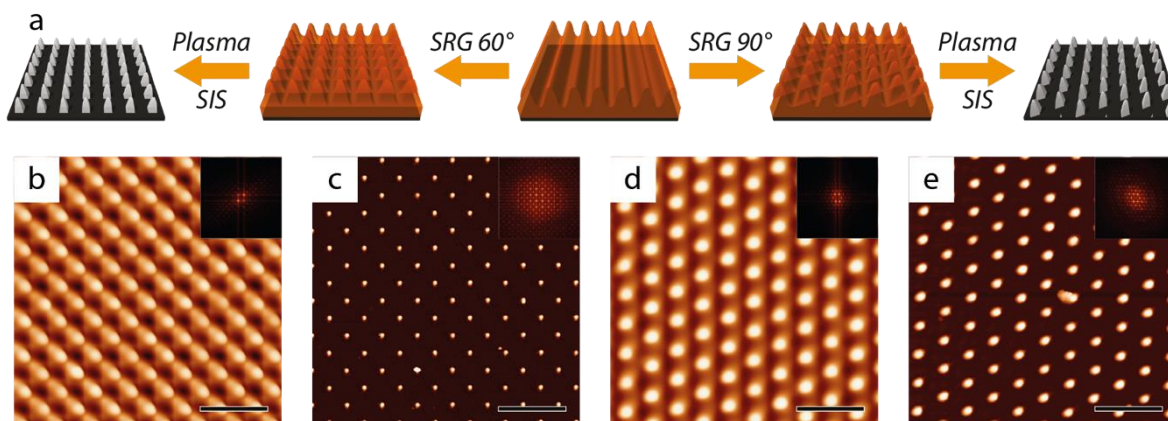


Figure 42. “Consecutive SRG” process. (a) In the middle is represented the wave pattern created by a first SRG. For the left route, a second SRG is made at 90° angle from the first, followed with plasma and infiltration, creating square or rectangle packed pillar depending of the SRG incident angle. For the right route, the same process is described with a 60° angle, creating perfect or distorted hexagonally packed pillars depending of the SRG incident angle. AFM height image of (b,c) tetragonal and (d,e) hexagonal pillar pattern created with this process. (b,d) before and (c,e) after plasma and infiltration. Insets are the corresponding FFTs. Scale bars: $1 \mu\text{m}$.

Finally, by modifying the order of the SRG and plasma/infiltration steps compared to the “repeated SRG” process, this so-called “consecutive SRG” process allow the production of pillars with controlled disposition, diameter and height. Figures 42.b-c show AFM images of this process before and after plasma/infiltration, with a 90° rotation angle between each SRG performed with a 45° incident angle. The resulting pattern is a perfect square packed pillar pattern with a 384 nm spacing. Performing this process by rotating the sample with a 60° angle instead of 90° leads to the formation of a hexagonally packed pillar pattern (Figures 42.d-e). Also, by changing the rotation angle and/or PPD between the two SRGs, it is possible to produce a plethora of different 2D textured surfaces.

This last process permits to create patterned substrates with the same hexagonal symmetry as out-of-plane cylinders or hexagonally packed spheres and could thus be used to promote long-range ordering and density multiplication by graphoepitaxy [12], [13].

II.3.B/ A large diversity of tunable nanostructures

Table 7 sums up some of the patterns achievable with the aforementioned processes, referencing the pattern name, the used process and the associated parameters. Here, the azobenzene film thickness, the total SRG duration and the plasma conditions are constant (i.e., 130 nm, 600 s and 20 sccm Argon - 200 W - 50 s, respectively).






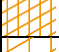



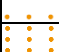
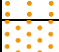

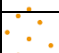

	Pattern structure	Process	First incident angle	Second incident angle	Rotation angle
	Narrow line & space	Unique SRG	45°	/	/
	Wide line & space	Unique SRG	21°	/	/
	Narrow square	Repeated SRG	45°	45°	90°
	Wide square	Repeated SRG	21°	21°	90°
	Rectangle	Repeated SRG	45° / 21°	21° / 45°	90°
	Narrow 60° lozenge	Repeated SRG	45°	45°	60°
	Wide 60° lozenge	Repeated SRG	21°	21°	60°
	General parallelogram	Repeated SRG	20°-70°	20°-70°	0°-90°
	Narrow square packed pillar	Consecutive SRG	45°	45°	90°
	Wide square packed pillar	Consecutive SRG	21°	21°	90°
	Rectangle packed pillar	Consecutive SRG	45° / 21°	21° / 45°	90°
	Narrow hexagonally packed pillar	Consecutive SRG	45°	45°	60°
	Wide hexagonally packed pillar	Consecutive SRG	21°	21°	60°
	Generally packed pillar	Consecutive SRG	20°-70°	20°-70°	0°-90°

Table 7. Patterns achievable by SRG nanotexturing processes developed during this Ph.D. with the corresponding experimental procedure. Narrow means 376 nm PPD and wide means 742 nm PPD.

Almost every structures have been formed onto silicon substrate, and were observed by SEM after the final immobilization of the structure by SIS (Figures 43.a-k).

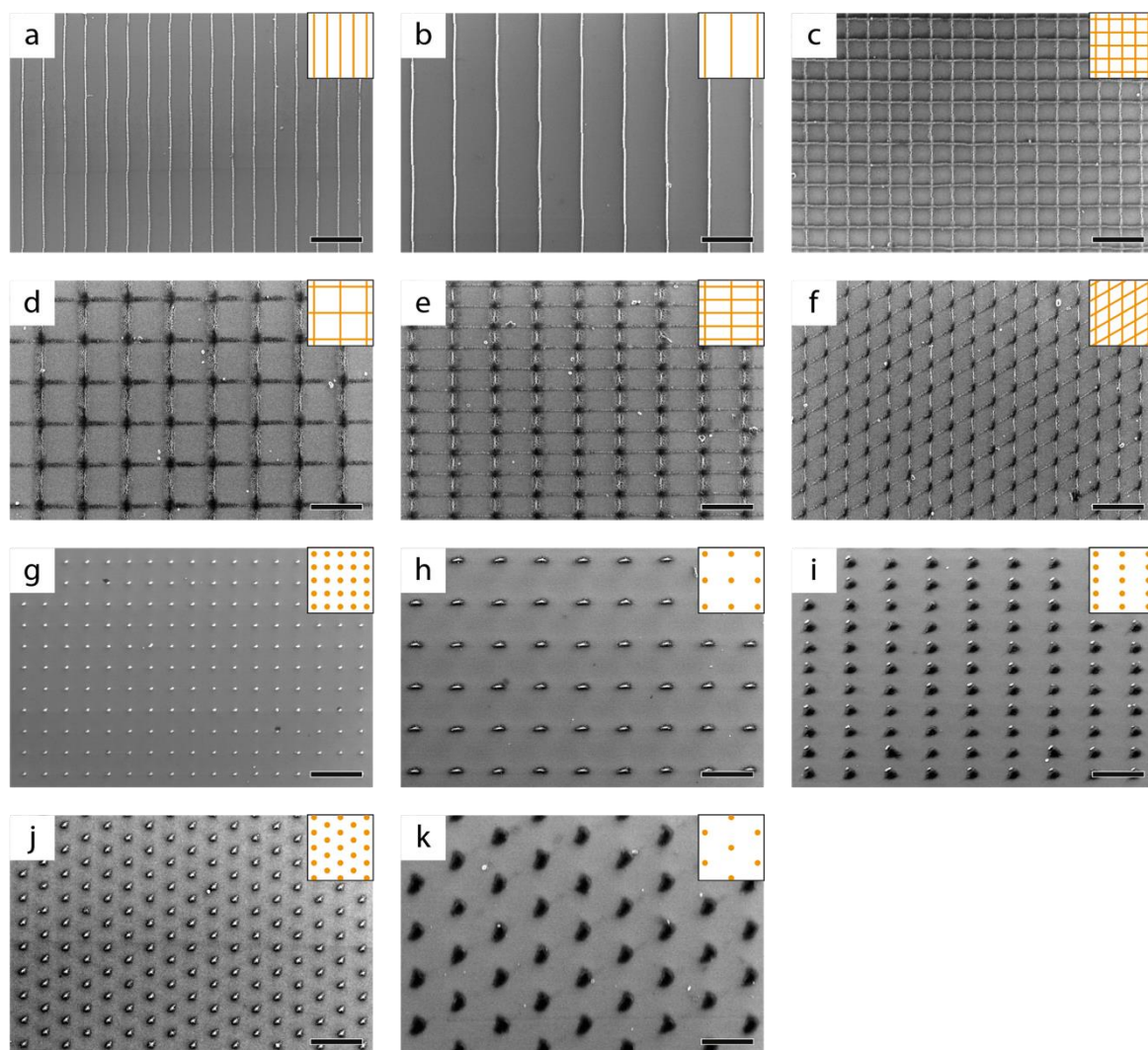


Figure 43. SEM pictures of (a) narrow line & space, (b) wide line & space, (c) narrow square, (d) wide square, (e) rectangle, (f) narrow lozenge, (g) narrow square packed pillar, (h) wide square packed pillar, (i) rectangle packed pillar, (j) narrow hexagonally packed pillar and (k) wide hexagonally packed pillar. Scale bars: 1 μm .

It is noteworthy that some of these images show dark structures instead of light ones (Figures 43.d-e,i,k). These artifacts are certainly due to surface electron charging, and AFM measurements demonstrated that the structures are not engraved into the silicon substrate. Besides, defect free and perfectly ordered patterns were observed over several mm^2 areas which is enough to perform DSA by graphoepitaxy. Obviously, this area can be easily enlarged by increasing the laser power and expanding the beam size in order to keep the same surface energy, i.e. $50 \text{ mW} \cdot \text{cm}^{-2}$.

II.3.C/ “Low cost” graphoepitaxy

These SRG enabled topographical patterns can be used as a nanotextured substrate to direct a subsequent BCP self-assembly by graphoepitaxy [13], [14]. Indeed, these nanostructures

have typical periodicities about few hundreds of nanometers with around 50 nm height, and are transformed into alumina, that cannot be damaged during BCP self-assembly process. Combining every nanopatterns achievable (14 from *Table 7*), BCP structures (lamellae, cylinders and spheres), orientations (in-plane or out-of-plane), and periodicity ratio between the nanopattern and the BCP domain spacing, leads to almost infinite cases to study. This part will present preliminary results of some of these combinations.

II.3.C.i/ Self-assembled lamellae on a line & space pattern

The simplest combination is to self-assemble out-of-plane lamellae into trenches produced by the “unique SRG” process. The objective is to increase the long-range ordering of the lamellar structure, from fingerprints to a unique grain of parallel lamellae orientated along or perpendicularly to the substrate pattern. This kind of graphoepitaxy has been already widely used using nanopatterned Si or SiO₂ substrate, and the orientation of lamellae with respect to the trenches is dictated by the commensurability ratio and the interfacial energy between the substrate/trenches and the BCP domains [15], [16].

A substrate was patterned with a line & space pattern using the “unique SRG” process, and a lamellar BCP was subsequently self-assembled on top of it (detailed process in *Annex 1.A/*). Prior to the BCP spin-coating, the patterned substrate surface was modified by grafting a PS-*r*-PMMA with a PS volume fraction $f_{PS} = 0.70$. This composition leads to a perfectly neutral interface toward this particular lamellar PS-*b*-PMMA (see *Chapter III.1/*) for the whole surface, i.e. for the trench bottom and walls. Then, the BCP thin film was deposited by spin-coating a PS₂₇-*b*-PMMA₂₂ at 1,5 wt.% in Propylene Glycol Methyl Ether Acetate (PGMEA) at 2000 rpm. Finally, an annealing treatment at 260 °C for 10 min yields to a 30 nm thick out-of-plane lamellar structure with 30 nm domain spacing.

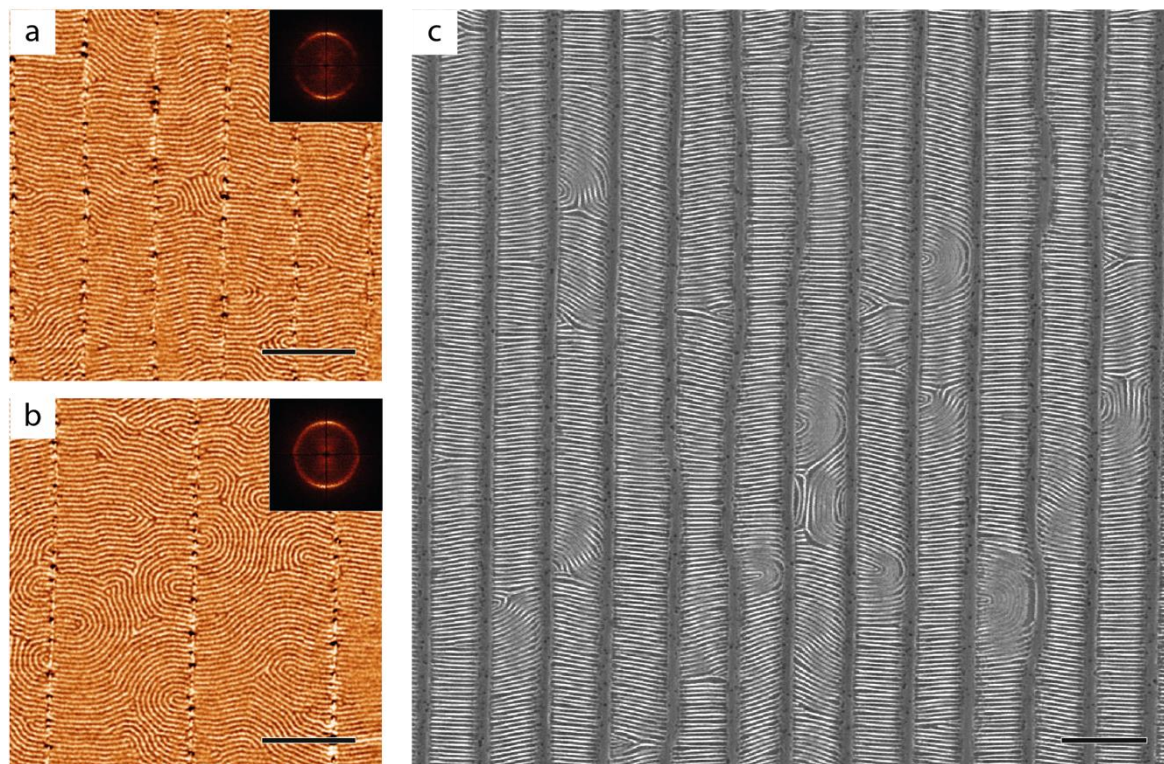


Figure 44. AFM phase image of a lamellar PS-*b*-PMMA on top of (a) 384 nm periodic “narrow line & space” pattern and (b) 780 nm “wide line & space” pattern made with the “unique SRG” process. Top right insets are the corresponding FFTs. (c) SEM picture of the “narrow line & space” case after PMMA infiltration by Al_2O_3 and PS removal by plasma. Scale bars: 500 nm.

Figure 44.a shows the resulting out-of-plane lamellae perpendicularly oriented with respect to the topographical pattern, as expected with a neutral interface configuration at the walls [16]. Indeed, the PS and PMMA domains are equally facing the whole pattern substrate surface, leading to the lowest interfacial energy compared to other configurations which would not have balanced exposition. Figure 44.b shows the same process on a wider pattern (780 nm versus 384 nm before) showing the same behavior, but with more defects as emphasized by the FFT insets. This difference on DSA quality is due to the formation of a weaker topographic field when the pattern is wider [6]. For the “narrow line & space” pattern, a subsequent infiltration of the PMMA domains has been performed followed by a plasma etching using the typical process (see Annex 1.B.ii/), leading to a well ordered and fully inorganic rectangle grid over a large area (Figure 44.c). It is noteworthy that such line & space pattern should also be able to orientate cylindrical or spherical morphologies for appropriate commensurability and thickness [17]–[19].

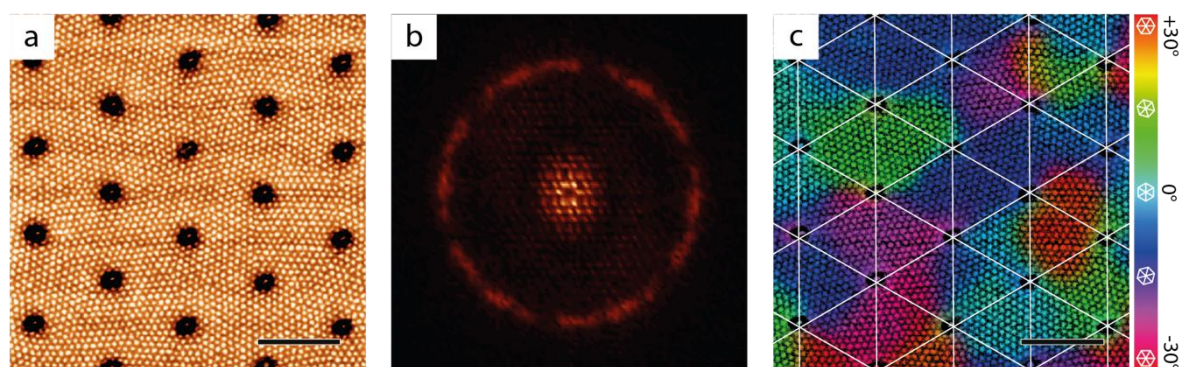
II.3.C.ii/ Self-assembled cylinders on a hexagonal packed pillar pattern

A second combination is the self-assembly of out-of-plane cylinders on top of a hexagonally packed pillar patterned substrate made with the “consecutive SRG” process. Indeed, the two structures have the same hexagonal symmetry, with a larger size for the pattern and a

smaller for the BCP structure. With the appropriate commensurability, the ordering of the cylinders should be dictated by the position of pillars, leading to the so-called density multiplication, as it has been observed for patterned substrates with nanolithography [12], [20].

In this case, a hexagonally packed pillar pattern was formed on a substrate, using the “consecutive SRG” process, and out-of-plane cylinders were self-assembled on top of it (detailed process in *Annex 1.A*). First, the surface energy of the pattern was modified by grafting a neutral PS-*r*-PMMA toward the hexagonally packed PMMA cylindrical phase, i.e. with $f_{PS} = 0.78$. Then, a thin film was deposited by spin-coating a 1.5 wt.% PS₃₃-*b*-PMMA₁₅ solution in PGMEA at 2000 rpm, followed by an annealing at 200 °C for 15 min, leading to a 30 nm thick film with 35 nm center-to-center out-of-plane cylindrical structure.

Figure 45.a shows that the PMMA cylinders are effectively positioned around the hexagonally packed pillars from the pattern. The FFT image (*Figure 45.b*) shows that a unique grain was not obtained, but preferential orientations of the BCP patterns were retrieved, leading to several well-defined grains. By processing the AFM image with a Matlab program (see *Annex 3.B*), the image was colored with respect to the orientation of the hexagonal structure (*Figure 45.c*). This image shows that each triangle formed by three pillars (emphasized by the white lines) mostly possesses a unique color. Also, the color changes are mostly happening along the triangle edges. This means that these triangles are each composed of a “unique” grain orientated by the topographic field induced by their three vertex pillars, and the major part of grain boundaries are localized at the triangle sides.



*Figure 45. (a) AFM image, (b) FFT and (c) orientational mapping of a cylinder forming PS-*b*-PMMA on top of a hexagonally packed pillar pattern made by a “consecutive SRG” process. The orientational map have been computed with Matlab, white lines are guides for the eyes. Scale bars: 400 nm.*

These various grain orientations and boundaries (i.e. defects) are explained by the incommensurability between the BCP intrinsic period and the pattern. Indeed, the substrate pattern exhibits an experimental center-to-center distance of 443 nm (i.e. $384 \times 2/\sqrt{3}$, exactly the value expected for a 60° angle geometry between two SRG forming 384 nm periodic lines), while the BCP has a 35 nm center-to-center distance, leading to a non-integer 12.6 ratio. Obviously, the

process can be improved by aiming at an integer ratio between the periodicities of the BCP and the pattern, and by lowering its value in order to strengthen the topographic field.

Accordingly, a ratio of 12 could be obtained by using a PS-*b*-PMMA with a center-to-center distance of 37 nm instead of 35 nm. However, this 2 nm center-to-center modification appears to be small enough for being spontaneously overpass by chain stretching if the energy benefit was high enough [7], [8]. This means that the topographic field induced by the “narrow hexagonally packed pillar” pattern is not strong enough to induce perfect DSA of 35 nm or 37 nm cylinders. In order to strengthen the topographical field, it is possible to lower the density multiplication ratio by reducing the periodicity of the pillar pattern or by increasing the BCP center-to-center distance.

This type of topographical pattern has also been used to direct the self-assembly of spherical BCPs which can produce hexagonal pattern in thin film [12], [21]. Interestingly, in this case, it has been observed that the directed self-assembly was still efficient for large density multiplication ratio, up to 16 due to the particular wetting configuration of the BCP spherical domains (only one block is in contact with the topographical pattern) [20].

II.3.C.iii/ Self-assembled cylinders in a square pattern

A third combination studied during this Ph.D. is the confinement of cylinder forming PS-*b*-PMMA inside a square structure. In this case, the difference between the pattern orthogonal symmetry and the BCP hexagonal symmetry would inexorably lead to incommensurate conditions. However, the constrained cylinders could rearrange to generate interesting non-native structures.

Experimentally, a square pattern was deposited on a silicon substrate using the “repeated SRG” process, forming 384 nm wide squares. Then, the same process as reported in the previous part was performed, leading to PMMA cylinders self-assembled on top of these squares. The resulting self-assembly (*Figure 46.a*) presents cylinders that are oriented in an in-plane configuration within the squares, and an out-of-plane orientation above the edge of the squares. This is explained by the film thickness difference within and above the square edges, which have a great impact on the orientation of cylinder-forming BCPs [22], [23], giving in-plane and out-of-plane cylinders in thicker and thinner regions, respectively.

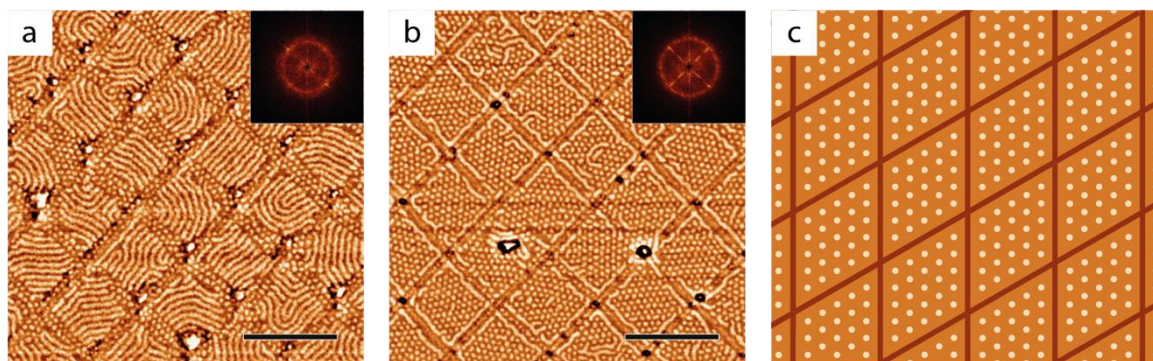


Figure 46. AFM phase images of cylinder-forming PS-*b*-PMMA formed from (a) 1,5 wt.% and (b) 1 wt.% solutions, on top of a square pattern made by a “repeated SRG” process. Top right insets are the corresponding FFTs. (c) Schematics of theoretical configuration allowing a commensurate self-assembly of PMMA cylinders in a 60° lozenge pattern. Scale bars: 400 nm.

To counterbalance this thickness effect, the BCP concentration solution was lowered from 1.5 wt.% to 1 wt.% (Figure 46.b). As a result, out-of-plane cylinders are mostly observed inside the square pattern even if neither preferential orientation nor long-range ordering is obtained (due to the geometrical incommensurability between both structures). However, in-plane cylinders are still visible on the square edges despite the conditions of surface neutrality. This type of confined cylinders within geometrical patterns (including square) were studied by Do *et al.* for non-neutral interfacial energy in order to stabilize the in-plane cylinder orientation. The results demonstrated as well the formation of interesting non-native structures [24].

As a side note, an interesting combination using a similar process would be to self-assemble cylinder-forming PS-*b*-PMMA on a 60° lozenge structure. Indeed, a commensurability could be obtained with the appropriate ratio between the lozenge size and the BCP domain spacing as schematized in Figure 46.c.

II.4/ Conclusions

In the first part of this chapter, a “exotic” DSA route has been developed with the possibility to orientate cylinders perpendicularly to a SRG pattern. This process is effectively more complex than standard DSA methods, e.g. graphoepitaxy or chemical epitaxy, because it requires a synthetic effort with the grafting of azobenzene moieties as well as the modification of well-mastered self-assembly processes. However, it might be interesting when it is not possible to perform surface modifications (topographical or chemical) before thin film self-assembly, for instance during a stacking process. Indeed, the standard lithography-based DSA processes are incompatible when the surface to modify is already a self-assembled BCP layer as the BCP layer would get damaged during the process.

The second part described the development of three different methods to perform substrate texturing by the generation of a nanostructured Al_2O_3 pattern, resulting in a plethora of different geometries with high order over several mm^2 . These patterns are around 50 nm thick with a periodicity of several hundred nanometers, which is the appropriate size for DSA by graphoepitaxy. Also, the fully inorganic composition of the pattern is perfectly adapted for BCP self-assembly processes based on thermal or solvent annealing as it allows both surface modification and improved stability of the topographical pattern.

Some preliminary experiments to direct the self-assembly of PS-*b*-PMMA thin films were performed to observe the compatibility of this method with the standard methodologies. This study clearly emphasized the important parameters to control for proper BCP self-assembly. Among others, the parameters of importance are:

- The film thickness with respect to pattern height, which can have a role on the orientation of the BCP structure (in-plane or out-of-plane);
- The commensurability ratio between the BCP domain spacing and the pattern periodicity, which should be appropriately defined in order to limit the defectivity of the BCP self-assembly;
- The combination between the BCP structure symmetry and the pattern geometry should be compatible.

II.5/ References

- [1] Y. Morikawa, T. Kondo, S. Nagano, and T. Seki, "Photoinduced 3D ordering and patterning of microphase-separated nanostructure in polystyrene-based block copolymer," *Chem. Mater.*, vol. 19, no. 7, pp. 1540–1542, 2007, doi: 10.1021/cm0630845.
- [2] H. Yu, A. Shishido, T. Iyoda, and T. Ikeda, "Photoinduced alignment of nanocylinders in an amphiphilic diblock liquid-crystalline copolymer by supramolecular cooperative motions," *Polym. Prepr. Japan*, vol. 55, no. 2, p. 3996, 2006.
- [3] K. Aissou *et al.*, "Nanoscale block copolymer ordering induced by visible interferometric micropatterning: A route towards large scale block copolymer 2D crystals," *Adv. Mater.*, vol. 25, no. 2, pp. 213–217, 2013, doi: 10.1002/adma.201203254.
- [4] Y. Rho *et al.*, "Laterally Ordered Sub-10 nm Features Obtained from Directed Self-Assembly of Si-Containing Block Copolymer Thin Films," *Small*, vol. 11, no. 48, pp. 6377–6383, 2015, doi: 10.1002/sml.201500439.
- [5] M. C. Spiridon *et al.*, "Optical Alignment of Si-Containing Nanodomains Formed by Photoresponsive Amorphous Block Copolymer Thin Films," *Macromolecules*, vol. 53, no. 1, pp. 68–77, 2020, doi: 10.1021/acs.macromol.9b01551.
- [6] S.-M. Park, M. P. Stoykovich, R. Ruiz, Y. Zhang, C. T. Black, and P. F. Nealey, "Directed Assembly of Lamellae-Forming Block Copolymers by Using Chemically and Topographically Patterned Substrates," *Adv. Mater.*, vol. 19, no. 4, pp. 607–611, 2007, doi: 10.1002/adma.200601421.
- [7] S. Xiao *et al.*, "Graphoepitaxy of cylinder-forming block copolymers for use as templates to pattern magnetic metal dot arrays," *Nanotechnology*, vol. 16, no. 7, pp. S324–S329, Jul. 2005, doi: 10.1088/0957-4484/16/7/003.
- [8] J. Y. Cheng, A. M. Mayes, and C. A. Ross, "Nanostructure engineering by templated self-assembly of block copolymers," *Nat. Mater.*, vol. 3, no. 11, pp. 823–828, 2004, doi: 10.1038/nmat1211.
- [9] D. Y. Kim, L. Li, X. L. Jiang, V. Shivshankar, J. Kumar, and S. K. Tripathy, "Polarized Laser Induced Holographic Surface Relief Gratings on Polymer Films," *Macromolecules*, vol. 28, no. 26, pp. 8835–8839, Dec. 1995, doi: 10.1021/ma00130a017.
- [10] X. L. Jiang, L. Li, J. Kumar, D. Y. Kim, and S. K. Tripathy, "Unusual polarization dependent optical erasure of surface relief gratings on azobenzene polymer films," *Appl. Phys. Lett.*, vol. 72, no. 20, pp. 2502–2504, 1998, doi: 10.1063/1.121400.
- [11] O. Sakhno, L. M. Goldenberg, M. Wegener, and J. Stumpe, "Deep surface relief grating in azobenzene-containing materials using a low-intensity 532 nm laser," *Opt. Mater. X*, vol. 1, no. October 2018, p. 100006, 2019, doi: 10.1016/j.omx.2019.100006.
- [12] I. Bitá, J. K. W. Yang, Y. S. Jung, C. A. Ross, E. L. Thomas, and K. K. Berggren, "Graphoepitaxy of Self-Assembled Block Copolymers on Two-Dimensional Periodic Patterned Templates," *Science (80-.)*, vol. 321, no. 5891, pp. 939–943, Aug. 2008, doi: 10.1126/science.1159352.
- [13] S. M. Nicaise, K. G. Amir Tavakkoli, and K. K. Berggren, "Self-assembly of block copolymers by graphoepitaxy," in *Directed Self-assembly of Block Co-polymers for Nano-manufacturing*, Elsevier, 2015, pp. 199–232.
- [14] I. Gunkel, "Directing Block Copolymer Self-Assembly on Patterned Substrates," *Small*, vol. 14, no. 46, pp. 1–8, 2018, doi: 10.1002/sml.201802872.
- [15] M. J. Maher *et al.*, "Directed self-assembly of silicon-containing block copolymer thin films," *ACS Appl. Mater. Interfaces*, vol. 7, no. 5, pp. 3323–3328, 2015, doi: 10.1021/am508197k.

- [16] E. Han, H. Kang, C. C. Liu, P. F. Nealey, and P. Gopalan, "Graphoepitaxial assembly of symmetric block copolymers on weakly preferential substrates," *Adv. Mater.*, vol. 22, no. 38, pp. 4325–4329, 2010, doi: 10.1002/adma.201001669.
- [17] C. Cummins *et al.*, "Parallel Arrays of Sub-10 nm Aligned Germanium Nanofins from an in Situ Metal Oxide Hardmask using Directed Self-Assembly of Block Copolymers," *Chem. Mater.*, vol. 27, no. 17, pp. 6091–6096, 2015, doi: 10.1021/acs.chemmater.5b02608.
- [18] R. Tiron *et al.*, "Optimization of block copolymer self-assembly through graphoepitaxy: A defectivity study," *J. Vac. Sci. Technol. B, Nanotechnol. Microelectron. Mater. Process. Meas. Phenom.*, vol. 29, no. 6, p. 06F206, 2011, doi: 10.1116/1.3659714.
- [19] J. Y. Cheng, C. A. Ross, E. L. Thomas, H. I. Smith, and G. J. Vancso, "Fabrication of nanostructures with long-range order using block copolymer lithography," *Appl. Phys. Lett.*, vol. 81, no. 19, pp. 3657–3659, 2002, doi: 10.1063/1.1519356.
- [20] L. Wan and X. Yang, "Directed self-assembly of cylinder-forming block copolymers: prepatterning effect on pattern quality and density multiplication factor," *Langmuir*, vol. 25, no. 21, pp. 12408–12413, 2009, doi: 10.1021/la901648y.
- [21] Q. Y. Tang and Y. Q. Ma, "High density multiplication of graphoepitaxy directed block copolymer assembly on two-dimensional lattice template," *Soft Matter*, vol. 6, no. 18, pp. 4460–4465, 2010, doi: 10.1039/c0sm00238k.
- [22] C. Park *et al.*, "Double textured cylindrical block copolymer domains via directional solidification on a topographically patterned substrate solidification on a topographically patterned substrate," vol. 848, no. April 2001, pp. 1999–2002, 2016, doi: 10.1063/1.1389766.
- [23] A. Knoll *et al.*, "Phase behavior in thin films of cylinder-forming block copolymers," *Phys. Rev. Lett.*, vol. 89, no. 3, pp. 355011–355014, 2002, doi: 10.1103/PhysRevLett.89.035501.
- [24] H. W. Do *et al.*, "Directed self-assembly of a two-state block copolymer system," *Nano Converg.*, vol. 5, no. 1, 2018, doi: 10.1186/s40580-018-0156-z.

CHAPTER III: A RICH VARIETY OF 2D-NANOSTRUCTURES OBTAINED BY PS-*b*-PMMA SELF-ASSEMBLY

III.1/ Introduction	108
III.2/ Formation of 2D nanostructures from PS-<i>b</i>-PMMA.....	110
III.2.A/ PS- <i>b</i> -PMMA self-assembly	110
III.2.B/ Structure hybridization.....	121
III.3/ Phase diagram exploration	124
III.3.A/ Different morphologies by changing the BCP composition.....	124
III.3.B/ Tuning the structure periodicities	131
III.4/ Preparation for iterative stacking.....	136
III.4.A/ Geometrical considerations	136
III.4.B/ Resulting 2D-structures.....	137
III.5/ Conclusions.....	142
III.6/ References.....	143



The BCP system chosen for this Ph.D. being PS-*b*-PMMA, a thorough study was performed to setup a sturdy basis about its phase behavior in thin film. The first part of this study deals with the development of robust processes to perform the BCP self-assembly in thin film, with several key parameters to control, such as the substrate surface energy, the film thickness and the annealing conditions. Also, the hybridization step was optimized to enable subsequent layering.

The second part of the study focuses of the different morphologies and periodicities that can be obtained using various PS-*b*-PMMA BCPs taking into account the variation of degree of polymerization and composition. Finally, using geometrical considerations, several specific structures chosen for the layering were precisely characterized.

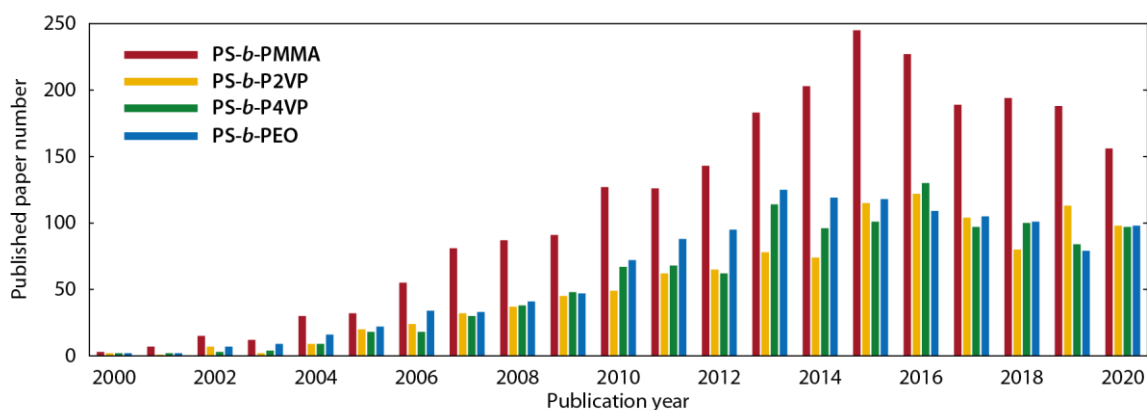
III.1/ Introduction

BCP self-assembly have been widely used to form well-ordered structures with a nanometric period. The simplest BCP architecture is the di-block, which can theoretically produce 4 different stable structures in bulk: lamellar, gyroidal, cylindrical and spherical. Interestingly, in the thin film regime, i.e. confined between two “fixed” boundaries (the substrate and the free interface), the phase behavior can differ and an additional parameter related to the orientation of the structure with respect to the “fixed” boundaries has to be taken into account. Accordingly, BCP self-assembly in thin film can produce line & space structures for out-of-plane lamellae or an in-plane monolayer of cylinders, and a hexagonal structure for out-of-plane cylinders or a monolayer of spheres.

The BCP chosen for this thesis is the PS-*b*-PMMA system due to the following reasons:

- The modulation of the substrate surface energy is usually done with PS-*r*-PMMA, which allows spanning surface energies from pure PS to pure PMMA;
- The well-documented self-assembly process by thermal annealing, due to the close surface energy of both blocks at the free surface;
- The high etching contrast between the PS and PMMA domains, allowing an efficient selective etching of PMMA;
- The compatibility of the PMMA block toward the SIS infiltration method;
- The controlled synthesis of PS-*b*-PMMA via a sequential living polymerization (i.e. anionic polymerization) which allows a fine tuning of the BCP chain length and composition combined with an overall low dispersity.

It is not surprising that this BCP is the most referenced in literature using “self-assembly” and “thin film” as keywords (*Figure 47*).



*Figure 47. Number of published papers versus the year of publication for the 4 main BCPs found in literature. The counting was made using Google Scholar with 3 keywords being the name of the BCP (PS-*b*-PMMA, PS-*b*-P2VP, PS-*b*-P4VP and PS-*b*-PEO), “self-assembly” and “thin film”.*

The aim of this chapter was thus to retrieve each interesting structure reachable with PS-*b*-PMMA for subsequent layering. A strong emphasis was placed on the process optimization to obtain the well-ordered structures combined to a high process robustness for the further scale-up using the stacking methods. Thus, the chapter is divided in three parts, the first one being the process development, the second being related to the screening of the reachable structures, and the last one being the selection and preparation of the different optimized layers that will be used for stacking in the next chapter.

III.2/ Formation of 2D nanostructures from PS-*b*-PMMA

III.2.A/ PS-*b*-PMMA self-assembly

The standard process to obtain self-assembled PS-*b*-PMMA thin films is composed of three different steps: the modification of the substrate surface energy, the deposition of a BCP film and the thermal annealing step (Figure 48).

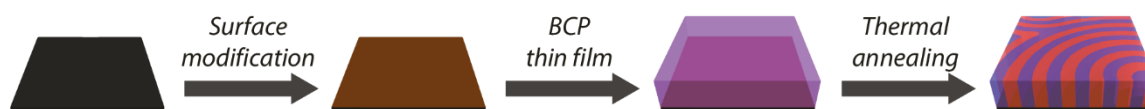


Figure 48. Schematics of the self-assembly process for the formation of nanostructured BCP films (here out-of-plane lamellae).

III.2.A.i/ Surface modification

The first step consists in tuning the substrate surface energy by modifying its chemistry, in order to either reach interfacial energy neutrality with respect to the two BCP domains, or to promote an affinity toward one specific domain. This modification is achieved by chemically grafting random copolymer (RCP) chains obtained from a (controlled) radical polymerization on the surface [1], [2]. The grafting is made by spin coating a thin film of the RCP, then annealing it at elevated temperature (promoting covalent grafting of the RCP chains at the surface), and rinsing away the non-grafted chains (the experimental process is detailed in Annex 1.A.). The most common RCP to control the domain orientation of PS-*b*-PMMA systems is PS-*r*-PMMA.

The parameters which influence the surface modification are the annealing conditions (time and temperature) and the RCP chemical characteristics (composition and molar mass). The objective is to reach a good grafting quality to perfectly screen the SiO₂ substrate surface while providing an appropriate surface energy for subsequent self-assembly. The first parameter is inherent to the grafting density and it has been observed that it is highly dependent on the film thickness and RCP molar mass. Experimental studies have demonstrated that the best subsequent BCP self-assemblies are obtained when the grafted film thickness is greater than twice the RCP radius of gyration R_g [3]. The usual RCP molar mass is between 2 and 10 kg/mol, thus the thickness required for the screening of the SiO₂ substrate should be higher than \approx 3-5 nm. Then, the second parameter depends on the BCP morphology and the targeted orientation. It is controlled by the RCP composition, i.e. the PS volume fraction [2], [4], but also the polymer end chain chemistry [5].

In order to cover a wide range of surface energies, different RCPs with M_n around 10 kg/mol were obtained from Arkema. These RCPs were synthesized with a “BlocBuilder MA” initiator, which decomposes into an initiator to trigger the polymerization, and a controller that

is used to control the kinetics, lowering the overall dispersity of the polymer (Figure 49). These two radical species lead to polymers with two different functionalized end chains.

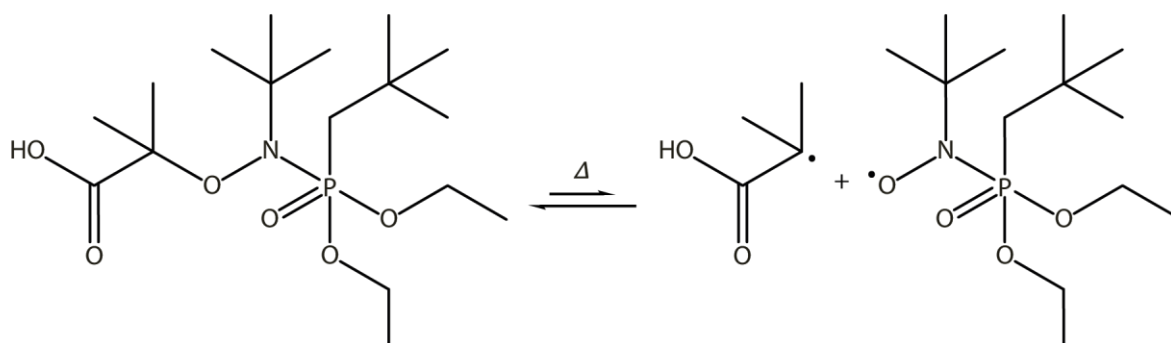


Figure 49. Chemical decomposition of Arkema "BlocBuilder MA" with heat, giving an initiator and a controller radical species.

Usually, the PS-*r*-PMMA used for substrate grafting are synthesized using TEMPO as initiator, leading to a hydroxyl end-functionalized chain [2], [5]. This terminal hydroxyl group is used to graft the chain onto the native silicon oxide layer by a dehydration mechanism initiated by heat. This reaction is slow, and thus requires a long thermal annealing treatment at a rather low temperature in order to avoid the RCP degradation (usually 140-160 °C for several days). However, on our case, with the BlocBuilder MA, the RCP chain is functionalized with a PO₃ group, allowing a fast-grafting reaction with SiO₂ (230 °C for 5 min).

Table 8 shows the characteristics of every RCP used in this study. It is noteworthy that a pure PS was synthesized using this particular initiator, but the synthesis of a pure PMMA was not attempted due to the poor control of this particular controlled radical polymerization with respect to methacrylate monomers. However, a "pure" PMMA behavior was obtained by combining styrene, MMA and trifluoroethyl methacrylate (TFEMA) monomers to the feed to produce PS-*r*-PMMA-*r*-poly(trifluoroethyl methacrylate) (PS-*r*-PMMA-*r*-PTFEMA). The addition of TFEMA repeating units in the RCP structure compensates in term of surface energy the low amount of styrene units [6], [7].

Name	f _{PS} ^a	M _n ^b (kg/mol)	PDI ^b	Initiator
11r56r33	0.11 ^c	7.5	1.76	BlocBuilder MA
40r60	0.40	12.3	1.53	BlocBuilder MA
49r51	0.49	13.4	1.38	BlocBuilder MA
63r37	0.63	12.4	1.30	BlocBuilder MA
69r31	0.69	11.2	1.32	BlocBuilder MA
75r25	0.75	13.6	1.23	BlocBuilder MA
87r13	0.87	12.3	1.30	BlocBuilder MA
100r0	1.00	12.3	1.19	BlocBuilder MA

Table 8. PS-*r*-PMMA macromolecular characteristics. ^af_{PS} is the volume fraction of PS estimated by ¹H NMR. ^bmeasured by SEC using PS standards for calibration. ^cThis polymer is PS-*r*-PMMA-*r*-PTFEMA 11%-56%-33%.

For PS-*b*-PMMA, only the control of the bottom interfacial energy is mandatory as the difference of surface energy with air is minimum at high temperature [8]. In addition, at elevated temperatures, the surface tension of both PS and PMMA are almost equivalent, providing therefore a natural “neutral” interaction between ambient air and the BCP domains. Then, the orientation of the structure is driven by the substrate surface energy: out-of-plane structures are obtained if the surface energy is neutral toward the self-assembled structure, while in-plane structures are obtained otherwise. Thus, a precise RCP composition is required for each structure in order to obtain out-of-plane structures (i.e. out-of-plane PS or PMMA cylinders and lamellae), even if a small composition drift is tolerated [4], [5]. Theoretically, it would have been expected a required RCP composition equal to the block ratio facing the substrate for out-of-plane structures (i.e. $f_{PS}^{RCP} = 0.30, 0.50$ and 0.70 for PS cylinders, lamellae and PMMA cylinders, respectively). However, the RCP composition is not directly linked to the effective surface energy, leading to non-linear relation between them. This can be explained by different reasons:

- Methyl methacrylate has a lower reactivity than styrene [9], [10], thus the RCP has a slightly gradient composition, leading to different effective RCP surface composition;
- The functionalized end chain which is not grafted to the surface can induce polar effects that affect surface interactions with BCPs [5];
- During annealing, PS and PMMA penetrates slightly the RCP thin film, modifying its effective composition [2];

In our case, the surface modification was experimentally optimized by observing the structure orientation with different RCP composition, until finding the desired one, without measuring the real surface energy. For this purpose, RCPs were mixed together to precisely tune the effective composition, thus the surface energy [4]. Blends were prepared in the liquid phase by mixing a vol_1 of RCP_1 solution to a vol_2 of RCP_2 solution (both solutions with the same 2 wt.% concentration). These mixtures were done only for RCP from two adjacent rows in *Table 8*, and a linear blend relation by volume was assumed since their composition were rather close:

$$f_{PS}^{RCP_{blend}} = \frac{vol_1 f_{PS}^{RCP_1} + vol_2 f_{PS}^{RCP_2}}{vol_1 + vol_2} \quad (11)$$

With this blending method, optimized RCP compositions used during this Ph.D. are:

- For in-plane structures with PS facing the substrate: $f_{PS}^{RCP} = 1$ (100r0);
- For in-plane structures with PMMA facing the substrate: $f_{PS}^{RCP} = 0.11$ (11r56r33);
- For out-of-plane PS cylinders within a PMMA matrix: $f_{PS}^{RCP} = 0.52$ (49r51:63r37 blend with 3:1 ratio);
- For out-of-plane lamellae: $f_{PS}^{RCP} = 0.70$ (69r31:75r25 blend with 3:1 ratio);

- For out-of-plane PMMA cylinders within a PS matrix: $f_{PS}^{RCP} = 0.78$ (75r25:87r13 blend with 3:1 ratio).

As mentioned before, we can see that the effective surface energy is indeed not directly linked to the RCP composition, since neutrality is not reached when the substrate surface energy is equal to the BCP composition [11], i.e. f_{PS}^{BCP} around 0.30, 0.50 and 0.70 for PS cylinders, lamellae and PMMA cylinders, respectively.

III.2.A.ii/ Block copolymer thin film

Once the substrate is grafted with the appropriate RCP brush, the second step consists in the spin coating of a BCP thin film (the experimental process is detailed in *Annex 1.A/*). As for the RCP, the BCP is dissolved in propylene glycol methyl ether acetate (PGMEA), which appears to be commonly used in the semiconductor industry for its environmental safety [12].

One major parameter for thin film self-assembly is the BCP film thickness as compared to the structure periodicity. Indeed, for in-plane orientation, the substrate- and air- facing domains geometrically depend on this thickness. Also, the bulk energetical contribution (i.e. interaction between the block sequences) versus the surface contribution (i.e. surface energies) will be modified with the thickness. Thus, the modification of the film thickness can lead to possible changes of orientation and/or structures [13], [14].

To target a specified BCP thickness by spin-coating, several parameters can be modified: the rotation speed ω , the concentration C and the solvent (as its viscosity and evaporation rate modify the resulting film thickness). In our case, it is possible to estimate that the thickness is linearly linked to $C/\sqrt{\omega}$ (see *Chapter 1.1.B.i/*). However, this estimation does not take in account the modification of viscosity related to the change of the polymer concentration during spin coating. *Figure 50* shows the evolution of the experimental thicknesses measured by AFM (see *Annex 2.A/*) for PS-*b*-PMMA films at different concentration in PGMEA for a 2000 rpm rotation speed. As expected, the relation is not linearly proportional with the simple estimation performed beforehand, but follow a relationship of $t \propto \alpha C^{2/3} + \beta C^2$ as predicted by the Meyerhofer model [15].

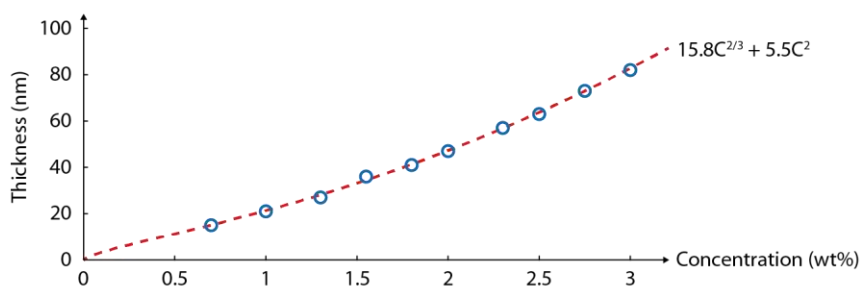


Figure 50. Dependency of a spin-coated thin film thickness at 2000 rpm with the solution concentration for a lamellar PS-*b*-PMMA dissolved in PGMEA.

A quantitative study for a lamellar PS-*b*-PMMA was done to emphasize the link between orientation, thickness and surface energy. A BCP forming lamellae was self-assembled (250 °C thermal annealing for 10 min) on substrates modified with various RCPs (f_{PS}^{RCP} from 0.47 to 0.86), and thicknesses, t , from 15 nm to 82 nm. Each film was observed with AFM and sorted in 4 different categories: out-of-plane, in-plane with a flat surface, in-plane with islands and holes, and mixed in-plane/out-of-plane (Figures 51.a-d). It is important to note that for PS-*b*-PMMA, the AFM phase channel provides a strong contrast between the PS and PMMA phases, with bright and dark regions corresponding to PMMA and PS, respectively.

The periodicity, denoted L_0 , was evaluated by FFT analysis of the fingerprint structure from out-of-plane lamellae and from island height or hole depth for in-plane lamellae, giving for each method the same value $L_0 = 28$ nm.

Interestingly, the in-plane structures (Figures 51.a-b,d) present an irregular dot pattern, which is not observed in similar studies [4], [5]. The majority bright color proves that the surface is composed of PMMA with small dots of PS, which is certainly poorly ordered perforations at the free surface. The presence of this structure is not fully understood yet, and the only difference with respect to the literature is the thermal annealing process (RTA 250 °C for 10 min under N₂ atmosphere versus “standard” thermal annealing 170-190 °C for 24-72 h under vacuum).

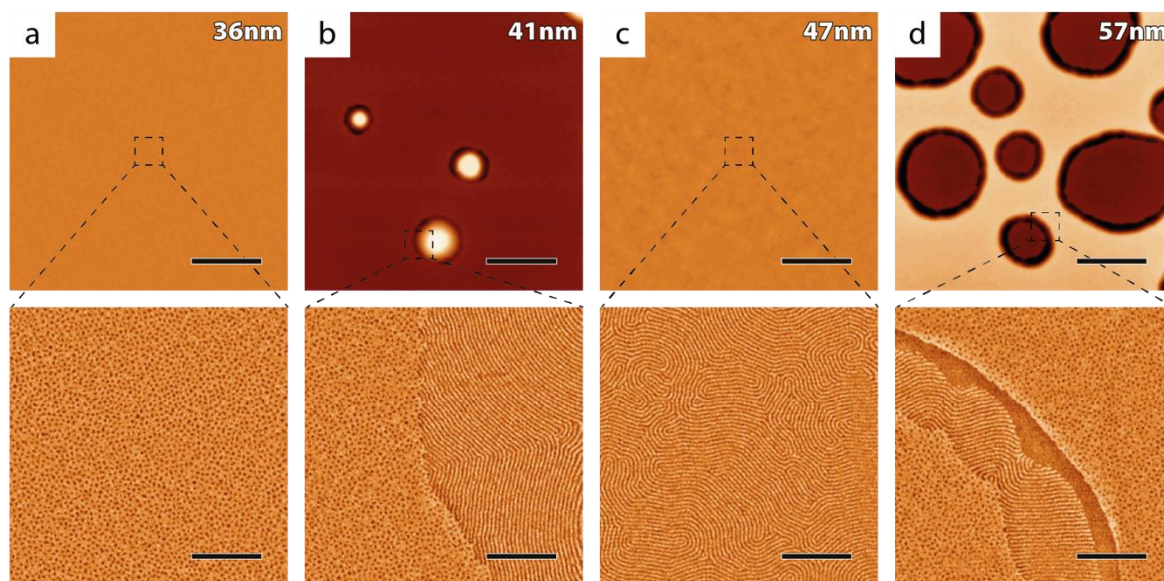


Figure 51. AFM images of a lamellar PS-*b*-PMMA with a 28 nm periodicity on a substrate modified with a $f_{PS}^{RCP} = 0,80$ at different thicknesses, giving (a) in-plane (36 nm), (b) mixed in-plane / out-of-plane (41 nm), (c) out-of-plane (47 nm) and (d) island/hole structure (57 nm). Top images are height channel with 5 μm scale bars, bottom images are phase channel with 500 nm scale bars.

The results from this study can be sorted into an experimental phase diagram (Figure 52.a), showing the out-of-plane window for lamellae depending on the thickness, which was already observed [4], [5], but the RCP composition for the window is not exactly the same, as explained before.

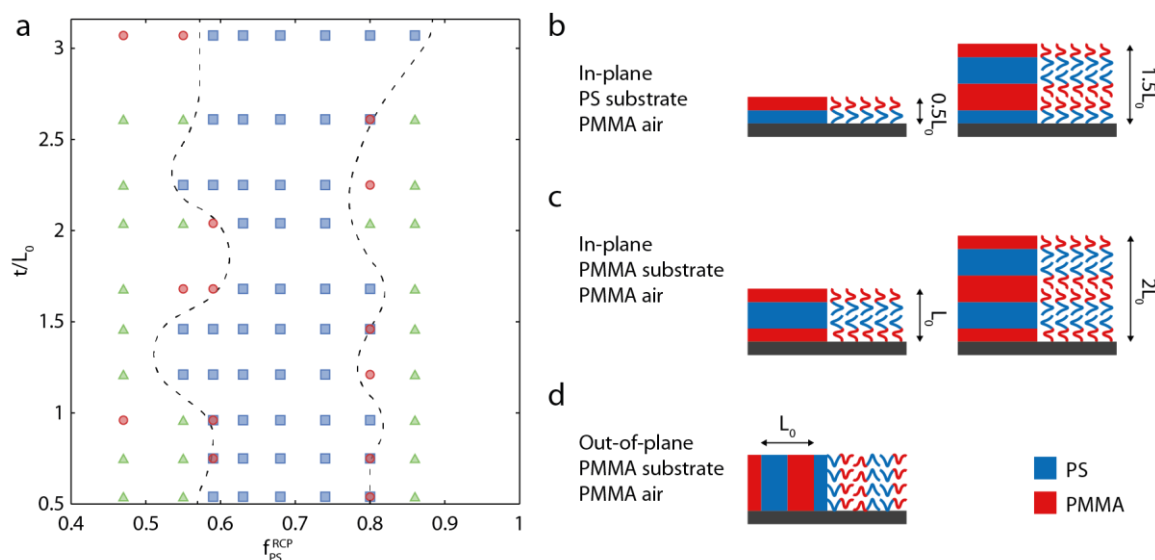


Figure 52. (a) Experimental lamellar PS-*b*-PMMA phase diagram in function of substrate coating composition and film thickness compared to BCP periodicity L_0 . Blue squares, red circles and green triangles correspond to out-of-plane, in-plane and island/hole orientations respectively. Dotted line delimits the “out-of-plane window”. Schematics of theoretical in-plane lamellae with (b) PS and (c) PMMA facing the substrate, and (d) out-of-plane lamellae.

It is important to note that the out-of-plane lamellar window possesses a range where the orientation is not dependent of the BCP thickness, around f_{PS}^{RCP} between 0.63 and 0.77 (for the

probed thickness range). Also, for out-of-plane structures, the lower surface energy at high temperature of PMMA leads to PMMA domains facing the air, as observed by AFM. For the substrate, PS domains wet it when f_{PS}^{RCP} is higher than neutrality, and PMMA when lower. These two different cases can happen for specific commensurate thicknesses, i.e. $t/L_0 = n$ when f_{PS}^{RCP} is lower than neutrality, and $t/L_0 = n + 0.5$ when it is higher (Figures 52.b-c). The experimental results corroborate this theory since the out-of-plane window is reduced when these specific in-plane structures are possible, e.g. for low f_{PS}^{RCP} when $t \approx L_0$. Finally, it is possible to observe that in-plane structures with a flat surface are quite rare outside the out-of-plane window, with instead mostly island/holes structures. This is explained by the perfect commensurate thickness required to provide unconstrained thus stable in-plane lamellae [16].

For a better understanding, a theoretical model has been developed to confirm the observed behavior. The model is based on the calculations of the energy of each structure configuration followed by a minimization process as regards to the RCP composition, f_{PS}^{RCP} , and film thickness t (taking into account the intrinsic structure periodicity L_0). The different effects taken into account for this model are:

- The substrate interfacial energy, corresponding to the interaction between the BCP and the substrate surface;
- The free surface interfacial energy, which is the interaction between the BCP and the atmosphere (air, inert gas or vacuum);
- The localization of the BCP chains in the volume, implying a stretching energy due to the chain distortion away from its equilibrium length, and repulsive interactions between chains from chemical difference between each block.

Each term was converted into energy costs per volume unit. The first term, denoted E_{s-f}^{vol} , is related to the difference between the bottom surface film composition f_{PS}^{bottom} and the RCP composition f_{PS}^{RCP} , multiplied by the interfacial tension between PS and PMMA, $\gamma_{PS/PMMA}$, and divided by the film thickness (Equation (12)).

$$E_{s-f}^{vol} = \frac{\gamma_{PS/PMMA} |f_{PS}^{bottom}(1 - f_{PS}^{RCP}) - (1 - f_{PS}^{bottom})f_{PS}^{RCP}|}{t} \quad (12)$$

Three cases are possible for a lamellar structure: either PS (PMMA, respectively) is at the bottom surface for in-plane lamellae ($f_{PS}^{bottom} = 0$ ($f_{PS}^{bottom} = 1$, respectively)), or the PS and PMMA domains are equally facing the substrate for out-of-plane lamellae ($f_{PS}^{bottom} = 0.5$).

The second term, denoted E_{f-a}^{vol} , is only dictated by the surface energy of the top film layer, depending on its composition f_{PS}^{top} and the PS and PMMA surface energies (γ_{PS} and γ_{PMMA} respectively) (Equation (13)).

$$E_{f-a}^{vol} = \frac{\gamma_{PS}f_{PS}^{top} + \gamma_{PMMA}(1 - f_{PS}^{top})}{t} \quad (13)$$

As for the substrate-film interface, three cases are possible ($f_{PS}^{top} = 0, 0.5$ or 1).

For the island/hole structure, an additional film-air interface is created, leading to a new energy cost, denoted $E_{i/h}^{vol}$. Since this structure appears for in-plane lamellae, the interface is composed at 50% PS and 50% PMMA. Also, the extra surface created over the total surface, $\alpha = S_{new}/S_{tot}$, is necessary to calculate the extra volume energy cost (Equation (14)).

$$E_{new\ f-a}^{vol} = \frac{\alpha(\gamma_{PS} + \gamma_{PMMA})}{2t} \quad (14)$$

In this model, islands or holes are supposed to be perfect cylinders with a radius, r , and a height, L_0 , leading to an area of the newly created surface, $S_{new} = 2\pi rL_0$, and an island/hole surface, $S_{i/h} = \pi r^2$. This creation of islands or holes is a phenomenon that happens at higher length scale than self-assembly, and we supposed that $r = 100L_0$, which it is the typical observed value from AFM images. Finally, it is assumed that the fraction of island/hole surface $f_{i/h} = S_{i/h}/S_{tot}$ represents 0% of the total surface for commensurate thickness, e.g. $t = nL_0$ when PMMA is facing the substrate, and 50% for perfectly incommensurate, e.g. $t = (n + 0.5)L_0$ when PMMA is facing the substrate. Between these two regimes, $f_{i/h}$ has been assumed to follow a linear evolution. Accordingly, $E_{new\ f-a}^{vol}$ can be rewritten as Equation (15).

$$E_{new\ f-a}^{vol} = \frac{L_0 f_{i/h} (\gamma_{PS} + \gamma_{PMMA})}{t \times r} \quad (15)$$

The third term is composed of two parts. The first one is the stretching energy penalty per molecule, denoted $E_{stretch}^{mol}$, which occurs when the chains are stretched to a distance R away from its radius of gyration, $R_g = l_k \sqrt{N/6}$, with l_k the Kuhn length and N the number of Kuhn units, k_b is the Boltzmann constant and T the temperature (Equation (16.1)). The second part is the repulsive interaction between the two blocks, leading to an energy penalty per molecule, denoted E_{χ}^{mol} , which depends on the Flory-Huggins parameter χ and the chain length (Equation (16.2)) [17].

$$E_{stretch}^{mol} = k_b T \frac{\pi^2}{12} \left(\frac{R}{R_g} \right)^2 \quad (16.1)$$

$$E_{\chi}^{mol} = k_b T \frac{\sqrt{\chi N}}{2} \left(\frac{R_g}{R} \right) \quad (16.2)$$

Combining these two equations and rescaling in volume energy with d the BCP density, M_n the BCP number averaged molecular weight and \mathcal{N}_a the Avogadro number, the total contribution related to the localization of the BCP chains can be rewritten as *Equation (17)*.

$$E_{chains}^{vol} = k_b T \left[\frac{\pi^2}{12} \left(\frac{R}{R_g} \right)^2 + \frac{\sqrt{\chi N}}{2} \left(\frac{R_g}{R} \right) \right] \frac{\mathcal{N}_a d}{M_n} \quad (17)$$

Interestingly, this equation shows a minimum reached for $R = R_{eq}$, which is the spontaneous chain distortion in a bulk system (*Equation (18)*). For instance, the lamellae periodicity can be estimated with this value, as $L_0 = 2R_{eq}$ [17].

$$R_{eq} = l_k \left(\frac{1}{2\pi^2 \sqrt{6}} \right)^{1/3} \chi^{1/6} N^{2/3} = R_g \left(\frac{3}{\pi^2} \right)^{1/3} (\chi N)^{1/6} \quad (18)$$

Finally, this chain contribution can be written for the out-of-plane or island/hole case, i.e. chains at an equilibrium state when $R = R_{eq}$ (*Equation (19.1)*) or the in-plane case with a flat surface, i.e. stretched chains when $R = t/n$, with n the number of stacked lamellae (*Equation (19.1)*).

$$E_{eq\ chains}^{vol} = k_b T \left[\frac{\pi^2}{12} \left(\frac{R_{eq}}{R_g} \right)^2 + \frac{\sqrt{\chi N}}{2} \left(\frac{R_g}{R_{eq}} \right) \right] \frac{d}{M_n} \mathcal{N}_a \quad (19.1)$$

$$E_{str\ chains}^{vol} = k_b T \left[\frac{\pi^2}{12} \left(\frac{t}{nR_g} \right)^2 + \frac{\sqrt{\chi N}}{2} \left(\frac{nR_g}{t} \right) \right] \frac{d}{M_n} \mathcal{N}_a \quad (19.2)$$

These hypotheses were coded in a Matlab code (see *Annex 3.F/*) to determine the most energetically stable structure, resulting in a theoretical phase diagram (*Figure 53*). The overall diagram is in a good agreement with experiments, with only a region at the bottom left far from reality. Such discrepancy is related to dewetting phenomena, which were not accounted in this approach.

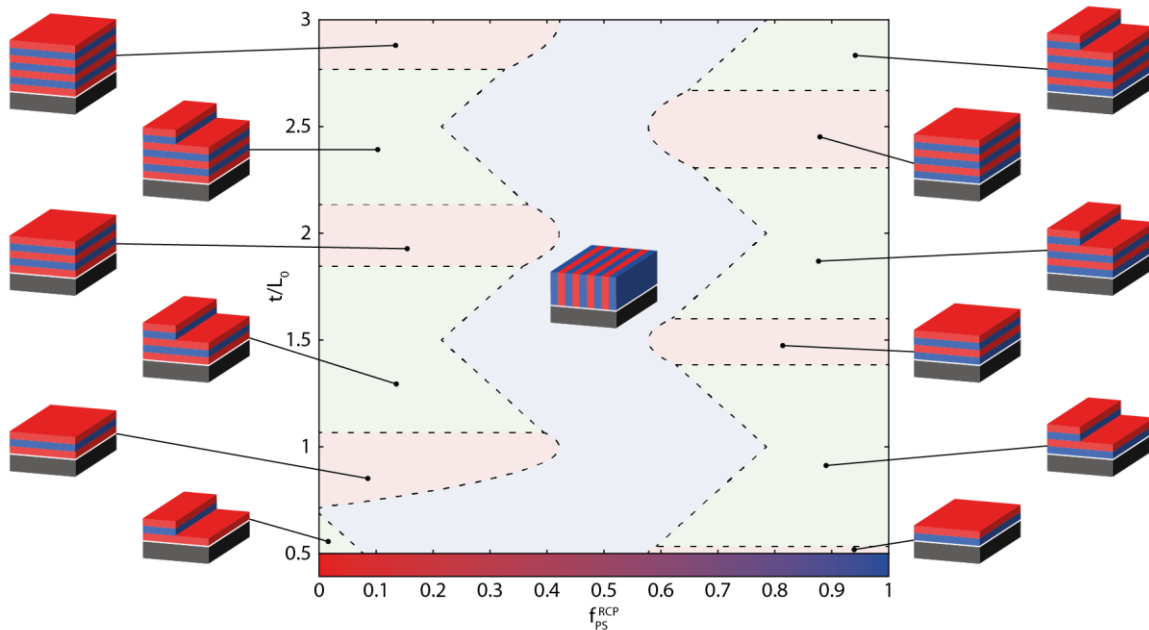


Figure 53. Theoretical phase diagram of the lamellae orientation as a function of the RCP composition and film thickness. Blue, red and green areas are the out-of-plane, in-plane and island/hole structure, respectively. (PS is in blue, PMMA is in red)

Interestingly, the theoretical phase diagram gives a f_{PS}^{RCP} window forming out-of-plane lamellae, as observed experimentally. This window range, around $f_{PS}^{RCP} = 0.4$ to 0.6 , is perfectly centered to $f_{PS}^{RCP} = 0.5$ which is exactly the BCP composition. However, this is not experimentally observed, which is explained by the difference between the substrate energy and the RCP composition as explained in *Chapter III.2.A.i/*. Thus, it is possible to shift this phase diagram with the observed difference to match the experimental phase diagram.

All these results highlight the importance of the substrate surface energy modification step and the BCP film thickness. Obviously, the second parameter that affects the self-assembly structure is the BCP composition and molecular weight. The same study might be performed for PS and PMMA cylindrical structures, leading to different out-of-plane f_{PS}^{RCP} window.

Thus, to target a specific structure and orientation, the substrate surface energy, the BCP composition and the film thickness should be chosen appropriately, with a tolerance window since self-assembly is driven by weak thermodynamic effects (i.e. soft matter). However, before observing these structures, a thermal annealing has to be performed, which is detailed in the next paragraph.

III.2.A.iii/ Thermal annealing

Due to the fast evaporation of PGMEA during spin-coating (taking place in ≈ 15 sec for 2000 rpm at room temperature) and the low segregation strength of PS-*b*-PMMA ($\chi = 0.038$ at

100 °C), the BCP film is trapped in a disordered state after solvent evaporation. For PS-*b*-PMMA, the usual method to provide chain mobility and promote self-assembly is a thermal annealing step (see *Chapter I.1.B.iii*). Two routes are commonly used for thermal annealing [18]:

- A conventional thermal annealing: a long annealing at low temperature to prevent the BCP deterioration (around 180 °C for several hours or days);
- A rapid thermal annealing (RTA): a short annealing at high temperature (around 250 °C for several minutes) with a fast heating and cooling rate using an RTA oven.

During this Ph.D., the annealing steps were performed with a RTA oven (see *Annex 1.A*) [18]. The temperature and duration were optimized according to the BCP structure, the periodicity and the desired orientation to provide the best self-assembly without polymer deterioration. Indeed, with a RTA process, the self-assembled structure quality increases due to the high chain mobility at elevated temperature, taking into account the limitations inherent to polymer degradation [19].

Interestingly, an effect of the annealing temperature on structure periodicity has been observed for the PS cylindrical structure. A PS-*b*-PMMA giving PS cylinders in a PMMA matrix was self-assembled on neutralized substrate in order to obtain an out-of-plane orientation after annealing. By increasing the annealing temperature and keeping the same duration (5 min), a slight increase of the structure periodicity was observed (*Figures 54.a-e*). The FFTs of the AFM images show that the periodicity increases from 29.4 nm to 32.2 nm (*Figure 54.f*), which correspond to a non-negligible 10% growth. This can be explained by the chain dilatation during annealing, which are frozen in this state during the quenching. Also, the overall structure quality (grain size and defect number) does not seem to be modified with the annealing temperature. However, this effect on the periodicity was not observed for other morphologies, certainly due to lower annealing temperatures (see *Table 10* in the next section). Indeed, the honeycomb periodicity starts to increase for temperatures above 270 °C, which are only necessary for this specific structure.

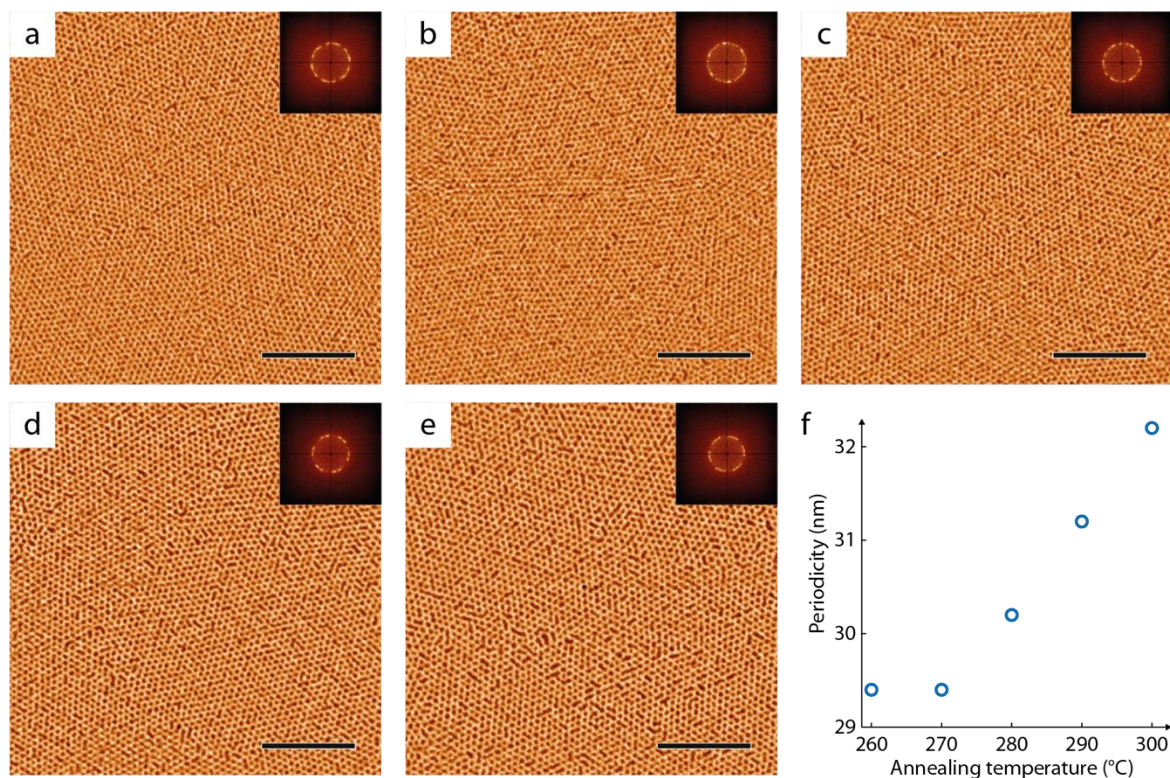


Figure 54. AFM phase images of the same out-of-plane PS cylinder forming PS-*b*-PMMA with different annealing temperature during 5 min: (a) 270 °C, (b) 290 °C and (c) 300 °C. Top right insets are the corresponding FFTs. Scale bars: 500 nm.

III.2.B/ Structure hybridization

BCP nanostructures in thin film have the potential to be hybridized in order to add further functionalities. During this Ph.D., we opted to immobilize the BCP structure using a selective Al₂O₃ infiltration step by SIS in the PMMA domains (see *Chapter I.2.D.i*) followed by an etching step using RIE to remove the PS domains (see *Chapter I.2.C*) (*Figure 55*).



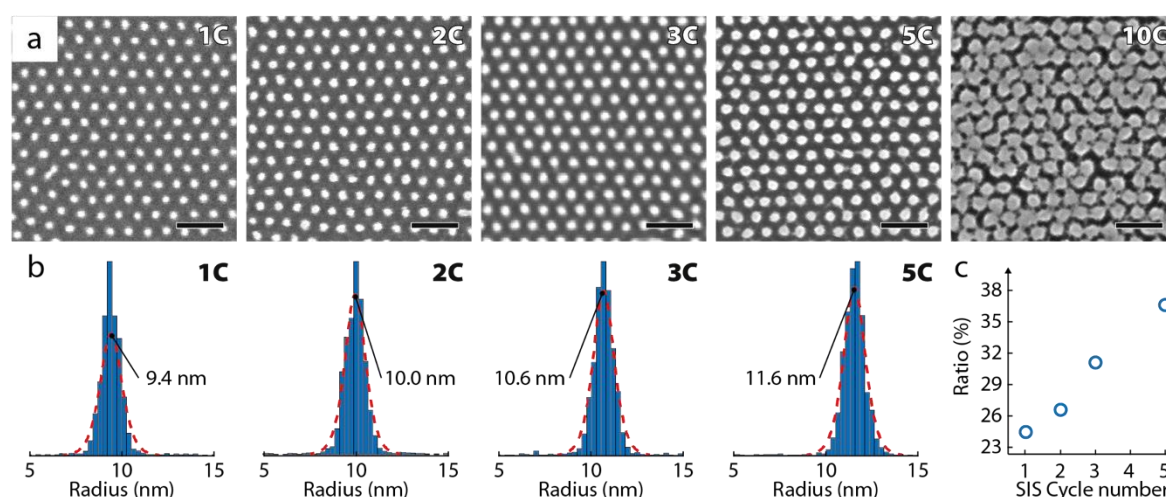
Figure 55. Schematics of the PMMA infiltration followed by a PS etching process for out-of-plane lamellae.

III.2.B.i/ PMMA infiltration by SIS

The first step of hybridization consists in infiltrating the PMMA domains with Al₂O₃ using a SIS process (see *Annex 1.B.i*). In our case, the metallic gaseous precursor for the formation of Al₂O₃ is the trimethyl aluminum (TMA), which is strongly selective to PMMA, leading to the formation of Al₂O₃ in PMMA, while the PS domains remain unchanged [20].

However, even if TMA is selective to PMMA, the number of infiltration cycles has an influence on the overall structure, hence it requires an optimization. Indeed, a too low number of infiltration steps leads to a fragile structure, while a too large number increases the Al₂O₃ domain

size until they coalesce. *Figure 56.a* shows SEM images of an out-of-plane PMMA cylindrical structure infiltrated by 1 to 10 SIS cycles, followed by a plasma etching (40 sccm O₂, 40 W, 40 sec). The PMMA domain growth is clear, with an onset of the coalescence for 5 cycles. A particle analysis was performed with ImageJ, giving the cylinder radius distributions (*Figure 56.b*), which were fitted with a logistic distribution to determine the mean radius. Then, *Figure 56.c* shows the occupied surface ratio of the cylinders within the unit cell, which is here a hexagonally packed cylindrical structure with a 36.2 nm center-to-center distance. The PMMA volume fraction for the formation of a PMMA cylindrical morphology is between 27% and 31% (see *Table 9*) which are the surface ratios achieved with 2 and 3 cycles (27.7% and 31.1%). Taking into account these results, a standard recipe has been devised based on 2 SIS cycles. Such recipe leads to well separated cylinders while providing sufficient mechanical integrity for the following steps, which can be easily enhanced by increasing the SIS cycle number to 3.



*Figure 56. (a) SEM images of PMMA cylinder forming PS-*b*-PMMA after SIS for different cycle number, followed by a plasma etching. (b) Corresponding cylinder radius distribution, fitted with a logistic distribution. (c) Cylinder to matrix surface ratio for different SIS cycle number. Scale bars: 100 nm*

During this Ph.D., TMA was chosen because it allows the infiltration of PMMA domains at low temperature, i.e. 85 °C, which is slightly lower than the glass transition, T_g , of PS and PMMA. Other precursors might be used by adapting the recipe to form different metal oxides within the PMMA matrix, as referenced in *Chapter 1.2.D.i/*.

III.2.B.ii/ PS etching for the formation of a topographical field

After infiltration of the PMMA domains with Al₂O₃, the PS domains can be partially removed to create a surface topography. Indeed, the PMMA domains swell during the SIS process leading to the generation of a 1 to 4 nm topography [21]. Further treatment of the infiltrated BCP layer by RIE plasma leads to a partial removal of the PS domains, thus enhancing the topographical

field. Such method allows a fine control of the depth of the topographical pattern which can be subsequently optimized with respect to the iterative self-assembly of a subsequent BCP layer.

In this study we opted for an oxygen RIE plasma (see *Annex 1.B.ii*/) for the selective etch of PS domains. In particular a 40 W, 40 sccm O₂, 40 s plasma was chosen as the standard etching recipe, increasing the topography from around 2 nm before plasma to around 10 nm after plasma in the case of a 29 nm periodic lamellar structure (*Figures 57.a-b*).

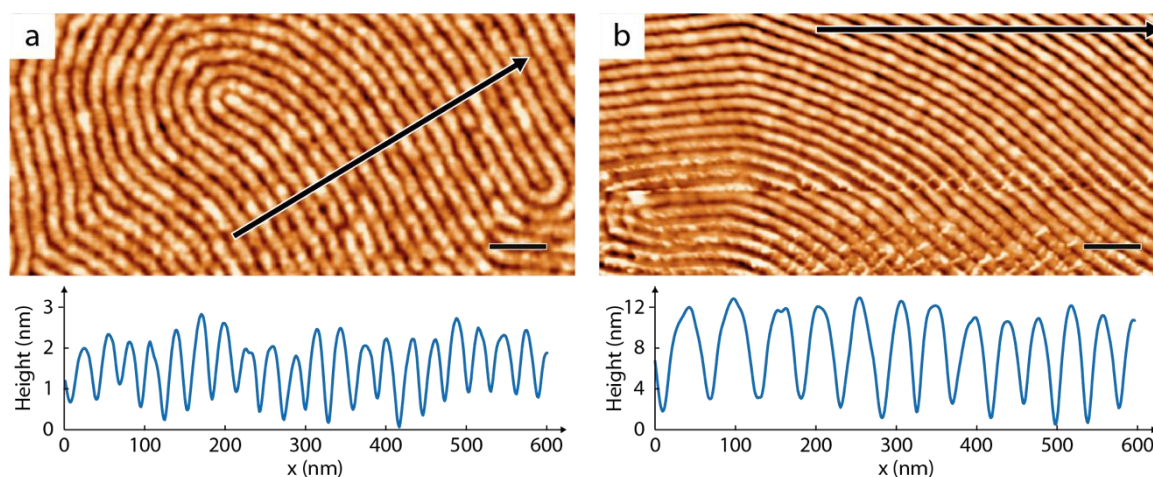


Figure 57. (top) AFM height images and (bottom) height profiles of 29 nm lamellar PS-*b*-PMMA (a) after SIS and (b) after SIS and O₂ plasma etching (40 sccm 40 W 40 sec). Scale bars: 100 nm.

As we can see on the *Figure 57.b*, it is difficult to characterize the depth of the Al₂O₃ pattern with tapping AFM, as artefacts occur after a few AFM scans. This is supposedly due to Al₂O₃ “dusts” sticking to the edges of tip, which happens even for a very slow scan speed (0.1 Hz). This is why the depth measurement was made at the top of the image, i.e. for the first scans. Also, the tip geometry has been controlled to verify that it is possible to reach the bottom of the trenches. In our case, the trenches are around 14.5 nm wide, and the tip has an angle of 40°, giving a maximum probe distance of 20 nm, which is higher than the 10 nm observed.

III.3/ Phase diagram exploration

In order to create a rich variety of 2D nanostructures, the PS-*b*-PMMA phase diagram was explored using polymers synthesized in our laboratory, or provided by Arkema and Polymer Source. The overall characteristics of the BCPs used for this study are summarized in *Table 9*, with the theoretical corresponding phase and periodicity estimated from the unified strong and weak segregation theory [17], [22] for which the treatment was automatized within a Matlab software (see *Annex 3.C/*).

Name	f_{PS}^{BCP} (1)	Mn (2)	PDI (2)	Structure (3)	Periodicity (3)	Source
11b50	0.18	61.5 kg/mol	1.09	PS spheres	33 nm	Polymer Source
8b10	0.44	18.2 kg/mol	1.2	Disordered	/	LCPO
15b41	0.27	56.1 kg/mol	1.18	PS cylinders	33 nm	Polymer Source
44b109	0.29	153.2 kg/mol	1.46	PS cylinders	64 nm	Polymer Source
13b12	0.51	25.2 kg/mol	1.16	Disordered	/	Arkema
27b22	0.55	49.6 kg/mol	1.07	Lamellae	30 nm	Arkema
85b78	0.52	162.9 kg/mol	1.04	Lamellae	65 nm	Polymer Source
21b8	0.72	29.2 kg/mol	1.12	PMMA cylinders	23 nm	Arkema
33b15	0.69	48.0 kg/mol	1.13	PMMA cylinders	31 nm	Arkema
101b37	0.73	138.2 kg/mol	1.14	PMMA cylinders	59 nm	Polymer Source
62b11	0.85	73.4 kg/mol	1.08	PMMA spheres	34 nm	Polymer Source

*Table 9. PS-*b*-PMMA macromolecular characteristics. (1) f_{PS} is the volume fraction of PS in the BCP estimated by 1H NMR. (2) Measured by SEC using PS standards as calibration. (3) Expected morphology and periodicity estimated from Matsen and Bates theoretical treatment.*

III.3.A/ Different morphologies by changing the BCP composition

In this part, BCPs with the same periodicity (≈ 30 nm), but with different compositions are examined in order to control both the self-assembled structures and its orientation. *Table 10* summarized the various protocols leading to optimized self-assembly for these particular BCPs.

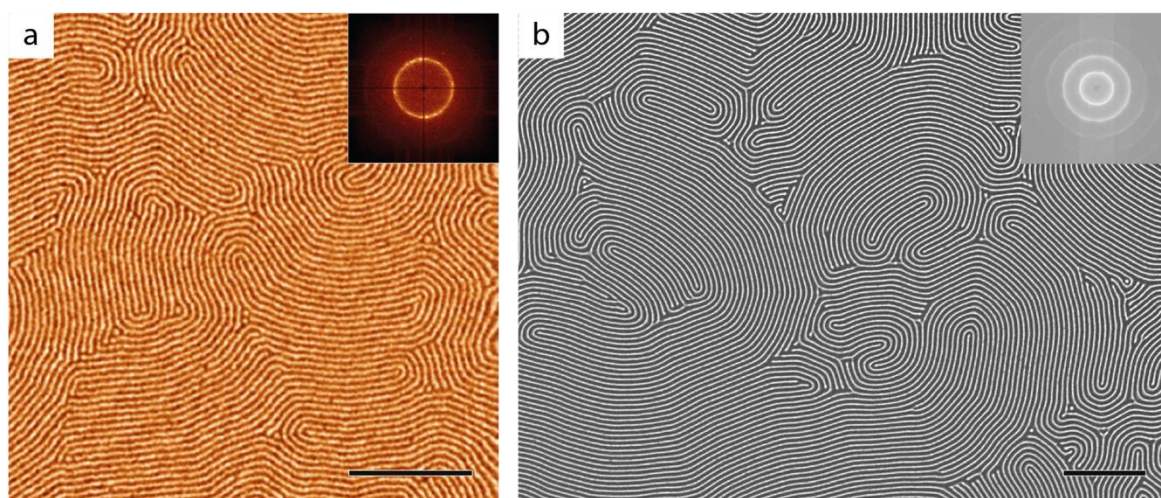
Aimed structure	Orientation	f_{PS}^{BCP}	BCP (1)	Spin-coating (2)	RTA annealing
PS spheres	Monolayer	0.13	11b50 - 0.75%	2000 rpm - 14 nm	190 °C - 5 min
PS cylinders	In-plane 1/2 layer	0.13	15b41 - 0.75%	2000 rpm - 14 nm	260 °C - 2 min
PS cylinders	Out-of-plane	0.52	15b41 - 1.5%	1500 rpm - 35 nm	290 °C - 5 min
Lamellae	Out-of-plane	0.70	27b22 - 1.5%	1500 rpm - 35 nm	260 °C - 10 min
PMMA cylinders	In-plane 1/2 layer	1	33b15 - 0.75%	2000 rpm - 14 nm	200 °C - 5 min
PMMA cylinders	In-plane 3/2 layer	1	33b15 - 1.9%	2000 rpm - 40 nm	220 °C - 10 min
PMMA cylinders	Out-of-plane	0.78	33b15 - 1.5%	1500 rpm - 35 nm	230 °C - 15 min
PMMA spheres	Monolayer	1	62b11 - 0.75%	2000 rpm - 14 nm	170 °C - 5 min
PMMA spheres	Bilayer	1	62b11 - 1.8%	2000 rpm - 38 nm	170 °C - 5 min

*Table 10. Optimized process parameters for the 5 different PS-*b*-PMMA with a ≈ 30 nm periodicity. (1) BCP name and concentration in PGMEA. (2) Rotation speed (at R.T.) and measured thickness using AFM.*

Every structure was observed with AFM after self-assembly, and with SEM after hybridization (SIS standard recipe with 2 cycles, and plasma 40 sec, 40 W, 40 sccm O₂). The resulting patterns are described in the following sections.

III.3.A.i/ Lamellar PS-*b*-PMMA for the formation of line & space patterns

As previously stated (see *Chapter III.2.A.ii/*), the substrate surface energy and the BCP film thickness greatly influence the orientation of lamellar structures in a thin film configuration. For iterative self-assembly, the out-of-plane structure is the most interesting as it will generate a topographical field after the SIS step that can be used to guide the self-assembly of a subsequent BCP layer. Using the optimized parameters summarized in *Table 3*, the *Figures 58.a-b* show the resulting out-of-plane lamellae with a fingerprint-like pattern.



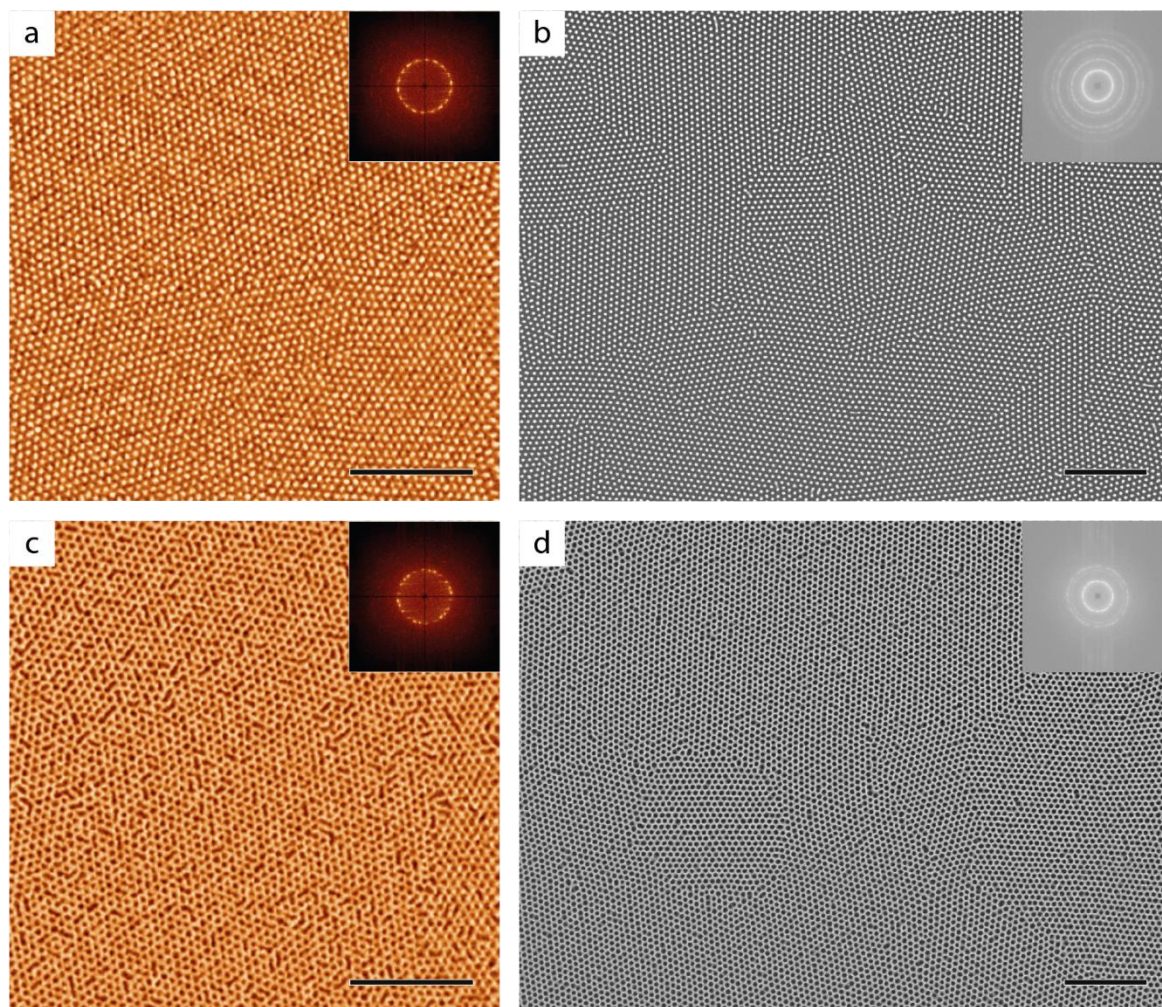
*Figure 58. Structural analysis of an out-of-plane lamellar PS-*b*-PMMA. (a) AFM phase image after thermal annealing, (b) SEM image after infiltration and plasma. Top right insets are the corresponding FFTs. Scale bars: 500 nm.*

The FFT of the AFM and SEM images were used to extract the periodicity of the structure at 29 nm and 31 nm, respectively. This small difference might be due to the apparatus calibration or linked to the SIS process which can induced a swelling of the BCP domains. It is noteworthy that the extracted periodicity is in agreement with the theoretical treatment (i.e. 30 nm).

III.3.A.ii/ Cylindrical PS-*b*-PMMA for the formation of dot, hole or line & space patterns

Two types of cylindrical structures are achievable using a PS-*b*-PMMA diblock architecture: either PS cylinders in a PMMA matrix, or the inverse. After hybridization, the PMMA domains are selectively infiltrated while the PS domains are etched. Accordingly, two different patterns are obtained for out-of-plane orientations: a dot pattern (PMMA cylindrical structure) and a honeycomb or hole pattern (PS cylindrical structure). For an in-plane orientation of the BCP structures, line & space patterns can be produced if carefully managing the BCP film thickness.

The out-of-plane structures generate a specific topographical pattern after hybridization, i.e. dots for PMMA cylinders, and holes for PS cylinders. As for out-of-plane lamellae, this will produce a topographic field that can be used for guiding the subsequent BCP layer. Using the optimized parameters summarized in *Table 3*, the *Figures 59.a-b* show the resulting out-of-plane PMMA cylinders with a hexagonally packed dot pattern, and the *Figures 59.c-d* show the resulting out-of-plane PS cylinders with a hexagonally packed hole pattern, often called honeycomb.



*Figure 59. Structural analysis of an out-of-plane (a-b) PMMA and (c-d) PS cylinder forming PS-*b*-PMMA. (a,c) AFM phase images after thermal annealing, (b,d) SEM images after infiltration and plasma. Top right insets are the corresponding FFTs. Scale bars: 500 nm.*

Using the FFT of the AFM images, a 32 nm and 31 nm periodicities were determined for PMMA and PS cylinders respectively, in agreement with theoretical calculations (31 nm and 33 nm respectively). Accordingly, a cylinder-to-cylinder distances of 37 nm and 36 nm were retrieved obtained by multiplying the periodicity by $2/\sqrt{3}$. Interestingly, we observed that the stability of the out-of-plane cylindrical morphology for both structures is conserved over a large range of thicknesses with respect to the results obtained on the lamellar structure. However, for PS cylinder structure, some holes are merging together along the grain boundaries because the

PMMA walls between them are too small. These defects are visible on both AFM and SEM images, meaning that it is not a defect resulting from the infiltration step.

For in-plane orientation, the structures produced after infiltration and plasma are highly dependent of the BCP layer thickness. As shown in *Figures 60.a-h*, four configurations (1/2 or 3/2 layers) were envisaged in this work. However, the 3/2 PS cylinders case (*Figure 60.d*) produced a similar topographical pattern as the 1/2 layer after hybridization (see *Figures 60.g-h*).

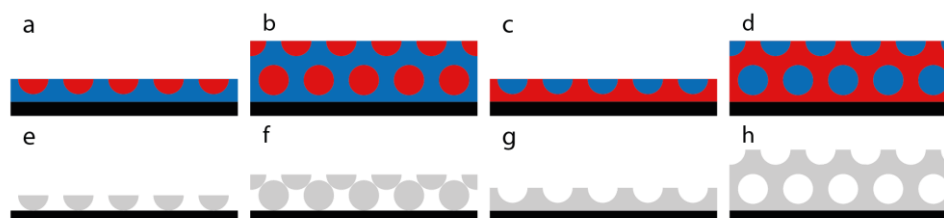


Figure 60. Schematics of in-plane (a) monolayer and (b) bilayer of PMMA and (c-d) PS cylinders before hybridization and (e-f) after PMMA infiltration and PS etching. (Red, blue and gray are PMMA, PS and Al_2O_3 respectively).

The 1/2 layer case can be obtained by reducing the BCP thickness to half the periodicity, i.e. around 15 nm, and by modifying the substrate surface interface to be PS or PMMA affine for PMMA or PS cylinders, respectively. Using the optimized parameters summarized in *Table 3*, the *Figures 61.a-b* and *Figures 61.c-d* show the resulting in-plane PMMA and PS cylinder 1/2 layers respectively, with a fingerprint-like pattern.

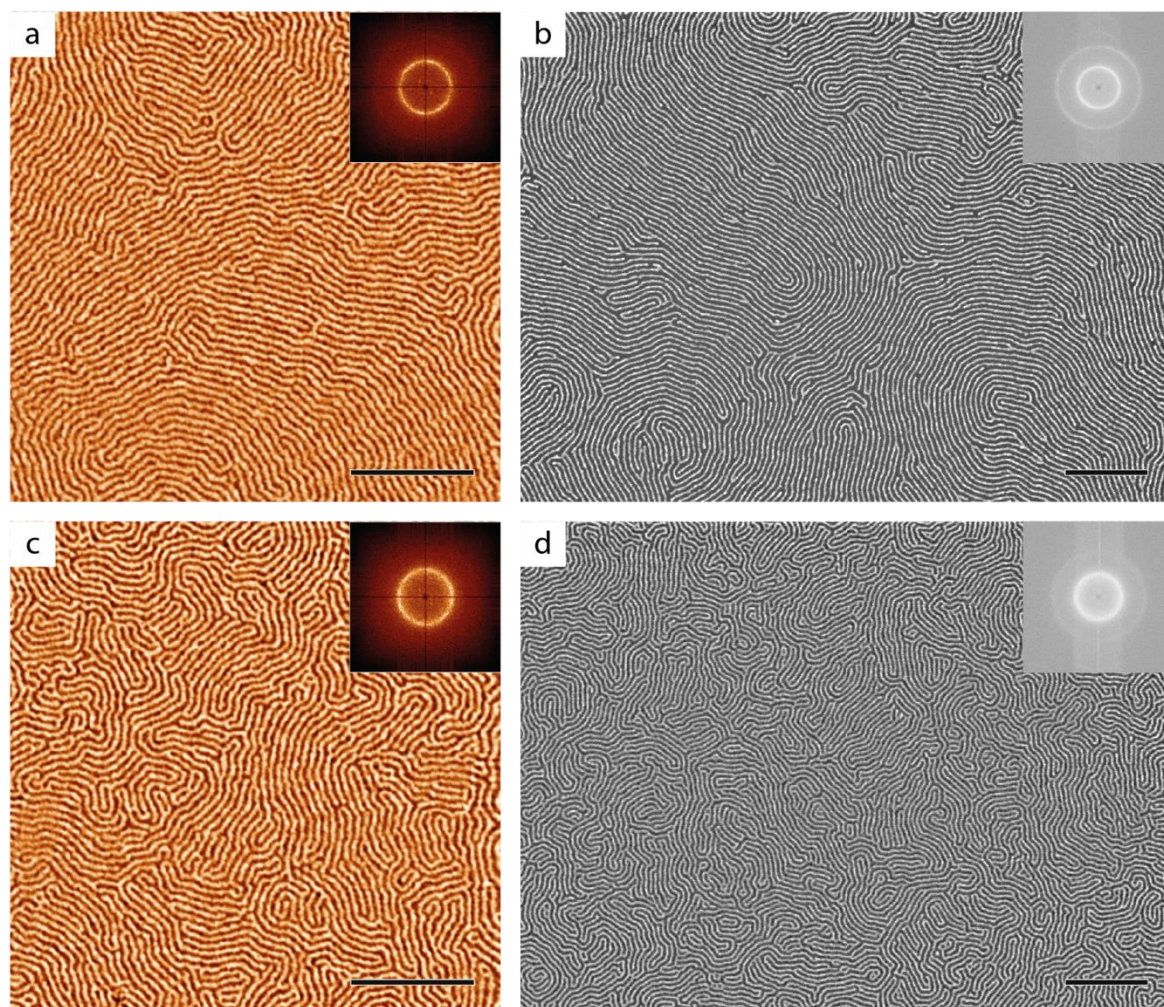


Figure 61. Structural analysis of an in-plane (a-b) PMMA and (c-d) PS 1/2 layer of cylinder forming PS-*b*-PMMA. (a,c) AFM phase images after thermal annealing, (b,d) SEM images after infiltration and plasma. Top right insets are the corresponding FFTs. Scale bars: 500 nm.

The overall pattern is similar to out-of-plane lamellae, but showing higher line roughness and more defects. The FFT of the AFM images of PMMA and PS cylinders give a 33 nm and 31 nm periodicities, respectively, which theoretically should be equal to the cylinder-to-cylinder distances measured from the out-of-plane structures. However, these values are significantly lower (33 nm vs 37 nm and 31 nm vs 36 nm), which can be explained by chain compressing due to the formation of half cylinders.

As schematized in *Figure 60.f*, PMMA cylinders can provide an interesting topographic pattern after hybridization, when the thickness is increased to provide a 3/2 layer. In this case, the thickness should be around 1.5 time the periodicity, i.e. 46 nm. Using the optimized parameters summarized in *Table 3*, the *Figures 62.a-b* show the resulting AFM image of in-plane 3/2 layer of PMMA cylinders with the same fingerprint pattern than the 1/2 layer.

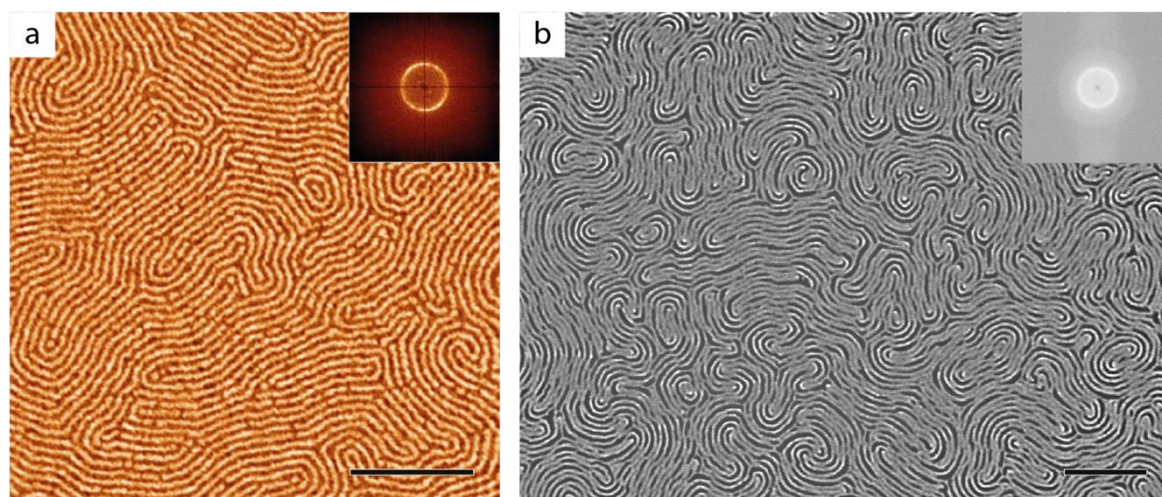


Figure 62. Structural analysis of an in-plane PMMA cylinder bilayer. (a) AFM phase image after thermal annealing, (b) SEM image after infiltration and plasma. Top right insets are the corresponding FFTs. Scale bars: 500 nm.

As predicted theoretically, the topographic pattern is indeed different after hybridization than the 1/2 layer, but due to cylinder collapsing during etching, the pattern is messy, and this structure is not suitable for further stacking because of the poor overall lateral order. However, the periodicity measured from the FFT did increase to 37 nm, which is now equal to the out-of-plane cylinder-to-cylinder distance as expected theoretically.

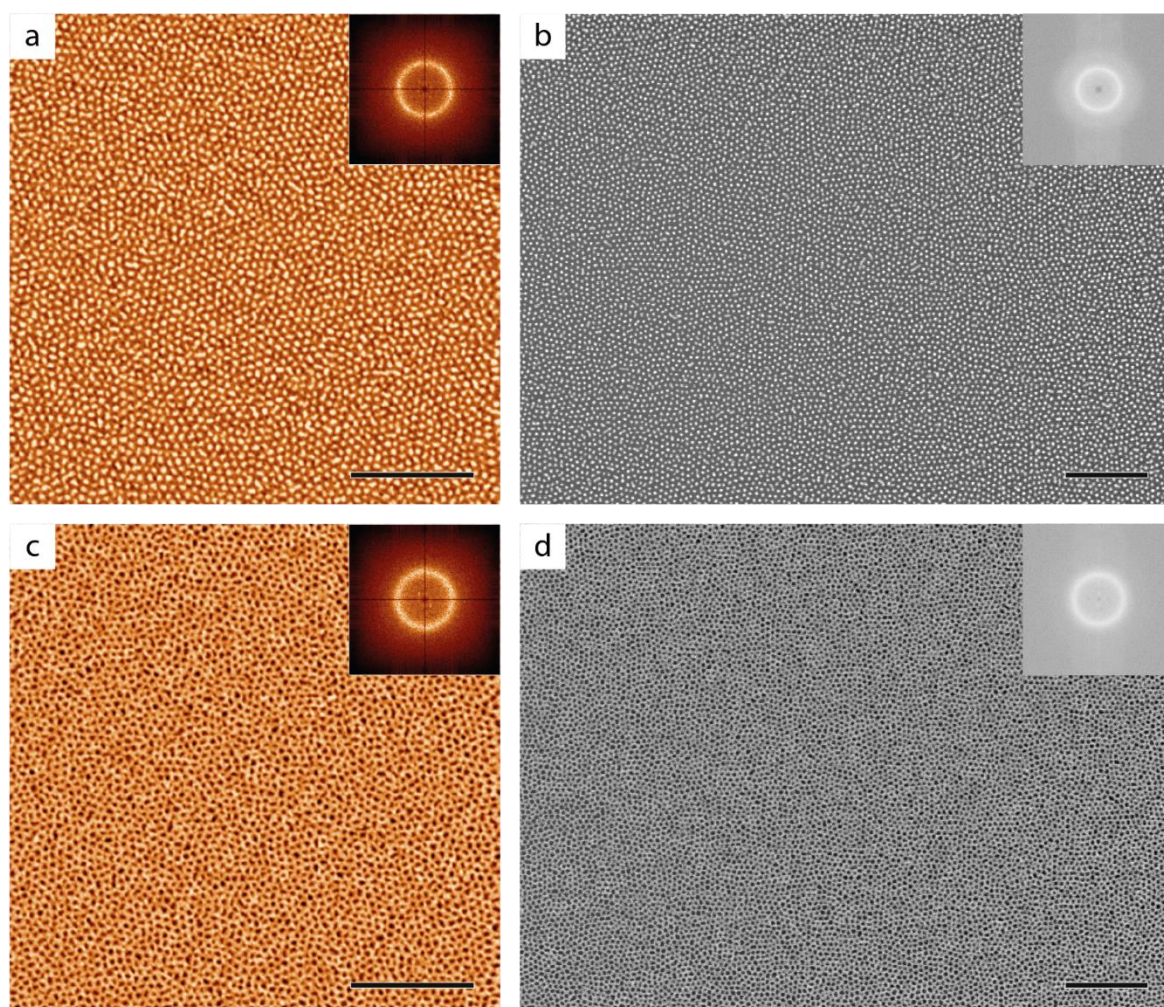
Even if these different in-plane structures are interesting for stacking methods; the requirement of a precise thickness of the BCP layer is too complex with respect to the production of fingerprint pattern from out-of-plane lamellae. Furthermore, the thermal annealing process had to be adapted for each situation in order to obtain well-defined self-assembled structures. Thus, these in-plane structures were not studied further.

III.3.A.iii/ Spherical PS-*b*-PMMA for the formation of dot or hole patterns

The last simple periodic structure obtained from PS-*b*-PMMA self-assembly is a spherical structure, which can be either PS spheres in a PMMA matrix or the opposite. In this case, there is no possible in-plane/out-of-plane classification since it is a 3D structure. However, it is possible to control the sphere packing as body-centered cubic (BCC) or hexagonally close packing (HCP), and the orientation of the plane at the free surface (BCC (100) or HCP (0002)) by controlling the thickness or by using directed self-assembly [23], [24]. We only studied the self-assembly of sphere-forming PS-*b*-PMMA for the 1/2 layer and 3/2 layer cases.

The 1/2 layer case can be obtained by reducing the thickness to half the periodicity, i.e. around 15 nm, and modify the substrate interface to be PS or PMMA affine for PMMA or PS

spheres, respectively. Using the optimized parameters summarized in *Table 3*, the *Figures 63.a-b* and *Figures 63.c-d* show the resulting 1/2 layer of PMMA and PS spheres respectively, showing the HCP expected structure [23].



*Figure 63. Structural analysis of a (a-b) PMMA and (c-d) PS 1/2 layer of spheres forming PS-*b*-PMMA. (a,c) Phase AFM image after thermal annealing, (b,d) SEM image after infiltration and plasma. Top right insets represent images FFT. Scale bars: 500 nm.*

Two kind of HCP spheres were obtained with this process, giving hexagonally packed dot and hole patterns, but with a lower order than the ones obtained from out-of-plane cylinders. The measured periodicity from the FFT analyses gives 32 nm and 31 nm for PMMA and PS spheres, respectively, giving a center-to-center distance of 37 nm and 36 nm respectively. These values are in good agreement with the theoretical 34 nm and 33 nm calculated periodicities. Contrarily to the in-plane 1/2 layer of cylinders which showed a smaller periodicity than expected, the spherical structures seem here unconstrained. Also, the poor order with no grains showing a single orientation might be explained by a shorter process optimization during this study.

As for in-plane cylinders, an interesting topographic pattern can be formed with two layers of HCP spheres, which should be obtained for 3/2 layer thickness, i.e. 46 nm [23]. Using the

optimized parameters summarized in *Table 3*, the *Figures 64.a-b* show the resulting 3/2 layers of PMMA spheres.

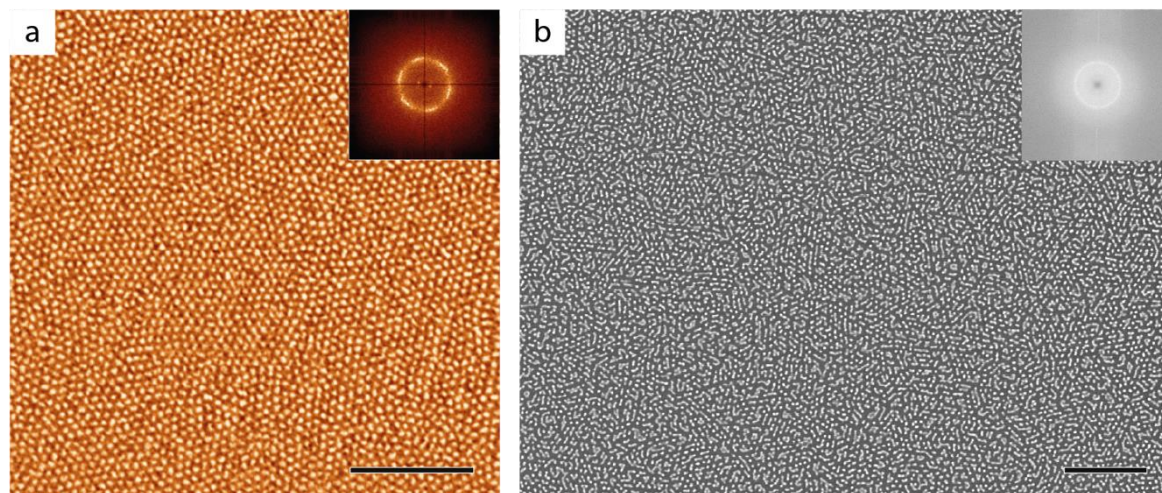


Figure 64. Structural analysis of a PMMA sphere bilayer. (a) AFM phase image after thermal annealing, (b) SEM image after infiltration and plasma. Top right insets are the corresponding FFTs. Scale bars: 500 nm.

The AFM phase image shows the same hexagonally packed structure and the same periodicity as in the monolayer case. Unfortunately, the collapse of the top layer of spheres during the plasma step was not vertical, leading to a poor overall self-assembled structure. This structure and etching step might be optimized to provide interesting well-ordered non-native patterns, which were obtained by a two-step process by Jin *et al.* for PS-*b*-PDMS [25].

III.3.B/ Tuning the structure periodicities

This part will focus on the tuning of the periodicity of the self-assembled structure by modifying the χN value to explore the phase diagram along vertical paths. This study is mandatory for further stacking, since precise size ratios will be required for commensurate stacking (see *Chapter III.4.A*).

In order to increase or lower the periodicity of a BCP structure, a possible route is to synthesize or buy plenty of different BCPs with the adequate composition and degree of polymerization. However, even if the anionic polymerization of PS-*b*-PMMA is well-mastered, it can be tedious and time-consuming. Besides, it is difficult to precisely target a periodicity despite the living-controlled character of the anionic polymerization. Nevertheless, this approach was successfully used to study the relationships between the degree of polymerization and the self-assembly properties (variation of domain spacing) [26], [27].

A second approach to modify the periodicity, which is the one used in this Ph.D., can overcome these difficulties by blending high and low molar mass BCPs with a similar f_{PS}^{BCP} . Indeed,

a blend behaves as an intermediate BCP according to the mixing ratio, which can be predicted theoretically [28].

As explained before, only out-of-plane structures will be studied for the stacking study, thus three different vertical paths were investigated:

- PS-*b*-PMMA BCPs with $f_{PS}^{BCP} \approx 0.50$, giving lamellar structure and a linear & space pattern after hybridization. This pattern will be named L for line & space;
- PS-*b*-PMMA BCPs with $f_{PS}^{BCP} \approx 0.70$, giving PMMA cylindrical structure and a hexagonally packed dot pattern after hybridization. This pattern will be named D for dot pattern;
- PS-*b*-PMMA BCPs with $f_{PS}^{BCP} \approx 0.30$, giving PS cylindrical structure and a hexagonally packed hole pattern after hybridization, also called honeycomb. This pattern will be named H for hole pattern.

For the sake of simplicity, until the end of this chapter and for the rest of the study, the patterns will be named with a letter describing the structure (L, D or H), followed by a number accounting for its the size (periodicity for line & space pattern and center-to-center distance for dot and hole patterns), e.g. H₄₀ for a hole pattern with a 40 nm center-to-center distance. Also, we opted to start from the well-mastered patterns presented in the previous part, i.e. L₂₉, D₃₇ and H₃₆.

First, the smallest self-assembling BCPs, i.e. close to the order-disorder transition, were targeted for the three different structures:

- For lamellae, the theoretical order-disorder transition is around $\chi N = 10.5$ for a symmetrical BCP, giving $N = 276$ in the PS-*b*-PMMA case, i.e. $M_n = 28$ kg/mol. This BCP has a theoretical periodicity of 20 nm. This specific BCP was not available, however, by using a smaller “lamellar” BCP which does not segregate, 13b12, and mixing it with the 27b22 BCP, smaller lamellae were obtained. The minimum periodicity obtained following this method was 22 nm lamellae (L₂₂) when 13b12 is mixed to 27b22 in a 4:1 volume ratio (*Figure 65.a*);
- For PMMA cylinders, the theoretical minimal periodicity is 23 nm for a 25 kg/mol PS-*b*-PMMA ($f_{PS}^{BCP} = 0.7$). Experimentally, this 23 nm periodicity has been reached with the 21b8 BCP (*Figure 65.b*), giving a 26 nm center-to-center distance (D₂₆);
- For PS cylinders, a 37 kg/mol PS-*b*-PMMA ($f_{PS}^{BCP} = 0.3$) should theoretically give the minimal achievable periodicity, 25 nm. As for lamellae, this polymer was not available, but the 15b41 periodicity has been lowered from 32 nm to 28 nm by blending it with 8b10 at a 1:4 volume ratio (*Figure 65.c*), giving a 32 nm center-to-center distance holes (H₃₂).

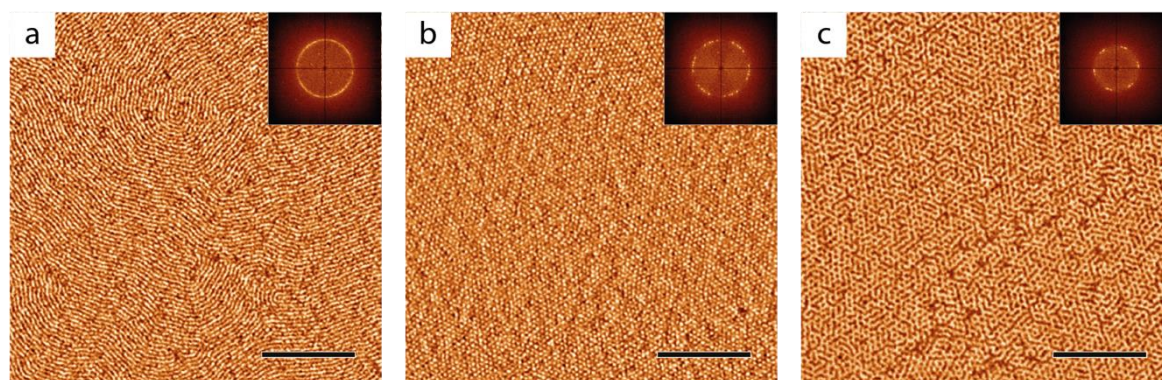


Figure 65. AFM phase images of the smaller PS-*b*-PMMA patterns reached for out-of-plane (a) lamellae (22 nm periodicity), (b) PMMA cylinders (23 nm periodicity) and (c) PS cylinders (28 nm periodicity). Top right insets are the corresponding FFTs. Scale bars: 500 nm.

Surprisingly, these very small BCP structures leads to poorly resolved patterns, i.e. the boundaries between the PS and PMMA domains are not sharp, even if a good long-range ordering (as proven with FFT insets) is obtained due to smaller BCP chains leading to a higher chain mobility. It is important to notice that the thermal annealing temperature had to be lowered by 30 °C for each case as compared to the standard processes in *Table 10*. This was required to prevent polymer degradation, which occurs at a lower temperature for low molecular weight BCPs [29].

Secondly, to reach bigger sizes, high molar mass polymers giving lamellae, PMMA cylinders and PS cylinders were used, leading to 3 larger patterns:

- For lamellae, 85b78 was self-assembled with the exact same process than 27b22 (see process in *Table 10*), leading to a poorer ordering than the standard line & space pattern presented in *Figure 66.a*. The FFT gives a 62 nm periodicity, close to the 65 nm predicted theoretically.
- For PMMA cylinders, 101b37 was self-assembled with the exact same process than 33b15 (see process in *Table 10*), showing a mixed in-plane/out-of-plane orientation (*Figure 66.b*), certainly due to the low thickness as compared to its periodicity (35 nm film thickness as compared to a 66 nm periodicity measured from the FFT). This value is higher than to the 59 nm predicted, but the mixed organization distorts the periodicity measured by FFT.
- For PS cylinders, 44b109 was self-assembled with the exact same process than 15b41 (see process in *Table 10*). As for PMMA cylinders, the structure is a mix between in-plane and out-of-plane cylinders (*Figure 66.c*). The FFT gives a 71 nm periodicity, again higher than the 64 nm expected.

The three structures present a poor ordering because the low χ value of PS-*b*-PMMA does not provide a strong enough segregation force to self-assemble long chains [30].

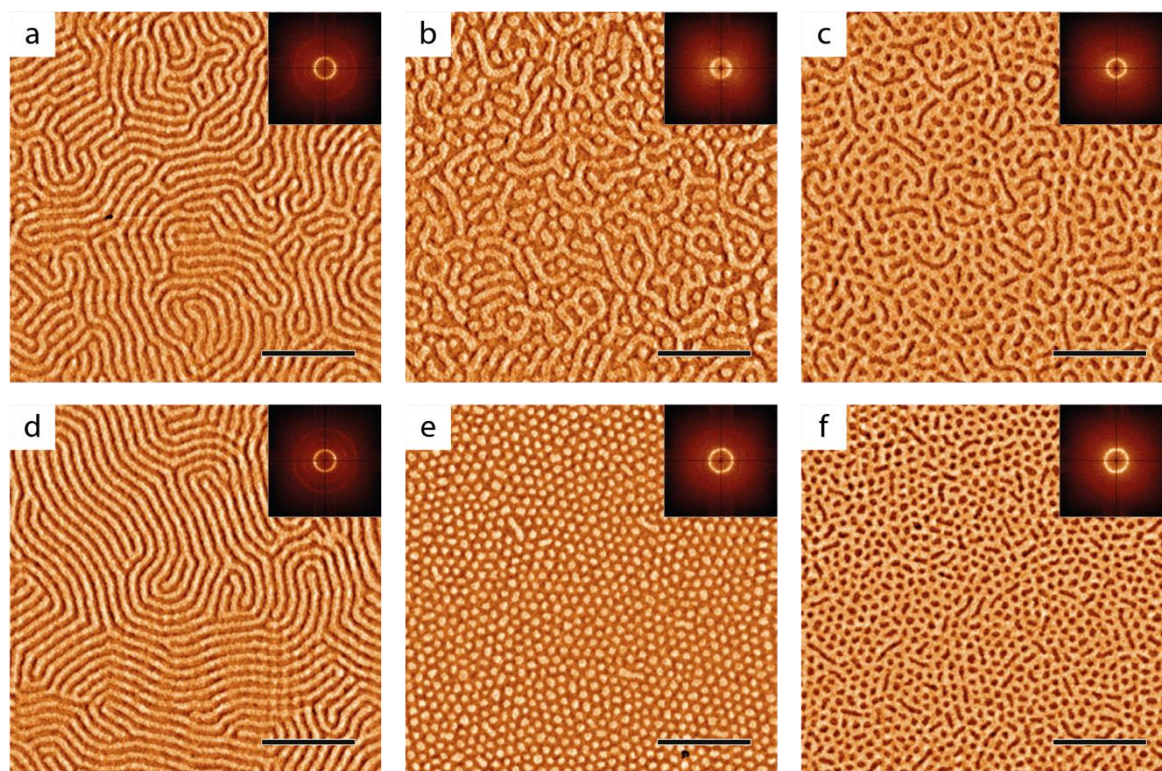


Figure 66. AFM phase images of the bigger PS-*b*-PMMA patterns reached for out-of-plane (a) lamellae (62 nm periodicity), (b) PMMA cylinders (66 nm periodicity) and (c) PS cylinders (71 nm periodicity). Optimized (d) lamellar pattern by increasing thickness from 35 nm to 163 nm (60 nm periodicity), (e) PMMA and (f) PS cylinders by blending it with smaller BCP (both 55 nm periodicity). Top right insets are the corresponding FFTs. Scale bars: 500 nm.

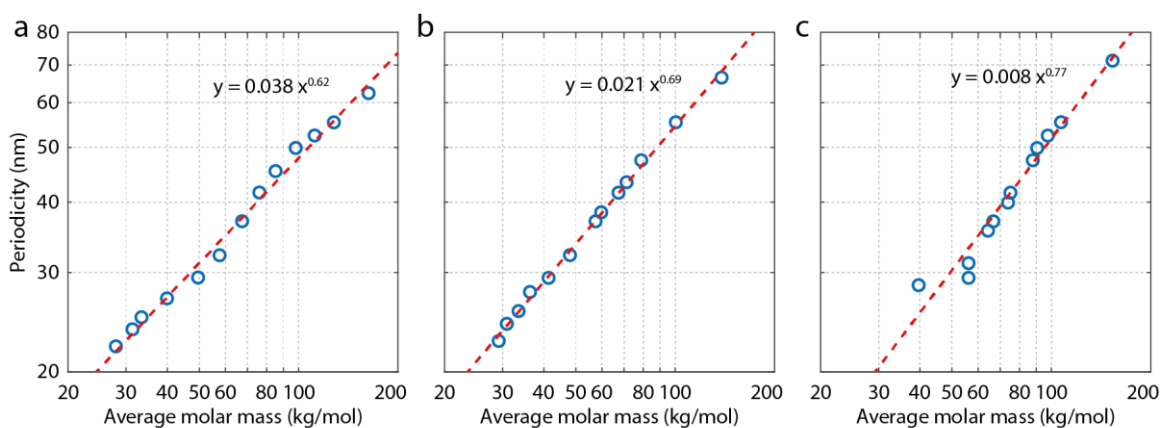
To increase the quality of the self-assembly and to obtain useful layers for further stacking, two different strategies were investigated: blending with a small amount of a low molecular weight BCP to increase the overall chain mobility [31], and increasing the thickness to modify the ratio between interfacial and bulk energies. For cylindrical structures, blending with a smaller BCP drastically removed the mixed orientation and increased the long-range order. For lamellae, the thickness increase has a strong impact on the self-assembly quality. However, in this case, thicker film with a much better lateral order can only be used for the first layer during stacking, but not for the subsequent layers (see *Chapter IV*).

The thermal annealing step did not require any modification and the optimized experimental processes for larger structures are:

- For lamellae, the solution concentration was increased to 4 wt.%, forming 163 nm thick films, leading to a well-ordered pattern (*Figure 66.d*) with a 60 nm periodicity (L_{60-t} , -t for thick), which is 2 nm lower than the “thin” one, certainly due to the reduction of defects;
- For PMMA cylinders, the 101b37 BCP was mixed with 33b15 in a 4:1 volume ratio (*Figure 66.e*), forming a well-ordered hexagonally packed cylinder array with a 55 nm periodicity, i.e. 64 nm center-to-center distance (D_{64});

- For PS cylinders, the 44b109 BCP was mixed with 15b41 in a 3:1 volume ratio (*Figure 66.f*), leading to a 55 nm periodicity, i.e. 64 nm center-to-center distance (H_{64}).

Then, blends between the three “standard” BCP patterns (L_{29} , D_{37} and H_{36}) and smaller (L_{22} , D_{26} and H_{32}) or bigger (L_{62} , D_{64} and H_{64}) ones were performed to apprehend the dependency between the blend ratio and the final structure size. The results for line & space, dot and hole patterns (*Figures 67.a-c*) show a power law dependency between the number average molecular weight of the blend and the structure periodicity. A 2/3 power exponent is theoretically expected [32], which is almost the value observed here.



*Figure 67. Evolution of the periodicity with the number average molecular weight of binary blends between the “standard” PS-*b*-PMMA and a lower or higher molar mass BCP for (a) lamellae, (b) PMMA cylinders and (c) PS cylinders. Blue dots are experimental periodicity measured from the AFM FFTs, and red dotted lines are the power fits.*

A noteworthy periodicity gap is observed for PS cylinders for low molecular weight (*Figure 67.c*) due to the thermal annealing temperature modification, which is not observable for other morphologies. Also, for large lamellae, this study was performed with standard thickness, i.e. 35 nm, since the thickness had no significant impact on the periodicity.

III.4/ Preparation for iterative stacking

Taking into account the results obtained in the previous parts, we can now precisely choose a BCP blend composition and the associated process to target a specific structure and periodicity, from L₂₂ to L₆₀, from D₂₆ to D₆₄, and from H₃₂ to H₆₄. Such versatility will be further used to produce interesting stacking behavior by playing on the commensurability between the self-assembled layers.

III.4.A/ Geometrical considerations

A quick reasoning about geometry is necessary because of the hexagonal symmetry of D and H structures, and the linear symmetry of L structure. *Figure 68.a* shows the 5 different noticeable ratios which can be reached within our periodicity range: 1, $2/\sqrt{3}$, $3/2$, $\sqrt{3}$ and 2. Obviously, the inverse values of these ratio will give the same interesting results.

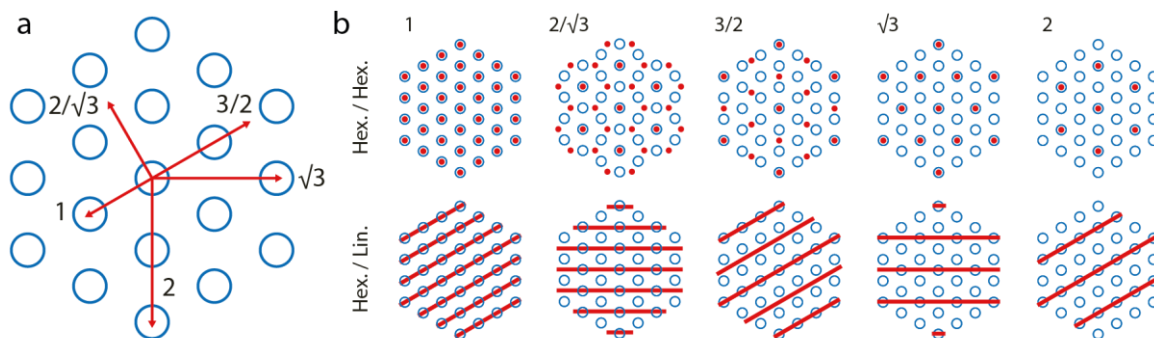


Figure 68. Schematics of (a) noticeable distances in a hexagonally packed structure and (b) resulting structure by adding a (top) red hexagonal or (bottom) linear array on top of the initial blue hexagonal array, with a size scaled with a given ratio.

The possible organizations with the 5 different periodicity ratios are described in *Figure 68.b*, showing the stacking of two hexagonal arrays, and the same for a hexagonal array and a linear one. Thus, the targeted sizes are obtained by multiplying or dividing the three standard sizes (28, 32 and 37 nm) by these 5 ratios (*Table 11*).

Ratio	$1/\sqrt{3}$	$2/3$	$\sqrt{3}/2$	1	$2/\sqrt{3}$	$3/2$	$\sqrt{3}$	2
Size for 28 nm	16 nm	19 nm	24 nm	28 nm	32 nm	42 nm	48 nm	56 nm
Size for 32 nm	18 nm	21 nm	28 nm	32 nm	37 nm	48 nm	56 nm	64 nm
Size for 37 nm	21 nm	25 nm	32 nm	37 nm	43 nm	56 nm	64 nm	74 nm

*Table 11. Listing of every size with noticeable ratio for a 28, 32 and 37 nm reference size. Shaded cells are the non-reachable size with the PS-*b*-PMMA used in this study.*

This table summarizes the large variety of noticeable sizes for stacking, even if some of them are not reachable due to the limited periodicity range obtained for PS-*b*-PMMA. Also, the sizes with less than 1 nm difference were merged together since it is the experimental precision of the size measure. Thus, the targeted periodicities for each BCP structure are the following:

- For lamellae: L₂₄, L₂₈, L₃₂, L₃₇, L₄₂, L₄₈, L₅₆ and the thick ones, L_{32-t}, L_{37-t}, L_{42-t}, L_{48-t}, L_{56-t};
- For PMMA cylinders: D₂₈, D₃₂, D₃₇, D₄₂, D₄₈, D₅₆, D₆₄;
- For PS cylinders: H₃₂, H₃₇, H₄₂, H₄₈, H₅₆ and H₆₄.

III.4.B/ Resulting 2D-structures

All the experiments for the target structures were carried out and analyzed by SEM and GISAXS after hybridization and a long plasma (called ashing (40 sccm O₂, 20 W, 3 min)) to remove all the PS, as presented in *Figures 69.a-b*.

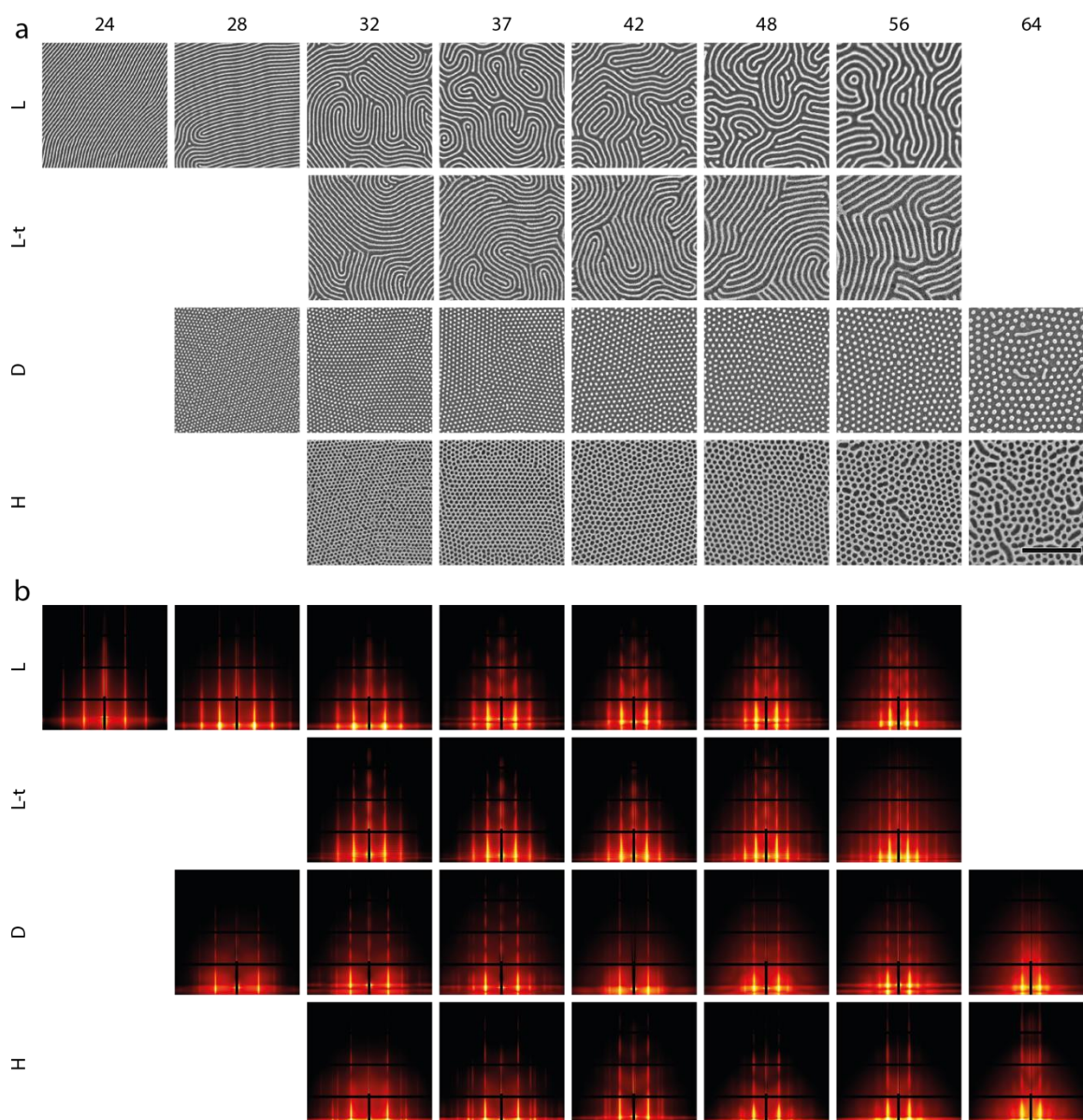


Figure 69. (a) SEM images and (b) GISAXS spectra of every targeted 2D-structures, rows with pattern type (L for line & space, L-t for thick line & space, D for dot and H for hole patterns) and column with pattern size (periodicity for line & space pattern, center-to-center distance for dot and hole patterns). Blank mean that the 2D-structure was inaccessible. Scale bar: 500 nm.

The overall structure quality was estimated by calculating the correlation length from large-scale SEM images (*Table 12*) (see *Annex 3.B/* for the computational details and *Annex 4/* for the large-scale images). The correlation length is a measure of the grain size, and a high value means that the structure is well-ordered. As we can observe from the SEM images, the lamellar lateral ordering is effectively increased by increasing the thickness, with an increase of the average correlation length of 50% between L_{32} to L_{42} , and more than 100% for higher periodicities. Also, these correlation lengths also prove that each morphology has better ordering and less defects for low M_n BCPs, as observed previously from AFM measurements.

These structures were also analyzed by GISAXS (*Figure 69.b*), which allows the precise determination of the structure, its orientation, and the periodicity (see *Annex 3.C/* for GISAXS details). The BornAgain software was used to simulate the GISAXS spectra. For instance, the L_{28} experimental spectrum (*Figure 70.a*) was simulated by creating a 19.2 nm high and 10.8 nm width perfectly sharp alumina lamellae with a 28.9 nm periodicity (*Figure 70.b*), giving a very similar spectrum.

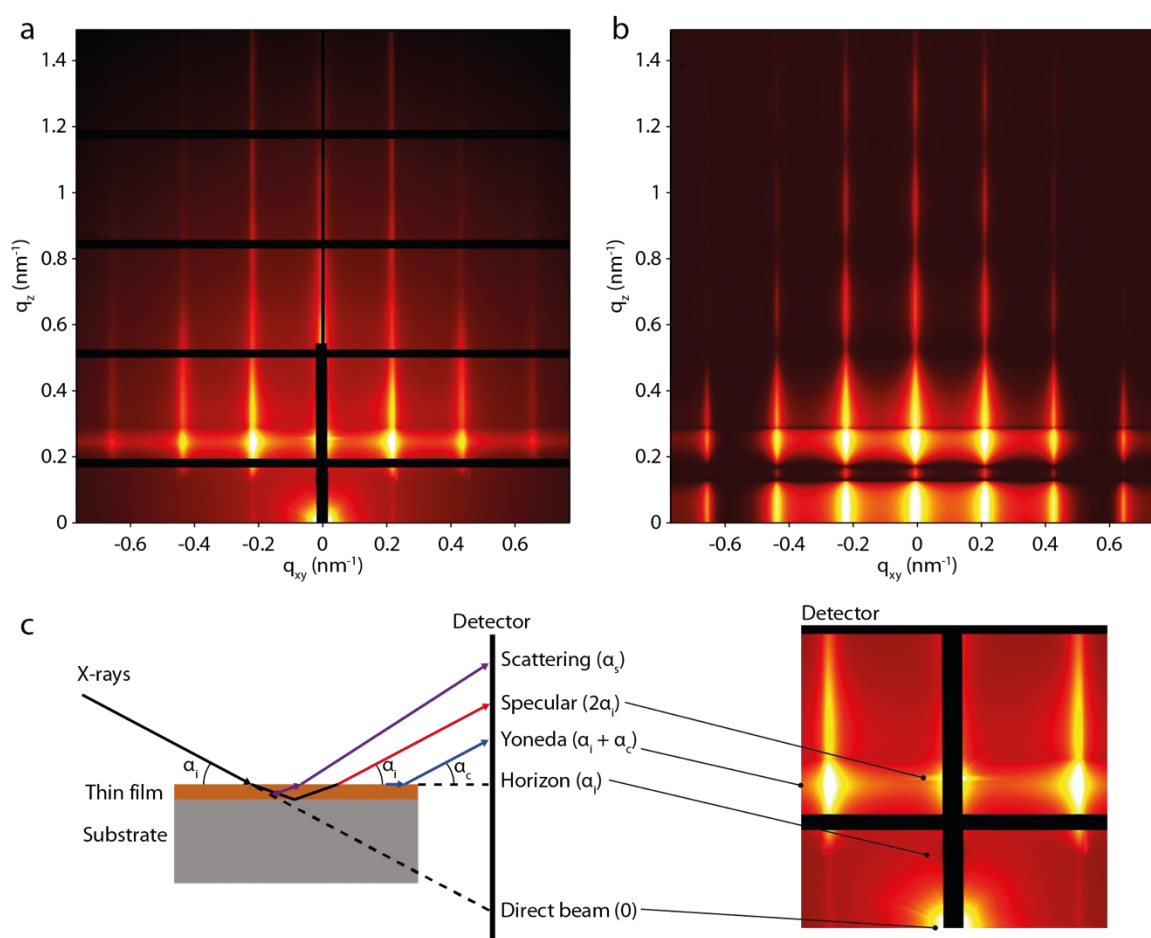


Figure 70. (a) Measured and (b) simulated GISAXS spectra of a L_{28} layer after hybridization and PS removal by 3 min plasma. (c) Schematics of the Ewald sphere representation for the GISAXS geometry, with the characteristic positions of the scattering signals along the q_z axis.

The interpretation the GISAXS spectra is divided in two parts:

- The z dimension along the q_z scattering vector, giving information about periodical pattern perpendicular to the substrate;
- The lateral dimension along the q_{xy} scattering vector, giving information about periodical pattern parallel to the substrate, which can be reduced to q_y due to the GISAXS geometry.

In our case, the GISAXS spectra do not show proper intensity signals, Bragg sheets or extinctions along the q_z scattering vector, which is in accordance with the out-of-plane orientation of the studied structures. However, some interesting information can be deduced from characteristic signals, thanks to the Ewald sphere representation (*Figure 70.c*). The specular peak is experimentally observed for $q_z = 0.252 \text{ nm}^{-1}$ which gives a scattered angle of 0.356° , which is very close to twice the theoretical incident angle used for the experiments, i.e. $2 \times 0.18^\circ$. Also a horizontal band is visible slightly below the specular peak, called the Yoneda band [33], due to waveguide modes and the roughness of the sample. In our case, the substrate surface is effectively rough due to the process: some Al_2O_3 can grow inside the PS domains, leading to porous Al_2O_3 residues [34]. Thus, the position of this band depends of the sample size and composition, and for instance, for L_{28} , this peak is centered for $q_z = 0.242 \text{ nm}^{-1}$, which gives a scattered angle of 0.342° . This band should be obtained for a scattered angle equal to the sum of the incident angle and the critical angle of the sample. Knowing the experimental incident angle thanks to the specular peak, it is possible to conclude that for L_{28} , the critical angle of this thin film is 0.164° , which is indeed lower than the Al_2O_3 critical angle value (0.289°) since the thin film is composed of not fully dense alumina due to SIS and voids.

Interestingly, for several GISAXS spectra, two Yoneda bands are observed, meaning that the vertical composition of the thin film is not constant. Another interesting effect is occurring for thick layers, with horizontal interferences around the Yoneda bands. This is due to remaining PS from the ashing process, which was optimized to remove the PS from the standard thickness, i.e. 35 nm, and not for the thicker ones (here 163 nm). This forms a rough interface parallel to the substrate surface, composed of PS and some Al_2O_3 , which produces narrow horizontal scattering.

For the lateral dimension, it is clear that every structure spectrum shows vertical bands (called Bragg rods), proving that the structures are indeed out-of-plane, as observed with the simulation of lamellae. Thus, these spectra can be integrated along q_y , which gives intensity plots over the scattering vector q_y (*Figure 71*). The scattering peak sequences and positions are then related to the structure morphology and periodicity (see *Chapter I.1.A.iii*/).

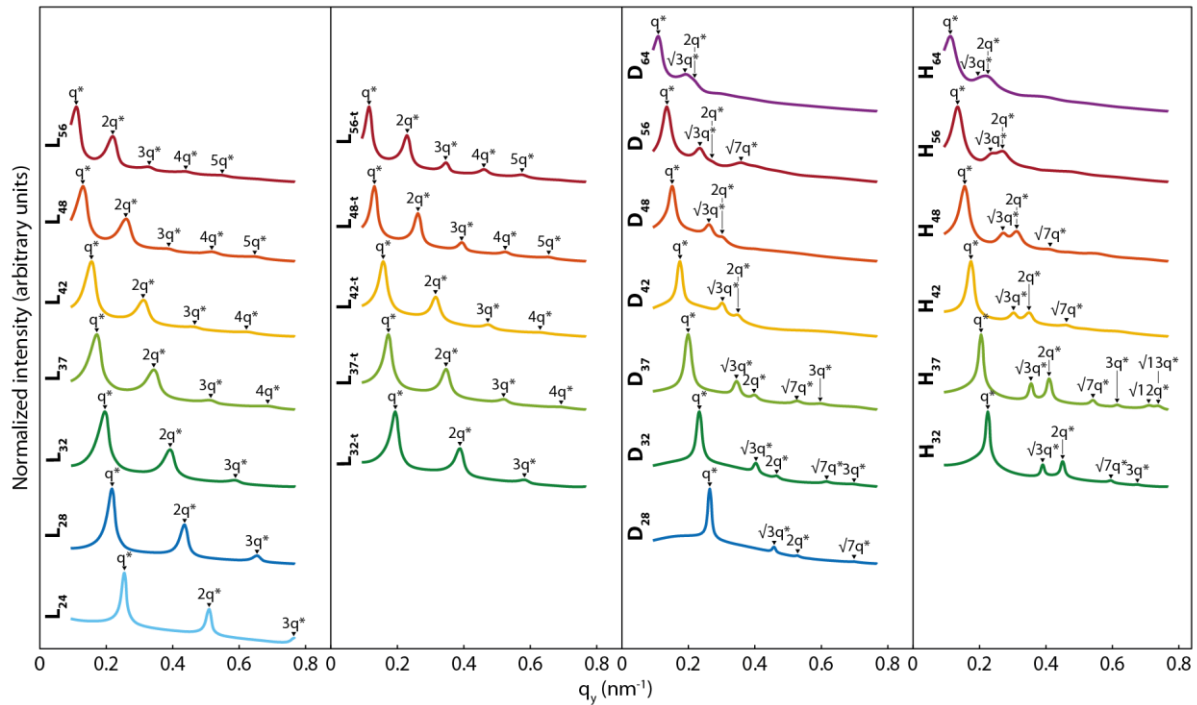


Figure 71. Integrated GISAXS spectra along q_y , giving an intensity vs scattering vector plot for line & space, thick line & space, dot and hole patterns (from left to right) with small to high periodicities (from bottom to top). Each peak position was enlightened.

Here, for each patterns the characteristic sequences are retrieved, with $q_y/q^* = 1, 2, 3, 4, 5$ for lamellae (line & space pattern) and $q_y/q^* = 1, \sqrt{3}, \sqrt{4}, \sqrt{7}, \sqrt{9}$ for hexagonally packed cylinders (dot and hole patterns). Then, by analyzing the position of the first peak, q^* , it is possible to retrieve the periodicity ($2\pi/q^*$) and the domains spacing, which is equal to the periodicity for line & space pattern and $2/\sqrt{3}$ times the periodicity for dot and hole patterns to obtain the cylinder-to-cylinder distance (Table 12).

Also, the width of the Bragg rods and the number of observable peaks is representative of the overall quality of the self-assembled structures. It is clearly observable that structures with a small periodicity are better ordered than the ones with high periodicity, corroborating the SEM results. Also, a slight improvement of structure quality can be observed between standard line & space and thick line & space patterns.

Interestingly, for most of the spectra, the Bragg rods show some extinctions along q_z due to the form factor of the structure, i.e. in our case, the thickness and the structure shape. Indeed, the structures are not perfect trenches, pillars or holes due to the plasma etching step. This is why the generated spectrum for lamellae shows these extinctions, due to perfectly parallel interface between the top of the sharp lamellae and the substrate surface, while the experimental spectrum does not. However, we can see that the extinctions are not at the same position for every sample, which means that this complex phenomenon depending on the structure, size, hybridization

process etc... could be deciphered by studying the variation of the Bragg rod intensity along q_z . This was not pursued during this study due to the extensive time needed for these simulations (limited computing power).

Finally, the *Table 12* sums up all the characterizations made for these different targeted 2D-structures.

Name	Blend composition	Annealing	Domains spacing	Correlation length
L ₂₄	27b22:13b12 1:1	230 °C - 10 min	24.7 nm	807 nm
L ₂₈	27b22	260 °C - 10 min	28.9 nm	359 nm
L ₃₂	27b22:85b78 4:1	260 °C - 10 min	32.4 nm	157 nm
L ₃₇	27b22:85b78 5:3	260 °C - 10 min	36.6 nm	126 nm
L ₄₂	27b22:85b78 1:1	260 °C - 10 min	40.3 nm	124 nm
L ₄₈	27b22:85b78 2:5	260 °C - 10 min	48.0 nm	101 nm
L ₅₆	27b22:85b78 1:7	260 °C - 10 min	56.8 nm	110 nm
L _{32-t}	27b22:85b78 4:1	260 °C - 10 min	32.4 nm	229 nm
L _{37-t}	27b22:85b78 5:3	260 °C - 10 min	36.3 nm	202 nm
L _{42-t}	27b22:85b78 1:1	260 °C - 10 min	39.9 nm	196 nm
L _{48-t}	27b22:85b78 2:5	260 °C - 10 min	48.0 nm	229 nm
L _{56-t}	27b22:85b78 1:7	260 °C - 10 min	54.5 nm	243 nm
D ₂₈	33b15:21b8 1:7	200°C - 15 min	27.5 nm	777 nm
D ₃₂	33b15:21b8 1:1	200°C - 15 min	31.2 nm	332 nm
D ₃₇	33b15	230°C - 15 min	36.3 nm	335 nm
D ₄₂	33b15:101b37 3:1	230°C - 15 min	41.5 nm	254 nm
D ₄₈	33b15:101b37 5:4	230°C - 15 min	47.9 nm	181 nm
D ₅₆	33b15:101b37 2:3	230°C - 15 min	53.5 nm	182 nm
D ₆₄	33b15:101b37 1:4	230°C - 15 min	66.5 nm	150 nm
H ₃₂	15b41:8b10 4:1	260°C - 5 min	32.2 nm	899 nm
H ₃₇	15b41	290°C - 5 min	35.4 nm	767 nm
H ₄₂	15b41:44b109 3:1	290°C - 5 min	41.5 nm	257 nm
H ₄₈	15b41: 44b109 3:2	290°C - 5 min	46.5 nm	202 nm
H ₅₆	15b41: 44b109 3:4	290°C - 5 min	54.2 nm	149 nm
H ₆₄	15b41: 44b109 1:3	290°C - 5 min	64.7 nm	136 nm

Table 12. Process parameters for all the targeted 2D-structures with the domain spacing measured by GISAXS and the correlation length by SEM image analysis (see Annex 3.B/).

III.5/ Conclusions

In this chapter, the experimental PS-*b*-PMMA phase diagram was explored in order to better apprehend the relationships between the BCP macromolecular characteristics and the self-assembled morphologies and periodicities. The self-assembly processes were also optimized in order to obtain self-assembled structures of good quality (low defectivity and high correlation length). Interestingly, the results were in good agreement with theoretical predictions, which will further help us to prepare the iterative layering of these BCP thin layers.

The self-assembly process was completed with an immobilization step consisting in transforming the PMMA domains into Al₂O₃ while partially removing the PS domains. Within all these structures, three particular structures were selected for subsequent layering because they produce 2D patterns which are invariant with the film thickness: the out-of-plane lamellae, the out-of-plane PMMA cylinders and the out-of-plane PS cylinders; forming after immobilization line & space, dot and hole patterns, respectively.

Then, by varying the BCP degree of polymerization, it was possible to screen the ranges of achievable periodicities, with a required process optimization due to the modification of BCP self-assembly with respect to the BCP chain length. Finally, a selection of characteristic dimensions according to geometrical considerations was done to prepare layers that would be stacked to form more complex 3D nanostructures. Also, this selection was characterized more thoroughly, with large SEM images and GISAXS analyses, in order to perform the stacking study on a sturdy basis.

III.6/ References

- [1] C. J. Hawker, E. Elce, J. Dao, W. Volksen, T. P. Russell, and G. G. Barclay, "Well-defined random copolymers by a 'living' free-radical polymerization process," *Macromolecules*, vol. 29, no. 7, pp. 2686–2688, 1996, doi: 10.1021/ma9515137.
- [2] P. Mansky *et al.*, "Controlling Polymer-Surface Interactions with Random Copolymer Brushes," *Science (80-.)*, vol. 275, no. March, pp. 1458–1461, 1997, doi: 10.1126/science.275.5305.1458.
- [3] K. Sparnacci *et al.*, "Ultrathin Random Copolymer-Grafted Layers for Block Copolymer Self-Assembly," *ACS Appl. Mater. Interfaces*, vol. 7, no. 20, pp. 10944–10951, 2015, doi: 10.1021/acsami.5b02201.
- [4] S. Ham *et al.*, "Microdomain orientation of PS-b-PMMA by controlled interfacial interactions," *Macromolecules*, vol. 41, no. 17, pp. 6431–6437, 2008, doi: 10.1021/ma8007338.
- [5] E. Han, K. O. Stuen, Y. H. La, P. F. Nealey, and P. Gopalan, "Effect of composition of substrate-modifying random copolymers on the orientation of symmetric and asymmetric diblock copolymer domains," *Macromolecules*, vol. 41, no. 23, pp. 9090–9097, 2008, doi: 10.1021/ma8018393.
- [6] H. J. Heo, D. J. Han, and E. H. Sohn, "Impact of trifluoromethyl groups on the control of surface and optical properties of poly(methyl methacrylate)," *J. Fluor. Chem.*, vol. 219, no. December 2018, pp. 92–97, 2019, doi: 10.1016/j.jfluchem.2019.01.001.
- [7] S. Wu, "Surface and interfacial tensions of polymer melts," *J. Colloid Interface Sci.*, vol. 31, no. 2, pp. 153–161, 1969, doi: 10.1016/0021-9797(69)90321-x.
- [8] P. Mansky, T. P. Russell, C. J. Hawker, J. Mays, D. C. Cook, and S. K. Satija, "Interfacial segregation in disordered block copolymers: Effect of tunable surface potentials," *Phys. Rev. Lett.*, vol. 79, no. 2, pp. 237–240, 1997, doi: 10.1103/PhysRevLett.79.237.
- [9] R. Leicht and J. Fuhrmann, "Comparative Recalculation of the Monomer Reactivity Ratios in Copolymerization for Styrene and Methyl Methacrylate.," *J. Polym. Sci. A1.*, vol. 21, no. 8, pp. 2215–2224, 1983, doi: 10.1002/pol.1983.170210806.
- [10] T. Fukuda, Y. D. Ma, and H. Inagaki, "Free-radical copolymerization. 3. Determination of rate constants of propagation and termination for styrene/methyl methacrylate system. A critical test of terminal-model kinetics," *Macromolecules*, vol. 18, no. 1, pp. 17–26, Jan. 1985, doi: 10.1021/ma00143a003.
- [11] C. C. Liu *et al.*, "Chemical patterns for directed self-assembly of lamellae-forming block copolymers with density multiplication of features," *Macromolecules*, vol. 46, no. 4, pp. 1415–1424, 2013, doi: 10.1021/ma302464n.
- [12] M. Jang, C. Yoon, J. Park, and O. Kwon, "Evaluation of Hazardous Chemicals with Material Safety Data Sheet and By-products of a Photoresist Used in the Semiconductor-Manufacturing Industry," *Saf. Health Work*, vol. 10, no. 1, pp. 114–121, 2019, doi: 10.1016/j.shaw.2018.08.001.
- [13] A. Knoll *et al.*, "Phase behavior in thin films of cylinder-forming block copolymers," *Phys. Rev. Lett.*, vol. 89, no. 3, pp. 355011–355014, 2002, doi: 10.1103/PhysRevLett.89.035501.
- [14] A. H. S. Lyakhova, G. J. A. Sevink, A. V. Z. Magerle, and A. Horvat, "Phase behavior in thin films of cylinder-forming modeling block copolymers : Mesoscale Phase behavior in thin films of cylinder-forming ABA block copolymers : Mesoscale modeling," vol. 1117, no. 2004, 2008, doi: 10.1063/1.1627325.
- [15] D. Meyerhofer, "Characteristics of resist films produced by spinning," *J. Appl. Phys.*, vol. 49,

- no. 7, pp. 3993–3997, 1978, doi: 10.1063/1.325357.
- [16] T. L. Morkved and H. M. Jaeger, “Thickness-induced morphology changes in lamellar diblock copolymer ultrathin films,” *Europhys. Lett.*, vol. 40, no. 6, pp. 643–648, 1997, doi: 10.1209/epl/i1997-00517-6.
- [17] M. W. Matsen and F. S. Bates, “Conformationally asymmetric block copolymers,” *J. Polym. Sci. Part B Polym. Phys.*, vol. 35, no. 6, pp. 945–952, Apr. 1997, doi: 10.1002/(SICI)1099-0488(19970430)35:6<945::AID-POLB9>3.0.CO;2-G.
- [18] P. W. Majewski and K. G. Yager, “Rapid ordering of block copolymer thin films,” *J. Phys. Condens. Matter*, vol. 28, no. 40, p. 403002, Oct. 2016, doi: 10.1088/0953-8984/28/40/403002.
- [19] M. Ceresoli *et al.*, “Evolution of lateral ordering in symmetric block copolymer thin films upon rapid thermal processing,” *Nanotechnology*, vol. 25, no. 27, 2014, doi: 10.1088/0957-4484/25/27/275601.
- [20] M. Biswas, J. A. Libera, S. B. Darling, and J. W. Elam, “New insight into the mechanism of sequential infiltration synthesis from infrared spectroscopy,” *Chem. Mater.*, vol. 26, no. 21, pp. 6135–6141, 2014, doi: 10.1021/cm502427q.
- [21] A. Rahman, P. W. Majewski, G. Doerk, C. T. Black, and K. G. Yager, “Non-native three-dimensional block copolymer morphologies,” *Nat. Commun.*, vol. 7, no. 1, p. 13988, Dec. 2016, doi: 10.1038/ncomms13988.
- [22] M. W. Matsen and F. S. Bates, “Unifying weak- and strong-segregation block copolymer theories,” *Macromolecules*, vol. 29, no. 4, pp. 1091–1098, 1996, doi: 10.1021/ma951138i.
- [23] S. Ji, U. Nagpal, W. Liao, C. C. Liu, J. J. De Pablo, and P. F. Nealey, “Three-dimensional directed assembly of block copolymers together with two-dimensional square and rectangular nanolithography,” *Adv. Mater.*, vol. 23, no. 32, pp. 3692–3697, 2011, doi: 10.1002/adma.201101813.
- [24] T. Segal-Peretz *et al.*, “Characterizing the three-dimensional structure of block copolymers via sequential infiltration synthesis and scanning transmission electron tomography,” *ACS Nano*, vol. 9, no. 5, pp. 5333–5347, 2015, doi: 10.1021/acsnano.5b01013.
- [25] C. Jin, B. C. Olsen, N. L. Y. Wu, E. J. Luber, and J. M. Buriak, “Sequential Nanopatterned Block Copolymer Self-Assembly on Surfaces,” *Langmuir*, vol. 32, no. 23, pp. 5890–5898, 2016, doi: 10.1021/acs.langmuir.6b01365.
- [26] F. Ferrarese Lupi *et al.*, “Fine tuning of lithographic masks through thin films of PS-b -PMMA with different molar mass by rapid thermal processing,” *ACS Appl. Mater. Interfaces*, vol. 6, no. 10, pp. 7180–7188, 2014, doi: 10.1021/am5003074.
- [27] X. Chevalier *et al.*, “Scaling-down lithographic dimensions with block-copolymer materials: 10-nm-sized features with poly(styrene)- block -poly(methylmethacrylate),” *J. Micro/Nanolithography, MEMS, MOEMS*, vol. 12, no. 3, p. 031102, Aug. 2013, doi: 10.1117/1.jmm.12.3.031102.
- [28] E. Sivaniah *et al.*, “Symmetric diblock copolymer thin films on rough substrates: Microdomain periodicity in pure and blended films,” *Macromolecules*, vol. 41, no. 7, pp. 2584–2592, 2008, doi: 10.1021/ma702465t.
- [29] A. Mamun, S. M. M. Rahman, S. Roland, and R. Mahmood, “Impact of Molecular Weight on the Thermal Stability and the Miscibility of Poly(ϵ -caprolactone)/Polystyrene Binary Blends,” *J. Polym. Environ.*, vol. 26, no. 8, pp. 3511–3519, 2018, doi: 10.1007/s10924-018-1236-1.
- [30] T. Xu *et al.*, “The influence of molecular weight on nanoporous polymer films,” *Polymer (Guildf)*, vol. 42, no. 21, pp. 9091–9095, 2001, doi: 10.1016/S0032-3861(01)00376-7.

- [31] D. O. Shin *et al.*, "A plasmonic biosensor array by block copolymer lithography," *J. Mater. Chem.*, vol. 20, no. 34, pp. 7241–7247, 2010, doi: 10.1039/c0jm01319f.
- [32] T. Hashimoto, M. Shibayama, and H. Kawai, "Domain-Boundary Structure of Styrene-Isoprene Block Copolymer Films Cast from Solution. 4. Molecular-Weight Dependence of Lamellar Microdomains," *Macromolecules*, vol. 13, no. 5, pp. 1237–1247, Sep. 1980, doi: 10.1021/ma60077a040.
- [33] Y. Yoneda, "Anomalous surface reflection of X rays," *Phys. Rev.*, vol. 131, no. 5, pp. 2010–2013, 1963, doi: 10.1103/PhysRev.131.2010.
- [34] F. E. Caligiore *et al.*, "Effect of the Density of Reactive Sites in P(S-r-MMA) Film during Al₂O₃ Growth by Sequential Infiltration Synthesis," *Adv. Mater. Interfaces*, vol. 6, no. 12, 2019, doi: 10.1002/admi.201900503.

CHAPTER IV: 3D-STRUCTURES FORMED BY ITERATIVE SELF-ASSEMBLY OF PS-*B*-PMMA FILMS

IV.1/ Introduction.....	148
IV.2/ General process for the formation of stacked nanostructures from BCP films	150
IV.2.A/ Formation of an immobilized BCP layer	150
IV.2.B/ Surface energy modification of the immobilized BCP layer via RCP grafting	150
IV.2.C/ Deposition of the 2 nd BCP layer and immobilization of the stacked structure	151
IV.2.D/ Structural characterization of the stacked BCP layers	152
IV.2.D/ The concept of responsive layering.....	153
IV.3/ Stacking of two layers with lamellar symmetry (L-L)	155
IV.3.A/ Stacked structures formed from lamellar PS- <i>b</i> -PMMA BCPs with the same periodicity ...	155
IV.3.B/ Rationalization of the mechanisms involved in the “responsive layering”	161
IV.3.C/ Stacking of two lamellar BCP layers with different periodicities	168
IV.4/ Hierarchical nanostructures by stacking two layers with a hexagonal symmetry ..	173
IV.4.A/ Expected configurations between the two stacked hexagonal patterns	173
IV.4.B/ Stacking of two dot patterns (D-D)	175
IV.4.C/ Stacking of two hole patterns (H-H)	181
IV.4.D/ Stacking of a dot pattern on top of hole pattern (H-D).....	185
IV.5/ Stacking of two layers with different symmetry	188
IV.5.A/ Expected configurations between two stacked patterns of different symmetry	188
IV.5.B/ Stacking of a dot pattern on top of a line & space pattern (L-D)	190
IV.5.C/ Stacking of a line & space pattern on top of a hole pattern (H-L)	194
IV.6/ Conclusions	197
IV.7/ References	198



This fourth chapter presents the general process of iterative layering of self-assembled BCP thin films that were previously immobilized (as described in the previous chapter). This process was optimized for two layers while the resulting layer configurations were analyzed by SEM and GISAXS.

An exhaustive study of every interesting stacking configuration was performed, by varying three different parameters between the two stacked layers: the morphologies (line & space, dot or hole patterns), the periodicity ratio (1:1, $2/\sqrt{3}$:1, $3/2$:1, $\sqrt{3}$:1 or 2:1), and the interfacial surface energy between the layers (neutral, PS-affine or PMMA-affine)

IV.1/ Introduction

The BCP self-assembly is an elegant method to form 2D or 3D patterns with a nanometric period at a very low cost (with only the polymeric material and a simple self-assembly process). Furthermore, the main drawback of this method inherent to the structural defectivity can be solved using “smart” DSA techniques, the most common being graphoepitaxy and chemical epitaxy. Nevertheless, the achievable patterns are also limited to the most thermodynamically stable self-assembled structures, giving for instance lamellae, cylinders, spheres and gyroids for a di-block architecture. Thus, three routes can be imagined to increase the complexity of self-assembled patterns which could open new avenues for technological applications:

- Pre-patterning (topographically or chemically) the substrate to induce specific fields that would force non-native self-assembly [1]–[3];
- Using more complex BCP architectures, with more than 2 blocks and different block arrangements with respect to a linear architecture [4], [5];
- Stacking “simple” layers made from di-block copolymers to obtain 3D structures [6].

The two first routes have a significant issue: they require more complex tools to reach the desired structure (nanolithography for pre-patterning, and chemical synthesis of complex BCPs). Interestingly, these three routes are not incompatible, and can be used together to produce even more complex structures [7], [8].

Accordingly, this chapter explores the “simple” stacking route, by performing iterative stacking of the 2D layers produced in *Chapter III*/. The first part will present the optimized processes to self-assemble a PS-*b*-PMMA thin film above a previously immobilized self-assembled layer. Importantly, it has been observed that the interfacial energy between the two layers can induce specific orientation and/or alignment of the second layer with respect to the first one. Besides, theoretical considerations corroborated with simulations have been developed to explain this “responsive layering” process.

Then, a study of every interesting stacking configuration was performed, varying three parameters:

- The layer patterns which can be line & space (L), dot (D) or hole (H) patterns, giving 6 potential bilayer stacking configurations (L-L, D-D, H-H, L-D, H-D and H-L);
- The ratio between the layer periodicities with five geometrically remarkable values (1:1, $2/\sqrt{3}:1$, $3/2:1$, $\sqrt{3}:1$ or 2:1);
- The interfacial energy between the layers (neutral, PMMA-affine or PS-affine).

The resulting structures have been sorted in three categories according to the geometry of stacked layers: both linear (L-L), both hexagonal (H-H, H-D and D-D), or mixed linear-hexagonal (L-D, H-L).

IV.2/ General process for the formation of stacked nanostructures from BCP films

The formation of 3D structures by iterative self-assembly was performed in a three-step process: the formation of a first immobilized BCP layer as described in the previous chapter, its surface modification, and the formation of a second BCP layer on top of it. In this study, three building bricks have been used for the implementation of the stacking methodology: out-of-plane lamellae for the formation of line & space pattern (L), out-of-plane PMMA cylinders for the formation of hexagonally packed dot pattern (D) and out-of-plane PS cylinders for the formation of hexagonally packed hole pattern (H).

IV.2.A/ Formation of an immobilized BCP layer

After the formation of a nanostructured thin film of PS-*b*-PMMA on a modified Si substrate, it is mandatory to “quench” the self-assembled pattern for the deposition of a subsequent BCP layer. As described in the previous chapter, the immobilization was performed by SIS in order to transform the PMMA domains into Al₂O₃. The last step of the SIS process is a plasma etching step used to “densify” the Al₂O₃ domains through the PMMA removal. During this step, the plasma treatment also etches partially the PS domains. This is of particular interest since: i) it allows a fine control of the topography of the first layer which can be further used to direct the self-assembly of the top layer [6], [9]; ii) it leads to the “screening” of the chemical fields of any underneath layer by providing a complete coverage of the surface. In addition to the topographical etch of the PS domains, the plasma treatment slightly crosslinks the PS domains which further assures a mechanical integrity of the layer with respect to solvation [10].

IV.2.B/ Surface energy modification of the immobilized BCP layer via RCP grafting

The immobilization process of the first nanostructured BCP film also yields to the generation of a stable platform for the subsequent tuning of interfacial energy between the stacked layers. Indeed, a standard ALD process was conducted after the plasma etching step in order to deposit a thin Al₂O₃ layer on top of the first layer. It further allows the modification of the surface energy by grafting an RCP layer from this continuous oxide layer. Experimentally, we opted to perform 10 cycles of standard ALD using TMA and H₂O at 85 °C. This process leads to the formation of an \approx 1 nm thick Al₂O₃ layer covering the whole surface [11]. The surface modification via the grafting of RCP chains was subsequently performed on the passivated surface without damaging the underneath structure (*Figure 72*).

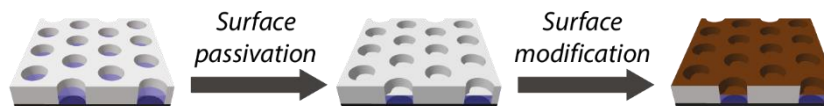


Figure 72. Schematics of the formation of an immobilized nanostructured layer from BCP self-assembly in thin film (here obtained from out-of-plane PS cylinders in a PMMA matrix infiltrated by Al_2O_3) followed by the deposition of a thin Al_2O_3 layer on top of the pattern in order to enable a further surface modification using RCP grafting.

As opposed to the study performed in the previous chapter using only “fully” neutral surface modification for the BCP domains (i.e. leading to an optimal out-of-plane orientation of the BCP domains), three different configurations within the “out-of-plane” window (neutral, “slightly” PMMA-affine, “slightly” PS-affine, denoted N, M and S respectively) were studied for the stacking of two BCP layers. Accordingly, different compositions of the grafted layers, f_{PS}^{RCP} , were used and obtained through blending different PS-*r*-PMMA copolymers with different compositions (see IV.2.D/ Structural characterization for details). The “slightly” PMMA-affine and “slightly” PS-affine compositions were defined as the minimal and maximal f_{PS}^{RCP} compositions for which an out-of-plane orientation of the BCP structures were observed for a 35 nm film thickness on a flat substrate.

Structure	PS cylinders (H)			Lamellae (L)			PMMA cylinders (D)		
	PMMA	Neutral	PS	PMMA	Neutral	PS	PMMA	Neutral	PS
f_{PS}^{RCP}	0.40	0.52	0.63	0.59	0.70	0.78	0.68	0.78	0.86
Name	M_H	N_H	S_H	M_L	N_L	S_L	M_D	N_D	S_D

Table 13. PS-*r*-PMMA blend compositions for “slightly” PMMA-affine, neutral and “slightly” PS-affine surface modifications adapted for PS cylinders, lamellae and PMMA cylinders.

IV.2.C/ Deposition of the 2nd BCP layer and immobilization of the stacked structure

After the passivation step, it is thus possible to perform the so-called iterative stacking. This step follows exactly the same process as described before for a flat substrate. Nevertheless, the self-assembly of the 2nd BCP layer takes place on a “patterned” substrate with both topographical and chemical fields. Experimentally, after the adequate surface energy modification of the first immobilized layer, a BCP thin film is spin-coated and thermally annealed to promote the self-assembly of the second layer. The PMMA domains are then infiltrated with Al_2O_3 by SIS (Figure 73) in order to stabilize the stacked structure.

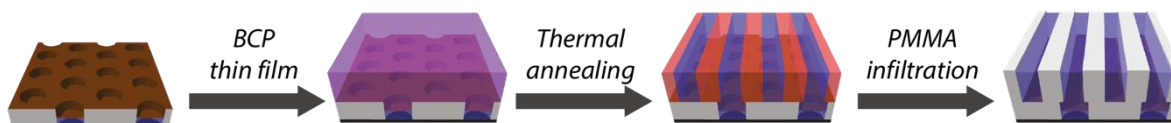


Figure 73. Schematics of the self-assembly process of the 2nd BCP layer leading to the immobilization of the stacked structure by SIS (here depicted for out-of-plane lamellar pattern on top of a hole pattern).

As observed on a flat substrate, an optimized composition of the RCP drives an out-of-plane orientation of the self-assembled BCP structure. It is noteworthy that the same RCP compositions in order to reach “full” neutrality for each structure was observed for the iterative stacking step. It means that the Al₂O₃ passivation layer behaves as the native silicon oxide layer in term of surface energy modification after RCP grafting.

Finally, the PS domains can be partially etched as done for the first layer to increase the topography and then the same iterative process can be performed again for the stacking of more than two BCP layers. The overall iterative structures formed following this process are labelled as the first layer name (structure and size), followed by the RCP name, and the second layer name, e.g. H₃₂-M_L-L₃₂ for a hole pattern with a period of 32 nm modified by a “slightly” PMMA-affine RCP layer with a top line & space pattern with a period of 32 nm. This labelling can be extended as well for more than 2 layers.

IV.2.D/ Structural characterization of the stacked BCP layers

After the stacking process of n ($n \geq 2$) self-assembled and hybridized PS-*b*-PMMA layers, non-native 3D-nanostructure are produced. To understand the stacking rules as a function of the BCP macromolecular parameters and the different self-assembly processes, it is required to precisely characterize the resulting structures. This can be done via direct visualization of the nanostructure by AFM or SEM, or using highly sensitive scattering techniques such as grazing small-angle X-ray scattering (GISAXS).

The most convenient method is the direct observation by top view SEM after an ashing step, i.e. removing the whole PS domains from the nanostructure, as performed by Rahman *et al.* [6]. The objective of this ashing step is to fully remove the PS domains, without deteriorating the inorganic nanostructure. Indeed, the overall Al₂O₃ structure is composed of very thin features, with characteristic sizes from 10 to 50 nm, which can be easily damaged during the ashing step. Thus, a low energy oxygen plasma treatment was performed (40 sccm at 20 W) for a duration optimized with respect to the stacked structure (*Figure 74.a*). Obviously, this duration is dependent on the number of layers to etch, but also on the kind of features (i.e. the Al₂O₃ content in the stacked structure). For instance, a hole structure which contains more Al₂O₃ than a dot structure for a constant thickness is more robust to the ashing step while the dot structure could collapse.

After ashing, it is possible to observe the top view projection of the 3D nanostructure with SEM. This was done routinely for bilayers to observe the produced structures, and to study the stacking orientation rules. *Figure 74.b* presents the stacking of a L₃₂ layer on top of a H₃₇ layer with

a PMMA-affine interfacial modification cropped to present a unique well-defined grain. Indeed, the FFT analysis of the SEM image (*Figure 74.c*) presents characteristic peaks of a hexagonal symmetry (bright dots arranged in a hexagonal array) from the H₃₇ pattern, with also the characteristic fringes of a linear symmetry (bright parallel fringes evenly separated) from the L₃₂ pattern. Interestingly, the bright lines are crossing the bright dots, due to the same periodicity of both layers (37 nm of H₃₇ is the domain spacing, leading to 32 nm periodicity).

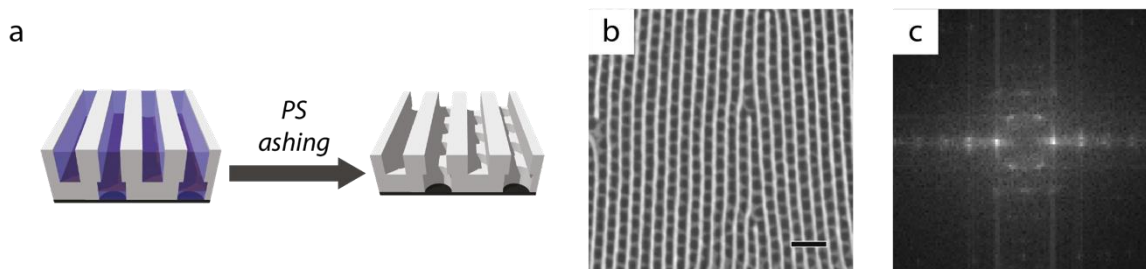


Figure 74. (a) Schematics of the PS complete removal step called ashing, leading to a fully inorganic 3D nanostructure (here depicted for a line & space pattern on top of a hole pattern). (b) SEM image of the ashed structure corresponding to the schematics (here formed with H₃₇-M_L-L₃₂), and (c) FFT analysis of the SEM image. Scale bar: 100 nm.

However, this method shows some limitations. Indeed, a top layer with a high Al₂O₃ content can “hide” a nanostructure formed by a BCP underlayer with a lower Al₂O₃ content. Experimentally, it was very difficult (even impossible in some cases) to observe dot patterns below line & space or hole pattern, and line & space pattern below hole pattern. This problematic is even more present during the characterization by top-view SEM of more than two stacked layers. Accordingly, the structural characterization of the stacked structures was also performed by “indirect” techniques such as GISAXS (see *Annex 2.C/*) to confirm the stacking rules and characteristic dimensions of the nanostructures. As a note, the $q_{xy} = q_y$ and q_z axes on the GISAXS images were not placed on the GISAXS images for the overall clarity of the assembled figures. Nevertheless, all GISAXS images presented in this chapter have the same size and the corresponding q_y and q_z axes are detailed on *Chapter III/Figures 70.a-b*.

IV.2.D/ The concept of responsive layering

The objective of this chapter is to decipher the stacking rules between two BCP layers for the nano-manufacturing of non-native structures from BCP self-assembly in thin films. This encompasses the understanding of the mechanisms driving the relative alignment and orientation of the top layer with respect to the bottom one – a concept so-called “responsive layering”. Considering two perfectly ordered BCP layers, the stacked nanostructures can be easily computed with the following parameters:

- The structure type of both layers (L, D or H);
- The ratio of the domain spacing of the BCP layers;

- The relative angle between both structures;
- The pattern translation along x and y axis between both structures.

The screening of all these parameters would lead to an “infinite” number of bilayered structures. However, it is possible to select specific bilayer configurations that would be thermodynamically more stable because of symmetry rules, as dictated by de Curie-Rosen principle [12]. To that extent, the stacked structure symmetry has been quantified with two parameters:

- The symmetry group of the produced pattern, also called the 2D wallpaper group, which can be one of the 17 possible groups [13];
- The size of the fundamental domain, i.e. the repetitive unit of the pattern, which should be the smallest possible.

Thus, it is possible to sort out the bilayered structures in two categories: i) the second layer is randomly configured (orientation and alignment) with respect to the first one (no registration mechanism); ii) a specific registration occurs which leads to a remarkable structure. In this case, the underneath mechanism linked to the registration of the 2nd layer with respect to the first one is called “responsive layering”; i.e. the first layer dictates the orientation and alignment of the 2nd layer.

IV.3/ Stacking of two layers with lamellar symmetry (L-L)

This part focuses on the simplest stacking configuration: two layers of line & space patterns created from lamellae forming PS-*b*-PMMA BCPs, called L-L stack. In general, the BCP lamellar morphology produces fingerprint patterns in thin films which have only a local translational order. The translational order of the lamellar morphology can be improved using directed self-assembly techniques, e.g. with graphoepitaxy or chemo-epitaxy. Thus, stacking two layers of such unidirectional structure have two remarkable orientations: the two line & space arrays are either parallel or orthogonal. Any other orientation between the layers clearly hints an independent self-assembly behavior between the layers which is characteristic of a “non-responsive layering”.

Interestingly, in the case of parallel orientation, the produced stacking is different than the 2D wallpaper group, and is called a line group. Indeed, in this case the pattern is infinitely repeated along the line direction. Thus, the pattern description is only made by the symmetry along the axis perpendicular to the lines. There are two possibilities: either there is a mirror reflection along this axis and the symmetry group is $p1m$, or the symmetry group is $p1$. In the other hand, for the perpendicular orientation, the pattern produced is 2D, and can be described by one of the 17 possible 2D wallpaper groups.

IV.3.A/ Stacked structures formed from lamellar PS-*b*-PMMA BCPs with the same periodicity

IV.3.A.i/ Expected configurations between the two stacked line & space patterns

In the case of stacking two line & space arrays with the same periodicity, responsive layering can lead to four particular bilayered structures:

- The top lamellar structure is parallel to the bottom line & space array, with either the PMMA or the PS domains being registered above the alumina lines, leading to a line pattern with the $p1m$ symmetry (Figures 75.b-c);
- The top lamellar structure is parallel to the bottom line & space array, with half-PMMA/half-PS domains being registered above the alumina lines, leading a line pattern with the $p1$ symmetry (Figure 75.d);
- The top lamellar structure is orthogonal to the bottom line & space array, leading to a 2D wallpaper grid pattern with a $p4mm$ symmetry (Figure 75.e).

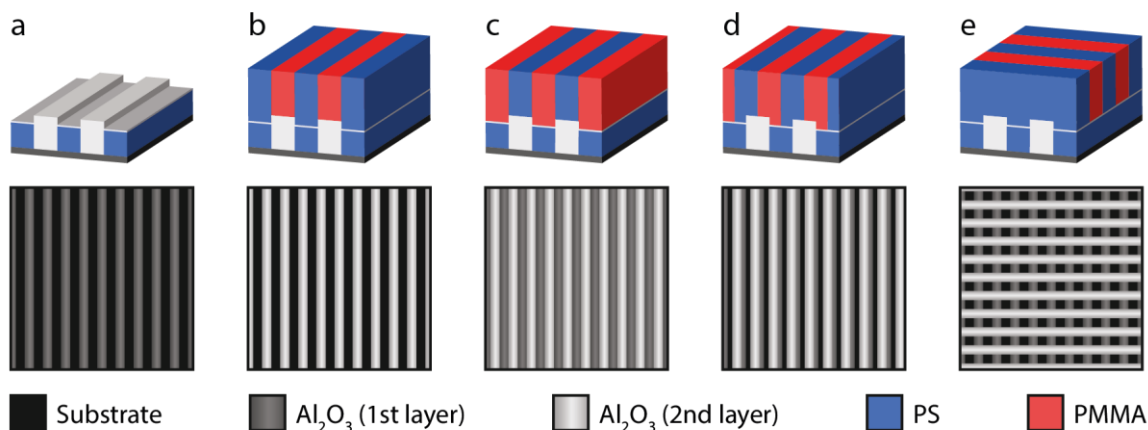


Figure 75. 3D schematics of (a) the Al_2O_3 line & space pattern after immobilization stacked with (b) the PMMA domains registered on top of the alumina lines, (c) the PS domains registered on top of the alumina lines, (d) half of the PMMA and PS domains registered on top of the alumina lines, (e) the PS-*b*-PMMA lamellar structure perpendicularly oriented to the Al_2O_3 lines. Bottom schemes are the expected idealized top-view SEM images.

Besides, a random orientation between both layers should be observed if no responsive layering occurs. It is possible to simulate the resulting top-view SEM image of a random orientation of the two patterns after ashing through the overlay of two SEM images with an arbitrary angle between them. For instance, *Figure 76* shows the result of such treatment with a random stacking configuration obtained from a top view SEM image of two L_{28} layers (L_{28} - L_{28}).

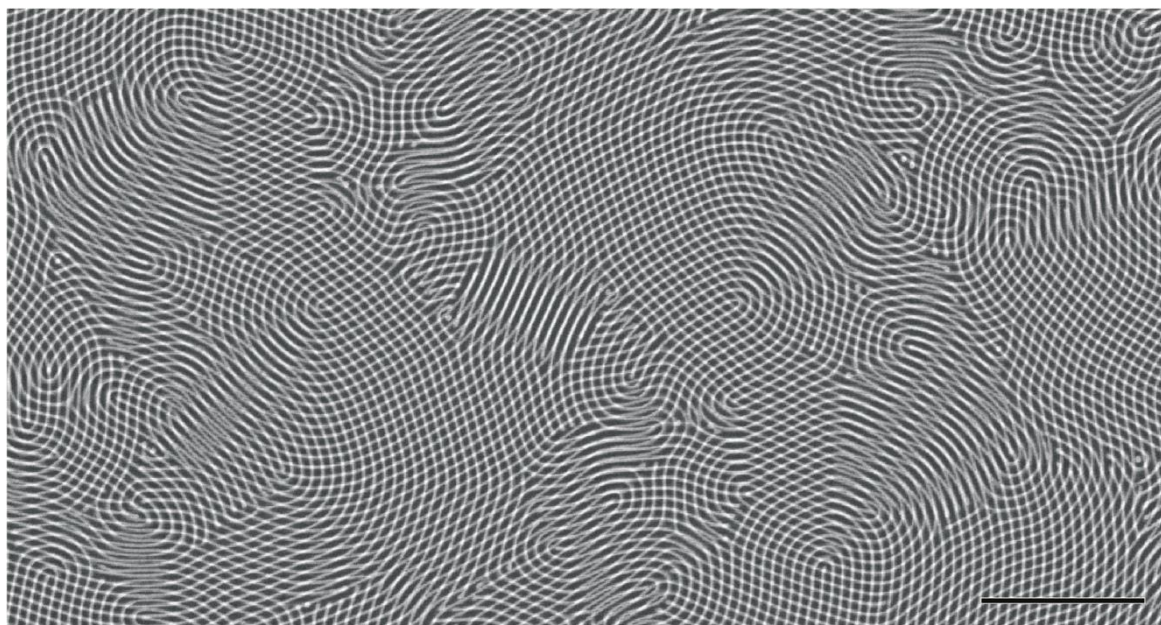
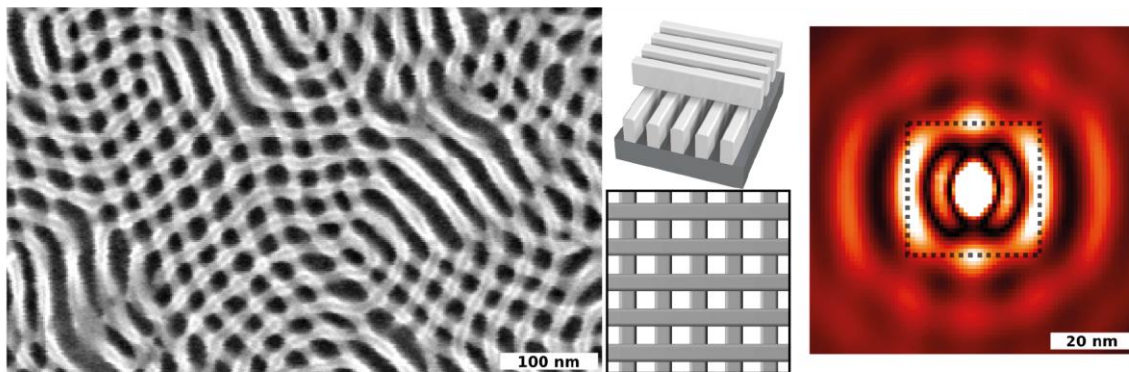


Figure 76. Simulated L_{28} - L_{28} random stacking top view SEM image made by overlaying the same L_{28} SEM image with an arbitrary rotation angle between them. Scale bar: 500 nm.

It is noteworthy that regions with parallel and perpendicular orientations are present in the simulated SEM image, but most of the regions are composed of crossing lines with a random angle, leading to a pattern composed of lozenges. Thus, responsive layering is only taking place if and only if a quantitative increase of one specific orientation can be observed with respect to the

generated image with a random orientation. Interestingly, the results of the stacking of two line & space patterns reported by Rahman *et al.* [6] (*Figure 77*) lacked such quantitative increase (i.e. experimental SEM images with characteristic features close to the random generated one). The conclusions drawn by the authors about “responsive layering” leading to an orthogonal arrangement of the two line & space patterns are consequently dubious.



*Figure 77. SEM image of two stacked layers of lamellar BCP with the associated 2D and 3D views of the idealized grid structure, and the FFT recalculated from the local configuration. Reprinted from Rahman *et al.* [6]*

IV.3.A.ii/ Experimental bilayered structures from lamellar PS-*b*-PMMA

Experimentally, we have studied the stacking of two L_{28} layers using the aforementioned process, with the three different interfacial coatings for lamellae, i.e. neutral, PMMA-affine or PS-affine (compositions of the grafted interfacial layers are summarized in *IV.2.D/ Structural characterization*). After the ashing of the PS domains by a long plasma treatment (4 min), the three different patterns were observed using SEM (*Figures 78.a-c*), showing the top-view projections of the superimposed layers. The corresponding GISAXS 2D pattern are given in *Figures 78.d-e*.

The neutral case (*Figure 78.a*) shows a decent grid pattern as compared to the random generated one, with an angle close to 90° between both layers. However, due to the inherent defectivity of BCP self-assembly, the translational order of the underlying line & space pattern is poor, which results in multiple defects (edge dislocations and disclinations for lamellar structure in thin films) localized mainly at the grain boundaries [14], [15]. The poor translational order of the first BCP layer inhibits thus the generation of a perfect grid without further use of directed self-assembly methods. The corresponding GISAXS pattern (*Figure 78.d*) is in accordance with the SEM image. Intense Bragg rods along q_y positioned in the characteristic $q_y/q^* = 1,2,3$ sequence confirmed the production of a line & space pattern with a common periodicity for the two superimposed layers with a measured $L_0 = 28.7$ nm which is identical to the L_{28} domain spacing. Accordingly, the characteristic size of the top self-assembled structure does not appear to be disturbed by the chemical and topographical fields induced by the underlying Al_2O_3 pattern. Even

if GISAXS is a powerful methodology for the characterization of complex nanostructured surfaces, the “polycrystalline” nature of the produced grid pattern (i.e. multiple angular orientations of the two grid arrays) does not permit to retrieve the angular configuration of the two superimposed line & space arrays.

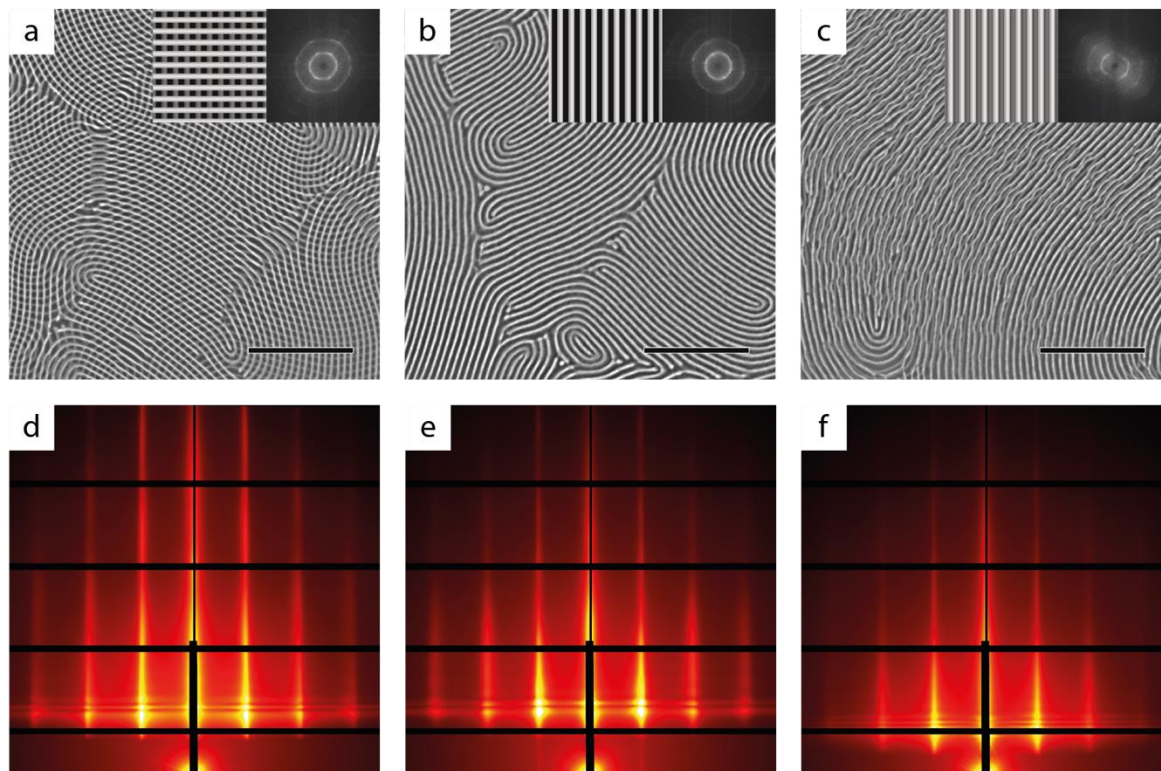


Figure 78. (top panel) SEM images and (bottom panel) corresponding GISAXS spectra of two stacked L_{28} layers with (a,d) N_L neutral interfacial layer, (b,e) M_L PMMA-affine interfacial layer and (c,f) S_L PS-affine interfacial layer. The top right insets show the idealized structures and FFTs. Scale bars: 500 nm.

Figure 78.b shows the structure obtained for two superimposed line & space patterns separated by a PMMA-affine interfacial layer. From such top-view image, a unique line & space pattern is observed. As the prolonged ashing by plasma treatment is expected to remove all organic materials (i.e. the non-hybridized PS domains), we conclude to a registration between the underlying Al_2O_3 lines and the PMMA domains of the top layer. Accordingly, a thicker Al_2O_3 line & space array is produced after the hybridization by SIS of the second BCP layer. The GISAXS data presented in Figure 78.e are in agreement with this assignment as a sequence of Bragg rods such as $q_y/q^* = 1,2,3$ is also retrieved. The periodicity of the thick line & space array was evaluated at $L_0 = 29.3$ nm, which is not significantly different than the L_{28} domain spacing.

Finally, the structure obtained for a PS-affine interfacial layer (Figure 78.c) is harder to analyze since the top layer is constituted of “wavy” lines. From the top-view SEM image, the top line & space array is collinear to the bottom one, but the registration between the bottom and top arrays differs from the previous case. As a PS-affine interfacial layer was inserted between the two

arrays, this structure results from a registration between the bottom alumina lines and the PS domains of the second BCP layer. Indeed, the hybridization by SIS of the second layer results in alumina lines positioned (at a different height) between the alumina lines of the first layer (see *Figure 75.c*). The ashing step leads to a collapse of the top layer structure by removing all the PS domains. This further results in the wavy pattern of the top array observed in *Figure 78.c*. The 2D GISAXS pattern recorded for this sample in *Figure 78.f* is coherent with this configuration as only two Bragg rods inherent to a weaker translational order of the structure are visible. Nevertheless, a characteristic sequence $q_y/q^* = 1,2$ is retrieved which confirms the formation of line & space arrays with a common periodicity $L_0 = 29.3$ nm.

IV.3.A.iii/ Long-range ordering of stacked line & space arrays

Even if a good understanding of the role of the interfacial layer between the two arrays has been established from the previous study, it is more difficult to conclude on the orientation control through the “responsive layering” approach. Indeed, the defectivity inherent to BCP self-assembly on flat substrate (poor translational order) results in polycrystalline structures with a low correlation length. To overcome this effect, a grooved patterned substrate was used to direct the self-assembly of the first BCP layer by graphoepitaxy.

The patterned substrates used in this study were generated by a combination 193 nm lithography and plasma etching in the LTM / CEA-LETI facility. They are composed of 60 nm deep parallel trenches, with a 70 nm width and a 140 nm periodicity (*Figure 79.a*). The PS-*b*-PMMA with a periodicity of 28 nm was self-assembled on the patterned substrate using the process described in *Chapter III*/ resulting in the formation of out-of-plane lamellae confined inside the grooves and oriented perpendicularly with respect to the orientation of the trenches as observed on the AFM phase image in *Figure 79.b*. This perpendicular orientation is coherent with the surface modification by a neutral RCP of the grooved substrate as already reported in the literature for lamellar PS-*b*-PMMA [16], [17]. This particular arrangement of the lamellae with respect to the grooved substrate is indeed expected as it provides the configuration with minimal energy due to both PS and PMMA domains facing a maximal interfacial area with the neutral RCP coating. It is noteworthy that the AFM height profile demonstrates that using this standard process, a topographical wave pattern with an amplitude of 6 nm remains from the underneath trenches. This topographical pattern would induce a strong topographic field orthogonal to the one formed at the time of the immobilization process. Even if the competition between the two topographical fields could be interesting to further tune the morphology of the stacked structures, it will be detrimental for a complete understanding on the “responsive layering” approach. In order to attenuate the topography induced by the grooved substrate, the BCP layer thickness was

increased by modifying the concentration of the BCP solution from 1.5 wt.% to 4 wt.%. This leads to a thicker BCP film (around 160 nm) for which a good translational order of the PS-*b*-PMMA lamellae is retained while the remaining topographical pattern has only an amplitude of 1 nm (Figure 79.c). Such amplitude was considered as negligible with respect to the topographical pattern created at the time of the BCP immobilization by the combined SIS and plasma treatments.

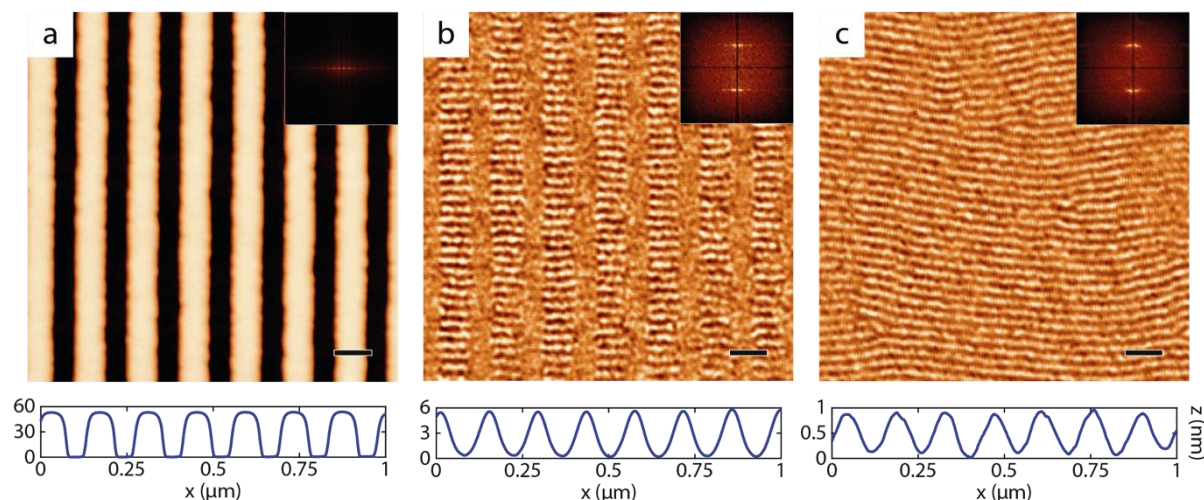


Figure 79. (a) AFM height image of the grooved substrate used for directed self-assembly. AFM phase images of (b) 35 nm and (c) 160 nm thick lamellae self-assembled on top of this pattern. Top right insets are the respective FFTs. The topographical profile is given for each image in the bottom panel. Scale bars: 100 nm.

This 1st layer being now a “unique” L_{28} grain with only a few dislocations, it is possible to perform the previously reported layering process using the standard thickness (35 nm) for the 2nd layer. The structures obtained for the different interfacial layers (i.e. neutral, PMMA-affine and PS-affine) are shown in Figures 80.a-c and validate the conclusions made in the previous paragraph, i.e. an orthogonal orientation of the 2nd layer is observed if the interfacial energy between the layers is perfectly neutral (L_{28} - N_L - L_{28}), and a parallel one if this interfacial energy is slightly affine to one of the BCP domains.

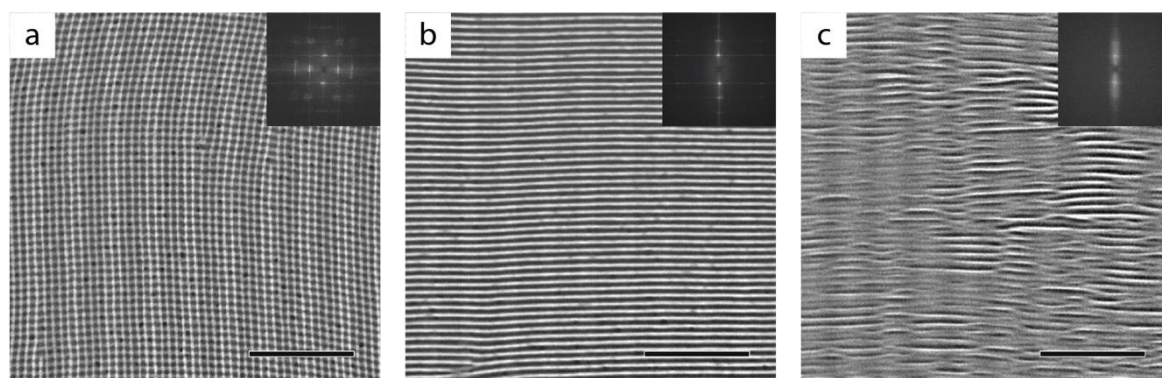


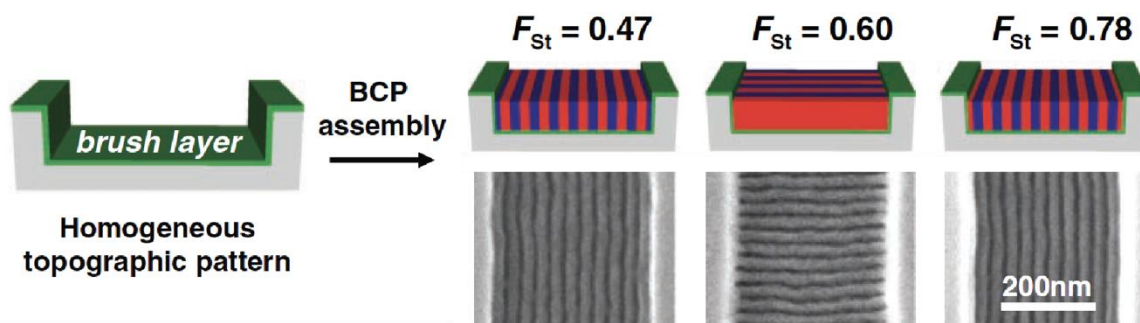
Figure 80. SEM images of (a) L_{28} - N_L - L_{28} , (b) L_{28} - M_L - L_{28} and (c) L_{28} - S_L - L_{28} on top of a grooved substrate (the initial trenches are vertically oriented on the SEM images) after the 4 min ashing treatment. Top right insets are FFTs of the corresponding SEM images. Scale bars: 500 nm.

Additionally, the two line & space arrays are perfectly stacked when the surface is affine to PMMA (L_{28} - M_L - L_{28}), while an interfacial layer affine to PS (L_{28} - S_L - L_{28}) leads to a collapse of the top line & space array inside the spaces of the bottom array as shown in *Figure 80.c*.

The results obtained using directed self-assembly methods are more robust than the previous ones, as they allow us to clearly distinguish the different stacking configurations. In particular, three highly ordered configurations have been observed with a clear responsive layering mechanism depending of the interfacial energy between the two BCP layers. The next paragraph will propose different hypotheses regarding the mechanisms involved in responsive layering.

IV.3.B/ Rationalization of the mechanisms involved in the “responsive layering”

The previous results underlined the role of the surface modification between the two BCP layers. Some insights on the mechanisms involved in the self-assembly of confined BCPs in thin films can be gained from the extensive works on the directed self-assembly of lamellar PS-*b*-PMMA systems by graphoepitaxy. In 2010, Han *et al.* [16] observed three possible orientations of PS-*b*-PMMA lamellae confined in grooved substrate depending on the surface modification with PS-*r*-PMMA (i.e. neutral and weakly affine towards PS or PMMA). In the study, the out-of-plane lamellae were strongly confined into the trenches (see *Figure 81*), and energetical considerations at the bottom surface and walls of the trenches were taken into account to explain the resulting configurations of the PS-*b*-PMMA lamellae: i) the out-of-plane lamellae are orthogonally orientated to the trenches if the substrate is fully neutral (i.e. neutral bottom surface and walls), or ii) the out-of-plane lamellae are collinearly oriented to the trenches due to the PS (PMMA) domain wetting at the walls for PS (PMMA) affine modification.



*Figure 81. Schematic of the directed assembly of lamellar PS-*b*-PMMA according to the styrene volume fraction (F_{St}) of the PS-*r*-PMMA brush layer coated on the topographical trench pattern, with the associated SEM images. Reprinted from Han *et al.* [16].*

In our case, the stacking process also leads to the generation of both topographical (PS/Al₂O₃ pattern) and chemical fields (modification of the top interface of the 1st immobilized BCP layer by different RCPs). Nevertheless, the 2nd BCP layer is not strongly confined by the topographical pattern created by the 1st layer as its thickness is important with respect to the 1st layer topography. Besides, the commensurability between the characteristic lengths of the two patterns is always respected since the experimental results were obtained for two L₂₈ BCP layers. Accordingly, the rationalization of the various experimental behaviors should be based on additional considerations which are commented in the following paragraphs.

IV.3.B.i/ Asymmetric surface areas due to the topographical field

A first consideration is related to the increased surface area due to the topography produced by the immobilization by SIS of the 1st BCP layer. Indeed, the line & space pattern is not sharp due to a gradient of block composition at the interface [18], related to the low segregation strength (i.e. χN product) of the PS-*b*-PMMA system under study [19] and the non-isotropic plasma etching process. It is rather composed of lines with curved walls, and the resulting bump profile has been modeled with a rectangle having perfectly rounded edges as shown in *Figure 82.a*. Thus, it is possible to geometrically estimate the surface variation with respect to a flat surface, as function of the bump height h and width w , i.e. the line thickness and its half periodicity, respectively:

$$\frac{S_{bump}}{S_{flat}} = \begin{cases} \frac{\pi}{2} + \frac{2h}{w} - 1 & \text{if } w \leq 2h \\ \frac{\pi \cdot h}{w} + 1 - \frac{2h}{w} & \text{if } w \geq 2h \end{cases} \quad (20)$$

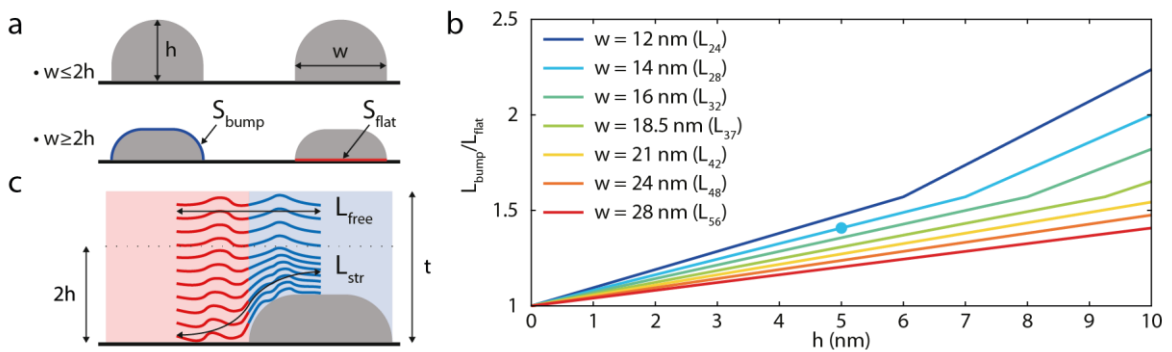


Figure 82. (a) Geometrical models used for the line & space pattern obtained from the immobilization of the first BCP layer with the characteristic dimensions and (b) excess interfacial length associated to the topography as function of bump height and width (blue dot is the simulated case taken into account for our experiments). (c) Scheme illustrating the chain stretching effect due to the 1st layer topography.

This excess interface with respect to a flat surface was evaluated for each lamellar periodicity studied during this work (*Figure 82.b*), and increases with the bump height h and decreases with the bump width w .

In the case of an interfacial treatment of the line & space pattern by PMMA- or PS- affine RCPs, an energetic gain is obtained when the affine block registers on top of the bump, due to an excess of affine area. However, this configuration generates chain stretching in the vicinity of the topographical pattern as shown in *Figure 82.c*, resulting in an energy penalty. Interestingly, this stretching penalty is completely relieved in the case of an orthogonal arrangement of the BCP domains of the 2nd layer (the substrate curvature is orthogonal to the BCP chains) which is experimentally obtained for a neutral interfacial treatment (formation of the orthogonal grid pattern after ashing).

These two antagonistic energetic contributions were evaluated using a Matlab code developed for the establishment of the orientational phase diagram of lamellar structures (see *Chapter III.2.A.ii/* for the model and *Annex 3.F/* for the Matlab code) taking into account the topographical field induced by the 1st immobilized BCP layer. Here we chose a patterned substrate corresponding to the L_{28} experimental case, i.e. a line & space pattern with a 28 nm periodicity and a 5 nm bump height (blue dot on the *Figure 82.b*). Besides, we assumed that only chains at a height lower than twice the bump height are constrained by the stretching penalty; thus the chains at a distance higher than $2h$ are “relaxed” with $L_{free} = L_{flat}$, and the chains at a distance lower are stretched from L_{free} to $L_{str} = (L_{flat} + L_{bump})/2$.

Finally, all possible orientations of the two layers were calculated leading to an orientational phase diagram shown in *Figure 83*. The orientational phase diagram is composed of two in-plane regions for strongly PMMA- or PS- affine interfacial layer compositions (not experimentally study) and one out-of-plane window divided in three different configurations depending of the affinity of the “near-neutral” layer, i.e. orthogonal to the topographical substrate (fully neutral case) or parallel to the topographical substrate with either PMMA or PS domains registered above the Al_2O_3 lines. The results are in full agreement with the experimental observations previously obtained on such stacked lamellar systems.

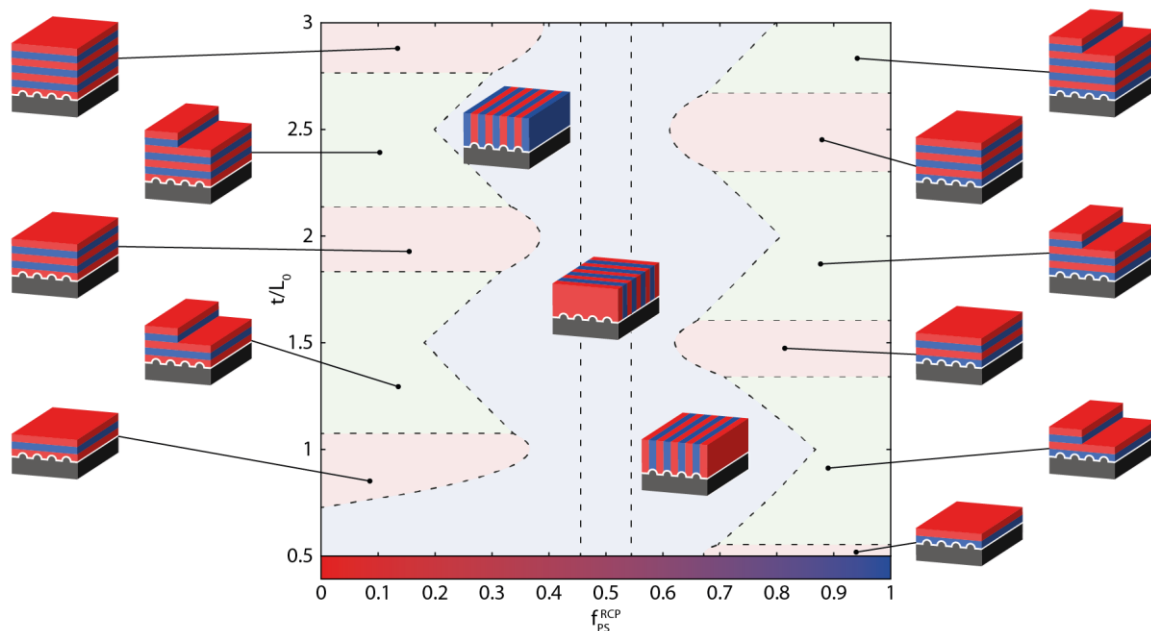


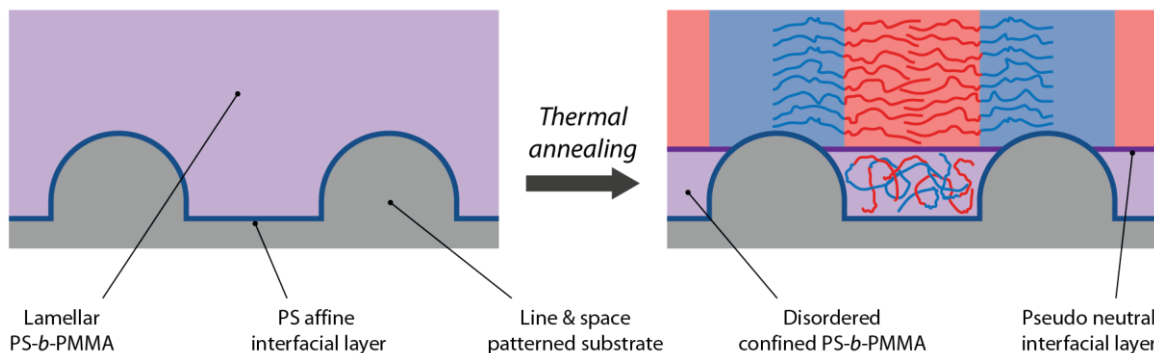
Figure 83. Theoretical phase diagram of the orientation of lamellae as a function of the RCP composition and film thickness on a patterned substrate with lines having the same periodicity than the second lamellar layer, and 5 nm height. Blue, red and green areas are the out-of-plane, in-plane and island/hole structures, respectively. (PS is in blue, PMMA is in red)

Interestingly, the overall structure of the phase diagram is not modified compared to the one obtained for a flat substrate (see *Chapter III/Figure 53*), with the same localization of the transitions between the out-of-plane, in-plane and island/hole windows. This means that the substrate patterning has a strong impact only for out-of-plane structures by orientating them orthogonally or collinearly, and does not increase or decrease the out-of-plane stability region. This can be understood as the energetical cost for chain compression above the bumps related to the in-plane configuration is lower than the affine interfacial energetical contribution for extreme values of f_{PS}^{RCP} .

This model qualitatively explained the self-assembly behavior visualized for two stacked L_{28} layers, but its generalization to other stacked configurations is difficult. Indeed, it is based on the comparison of energetical costs for each possible configuration which accordingly have to be preliminary defined to be simulated. Thus, it requires to be able to identify all these configurations, which was rather simple for the L_{28} - L_{28} case based on geometrical arguments. Nevertheless, it would be rather tedious for more complex layering configurations such as the ones with a hexagonal symmetry. Besides, an orthogonal configuration window between two collinear ones is retrieved by simulation only if the bump height is lower than 5.5 nm, and for higher values, the whole out-of-plan window has an orthogonal configuration. The experimental bump height measured with AFM is ≈ 10 nm (see *Chapter III/Figure 57*), which means that this model might be too simplistic to be quantitatively used as it lays on a strong argument related to the chain compression / stretching.

IV.3.B.ii/ Pseudo-chemical epitaxy via the disordering of PS-*b*-PMMA chains induced by a strong spatial confinement

For affine interface, the parallel orientation can also be explained by supposing that some confined PS-*b*-PMMA chains of the 2nd layer are trapped in a disordered state within the topographic space created by the line & space pattern from the 1st layer (*Figure 84*). This mechanism leans on the close to neutrality surface energy of PS- and PMMA- affine interfacial layers, and the low segregation strength of PS-*b*-PMMA (small χ), leading to possible disordered trapped chains. Indeed, both theoretical and experimental works have reported a drastic increase of χN value for the order-disorder transition upon confinement for a ratio between the spatial confinement size and the polymer gyration radius of around 1.4~1.5 [20], [21]. Thus, for a given χN , reaching a ratio lower than this value means that the BCP is disordered within the confinement walls. In the L_{28} - L_{28} , the trench width is half the period, around 14 nm here, and the R_g of this BCP is approximately 10 nm, giving a ratio of ~ 1.4 which effectively corresponds to a disordered state. Thus, a pseudo perfectly neutral interface toward the PS and PMMA domains is generated between the Al_2O_3 lines, while a weakly preferential coating is still present above them due to the RCP grafting. Accordingly, a self-assembly mechanism driven by chemical epitaxy occurs, leading to an energetical gain for the collinear configuration between the two line & space patterns as shown in *Figure 84*, since a domain is facing an affine interface and the other a neutral one.



*Figure 84. Schematics of the responsive layering mechanism based on the disordering of PS-*b*-PMMA chains inside the topographic spaces created by the line & space pattern from the 1st layer. Such mechanism leads to a collinear stacking of both line & space patterns for lamellar BCP with the same periodicity. The example shows the case where the interfacial layer is PS-affine, leading to the registration of PS lamellae on top of Al_2O_3 lines of the 1st layer.*

For perfectly neutral interface, the collinear orientation does not generate an energetical gain since both domains wet neutral interfaces (either from the grafting of the RCP on the top of the Al_2O_3 lines or from the disordering of the PS-*b*-PMMA inside the topographic pattern). Thus, the most stable configuration is the orthogonal orientation of the two line & space patterns, as no chain stretching is involved in this configuration. As opposed, this pseudo-chemical epitaxy

mechanism (based on the balance between the energy cost related to the confinement of disordered BCP chains and the energy gain linked to the registration of the affine domains above the Al₂O₃ lines) should lead to a collinear arrangement of the line & space patterns for slightly affine modification of the Al₂O₃ lines, as observed experimentally. Obviously, a switch to in-plane orientation of the 2nd lamellar structure should occur for an interfacial modification with strongly affine materials (not experimentally studied here).

Interestingly, this mechanism is not dependent of the height of the topographic pattern created by the immobilization of the 1st BCP layer, but only on the pattern shape. Indeed, the configuration of the top BCP layer is only dictated by the maximization of the relative surface areas between the affine block and the alumina pattern with respect to the neutral layer between the alumina pattern.

IV.3.B.iii/ Dissipative Particles Dynamics (DPD) simulations

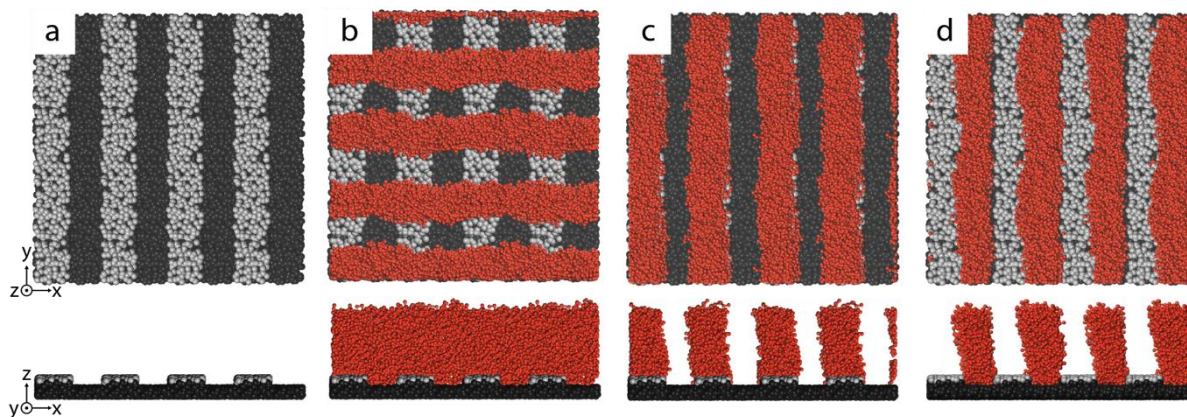
In order to strengthen the results obtained from the rather simplistic description of the BCP behavior on top of a corrugated substrate, dissipative particles dynamics (DPD) modeling can be employed [9], [22]. In DPD simulations, dynamic and rheological properties of BCP chains can be simulated in which the chains are simplified into linear connected beads (every bead represents a group of repeating units). In our case, the physical reduced parameters of the beads (for instance the distance between them, modeled as a harmonic oscillator, called harmonic bond) were chosen to mimic either PS or PMMA, and the BCP architecture was then generated by connecting the appropriate amount of each bead, e.g. 10 beads of PS with 10 beads of PMMA for a lamellar BCP. In DPD, in addition to the harmonic bond between the polymer beads, the interaction between every bead is described as a repulsive force. The repulsion between PS and PMMA beads is set as the maximum repulsion in the system while similar beads are characterized by a minimum one.

To perform the simulation and observe the self-assembly behavior, a periodic 3D box is generated with a high-density impenetrable substrate at the bottom and a “flexible” air layer at the top based of unconstrained single beads. Then, a determined number of bead-shaped BCP chains is randomly introduced between the substrate and the air taking into account the overall density of the system. The bead-shaped BCP chains are let to interact in presence of thermal fluctuations and drag forces with specified repulsion energies between them, the substrate and the air. After a sufficient reorganization time, the BCP chains self-organize to a final configuration.

By adding a topography to the substrate (gray beads in *Figure 85.a*) and by changing the repulsion energies between the PS and PMMA beads with respect to the substrate, it is possible to

mimic the stacking process for different interfacial affinity. This was made for lamellae stacked on top of a line & space patterned substrate for 3 different substrate-polymer interactions (*Figures 85.b-d*):

- The same interaction parameter (i.e. no specific repulsive interaction, mimicking the neutral case), resulting in a orthogonal orientation between the layers (*Figure 85.b*);
- The same interaction parameter on the pattern depressions between the substrate and both PS and PMMA domains (i.e. neutral), and a higher repulsive value for PS beads on the pattern heights with respect to the PMMA beads (i.e. PMMA-affine), resulting in the registration of the PMMA domains on top of the pattern bumps (*Figure 85.c*);
- The same interaction parameter on the pattern depressions between the substrate and both PS and PMMA domains (i.e. neutral), and a higher repulsive value for PMMA beads on the pattern height with respect to the PS beads (i.e. PS-affine), resulting in the registration of the PS domains on top of the pattern bumps (*Figure 85.d*).



*Figure 85. Top (top panel) and side (bottom panel) views of (a) a simulated grooved substrate with the topographic line & space pattern created by the immobilization of the 1st BCP layer (the lines are in gray), covered by commensurate PS-*b*-PMMA lamellae (PMMA domains in red, PS domains were removed for clarity) with (b) neutral interface, (c) PMMA-affine interface and (d) PS-affine interface. The images are the result of the concatenation of 4 times the same simulated box.*

These simulations are coherent with the experimental observations, which strengthen our understanding of the interplay between interfacial modulation and self-assembly by “responsive layering”. Interestingly, this model is close to the pseudo-chemical epitaxy mechanism exposed in the previous paragraph, as the small affine bumps (grey beads) on top of a neutral substrate (dark beads) represent the Al₂O₃ lines & space pattern filled with confined disordered PS-*b*-PMMA chains.

This work was performed in collaboration with the Dr. Pablo Argudo, a post-doc in the group, and is still on-going for the other structures, with very promising results.

IV.3.C/ Stacking of two lamellar BCP layers with different periodicities

Until now, the study was limited to the stacking of two L_{28} layers with the same periodicity. Nevertheless, it is possible to form lamellar structures with different periodicities by increasing the overall degree of polymerization of the BCP. However, the control of the self-assembly (correlation length of the structure, stability of the out-of-plane lamellar region) is more difficult for these high periodicities. As observed in *Chapter III*/, higher BCP film thickness (around 160 nm) seems to be mandatory in order to achieve a proper self-assembly for the higher probed periodicities. This restricts the use of the lamellar structures with high periodicity to the 1st layer as the final ashing treatment leads to a collapse of the bilayer arrays when thick films are employed for the 2nd layer. We decided thus to only generate bilayer structures with L_{24} or L_{28} as top layer.

IV.3.C.i/ Mesh formation with tunable sizes

For the general case, i.e. random ratio between the two layer periodicities, e.g. L_n and L_m , the only configuration that presents a remarkable symmetrical structure is the orthogonal one. Indeed, the parallel orientation will create a moiré pattern with a $n \times m$ periodicity, which cannot be energetically stable if n/m ratio ($n > m$) is not an integer. Indeed, in this case, the fundamental domain of the line pattern will be drastically higher than the two initial layer patterns. Also, within the moiré pattern, there are plenty of stacking configurations of the second layer that are not perfectly registered, i.e. leading to an energetical gain.

Consequently, a neutral interface was used for the stacking of L_{28} above each thick layers with higher periodicity, L_{32-t} to L_{56-t} to target the orthogonal orientation. The same standard process was performed, with a final ashing step of 4 min. The resulting SEM pictures (*Figures 86.a-e*) showed well-ordered rectangle meshes, which is consistent with the expected configuration observed with L_{28} bilayer stacking. The structure symmetry analysis of these rectangular meshes gives a p2mm 2D wallpaper group [13].

As observed with the L_{28} - N_L - L_{28} case (*Figure 78.a*), each configuration leads to a grid pattern, with large areas presenting arrays with an angle close to 90° between both layers (see third row of *Figure 86*). Such stacking configuration allows the formation of a rectangle pattern with characteristic dimensions related to the two BCP periodicities.

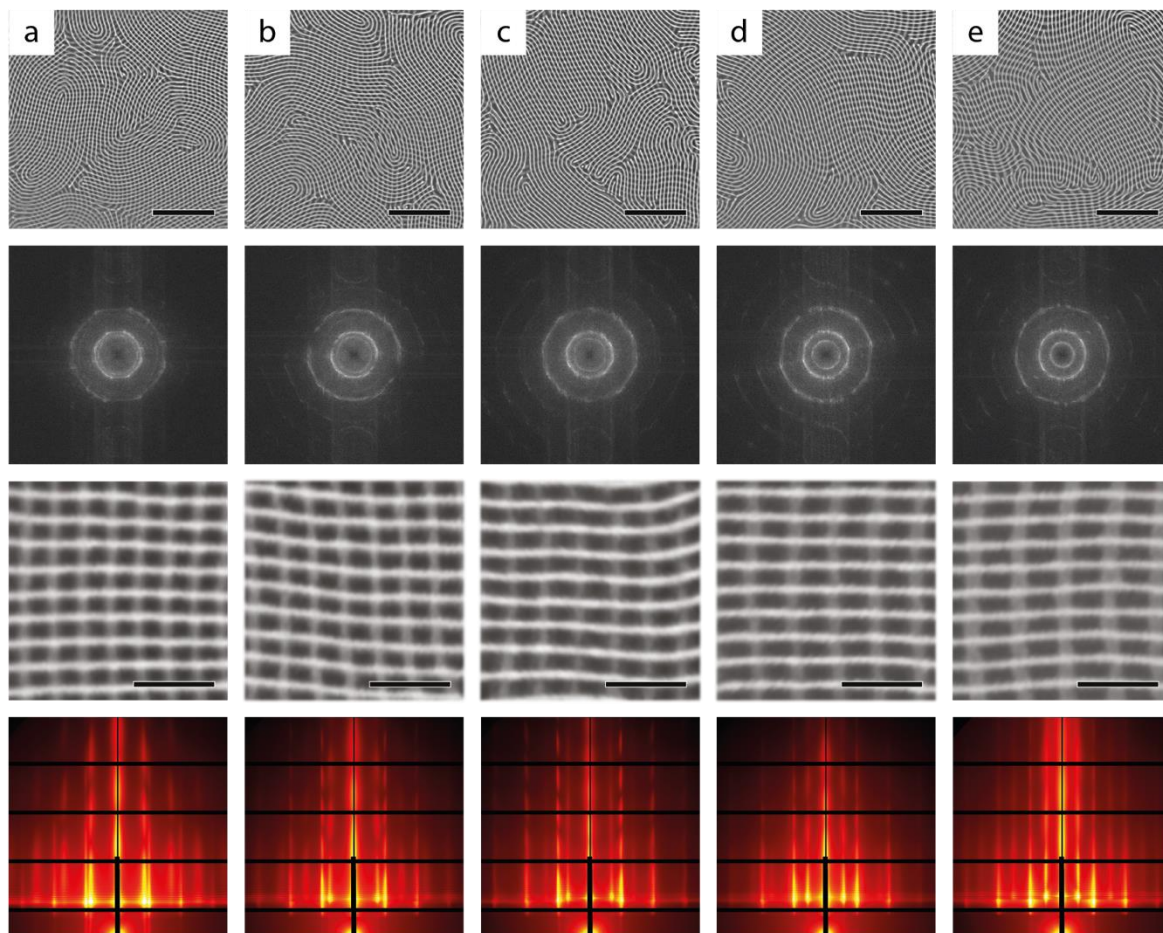


Figure 86. SEM images of nanomeshes formed by the stacking of L_{28} on top of (a) L_{32-t} , (b) L_{37-t} , (c) L_{42-t} , (d) L_{48-t} and (e) L_{56-t} . First row: low magnification SEM images (scale bars: 500 nm), second row: associated FFTs, third row: zoomed areas displaying a “perfect” orientation (scale bars: 100 nm), and fourth row: corresponding GISAXS patterns.

The GISAXS patterns are in perfect accordance with the SEM images, with intense Bragg rods along q_y positioned at two characteristic sequences $q_y/q^* = 1, 2, 3$ for q^* that can be associated to the first layer and the second layer periodicities as detailed in Table 14. Interestingly, the characteristic size of both layers is not disturbed by the stacking process as it is possible to retrieve the ratios between the periodicities of both structures.

Configuration	q^*_1 (nm ⁻¹)	$L_{0,1}$ (nm)	q^*_2 (nm ⁻¹)	$L_{0,2}$ (nm)	q_y/q^*_1	q_y/q^*_2
L_{32-t} - N_L - L_{28}	0.189	33.2	0.223	28.2	1, 1.99, 3, 3.97	1, 2, 3
L_{37-t} - N_L - L_{28}	0.167	37.6	0.222	28.3	1, 1.99, 3.02, 3.98	1, 2, 2.99
L_{42-t} - N_L - L_{28}	0.154	40.8	0.222	28.3	1, 1.99, 2.90	1, 2.01 , 3
L_{48-t} - N_L - L_{28}	0.126	49.9	0.222	28.3	1, 2.01, 3.02, 4.02	1, 2, 2.98
L_{56-t} - N_L - L_{28}	0.113	55.6	0.224	28.0	1.01, 1.98 , 3.01, 3.96 , 4.97, 5.93	1, 2, 2.99

Table 14. Bragg rod positions obtained from GISAXS patterns for different orthogonal meshes produced by the stacking of two layers of lamellar PS-*b*-PMMA with different periodicity and a neutral interface between them. The ratios in bold are the ones that are shared between both lamellar structures.

Interestingly, we can notice on the GISAXS patterns a small shift of the position of the Yoneda band for the 1st and the 2nd layers. This shift is linked to the height difference (in the z direction) of the layers in the stacked structure. Nevertheless, the GISAXS pattern can be decomposed as the sum of the two individual GISAXS patterns obtained for a unique layer. Unfortunately, no specific signals related to a perfect orthogonal stacking was observed due to the “polycrystalline” nature of the grid pattern at larger scale.

Combining such strategy for the formation of nanomeshes with directed self-assembly methods could lead to the generation of perfectly ordered nanomeshes, with a very precise control over the feature size, i.e. from 24 nm to 56 nm by using the library of PS-*b*-PMMA used in this study. Such grid arrangement could have very interesting optical properties, which will be further discussed in the *Chapter V*.

IV.3.C.ii/ Specific case of 2:1 periodicity ratio

Within the range of available periodicities for the stacking of line & space structures (L_{24} to L_{56}), the 2:1 specific ratio is particularly interesting as it would not result in the formation of a random moiré-like structure for non-neutral interfacial layers. Indeed, two layers with this particular ratio can obviously produce a rectangular nanomesh array, as shown for the L_{56-t} - N_L - L_{28} in *Figure 86.e*, but could also lead to two different structures: the PMMA domains are registered either on each edge of the underlying Al_2O_3 lines (*Figure 87.b*) or on top and between the underlying Al_2O_3 lines (*Figure 87.c*). Interestingly those two structures belong to the $p1m$ line group, with a fundamental domain that includes a mirror line.

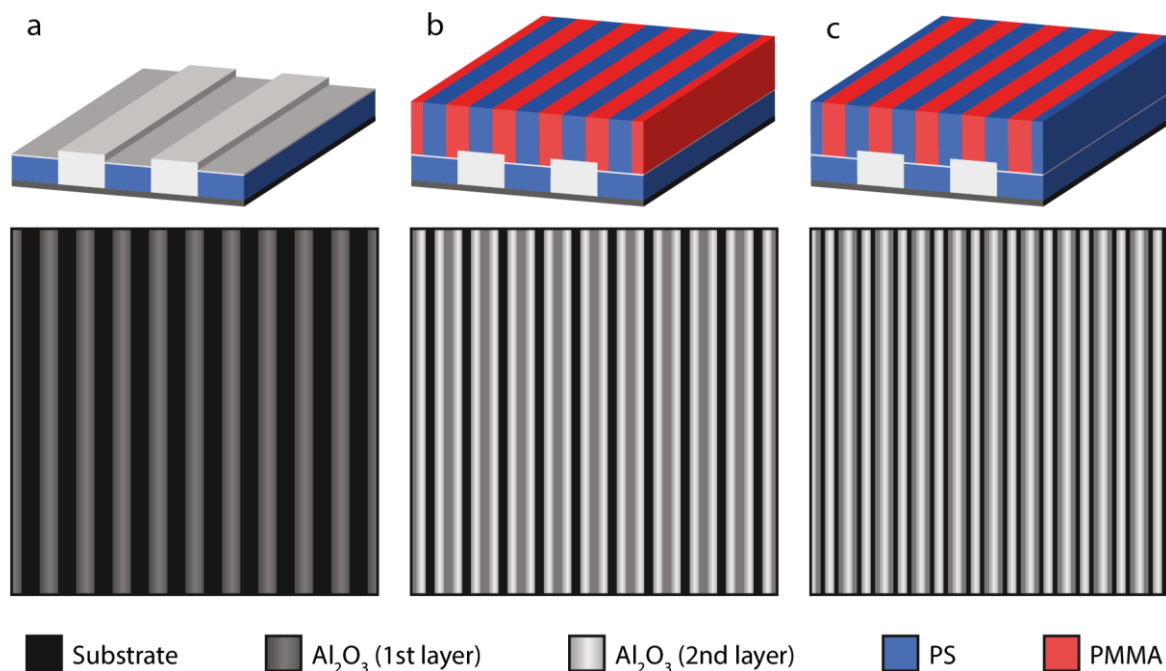


Figure 87. 3D schematics of (a) the line & space pattern produced after hybridization of a large lamellar PS-*b*-PMMA, stacked with a collinear arrangement of a smaller lamellar PS-*b*-PMMA pattern (of half the periodicity) registered with PMMA domains (b) on top of the Al_2O_3 line edges and (c) on top and between the Al_2O_3 lines. The bottom schemes show the expected idealized top view SEM images.

The difference between these two arrangements is clear: either the PMMA or the PS domains of the 2nd layer are registered at the edges of the underneath Al_2O_3 line & space pattern. For this very specific 2:1 ratio, arguments based on the pseudo-chemical epitaxy mechanism cannot help us to predict the resulting layered structures as both the PS and PMMA domains of the 2nd layer are in contact with the same surface area of the Al_2O_3 pattern. However, with the asymmetric surface hypothesis, the produced structure would depend on the surface area between the domains registered on top of the bumps and the domains registered on the edge of the bumps. Here, the line & space pattern is large leading to the $w \geq 2h$ case from Figure 82.a. With this topographic model in mind, additional surface area is created near the edges of the bumps. Thus, the configuration depicted in Figure 87.b is expected for a PMMA-affine layer, while the configuration of Figure 87.c is expected for a PS-affine layer.

Experimentally, both cases were observed by stacking L_{24} on top of L_{48-t} with either S_L or M_L surface modification, leading to the two different predicated configurations. For the PMMA-affine case (Figure 88.a), the PMMA domains are registered on each edge of the underlying Al_2O_3 lines, leading to the structure predicted in Figure 87.b. Conversely, for the PS-affine case (Figure 88.b), the PMMA domains are registered on top and between the underlying Al_2O_3 lines, leading to the structure predicted in Figure 87.c. The overall quality of the resulting structures is low due to the ashing treatment that induces the narrow lines situated at the top to collapse during ashing

(due to their small widths, here 12 nm). Importantly, the results are coherent with the asymmetric surface hypothesis as explained previously.

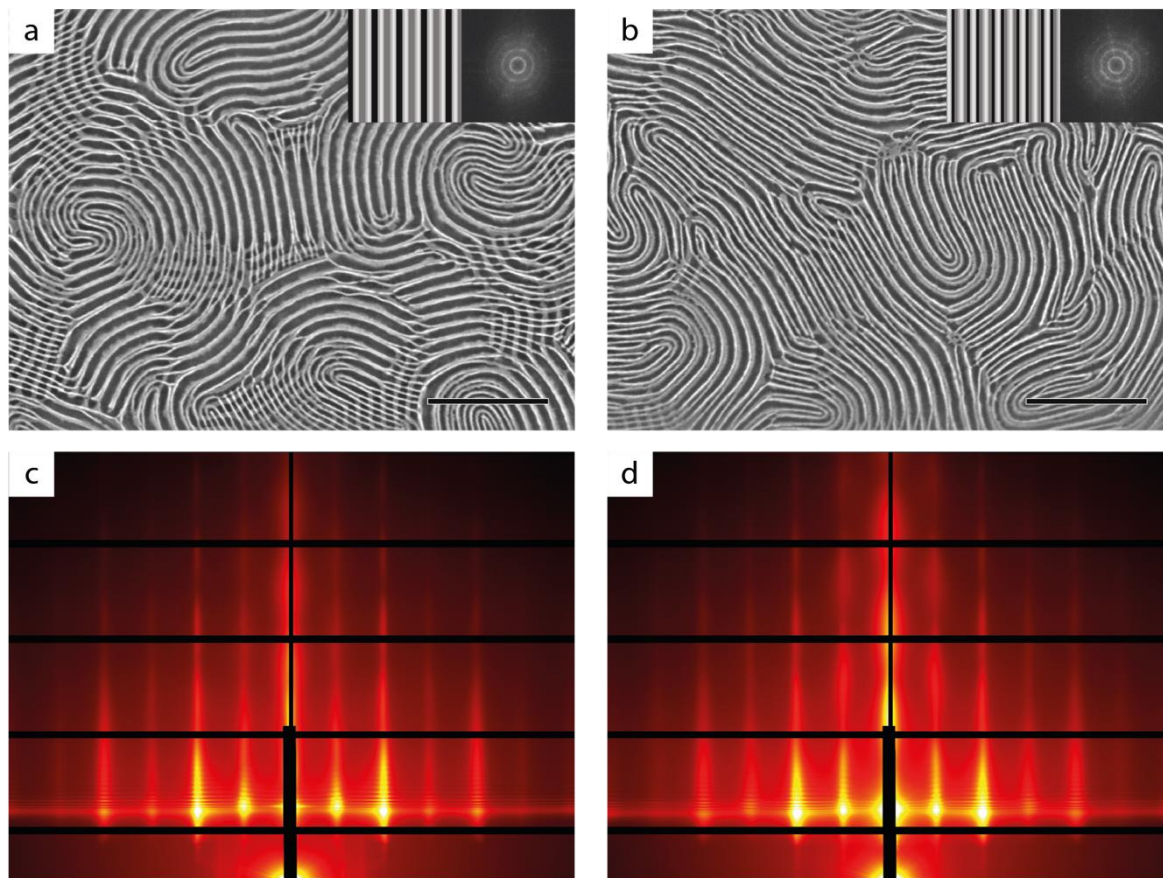


Figure 88. (top) SEM images and (bottom) corresponding GISAXS spectra of ashed L_{24} hybridized layer on top of a L_{48-t} layer with (a,c) PMMA-affine surface modification, M_L , and (b,d) PS-affine surface modification, S_L . Top right insets are the idealized structures and FFTs. Scale bars: 500 nm.

For both structures, the GISAXS patterns present intense Bragg rods localized at the characteristic positions for line & space pattern, i.e. $q_y/q^* = 1,2,3,4,5$, with higher intensity for first and fourth rods as compared to the others as they are associated with scattering events for both the large and small lamellar patterns (Figures 88.c-d). Indeed, for a particular 2:1 ratio between the periodicities of both layers, the 1st (2nd) Bragg rod of the L_{24} layer is positioned at the same position that the 2nd (4th) Bragg rod of the L_{56-t} layer. The analysis of the peak positions of each pattern confirms the periodicities of the large and small line & space patterns (i.e. $L_0=49.7$ nm for the large periodicity and $L_0=24.8$ nm for the small periodicity). No difference between the two configurations were noticed, except for sharper Bragg rods in the PMMA-affine pattern case, certainly due to a lower extent of lamellae collapsing. Indeed, for this case, the small top lines are positioned on the edges of underneath Al_2O_3 lines, while for the other case, half of the small lines are positioned between them, i.e. on PS surface passivated with 1 nm alumina, which breaks during ashing. Thus, the small top lines are obviously more prone to collapse when the material below them is getting etched (i.e. above PS), compared to the opposite case (i.e. above alumina).

IV.4/ Hierarchical nanostructures by stacking two layers with a hexagonal symmetry

A second type of commensurate stacking between BCP layers can be obtained by using BCP structures with a hexagonal symmetry, i.e. hexagonal packed cylinders for a di-block architecture. As shown previously, such BCP structures in thin films can lead to either dots (PMMA cylindrical structure) or holes (PS cylindrical structure) through a subsequent immobilization of the nanostructured thin films by SIS. Contrarily to the limited number of stacked configurations for L-L stacking as explained from symmetry considerations (i.e. either 1D symmetry in the case of a collinear stacking or 2D grids in the case of orthogonal stacking), the stacking of two 2D hexagonal structures can produce a plethora of 2D periodic structures, which in the case of responsive layering, will produce remarkable symmetrical structures with specific ratio between the stacked structure periodicities. Since BCP self-assembly can generate two different hexagonal structures, i.e. the dot and hole arrays, it is possible to perform four different stacking configurations, which are dot-dot (D-D), hole-hole (H-H), dot-hole (D-H) or hole-dot (H-D). However, the analysis by top view SEM requires that the top layer has a lower alumina coverage with respect to the bottom layer in order to fully decipher the stacked configuration. Thus, the D-H case was not studied during this Ph.D., but the conclusions made for the three other cases could be easily transposed to this case. For the same reasons, the study was performed with the BCP layer of the highest periodicity as the 1st layer.

IV.4.A/ Expected configurations between the two stacked hexagonal patterns

As explained in *Chapter III/ Figure 68.b*, there are 5 different ratios experimentally achievable between the two BCP periodicities which could geometrically generate a commensurate stacking between the two hexagonal patterns, and thus would produce remarkable patterns with high symmetry unit cell. It is possible to inventory all the geometrically stable structures which might be experimentally reachable according to several parameters:

- The ratio between the structure periodicities: 1:1, $2/\sqrt{3}$:1, 3/2:1, $\sqrt{3}$:1 and 2:1;
- The relative rotation angle between the two stacked layers: 0° or 30°;
- The type of building bricks used to generate the stacked structure: D-D, H-H or H-D;
- The registration of the second layer pattern with respect to the bottom layer pattern: PMMA (dots) or PS (holes) cylinders of the top layer can be either registered above the Al₂O₃ pattern (called in the following text “above” registration), or in the interstices of the Al₂O₃ pattern (called in the following text “between” registration) or at the edges of the Al₂O₃ pattern (called

in the following text “edge” registration). It can also be a combination of these configurations depending of the periodicity ratio.

It is noteworthy that the ratio between the layer periodicities and the relative rotation angle between layers are related: for ratios equal to 1:1, 3/2:1 and 2:1, a remarkable 2D wallpaper (i.e. high symmetry group) with small fundamental domain is produced only if the angle between the structures is 0°, while for ratios equal to $2/\sqrt{3}$:1 and $\sqrt{3}$:1, the angle should be 30°. *Table 15* sums up the possible configurations for D-D stacking with the simulated sketches, the fundamental domains and the wallpaper groups. D-D stacking was chosen to display the resulting structures as they are the more self-explanatory with respect to the simulated sketches from H-H or H-D because of superposed patterns.

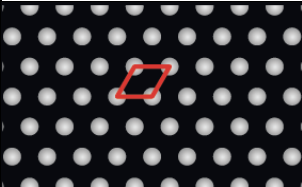
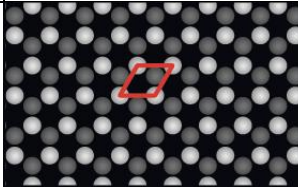
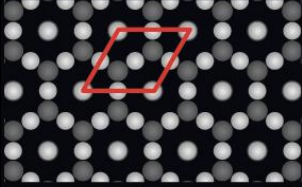
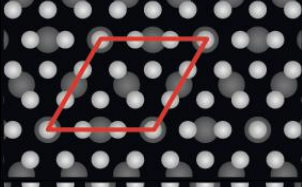
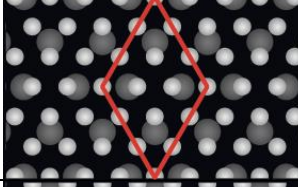
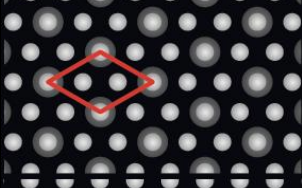
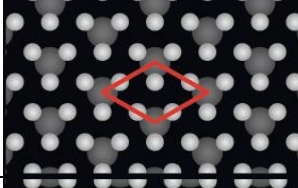
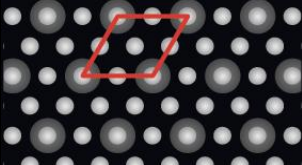
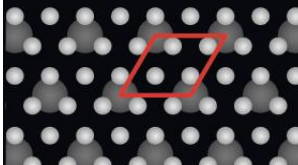
Ratio Angle	Stacking type Wallpaper group	SEM predicted image	Stacking type Wallpaper group	SEM predicted image
1:1 0°	Above p6mm		Between p3m1	
$2/\sqrt{3}$:1 30°	Above & Between p6mm			
3/2:1 0°	Above & Edge p6mm		Above, Between & Edge c2mm	
$\sqrt{3}$:1 30°	Above & Between p6mm		Edge p31m	
2:1 0°	Above & Between p6mm		Edge & Between p3m1	

Table 15. Schematics of 2D wallpapers obtained by stacking two layers of hexagonally packed dots with a given periodicity ratio and relative rotation angle between the two hexagonal patterns. Red lines specify the pattern fundamental domain, with rotation center and reflection axis from the wallpaper group.

With the asymmetric surface area model developed previously for the L-L stacking case, the most stable structures should be obtained if there is only one stacking type, i.e. “above”, “between” or “edge”, to avoid competition between energetical gains and costs from affine

surfaces. Also, the combination of “above” & “between” should be considered, as observed with the 2:1 ratio for collinear lamellar structures.

A systematic study for the three aforementioned cases, i.e. D-D, H-H and H-D, was performed to experimentally observe the stacking configuration for each ratio between the BCP layers and by varying the interfacial affinity between the two layers (i.e. neutral, PS-affine or PMMA-affine layers). In the following, we have restricted our analysis to the most remarkable cases, for which we have been able to obtain robust experimental results (i.e. low defectivity of the stacked structures).

IV.4.B/ Stacking of two dot patterns (D-D)

For this specific case, a particular attention should be paid to the ashing plasma step, as it can induce a collapse of the overall structure. Indeed, both the top and bottom layers are mechanically fragile since they are composed of disjointed dot arrays with no lateral cohesion. In order to reduce this phenomenon, different modifications of the common process were explored:

- The modification of the ashing process to reduce the plasma harshness (in particular the isotropic physical plasma);
- An increase of the dot mechanical stability by performing a larger number of SIS cycles (3 or 4 SIS cycles instead of 2);
- A reduction of the height of the dots (i.e. by a reduction of the BCP film thickness) which would require a shorter ashing duration in order to produce the final stacked structure.

The best results were obtained by reducing the thickness of the 2nd BCP layer through the increase of the spin-coating speed from 1500 rpm to 2000 rpm. As a consequence, the ashing step duration could be reduced to 3 min which prevents the collapse of the structure.

The first experimental parameter which was explored is the effect of the interfacial energy between BCP layers with the same periodicity. For that extent, we have simulated the top-view SEM image of a stacking configuration without registration between the two layers. The result is presented in *Figure 89*, in which multiple grains with different patterns are visible. Indeed, according to the angle between the BCP grains of both layers, several symmetrical structures can emerge. However, the majority of these structures present a subsequent higher fundamental domain size compared to the ones from both layers, and have all three stacking types, i.e. “above”, “between” & “edge”. Thus, even if some of these structures might seem highly symmetrical and remarkable, it seems very unlikely to observe them all experimentally if a proper “responsive layering” process occurs, except for the two most symmetrical structures expected in the *Table 15*, which are also present in this random image.

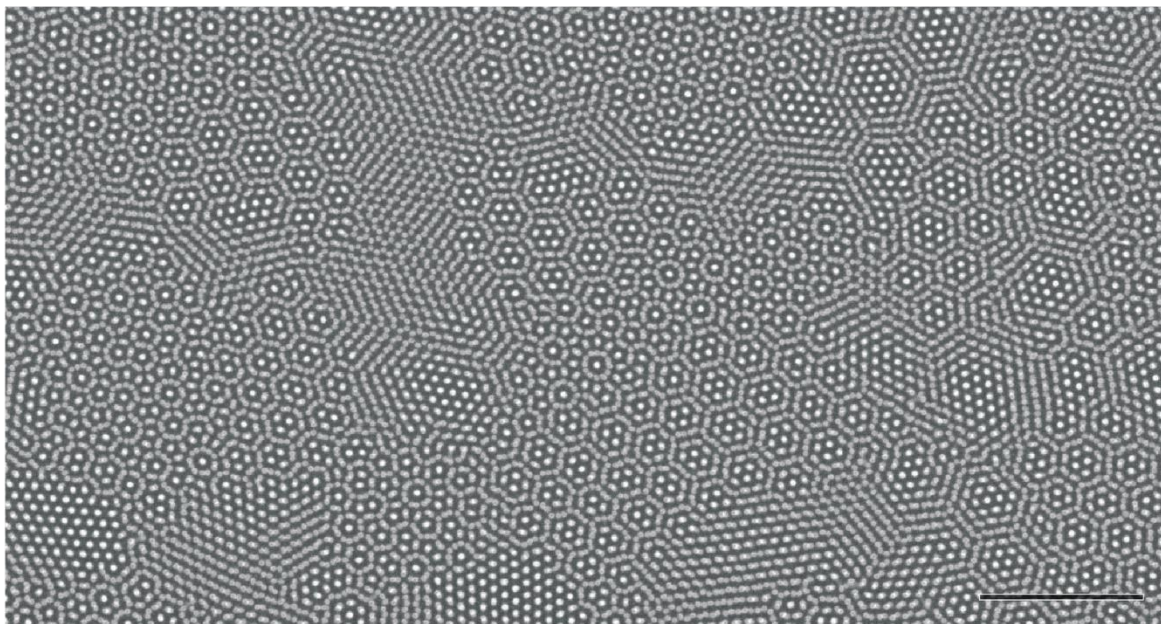


Figure 89. Simulated D_{37} - D_{37} random stacking configuration made by overlaying the same D_{37} SEM image with a random rotation angle between them. Scale bar: 500nm.

Experimentally, two layers of D_{37} were stacked using the process described above, using N_D , M_D or S_D surface modification, and then gently ashed to prevent the collapse of the top dots. The top-view SEM images resulting of the various stacking configurations are shown in *Figures 90.a-c*, with the associated GISAXS patterns in *Figures 90.d-f*.

The differences between these three SEM images evidence a potential “responsive layering” process and the importance of the interfacial energy between the two stacked layers. In the case of a neutral interfacial layer, the simulated and experimental images (*Figure 89* and *Figure 90.a*) are quite similar even if the experimental one presents many defects due to the collapse of the dot pattern during the ashing step. This behavior means that a random relative rotation angle between both layer grains is observed, without one unique structure that would be more stable. Thus, for a fully neutral layer, the topographical constraints are not enough to induce a preferential layering, i.e. responsive layering, which was yet proposed as a mechanism to explain the results obtained by Rahman *et al.* [6].

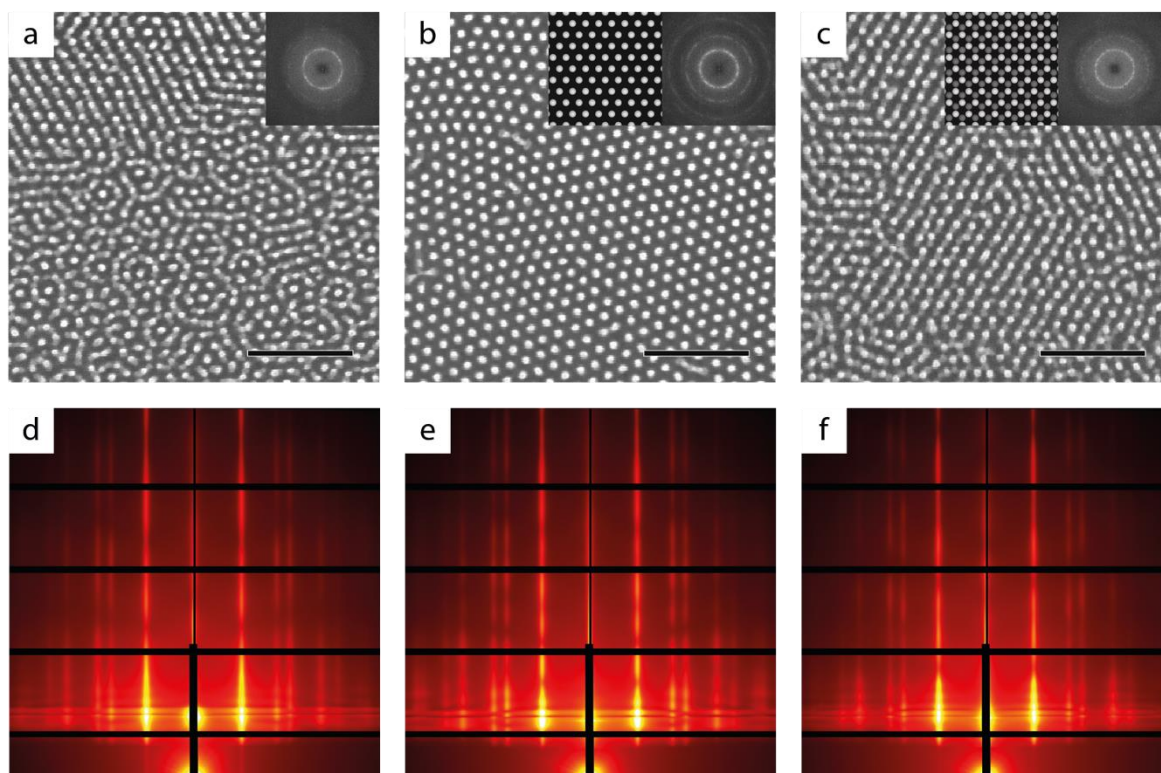


Figure 90. (top) SEM images and (bottom) corresponding GISAXS patterns of two stacked D_{37} layers with (a,d) N_D neutral layer, (b,e) M_D PMMA-affine layer and (c,f) S_D PS-affine layer. Top right insets are the idealized structures and the FFTs of the SEM images. Scale bars: 250 nm.

For the PMMA-affine case, the structure is similar to a single dot pattern resulting for the self-assembly of a unique BCP layer. This means that “responsive layering” occurs in this case as a registration between the PMMA cylinders of the 2nd layer and the Al_2O_3 dots of the 1st layer is evident. This “above” stacking configuration is in perfect correlation with the pseudo-chemical epitaxy mechanism that would lead to an energetical gain for this particular type of stacking. Indeed, in this case, the PMMA domains are registered on top of the Al_2O_3 topographical pattern which is coated with a PMMA-affine layer, while the PS domains registered on top of the hollows are in contact with disordered BCP chains that behave like a neutral layer.

Finally, the PS-affine case exhibits a “between” stacking type, slightly different from the one expected from a purely symmetrical point of view: the PMMA cylinders of the 2nd layer are experimentally positioned in the vicinity of two underneath Al_2O_3 dots, while the arrangement leading to the highest symmetry would be in the vicinity of three Al_2O_3 dots. However, both stacking configurations are in accordance with the pseudo-chemical epitaxy mechanism. Indeed, the Al_2O_3 dots are in both cases fully covered with PS domains, for which an energetical gain is expected due to the PS-affine interfacial layer, while the Al_2O_3 pattern hollow part with the pseudo neutral energy due to disordered BCP chains will lead to the same interfacial energy cost whatever is the position of the PMMA cylinders.

The GISAXS patterns of the three stacking configurations (*Figures 90.a-c*) showed similar features with extended Bragg rods along the q_y direction. It is not possible to differentiate the stacking configurations from such patterns due the random orientation between grains of each layer leading to a “polycrystalline” overall structure. Nevertheless, we retrieved the same sequence $q_y/q^* = 1, \sqrt{3}, \sqrt{4}, \sqrt{7}, \sqrt{9}$ characteristic of a hexagonal packing. The extracted periodicity of the structure is $L_0=31.6$ nm, giving a 36.5 nm domain spacing, perfectly comparable to the D_{37} single layer.

A second interesting case based on the variation of the periodicities between the two layers for a neutral interfacial configuration was evaluated using the $2/\sqrt{3}:1$ and $3/2:1$ ratios (i.e. $D_{37}\text{-}N_D\text{-}D_{42}$ and $D_{32}\text{-}N_D\text{-}D_{42}$). Here the dot pattern with the largest periodicity was used as a top layer as it reduced the collapse of the structure during the ashing step. *Figures 91.a-b* show the resulting SEM images in good accordance with our predications based on symmetry considerations (see *Table 15*, “above” & “between” type for $D_{37}\text{-}N_D\text{-}D_{42}$ and “above” & “edge” type for $D_{32}\text{-}N_D\text{-}D_{42}$).

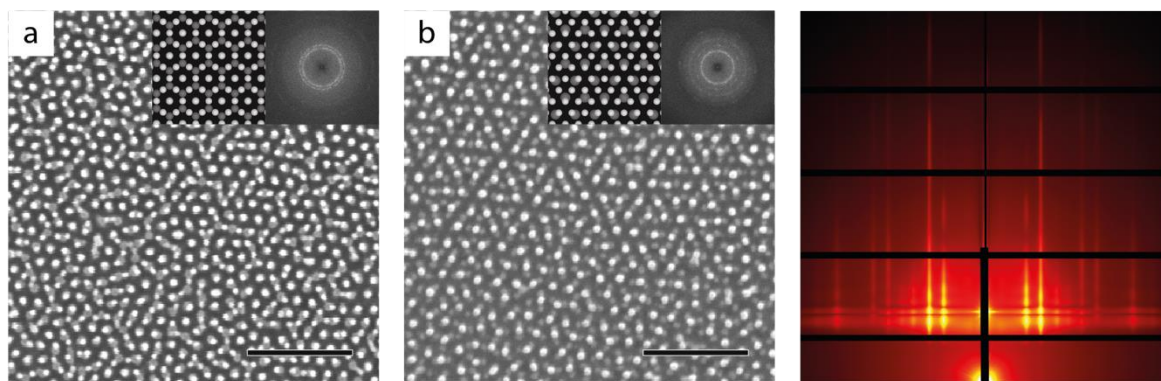


Figure 91. SEM images of (a) $D_{37}\text{-}N_D\text{-}D_{42}$ and (b,c) $D_{32}\text{-}N_D\text{-}D_{42}$, with (c) its GISAXS corresponding pattern. Top right insets are the idealized structures and the corresponding FFTs. Scale bars: 250 nm.

For the $2/\sqrt{3}:1$ ratio, the observed structure shows some similarities with the expected one based on geometrical packing considerations; however, the overall translational order is very weak. Effectively, within the wallpaper fundamental domain, it is possible to see that 1/3 of underneath dots are capped with PMMA cylinders and 2/3 with the PS matrix, meaning that both affine interfacial energy types are in competition. This uneven balance between both domains should tend to have a stabilization of the structure for PS-affine coating. However, the same stacking structures were found experimentally between the affine and neutral cases, meaning that this competition is too weak to drive the “responsive layering” mechanism. Thus, the resulting structure is closer to a random stacking.

As for the $3/2:1$ ratio, the same structures were also observed with the three interfacial configurations, but it is possible to clearly observe non negligible regions with remarkable

orientation between two layers corresponding to the expected structure. Nevertheless, the translational order of the structures is still weak which might be due to a low energetical gain from such stacking configuration with respect to a “random” one. Indeed, responsive layering is not occurring due to interfacial interactions since the three cases (neutral, PS-affine and PMMA-affine) led to the same results.

As for the GISAXS pattern, only the D_{32} - N_D - D_{42} structure that present somehow a responsive layering was analyzed (*Figure 91.c*), exhibiting the characteristic Bragg rods of two cylinder forming structures with a different periodicity. Indeed, it is possible to sort these peaks in two sequences of values positioned at $q_y/q^* = 1, \sqrt{3}, \sqrt{4}, \sqrt{7}$, with a first $q^*_1 = 0.172 \text{ nm}^{-1}$ giving a periodicity of 36.5 nm (i.e. a domain spacing of 42.2 nm associated to D_{42}), and a second $q^*_2 = 0.234 \text{ nm}^{-1}$ associated to D_{32} with a 31 nm periodicity. This GISAXS pattern exhibits the characteristic signals of the two monolayers.

More robust experimental results were obtained for a $\sqrt{3}:1$ ratio between the two layers (i.e. D_{56} on top of D_{32}) with the three different surface modifications. Interestingly, both predicted structures were obtained with a good translational order using M_D (*Figure 92.a*) and S_D (*Figure 92.b*) interfacial layers. For the PMMA-affine interfacial layer, the obtained structure is clearly of “edge” type leading to raspberry-like or planet-satellite nanostructures [23], which could have interesting optoelectronic properties [24]. This result is in accordance with the pseudo-chemical epitaxy mechanism as the majority of small PMMA domains are positioned on top of the Al_2O_3 large dots coated with the PMMA-affine layer. Interestingly, for a PS-affine interfacial layer, the “above” & “between” expected structure is obtained, with unfortunately some defects due to the collapse of the “between” positioned dots. In this case, every underneath alumina dots are effectively capped with a PMMA cylinder which is not in accordance with the pseudo-chemical epitaxy mechanism. However, by using the relative cylinder size compared to the periodicity obtained in *Chapter III.2.B.i/*, it is possible to estimate that the D_{56} and D_{32} radii are 14.8 nm and 8.6 nm respectively, leading to a surface area of 688 nm² and 232 nm². Thus, the percentage covered with PMMA is effectively 34% while 66% for PS, giving an interfacial energetical gain for the PS-affine coating, which make the result in accordance with the model.

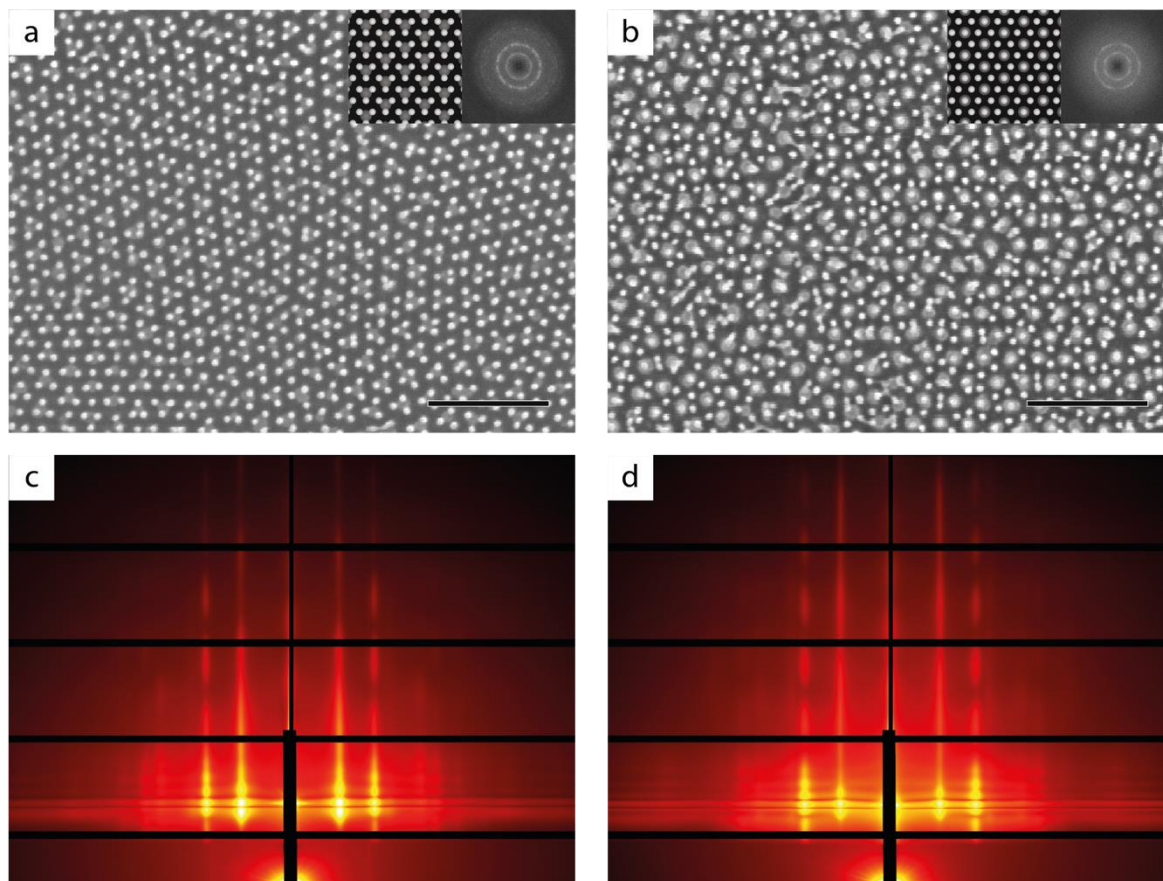


Figure 92. (top) SEM images and (bottom) corresponding GISAXS patterns of two stacked D_{56} - D_{32} layers with (a,c) M_D PMMA-affine and (b,d) S_D PS-affine layers. Top right insets are the idealized structures and FFTs. Scale bars: 250 nm.

It is noteworthy to mention that the same $1/3:2/3$ uneven balance between PS and PMMA interfaces was observed for the $2/\sqrt{3}:1$ ratio case, without any responsive layering. This difference cannot be explained with the pseudo-chemical epitaxy mechanism, and might be due to higher chain stretching and bending in the $2/\sqrt{3}:1$ ratio case inherent to a denser structure (closer periodicity between both layers).

The corresponding GISAXS patterns (Figures 92.c-d) showed Bragg rods characteristic of the hexagonal packing of the dots with a sequence $q_y/q_1^* = 1, \sqrt{3}, \sqrt{4}, \sqrt{7}, \sqrt{9}, \sqrt{12}$. The analysis of the peak positions leads to a cylindrical structure with a periodicity of 46.9 nm, i.e. a domain spacing of 54.1 nm associated to the D_{56} structure. Interestingly, the second peak of the sequence is way more intense than the one observed from the sole D_{56} structure. Effectively, this $q_2^* = \sqrt{3} \times q_1^*$ peak corresponds also to the first peak from a 31.8 nm cylindrical domain spacing which can be associated to the stacked. It is also possible to retrieve the sequence associated to the D_{32} hexagonal structure ($q_y/q_2^* = 1, \sqrt{3}, \sqrt{4}, \sqrt{7}$). Interestingly, the peak intensities linked to D_{32} are lower than the one observed from a D_{32} monolayer (see Chapter III/Figure 71). This is certainly

due to the registration of D_{32} pattern above a D_{56} pattern leading to a transfer of its weak translational order.

Finally, we were not able to obtain reliable results for the 2:1 ratio. This is due to poor self-assembly of the D_{64} layer as presented in the previous chapter. Our efforts to use a configuration based on D_{28} on top of D_{56} did not succeed due to the collapse of the small D_{28} during ashing. Nevertheless, it is very likely that the “above” & “between” stacking configuration would be obtained for a S_D interface modification taking in consideration the same argument than for D_{56} - S_D - D_{32} (i.e. a high dissymmetry of surface areas between PMMA and PS domains above the big dots, here 26% PMMA and 74% PS).

IV.4.C/ Stacking of two hole patterns (H-H)

For the stacking of two layers of holes, the ashing step is less problematic since the honeycomb Al_2O_3 matrix is more rigid. However, this configuration has an important drawback as the extended coverage of the honeycomb pattern can prevent the observation of the stacked configuration using top-view SEM. Experimentally, in this H-H case, the plasma time for the ashing step was increased to 5 min to “melt” both layers together, leading to a structure with the two patterns merged together which is easier for the top-view SEM image analysis.

As for L-L and D-D, the first study was performed by stacking two hole layers with the same domain spacing, here H_{37} , with the three different interfacial configurations, i.e. N_H , M_H and S_H . The produced structures were observed with SEM after ashing (*Figures 93.a-c*), and the GISAXS patterns are presented in *Figures 93.d-f*. Interestingly, the FFT of the SEM images showed well-defined discrete signals related to the high correlation length of the H_{37} grains as observed in *Chapter III/*.

The analysis of the SEM images leads to similar conclusions than for D_{37} - D_{37} stacking: a random registration for N_H , an “above” registration for M_H , and a “between” registration for S_H . It is noteworthy that these configurations are coherent with the pseudo-chemical epitaxy hypothesis: for instance, with a PMMA-affine layer, the matrix surrounding the holes is attractive to PMMA, while the holes are filled with disordered PS-*b*-PMMA chains resulting in a neutral interface. Thus, the PMMA domains “benefit” from a registration on top of the underneath honeycomb Al_2O_3 matrix, leading to PS cylinders registered on top of the holes of the 1st layer. Interestingly, for the PS-affine case, the predominance of triangular features proves that the holes of the 2nd layer are positioned at the interstices between three holes of the 1st layer. This behavior differs from the one previously observed for two layers of dots. Indeed, the structure registration in the case of hole-hole stacking is dictated by the position of PS cylinders, which have a maximized

interface with the PS-affine coated Al₂O₃ honeycomb pattern if they are placed between three holes. Indeed, if they are placed between two holes, the edge of the cylinder will be slightly aligned with the edge of the underneath hole. However, the area difference between both case is low, which is why it is possible to observe this second configuration in some areas (see the bottom left part of the *Figure 93.c*)

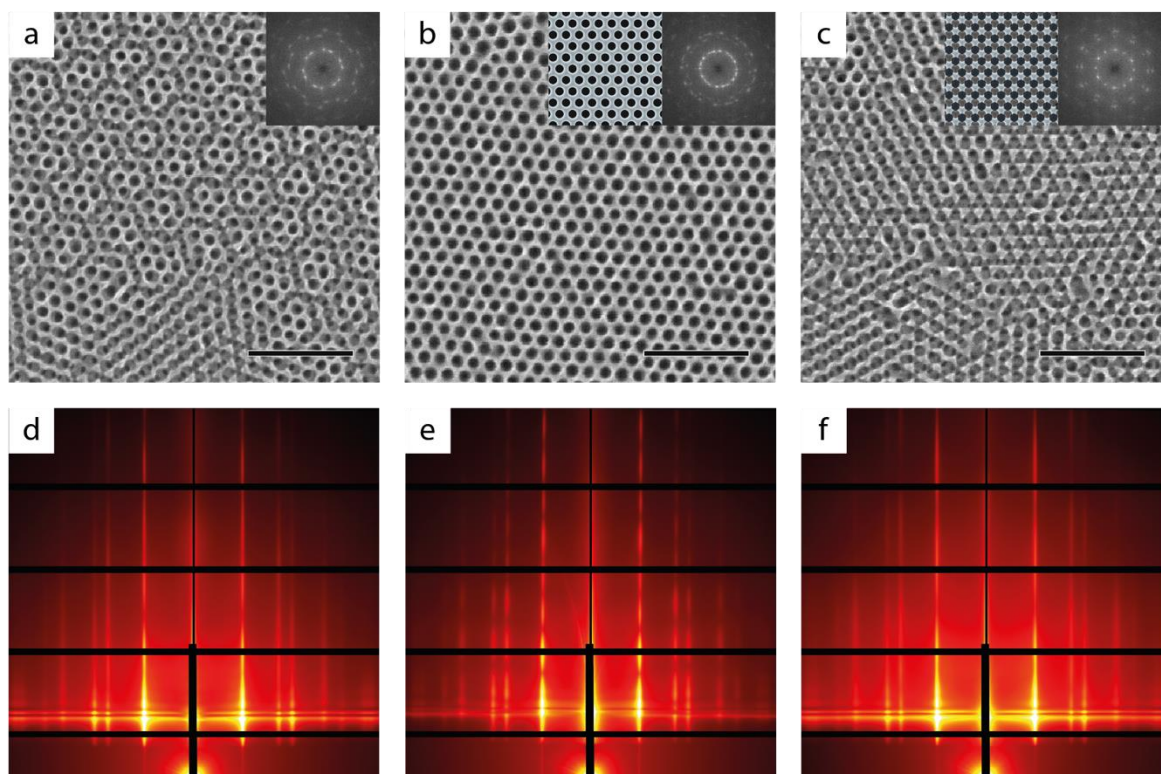


Figure 93. (top) SEM images and (bottom) corresponding GISAXS patterns of two stacked H₃₇ layers with (a,d) N_H neutral, (b,e) M_H PMMA-affine and (c,f) S_H PS-affine layers. Top right insets are the idealized structures and FFTs. Scale bars: 250 nm.

Each structure was analyzed with GISAXS (*Figures 93.d-f*), leading to three very similar patterns. Indeed, intense Bragg rods can be observed at the $q_y/q^* = 1, \sqrt{3}, \sqrt{4}, \sqrt{7}, \sqrt{9}, \sqrt{12}$ positions (i.e. characteristic of a hexagonal pattern), with the same $q^* = 0.205 \text{ nm}^{-1}$ corresponding to a 35.4 nm domain spacing. This value is exactly the same value measured for H₃₇ structure in a monolayer configuration.

A particular interest was given to the neutral modification, since it is possible to precisely observe the stacking configuration without the collapsing issue encountered for dots. A large field top-view SEM image is presented in *Figure 94*, highlighting the presence of several sub-structures. It is possible to colorize the SEM image into five different zones depending of the rotation angle between both layers. Accordingly, several stacking configurations appear to be more stable than others, even if the coexistence between these five structures underlines their close stability in term of energy.

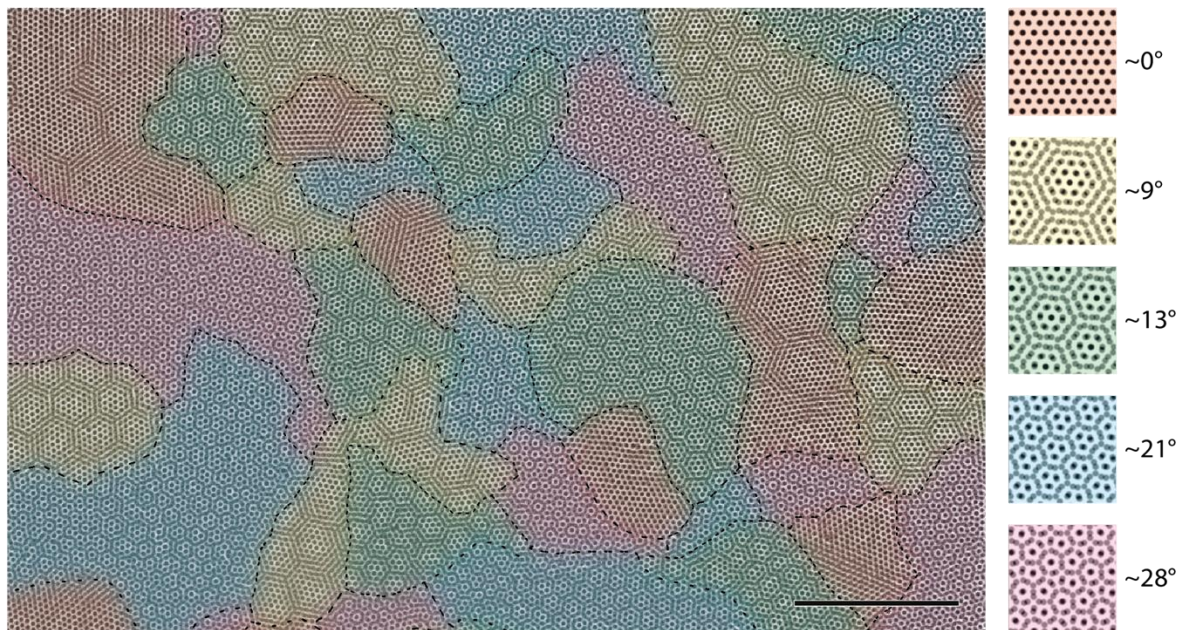


Figure 94. Experimental large SEM image of H_{37} - N_H - H_{37} , colored according to the rotation angle between both layers sorted following 5 main angle. Scale bar: $1 \mu\text{m}$.

A complementary study was performed to try to enhance the stability of a specific sub-structure observed experimentally by modifying several parameters (i.e. RCP composition to reach a non-perfect neutrality, second layer film thickness to modify the balance between interfacial and volume effects or the annealing temperature to unlock metastable energy wells). Unfortunately, we did not manage to fully stabilize a particular sub-structure by the tuning of these parameters.

A simulated image was generated by stacking two H_{37} SEM images with a random angle (Figure 95). Interestingly, it is possible to visualize the same interesting sub-structures. The similar overall shapes of both simulated and experimental images tends to prove that the orientation is effectively random. Effectively, the well-ordered sub-structures are produced by the stacking of two well-ordered grains from both layers, with a random angle, as observed with the grain boundaries from the simulated image. Indeed, these boundaries were created on both monolayers and were superposed, separating perfectly the new grains from the stacking. Finally, there is not any responsive layering in this case, which is consistent with previous stacking observed with neutral interfacial coating.

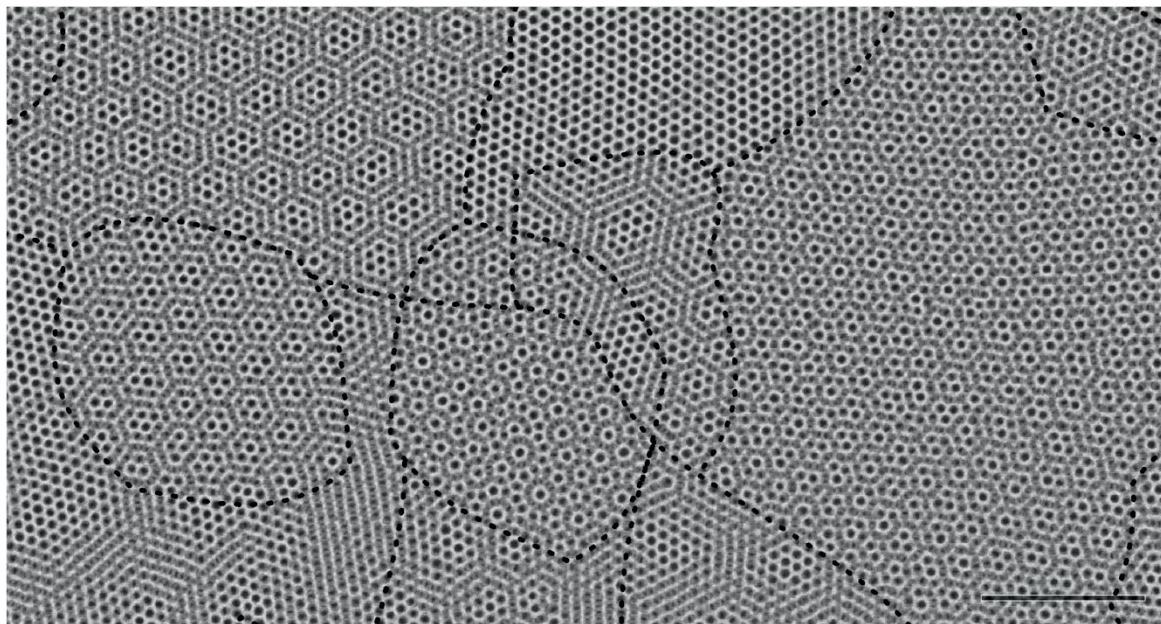


Figure 95. Simulated H_{37} - H_{37} random stacking made by overlaying twice the same H_{37} SEM image with a random rotation angle between them. Dot lines are the superposed grain boundaries obtained from each SEM image. Scale bar: 500nm.

Another interesting study of H-H stacking can be performed by varying the ratios between the layer periodicities. Figures 96.a-b show the SEM images for the $2/\sqrt{3}:1$ and $3/2:1$ ratios with a neutral interfacial layer (i.e. H_{42} - N_H - H_{37} and H_{56} - N_H - H_{37}).

Both results present similar 2D wallpaper patterns as depicted for D-D in the Table 15 transposed to the H-H case with the “above” & “between” and “above” & “edge” stacking types for $2/\sqrt{3}:1$ and $3/2:1$ ratios, respectively, with a weak translational order is obtained due to the low pattern quality of the 1st layer (H_{42} and H_{56} here). Unfortunately, the obtained configurations cannot be explained by the pseudo-chemical epitaxy model, and thus no difference were observed with PS- or PMMA- affine coatings. Interestingly, the SEM image obtained for H_{42} - N_H - H_{37} seems in better agreement with the expected ideal structure than the SEM image retrieved for a D-D configuration with the same $2/\sqrt{3}:1$ ratio.

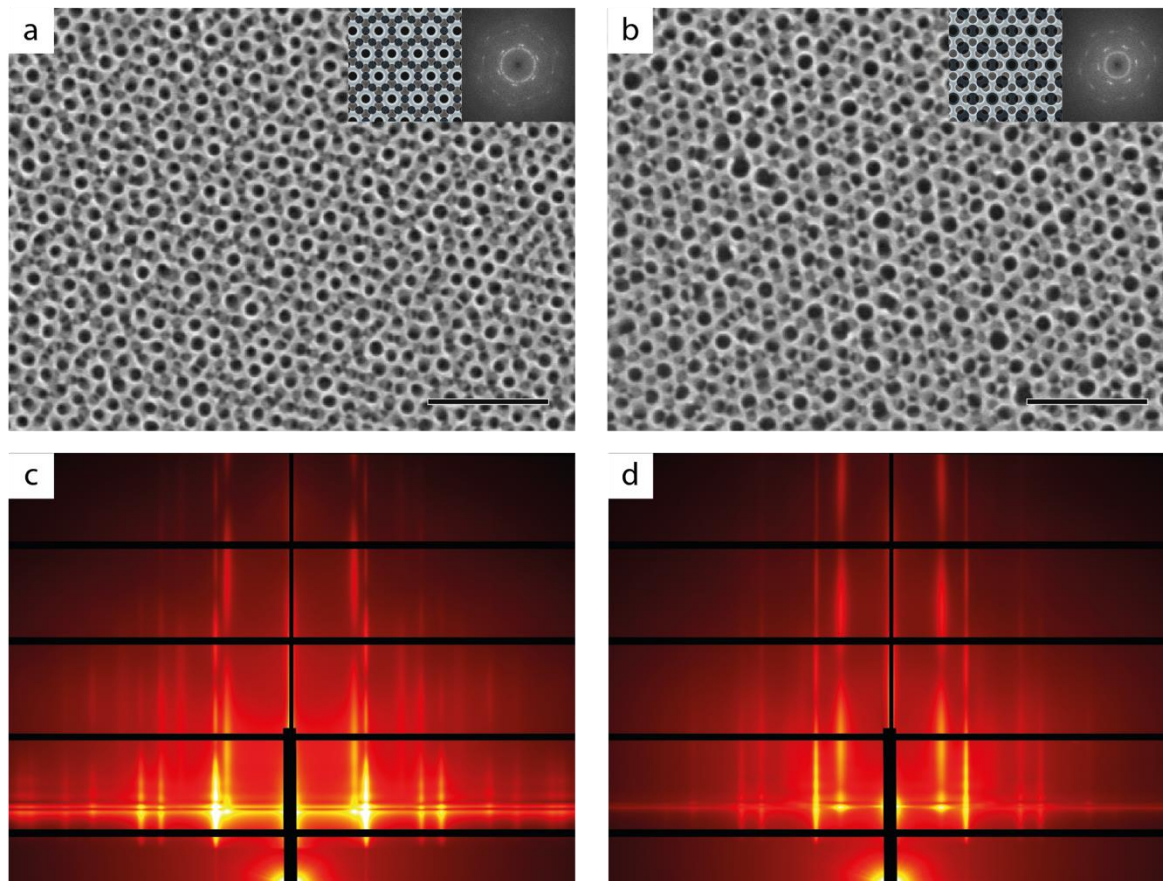


Figure 96. (top) SEM images and (bottom) corresponding GISAXS patterns of (a,c) H_{42} - N_H - H_{37} and (b,d) H_{56} - N_H - H_{37} . Top right insets represent idealized structures and image FFTs. Scale bars represent 250 nm.

The GISAXS pattern of the H_{42} - N_H - H_{37} structure (Figure 96.c) exhibits intense Bragg rods that can be separated in two families, one for H_{42} and one for H_{37} . Thus, it is possible to retrieve the intensity peak sequence for a particular hexagonal array such as $q_y/q^*_1 = 1, \sqrt{3}, \sqrt{4}, \sqrt{7}$, corresponding to a domain spacing of 41.9 nm (i.e. the H_{42} structure), and $q_y/q^*_2 = 1, \sqrt{3}, \sqrt{4}, \sqrt{7}, \sqrt{9}, \sqrt{12}, \sqrt{13}$, corresponding to a domain spacing of 35.4 nm (i.e. the H_{37} structure). The GISAXS pattern obtained for the H_{56} - N_H - H_{37} structure (Figure 96.d) shows the same characteristic features with two sequence of Bragg rods related to hexagonal patterns of 53 nm and 35.4 nm periodicities.

Unfortunately, the $\sqrt{3}:1$ and $2:1$ ratios did not produce stacking configurations that could be analyzed as a very poor ordering of BCP layers with large domain spacing had to be used as a first layer.

IV.4.D/ Stacking of a dot pattern on top of hole pattern (H-D)

A last stacking configuration using the hexagonal symmetry produced by BCP self-assembly is by mixing dot and hole features. The hole layer was positioned as the 1st layer since it

allows an easier visualization by SEM. As for the other cases, every combination of H-D stacking was tested, and below is only presented the most robust results.

Figures 97.a-c show the SEM images of the stacking configurations obtained for $H_{37}\text{-}M_D\text{-}D_{37}$, $H_{37}\text{-}S_D\text{-}D_{37}$ and $H_{56}\text{-}S_D\text{-}D_{32}$ (standard process with an ashing step of 4 min). It is important to note that the interfacial layer composition is only affecting the top BCP layer. Thus, M_D , N_D and S_D RCP materials were used for this study.

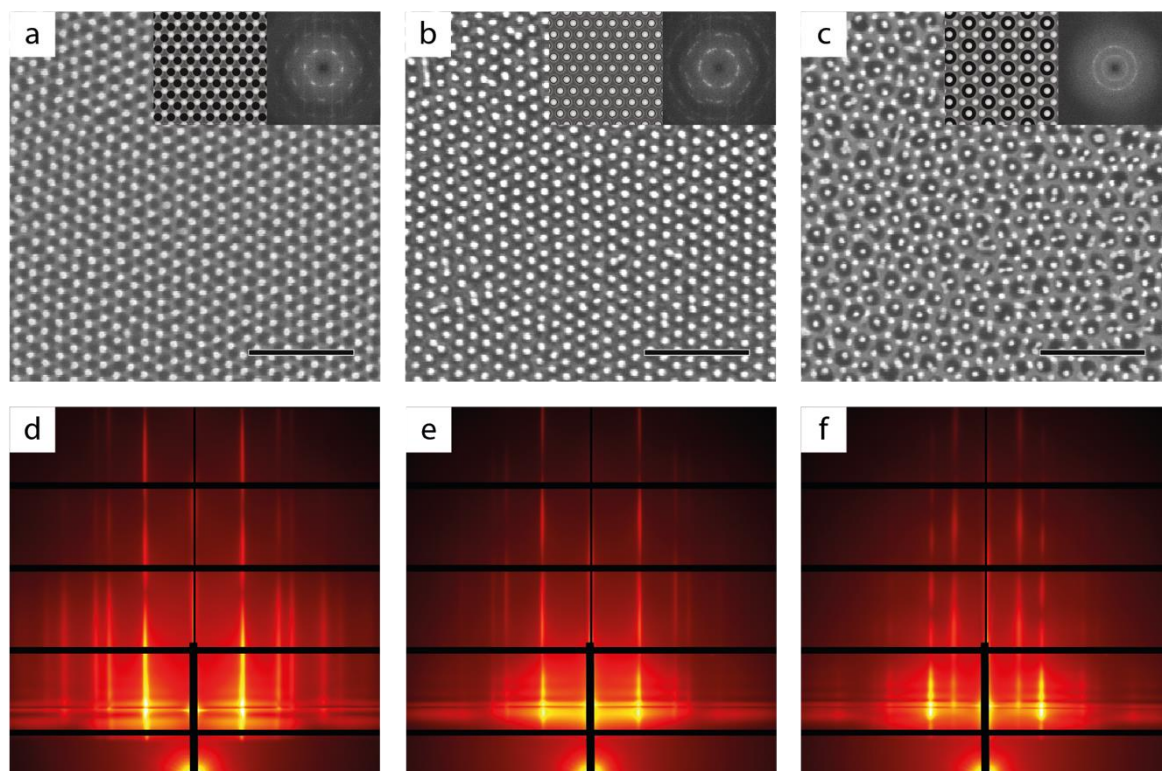


Figure 97. (top) SEM images and (bottom) corresponding GISAXS spectra of (a,d) $H_{37}\text{-}M_D\text{-}D_{37}$, (b,e) $H_{37}\text{-}S_D\text{-}D_{37}$ and (c,f) $H_{56}\text{-}S_D\text{-}D_{32}$. Top right insets are the idealized structures and FFTs. Scale bars: 250 nm.

As observed for the other stacking configurations with a 1:1 ratio, it is possible to observe completely different configurations depending of the affinity of the interfacial layer. PMMA-affine and PS-affine layers lead to “between” and “above” stacking configurations, respectively (*Figures 97.a-b*). These results are in agreement with the pseudo-chemical epitaxy hypothesis: for instance, for the $H_{37}\text{-}M_D\text{-}D_{37}$ case, the Al_2O_3 honeycomb matrix is coated by a PMMA-affine layer and the holes are filled with “neutral” disordered PS-*b*-PMMA chains. Accordingly, the PMMA cylinders from the dot layer are positioned at the interstices between three holes leading to a “between” stacking type.

The GISAXS patterns obtained for the 1:1 ratio (*Figures 97.d-e*) are coherent with the stacking configurations observed by SEM and the use of hexagonal patterns with a 37 nm domain

spacing. Indeed, it is possible to retrieve a unique sequence of Bragg rods $q_y/q^* = 1, \sqrt{3}, \sqrt{4}, \sqrt{7}, \sqrt{9}$ with a 35.7 nm periodicity.

Finally, the $\sqrt{3}:1$ ratio with a PS-affine interfacial layer yields to an “above” & “between” stacking type (*Figure 97.c*), which is coherent with the pseudo-chemical epitaxy model. With this configuration, the PMMA domain area registered above the Al_2O_3 pattern is smaller than for the “edge” configuration, as expected for a PS-affine interfacial layer. It is noteworthy that the M_H interfacial layer case leads to the “edge” stacking type (not presented here) in accordance with the previous rationalization, even if the “above” & “between” configuration was retrieved in some region.

The associated GISAXS pattern (*Figure 97.f*) exhibits the characteristic peaks of H_{56} and D_{32} with measured periodicities of 53.3 nm and 31.4 nm, very close to the 54.2 nm and 31.2 nm measured from individual layers. Also, it is very clear that the D_{32} signals are drastically weaker in the stacked configuration with respect to the ones observed for an individual layer. This is linked to the highly disrupted positioning of the dots on top of the H_{56} layer.

IV.5/ Stacking of two layers with different symmetry

It is possible to imagine four different stacking configurations of layers showing distinct symmetries, which are L-D, D-L, L-H and H-L. As previously mentioned, D-L and L-H stacking configurations were not thoroughly studied due to the difficulty to analyze the resulting top-view SEM images. Besides, an important challenge with mixed stacking is the strongly different grain shapes and defects obtained from the BCP self-assembly. At one hand, for line & space pattern, i.e. lamellar BCP structure, a fingerprint pattern with randomly positioned defects such as dislocations and disclinations is produced [25]. At the other hand, for dot or hole patterns, i.e. cylindrical BCP structure, highly ordered grains of hexagonal packed features are produced and the defects are localized at the grain boundaries. Thus, the dot or hole patterns are strongly constrained when subject to registration fields over “wavy” lines.

IV.5.A/ Expected configurations between two stacked patterns of different symmetry

Firstly, it is interesting to predict the expected structures taking into account geometrical packing (i.e. leading to the smallest fundamental domain with the highest symmetry group), from the several ratios selected with geometrical considerations as explained in *Chapter III/ Figure 68.b*. The same parameters listed for stacking two layers with hexagonal symmetries can be taking into account here, leading to a list of potential bilayers structures. For the sake of simplicity, D-L stacking configurations was solely inventoried in the *Table 16*, referencing the simulated sketches, the fundamental domains and the wallpaper groups [13], leading to structures that could not be natively achieved from di-BCPs.

It is noteworthy that the ratio between the two structures is calculated from their periodicities and not from the domain spacing. For instance, a 1:1 ratio is obtained by stacking L_{28} with D_{32} , since D_{32} means that the cylinder-to-cylinder distance is 32 nm, i.e. a periodicity of $32 \times \sqrt{3}/2 = 28$ nm. Also, for large dot pattern on top of small line & space pattern, the “above” & “between” stacking types enclose the “edge” type since the dots are larger than the width of the lines. This was highlighted in the table by an “(edge)” nomenclature.

Ratio Angle	Stacking type Wallpaper group	SEM predicted image	Stacking type Wallpaper group	SEM predicted image
1:1 0°	Above c2mm		Between c2mm	
2/√3:1 30°	Above & Between p2mm		Edges p2mg	
3/2:1 0°	Above & Edges c2mm		Between & Edges c2mm	
√3:1 30°	Above & Edge c2mm		Between & Edge c2mm	
2:1 0°	Above & Between p2mm		Edge p2mg	
1: 2/√3 30°	Above & Edge c2mm		Between & Edge c2mm	
1:3/2 0°	Above, Between (& Edge) p2mm		Edge p2mg	
1:√3 30°	Above (& Edge) c2mm		Between (& Edge) c2mm	
1:2 0°	Above (& Edge) c2mm		Between (& Edge) c2mm	

Table 16. Schematics of the nanostructures obtained by stacking a layer of hexagonally packed dots above parallel lines, with a given periodicity ratio and a relative rotation angle between them. Red lines specify the pattern fundamental domain, with rotation center and reflection axis from the wallpaper group.

As for the previous cases, a systematic study was performed to observe the stacking for each ratio and with neutral, PS-affine layer and PMMA-affine layers between the two BCP layers.

IV.5.B/ Stacking of a dot pattern on top of a line & space pattern (L-D)

Interesting stacking configurations were observed for the 1:1 ratio using PS- and PMMA-affine interfacial layers to modify the stacking type. *Figures 98.a-b* show the typical SEM images obtained for both cases, using the $L_{32-t}M_D-D_{37}$ and $L_{28-t}M_D-D_{32}$ stacking configurations.

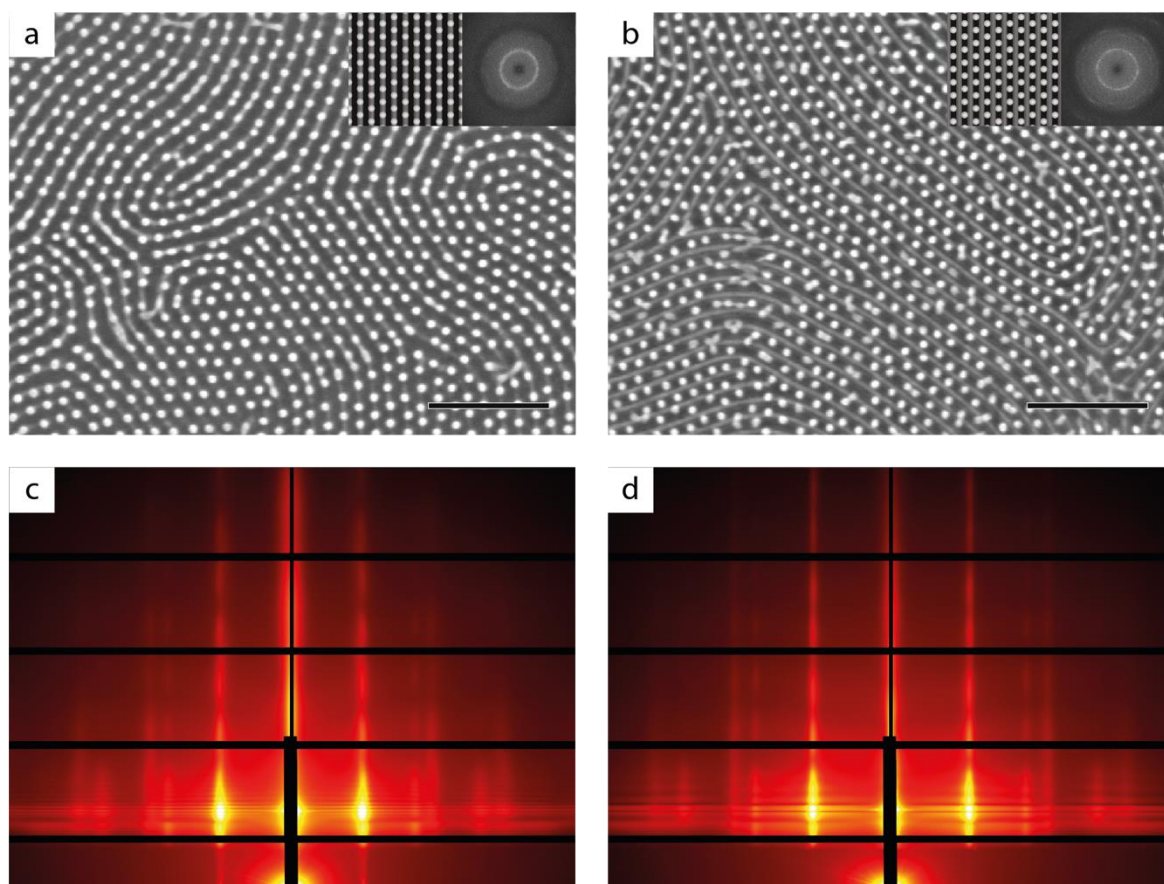


Figure 98. (top) SEM images and (bottom) corresponding GISAXS patterns of (a,c) $L_{32-t}M_D-D_{37}$ and (b,d) $L_{28-t}M_D-D_{32}$. Top right insets are the idealized structures and FFTs. Scale bars: 250 nm.

For the PMMA-affine case, the obtained structure is clearly composed of dots perfectly registered on top of Al_2O_3 lines, which is consistent with pseudo-chemical epitaxy mechanism hypothesis. Indeed, the PMMA cylinders are positioned on top of the PMMA-coated Al_2O_3 lines, while the surrounding PS matrix is predominantly placed on the neutral spaces filled with disordered PS-*b*-PMMA chains. For the PS-affine case, the opposite structure is observed, i.e. dots perfectly registered between the Al_2O_3 line pattern, which is also expected from the pseudo-chemical epitaxy hypothesis. Indeed, in this case, the PS-affine coated Al_2O_3 pattern is fully

covered with PS domains which lowers the interfacial energy of the system, while the neutral space between the lines is alternatively covered with PS and PMMA, which does not modify the overall energy cost.

Unfortunately, the inherent defectivity of BCP self-assembly limits the correlation length of the stacked structures, in particular due to the grain boundaries of the underneath lamellar structure. Nevertheless, this could be easily solved by using DSA methods for the first layer as demonstrated in the previous chapter.

The GISAXS pattern for the PMMA-affine case (*Figure 98.c*) presents intense Bragg rods with the characteristic hexagonal sequence i.e. $q_y/q^* = 1, \sqrt{3}, \sqrt{4}, \sqrt{7}, \sqrt{9}$, which gives a structure periodicity of 32.4 nm, i.e. a cylinder-to-cylinder distance of 37.4 nm. As expected with the 1:1 ratio, the lamellar structure signals are “hidden” by the cylinder ones, corroborating the similar periodicity for the two structures. Similar features were observed for the PS-affine case as shown in *Figure 98.c* and a 29.5 nm periodicity was extracted from the position of the first Bragg rod corresponds to a cylinder-to-cylinder distance of 34.1 nm. Interestingly, for both the PMMA- and PS- affine cases, the cylinder-to-cylinder distance measured by GISAXS is higher than the one measured for a single layer on a flat substrate. It means that the layering induces some chain stretching to match the topographical field created by the immobilization of the 1st layer.

The next series of results were sorted according to whether the stacking ratio was greater or less than 1, i.e. small dot pattern above large line & space pattern or large dot pattern above small line & space pattern.

Figures 99.a-c show the SEM images observed for the first type of stacking ratio, i.e. small dot pattern on top of large line & space Al_2O_3 pattern, experimentally obtained with $\text{L}_{56\text{-t}}\text{-N}_{\text{D}}\text{-D}_{37}$, $\text{L}_{56\text{-t}}\text{-S}_{\text{D}}\text{-D}_{32}$ and $\text{L}_{56\text{-t}}\text{-M}_{\text{D}}\text{-D}_{32}$ stacking configurations.

As presented in the *Table 16*, the $\sqrt{3}:1$ ratio could lead to two different remarkable structures, one being composed of “above” & “edge” stacking types, and the other one composed of “between” & “edges” stacking types. Taking into account the pseudo-chemical epitaxy mechanism, the first stacking type should be obtained using a PMMA-affine coating, while the second one is expected for a PS-affine coating. However, no difference was experimentally observed depending of the interfacial layer used for the stacking. The best results were obtained for a neutral interfacial layer (*Figure 99.a*) with both “above” & “edge” stacking types. A tentative explanation for this behavior could be related to the small difference in energy between the two expected structures or additional parameters such as chain stretching that have not been taken into account for the determination of the predicated structures in *Table 3*. The GISAXS pattern

associated to the $\sqrt{3}:1$ ratio (*Figure 99.d*) exhibits intense Bragg rods that can be sorted into two different sequences, i.e. L_{56-t} with $q_y/q_1^* = 1,2,3$ and $q_1^* = 0.114 \text{ nm}^{-1}$ giving a periodicity of 55.1 nm, and D_{37} with $q_y/q_2^* = 1, \sqrt{3}, \sqrt{4}, \sqrt{7}, \sqrt{9}$ and $q_2^* = 0.198 \text{ nm}^{-1}$ giving a periodicity of 31.7 nm.

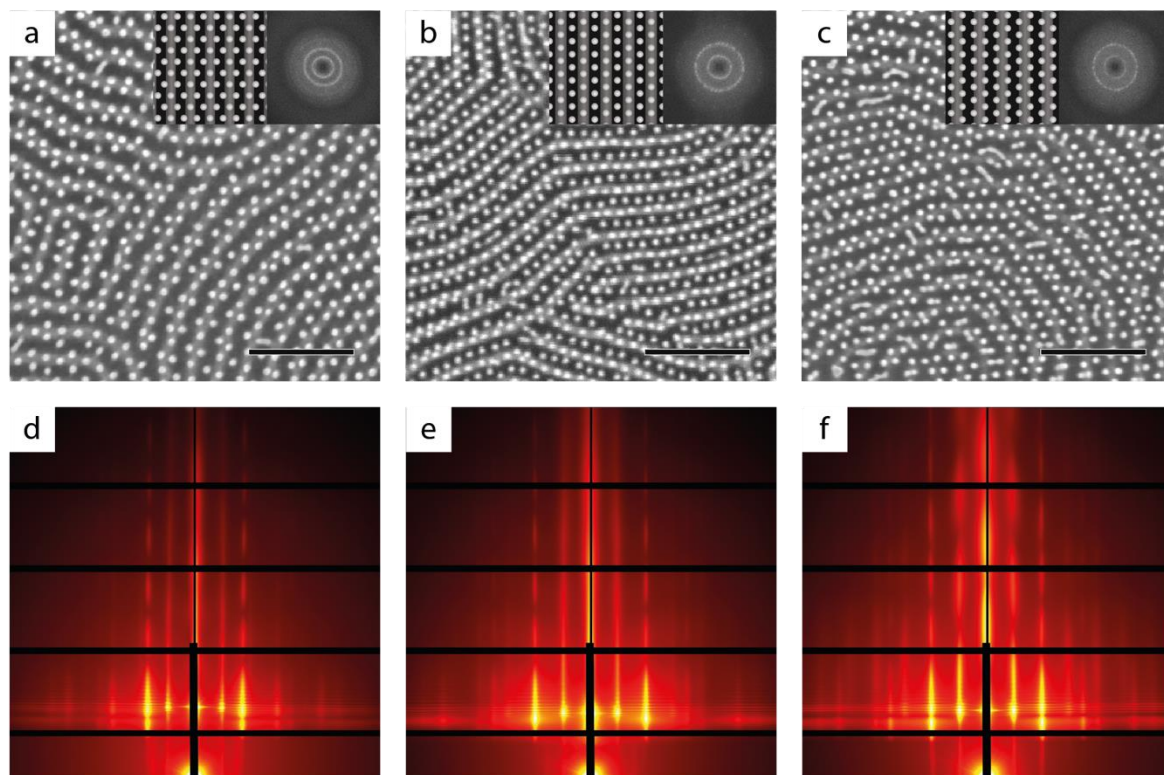


Figure 99. (top) SEM images and (bottom) corresponding GISAXS patterns of (a,d) $L_{56-t}ND-D_{37}$, (b,e) $L_{56-t}SD-D_{32}$ and (c,f) $L_{56-t}MD-D_{32}$. Top right insets are the idealized structures and FFTs. Scale bars: 250 nm.

For the 2:1 ratio, the two structures observed with PS- and PMMA- affine interfacial layers are strikingly different (*Figures 99.b-c*) and the SEM analysis concludes to a “above” & “between” stacking type for PS-affine interfacial layer and an “edge” stacking type for the PMMA-affine interfacial layer. For this specific 2:1 ratio, the pseudo-chemical epitaxy model is limited because both expected and observed stacking configurations are completely equivalent in term of interfaces. Indeed, for both configurations, exactly half of PMMA dots are above the line pattern: either one dot is registered above a line for one registered in between lines (PS-affine case), or each dot is positioned at the edge of the Al_2O_3 lines (PMMA-affine case). Nevertheless, the asymmetric surface area hypothesis allows rationalizing the observed stacking configurations. Indeed, an excess surface area is created along the edges of the Al_2O_3 lines (at the bump curvature), leading to the specific registration of the affine block over these edges. For the PMMA-affine interfacial layer, the PMMA domains would then be registered on the edges of the lines, which gives the observed “between” stacking type. In the other hand, the “above” & “between” structure leads to the alumina line edges fully covered with the PS block, which would lower the configurational energy for the PS-affine case. Both GISAXS patterns from the 2:1 ratio cases

(Figures 99.e-f) show the same overall characteristics. The analysis of the Bragg peak positions gives the characteristic sequences from lamellae and cylinders (with some superimposed Bragg rods due to the commensurate ratio), i.e. $q_y/q^*_1 = 1, 2, 3, 4$ and $q_y/q^*_2 = 1, \sqrt{3}, \sqrt{4}, \sqrt{7}$, giving 55.1 nm and 27.2 nm periodicities, respectively (i.e. a 31.4 nm domain spacing for cylinders).

For the other ratios between the two structures, the experimental results were not conclusive, in part due to the ability of BCP structure to stretch in order to accommodate topographical and chemical fields. As an example, for the $2/\sqrt{3}:1$ ratio, the PMMA cylindrical structure slightly expanded to reach the 1:1 ratio, yielding thus to similar stacking configurations as observed before, with obviously more defects due to the stretching constraints. As for the $3/2:1$ ratio, the predicted structures have a rather higher fundamental wallpaper domain sizes compared to the other ones, leading to a poorer overall symmetry which are thus less stable structures from a thermodynamical point of view.

For the stacking of large dot pattern over smaller line & space pattern, Figures 100.a-b show two remarkable structures which were obtained using $L_{28}-N_D-D_{48}$ and $L_{28}-N_D-D_{56}$ stacking configurations.

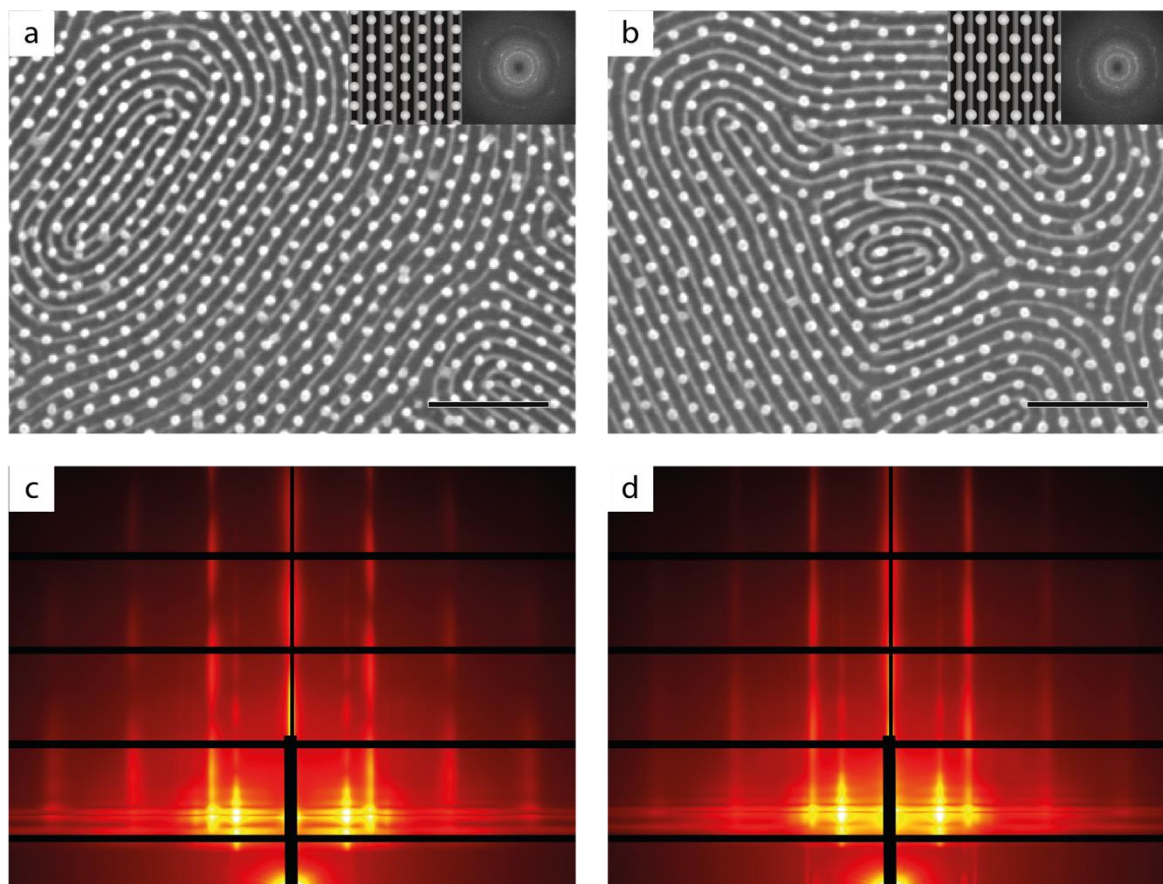


Figure 100. (top) SEM images and (bottom) corresponding GISAXS patterns of (a,c) $L_{28}-N_D-D_{48}$ and (b,d) $L_{28}-N_D-D_{56}$. Top right insets are the idealized structures and FFTs. Scale bars: 250 nm.

The structure obtained for the 1:3/2 ratio is not very well defined since it appears to be a mix of the three stacking types, i.e. “above”, “between” & “edge”. We rationalize this result taking into account the large size of the dots with respect to the line width which could favor the collapse of the dots at different positions during the ashing step. However, the structure obtained for the 1: $\sqrt{3}$ ratio is consistent with a “above” stacking type as predicted. For these two stacking configurations, no difference between PS-affine, PMMA-affine or neutral interfacial layers were observed even if the best self-assembly results were obtained for a neutral layer. This might be explained by the fact that the pseudo-chemical epitaxy mechanism is not valid for stacking configurations based on top features larger than the underneath Al₂O₃ lines. Indeed, there is no configuration which would preferentially stabilize the PS or PMMA domains on top of Al₂O₃ lines. However, responsive layering is still observed due to the topographical field related to the immobilization of the 1st BCP layer. The GISAXS pattern of the L₂₈-N_D-D₄₈ stacking configuration (*Figure 100.c*) presents intense Bragg rods corresponding to the L₂₈ line & space pattern (i.e. $q_y/q_1^* = 1,2,3$ with a periodicity of 29.1 nm). Also, Bragg rods of weaker intensity can be observed along the hexagonal structure sequence, i.e. $q_y/q_2^* = 1, \sqrt{3}, \sqrt{4}, \sqrt{7}$ with a periodicity of 41.9 nm, i.e. a cylinder-to-cylinder distance of 48.4 nm, associated to the D₄₈ structure. For the L₂₈-N_D-D₅₆ (*Figure 100.d*), similar conclusions can be drawn from the GISAXS pattern with a sequence of Bragg rods shifted to lower q values for the D₅₆ structure (domain spacing of 54.1 nm).

IV.5.C/ Stacking of a line & space pattern on top of a hole pattern (H-L)

The last type of stacking studied during this Ph.D. is the hole and line & space stacking configuration, which would have similar expected 2D wallpaper symmetries as L-D stacking. However, in this case, the stacking would not present the grain shape issue encountered previously, i.e. the hexagonally packed cylinder within a sole grain bending along curvy lines from the underneath fingerprint pattern. Indeed, in this H-L case, it is the lamellae that would have to get aligned on a underneath hole pattern within a sole grain. In this case, some bilayer grains will have a perfect order if responsive layering occurs, which should be easier to analyze. As for the previous case, it is possible to split this study in three parts: the 1:1 ratio, and the ratios above and below 1.

Figures 101.a-b present the first case, i.e. 1:1 ratio, with PMMA- or PS-affine interfacial layer, produced by stacking L₃₂ on top of H₃₇, i.e. H₃₇-M_L-L₃₂ and H₃₇-S_L-L₃₂.

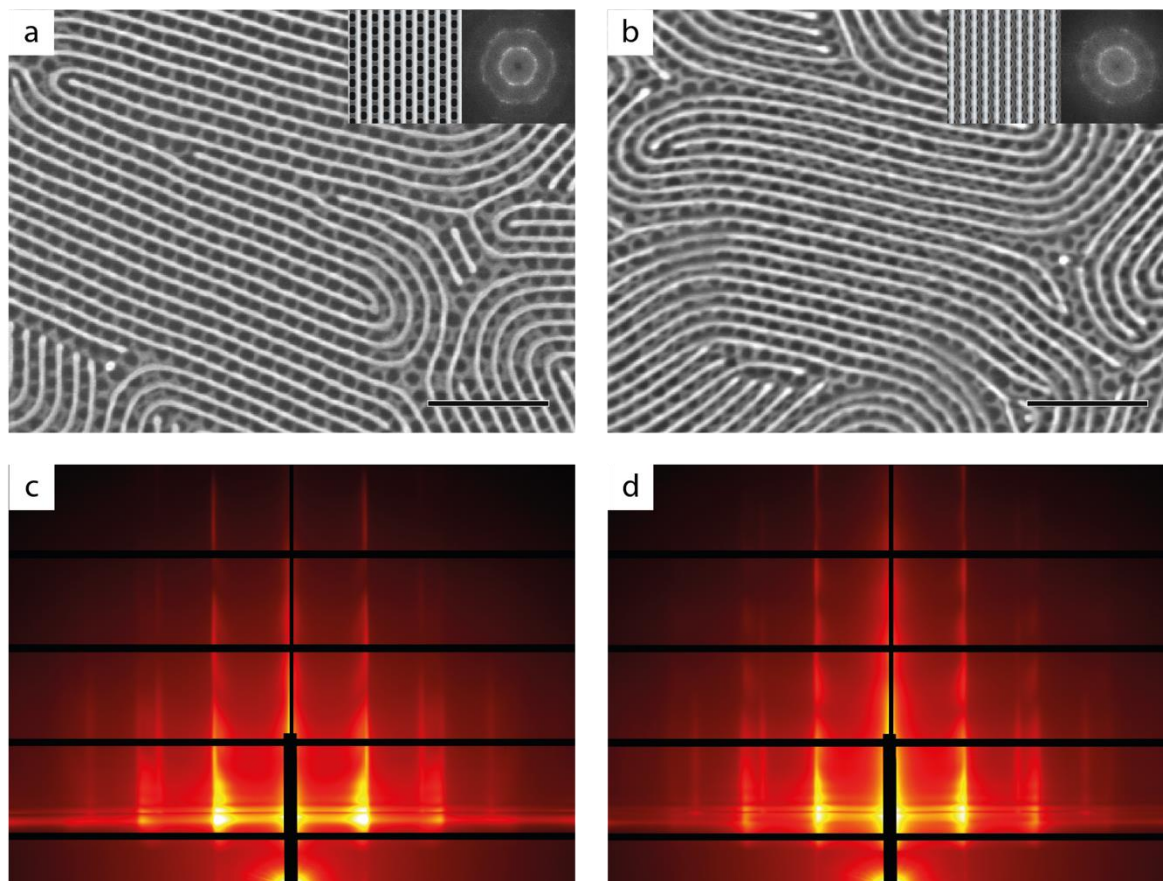


Figure 101. SEM images (top) and corresponding GISAXS patterns (bottom) of (a,c) $H_{37}\text{-M}_L\text{-L}_{32}$ and (b,d) $H_{37}\text{-S}_L\text{-L}_{32}$. Top right insets represent idealized structures and image FFTs. Scale bars: 250 nm.

As expected, and observed for every 1:1 ratio configuration, the structures are exactly the ones predicted from packing considerations, i.e. the PMMA lamellae registered between or above the holes formed by the Al_2O_3 honeycomb pattern. Interestingly, both stacking configurations can be fully explained using the pseudo-chemical epitaxy mechanism, clearly underlining responsive layering. For the PMMA-affine case, i.e. lines registered between holes, the PMMA domains are fully facing the underneath Al_2O_3 pattern coated with the PMMA-affine layer. For the PS-affine case, the same process is occurring, with PS instead of PMMA. Interestingly, for both cases, the non-affine lamellar domains are registered on top of holes, i.e. sequentially facing neutral conditions from disordered BCP chains trapped in the hole and non-affine areas from the Al_2O_3 pattern. This induces an energetical cost, that is fortunately lower than the energetical gain of the responsive layering. It is important to note that for both structures, lines are effectively mostly directed collinearly within a hole grain, and bend along the grain boundaries.

As expected, the associated GISAXS spectra (Figures 101.c-d) present similar features with intense Bragg rods positioned at a first characteristic sequence $q_y/q_1^* = 1,2,3$ of lamellar structure, with a measured periodicity of 31.4 nm, and a second characteristic sequence $q_y/q_2^* =$

$1, \sqrt{3}, \sqrt{4}, \sqrt{7}, \sqrt{9}$ of hexagonally packed cylinders, with a measured domain spacing of 36.3 nm. This analysis is in accordance with the two stacked structures, i.e. L_{32} and H_{37} .

For stacking ratios above 1, i.e. small line & space pattern above large hole pattern, the study was performed using L_{28} . *Figures 102.a-c* present the SEM images of the $2/\sqrt{3}:1$, $3/2:1$ and $\sqrt{3}:1$ ratios, obtained from H_{42} - M_L - L_{28} , H_{48} - S_L - L_{28} and H_{56} - S_L - L_{28} stacking configurations, respectively.

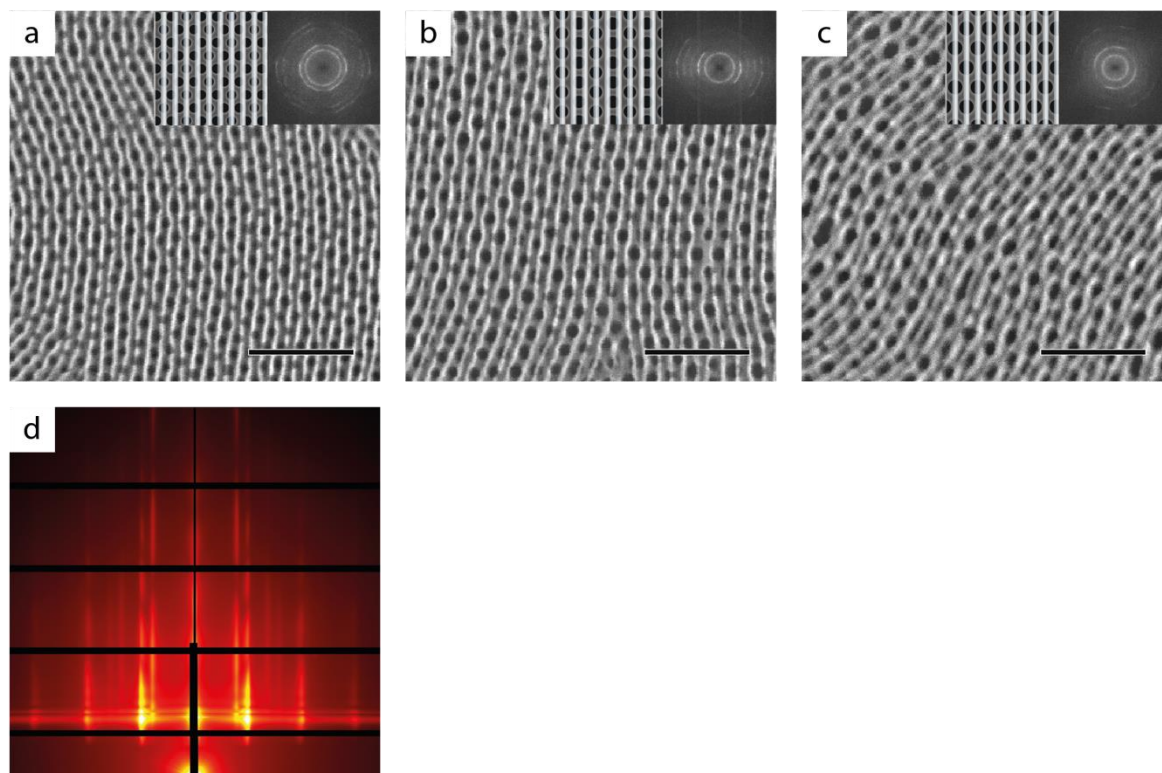


Figure 102. (top) SEM images and (bottom) corresponding GISAXS patterns of L_{28} stacked on top of (a,d) H_{42} with PMMA-affine layer, (b) H_{48} with PS-affine layer and (c) H_{56} with PS-affine layer. Top right insets are the idealized structures and FFTs. Scale bars: 250 nm.

Interestingly, similar results were obtained by stacking L_{28} on top of H_{42} , H_{48} and H_{56} , and that independently of the interfacial layers used. For all three experiments, the most stable configuration always involved the registration of the lines on top or between holes. It seems that in these cases, the topographic contribution is higher than the interfacial one, explaining why there is no impact of the interfacial layer affinity on the registration of the second layer.

The GISAXS pattern from the $2/\sqrt{3}:1$ ratio case (*Figure 102.d*) exhibits as usually the two characteristic sequences related to the stacked structures: $q_y/q_1^* = 1,2,3$ for L_{28} with a measured 28.3 nm periodicity, and $q_y/q_2^* = 1, \sqrt{3}, \sqrt{4}$, for H_{42} with a measured 41.2 nm domain spacing. Unfortunately, the GISAXS spectra of the two other cases, i.e. H_{48} - S_L - L_{28} and H_{56} - S_L - L_{28} were not recorded.

IV.6/ Conclusions

In this study, an efficient process to stack two layers of PS-*b*-PMMA thin films using an immobilization step have been developed. With geometrical and symmetrical considerations, it has been possible to list the potential bilayers patterns that were targeted. Then, an exhaustive study has permitted to reach a consequent number of these non-native patterns (some of them observed for the first time using BCP self-assembly).

Amongst all those bilayer patterns, it has been possible to reference 7 of the 17 2D-wallpaper groups, and the 2 possible line groups, only by stacking layers that belong to the p1m line group (line & space pattern) and p6mm 2D-wallpaper group (dot and hole patterns). Besides, we have proposed a model that allows explaining the relative configurations between the layers as a function of interfacial energy considerations and a disordering of PS-*b*-PMMA chains under confinement.

To conclude, we have shown that it is possible to control and predict the orientation and alignment of a PS-*b*-PMMA thin film stacked above an immobilized pattern. This work permits to form a toolbox that could be used to produce complex 3D structures from BCP self-assembled thin film.

IV.7/ References

- [1] M. P. Stoykovich *et al.*, "Directed Self-Assembly of Block Copolymers for Nanolithography: Fabrication of Isolated Features and Essential Integrated Circuit Geometries," *ACS Nano*, vol. 1, no. 3, pp. 168–175, Oct. 2007, doi: 10.1021/nn700164p.
- [2] A. Tavakkoli K. G., A. F. Hannon, K. W. Gotrik, A. Alexander-Katz, C. A. Ross, and K. K. Berggren, "Rectangular symmetry morphologies in a topographically templated block copolymer," *Adv. Mater.*, vol. 24, no. 31, pp. 4249–4254, 2012, doi: 10.1002/adma.201104895.
- [3] S. M. Park, G. S. W. Craig, Y. H. La, H. H. Solak, and P. F. Nealey, "Square arrays of vertical cylinders of PS-*b*-PMMA on chemically nanopatterned surfaces," *Macromolecules*, vol. 40, no. 14, pp. 5084–5094, 2007, doi: 10.1021/ma0702344.
- [4] C. Tang *et al.*, "Square packing and structural arrangement of ABC triblock copolymer spheres in thin films," *Macromolecules*, vol. 41, no. 12, pp. 4328–4339, 2008, doi: 10.1021/ma800207n.
- [5] Y. Mogi, M. Nomura, H. Kotsuji, K. Ohnishi, Y. Matsushita, and I. Noda, "Superlattice Structures in Morphologies of the ABC Triblock Copolymers," *Macromolecules*, vol. 27, no. 23, pp. 6755–6760, 1994, doi: 10.1021/ma00101a013.
- [6] A. Rahman, P. W. Majewski, G. Doerk, C. T. Black, and K. G. Yager, "Non-native three-dimensional block copolymer morphologies," *Nat. Commun.*, vol. 7, no. 1, p. 13988, Dec. 2016, doi: 10.1038/ncomms13988.
- [7] A. Tavakkoli K. G., S. M. Nicaise, K. R. Gadelrab, A. Alexander-Katz, C. A. Ross, and K. K. Berggren, "Multilayer block copolymer meshes by orthogonal self-assembly," *Nat. Commun.*, vol. 7, pp. 1–10, 2016, doi: 10.1038/ncomms10518.
- [8] V. P. Chuang, J. Gwyther, R. A. Mickiewicz, I. Manners, and C. A. Ross, "Templated self-assembly of square symmetry arrays from an ABC triblock terpolymer," *Nano Lett.*, vol. 9, no. 12, pp. 4364–4369, 2009, doi: 10.1021/nl902646e.
- [9] H. Huang, R. Liu, C. A. Ross, and A. Alexander-Katz, "Self-directed self-assembly of 3D tailored block copolymer nanostructures," *ACS Nano*, vol. 14, no. 11, pp. 15182–15192, Nov. 2020, doi: 10.1021/acsnano.0c05417.
- [10] E. Occhiello, M. Morra, P. Cinquina, and F. Garbassi, "Hydrophobic recovery of oxygen-plasma-treated polystyrene," *Polymer (Guildf.)*, vol. 33, no. 14, pp. 3007–3015, Jan. 1992, doi: 10.1016/0032-3861(92)90088-E.
- [11] D. Pan, L. Ma, Y. Xie, T. C. Jen, and C. Yuan, "On the physical and chemical details of alumina atomic layer deposition: A combined experimental and numerical approach," *J. Vac. Sci. Technol. A Vacuum, Surfaces, Film.*, vol. 33, no. 2, p. 021511, 2015, doi: 10.1116/1.4905726.
- [12] J. Rosen, "The symmetry principle," *Entropy*, vol. 7, no. 4, pp. 308–313, 2005, doi: 10.3390/e7040308.
- [13] E. Hitzer and C. Perwass, "Full Geometric Description of All Symmetry Elements of Crystal Space Groups By the Suitable Choice of Only Three Vectors for Each Bravais Cell or Crystal Family," 2005.
- [14] S. O. Kim *et al.*, "Defect structure in thin films of a lamellar block copolymer self-assembled on neutral homogeneous and chemically nanopatterned surfaces," *Macromolecules*, vol. 39, no. 16, pp. 5466–5470, 2006, doi: 10.1021/ma060087u.
- [15] S. M. Hur, V. Thapar, A. Ramírez-Hernández, P. F. Nealey, and J. J. De Pablo, "Defect Annihilation Pathways in Directed Assembly of Lamellar Block Copolymer Thin Films," *ACS Nano*, 2018, doi: 10.1021/acsnano.8b04202.

- [16] E. Han, H. Kang, C. C. Liu, P. F. Nealey, and P. Gopalan, "Graphoepitaxial assembly of symmetric block copolymers on weakly preferential substrates," *Adv. Mater.*, vol. 22, no. 38, pp. 4325–4329, 2010, doi: 10.1002/adma.201001669.
- [17] S. M. Park, M. P. Stoykovich, R. Ruiz, Y. Zhang, C. T. Black, and P. F. Nealey, "Directed assembly of lamellae-forming block copolymers by using chemically and topographically patterned substrates," *Adv. Mater.*, vol. 19, no. 4, pp. 607–611, 2007, doi: 10.1002/adma.200601421.
- [18] D. F. Sunday *et al.*, "Characterizing the Interface Scaling of High χ Block Copolymers near the Order-Disorder Transition," *Macromolecules*, vol. 51, no. 1, pp. 173–180, 2018, doi: 10.1021/acs.macromol.7b01982.
- [19] M. W. Matsen and M. Schick, "Self-assembly of block copolymers," *Curr. Opin. Colloid Interface Sci.*, vol. 1, no. 3, pp. 329–336, 1996, doi: 10.1016/s1359-0294(96)80128-2.
- [20] B. Miao, D. Yan, C. C. Han, and A. C. Shi, "Effects of confinement on the order-disorder transition of diblock copolymer melts," *J. Chem. Phys.*, vol. 124, no. 14, 2006, doi: 10.1063/1.2187492.
- [21] A. Alexander-Katz and G. H. Fredrickson, "Diblock copolymer thin films: A field-theoretic simulation study," *Macromolecules*, vol. 40, no. 11, pp. 4075–4087, 2007, doi: 10.1021/ma070005h.
- [22] H. Huang and A. Alexander-Katz, "Dissipative particle dynamics for directed self-assembly of block copolymers," *J. Chem. Phys.*, vol. 151, no. 15, 2019, doi: 10.1063/1.5117839.
- [23] A. Alvarez-Fernandez *et al.*, "Large area Al₂O₃-Au raspberry-like nanoclusters from iterative block-copolymer self-assembly," *RSC Adv.*, vol. 10, no. 67, pp. 41088–41097, 2020, doi: 10.1039/d0ra08730k.
- [24] C. Rossner and A. Fery, "Planet-satellite nanostructures from inorganic nanoparticles: From synthesis to emerging applications," *MRS Commun.*, vol. 10, no. 1, pp. 112–122, 2020, doi: 10.1557/mrc.2019.163.
- [25] J. N. Murphy, K. D. Harris, and J. M. Buriak, "Automated defect and correlation length analysis of block copolymer thin film nanopatterns," *PLoS One*, vol. 10, no. 7, pp. 1–32, 2015, doi: 10.1371/journal.pone.0133088.

CHAPTER V: OUTLOOK FOR BCP ITERATIVE SELF-ASSEMBLY

V.1/ Introduction	202
V.2/ Beyond the stacking of two layers	203
V.3/ Optically active structures from BCP self-assembly	205
V.3.A/ Bibliographical study.....	205
V.3.B/ Tailored 3D-nanogrid targeting optics.....	209
V.3.C/ Experimental challenges.....	210
V.4/ Electronic devices from BCP self-assembly	212
V.4.A/ Bibliographical study.....	212
V.4.B/ 3D-nanopillars memory device	214
V.4.C/ Experimental challenges.....	215
V.5/ Conclusions	218
V.6/ References	219

All along this manuscript, a robust process was developed to stack BCP immobilized layers, in order to form on-demand complex 3D nanostructures. Interestingly, we demonstrated that this iterative process leads to a good control of the final structure, e.g. pattern morphology, periodicity or block functionality by hybridization.

In this last chapter, a preliminary study for stacking more than two layers was performed, which is mandatory to extrapolate the process to form more complex 3D nanostructures. This proof-of-concept study was performed by successfully stacking 3 layers.

Besides, we will present the structural design of two potential applications: a 3D gold nanogrid which might exhibit interesting optical properties, and a 3D-nanopillar array for data storage purpose. Nonetheless, these configurations are still highly conceptual, with several manufacturing challenges, which were not fully resolved during this study. Finally, a general conclusion and perspectives about this Ph.D. is presented.

V.1/ Introduction

Currently, the major use of BCP thin films in the industry is related to the formation of masks for nano-manufacturing with applications in the fabrication of electronic devices. Indeed, the periodical nanostructures produced with this technique allow the generation of a large range of patterns with tunable feature sizes at a low process cost (with respect to common top-down photo-lithography) [1]–[3]. However, even if BCP self-assembly is a bottom-up technique (the pattern is made directly from the deposited BCP layer), the use of BCP thin film as a photo-lithography mask transforms this method into a top-down approach (*Figure 103*). Indeed, the final structure would be made by “carving” a substrate of interest for the desired application.

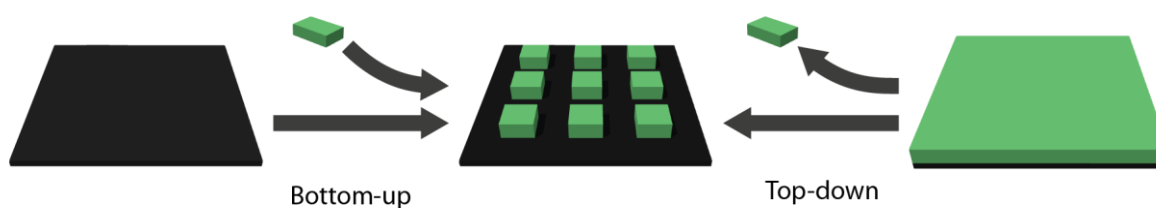


Figure 103. Schematics of bottom-up versus top-down approaches for device nanofabrication. Bottom-up consists in adding material on a substrate, while top-down consists in removing material from a layer of interest for the applications.

Alternatively, BCP thin films can be hybridized to directly generate functionalized nanostructures (thus a fully bottom-up approach). Depending of the type of hybridized materials (metals / dielectrics / ceramics / oxides), applications in various technological fields, such as optics, catalysis, energy or filtration, have been reported in the literature [4], [5]. Unfortunately, even if clear methodologies are established in order to produce the hybridized structures, successful integrations into functional devices are scarce due to the inherent limitation of BCP self-assembly; i.e. the self-assembly phenomenon is driven by a thermodynamic process, which drastically limit the variety of achievable structures and patterns. Obviously, these two approaches are not incompatible, with DSA using graphoepitaxy to remove self-assembly defects as a prime example. DSA methods also allow the generation of tailored structures inaccessible natively by constraining the BCP self-assembly within adequate patterns [6], [7].

During this Ph.D., an efficient layer-by-layer process to form 3D nanostructures was developed, with a controlled registration between layers. Interestingly, this bottom-up approach can be used to produce specific multilayered structures following a rather simple process, which might unlock the possibility to produce complex functional devices. This last prospective chapter will focus on two possible applications in optics and nanoelectronics and will describe the envisioned hybridized structures and the processes associated to their fabrication.

V.2/ Beyond the stacking of two layers

Firstly, a preliminary study was performed to observe the effective possibility to transfer the conclusions made from the stacking of two BCP layers to more than two BCP layers. Indeed, the process was designed to be compatible for the stacking of any number of layers. Interestingly, only the previous layer should influence on the self-assembly of the next layer through responsive layering. To verify this hypothesis, the stacking of three BCP layers were performed on selected configurations allowing a facile characterization by top-view SEM. The two stacking configurations chosen were $H-M_L-L-M_D-D$ and $L-N_L-L-M_D-D$ with a ratio between the periodicities equal to 1. The expected structures for the two envisioned configurations are displayed in *Figures 104.a-b*.

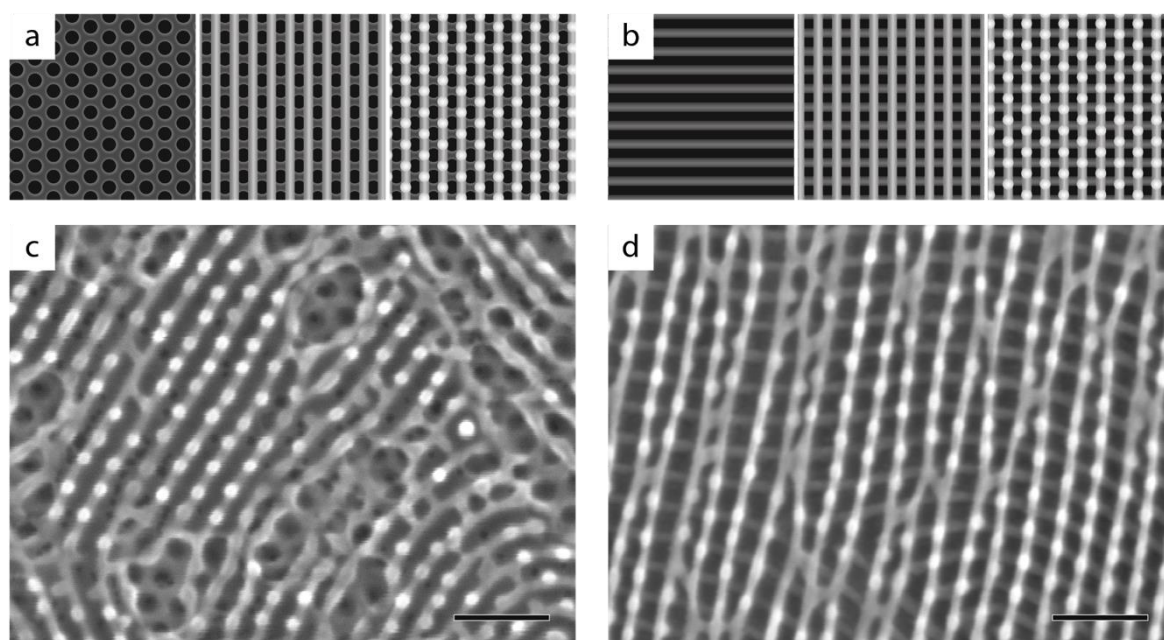


Figure 104. Idealized schematics of three-layer stacking of (a) $H-M_L-L-M_D-D$ and (b) $L-N_L-L-M_D-D$ with the same periodicity. SEM images of (c) $H_{32}-M_L-L_{28}-M_D-D_{32}$ and (d) $L_{28}-N_L-L_{28}-M_D-D_{32}$. Scale bars: 100 nm.

The $H_{32}-M_L-L_{28}-M_D-D_{32}$ (Figure 104.c) and $L_{28}-N_L-L_{28}-M_D-D_{32}$ (Figure 104.d) stacking configurations were generated using the standard process. It is noteworthy that a longer ashing process was necessary to reveal the three-layered structures. Unfortunately, such long ashing step (20 min was required to visualize the hole pattern at the bottom) led to the collapse of the dot pattern (even some parts of the line & space pattern) for the $H_{32}-M_L-L_{28}-M_D-D_{32}$ configuration. Only 6 min of ashing were required for the $L_{28}-N_L-L_{28}-M_D-D_{32}$ configuration and a three-layered structure is clearly visible on the SEM image. It is composed of two line & space patterns orthogonally arranged in a grid (due to the neutral interfacial layer) with the third dot pattern registered on top of the Al_2O_3 lines of the 2nd layer. This is in full accordance with the expected structure and the results obtained for each individual bilayer stacking. Accordingly, the iterative

self-assembly methods devised for the stacking of two layers seems to be fully transposable to more complex iterative layering. However, as experimentally observed for the $H_{32}-M_L-L_{28}-M_D-D_{32}$ stacking configuration, a bottleneck linked to such process is the ashing step which can lead to a collapse of the top structures. An alternative would be to preserve the structural integrity of each layer by a dual hybridization of the two BCP domains.

It is also important to note that for both of these examples, the relative orientation angle between the first and third layers is correlated through the second layer. However, the positioning of the features of the third layer is decorrelated from the localization of the features of the first layer. In other words, the position of top dots along the lines from the second layer is not dictated by the first layer. Indeed, the *Figure 104.d* clearly shows that the dots are not registered along the first line & space pattern, with all three possible stacking configurations. It means that the topographical field generated by the second layer does not integrate the topographical field from the first one.

V.3/ Optically active structures from BCP self-assembly

An interesting property of BCP self-assembly is that the resulting nanostructure shows feature size in the 10-100 nm range, which is slightly below the visible wavelength, and thus can promote optical properties by light-matter interactions [8]. This part will focus on the opportunities to use iterative stacking to obtain optically active nanostructures and devices.

V.3.A/ Bibliographical study

V.3.A.i/ Photonic crystals

The term “photonic crystal” describes objects presenting a periodical nanostructure in which the refractive index is not constant, leading to a modification of the light propagation. The periodicity can be along one, two or three directions, leading to 1D, 2D or 3D photonic crystals. Photonic crystals can have important applications for many optical purposes since it can manipulate light propagation, such as structural colored coatings [9], solar cells [10] or optical sensors [11].

BCPs have been used to produce 1D, 2D and 3D photonic crystals [12], [13]. For instance, 1D photonic crystal were generated using in-plane lamellae (*Figures 105.a,d*), 2D from out-of-plane cylinders (*Figures 105.b,e*) and 3D from gyroid (*Figures 105.c,f*), leading to high reflectivity at a specific wavelength linked to the nanostructure periodicity.

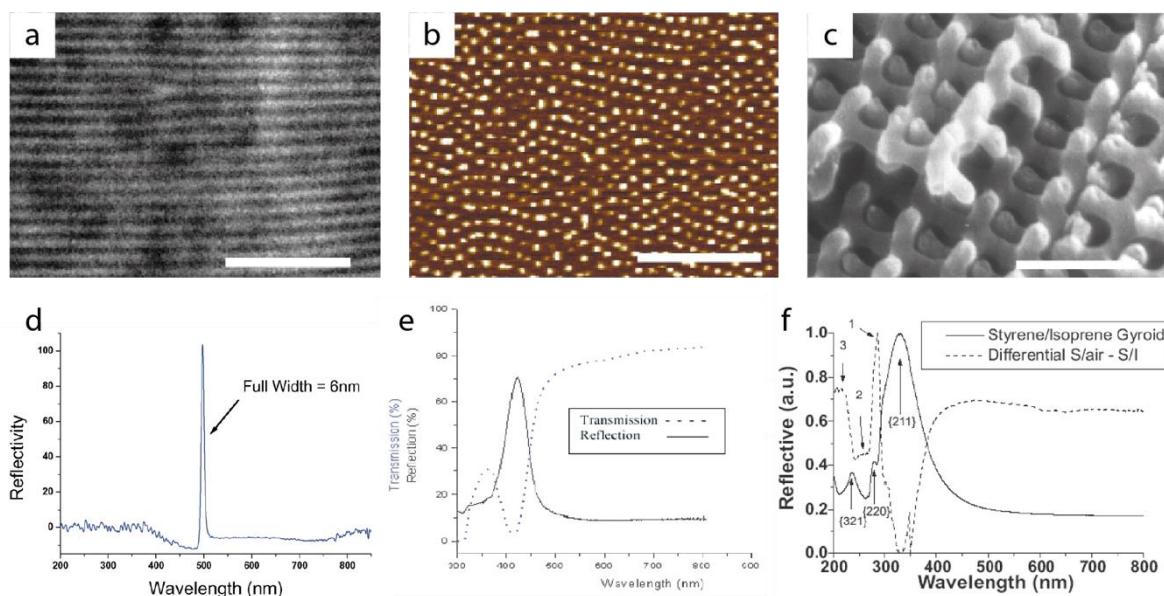


Figure 105. (a) SEM image from an in-plane lamellar PS-b-PI (scale bar: 1 μm) and (d) the associated reflectance spectrum. (b) AFM phase image of an out-of-plane cylinder PS-b-PI (scale bar: 1 μm) and (e) the associated reflectance spectrum. (c) SEM image of a double gyroid PS-b-PI after PI etching by UV/O₃ (scale bar: 250 nm) and (f) the associated reflectance spectrum [12].

To increase the contrast of refractive indexes between the two BCP domains, and thus modify further the optical properties, an infiltration step using metal impregnation or SIS can be performed to incorporate inorganic material, as detailed in *Table 17* for some examples.

Material	n	k	Ref
PS	[1.58 – 1.63]	0	[14]
PMMA	[1.48 – 1.51]	0	[14]
Al ₂ O ₃	1.72	0	[15]
Au	[0.13 – 1.46]	[4.1 – 1.9]	[16]

Table 17. Optical properties of several materials in the visible light range (380 nm – 700 nm) with the refractive index n and the extinction coefficient k .

V.3.A.ii/ Optical metamaterials

A second type of optically active nanostructures are called optical metamaterials. As defined by Zheludev, “Metamaterials are artificial media structured on a size scale smaller than the wavelength of external stimuli” [17], i.e. the visible wavelengths in our case. These objects show properties that are not observed in the nature. The main interest for optical metamaterials is reaching negative refractive indexes [18], which can be obtained by modulating the electronic and magnetic fields from the light wave. This “unnatural” behavior can be used in many applications for optics, in particular for imaging and nanolithography in order to reach resolutions higher than the diffraction limit [19].

Several methods have been developed to generate optical metamaterials, including the use of BCP self-assembly since they exhibit periodical features effectively smaller than the visible wavelengths [20]. For this specific application, the polymer dielectric properties are not compatible, thus a hybridization of at least one of the BCP phase is mandatory to reach the targeted electromagnetic properties, which is usually performed by metallic infiltration.

In 2011, Hur *et al.* theoretically demonstrated that a chiral gyroid structure formed from BCP self-assembly and hybridized with gold in one of its domains, should lead to a chiral 3D metamaterial exhibiting negative refractive index [21]. Experimentally, this structure was obtained, and showed interesting optical properties such as linear and circular dichroisms, but not yet a negative refractive index (*Figures 106.a,c*) [22]. Other metamaterials were obtained from BCP self-assembly, such as shear directed in-plane cylinders hybridized with gold or silver, exhibiting an anisotropic optical response depending on the angle between the incident light and the cylinder direction (*Figures 106.b,d*) [23].

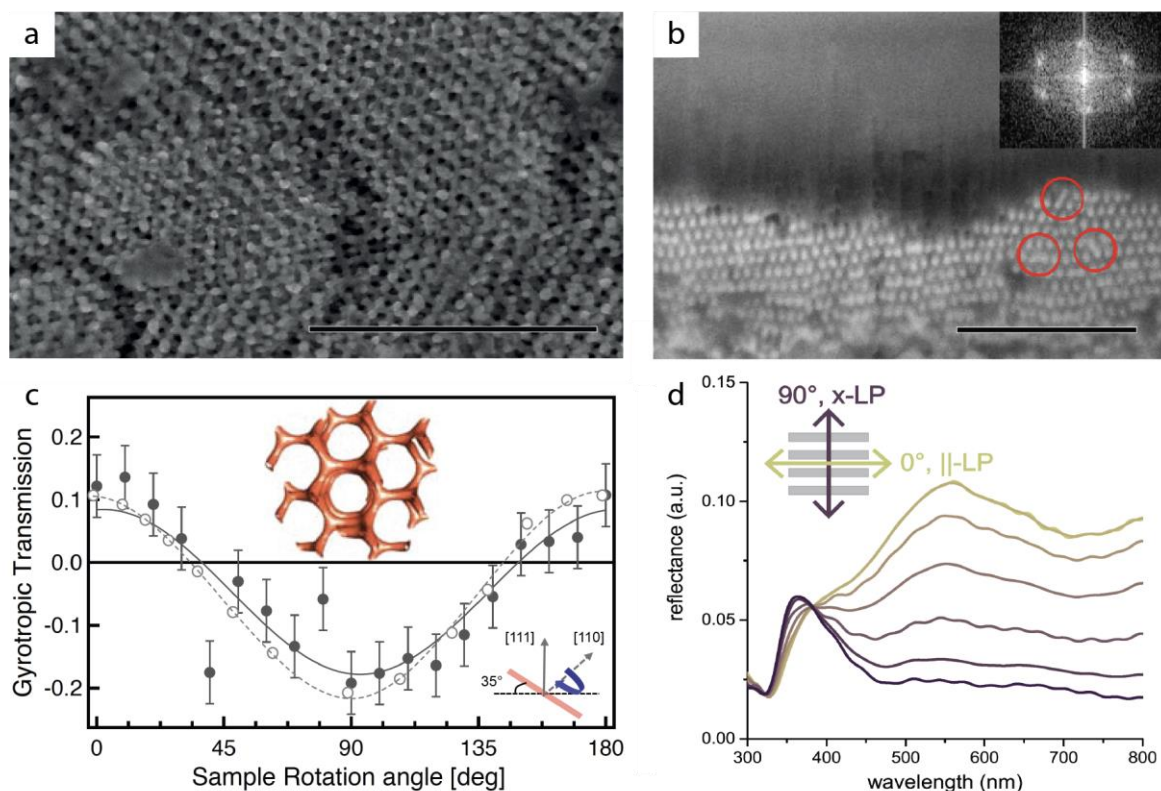


Figure 106. SEM image of a (a) gyroid forming PI-*b*-PS-*b*-PEO [22] and (b) cylinder forming PS-*b*-PMMA [23], with PI and PMMA blocks etched and filled with gold by electrodeposition before full polymer removal. (c) Difference between the transmission spectra in left and right light polarization channels as the sample (a) is rotated around the [110] axis. (d) Polarization-dependent reflectance spectra of the sear aligned cylindrical sample (b). Scale bars: 500 nm.

V.3.A.iii/ Plasmonic nanostructures

Another functional property triggered by periodical nanostructures is the plasmonic effect. It is related to the interactions between electrons from metallic nanoparticles and the incident light. Indeed, a plasmonic oscillation can occur between nanoparticles and light, even if the wavelength is higher than the particle size. Such interaction is due to the metal-dielectric interface between the particles and surrounding matrix, e.g. air. Interestingly, in the case of monodisperse nanoparticle distribution, this plasmonic effect occurs for a very narrow wavelength band that will produce the electron oscillation. For nanoparticles built from periodical nanostructure, for instance BCP self-assembled thin film, a plasmonic nanosurface is produced, which can have a large range of optical applications such as in solar cells [24] or optical sensors [25].

In term of BCPs, plasmonic nanosurfaces can be obtained with gold impregnated out-of-plane cylinders leading to hexagonally packed gold nanoparticles (Figures 107.a,c) [26], but also with the inverse structure, i.e. gold honeycomb [27] (Figures 107.b,d), since the interface of both nanopatterns is similar, i.e. a nanometric periodic array between air and metallic gold.

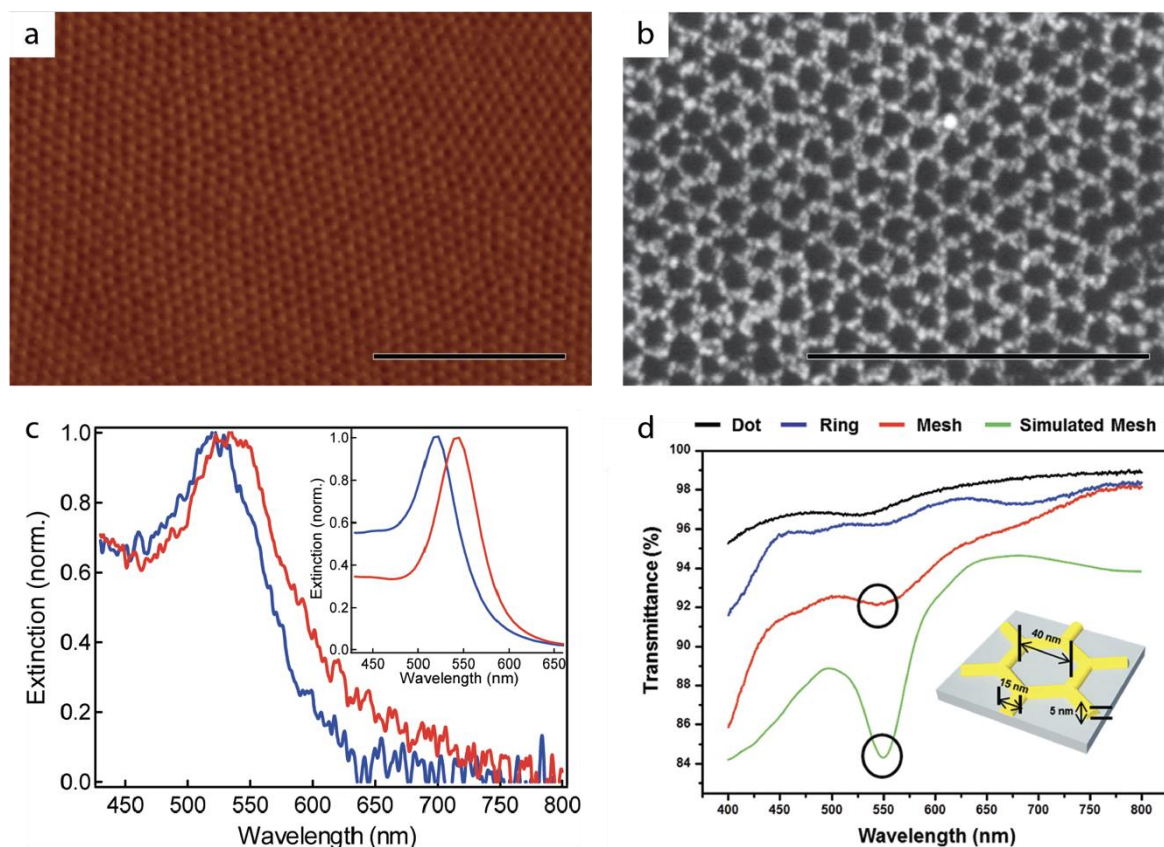


Figure 107. (a) AFM image of out-of-plane PS-*b*-P4VP cylinders infiltrated with a gold salt solution and etched in order to produce an array of gold nanoparticles [26]. (b) SEM image of a metallic nanopattern produced from out-of-plane PS-*b*-P4VP cylinders infiltrated with a gold salt solution and etched in order to obtain a gold nanomesh [27]. (c) Extinction spectra of the sample (a) taken at (red) normal and (blue) 70° off-normal incidence with the simulated spectra in inset. (d) UV-Vis transmittance spectra of nanodots array, nanoring array, nanomesh and simulated spectra for the nanomesh depicted in the inset. Black circles indicate the plasmonic resonance wavelength. Scale bars: 500 nm.

Within our laboratory, Dr. Cian Cummins *et al.* developed another route to form inorganic 2D plasmonic nanosurfaces using PS-*b*-PMMA. The method used was a gold evaporation on top of an porous PS-*b*-PMMA hole pattern followed by a lift off of the PS matrix. Interestingly, the hexagonally packed gold nanodot nanosurface presented near-perfect absorbance at 600 nm wavelength when produced above a gold coated substrate capped with an alumina spacer [28].

The bibliographic details of the published manuscript are:

C. Cummins, Q. Flamant, R. Dwivedi, A. Alvarez-Fernandez, N. Demazy, A. Bentaleb, G. Pound-Lana, M. Zelsmann, P. Barois, G. Hadziioannou, A. Baron, G. Fleury, V. Ponsinet, "An Ultra-Thin Near-Perfect Absorber via Block Copolymer Engineered Metasurfaces" *J. Colloid Interface Sci.*, vol. 609, pp. 375-383, 2022.

<https://doi.org/10.1016/j.jcis.2021.11.163>

V.3.B/ Tailored 3D-nanogrid targeting optics

The possibility to iteratively stack 2D well-ordered layers with a defined configuration allows the creation of tailored 3D-nanostructures containing both dielectric and metallic materials through BCP hybridization done at each layering step. Here, a targeted nanostructure is a stack of several orthogonal arrays of out-of-plane lamellae, with each layer having one block hybridized into a conductive material and the other hybridized into a dielectric material (*Figure 108*). It was already observed that a perfectly aligned wire array presents interesting polarization properties due to the nanometric periodicity [29]. Also, the stacking will produce a more complex 3D-nanogrid, which might exhibit other interesting properties, as already observed with a ZnO nanomesh device that shows a different conductivity according to the ambient illumination [30]. The desired stacking configuration could be easily achieved by stacking line & space arrays with a neutral interfacial coating to promote the orthogonal orientation between the patterns.

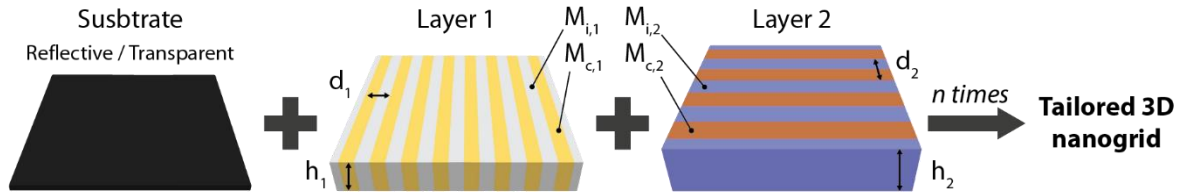


Figure 108. Schematics of the responsive layering process of orthogonal lamellar BCP layers hybridized into conductive/insulator lines for the formation of a tailored 3D-nanogrid. d_j , h_j , $M_{c,j}$, $M_{i,j}$ represent the lamellar domain spacing, layer height, conductive material and insulator material of the j -layer.

This structure can be tailored to target specific behaviors which could be optimized with simulations. The different parameters that can be tuned are:

- The device substrate which can be a silicon wafer for its reflective properties, or a smooth transparent glass wafer for transmission purpose;
- The composition of the conductive material, M_c , with for instance gold, silver or copper, and the composition of the insulator material, M_i , with for instance Al_2O_3 or TiO_2 ;
- The lamellar domain spacing, d , to target a specific wavelength, or the combination of different domain spacing for each layer in order to be responsive to different wavelengths;
- The height, h , of each layer to modify the periodicity along the height axis.

Finally, this on-demand 3D-structure would be formed of n layers having 1D specific in-plane plasmonic effects which are vertically and orthogonally stacked. This stacking would exhibit another periodicity in the height axis, and an orthogonal arrangement between each layer, which could both produce plasmonic effects.

V.3.C/ Experimental challenges

The main challenge for the formation of such device is the hybridization of PS or PMMA domains into a conductive material. As detailed in the *Chapter 1.2/*, several routes have been developed to selectively transform a BCP domain into gold or other metals. Nevertheless, only two are fully compatible with iterative stacking (i.e. keeping the structural integrity of the BCP pattern during the hybridization), which are liquid phase metal salt impregnation and electrodeposition.

For the first route, PS-*b*-PMMA is unfortunately not a suitable candidate for impregnation due to low affinity between metallic salts and PMMA. A solution could be to use PS-*b*-P2VP or PS-*b*-P4VP which can be easily impregnated with gold for instance [27], [31], [32]. However, the standard annealing process for these BCPs is based on an exposition to solvent vapors (solvent vapor annealing), which might have a strong impact on the stacking method developed during this work.

The second route seems more adapted to our process, since it only requires to add an electrode below the first BCP layer in order to perform electrodeposition. By selectively removing one of the domains of the PS-*b*-PMMA structure, it would be possible to growth metal in the created voids. For the electrode, it is possible to coat a wafer with a thin layer of gold using an evaporation method, which is compatible with subsequent self-assembly, as proven with *Figures 109.a-b* that show two self-assembled bilayers on top of a gold coated wafer, using the standard process described in the previous chapters. However, this electrode should be thick enough for electrodeposition, i.e. around 150 nm, leading to a reflective surface, preventing the transmission of light. An alternative would be to use ITO coated substrate even if the higher roughness on such kind of substrate could be detrimental to BCP self-assembly.

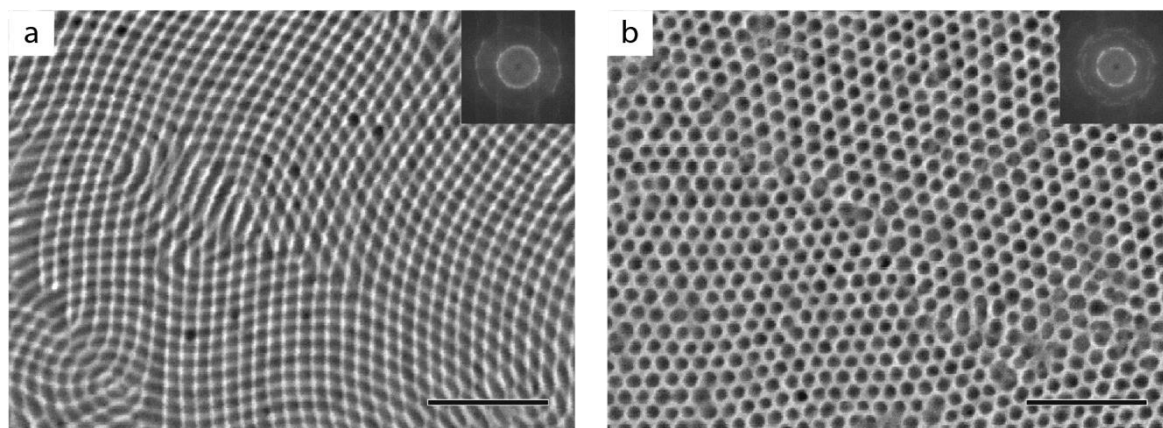


Figure 109. SEM images of (a) L_{32} - N_L - L_{32} and (b) H_{37} - M_H - H_{37} stacking configurations on top a 150 nm gold coated silicon wafer. Top right insets are the FFTs. Scale bars: 250 nm.

Two possible pathways can be devised to perform the electrodeposition (i.e. for the formation of voids into a BCP thin layer): either a selective plasma etching of the PMMA domains followed by a subsequent metal growth (metal / PS structure), or the SIS of alumina in the PMMA domains combined with the PS removal for a subsequent metal growth (metal / alumina structure). A particular attention had to be paid to the electrodeposition parameters (voltage and duration) to grow the metal at a lower height than the surrounding matrix in order to preserve a topographical pattern for the subsequent responsive layering process. Additionally, the metallic domains created during the electrodeposition process should not be covered to be able to pursue further metal growth at the second layer level. Thus, the second process seems more interesting because it produces a fully inorganic layer that does not require an alumina passivation layer to prevent PS removal during the RCP grafting process.

Some preliminary tests were performed with this second process; however, no conclusive results were obtained, certainly due to the very small pattern size (some tenth of nanometer width and height), which requires an optimization of the electrodeposition parameters.

V.4/ Electronic devices from BCP self-assembly

This part will focus on potential avenues of the developed stacking method for the design of electronic devices. The main constraint is to develop a device architecture, which is compatible with the layer-by-layer process that was developed along this Ph.D.

V.4.A/ Bibliographical study

Unfortunately, the transformation of BCP functionalized nanostructures into functional electronic devices are scarce due to the difficulty to produce perfectly ordered patterns which is usually required for this type of applications. Indeed, contrarily to optical applications, functional properties do not emerge from structure averaging. Yet, several potential applications have been developed, and this part will focus one two of them: transistors and data storage.

V.4.A.i/ Transistors

One very important electronic component for actual electronic devices are transistors. These are usually made from doped silicon, and etched to the appropriate shape. This lithographic step might be improved using BCP masks in order to increase the final resolution. For instance, BCP masks were used to selectively etch a graphene layer, leading to the formation of graphene nanoribbon arrays (GNR), which can be used to produce field-effect transistors [33].

However, BCP nanostructures might be directly used to produce intricate structure-function relationships. Chi *et al.* demonstrated the use of BCP self-assembly to produce field-effect transistors [34]. They used a PS-*b*-P4VP BCP to produce different nanostructures, such as spheres, in-plane and out-of-plane cylinders, containing small ferrocene molecules mainly dispersed in the P4VP domains. The produced composite sandwiched between appropriate electrodes exhibited interesting charge-storage properties which can be used for memory device for instance, known as non-volatile organic memories. A similar result was also observed with gold nanoparticles formed within P4VP domains [35].

Another use of BCPs for transistor applications has been demonstrated with the performance improvement of pentacene thin film transistors. Indeed, Jo *et al.* added an out-of-plane PS-*b*-PMMA self-assembled layer between a substrate (SiO_2) and a pentacene thin film, which increased the electron mobility within the overall field effect transistor, due to low PS resistivity which matrix has a continuous pathway perpendicular to the film with this morphology [36], [37].

V.4.A.ii/ Data storage

One specific BCP arrangement can be very interesting for data storage application: the hexagonally packed dots array formed by out-of-plane cylinders or spheres. Indeed, they form laterally periodical spaced objects that can each store one binary information, e.g. with magnetic field orientation. Two distinct ways to form these 2D layers of nanodots are referenced:

- Using the BCP self-assembled layer as a mask to etch the underneath thin layer that already possesses the desired properties for data storage [38]–[40] (*Figures 110.a,d*) which is similar to a top-down approach performed with a conventional lithographic mask;
- Using the BCP layer as a template to hybridize one of the BCP domain with a material having the desired properties for data storage, by electrodeposition, sputtering or infiltration [41]–[44] (*Figures 110.b,e*) which is a bottom-up approach.

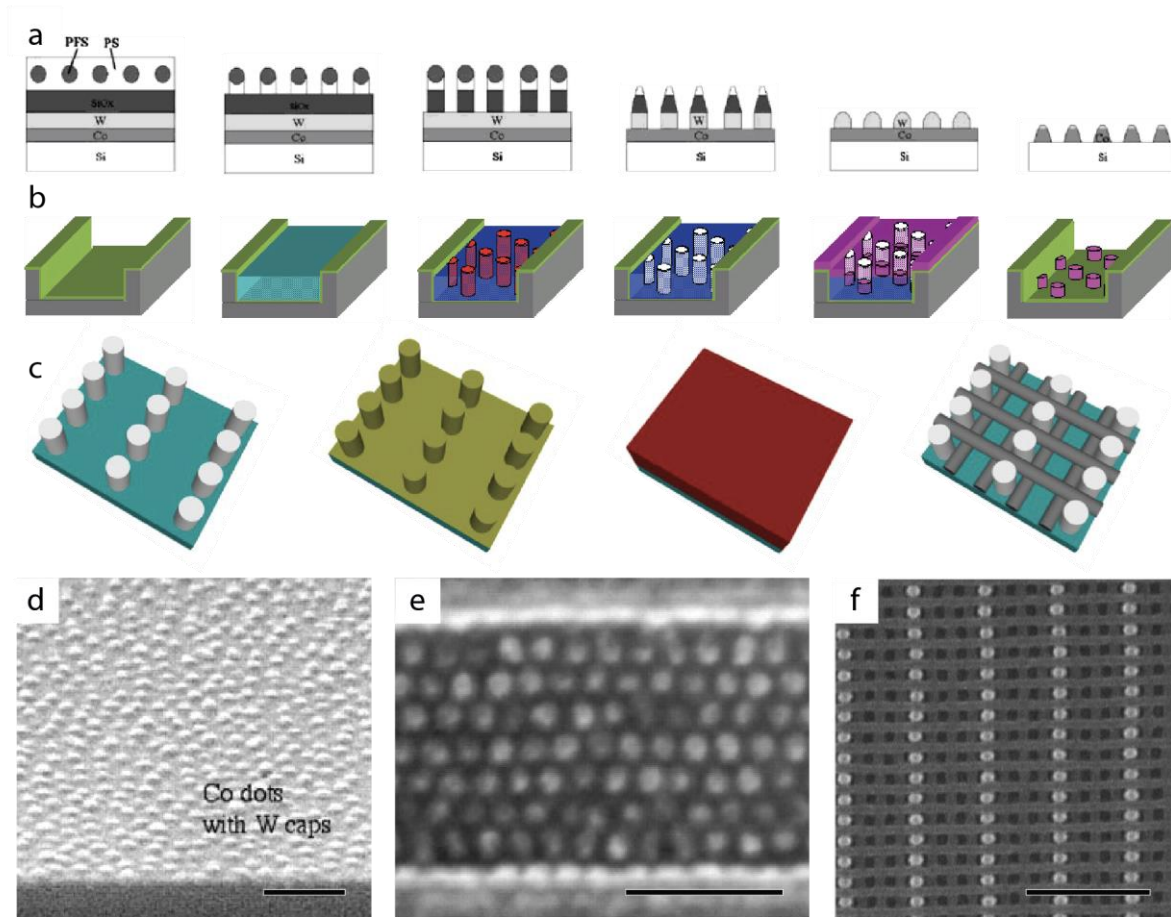


Figure 110. Schematics of the formation of a cobalt dot array (a) using PS-b-PFS sphere mask above a cobalt layer and (b) using PS-b-PMMA out-of-plane cylinders to form a hexagonally packed hole template which is subsequently filled by cobalt. (c) Schematics of the fabrication of 3D PS-b-PDMS in-plane cylindrical structure above a nano-templated substrate. SEM image of (d) W-capped cobalt dot array produced with process (a), (e) magnetic cobalt dot arrays produced with process (b), and (f) 3D structure formed from two layers of ceramized PDMS cylinder arrays produced with process (c). Scale bars:200 nm.

For the bottom-up approach, several materials can be used for their ferromagnetic, antiferromagnetic or ferroelectric properties such as cobalt, chromium or lead zirconate titanate,

respectively. However, this approach produces 2D flat structure and does not take advantage of the possibility to stack BCP layers to form 3D structures.

More recently, another type of memory has been developed by Intel and Micron Technology, called 3D cross-point memory, and requires the precise orientation of nanowires in 3D. Tavakkoli *et al.* showed that this more complex 3D nanostructure can be produced by ordering a bilayer of in-plane cylinders using nanoposts to control the self-assembly [45] (*Figures 110.c,f*). Accordingly, the structure is composed of two rows of cylinders (obtained by selecting an appropriate BCP layer thickness), and it is not possible to further tune the pattern configuration. Interestingly, the layer-by-layer approach developed in this Ph.D. should be able to generate more complex configurations and to reach tailored 3D-nanostructure which might be better adapted to the cross-point memory application.

V.4.B/ 3D-nanopillars memory device

An interesting use of the layer-by-layer approach can be imagined to improve the data storage capacity. Indeed, some groups used out-of-plane cylinders subsequently functionalized with a ferromagnetic material to form dots that can store data, known as metal nanodot memory. However, this type of device produces a 2D memory array, which capacity is dictated by the dot density. For instance, if the distance between each dot is 30 nm, it gives around 1.3×10^{11} dots/cm² density, which correspond to around 130 Gb/cm² by assuming that each dot can store 1 bit. In 2012 the areal density value of hard disk drives was around this value [46] and reached the value of 170 Gb/cm² in 2021 [47]. The theoretical value obtained with BCP is relatively high, but already obtained using other technologies. However, it could be drastically enhanced by stacking dot patterns on top of each other, to create pillars that could each store more than one bit. In the case of a stack of 8 layers separated with an intermediate conductive electrode, this would lead to the direct storage of an octet. *Figure 111* proposes a potential process to fabricate this type of 3D device.

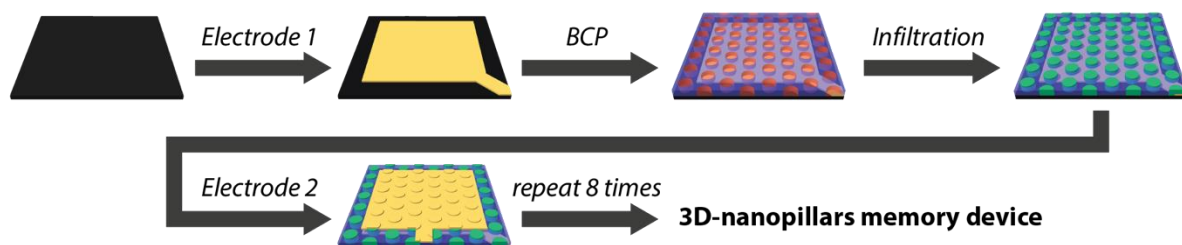


Figure 111. Schematics of the responsive layering process of registered out-of-plane cylinders hybridized into an appropriate material and separated by a conductive electrode for the formation of a 3D-nanopillars memory device.

The electrode deposition step could be performed with gold sputtering and the appropriate mask to form the desired layer shape. The BCP step can be performed as detailed in this manuscript, using the adequate RCP composition to obtain the correct responsive layering response. It is noteworthy that the infiltration step has to transform the cylindrical domains into a material with the appropriate electric and/or magnetic properties while the other domains should retain their isolator properties.

V.4.C/ Experimental challenges

With this approach using 3D-nanopillars, the main limitation inherent to BCP self-assembly, i.e. the formation of defects and grains, could be resolved by directed self-assembly methods. However, a strong experimental challenge remains: how can we hybridize the cylindrical domains with an adequate material? The candidate retained for this study was bismuth ferrite (BiFeO_3) denoted BFO, which has a multiferroic behavior above room temperature, i.e. magnetic and ferroelectric properties, considered as a very promising material for memory devices [48].

V.4.C.i/ PMMA infiltration

Considering the works done during this Ph.D., *PS-*b*-PMMA* would be a candidate of interest as methods to stack such BCP layers have been shown to produce well-defined 3D structures. However, *PS-*b*-PMMA* is not compatible with liquid phase infiltration, e.g. metallic salt infiltration, and one should focus on vapor phase infiltration methods, e.g. SIS. In this case, the metal oxide is produced within the PMMA phase, thus the requirements for this method are:

- The formation of a metal oxide that possesses electric or magnetic properties that can be compatible with data storage at room temperature;
- The precursor(s) used for the SIS are small and mobile enough to penetrate the PMMA domains. They also need to be able to form specific interactions with PMMA to ensure a selective localization;
- The SIS reaction should occur below *PS-*b*-PMMA* order-disorder temperature to preserve the self-assembled structure during the process.

Several research groups described the ALD growth of BFO thin films, exhibiting good electromagnetic properties [49]–[55]. These syntheses were performed using different precursors at different temperatures. For bismuth, the $\text{Bi}(\text{CH}_3)_3$ precursor seems a good candidate since it is very similar to TMA which is used for the formation of Al_2O_3 in the PMMA domains. Unfortunately, the precursors for iron used in these syntheses are rather large and might not be selectively incorporate into the PMMA domains. Another precursor used to grow Fe_2O_3 is FeCl_3

[56] which might be interesting for SIS. However, the presence of chlorine in the precursor is not very convenient as it produces HCl which is highly corrosive for the ALD tool.

For the reaction temperature, the reported ALD window is between 150°C and 250°C which might be too high for SIS of BCP patterns. However, the ALD and SIS processes are slightly different, and it might be possible to perform the reaction at lower temperature using long exposure times. Also, a second annealing at the end of the reaction at around 500 °C to 700 °C is mandatory to crystalize the BFO. This would in parallel remove the PS domains which could impart the mechanical integrity of the BCP pattern.

To conclude, this SIS route seems promising because it would create a fully inorganic memory storage device, and would be easy to perform from a self-assembly point-of-view. However, strong challenges remain with in particular the SIS of BFO and the final annealing treatment.

V.4.C.ii/ BCP modification

A second possible route would be to employ a different BCP system than PS-*b*-PMMA. It should be compatible with metallic salt impregnation, such as PS-*b*-PxVP (x=2 or 4, see *Chapter.2.D.ii/*). Interestingly, the formation of a BFO thin film by spin coating a solution containing Bi and Fe precursors followed by a baking step to crystalize the oxide have been reported in the literature [57]. The precursors used during this study were iron acetylacetonate (Fe(Acac)₃) and bismuth nitrate (Bi(NO₃)₃·5H₂O), and it would be interesting to see if these molecules selectively interact with the PxVP block.

A preliminary study was performed to observe the infiltration of these two precursors within an out-of-plane cylinder forming PS-*b*-P2VP thin film. For this experiment, a 0.5 wt.% solution of PS-*b*-P2VP (M_n(PS) = 135 kg/mol and M_n(P2VP) = 53 kg/mol) in PGMEA was spin coated at 2000 rpm on top of a silicon substrate grafted with the 75r25 RCP. Then the thin film was solvent annealed in a chamber containing THF vapors during 10 min to promote the self-assembly (*Figure 112.a*). This film was subsequently infiltrated with a 1 wt.% iron acetylacetonate (Fe(acac)₃) and bismuth nitrate (Bi(NO₃)₃·5H₂O) stoichiometric solution in a mixture of acetic acid and 1,3-propanediol (4:1 vol:vol), by immersing the sample in this solution during 5 min. The infiltrated structure was etched during 20 min using UV/O₃ treatment leading to nanodots composed of Bi and/or Fe oxides (*Figure 112.b*).

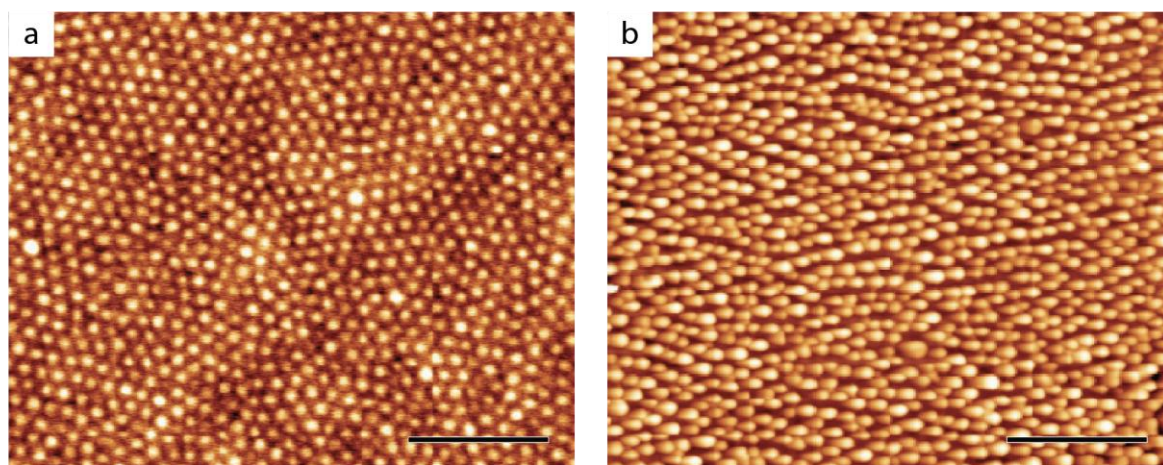


Figure 112. AFM height image of out-of-plane cylinder forming PS-*b*-P2VP (a) after self-assembly by THF solvent annealing and (b) after impregnation with a Bi and Fe solution followed by an UV/O₃ etching. Scale bars: 500 nm.

Interestingly, performing the same process with a solution containing only one of the two precursor leads to similar results, meaning that both precursors are actually infiltrated in the P2VP domains. However, the kinetics might not be the same, and a specific ratio between precursors might be needed to obtain the appropriate BFO stoichiometry.

PS-*b*-P4VP thin films were also tested, leading to a significant lower oxide growth within the P4VP block, which might be due to weaker interactions between the precursors and the nitrogen lone pair in the *para* position. Finally, it was demonstrated that the acetic acid is required for a good infiltration, as expected from the solubility of both precursors [58].

This preliminary work was performed in collaboration by Estelle Pinto Dos Santos, an intern that spent two months in the group.

This could solve the difficulty to grow BFO into PMMA by SIS, however, the pyrolysis step is still required, thus PS should be transformed into an inorganic material. However, since the BCP is not PS-*b*-PMMA anymore, it could be intelligent to choose a BCP that could also solve this issue, with a second block that can be transformed into inorganic material, such as PDMS that can be ceramized, or any another block that could be selectively hybridized with a different process.

V.5/ Conclusions

In this chapter, we presented the proof-of-concept for the stacking of three layers, which successfully enable the deployment of this stacking process for n layers, i.e. the iterative formation of 3D nanostructures. Then, to illustrate it, two potential devices were proposed: a 3D gold nanogrid for optical application, and a hexagonally packed pillar for stacked data storage.

For both proposals, a quick bibliographic survey was performed to define the state-of-the-art on the BCP based devices in the same field. Then, an ideal structure made by iterative layering was proposed, with an imagined process to achieve it. Finally, the experimental challenges about the process were listed, because it requires more complex BCP structure modification than only Al_2O_3 infiltration and PS plasma removal. Interestingly, some preliminary studies were performed to propose solutions, such as gold electrodeposition growth and selective BiFeO_3 infiltration within a P2VP block.

V.6/ References

- [1] M. P. Stoykovich *et al.*, “Directed Self-Assembly of Block Copolymers for Nanolithography: Fabrication of Isolated Features and Essential Integrated Circuit Geometries,” *ACS Nano*, vol. 1, no. 3, pp. 168–175, Oct. 2007, doi: 10.1021/nn700164p.
- [2] H.-C. C. Kim, S.-M. M. Park, W. D. Hinsberg, and I. R. Division, “Block Copolymer Based Nanostructures: Materials, Processes, and Applications to Electronics,” *Chem. Rev.*, vol. 110, no. 1, pp. 146–177, 2010, doi: 10.1021/cr900159v.
- [3] I. W. Hamley, “Nanostructure fabrication using block copolymers,” *Nanotechnology*, vol. 14, no. 10, 2003, doi: 10.1088/0957-4484/14/10/201.
- [4] J. K. Kim, S. Y. Yang, Y. Lee, and Y. Kim, “Functional nanomaterials based on block copolymer self-assembly,” *Prog. Polym. Sci.*, vol. 35, no. 11, pp. 1325–1349, 2010, doi: 10.1016/j.progpolymsci.2010.06.002.
- [5] N. Demazy, C. Cummins, K. Aissou, and G. Fleury, “Non-Native Block Copolymer Thin Film Nanostructures Derived from Iterative Self-Assembly Processes,” *Adv. Mater. Interfaces*, vol. 1901747, pp. 1–11, 2019, doi: 10.1002/admi.201901747.
- [6] J. Y. Cheng, C. A. Ross, H. I. Smith, and E. L. Thomas, “Templated self-assembly of block copolymers: Top-down helps bottom-up,” *Adv. Mater.*, vol. 18, no. 19, pp. 2505–2521, 2006, doi: 10.1002/adma.200502651.
- [7] C. J. Hawker and T. P. Russell, “Block copolymer lithography: Merging ‘bottom-up’ with ‘top-down’ processes,” *MRS Bull.*, vol. 30, no. 12, pp. 952–966, 2005, doi: 10.1557/mrs2005.249.
- [8] P. Mokarian-Tabari *et al.*, “Large Block Copolymer Self-Assembly for Fabrication of Subwavelength Nanostructures for Applications in Optics,” *Nano Lett.*, vol. 17, no. 5, pp. 2973–2978, 2017, doi: 10.1021/acs.nanolett.7b00226.
- [9] H. S. Lee, T. S. Shim, H. Hwang, S. M. Yang, and S. H. Kim, “Colloidal photonic crystals toward structural color palettes for security materials,” *Chem. Mater.*, vol. 25, no. 13, pp. 2684–2690, 2013, doi: 10.1021/cm4012603.
- [10] W. Liu, H. Ma, and A. Walsh, “Advance in photonic crystal solar cells,” *Renew. Sustain. Energy Rev.*, vol. 116, no. September, p. 109436, 2019, doi: 10.1016/j.rser.2019.109436.
- [11] R. V. Nair and R. Vijaya, “Photonic crystal sensors: An overview,” *Prog. Quantum Electron.*, vol. 34, no. 3, pp. 89–134, 2010, doi: 10.1016/j.pquantelec.2010.01.001.
- [12] C. Park, J. Yoon, and E. L. Thomas, “Enabling nanotechnology with self assembled block copolymer patterns,” *Polymer (Guildf.)*, vol. 44, no. 22, pp. 6725–6760, 2003, doi: 10.1016/j.polymer.2003.08.011.
- [13] B. A. C. Edrington *et al.*, “Polymer-Based Photonic Crystals,” no. 6, pp. 421–425, 2001, doi: 10.1002/1521-4095(200103).
- [14] X. Zhang, J. Qiu, X. Li, J. Zhao, and L. Liu, “Complex refractive indices measurements of polymers in visible and near-infrared bands,” *Appl. Opt.*, vol. 59, no. 8, p. 2337, 2020, doi: 10.1364/ao.383831.
- [15] M. R. Querry, “Optical Constants, Report No. AD-A158 623,” *Crdc*, vol. CR-85034, pp. 1–413, 1985, [Online]. Available: <https://apps.dtic.mil/dtic/tr/fulltext/u2/a158623.pdf>.
- [16] P. B. Johnson and R. W. Christy, “Optical Constants of the Noble Metals,” *Phys. Rev. B*, vol. 6, no. 12, pp. 4370–4379, Dec. 1972, doi: 10.1103/PhysRevB.6.4370.
- [17] N. I. Zheludev, “Applied physics. The road ahead for metamaterials,” *Science*, vol. 328, no. 5978, pp. 582–583, Apr. 2010, doi: 10.1126/science.1186756.

- [18] W. Cai and V. Shalaev, *Optical Metamaterials*. New York, NY: Springer New York, 2010.
- [19] V. M. Shalaev, "Optical negative-index metamaterials," *Nat. Photonics*, vol. 1, no. 1, pp. 41–48, Jan. 2007, doi: 10.1038/nphoton.2006.49.
- [20] A. Alvarez-Fernandez *et al.*, "Block Copolymer Directed Metamaterials and Metasurfaces for Novel Optical Devices," *Adv. Opt. Mater.*, vol. 9, no. 16, 2021, doi: 10.1002/adom.202100175.
- [21] K. Hur, Y. Francescato, V. Giannini, S. A. Maier, R. G. Hennig, and U. Wiesner, "Three-dimensionally isotropic negative refractive index materials from block copolymer self-assembled chiral gyroid networks," *Angew. Chemie - Int. Ed.*, vol. 50, no. 50, pp. 11985–11989, 2011, doi: 10.1002/anie.201104888.
- [22] S. Vignolini *et al.*, "A 3D optical metamaterial made by self-assembly," *Adv. Mater.*, vol. 24, no. 10, pp. 23–27, 2012, doi: 10.1002/adma.201103610.
- [23] C. Kilchoer *et al.*, "Hyperbolic Optical Metamaterials from Shear-Aligned Block Copolymer Cylinder Arrays," *Adv. Photonics Res.*, vol. 1, no. 2, p. 2000037, 2020, doi: 10.1002/adpr.202000037.
- [24] A. Polemi and K. L. Shuford, "Two-dimensional plasmonic nanosurface for photovoltaics," *J. Appl. Phys.*, vol. 110, no. 11, 2011, doi: 10.1063/1.3667194.
- [25] A. S. Urban, S. Carretero-Palacios, A. A. Lutich, T. Lohmüller, J. Feldmann, and F. Jäckel, "Optical trapping and manipulation of plasmonic nanoparticles: Fundamentals, applications, and perspectives," *Nanoscale*, vol. 6, no. 9, pp. 4458–4474, 2014, doi: 10.1039/c3nr06617g.
- [26] P. A. Mistark *et al.*, "Block-Copolymer-Based Plasmonic Nanostructures," *ACS Nano*, vol. 3, no. 12, pp. 3987–3992, Dec. 2009, doi: 10.1021/nn901245w.
- [27] J. H. Mun *et al.*, "Nanodomain swelling block copolymer lithography for morphology tunable metal nanopatterning," *Small*, vol. 10, no. 18, pp. 3742–3749, 2014, doi: 10.1002/smll.201400600.
- [28] C. Cummins *et al.*, "An Ultra-Thin Near-Perfect Absorber via Block Copolymer Engineered Metasurfaces," *J. Colloid Interface Sci.*, vol. 609, pp. 375–383, Mar. 2022, doi: 10.1016/j.jcis.2021.11.163.
- [29] S. Y. Kim, J. Gwyther, I. Manners, P. M. Chaikin, and R. A. Register, "Metal-containing block copolymer thin films yield wire grid polarizers with high aspect ratio," *Adv. Mater.*, vol. 26, no. 5, pp. 791–795, 2014, doi: 10.1002/adma.201303452.
- [30] A. Subramanian, G. Doerk, K. Kisslinger, D. H. Yi, R. B. Grubbs, and C.-Y. Nam, "Three-Dimensional Electroactive ZnO Nanomesh Directly Derived from Hierarchically Self-Assembled Block Copolymer Thin Films," *Submitted*, pp. 9533–9546, 2019, doi: 10.1039/C9NR00206E.
- [31] J. Chai, D. Wang, X. Fan, and J. M. Buriak, "Assembly of aligned linear metallic patterns on silicon," *Nat. Nanotechnol.*, vol. 2, no. 8, pp. 500–506, 2007, doi: 10.1038/nnano.2007.227.
- [32] J. Chai and J. M. Buriak, "Using Cylindrical Domains of Block Copolymers To Self-Assemble and Align Metallic Nanowires," *ACS Nano*, vol. 2, no. 3, pp. 489–501, Mar. 2008, doi: 10.1021/nn700341s.
- [33] J. Arias-Zapata *et al.*, "Engineering Self-Assembly of a High- χ Block Copolymer for Large-Area Fabrication of Transistors Based on Functional Graphene Nanoribbon Arrays," *Chem. Mater.*, vol. 31, no. 9, pp. 3154–3162, 2019, doi: 10.1021/acs.chemmater.8b04936.
- [34] H. Y. Chi, H. W. Hsu, S. H. Tung, and C. L. Liu, "Nonvolatile Organic Field-Effect Transistors Memory Devices Using Supramolecular Block Copolymer/Functional Small Molecule

- Nanocomposite Electret," *ACS Appl. Mater. Interfaces*, vol. 7, no. 10, pp. 5663–5673, 2015, doi: 10.1021/acsami.5b00338.
- [35] W. L. Leong *et al.*, "Non-volatile organic memory applications enabled by in situ synthesis of gold nanoparticles in a self-assembled block copolymer," *Adv. Mater.*, vol. 20, no. 12, pp. 2325–2331, 2008, doi: 10.1002/adma.200702567.
- [36] P. S. Jo *et al.*, "Self assembled block copolymer gate insulators with cylindrical nanostructures for pentacene thin film transistor," *Macromol. Res.*, vol. 18, no. 8, pp. 777–786, 2010, doi: 10.1007/s13233-010-0805-5.
- [37] P. S. Jo *et al.*, "Controlled topology of block copolymer gate insulators by selective etching of cylindrical microdomains in pentacene organic thin film transistors," *Adv. Funct. Mater.*, vol. 18, no. 8, pp. 1202–1211, 2008, doi: 10.1002/adfm.200701034.
- [38] J. Y. Cheng, C. A. Ross, V. Z. H. Chan, E. L. Thomas, R. G. H. Lammertink, and G. J. Vancso, "Formation of a cobalt magnetic dot array via block copolymer lithography," *Adv. Mater.*, vol. 13, no. 15, pp. 1174–1178, 2001, doi: 10.1002/1521-4095(200108)13:15<1174::AID-ADMA1174>3.0.CO;2-Q.
- [39] K. Liu, S. M. Baker, M. Tuominen, T. P. Russell, and I. K. Schuller, "Tailoring exchange bias with magnetic nanostructures," *Phys. Rev. B - Condens. Matter Mater. Phys.*, vol. 63, no. 6, pp. 604031–604034, 2001, doi: 10.1103/PhysRevB.63.060403.
- [40] K. Naito, H. Hieda, M. Sakurai, Y. Kamata, and K. Asakawa, "2.5-Inch disk patterned media prepared by an artificially assisted self-assembling method," *INTERMAG Eur. 2002 - IEEE Int. Magn. Conf.*, vol. 38, no. 5, pp. 1949–1951, 2002, doi: 10.1109/INTMAG.2002.1000594.
- [41] T. Thurn-Albrecht *et al.*, "Ultrahigh-density nanowire arrays grown in self-assembled diblock copolymer templates," *Science (80-.)*, vol. 290, no. 5499, pp. 2126–2129, 2000, doi: 10.1126/science.290.5499.2126.
- [42] S. Xiao *et al.*, "Graphoepitaxy of cylinder-forming block copolymers for use as templates to pattern magnetic metal dot arrays," *Nanotechnology*, vol. 16, no. 7, pp. S324–S329, Jul. 2005, doi: 10.1088/0957-4484/16/7/003.
- [43] A. J. Hong *et al.*, "Metal nanodot memory by self-assembled block copolymer lift-off," *Nano Lett.*, vol. 10, no. 1, pp. 224–229, 2010, doi: 10.1021/nl903340a.
- [44] J. Varghese *et al.*, "Fabrication of arrays of lead zirconate titanate (PZT) nanodots via block copolymer self-assembly," *Chem. Mater.*, vol. 25, no. 8, pp. 1458–1463, 2013, doi: 10.1021/cm303759r.
- [45] A. K. G. Tavakkoli, "Templating Three-Dimensional Self-Assembled Structures in Bilayer Block Copolymer Films A. Tavakkoli K. G.," vol. 1294, no. 2012, pp. 1294–1299, 2013, doi: 10.1126/science.1218437.
- [46] B. Marchon, T. Pitchford, Y.-T. Hsia, and S. Gangopadhyay, "The Head-Disk Interface Roadmap to an Areal Density of Tbit/in²," *Adv. Tribol.*, vol. 2013, pp. 1–8, 2013, doi: 10.1155/2013/521086.
- [47] G. Albuquerque, S. Hernandez, M. T. Kief, D. Mauri, and L. Wang, "HDD Reader Technology Roadmap to an Areal Density of 4 Tbps and Beyond," *IEEE Trans. Magn.*, vol. 9464, no. c, 2021, doi: 10.1109/TMAG.2021.3081042.
- [48] R. Safi and H. Shokrollahi, "Physics, chemistry and synthesis methods of nanostructured bismuth ferrite (BiFeO₃) as a ferroelectro-magnetic material," *Prog. Solid State Chem.*, vol. 40, no. 1–2, pp. 6–15, Jun. 2012, doi: 10.1016/j.progsolidstchem.2012.03.001.
- [49] Y. T. Liu, C. S. Ku, S. J. Chiu, H. Y. Lee, and S. Y. Chen, "Ultrathin oriented BiFeO₃ films from deposition of atomic layers with greatly improved leakage and ferroelectric properties," *ACS Appl. Mater. Interfaces*, vol. 6, no. 1, pp. 443–449, 2014, doi: 10.1021/am404498y.

- [50] A. V. Plokhikh *et al.*, "Formation of BiFeO₃ from a Binary Oxide Superlattice Grown by Atomic Layer Deposition," *ChemPhysChem*, vol. 18, no. 15, pp. 1966–1970, 2017, doi: 10.1002/cphc.201700407.
- [51] C. D. Pham, J. Chang, M. A. Zurbuchen, and J. P. Chang, "Synthesis and Characterization of BiFeO₃ Thin Films for Multiferroic Applications by Radical Enhanced Atomic Layer Deposition," *Chem. Mater.*, vol. 27, no. 21, pp. 7282–7288, 2015, doi: 10.1021/acs.chemmater.5b02162.
- [52] P. Jalkanen *et al.*, "Magnetic properties of polycrystalline bismuth ferrite thin films grown by atomic layer deposition," *J. Phys. Chem. Lett.*, vol. 5, no. 24, pp. 4319–4323, 2014, doi: 10.1021/jz502285f.
- [53] A. R. Akbashev, G. Chen, and J. E. Spanier, "A facile route for producing single-crystalline epitaxial perovskite oxide thin films," *Nano Lett.*, vol. 14, no. 1, pp. 44–49, 2014, doi: 10.1021/nl4030038.
- [54] F. Zhang *et al.*, "Atomic Layer Deposition of BiFeO₃ Thin Films Using β -Diketonates and H₂O," *J. Phys. Chem. C*, vol. 117, no. 46, pp. 24579–24585, Nov. 2013, doi: 10.1021/jp4080652.
- [55] M. Coll *et al.*, "Nanocrystalline Ferroelectric BiFeO₃ Thin Films by Low-Temperature Atomic Layer Deposition," *Chem. Mater.*, vol. 27, no. 18, pp. 6322–6328, 2015, doi: 10.1021/acs.chemmater.5b02093.
- [56] A. Tanskanen, O. Mustonen, and M. Karppinen, "Simple ALD process for ϵ -Fe₂O₃ thin films," *APL Mater.*, vol. 5, no. 5, 2017, doi: 10.1063/1.4983038.
- [57] M. Tomczyk, D. G. Stroppa, I. M. Reaney, and P. M. Vilarinho, "Growth of BiFeO₃ thin films by chemical solution deposition: The role of electrodes," *Phys. Chem. Chem. Phys.*, vol. 19, no. 22, pp. 14337–14344, 2017, doi: 10.1039/c7cp01842h.
- [58] C. Gutiérrez-Lázaro *et al.*, "Solution synthesis of BiFeO₃ thin films onto silicon substrates with ferroelectric, magnetic, and optical functionalities," *J. Am. Ceram. Soc.*, vol. 96, no. 10, pp. 3061–3069, 2013, doi: 10.1111/jace.12569.

GENERAL CONCLUSIONS

BCP self-assembly in a thin film configuration has been the focus of intense research activity over the past decade since it can produce a variety of patterns at a nanometric scale through “low cost” processes. Indeed, this technology only requires the thoughtful design of BCP architectures associated with the optimization of self-assembly processes, while a thermodynamic driving force performs the remaining work. Nevertheless, this spontaneous ordering exhibits several issues that have been the focus of important research works: i) the limited number of achievable structures, and ii) the presence of defects within the self-assembled structure. Several solutions were proposed to overcome these challenges, such as the modification of the BCP architecture toward more complex BCP configurations (i.e. number of blocks, number of chemistries, arrangement of blocks (linear, star, graft, etc.)) and the establishment of directed self-assembly methodologies. Among all the methods expanding the scope of BCP self-assembly, a layer-by-layer approach was the main focus of this Ph.D. as it allows the generation of non-native BCP morphologies, and the implementation of registration mechanisms between the layers that can be further used as a directed self-assembly method.

For this study, the PS-*b*-PMMA system was chosen as its self-assembly is well-described in the literature and shows a good correlation with theoretical predictions. Accordingly, it is a good candidate to study the layering mechanisms in order to produce complex nanostructures with defined arrangement in the 3D space. Using this system, we demonstrated that every simple di-BCP nanostructure is achievable in thin films, i.e. PS/PMMA lamellae, hexagonal packing of PS or PMMA cylinders and hexagonal close-packed PS or PMMA spheres. A focus was given on the lamellar and cylindrical structures in order to generate in a thin film configuration, leading to line & space, dot and hole patterns after hybridization. We further developed an adequate process to stack these various structures using a “responsive layering” mechanism in order to control the registration of the layers between them. In particular, different stacking configurations (above, between or edges) were obtained depending of the topographical and chemical fields between the layers. Thus, we demonstrated the controlled formation of a cornucopia of 3D nanostructures that are non-native to BCP self-assembly.

This opens avenues to perform reverse engineering with BCPs to produce complex devices as proposed in the last chapter. Indeed, with this approach, it is possible to design an ideal targeted 3D-nanostructure, and then optimize a layering process to manufacture it. In summary, we have

developed a methodology which could, in the long term, produce tailored nanometric 3D-nanostructures (from 24 nm to 64 nm) with on-demand functionalities specific to each layer size.

It is noteworthy that the annihilation of defects was not thoroughly tackled during this Ph.D., but we have shown that the layering process performed in this study is compatible with directed self-assembly methods, e.g. graphoepitaxy and chemical epitaxy, which are the most powerful tools to form long range ordered BCP structures. An alternative directed self-assembly method was also proposed and is based on the formation of Al_2O_3 patterns obtained from the SRG of azobenzene-containing layers. These patterns were successfully used to direct PS-*b*-PMMA self-assembly using the topographical fields produced from the SRG mechanism.

By way of conclusion, we have proposed during this Ph.D. a novel layering approach based on BCP self-assembly and hybridization methods of the resulting nanostructured layers. Even if additional studies to fully decipher the registration mechanisms are still needed, solid foundations were laid in order to rationalize the intricate relationships between the self-assembly of the different layers. Besides, we have demonstrated that this method could be extended to more than two BCP layers which could further widen the scope of applications of the iterative layering approach to the manufacturing of practical technological devices.

ANNEX

1/ Thin film process	230
1.A/ Self-assembly	230
1.B/ Hybridization	231
2/ Thin film characterization	235
2.A/ Atomic Force Microscopy (AFM)	235
2.B/ Scanning Electron Microscopy (SEM).....	236
2.C/ Grazing Incidence Small Angle X-ray Scattering (GISAXS)	237
3/ Matlab programs & simulations	239
3.A/ Plasma etching waves simulation	239
3.B/ Hexagonally packed dots image analysis	241
3.C/ Di-block copolymers theoretical pitch and phase diagram position calculation	243
3.D/ SAXS intensity plot fitting to determine χ parameter	244
3.E/ Triply-Periodic Minimal Surface 3D modelling and 2D-slicing	256
3.F/ Lamellae stacking orientation	266
3.G/ NanoScope AFM image viewer and processing.....	271
4/ 2D-structures large SEM images	276
5/ References	289

1/ Thin film process

1.A/ Self-assembly

The standard process to obtain self-assembly from PS-*b*-PMMA is composed on three different steps: modification of the substrate surface energy, deposition of a BCP film and thermal annealing (*Figure 113*).

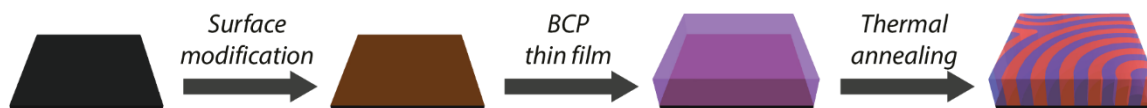


Figure 113. Schematics of the self-assembly process for the formation of nanostructured BCP film (here out-of-plane lamellae).

The overall process is performed in a cleanroom in order to prevent the formation of defects in the BCP layer induced by dust, and the detailed steps are the following:

- A silicon wafer is cut at the desired size and cleaned in a PGMEA bath three times separated by a drying step with a nitrogen flow;
- A 1.5 wt.% PS-*r*-PMMA in PGMEA is spin coated a 1500 rpm on the substrate;
- The PS-*r*-PMMA layer is heated at 230 °C for 5 min, to promote the grafting of polymer chains;
- The surface modified substrate is cleaned following the same process as previously in order to remove non-grafted PS-*r*-PMMA chains;
- A PS-*b*-PMMA in a PGMEA solution is spin coated on this surface modified substrate;
- The thin film is thermally annealed in an RTA oven, in order to promote BCP chain mobility (i.e. BCP self-assembly).

For the surface energy modification step, the concentration of the PS-*r*-PMMA solution is not critically important since non-grafted polymer chains are removed by a rinsing step after grafting. Nevertheless, the process should lead to a homogeneous coverage of the whole substrate and studies have showed that a minimum layer thickness (depending of the molecular weight of the PS-*r*-PMMA chains) is required to efficiently screen surface interactions with the substrate [1], [2]. Here, the PS-*r*-PMMA film thickness is around 40 nm before grafting, which covers perfectly the substrate. The temperature and duration of the annealing step (5 min at 230 °C) should be sufficient to promote grafting without degrading the polymer. Importantly, the PS-*r*-PMMA composition should be precisely chosen because it will dictate the subsequent substrate surface energy, and thus the ability to control the orientation of the BCP structure.

For the deposition of the BCP layer, a critical parameter is the BCP film thickness after annealing. It can be controlled through the concentration of the BCP solution, the viscosity of the solvent as well as by the spin-coating speed (see *1.1.B.i*). The formation of a particular BCP

structure is controlled by the PS-*b*-PMMA composition and molecular weight, which will determine the morphology and its periodicity (see *I.1.D*).

Finally, the thermal annealing is performed in a rapid thermal annealing (RTA) oven, under a N₂ atmosphere with a controlled heating ramp, annealing temperature, annealing duration and cooling ramp. The optimal temperature and duration are highly dependent of the BCP macromolecular characteristics. A standardized recipe for a PS-*b*-PMMA is the following (*Figure 114.a*):

- Three cycles of vacuum / N₂ purge of 10 s each at 50 °C;
- A heating ramp from 50 °C to the desired temperature in 10 s;
- The temperature of the chamber is maintained during a chosen duration;
- A N₂ flow is then applied to the chamber to cool it to room temperature, reducing the temperature below 100 °C in less than 40 s.

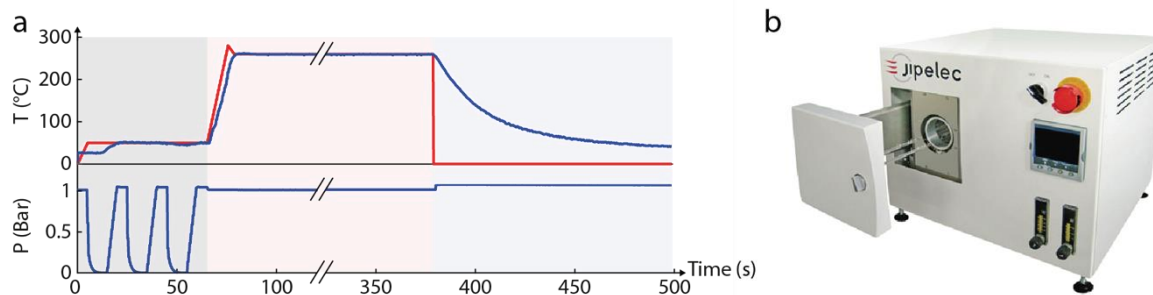


Figure 114 (a) RTA standard recipe with the input temperature ramp (red) and actual temperature ramp (blue) in the top panel, and the chamber pressure in bottom panel. The gray, red and blue backgrounds represent the purging cycles at 50 °C, the thermal annealing step (here 260 °C for 5 min) and the cooling ramp, respectively. (b) The RTA apparatus used during this Ph.D.

During this Ph.D., the rapid thermal annealing step was performed using a Jipelec JetLight RTA furnace (*Figure 114.b*)

1.B/ Hybridization

BCP nanostructures in thin film have the potential to be hybridized in order to add further functionalities. During this Ph.D., we opted to immobilize the BCP structure using a selective Al₂O₃ infiltration step by SIS in the PMMA domains (see *Chapter I.2.D.i*) followed by an etching step using RIE to remove the PS domains (see *Chapter I.2.C*) (*Figure 115*).

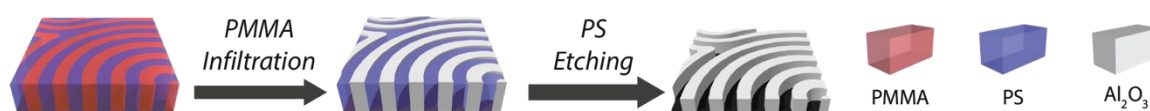


Figure 115. Schematics of the PMMA infiltration followed by PS etching process for out-of-plane lamellae.

1.B.i/ Sequential Infiltration Synthesis (SIS)

The SIS is a technique that permits to transform an organic matrix into metal oxides, using an atomic layer deposition (ALD) tool in an “exposure” mode. The general process is based on the infiltration of metallic gaseous precursors into an organic matrix followed by their oxidation to form the oxide species. In the case of PS-*b*-PMMA, the metallic gaseous precursor for the formation of Al₂O₃ are trimethyl aluminum and water (trimethyl aluminum (TMA) is strongly selective to PMMA, leading to the formation of Al₂O₃ in PMMA, while the PS domains remain unchanged (see *Chapter 1.2.D.i*)).

Experimentally, the sample is placed into the ALD chamber heated at 85 °C within a glovebox, and the standard SIS procedure is the following (*Figure 116.a*):

- The sample is cleaned with a 20 sccm N₂ flow during 2 min.
- A sequence of two infiltration cycles, which are described in *Figure 116*, is carried out. A cycle is composed of two static TMA infiltration of 1 min separated by a 10 s N₂ purge, followed by the same process but with water instead of TMA. Static infiltration means that the outer valve is closed while a precursor is pulsed into the chamber and the nitrogen flow is reduced to 5 sccm, leading to a slow increase of the pressure. A purge means that the outer valve is reopened, and the nitrogen flow is increased at 20 sccm for 5 s to remove the excess of precursors and then reduced to 5 sccm for the remaining 5 s to stabilize the flow before the next infiltration.
- The sample is finally cleaned with a step of a 20 sccm N₂ flow during 2 min, to remove by-products and unreacted precursors.

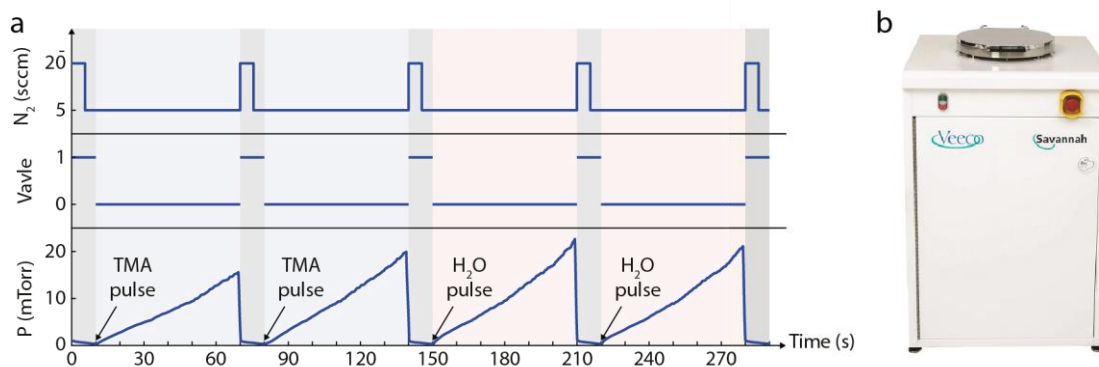


Figure 116. (a) SIS infiltration cycle sequence over time with the N₂ gas flow in the top panel, outer valve position in the middle panel (0=close, 1=open) and experimental chamber pressure in the bottom panel. The blue, red and gray backgrounds represent static TMA infiltration, static H₂O infiltration and N₂ purge respectively. (b) The ALD apparatus used during this Ph.D.

Different pressure peak values are observed between the first and second static TMA infiltration, from 15 mTorr to 20 mTorr (identical behavior for the first and second cycles). This pressure difference means that a TMA consuming reaction happens during first infiltration, which

can be related to the TMA absorption within the PMMA matrix, the TMA adsorption at the chamber surface or the TMA reaction with residual traces of water or oxygen. However, for recipes with more than two static TMA infiltrations, the same pressure peak value, around 20 mTorr, is observed for the second infiltration and all the subsequent infiltrations. Furthermore, no changes were observed regarding the final Al₂O₃ structure when applying more than two static infiltrations. Thus, a TMA excess in the chamber is reached after two infiltrations, and there is no interest to perform more than two infiltrations. Also, two static infiltrations were chosen for static water infiltrations for symmetry, even if no pressure peak decrease was observed.

During this Ph.D., SIS was performed using a Cambridge Nanotech Savannah S100 ALD machine within a glovebox (*Figure 116.b*).

1.B.ii/ Plasma etching

After infiltration, an etching treatment is necessary in order to remove the PS phase for further characterization or layer stacking. Dry etching with reactive ion etching (RIE) plasma is widely used in the BCP nanotechnology field since it can selectively etch one phase with respect to the other (see *Chapter 1.2.C/*). A plasma is generated with a strong radio frequency electromagnetic field that will strip off electrons from the gas. Then, this ionized gas can etch a polymeric target sample by:

- Chemical reactions with reactive species (i.e. radicals or ions), called chemical etching;
- Ion bombardment on the surface, called physical etching;
- UV radiation generated during the plasma formation, which can dissociate chemical bonds leading to polymer fragmentation.

With the RIE configuration, i.e. a sample deposited on top of the power electrode and below the shower head connected to the ground, the reactive ion bombardment is essentially vertical, leading to an anisotropic physical etching. However, for polymeric samples, isotropic chemical etching and UV fragmentation are not negligible. Thus, a competition between these three etching processes occurs and an optimization of the process is required to optimize the plasma anisotropy. Also, the process generates heat at the power electrode (which could be detrimental to the BCP thin film), which is regulated by a chiller.

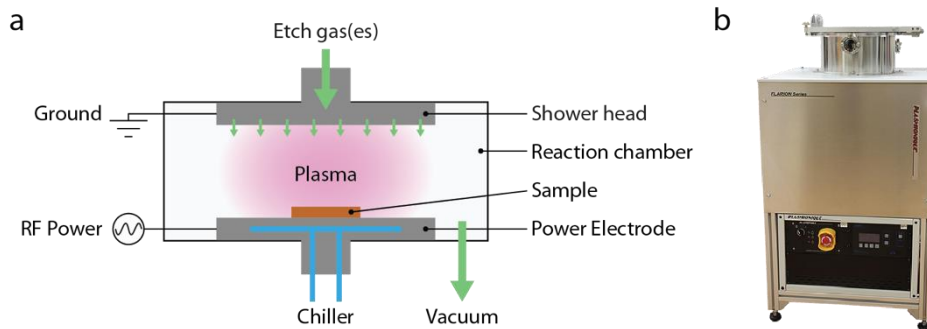


Figure 117. (a) Plasma RIE operating schematics and (b) the plasma apparatus used during this Ph.D.

There is no universal plasma recipes, since RIE etching is highly dependent of the etching tool, the chamber geometry, the polymer composition and structure, the film thickness, etc. However, the general procedure is the following:

- A sample is inserted in a plasma chamber chilled at 18 °C under dynamic vacuum (target: 80 mTorr);
- A gas or a mixture of gases (Argon, Oxygen or CF_4) is introduced with a certain gas flow (usual range is 20-40 sccm);
- A 30 s pause is observed to stabilize the chamber pressure (usual range is 150-170 mTorr according to the gas flow);
- The plasma is produced at the desired power (usual range is 20-40 W) for a chosen duration according to the targeted etching thickness;
- The plasma is turned off and the gas valve is closed. After few seconds of dynamic vacuum to remove by-products from the chamber, the sample is taken out from the chamber.

During this Ph.D., plasma etching was performed using a Plasmionique FLARION Series Plasma Etcher (*Figure 117.b*).

2/ Thin film characterization

To characterize BCP thin films, two direct imaging techniques have been used during this Ph.D. to probe the surface topography and the domain spatial arrangement: AFM and SEM. These techniques were routinely used to observe the nanostructured BCP thin films as well as to estimate critical dimensions and the overall quality of the self-assembled structures.

2.A/ Atomic Force Microscopy (AFM)

The AFM is a high-resolution imaging technique which produces an image by probing a sample surface with a tip, mounted on an oscillating cantilever near its resonance frequency, which will be deflected by surface interaction when the tip is close enough to the surface (*Figure 118.a*). This information is amplified from a laser reflection onto the cantilever surface and is recorded by a highly sensitive photodiode. The cantilever deflection is related with the interactions between the tip and surface, and two information can be obtained simultaneously:

- The sample topography (height channel) measured by the cantilever flexion modification with surface height differences;
- The surface composition (phase channel), measured by the modification of the phase shift between the drive and the response, due to attractive or repulsive forces between the tip and the surface (adhesion, stiffness, dissipation and viscoelasticity).

It is also possible to use conductive, magnetic or electroactive tips to probe the electrical, magnetic or piezoelectric response of a surface.

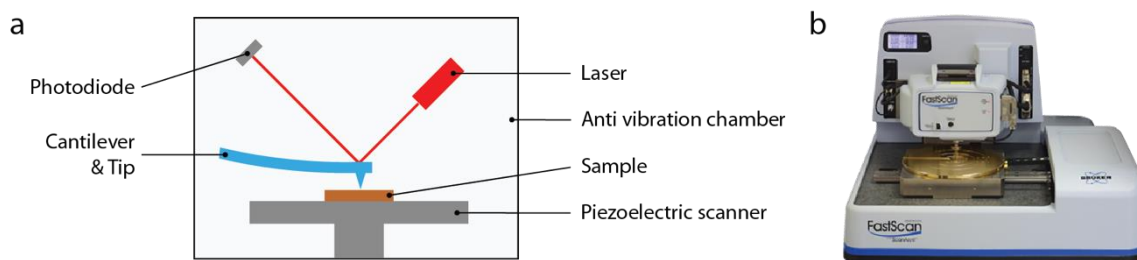


Figure 118. (a) AFM operating schematics and (b) the AFM apparatus used during this Ph.D.

The typical resolution of the AFM technique is the nanometer scale; its compatibility with thin film, and the possibility to differentiate chemical contrast makes it one of the most used imaging tools for the characterization of BCP thin films. Indeed, for self-assembled structures, the phase channel will spatially differentiate the two (or more) BCP components on the surface, giving structural information. Indeed, each block has different physical-chemical properties (in particular viscoelastic properties) that will modify the interaction forces with the tip. Also, the height channel can corroborate this structural information when a slight bump over the low

surface energy block appears, or after selective etching of one block leading to high topography differences.

During this Ph.D., a Bruker Dimension FastScan AFM (*Figure 118.b*) was used in tapping mode, with Fastscan-A probes (triangular tip with a 5 nm radius, cantilever spring constant of 18 N.m⁻¹ and resonance of 1400 KHz). This configuration allows a fast-scanning speed, leading to usually 1 min scan duration per image. Images were captured with Nanoscope 9.4 software from Bruker and the treatment of images has been made with a Matlab software developed for this purpose (see 3.G/ NanoScope AFM image viewer and processing)

2.B/ Scanning Electron Microscopy (SEM)

The SEM is an ultrahigh resolution imaging technique which produces images by scanning a sample surface with an electron focused beam under vacuum (*Figure 119.a*). An image is produced by the signal detected along the scan position. For the most common SEM mode, the signal is produced by secondary electrons emitted by the sample surface (and slightly below) atoms which were excited by the electron beam. Thus, the resolution is determined by the number of secondary electrons emitted by the surface, which depends among other on the sample topography and conductivity. For non-conductive samples, the electron beam will charge the surface with electrons which could not be evacuated, leading to a drastic lowering of contrast and resolution. To overcome this problem, it is possible to lower the electron beam voltage, but this will also lower the resolution. To bypass this issue, an electron beam deceleration function called gentle beam super high resolution (GBSH) can be applied on the particular SEM used in this study. This deceleration is made by applying a negative bias to the stage, thus lowering the effective electron beam voltage. This function decreases the charging effect while not (drastically) affecting the resolution.

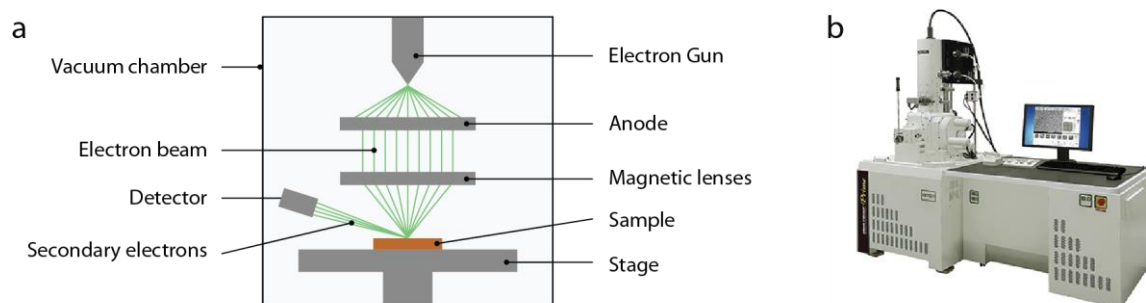


Figure 119. (a) SEM operating schematics and (b) the SEM apparatus used during this Ph.D.

The typical resolution is below a nanometer, which is a very interesting for BCP analysis. However, for “standard” self-assembled BCPs, e.g. PS-*b*-PMMA, the topography and conductivity contrast between each block are too small for being differentiated with SEM. Thus, a treatment is

required to increase this contrast: by selective etching of one phase to increase topography, by selective infiltration of one phase to modify its composition and conductivity, or by combining these two treatments.

During this Ph.D., a 7800-E Prime SEM from Jeol has been used (*Figure 119.b*) with an acceleration voltage of 15 kV with GBSH mode. For PS-*b*-PMMA imaging, PMMA was infiltrated with alumina and the PS phase was removed, leading to a high topographic contrast with a strong conductivity ratio.

2.C/ Grazing Incidence Small Angle X-ray Scattering (GISAXS)

GISAXS is a characterization technique that uses X-ray scattering to observe the nanostructure of thin films in a reflection mode. Indeed, the grazing incidence induces a substrate total reflection, and scattering within the film over long lateral distances. Then, a detector placed far away from the sample records the scattering, giving signals at defined position according to the studied diffractive nanostructure. Considering the beamline parameters, i.e. the X-ray wavelength λ , the incidence angle α_i , the distance between the sample and the detector L , and the detector pixel size u_{pix} it is possible to convert the detector pixel grid u_{xy} and u_z into scattered angles θ_s and α_s and then into scattered vector q_{xy} and q_z (*Equations (21) and (22)*, and *Figure 120.a*)

$$q_{xy} = \frac{4\pi}{\lambda} \sin\left(\frac{\theta_s}{2}\right) \quad \text{and} \quad \theta_s = \text{atan}\left(\frac{u_{xy} \times u_{pix}}{L}\right) \quad (21)$$

$$q_z = \frac{2\pi}{\lambda} \sin(\alpha_s) \quad \text{and} \quad \alpha_s = \text{atan}\left(\frac{u_z \times u_{pix}}{L}\right) \quad (22)$$

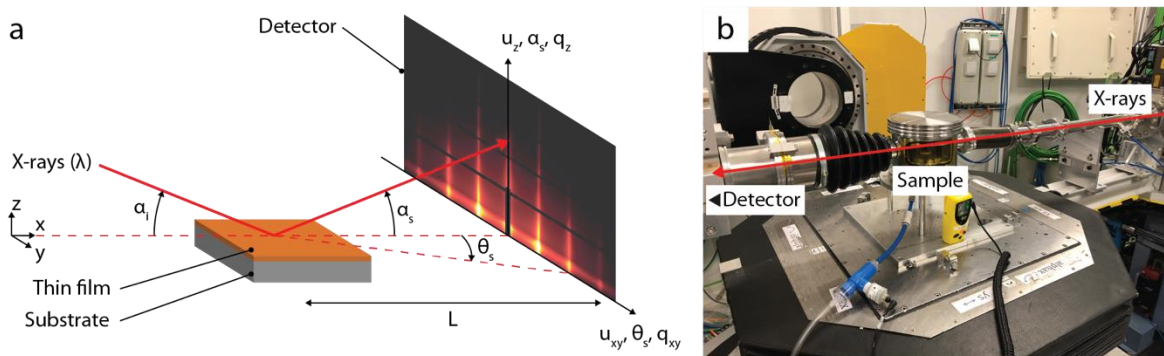


Figure 120. (a) GISAXS operating schematics and (b) the Sirius beamline from Soleil synchrotron used during this Ph.D.

Experimentally, the GISAXS experiments were performed on the Sirius beamline at the Soleil synchrotron (*Figure 120.b*), with a wavelength $\lambda = 0.155$ nm, a detector distance $L = 4445$ mm, a rectangular detector composed of 981×1043 pixels with a pixel size $u_{pix} = 0.172$ cm, and an X-ray incident angle $\alpha_i = 0.18^\circ$. This incident angle is below the critical angle of Si and SiO_2 ,

which are 0.224° and 0.239° respectively, meaning that X-rays will be fully reflected by the substrate, and then the measured spectra will depend only on the thin film surface, i.e. the nanostructure from BCP self-assembly. Also, the sample is placed in a chamber filled with helium to remove the air scattering background noise. The acquisition of GISAXS patterns were composed of 10 scans of 30 s each to improve signal-to-noise ratio.

3/ Matlab programs & simulations

This part describes the programs and simulations developed with Matlab 2021.a. The programs were developed with “App Designer” tool from Matlab, allowing the creation of standalone software, meaning that it can be used without Matlab software and Matlab license. No code will be presented, but only functionalities and usage. However, the programs can be shared on demand. For simulations, the complete code will be presented, which can be freely copied.

3.A/ Plasma etching waves simulation

```
function [x,z,p,h] = etchfilm(t,a,f,w,e,s)
% Created by Nils Demazy @ LCPO, Bordeaux
% Last update: August 24, 2021

%% INPUTS %%
% t = thickness: film thickness in nm
% a = amplitude: waves amplitude (peak to valley) in nm
% f = frequency: waves frequencies
% w = width: integer that determine simulation size = width*frequency
% e = etching: total etching in nm (e=t+a/2 for total etching)
% s = snapshot: number of printed curves

%% OUTPUTS %%
% x,z = x and z coordinate of the film at the end of the etching
% p = pickheight: maximum height of the film calculated for each snapshot
% h = halfwidth: width at lines half height for each snapshot

%% INITIALIZATION %%
x = 0 : 0.1 : w*f; % observable windows width, from 0 to chosen width
z = t+a/2*sin(2*pi*(x-f/4)/f); % simulated initial film height
k = 1; % snapshot counter
p = zeros(s,1); % initialization peakheight array
h = zeros(s,1); % initialization halfwidth array
etchstep = 0.01; % each step would etch 0.01nm of the film
% creation colormap for plot
blue = [43 75 155]/255;
red = [229 37 33]/255;
colormap = zeros(3,s);
colormap(1,:) = linspace(blue(1),red(1),s);
colormap(2,:) = linspace(blue(2),red(2),s);
colormap(3,:) = linspace(blue(3),red(3),s);
% initialization figure plot
fig = figure;
hold on
xlim([0 w*f]);
ylim([0 t+a/2+20]);
xlabel("x (nm)");
ylabel("z (nm)");
box on

%% CALCULATION %%
for i = 1 : e/etchstep+1
    for j = 1 : length(x)
        % calculating normal vector to the surface
        if j == 1 % extreme left of the film
            v = [x(j+1)-x(j) z(j)-z(j+1)];
        elseif j == length(x) % extreme right of the film
            v = [x(j)-x(j-1) z(j-1)-z(j)];
        else
            if z(j-1) == 0 % from cleaned surface to film specific case
                v = [x(j+1)-x(j) z(j)-z(j+1)];
            elseif z(j+1)==0 % from film to cleaned surface specific case
                v = [x(j)-x(j-1) z(j-1)-z(j)];
            else % normal case
                v = [x(j+1)-x(j-1) z(j-1)-z(j+1)];
            end
        end
    end
end
```

```

% etching film
X(j) = x(j)-etchstep*v(2)/norm(v);
Z(j) = z(j)-etchstep*v(1)/norm(v);
% if film is totally etched
if Z(j) <= 0
    Z(j) = 0;
end
end
% removing artifacts
X1 = X;
Z1 = Z;
for j = 1 : length(X)-1
    if X(j+1) <= X(j)
        X1(j) = mean([X(j),X(j+1)]);
        Z1(j) = mean([Z(j),Z(j+1)]);
        X1(j+1) = NaN;
        Z1(j+1) = NaN;
    end
end
X1(find(isnan(X1))) = [];
Z1(find(isnan(Z1))) = [];
clear x z X Z
x = X1;
z = Z1;
clear X1 Z1
% when a snapshot should be taken
if mod(i,round(e/((s-1)*etchstep))) == 1
    figure(fig)
    plot(x,z,'Color',colormap(:,k),'LineWidth',2)
    % calculating peak height and halfwidth
    p(k) = max(z);
    if find(z==0)
        if find (z>0)
            left = find(z-p(k)/2>0,1);
            h(k) = find(z(left+1:end)-p(k)/2<0,1)*0.1;
        else
            h(k) = 0;
        end
    else
        h(k) = 0;
    end
    k = k+1;
end
end
aspectratio = p./h; % calculating aspect ratio

%% PLOTS %%
figure
subplot(211)
plot(p,'Color',blue,'LineWidth',2)
xlim([1 s])
xticklabels({})
xlabel("Plasma etching duration (au)")
ylabel("Peak height (nm)");
box on
subplot(212)
plot(aspectratio,'Color',red,'LineWidth',2)
xlim([1 s])
yl = ylim;
ylim([0,yl(2)]);
xticklabels({})
xlabel("Plasma etching duration (au)")
ylabel("Aspect Ratio");
box on
end

```

Chapter II/Figure 40.a has been plotted using `etchfilm(130,100,372,2,165,20)`, and *Chapter II/Figure 40.b* using `etchfilm(130,100,372,2,165,100)` for more accuracy.

3.B/ Hexagonally packed dots image analysis

One of the most common ways for the characterization of BCP self-assembly is direct imaging with AFM or SEM. It is noteworthy that a contrast between the BCP phases is required for successful visualization of the BCP structure. These images can be further analyzed to obtain quantitative information, including important parameters for BCP characterization, such as the orientational / translational quality of the structure, the type and position of defects, and the correlation length (grain size).

For line/space pattern (i.e. lamellae or in-plane cylinders), a software based on ImageJ has been developed by Murphy et al.[3] in 2015, providing all these parameters from a SEM image (or a contrasted enough AFM image converted in black and white). An equivalent software for dot structures (out-of-plane cylinders or spheres) is not currently available, which is the reason why a software was developed in this Ph.D. work.

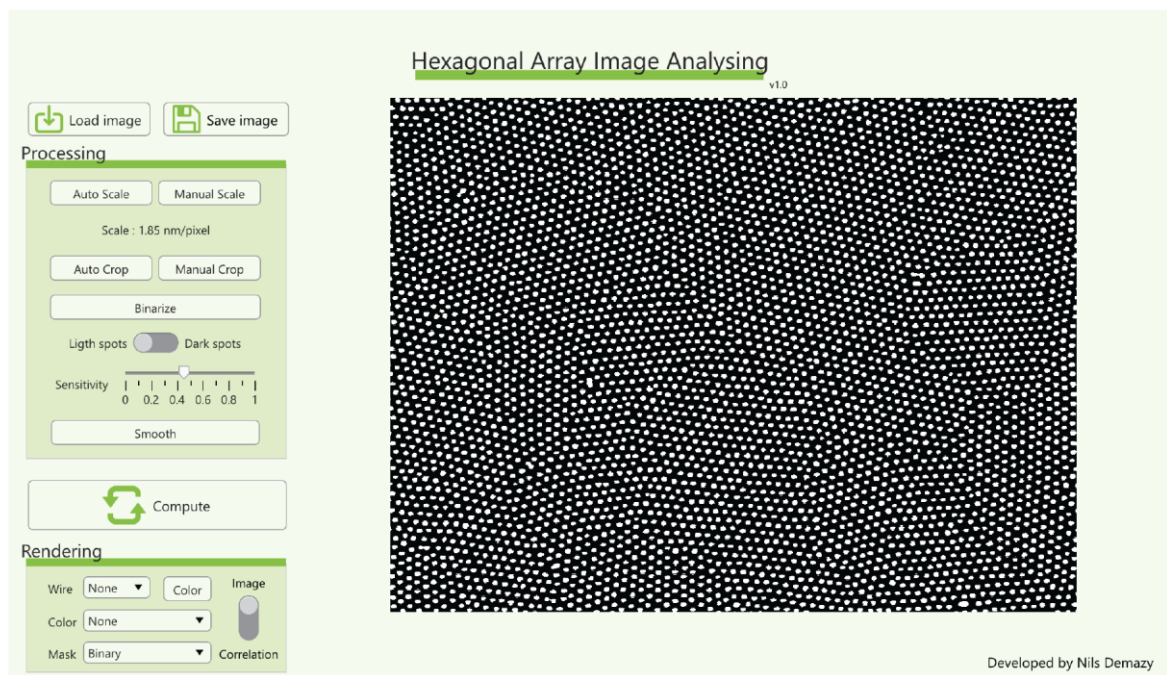


Figure 121. Hexagonal Array Image Analyzing window with processing and rendering parameters on the left, and resulting image on the right.

The software is presented as a unique window (Figure 121), and designed to be straightforward, with the following steps:

- First, load the image to analyze (Figure 122.a). Better results are obtained with black and white tiff image from SEM with flattened background and enhanced contrast;
- Then, complete the “Processing” tab by giving length scale of the image, by cropping if necessary, by binarizing the image and by optimizing threshold and smooth (Figure 122.b). A switch button can invert the picture contrast to process honeycomb (dark holes) structures

instead of hexagonal dots (bright dots). An automatic tool has been designed for SEM images obtained during this Ph.D.;

- Press “Compute” button, and wait until the “Wait” bar is over, which can be long, according to the number of dots to analyze (and not the size of the image);
- Choose between all “Rendering” options to obtain the desired image which can be saved (Figures 122.c-h). Also, a button permits to switch from “Image” to “Correlation” (Figure 122.i).

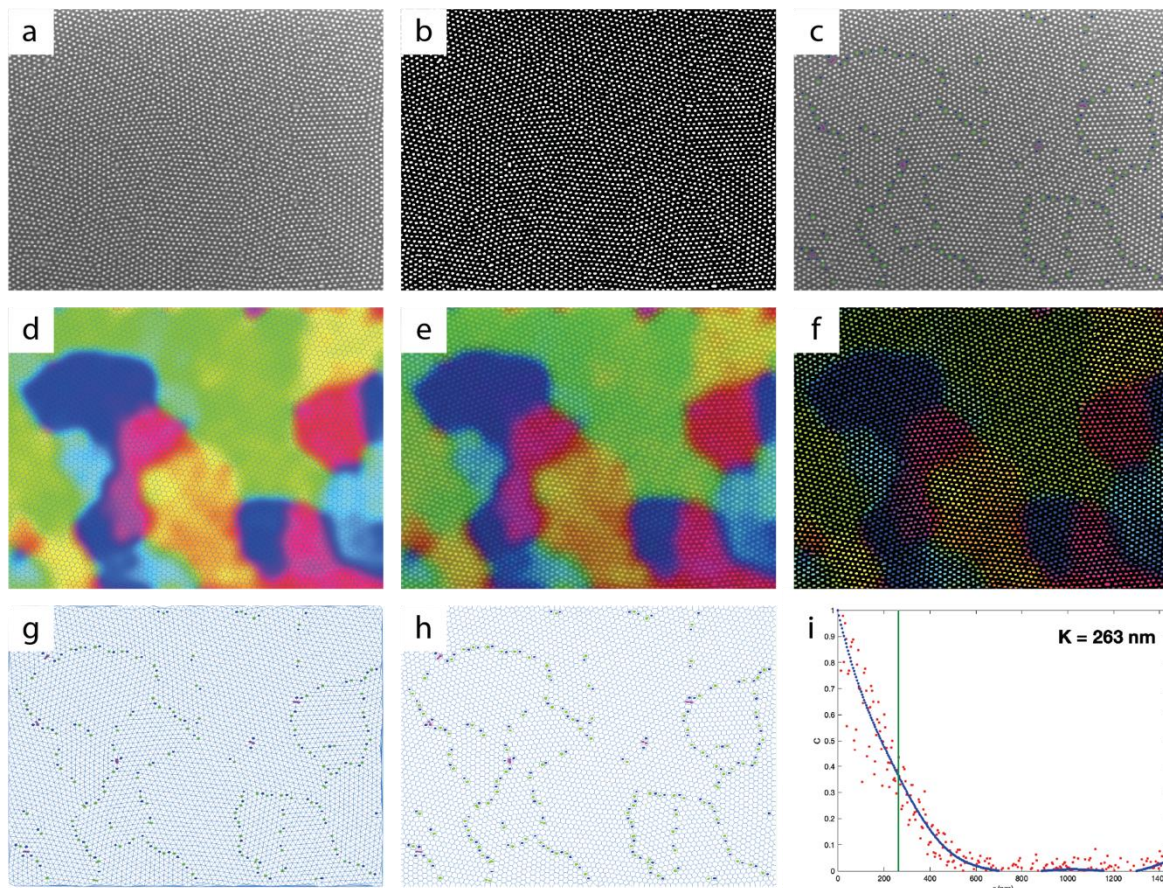


Figure 122. (a) Initial SEM image with out-of-plane cylinders made from PS_{33} - b - $PMMA_{16}$. (b) Binarized image, (c) SEM image and defects (4, 5, 7 and 8 neighbors gives red, blue, green and purple dots respectively), (d) orientation map and Delaunay mesh, (e) SEM image and orientation map, (f) binarized image and orientation map, (g) Voronoi mesh and defects, (h) Delaunay mesh and defects. (i) Correlation length with in red the raw data, in blue the smoothed data, and in green the correlation length, K .

Beyond a visual analysis of the image to observe grain size and defect type, the correlation length provides a value for quantitative comparison of the quality of self-assembly. Furthermore, to produce results that can be compared with the results produced with the ImageJ software, the correlation length calculation should be identical: the blue line $C(r)$ is fitted with an exponential decay like $e^{-\frac{r}{K}}$, giving a correlation length K when the blue line crosses $e^{-1} = 0,368$ (green line in (Figure 122.i).

3.C/ Di-block copolymers theoretical pitch and phase diagram position calculation

Within BCP self-assembly, the simplest and most studied architecture is the AB di-block architecture. A colossal theoretical work has been initiated since 1942 to understand and predict their behavior (see *Chapter I.1.A*). For the conception and design of the experimental works done during this Ph.D., a software has been developed to position a particular BCP system into a theoretical phase diagram [4]. It allows the prediction of the self-assembled structure, and the estimation of its critical dimension [5].

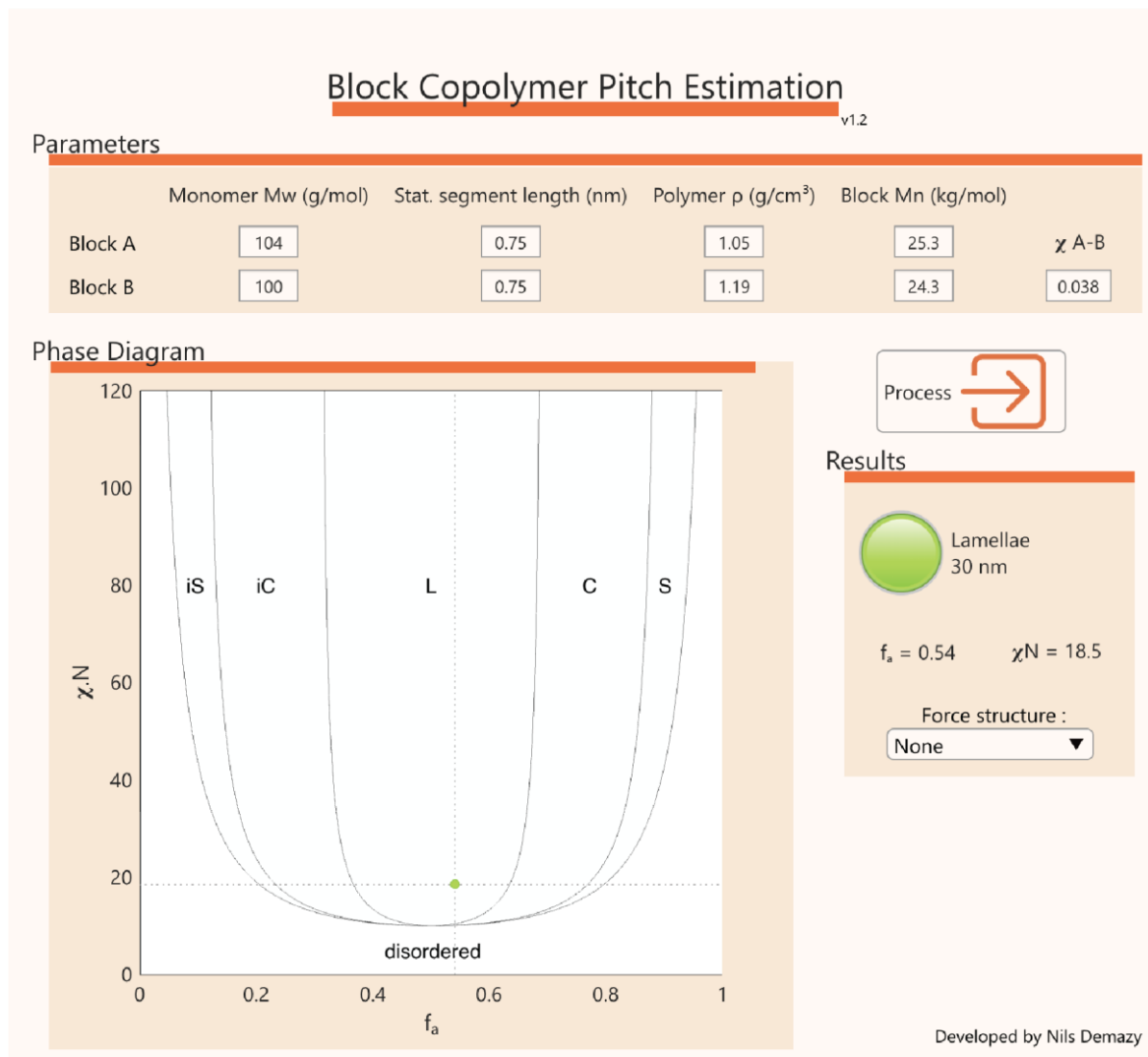


Figure 123. Block Copolymer Pitch Estimation window with the example of a PS-*b*-PMMA giving lamellar structure with a 30 nm estimated domain spacing.

The program needs some experimental values for each block to perform the various calculation, which should be filled in the “Parameters” panel (Figure 123). These parameters are the repeating unit molecular weight, the statistical segment length, the density and the number average molecular weight of each block, as well as the Flory-Huggins parameter of the

corresponding BCP. When all fields are fulfilled, the “Process” button appears. Pressing this button will place a mark on the theoretical phase diagram plot: in green if the structure is ordered, in orange if near the order-disorder transition, and in red if disordered. Furthermore, a “Results” panel appears, showing the corresponding structure with the theoretical domain spacing, the volume fraction and the segregation strength χN . Also, it is possible to force a BCP self-assembly into a particular structure to estimate the corresponding domain spacing.

3.D/ SAXS intensity plot fitting to determine χ parameter

One way to estimate the Flory Huggins parameter χ relies on using Small Angle X-ray Scattering of a BCP system in the disordered state (more precisely in the range of density fluctuations below the order-disorder transition). Indeed, the SAXS intensity profiles of such kind of spatial arrangements are theoretically described as a Gaussian, which shape depends on the macromolecular parameters of the studied BCP (in particular the χ value) (see *Chapter I.1.A.iv/*). A fitting software has been developed to fit the intensity plots obtained for different temperatures as a function of the BCP physical-chemical parameters, which subsequently leads to an accurate determination of $\chi(T)$.

The software is presented as a unique window (*Figure 124*), and the procedure to use it is the following:

- First, load a SAXS data file. It should be a *.txt* file with two tabulation separated rows, one for the scattering vector q and one for the intensity S . A “Raw SAXS Data” curve appears, showing $S = f(q)$ with gray dots;
- Then the BCP properties should be filled: the number averaged block molecular weight, the block dispersities, the repeating unit molar mass, and the monomer density. A list of some pre-filled parameters for usual polymers might help. When all parameters are fulfilled, a “SAXS Data without Background” (blue dots) and a “Fitting curve” (red line) curves appear;
- The “In-parameters” table should be optimized to have the red curve near the blue curve. X scale and Y scale might help to have more visibility. K is a proportionality constant which modulates the red curve amplitude. bA and bB are the statistical segment lengths of block A and B, respectively, and a switch can force to fix their value. It is important to note that these two parameters have a great impact on the fitting (even if the tabulated values in the literature are questionable). The best procedure is to fix the most well-known value (here the PS at 0.75 nm), and let the other one vary. If the fitting gives non-meaningful value (i.e. below 0.3 nm or above 1.5 nm), it means that the fit is not physically sound and the parameters should be modified. a and b are two parameters to remove the intensity decay background, transforming the gray dots in blue dots by subtracting $b \times q^{-a}$;

- When the red curve is close to the experimental values, cursors (red triangles on the image) should be placed to remove data that are not required for the fitting process. They can be displaced with the “Remove low/high q data” sliders. Essentially, it permits to “focus” the algorithm on the fitting of the correlation hole scattering peak;
- Press the “Fit data” button. If everything is ok, a green button appears, and the χ value is given at the bottom right of the window. The parameters for the fit are printed in the “Out-parameters” table. It is also possible to export image and raw data.

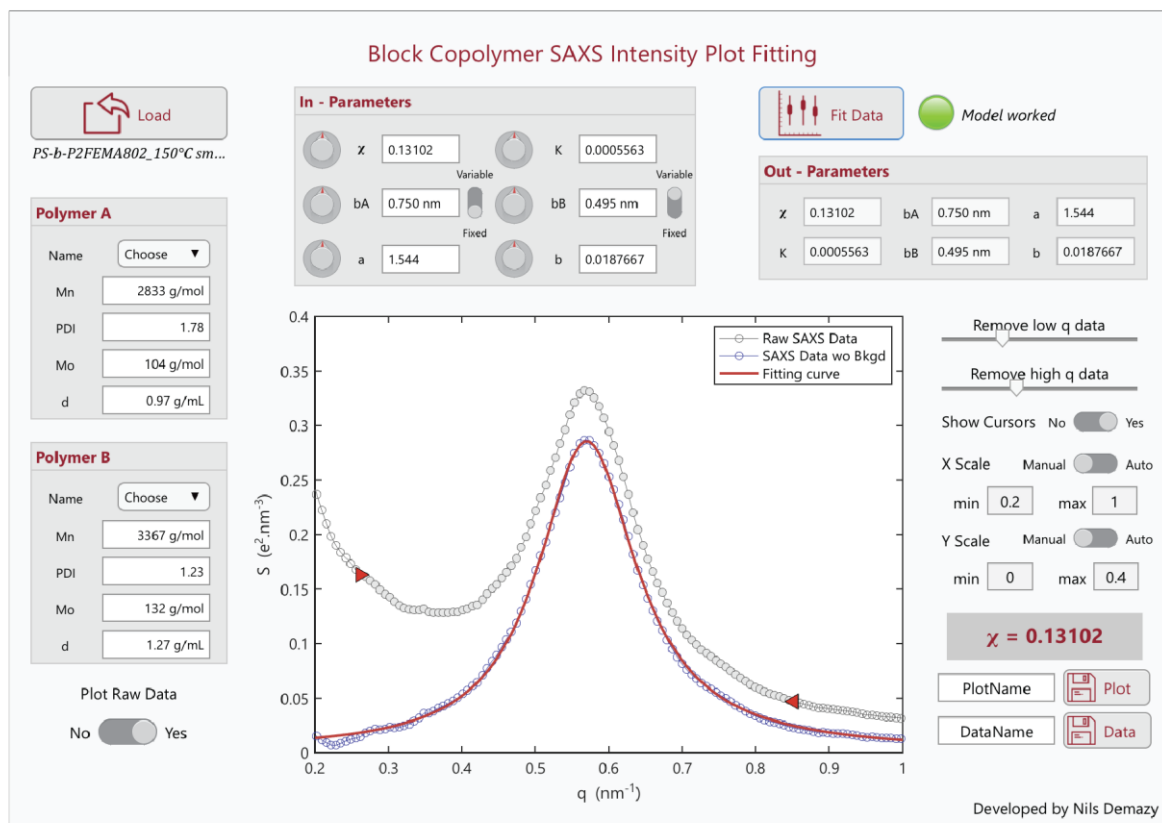


Figure 124. BCP SAXS Intensity Plot Fitting window with the example of a PS-*b*-P2FEMA SAXS spectrum in a disordered state.

Within the laboratory, some studies are performed on high- χ low- N BCPs to target the formation of sub-10 nm domain spacing [6]. During this Ph.D. this software was used to determine the χ values of several of these systems, leading to a published article on PS-*b*-P2FEMA [7] and one submitted one on PDHS-*b*-PTMSS.

The bibliographic details of the published manuscript are:

C. Cummins, D. Mantione, F. Cruciani, G. Pino, N. Demazy, Y. Shi, G. Portale, G. Hadziioannou, G. Fleury, “Rapid Self-Assembly and Sequential Infiltration Synthesis of High χ Fluorine-Containing Block Copolymers” *Macromolecules*, vol. 53, no. 15, pp. 6246–6254, 2020.

<https://doi.org/10.1021/acs.macromol.0c01148>

The bibliographic details of the submitted manuscript are:

G. Pino, C. Cummins, D. Mantione, N. Demazy, A. Alvarez-Fernandez, S. Guldin, G. Fleury, G. Hadziioannou, E. Cloutet, C. Brochon, "Design and morphological investigation of high- χ catechol-containing styrenic block copolymers"

Rapid Self-Assembly and Sequential Infiltration Synthesis of High χ Fluorine-Containing Block Copolymers

Cian Cummins, Daniele Mantione,* Federico Cruciani, Guillaume Pino, Nils Demazy, Yulin Shi, Giuseppe Portale, Georges Hadziioannou, and Guillaume Fleury*

Cite This: *Macromolecules* 2020, 53, 6246–6254

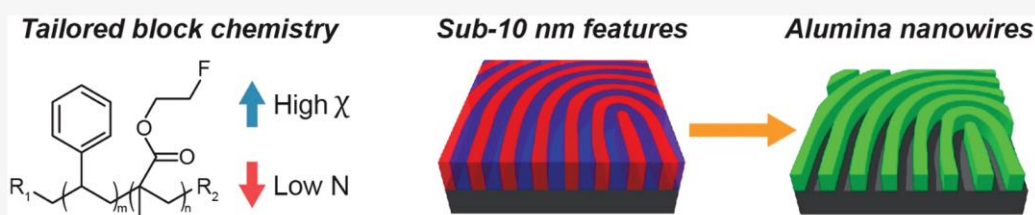
Read Online

ACCESS |

Metrics & More

Article Recommendations

Supporting Information



ABSTRACT: We leverage the attractive properties of a high χ –low N BCP, i.e., poly(styrene)-*block*-poly(2-fluoroethylmethyl acrylate) (PS-*b*-P2FEMA), and illustrate its utility for next-generation nanomanufacturing. The synthesis, physical characterization, and thin film self-assembly of a series of lamellar and cylindrical PS-*b*-P2FEMA BCPs are delineated. PS-*b*-P2FEMA BCPs with total molecular weights ranging from 7 to 22 kg mol⁻¹ were synthesized by using reversible addition–fragmentation chain-transfer (RAFT) polymerization. Temperature-resolved small-angle X-ray scattering (SAXS) measurements revealed a large χ value (0.13 at 150 °C) for PS-*b*-P2FEMA. Solvothermal vapor annealing of PS-*b*-P2FEMA films produced highly oriented fingerprint patterns in as short as 60 s. Lamellar period sizes ranged from 25.9 down to 14.2 nm with feature sizes as small as 7 nm observed. We also demonstrate the integration feasibility of PS-*b*-P2FEMA BCPs through alumina hardmask formation using sequential infiltration synthesis. The highly favorable characteristics of the P2FEMA-based BCPs detailed here provide a versatile material option to the current library of available BCPs for sub-10 nm nanolithography.

INTRODUCTION

Thin film block copolymer (BCP) self-assembly is a powerful means to fabricate nanoscale templates with diverse applications, e.g., Li-ion batteries, solar cells, waveguides, and membrane filtration among others.^{1–5} Owing to the spontaneous self-assembly of BCPs, nanoscale features can be formed depending on respective volume fraction (f_i) of the constituent polymers. Morphologies of BCPs can be tailored through f_i , whereby increasing one block with respect to the other transitions from spherical, cylindrical, gyroidal, and lamellar features. Aggressive scaling of semiconductor features has pushed the limits of optical lithography patterning, and there is a pressing need to develop novel materials to further advance scaling. Both in-plane and out-of-plane cylinder orientations and out-of-plane lamellar structures can be used to fabricate logic and memory features.^{6,7} Directed self-assembly (DSA) of BCPs is considered a strong candidate whereby patterns are chemically or physically guided to align with respect to the substrate.^{8,9} DSA-BCP technology is envisaged to complement 193 nm immersion lithography and extreme ultraviolet lithography for semiconductor and data storage needs. DSA patterning offers a tremendously attractive methodology that is regarded as low cost and CMOS compatible given the parallels with contemporary resist

development (i.e., spin, bake, strip, and etch).¹⁰ Diffraction limits of top-down optical lithography have thus led to the exploration of new material chemistries and synthetic strategies to advance scaling. In particular, novel BCPs are required to scale to smaller periods beyond the workhorse material poly(styrene)-*block*-poly(methyl methacrylate) (PS-*b*-PMMA).

Newly synthesized block copolymers (BCPs) that possess a high Flory–Huggins interaction parameter (χ) and a low degree of polymerization (N) are now needed to define ultrasmall periods for logic applications.¹¹ As N needs to be low for ultrasmall periods, a high χ is therefore advantageous to satisfy that the product of χ and N is greater than 10.5 to allow microphase separation.¹² To achieve this goal, novel strategies are necessary to formulate high χ –low N BCPs that also exhibit high etch contrast or an ability to selectively infiltrate a block for pattern transfer purposes.¹³ In this vein, Willson and co-workers championed the use of silicon containing BCPs to

Received: May 15, 2020

Revised: June 25, 2020

Published: July 20, 2020



reach sub-20 nm periods beyond the well-studied PS-*b*-poly(dimethylsiloxane) (PS-*b*-PDMS) system, e.g., poly(styrene-*b*-trimethylsilylstyrene-*b*-styrene), poly(trimethylsilylstyrene-*b*-lactide),¹⁴ poly(5-vinyl-1,3-benzodioxole-*b*-pentamethylsilylstyrene) (PVBD-*b*-PDSS),¹⁵ and poly(trimethylsilylstyrene-*b*-*p*-methoxystyrene) (PTMSS-*b*-PMOST).¹⁶ Furthermore, another silicon-based BCP, poly(1,1-dimethylsilylacyclobutane)-*b*-PMMA (PDMSB-*b*-PMMA), was introduced by Aissou et al. to pattern sub-10 nm period sizes in 10 min under thermal annealing.¹⁷ Hydroxystyrene-based BCP reports have shown that extremely high χ materials can be attained due to the incompatibility of constituent polymers.^{18–20} For example, Wang et al. recently detailed the RAFT synthesis of poly(pentadecafluorooctyl methacrylate)-*b*-poly(hydroxystyrene) (PPDFMA-*b*-PHS) that possessed a χ of 0.48, enabling an L_0 of 9.8 nm in lamellar thin films.²¹ Other notable hydroxystyrene-based BCPs include poly(3-hydroxystyrene)-*b*-poly(dimethylsiloxane) (P3HS-*b*-PDMS),²² poly(dihydroxystyrene)-*b*-polystyrene (PDHS-*b*-PS) with an L_0 of 5.9 nm,²³ P3HS-*b*-tBuSt, and P4HS-*b*-tBuSt demonstrating an L_0 of 8.8 nm.²⁴ Fluorine-based BCPs also present an appealing way to facilitate the development of high χ materials and offer the possibility of fast microphase separation due to the mobility of fluorinated blocks with low coefficients of friction.²⁵ Because high χ BCPs typically possess vastly different chemistries (e.g., organic vs inorganic blocks), the contrast in surface free energy (SFE) can result in large scale dewetting²⁶ as well as preferential wetting layer formation at the polymer/air or polymer/substrate interfaces. To overcome such problematic scenarios, a novel strategy by Hayakawa and co-workers reported the use of poly(2,2,2-trifluoroethyl methacrylate) (PTFEMA) to balance SFEs with a silicon containing moiety where $L_0 = 11$ nm was attained and DSA demonstrated.²⁷ A similar approach has been employed for PS-*b*-poly[2-hydroxy-3-(2,2,2-trifluoroethylsulfanyl)propyl methacrylate] (PS-*b*-PHFMA) producing $L_0 = 9.6$ nm. Jo et al. showed that the synthesis of PS-*b*-poly(2,2,2-trifluoroethyl acrylate) (PS-*b*-PTFEAs) via transesterification of PS-*b*-poly(*tert*-butyl acrylate) (PS-*b*-PtBAs) resulted in an extremely high χ and demonstrated an $L_0 = 10.1$ nm.²⁸ Likewise, Li et al. exemplified the flexibility of a series of PS-*b*-poly(pentadecafluorooctyl methacrylate) (PS-*b*-PPDFMA) BCPs that were shown to self-assemble in 1 min with cylindrical systems ($L_0 = 14.3$ nm) showing promise for DSA.²⁹

Herein, we describe the RAFT polymerization of lamellar and cylindrical PS-*b*-P2FEMA BCPs (termed SFEMA herein) for sub-10 nm nanolithography that can be patterned in a facile manner, i.e., short times and minimal processing steps. Ordered lamellar features were developed with periods ranging from 25.9 down to 14.2 nm with feature sizes as small as 7 nm. After optimization through solvothermal vapor annealing, AlO_x patterns with feature sizes of 11 nm were developed by using sequential infiltration synthesis (SIS) of SFEMA BCPs. The series of SFEMA BCPs reported in this article provides a viable pathway to 7 nm half-pitch periods and sub-10 nm BCP feature sizes that are amenable to rapid self-assembly, i.e., ≈ 3 min. Our work represents significant progression of the BCP nanolithography toolbox from a materials and processing standpoint of a new fluorine-containing BCP.

EXPERIMENTAL SECTION

Materials. Styrene and trifluorostyrene were purchased from Sigma-Aldrich. 2-Fluoroethanol was purchased from ABCR. All other

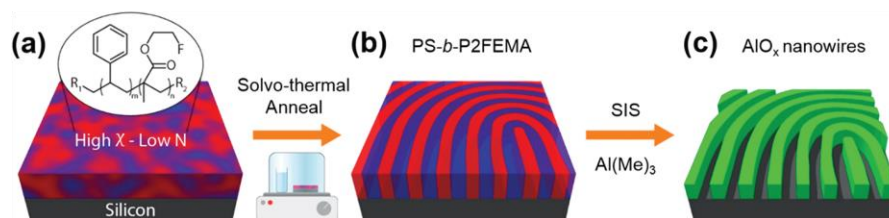
chemicals were supplied from Fisher Scientific. TLC were performed on aluminum precoated plates (silica gel 40–60 Å 400 mesh, F254, Aldrich) using hexane:ethyl acetate (Hex:AcOEt) as eluent. Silica gel high-purity grade, pore size 60 Å, 230–400 mesh particle size 40–63 μm was used for flash column chromatography. Solvents used for solvothermal vapor annealing were purchased from Sigma-Aldrich and were used as received. The density of P2FEMA at 25 °C was measured by pycnometer. Details are described in the [Supporting Information](#) (section 1, Materials and Methods).

Synthesis of 2FEMA. To a solution of methacrylic acid (4.35 mL; 4.65 g, 54 mmol, 1.1 equiv) in 250 mL of dry DCM, DCC (12.57 g; 61 mmol, 1.3 equiv) was added and left stirring for 30 min under argon. Afterward, 2-fluoroethanol (2.75 mL; 3 g, 47 mmol, 1 equiv) and DMAP (0.969 g; 4.7 mmol, 0.17 equiv) were added, and the reaction mixture was held at 0 °C by using an ice bath. The mixture was kept for 48 h at room temperature under an argon atmosphere. After the reaction, monitored by TLC, had reached completion, the reaction mixture was filtered to eliminate the urea salts that precipitated during the reaction. The product containing filtrate was diluted with an extra 250 mL of DCM and rinsed three times with 100 mL of water. The organic phase was dried over Na₂SO₄ and concentrated. The concentrated product was then loaded onto a silica gel column and purified by flash column chromatography by using a mixture of hexane:ethyl acetate 8:2 ($R_f = 0.68$) to give the product as a colorless oil (5.5 g, 89%). FT-IR $\nu_{\text{max}}/\text{cm}^{-1}$: 3108 (=C–H), 2975, 2939 (C–H), 1710 (C=O), 1474 (C=C), and 1111 (C–F). ¹H NMR (400 MHz, chloroform-*d*): δ 6.15 (dd, $J = 1.6, 0.9$ Hz, 1H), 5.59 (p, $J = 1.6$ Hz, 1H), 4.70–4.64 (m, 1H), 4.59–4.53 (m, 1H), 4.42–4.38 (m, 1H), 4.35–4.31 (m, 1H), 1.94 (dd, $J = 1.6, 1.0$ Hz, 3H). ¹³C NMR (101 MHz, chloroform-*d*): δ 167.19, 135.93, 126.25, 82.28, 80.59, 63.76, 63.56, 18.27. ¹⁹F NMR (377 MHz, chloroform-*d*): δ –222.10.

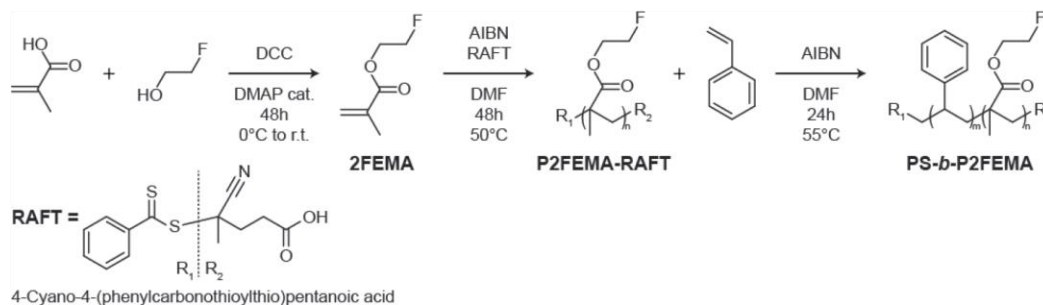
Synthesis of P2FEMA_RAFT. P2FEMA_RAFT was prepared according to a previously reported literature procedure using Azobisisobutyronitrile (AIBN) as an initiator.²⁷ The RAFT agent used in this work is 4-cyano-4-((phenylcarbonothioyl)thio)pentanoic acid.³⁰ The oven-dried Schlenk was charged with a stir bar and left to cool to room temperature under vacuum. The reagents were poured in sequence starting from 1 mL of dry DMF for each gram of monomer used, RAFT agent (1 equiv), AIBN (0.5 equiv), and the monomer 2FEMA [equiv = target(M_n)/monomer(M_w)] followed by four freeze–pump–thaw cycles to remove traces of oxygen. The Schlenk was then filled with argon, sealed, and left for 2 days at 50 °C under stirring. After cooling to room temperature, the solution or in the case of a solid dissolved in a minimum amount of THF (in some cases the solubilization required 2–4 h of sonication) was directly precipitated dropwise in pentane/methanol with an 8:2 ratio. The purification through precipitation was repeated twice to remove small traces of coupling defects. The M_n , dispersity (D), NMR, and yields of respective polymers are detailed in the [Supporting Information](#) (section 2.2).

Synthesis of SFEMA Diblock Copolymers. Following the guidelines of the previous synthesis, the oven-dried Schlenk was charged with a stir bar, 1 mL of dry DMF for each 0.3 g of P2FEMA_RAFT (1 equiv), AIBN (0.5 equiv), and the amount of styrene desired to have a range of M_n for different volume fractions. The vessel was subjected to three freeze–pump–thaw and then left stirring at 55 °C for 24 h. The mixture was directly precipitated dropwise in EtOH, 100 mL for each gram of polymer batch. In this case the precipitation was performed four times to guarantee an acceptable dispersity (D) of the polymer batches. The number-average molar masses (M_n), the weight-average molar masses (M_w), the molar mass distributions ($D = M_w/M_n$), and the volume fractions of SFEMA BCPs were determined by a combination of NMR and SEC. Volume fractions, M_n , D , NMR, and yields are detailed in the [Supporting Information](#) (section 2.3).

Nuclear Magnetic Resonance (NMR). NMR spectra were all recorded at ambient temperature by using a liquid-state 400 MHz NMR spectrometer (Bruker AVANCE I) with 5 mm BBFO probe in the appropriate deuterated solvent. Data are reported in chemical shift

Scheme 1. Process Flow for SFEMA Self-Assembly and AlO_x Nanowire Formation

Scheme 2. Synthesis of SFEMA BCP Materials via Reversible Addition–Fragmentation Chain Transfer Polymerization



(ppm), multiplicity (s, singlet; d, doublet; t, triplet; dd, double doublet; q, quartet; the signals are referenced to the residual solvent $\text{DMSO}-d_6$ ($\delta = 2.50$ ppm ^1H , 39.520 ppm ^{13}C); CDCl_3 ($\delta = 7.26$ ppm, 77.160 ppm ^{13}C); α,α,α -trifluorotoluene as internal standard ($\delta = -63.90$ ppm).

Size Exclusion Chromatography (SEC). SEC measurements were performed with a Viscotek TDAmx system from Malvern Instruments that consists of an integrated solvent and sample delivery module (GPCmax) and a Tetra Detector Array (TDA). THF was used as the mobile phase at a flow rate of 0.8 mL/min and TCB as a flow rate marker. All polymers were injected (100 μL of solution) at a concentration of 5 mg/mL after filtration through a 0.45 μm pore-size membrane. The separation was performed on two Agilent columns [2 \times PLgel 5 μm Mixed C (300 \times 7.5 mm 2)] and a guard column (PL gel 5 μm). Columns and detectors were maintained at 30 $^\circ\text{C}$. Relative molecular weights and dispersity were determined thanks to a conventional calibration obtained with polystyrene narrow standards.

Small-Angle X-ray Scattering (SAXS) Characterization. SAXS experiments were performed at the Centre de Recherche Paul Pascal (CRPP) at Université de Bordeaux using a high-resolution X-ray spectrometer Xeuss 2.0 from Xenocs operating with radiation wavelength of $\lambda = 1.54$ Å. 2D scattering patterns were collected by using a PILATUS 300 K Dectris detector with a sample-to-detector distance of 1635 mm. The beam center position and the angular range were calibrated by using a silver behenate standard sample. The SAXS patterns were radially averaged around the direct beam position by using the Xenocs XSACT software. Temperature-dependent SAXS experiments were performed at the MINA (Multipurpose Instrument for Nanostructured Analysis) beamline in Groningen (Netherlands) by employing a rotating anode X-ray source with radiation wavelength of $\lambda = 1.54$ Å. The beam is collimated by using Monteil optics and a set of three Pt pinholes. The beam size at the sample position was 250 \times 250 μm^2 . SAXS patterns were recorded by using a Vantec2000 detector (Bruker) with pixel size 68 \times 68 μm^2 placed 3000 mm away from the sample. The beam center and the sample-to-detector distance were calibrated by using the position of diffraction peaks from a standard silver behenate powder. The SAXS patterns were radially averaged around the direct beam position by using the Fit2D software. After radial averaging, the background signal from the empty cell was subtracted to all the sample profiles.

Thin Film Self-Assembly. Silicon substrates, with a native silicon dioxide layer (≈ 2 nm), were diced into 1 \times 1 cm 2 pieces and ultrasonicated in toluene for 10 min. Prior to deposition, substrates

were blown dry with N_2 . Substrates were exposed to UV/ O_3 for 10 min to remove any organic material and to hydroxylate the surface. Following treatment, 1–1.5 wt % SFEMA solutions were made up in toluene and left stirring until fully dissolved. SFEMA films were deposited upon the modified wafers at 4000 rpm for 30 s, with a ramp of 5 s. SFEMA films were subsequently exposed to chloroform or toluene solvent vapors in glass jars (total volume, 50 cm 3) from 1 to 30 min to induce self-assembly. For solvothermal vapor annealing, jars were placed on a hot plate at 50 $^\circ\text{C}$.

Thin Film Characterization Methods. BCP surfaces were characterized by an atomic force microscope (AFM) using a Dimension FastScan AFM (Bruker) in tapping mode. Silicon cantilevers (Fastscan-A) with a typical tip radius of ≈ 5 nm were used. The resonance frequency of the cantilevers was ≈ 1.25 kHz. A JEOL 7800-E Prime scanning electron microscope (SEM) was used at low voltage acceleration (1 kV) in the superhigh-resolution gentle beam (GBSH) mode to characterize metal oxide nanostructures formed.

Atomic Layer Deposition (ALD) Exposure. Sequential infiltration synthesis (SIS) of AlO_x was performed by using an ALD (Ultratech SAVANNAH G2) tool in exposure mode. This mode allowed Al_2O_3 SIS using an alternating exposure of P2FEMA-based BCP thin films to trimethylaluminum (TMA) and deionized water at 80 $^\circ\text{C}$ with a purge under N_2 gas flow after each exposition.³¹ During exposure time, pressure in the ALD chamber increased, leading to an infiltration of species in P2FEMA microdomains; then during purge time, unreacted precursor was removed by N_2 flow. Exposure and purge times used in this experiment were 60 and 300 s, respectively, for both precursors. Here we used three cycles (TMA/purge/ H_2O /purge) of SIS to form AlO_x nanostructures. Following SIS treatments, film were then plasma treated with O_2 plasma (60 W, 60 s, 20 sccm) to remove polymer and create AlO_x features.

RESULTS AND DISCUSSION

SFEMA Design, Synthesis, and Characterization. We have synthesized several lamellar and cylindrical forming PS-*b*-P2FEMA BCPs and examined their ability to form well-defined features for nanolithography. Our objectives included (i) patterning of sub-20 nm periods and feature sizes, (ii) demonstration of fast self-assembly, e.g., <5 min, and (iii) compatibility with standardized hardmask practices for potential pattern transfer. Scheme 1 outlines the overall

Table 1. Characteristics of SFEMA BCPs

BCP	M_n SEC ^a (kg mol ⁻¹)	M_n NMR ^b (kg mol ⁻¹)	\mathcal{D} ^a	vol fract (P2FEMA/PS) ^c	d -spacing ^d (nm)	morphology (orientation) ^d	feature size ^e (nm)
SFEMA1	22	23.4	1.3	38/62	27.3	Lam (L)	10.2
SFEMA2	18	18.6	1.3	44/56	26.1	Lam (L)	10.1
SFEMA3	17	17.2	1.4	22/78	21.6	Hex (L)	9.4
SFEMA4	14	13.8	1.4	21/79	20.9	Hex (L)	11.9
SFEMA5	10	9.7	1.4	37/63	17.9	Lam (L)	8.3
SFEMA6	8	8.8	1.4	54/46	14.6	Lam (L)	8.1
SFEMA7	7	6.7	1.4	33/67	14.9	Lam (L)	7.3
SFEMA8	6.4	6.3	1.2	49/51		Dis	

^aMolecular weights (M_n) and dispersity (\mathcal{D}) evaluated by SEC using polystyrene standards. ^bMolecular weights (M_n) evaluated from ¹H NMR. ^cVolume fractions determined by ¹H NMR using the densities of PS (1.05 g/cm³) and P2FEMA (1.27 g/cm³) as measured by pycnometer) at 25 °C. ^d d -spacing obtained from SAXS with the morphologies determined by the q/q^* series, where q^* is the position of the first-order peak. Lam and Hex indicate lamellar and hexagonally packed cylindrical morphologies, respectively. ^eRespective feature sizes determined from AFM images.

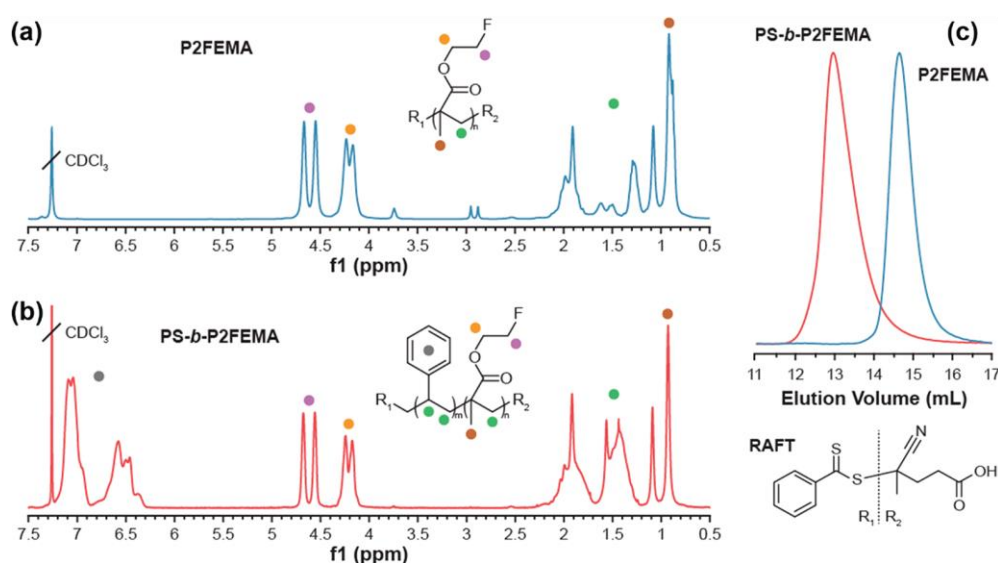


Figure 1. (a) ¹H NMR spectrum of P2FEMA-RAFT-A in chloroform-*d*. (b) ¹H NMR spectrum of SFEMA2 in chloroform-*d*. (c) SEC overlapped curves (P2FEMA-macro-RAFT is in blue and SFEMA2 is in red).

process flow for high χ -low N SFEMA BCPs, with the molecular structure shown in (a), SFEMA self-assembled patterns displayed in (b), and aluminum oxide (AlO_x) nanowires shown in (c) after sequential infiltration synthesis (SIS).

The synthesis and key characteristics of SFEMA BCPs synthesized by RAFT and studied in thin film form are outlined in Scheme 2 and Table 1. We have pursued the synthesis of a modified methyl methacrylate block functionalized with a single fluorine atom to develop a high χ BCP material. The reason for this pursuit is twofold. First, SFEMA BCPs of low molecular weight are capable of fabricating ultralow feature sizes (sub-10 nm), but critically the new materials do not exhibit large scale dewetting in thin film form as occurs in BCPs of vastly contrasting surface energies (e.g., PDMS containing BCPs).^{32,33} Moreover, low-fluorinated polymerizable molecules are not commercially available, which provided further motivation for us to design and synthesize a monofluorinated derivative of ethyl methacrylate.

Using 2-fluoroethanol and methacrylic acid via a Steglich esterification with dicyclohexylcarbodiimide (DCC) as a condensing agent and (dimethylamino)pyridine (DMAP) as a catalyst, we routinely synthesized 2FEMA with high yield

(over 80%). RAFT polymerization was chosen as it is a versatile technique allowing polymerization of a range of functionalized monomers (unlike anionic polymerization) and produces BCPs with low \mathcal{D} that are free of metal contamination. A standard, widely used RAFT agent was adopted to maintain a fast and approachable synthesis using commercially available reagents. 4-Cyano-4-(phenylcarbonothioylthio)pentanoic acid was used as the RAFT agent and azobis(isobutyronitrile) (AIBN) as a free radical initiator. The sequence of blocks was determined, as 2FEMA is much less reactive than styrene, and therefore the styrene-RAFT is not suitable. Thus, a series of P2FEMA-RAFT agents were synthesized and used to create desired SFEMA BCP materials. The polymers were characterized via nuclear magnetic resonance (NMR), SEC, and FT-IR, confirming the predicted structures (see the Supporting Information, section 2).

Figures 1a,b show the ¹H NMR spectra of the P2FEMA-macro-RAFT (top spectrum) and SFEMA2 (bottom spectrum). The ¹H NMR spectrum of SFEMA2 BCP clearly displays the aromatic group of the styrene from 6 to 7.5 ppm (grey dot), which is absent in the P2FEMA macro-RAFT (top). The aliphatic backbone is creating complex multiplets in between 1 and 2 ppm (green dots), while the methylenes of

the fluorinated ethanoate residue appear clearly as two doublets around 4.5 ppm in both P2FEMA-macro-RAFT and the SFEMA2 cases (purple and orange dots). Representative chromatograms are given in Figure 1c, showing the narrow dispersity for respective materials and the molecular mass increase, transitioning from the macro-RAFT (blue curve) to SFEMA2 (red curve).

Bulk Microphase Segregation. SFEMA BCP bulk phase behavior was probed by SAXS to establish respective BCP morphologies and domain spacing values. All samples were thermally annealed at 120 °C overnight prior to SAXS analysis. Measurements of the annealed samples were performed at 25 °C. Figure 2a displays SAXS patterns obtained for SFEMA1–

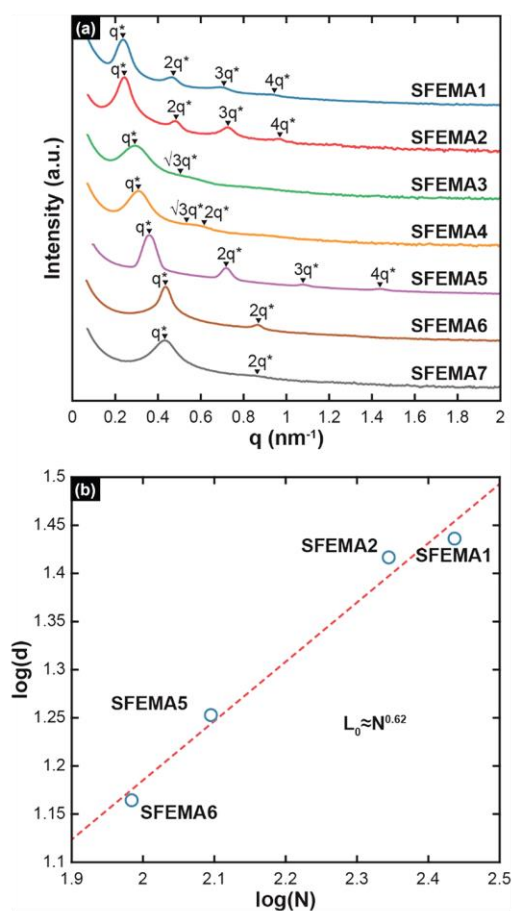


Figure 2. (a) Representative SAXS profiles acquired at 25 °C for bulk analysis of SFEMA BCPs. Data have been shifted vertically for clarity. (b) Plot of the scaling relationship of lamellar SFEMA BCP d -spacing (d) with respect to total degree of polymerization (N) based on 118 Å³ reference volume for BCPs with a nearly constant composition.

7. The peaks observed confirmed the ability of these BCPs to form segregated structures in the bulk with M_n as low as 7 kg/mol. SFEMA BCPs labeled SFMEA1, SFMEA2, SFMEA5, SFMEA6, and SFMEA7 in Figure 2a display peaks positioned at q/q^* with ratios of 1:2:3:4 indicative of lamellar morphologies. Additionally, SAXS profiles of SFMEA3 and SFMEA4 show peak positions tentatively assigned to cylindrical systems in accordance with BCP composition and BCP thin film self-assembly behavior. Periods ranged from 27.3 to 14.6 nm for lamellar SFEMA BCPs ($d = 2\pi/q^*$, where

d is the domain spacing and q^* is the primary peak position), as summarized in Table 1. Figure 2b displays the scaling relationship of lamellar BCP periods SFEMA1, -2, -5, and -6 versus the total degree of polymerization of respective BCPs based on 118 Å³ reference volume. The experimental results for this series of SFEMA with a nearly constant composition exhibit a power law of $d \approx N^{0.62}$, in agreement with the strong segregation theory, i.e., $d \approx bN^{2/3}\chi^{1/6}$ where b is the statistical segment length.

Determination of χ for SFEMA. We subsequently determined the Flory–Huggins parameter of this system using temperature resolved SAXS. The absolute intensity calibrated with a low-density polyethylene standard was plotted against the primary scattering vector, q , for the disordered SFEMA8 sample (overall $M_n = 6.4$ kg/mol). A mean-field expression for the segment–segment interaction corrected from the effects of molecular weight dispersity and segmental volume asymmetry parameter has been extracted from these scattering profiles,^{34–36} and the results are presented in Figure 3a (Supporting Information section 4 details the model used here together with data analysis carried

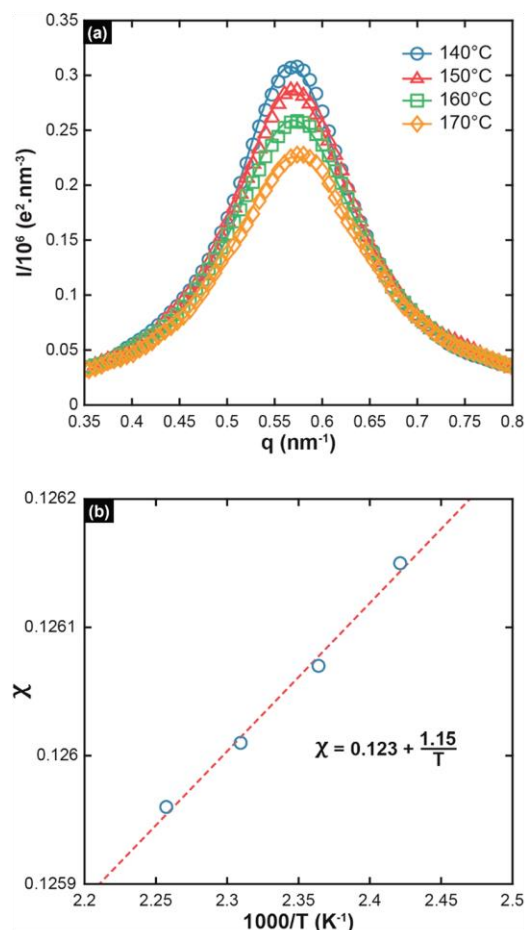


Figure 3. Determination of SFEMA χ by using Liebler mean-field theory. (a) Temperature-resolved SAXS intensity profiles of disordered SFEMA8 fitted by the mean-field theory at the vicinity of the scattering maximum associated with density fluctuations at 140 °C (blue circles), 150 °C (red triangles), 160 °C (green squares), and 170 °C (yellow diamonds). (b) Plot showing the linear dependence of χ calculated as a function of $1/T$.

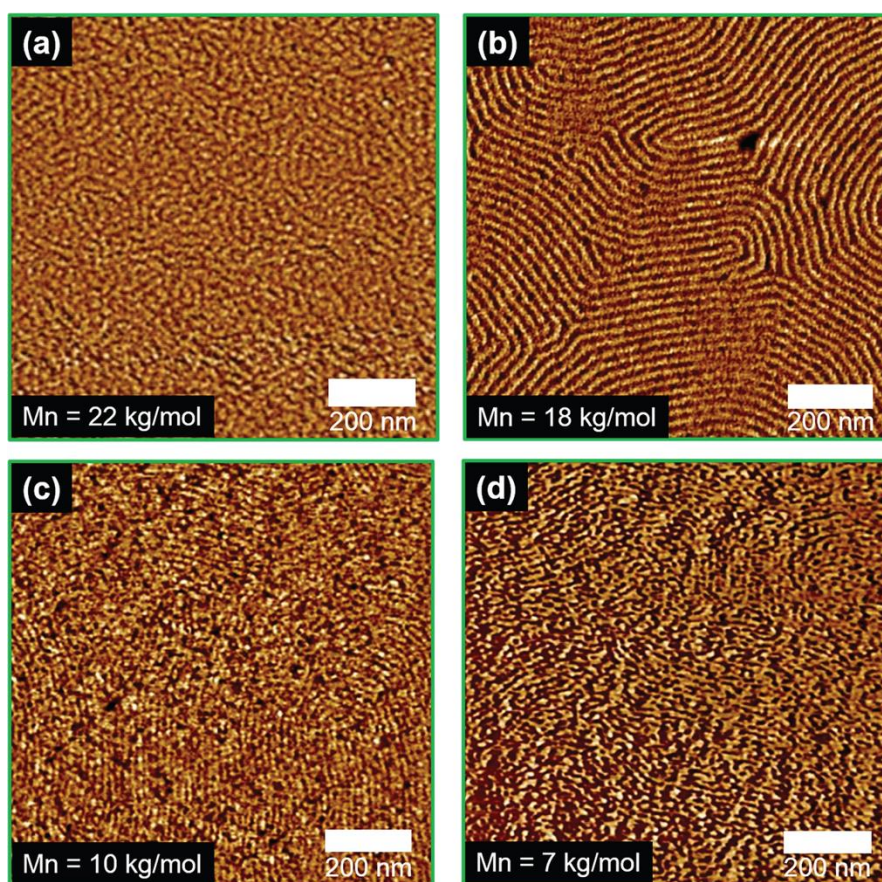


Figure 4. AFM phase images of self-assembled lamellar SFEMA BCP films on silicon surfaces with total molecular weights of (a) $M_n = 22$ kg/mol (SFEMA1), (b) $M_n = 18$ kg/mol (SFEMA2), (c) $M_n = 10$ kg/mol (SFEMA5), and (d) $M_n = 7$ kg/mol (SFEMA7). SFEMA films were solvothermal annealed in a CHCl_3 atmosphere at 50°C for less than 3 min.

out). The resulting temperature-dependent Flory–Huggins parameter can be expressed as $\chi = 1.15 \times T^{-1} + 0.123$, which is equivalent to a value of 0.13 at 150°C , over 4 times the value reported for PS-*b*-PMMA (0.03).³⁶ This value supersedes commercially available “high χ ” BCPs including PS-*b*-PDMS (0.11) and PS-*b*-PLA (0.075).³⁷ Our SFEMA BCPs also challenge more recently published BCPs including poly-(cyclohexylethylene)-*b*-PMMA (0.18)³⁸ and PMOST-*b*-PTMSS (0.046).³⁹ Such comparisons to the state-of-the-art literature illustrate the potential use of PS-*b*-P2FEMA for future nanomanufacturing.

SFEMA Thin Film Self-Assembly. Processing new BCPs in thin film form and precisely manipulating conditions to achieve desired orientation is paramount. Moreover, developing processes toward relevant features in rapid time scales is also desirable and is a central focus here. Lamellar BCP systems are extremely practical for pattern transfer as the vertical sidewalls of the original etch mask are advantageous for fidelity. Therefore, this section examines lamellar systems.

We screened several solvents to establish the optimum deposition conditions. PS is well-known to dissolve in toluene because of similar solubility values (Hansen solubility parameters for PS, $\delta_d = 18.6 \text{ MPa}^{1/2}$, $\delta_p = 1.0 \text{ MPa}^{1/2}$, $\delta_h = 4.1 \text{ MPa}^{1/2}$, and toluene, $\delta_d = 18.0 \text{ MPa}^{1/2}$, $\delta_p = 1.4 \text{ MPa}^{1/2}$, and $\delta_h = 2.0 \text{ MPa}^{1/2}$, where δ_d is the dispersive force, δ_p is the polar force, and δ_h is hydrogen bonding).⁴⁰ In addition, we also observed clear solutions from P2FEMA homopolymer–

toluene solutions, inferring good solubility of P2FEMA in toluene. Thus, toluene was chosen for deposition of SFEMA and BCP film thicknesses were varied from ≈ 15 to 30 nm. Using such thin films is necessary to avoid image transfer issues during pattern transfer as pattern collapse of features is circumvented.⁴¹

We investigated SFEMA BCP self-assembly on UV/O₃-treated silicon and observed no large-scale dewetting of SFEMA BCPs. Initial experiments inferred the amenable nature of the PS and P2FEMA blocks materials on UV/O₃ modified silicon surfaces. However, as-cast films only exhibit ill-defined segregated structures (see Figure S29), and solvent vapor annealing was applied to the SFEMA films to increase polymer chain mobility and therefore enhance ordering of the resulting nanostructures. Additionally, such treatment allows to mitigate preferential interactions at the BCP bottom and top interfaces, thus promoting out-of-plane orientations of the BCP features. Cylinder systems were also investigated (and are detailed in Figure S30) to fabricate vertical nanofeatures and expand the overall applicability of the family of SFEMA BCPs synthesized. For lamellar systems, we observed microphase separation in thin films annealed under a chloroform or toluene atmosphere. Patterns were typically formed in less than 30 min. We subsequently examined the use of solvothermal annealing (STVA) at 50°C to produce line-space features with larger correlation lengths. Moreover, STVA accelerates the

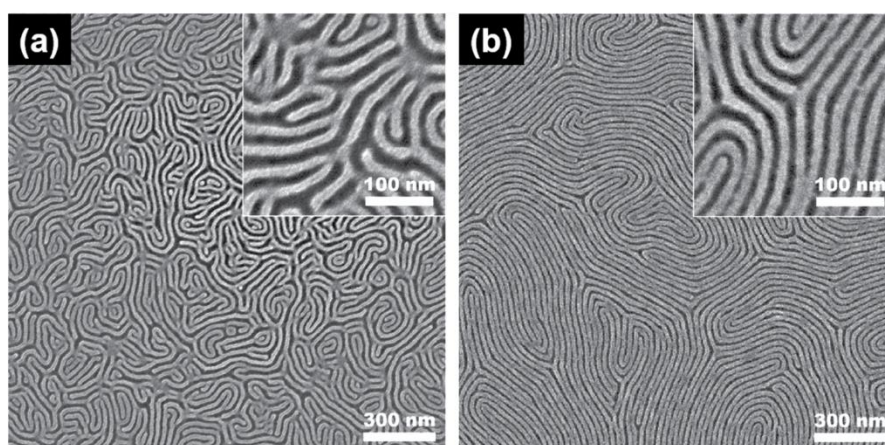


Figure 5. Large-area scanning electron microscopy image of AlO_x features developed from SIS treatment of (a) SFMEA 2 and (b) SFEMA 5. Period is ≈ 25 nm with feature sizes ≈ 14 nm for SFMEA 2. Period is ≈ 18 nm with feature sizes ≈ 11 nm for SFEMA 5. Insets show high-resolution images of AlO_x feature definition.

microphase separation^{42–44} process to as short as 3 min (vide supra).

Figure 4a–d displays line-space features from SFEMA BCPs following STVA treatment for less than 3 min. The d -spacings were measured at 25.9 nm for SFMEA1 (Figure 4a), 24.5 nm for SFEMA2 (Figure 4b), 16.4 nm for SFEMA5 (Figure 4c), and 14.2 nm for SFEMA7 (Figure 4d). Despite other reports based on fluorine-containing BCPs requiring an etch procedure to reveal microdomains, we observed well-defined patterns after STVA alone. We assert that this is due to the presence of only one fluorine atom in the P2FEMA block. However, one should note that dewetting of films was observed after longer annealing periods, e.g., greater than 10 min, particularly in low molecular weight SFEMA (<10 kg mol^{-1}) which is possibly a result of the enhanced fluorine polymer block–solvent interaction at the free surface, resulting in film instability and ultimately leading to film rupture. However, longer annealing times were not required as microphase-separated patterns were observed in less than 3 min as evidenced in Figure 4.

Alumina Nanowire Fabrication. To be considered further for nanolithography applications, we evaluated the possibility of converting the P2FEMA block to a hardmask material. Hardmask formation is a desired attribute for semiconductor processing as it allows enhanced etching contrast for high aspect ratio features.^{45–49} Enhanced etching can ultimately lead to better edge definition (lower line edge roughness) than all polymeric based BCPs. Given the chemical similarity between PMMA and P2FEMA which both share carbonyl groups, we used SIS to infiltrate the P2FEMA microdomains. After precursor exposure, films were subsequently oxygen plasma treated to create AlO_x nanowire replicas. The large-scale AlO_x line-space features shown in Figure 5 for SFEMA2 and SFEMA5 were exposed to three cycles of TMA/ H_2O precursors. Highly defined features with excellent uniformity were observed (see the insets in Figure 5) demonstrating the versatility of SFEMA BCPs for nanolithography use.

A multitude of reasons make SFEMA BCPs synthesized here appealing for sub-10 nm nanolithography. First, the high χ (0.13 at 150 °C) nature allows access to small periods and interfacial widths at low N , which is a considerable barrier to

further progression of PS-*b*-PMMA BCPs. Importantly, we have shown that fast self-assembly (in a matter of seconds) can be induced through STVA practices. It is also notable that SFEMA BCPs appear from our investigation not to present with a wetting layer at the polymer/air interface. This therefore eliminates the need for an additional trim plasma etch as required for silicon (and other)-containing BCPs. We suspect the absence of such a wetting layer is a result of P2FEMA possibly possessing a higher surface free energy value contrary to the more abundant fluorine-containing BCPs studied hitherto.

CONCLUSIONS

We have described the RAFT synthesis and characterization of a new fluorine-containing BCP system, PS-*b*-P2FEMA, for sub-10 nm nanolithography needs. The high χ (0.13 at 150 °C) SFEMA BCP modified with a fluorine-containing block favors rapid microphase separation even at low N (i.e., 7 kg/mol). Self-assembly of lamellar SFEMA was shown to form line-space patterns with periods of 14 nm in as short as 60 s. We have also evaluated the use of SFEMA thin films for generating well-defined AlO_x nanowires using industry compatible SIS. The rapid assembly and the compatibility demonstrated with SIS therefore position SFEMA BCPs as a useful candidate to pattern ultralow nanodimensions. In addition, we are currently exploring the thermal annealing of these materials given SFEMA block's relatively low T_g (≈ 90 °C), and results will be reported in due course to expand the processing options for this highly promising BCP material. Likewise, integrating such useful systems with directed self-assembly processes to dictate feature alignment will also be investigated.

ASSOCIATED CONTENT

Supporting Information

The Supporting Information is available free of charge at <https://pubs.acs.org/doi/10.1021/acs.macromol.0c01148>.

Experimental details; Figures S1–S30 (PDF)

AUTHOR INFORMATION

Corresponding Authors

Daniele Mantione – CNRS, Bordeaux INP, LCPO, UMR 5629, Univ. Bordeaux, F-33600 Pessac, France; orcid.org/

0000-0001-5495-9856; Email: daniele.mantione@u-bordeaux.fr

Guillaume Fleury – CNRS, Bordeaux INP, LCPO, UMR 5629, Univ. Bordeaux, F-33600 Pessac, France; orcid.org/0000-0003-0779-191X; Email: guillaume.fleury@u-bordeaux.fr

Authors

Cian Cummins – CNRS, Bordeaux INP, LCPO, UMR 5629 and CNRS, Centre de Recherche Paul Pascal, UMR 5031, Univ. Bordeaux, F-33600 Pessac, France; orcid.org/0000-0001-6338-3991

Federico Cruciani – CNRS, Bordeaux INP, LCPO, UMR 5629, Univ. Bordeaux, F-33600 Pessac, France

Guillaume Pino – CNRS, Bordeaux INP, LCPO, UMR 5629, Univ. Bordeaux, F-33600 Pessac, France

Nils Demazy – CNRS, Bordeaux INP, LCPO, UMR 5629, Univ. Bordeaux, F-33600 Pessac, France

Yulin Shi – Zernike Institute for Advanced Materials, University of Groningen, NL-9747 AG Groningen, The Netherlands

Giuseppe Portale – Zernike Institute for Advanced Materials, University of Groningen, NL-9747 AG Groningen, The Netherlands; orcid.org/0000-0002-4903-3159

Georges Hadziioannou – CNRS, Bordeaux INP, LCPO, UMR 5629, Univ. Bordeaux, F-33600 Pessac, France; orcid.org/0000-0002-7377-6040

Complete contact information is available at:

<https://pubs.acs.org/10.1021/acs.macromol.0c01148>

Notes

The authors declare no competing financial interest.

ACKNOWLEDGMENTS

The authors are sincerely grateful for financial support from the University of Bordeaux and the LabEx AMADEus (ANR-10-LABEX-0042-AMADEUS). The authors thank Ahmed Bentaleb (CRPP, University of Bordeaux) for SAXS assistance. The authors also thank the LCPO support staff—Aude Manson, Melanie Bousquet, Ellena Karnezis, and Gilles Pecastaings—for their endless everyday help. This work was performed within the framework of the Equipex ELORPrint-Tec ANR-10-EQPX-28-01 with the help of the French state's Initiative d'Excellence IdEx ANR-10-IDEX-003-02.

REFERENCES

- Orilall, M. C.; Wiesner, U. Block copolymer based composition and morphology control in nanostructured hybrid materials for energy conversion and storage: solar cells, batteries, and fuel cells. *Chem. Soc. Rev.* **2011**, *40* (2), 520–535.
- Abetz, V. Isoporous Block Copolymer Membranes. *Macromol. Rapid Commun.* **2015**, *36* (1), 10–22.
- Hu, H.; Gopinadhan, M.; Osuji, C. O. Directed self-assembly of block copolymers: a tutorial review of strategies for enabling nanotechnology with soft matter. *Soft Matter* **2014**, *10* (22), 3867–3889.
- Demazy, N.; Cummins, C.; Aissou, K.; Fleury, G. Non-Native Block Copolymer Thin Film Nanostructures Derived from Iterative Self-Assembly Processes. *Adv. Mater. Interfaces* **2020**, *7* (5), 1901747.
- Gabinet, U. R.; Osuji, C. O. Optical materials and metamaterials from nanostructured soft matter. *Nano Res.* **2019**, *12* (9), 2172–2183.
- Luo, Y.; Montarnal, D.; Kim, S.; Shi, W.; Barteau, K. P.; Pester, C. W.; Hustad, P. D.; Christianson, M. D.; Fredrickson, G. H.; Kramer, E. J.; Hawker, C. J. Poly(dimethylsiloxane-*b*-methyl

methacrylate): A Promising Candidate for Sub-10 nm Patterning. *Macromolecules* **2015**, *48* (11), 3422–3430.

(7) Pitet, L. M.; Wuister, S. F.; Peeters, E.; Kramer, E. J.; Hawker, C. J.; Meijer, E. W. Well-Organized Dense Arrays of Nanodomains in Thin Films of Poly(dimethylsiloxane)-*b*-poly(lactide) Diblock Copolymers. *Macromolecules* **2013**, *46* (20), 8289–8295.

(8) Ji, S.; Wan, L.; Liu, C.-C.; Nealey, P. F. Directed self-assembly of block copolymers on chemical patterns: A platform for nanofabrication. *Prog. Polym. Sci.* **2016**, *54*, 76–127.

(9) Cummins, C.; Morris, M. A. Using block copolymers as infiltration sites for development of future nanoelectronic devices: Achievements, barriers, and opportunities. *Microelectron. Eng.* **2018**, *195*, 74–85.

(10) Bates, C. M.; Maher, M. J.; Janes, D. W.; Ellison, C. J.; Willson, C. G. Block Copolymer Lithography. *Macromolecules* **2014**, *47* (1), 2–12.

(11) Maher, M. J.; Mori, K.; Sirard, S. M.; Dinhl, A. M.; Bates, C. M.; Gurer, E.; Blachut, G.; Lane, A. P.; Durand, W. J.; Carlson, M. C.; Strahan, J. R.; Ellison, C. J.; Willson, C. G. Pattern Transfer of Sub-10 nm Features via Tin-Containing Block Copolymers. *ACS Macro Lett.* **2016**, *5* (3), 391–395.

(12) Bates, F. S.; Fredrickson, G. H. Block Copolymer Thermodynamics - Theory and Experiment. *Annu. Rev. Phys. Chem.* **1990**, *41*, 525–557.

(13) Cummins, C.; Ghoshal, T.; Holmes, J. D.; Morris, M. A. Strategies for Inorganic Incorporation using Neat Block Copolymer Thin Films for Etch Mask Function and Nanotechnological Application. *Adv. Mater. (Weinheim, Ger.)* **2016**, *28* (27), 5586–618.

(14) Bates, C. M.; Seshimo, T.; Maher, M. J.; Durand, W. J.; Cushen, J. D.; Dean, L. M.; Blachut, G.; Ellison, C. J.; Willson, C. G. Polarity-Switching Top Coats Enable Orientation of Sub-10-nm Block Copolymer Domains. *Science* **2012**, *338* (6108), 775–779.

(15) Lane, A. P.; Yang, X.; Maher, M. J.; Blachut, G.; Asano, Y.; Someya, Y.; Mallavarapu, A.; Sirard, S. M.; Ellison, C. J.; Willson, C. G. Directed Self-Assembly and Pattern Transfer of Five Nanometer Block Copolymer Lamellae. *ACS Nano* **2017**, *11* (8), 7656–7665.

(16) Cushen, J.; Wan, L.; Blachut, G.; Maher, M. J.; Albrecht, T. R.; Ellison, C. J.; Willson, C. G.; Ruiz, R. Double-Patterned Sidewall Directed Self-Assembly and Pattern Transfer of Sub-10 nm PTMSS-*b*-PMOST. *ACS Appl. Mater. Interfaces* **2015**, *7* (24), 13476–13483.

(17) Aissou, K.; Mumtaz, M.; Fleury, G.; Portale, G.; Navarro, C.; Cloutet, E.; Brochon, C.; Ross, C. A.; Hadziioannou, G. Sub-10 nm Features Obtained from Directed Self-Assembly of Semicrystalline Polycarbosilane-Based Block Copolymer Thin Films. *Adv. Mater.* **2015**, *27* (2), 261–265.

(18) Li, M.; Douki, K.; Goto, K.; Li, X.; Coenjarts, C.; Smilgies, D. M.; Ober, C. K. Spatially Controlled Fabrication of Nanoporous Block Copolymers. *Chem. Mater.* **2004**, *16* (20), 3800–3808.

(19) Bosworth, J. K.; Paik, M. Y.; Ruiz, R.; Schwartz, E. L.; Huang, J. Q.; Ko, A. W.; Smilgies, D.-M.; Black, C. T.; Ober, C. K. Control of Self-Assembly of Lithographically Patternable Block Copolymer Films. *ACS Nano* **2008**, *2* (7), 1396–1402.

(20) Bosworth, J. K.; Black, C. T.; Ober, C. K. Selective Area Control of Self-Assembled Pattern Architecture Using a Lithographically Patternable Block Copolymer. *ACS Nano* **2009**, *3* (7), 1761–1766.

(21) Wang, C.; Li, X.; Deng, H. Synthesis of a Fluoromethacrylate Hydroxystyrene Block Copolymer Capable of Rapidly Forming Sub-5 nm Domains at Low Temperatures. *ACS Macro Lett.* **2019**, *8* (4), 368–373.

(22) Azuma, K.; Sun, J.; Choo, Y.; Rokhlenko, Y.; Dwyer, J. H.; Schweitzer, B.; Hayakawa, T.; Osuji, C. O.; Gopalan, P. Self-Assembly of an Ultrahigh- χ Block Copolymer with Versatile Etch Selectivity. *Macromolecules* **2018**, *51* (16), 6460–6467.

(23) Kwak, J.; Mishra, A. K.; Lee, J.; Lee, K. S.; Choi, C.; Maiti, S.; Kim, M.; Kim, J. K. Fabrication of Sub-3 nm Feature Size Based on Block Copolymer Self-Assembly for Next-Generation Nanolithography. *Macromolecules* **2017**, *50* (17), 6813–6818.

- (24) Kanimozhi, C.; Kim, M.; Larson, S. R.; Choi, J. W.; Choo, Y.; Sweat, D. P.; Osuji, C. O.; Gopalan, P. Isomeric Effect Enabled Thermally Driven Self-Assembly of Hydroxystyrene-Based Block Copolymers. *ACS Macro Lett.* **2016**, *5* (7), 833–838.
- (25) Maeda, R.; Hayakawa, T.; Ober, C. K. Dual Mode Patterning of Fluorine-Containing Block Copolymers through Combined Top-down and Bottom-up Lithography. *Chem. Mater.* **2012**, *24* (8), 1454–1461.
- (26) Brassat, K.; Lindner, J. K. N. Nanoscale Block Copolymer Self-Assembly and Microscale Polymer Film Dewetting: Progress in Understanding the Role of Interfacial Energies in the Formation of Hierarchical Nanostructures. *Adv. Mater. Interfaces* **2020**, *7* (5), 1901565.
- (27) Nakatani, R.; Takano, H.; Chandra, A.; Yoshimura, Y.; Wang, L.; Suzuki, Y.; Tanaka, Y.; Maeda, R.; Kihara, N.; Minegishi, S.; Miyagi, K.; Kasahara, Y.; Sato, H.; Seino, Y.; Azuma, T.; Yokoyama, H.; Ober, C. K.; Hayakawa, T. Perpendicular Orientation Control without Interfacial Treatment of RAFT-Synthesized High- χ Block Copolymer Thin Films with Sub-10 nm Features Prepared via Thermal Annealing. *ACS Appl. Mater. Interfaces* **2017**, *9* (37), 31266–31278.
- (28) Jo, S.; Jeon, S.; Jun, T.; Park, C.; Ryu, D. Y. Fluorine-Containing Styrenic Block Copolymers toward High χ and Perpendicular Lamellae in Thin Films. *Macromolecules* **2018**, *51* (18), 7152–7159.
- (29) Li, X.; Li, J.; Wang, C.; Liu, Y.; Deng, H. Fast self-assembly of polystyrene-*b*-poly(fluoro methacrylate) into sub-5 nm microdomains for nanopatterning applications. *J. Mater. Chem. C* **2019**, *7* (9), 2535–2540.
- (30) Moad, G.; Rizzardo, E.; Thang, S. H. Living Radical Polymerization by the RAFT Process – A Third Update. *Aust. J. Chem.* **2012**, *65* (8), 985–1076.
- (31) Peng, Q.; Tseng, Y.-C.; Darling, S. B.; Elam, J. W. A Route to Nanoscopic Materials via Sequential Infiltration Synthesis on Block Copolymer Templates. *ACS Nano* **2011**, *5* (6), 4600–4606.
- (32) Girardot, C.; Böhme, S.; Archambault, S.; Salaün, M.; Latur-Romain, E.; Cunge, G.; Joubert, O.; Zelsmann, M. Pulsed Transfer Etching of PS–PDMS Block Copolymers Self-Assembled in 193 nm Lithography Stacks. *ACS Appl. Mater. Interfaces* **2014**, *6* (18), 16276–16282.
- (33) Borah, D.; Cummins, C.; Rasappa, S.; Senthamaikannan, R.; Salaun, M.; Zelsmann, M.; Lontos, G.; Ntetsikas, K.; Avgeropoulos, A.; Morris, A. M. Nanopatterning via Self-Assembly of a Lamellar-Forming Polystyrene-*block*-Poly(dimethylsiloxane) Diblock Copolymer on Topographical Substrates Fabricated by Nanoimprint Lithography. *Nanomaterials* **2018**, *8* (1), 32.
- (34) Leibler, L. Theory of Microphase Separation in Block Copolymers. *Macromolecules* **1980**, *13* (6), 1602–1617.
- (35) Sakurai, S.; Mori, K.; Okawara, A.; Kimishima, K.; Hashimoto, T. Evaluation of segmental interaction by small-angle x-ray scattering based on the random-phase approximation for asymmetric, polydisperse triblock copolymers. *Macromolecules* **1992**, *25* (10), 2679–2691.
- (36) Zhao, Y.; Sivaniah, E.; Hashimoto, T. SAXS Analysis of the Order–Disorder Transition and the Interaction Parameter of Polystyrene-*block*-poly(methyl methacrylate). *Macromolecules* **2008**, *41* (24), 9948–9951.
- (37) Sinturel, C.; Bates, F. S.; Hillmyer, M. A. High χ –Low N Block Polymers: How Far Can We Go? *ACS Macro Lett.* **2015**, *4* (9), 1044–1050.
- (38) Kennemur, J. G.; Yao, L.; Bates, F. S.; Hillmyer, M. A. Sub-5 nm Domains in Ordered Poly(cyclohexylethylene)-*block*-poly(methyl methacrylate) Block Polymers for Lithography. *Macromolecules* **2014**, *47* (4), 1411–1418.
- (39) Durand, W. J.; Blachut, G.; Maher, M. J.; Sirard, S.; Tein, S.; Carlson, M. C.; Asano, Y.; Zhou, S. X.; Lane, A. P.; Bates, C. M.; Ellison, C. J.; Willson, C. G. Design of high- χ block copolymers for lithography. *J. Polym. Sci., Part A: Polym. Chem.* **2015**, *53* (2), 344–352.
- (40) Hansen, C. M. *Hansen Solubility Parameters: A User's Handbook*; CRC Press: 2007.
- (41) Ruiz, R.; Wan, L.; Lille, J.; Patel, K. C.; Dobisz, E.; Johnston, D. E.; Kisslinger, K.; Black, C. T. Image quality and pattern transfer in directed self assembly with block-selective atomic layer deposition. *J. Vac. Sci. Technol., B: Nanotechnol. Microelectron.: Mater., Process., Meas., Phenom.* **2012**, *30* (6), 06F202.
- (42) Cummins, C.; Mokarian-Tabari, P.; Andrezza, P.; Sinturel, C.; Morris, M. A. Solvothermal Vapor Annealing of Lamellar Poly(styrene)-*block*-poly(d,l-lactide) Block Copolymer Thin Films for Directed Self-Assembly Application. *ACS Appl. Mater. Interfaces* **2016**, *8* (12), 8295–8304.
- (43) Gotrik, K. W.; Ross, C. A. Solvothermal Annealing of Block Copolymer Thin Films. *Nano Lett.* **2013**, *13* (11), 5117–5122.
- (44) Lundy, R.; Flynn, S. P.; Cummins, C.; Kelleher, S. M.; Collins, M. N.; Dalton, E.; Daniels, S.; Morris, M. A.; Enright, R. Controlled solvent vapor annealing of a high [small χ] block copolymer thin film. *Phys. Chem. Chem. Phys.* **2017**, *19* (4), 2805–2815.
- (45) Cummins, C.; Gangnaik, A.; Kelly, R. A.; Borah, D.; O'Connell, J.; Petkov, N.; Georgiev, Y. M.; Holmes, J. D.; Morris, M. A. Aligned silicon nanofins via the directed self-assembly of PS-*b*-P4VP block copolymer and metal oxide enhanced pattern transfer. *Nanoscale* **2015**, *7* (15), 6712–6721.
- (46) Cummins, C.; Gangnaik, A.; Kelly, R. A.; Hydes, A. J.; O'Connell, J.; Petkov, N.; Georgiev, Y. M.; Borah, D.; Holmes, J. D.; Morris, M. A. Parallel Arrays of Sub-10 nm Aligned Germanium Nanofins from an In Situ Metal Oxide Hardmask using Directed Self-Assembly of Block Copolymers. *Chem. Mater.* **2015**, *27* (17), 6091–6096.
- (47) Tseng, Y.-C.; Peng, Q.; Ocola, L. E.; Czaplewski, D. A.; Elam, J. W.; Darling, S. B. Etch properties of resists modified by sequential infiltration synthesis. *J. Vac. Sci. Technol., B: Nanotechnol. Microelectron.: Mater., Process., Meas., Phenom.* **2011**, *29* (6), 06FG01.
- (48) Tseng, Y.-C.; Peng, Q.; Ocola, L. E.; Elam, J. W.; Darling, S. B. Enhanced Block Copolymer Lithography Using Sequential Infiltration Synthesis. *J. Phys. Chem. C* **2011**, *115* (36), 17725–17729.
- (49) Tseng, Y.-C.; Mane, A. U.; Elam, J. W.; Darling, S. B. Enhanced Lithographic Imaging Layer Meets Semiconductor Manufacturing Specification a Decade Early. *Adv. Mater.* **2012**, *24* (19), 2608–2613.

3.E/ Triply-Periodic Minimal Surface 3D modelling and 2D-slicing

The gyroid morphology is a particular bi-continuous self-assembled di-BCP structure which was not studied in this Ph.D., because it is a 3D structure that requires thicker films for proper stabilization, e.g. 500 nm [8]. Conversely to classic structures, i.e. lamellae, cylinders and spheres, the gyroid phase and other multi-continuous BCP phases are more complex and can be described using triply-periodic minimal surfaces (TPMS) [9], [10]. A software was developed to better apprehend experimental microscopy results by modeling different TPMSs and slicing them in a chosen plan (*Figure 125*). This software permits to understand which structure is observed with the associated plan, or to predict the theoretical most stable plan that should be observed. This software has many features which will not be presented here, but are explained in the software.

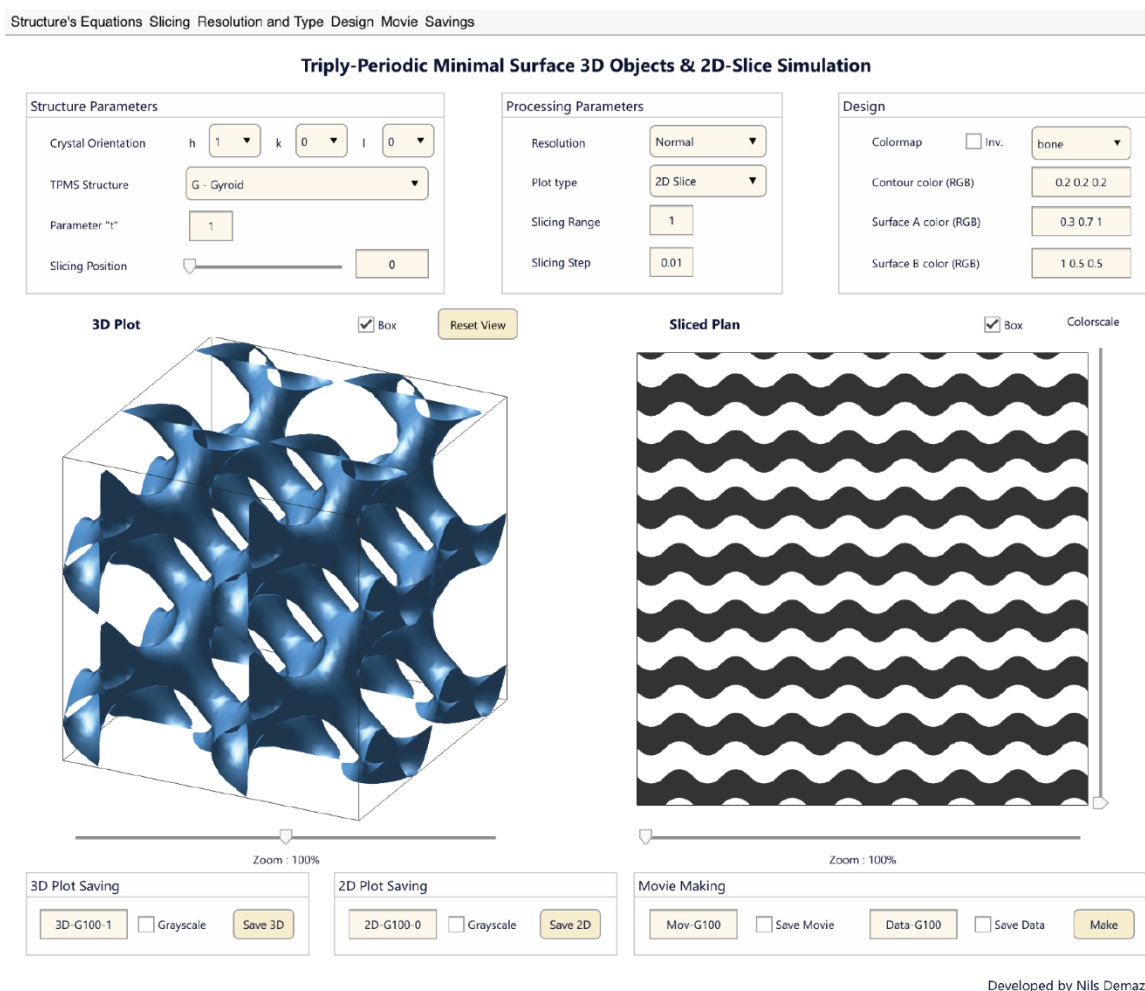


Figure 125. Triply-Periodic Minimal Surface 3D Objects & 2D-Slice Simulation window with the example of a gyroid sliced along the 100 plan.

Within our laboratory, K. Aissou *et al.* studied triblock copolymers which self-assemble in a variety of multi-continuous structures. This aforementioned software was used to better understand the morphological features of a particular PDMSB-*b*-PS-*b*-PMMA sample. Indeed, the

SEM images of the 3D structure showed several periodic patterns depending of the observed plans. A diamond-type structure was confirmed using the software simulation, which is different than the di-BCP gyroid structure as each structure node are connected to four other ones, against three for the gyroid [11].

The bibliographic details of the published manuscript are:

K. Aissou, M. Mumtaz, N. Demazy, G. Pécastaings, G. Fleury, and G. Hadziioannou, "Periodic Bicontinuous Structures Formed on the Top Surface of Asymmetric Triblock Terpolymer Thick Films" *ACS Macro Letters*, vol. 8, no. 8, pp. 923–930, 2019.

<https://doi.org/10.1021/acsmacrolett.9b00403>

Periodic Bicontinuous Structures Formed on the Top Surface of Asymmetric Triblock Terpolymer Thick Films

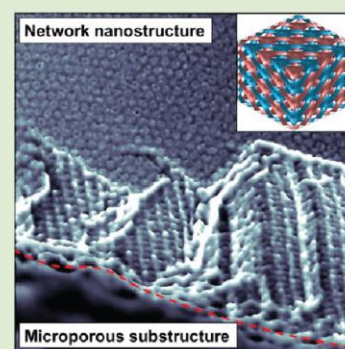
Karim Aissou,^{*,†} Muhammad Mumtaz,[‡] Nils Demazy,[‡] Gilles Pécastaings,[‡] Guillaume Fleury,[‡] and Georges Hadziioannou[‡]

[†]Institut Européen des Membranes, Université de Montpellier - CNRS - ENSCM, 300 Avenue du Professeur Emile Jeanbrau, F-34090 Montpellier, France

[‡]Laboratoire de Chimie des Polymères Organiques, Université Bordeaux, CNRS, Bordeaux INP, LCPO, UMR 5629, F-33600 Pessac, France

Supporting Information

ABSTRACT: The combination of the nonsolvent-induced phase separation (NIPS) process with a solvent vapor annealing (SVA) treatment is used to produce asymmetric and hydrophobic thick films having different long-range ordered network nanostructures, which are inaccessible via currently available membrane fabrication methods. We show that the disordered phase generated by NIPS on the material top surface can be transformed into a highly ordered bicontinuous network nanostructure during the SVA process without disrupting the substructure morphology. For instance, by using a straightforward blending approach, either a triply periodic alternating diamond (D^A) structure or a core-shell perforated lamellar (PL) phase was demonstrated on the skin layer of fully hydrophobic poly(1,1-dimethyl silacyclobutane)-*block*-polystyrene-*block*-poly(methyl methacrylate) (PDMSB-*b*-PS-*b*-PMMA) thick films. Such a material fabrication method, enabling the formation of a sponge-like substructure topped by a network phase having an excellent long-range order, provides an appealing strategy to facilitate the manufacture of next-generation membranes at large scale since these bicontinuous morphologies obviate the need of the nanochannel alignment.



Asymmetric and isoporous block copolymer (BCP) membranes are promising materials to achieve a better figure of merit compared to the state-of-the-art membranes as their unique architecture allows overcoming the ubiquitous permeability–selectivity trade-off.^{1–4} To produce such kinds of high-performance materials, Peinemann et al.⁵ have used an elegant approach which combines the self-assembly of BCPs into an out-of-plane cylindrical nanostructure on the material top surface with the formation of a macroporous substructure generated by nonsolvent-induced phase separation (NIPS). However, a perfect control of the nanopore formation is challenging to achieve with the SNIPS method (*i.e.*, self-assembly + NIPS) due to the fact that, at best, a kinetically trapped morphology derived from a micellization process is formed on the material skin layer when appropriate manufacturing conditions can be defined.^{6–8} Indeed, the complex exchange/migration of the nonsolvent occurring during the porosity formation allows isoporous membranes with pores extending over the top separation layer to be solely demonstrated for specific amphiphilic AB- and ABC-type BCP systems since the hydrophilic block plays a crucial role in creating pores during the precipitation process.^{9–14}

To produce innovative membranes with smart nanopores (*e.g.*, thermo-, ion-, and/or pH-responsive channels),^{15–18} a large panoply of chemically distinct amphiphilic BCP materials has been generated by SNIPS. In addition, the self-assembly of

blends of two chemically interacting amphiphilic BCPs was revealed to be a powerful strategy to achieve highly porous membranes with pore diameters as small as 1.5 nm.¹⁹ However, so far, only a few of these chemically distinct amphiphilic BCP membranes exhibit a dense top surface with long-range ordered nanopores.

The more challenging fabrication of fully hydrophobic BCP materials with an asymmetric structure or ordered pores over the whole film has been recently demonstrated by SNIPS²⁰ or a strategy related to SNIPS,²¹ respectively. For the asymmetric material, although a complete pore formation was evidenced on the top layer during the SNIPS process, the resulting BCP morphology was arranged into a short-range ordered array with a broad pore size distribution, limiting the selectivity of the top separation layer.²⁰

In this work, we efficiently combine the NIPS process and the solvent vapor annealing (SVA) approach to demonstrate that fully hydrophobic triblock terpolymer thick films can also be manufactured with a sponge-like morphology topped by a long-range ordered nanostructure. We show that no effort is required to preorder the poly(1,1-dimethyl silacyclobutane)-*block*-polystyrene-*block*-poly(methyl methacrylate) (PDMSB-

Received: May 27, 2019

Accepted: June 12, 2019

Published: July 16, 2019

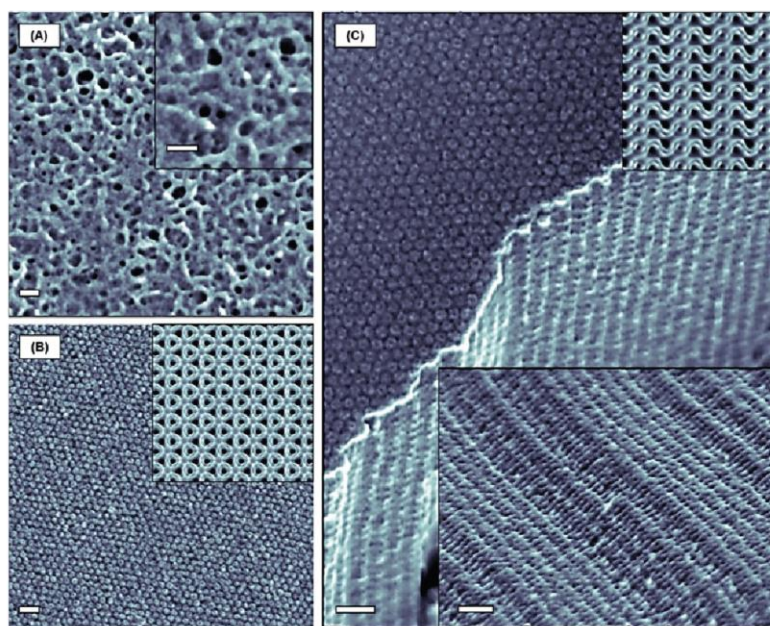


Figure 1. Top-view SEM images of blended (25 wt %) PDMSB-*b*-PS-*b*-PMMA thick films manufactured by NIPS then exposed to a CHCl₃ vapor during different times: (a) 0 h and (b, c) 3 h. The disordered phase generated by NIPS on the top surface membrane is transformed into a highly ordered D^A structure after the SVA treatment. Insets: Magnified SEM image showing (a) the dense regions formed by collapsed micelles after the NIPS process and (c) the D^A (210) pattern. Additionally, simulated cross-sectional images of the D^A structure cut parallel to (b) the (111) plane and (c) the (210) plane are presented. Scale bars: 100 nm.

b-PS-*b*-PMMA) terpolymers on the material top surface during the NIPS process since the SVA treatment transforms the kinetically trapped poorly ordered phase into a well-defined nanostructure. To obviate the need of alignment of the BCP nanodomains, we show that different network structures such as the alternating diamond (D^A) and perforated-lamellar (PL) phases can be readily produced on the top surface layer by using a simple blending strategy. As all the material architectures, consisting of a sponge-like substructure topped by a network structure having a high-areal density of well-defined continuous nanopathways, are highly desired for the next-generation membranes, the NIPS-SVA process could be envisioned as a promising methodology toward the reproducible manufacturing in large scale of asymmetric and isoporous BCP membranes.

The PDMSB-*b*-PS-*b*-PMMA used in this work was prepared by a sequential anionic polymerization, as described previously,²² to achieve a perfect control of the molecular weight, M_n (34 kg mol⁻¹), with a narrow dispersity ($\mathcal{D} = 1.11$) and a symmetric volume composition, Φ ($\Phi_{\text{PDMSB}} = 0.32$, $\Phi_{\text{PS}} = 0.36$, $\Phi_{\text{PMMA}} = 0.32$). This triblock terpolymer is nonfrustrated²³ since the Flory–Huggins interaction parameter, $\chi_{\text{PDMSB-PMMA}}$, between the two end blocks (i.e., PDMSB and PMMA) is higher than the other pairs, $\chi_{\text{PDMSB-PS}}$ and $\chi_{\text{PS-PMMA}}$ ($\chi_{\text{PS-PMMA}} \approx 0.04 < \chi_{\text{PDMSB-PS}} \approx 0.07 < \chi_{\text{PDMSB-PMMA}} \approx 0.2$).^{22,24,25} Note that both (spin-coated) thin films and (drawn) asymmetric thick films made of this nonfrustrated terpolymer exhibit a 39 nm period core–shell cylindrical structure having an in-plane orientation (i.e., an undesirable nanodomain orientation) when exposed to a chloroform (CHCl₃) vapor (see Figure S1).²¹ A preferential swelling of the PDMSB domains under a CHCl₃ stream causes the core–shell cylindrical structure to differ from the bulk morphology since the SAXS profile of the thermally annealed (24 h, 180

°C) PDMSB-*b*-PS-*b*-PMMA sample shows a first-order peak, q^* , at 0.173 nm⁻¹ and higher-order peaks located at $q/q^* = 1, 2, 3, 4, 5, 6, 7,$ and 8 , consistent with a lamellar phase having a period of ~ 36.3 nm (see Figure S2).

To alleviate the need for domain alignment, different highly ordered network structures were produced on the top surface layer by blending the PDMSB-*b*-PS-*b*-PMMA thick films with either 25 or 35 wt % of PDMSB-*b*-PS chains ($\Phi_{\text{PDMSB}} = 0.29$, $M_n = 21.6$ kg mol⁻¹, and $\mathcal{D} = 1.09$). Importantly, blends of this triblock terpolymer with different amounts of a small PS homopolymer (hPS, 3 kg mol⁻¹) gave access to well-ordered cylindrical or spherical nanodomains on a denser sponge-like substructure. Here, the possible miscibility of PMMA domains with the small hPS chains, due to the low $\chi_{\text{PS-PMMA}}$ value, should be taken into account to explain the different phase behaviors of such blends.

Blended PDMSB-*b*-PS-*b*-PMMA thick films were drawn into a silicon substrate from an 18 wt % polymer solution in a disolvent mixture of 1,4-dioxane and tetrahydrofuran (DOX/THF: 80/20 by weight) using a doctor's blade set at a gate height of 225 μm . After the thick film was casted, the disolvent mixture was allowed to evaporate for 15 s to form a dense top surface layer. The blended PDMSB-*b*-PS-*b*-PMMA thick films were then plunged in a water bath in order to induce the formation of a sponge-like substructure by NIPS. Note that a fluorine-rich reactive ion etching (RIE) plasma was performed to partially and preferentially remove PDMSB and PMMA domains, respectively, prior to taking scanning electronic microscopy (SEM) images (plasma conditions are 40 W, 17 sccm CF₄ and 3 sccm O₂, 180 mTorr, 45 s).

The SEM image presented in Figure 1a shows the resulting top surface morphology of a blended (25 wt %) PDMSB-*b*-PS-*b*-PMMA thick film generated by NIPS for a solvent evaporation time of 15 s. In such conditions, the material

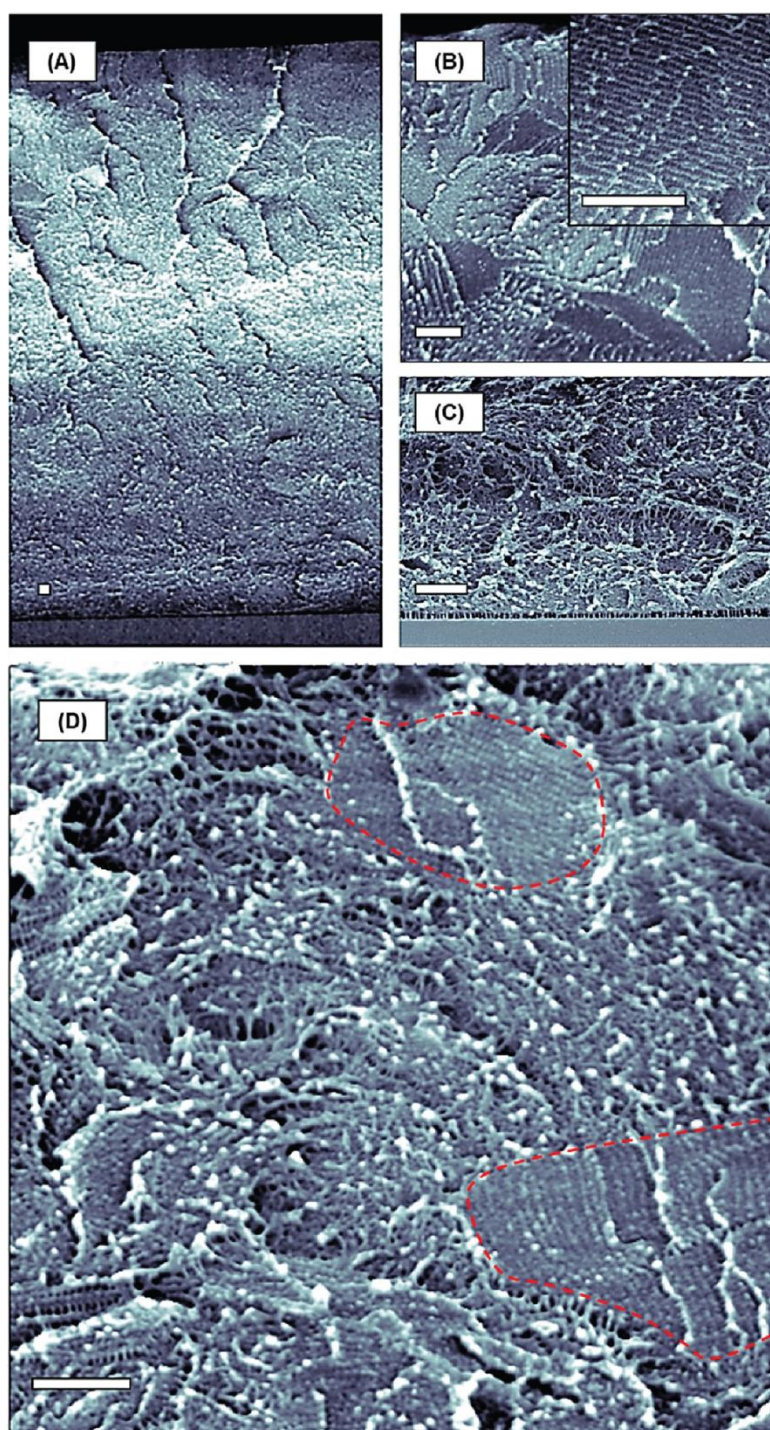


Figure 2. Cross-sectional SEM views of a blended (25 wt %) PDMSB-*b*-PS-*b*-PMMA thick film ($t \sim 24 \mu\text{m}$) generated by NIPS-SVA (3 h, CHCl_3) showing: (a) the full material on a Si substrate, (b) the D^A structure formed within the material top layer, (c) the sponge-like substructure in the vicinity of the substrate, and (d) ordered D^A grains delimited by red dashed lines in the sponge-like substructure. Inset: magnified SEM view showing the complex D^A structure. Scale bars: $0.5 \mu\text{m}$.

top layer consists of dense regions formed by collapsed micelles (gray) which coexist with sub-100 nm diameter pores (black) randomly distributed across the surface. Conversely, a highly ordered hexagonal nanoring-like array with a period of 38.5 nm is produced when the thick film is afterward exposed to a CHCl_3 vapor during 3 h (see Figure 1b). This nanoring-

like array pattern is consistent with the characteristic (111) crystallographic plane of an alternating diamond (D^A , space group $Fd\bar{3}m$) structure oriented parallel to the air surface since it qualitatively resembles the simulated cross-sectional view cut parallel to the D^A (111) plane (see Figure 1b inset) and to the D^A (111) pattern recently observed in bulk from binary blends

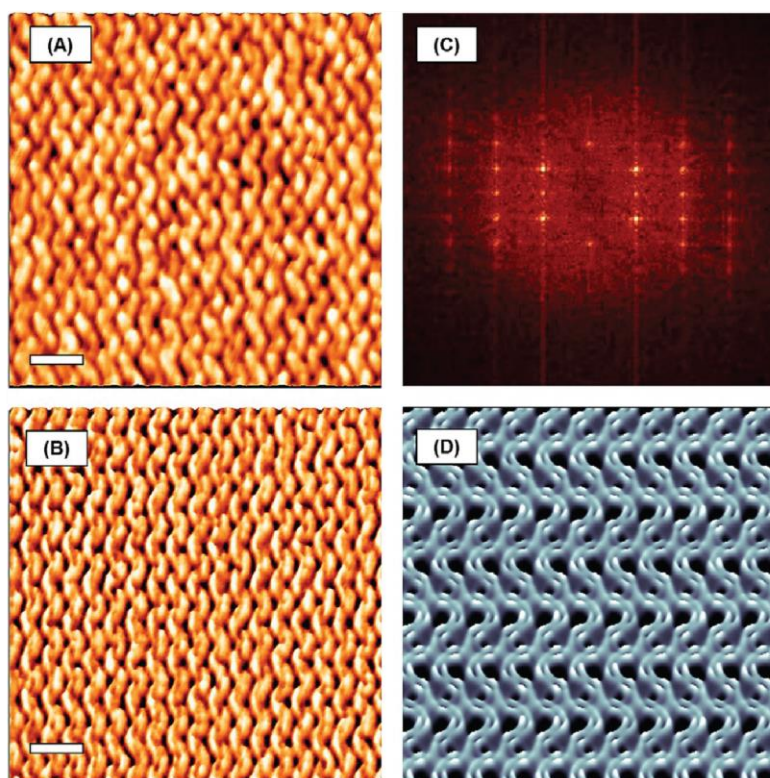


Figure 3. AFM (a) topographic and (b) phase views showing the D^A (310) plane oriented parallel to the air surface of a blended (25 wt %) PDMSB-*b*-PS-*b*-PMMA thick film generated by NIPS-SVA (3 h, CHCl_3). (c) The 2D-FFT of the topographic image reveals that the wavy stripe pattern has $c2mm$ symmetry. (d) Simulated cross-sectional image of the D^A structure cut parallel to the (310) plane. Scale bars: 100 nm.

of polyisoprene-*b*-PS-*b*-poly(2-vinylpyridine) (PI-*b*-PS-*b*-P2VP).²⁶ The presence of the D^A (210) pattern as shown in Figure 1c further confirms the formation of a D^A structure, which consists of two chemically distinct (PDMSB and PMMA) and mutually interwoven networks embedded in a PS matrix (see Figure S3). The D^A (210) pattern presents wavy stripes ordered into a rectangular array with the lattice parameters $a = 45$ nm and $b = 21$ nm. The ratio a/b equal to 2.14 is quite similar to the one determined from the simulated (210) plane of the D^A structure shown in Figure 1c inset ($a/b = 2.25$).

In the regions of the thick film where the nanoring pattern is observed on the top surface layer, it turns out that the fracture propagations of the D^A structure occur preferentially along the (210) plane with a relative flatness inside the grains having a single orientation of the wavy stripe motif. This relative flatness is a good indication of a nontraumatic propagation of the fracture along the wavy stripe pattern having a PS matrix area fraction of $\sim 57\%$ (determined from a binarization of the simulated D^A (210) plane) and could explain the frequent observation of the D^A (210) plane. Importantly, this several micrometers thick D^A structure differs from the core-shell cylindrical morphology having a period of ~ 33 nm observed in thin-film configuration after the SVA treatment (3 h, CHCl_3).²² This phenomenon is probably due to the fact that the 70 nm thick PDMSB-*b*-PS-*b*-PMMA layer blended with 25 wt % of PDMSB-*b*-PS chains is too thin to allow the formation of the D^A structure, as recently shown from sub-100 nm thick PDMSB-*b*-PS films for which a cylindrical phase was observed

for film thicknesses below the unit cell dimension of the double gyroid (DG, $Ia\bar{3}d$) structure.²⁷

To demonstrate that the asymmetric structure of the blended (25 wt %) thick films has not been destroyed during the SVA process, representative SEM images showing the lower, middle, and upper regions of a solvent-annealed (3 h, CHCl_3) PDMSB-*b*-PS-*b*-PMMA thick film are presented in Figure 2. The cross-sectional SEM view presented in Figure 2a indicates that the blended PDMSB-*b*-PS-*b*-PMMA thick film deposited on a silicon substrate has a thickness of ~ 24 μm . A nanostructured 3D morphology of over 4 μm in thickness can be observed on the material top surface (see Figure 2b), while a sponge-like substructure is clearly visible close to the Si substrate (see Figure 2c). Although the disordered sponge-like morphology and the network structure are always separated from one another by a well-defined interface (see Figure S4), some nanostructured grains drown in the sponge-like substructure can be seen in the middle of the blended PDMSB-*b*-PS-*b*-PMMA thick film, like those surrounded by the dashed red lines in Figure 2d. Importantly, in spite of the presence of a few nanostructured grains in the middle of the polymeric layer (revealing that the CHCl_3 vapor is able to deeply penetrate the material), the asymmetric structure of the blended material generated by NIPS is not disrupted during the post SVA process. This phenomenon is due to the fact that the sponge-like substructure must densify prior to being transformed into a well-ordered D^A phase, implying a strong collapse of the blended PDMSB-*b*-PS-*b*-PMMA thick film.

For short time durations of the SVA process ($t < 1$ h), the characteristic D^A (111) pattern is the most frequently observed

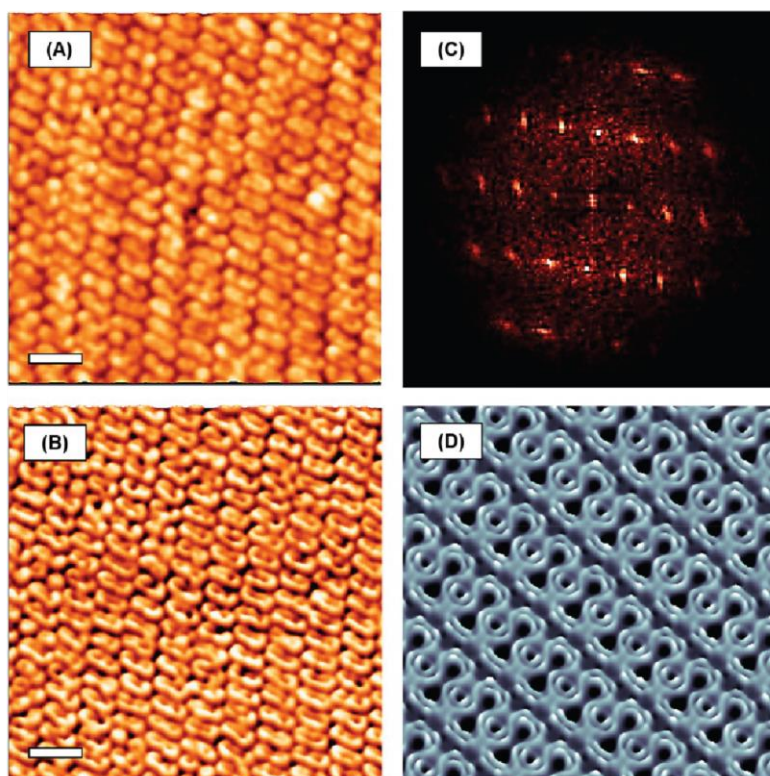


Figure 4. AFM (a) topographic and (b) phase views showing the D^A (311) plane oriented parallel to the air surface of a blended (25 wt %) PDMSB-*b*-PS-*b*-PMMA thick film generated by NIPS-SVA (3 h, CHCl_3). (c) The 2D-FFT of the topographic image indicates that the lozenge-like features are arranged in an oblique lattice. (d) Simulated cross-sectional image of the D^A structure cut parallel to the (311) plane. Scale bars: 100 nm.

on the free surface of the blended (25 wt %) thick film. In contrast, the (310) and (311) motifs of the D^A structure can also be encountered at the material–air interface when the time duration of the SVA process is increased. For instance, the atomic force microscopy (AFM) topographic and phase images taken from a blended (25 wt %) PDMSB-*b*-PS-*b*-PMMA thick film exposed to a CHCl_3 vapor for 3 h and then treated by a CF_4/O_2 RIE plasma show the typical wavy stripe pattern of the D^A (310) plane oriented parallel to the air surface (see Figure 3a,b).

The 2D fast Fourier transform (FFT) of the AFM topographic image indicates that these wavy stripes are arranged into a centered rectangular array with the lattice parameters $a = 74.1$ nm and $b = 40.7$ nm (see Figure 3c). The ratio a/b equal to 1.82 is very close to the one determined from the simulated D^A (310) plane presented in Figure 3d ($a/b = 1.78$). These wavy stripes are often confined inside macro-sized grains ($>1.5 \mu\text{m}^2$), indicating a high crystalline quality of the alternating diamond morphology formed on the sponge-like substructure (see Figure S5). Lozenge-like features arranged in an oblique lattice can also be observed on the material free surface as shown on the AFM topographic and phase views presented in Figure 4a,b.

The 2D-FFT presented in Figure 4c indicates that this lozenge-like pattern ($a = 64.5$ nm, $b = 36.3$ nm, and $\gamma \approx 100^\circ$) has a ratio a/b equal to 1.77 which is quite similar to the one determined from the simulated D^A (311) plane shown in Figure 4d ($a/b = \sqrt{3} \sim 1.73$). This lozenge-like motif can also be encountered inside large grains as shown on the AFM and

SEM images presented in Figure S6. Note that other crystallographic planes of the D^A structure have also been observed within the material skin layer, which fully supports the formation of a well-developed network morphology during the SVA treatment (see Figure S7).

Varying the amount of PDMSB-*b*-PS chains within the PDMSB-*b*-PS-*b*-PMMA material was revealed to be an efficient strategy to achieve another long-range ordered network structure on the material skin layer. Indeed, a perforated layer (PL) is produced on the top surface of solvent-annealed (3 h, CHCl_3) PDMSB-*b*-PS-*b*-PMMA thick films blended with 35 wt % of PDMSB-*b*-PS chains as depicted in Figure 5a. For such morphology consisting of a PMMA-rich phase enclosed in PS lamellae and PDMSB lamellae perforated by PMMA/PS core–shell cylinders, two different patterns, corresponding to the (001) and (101) crystallographic planes of the PL structure, are commonly observed on the material skin layer. The top view SEM image presented in Figure 5b shows that the PL (001) pattern consists of PMMA/PS core–shell perforations ordered into a well-ordered hexagonal array having a period of ~ 27 nm. A hexagonal packing of perforations is commonly observed for the perforated layer structures in which the perforations are generally arranged into an AB or ABC stacking.^{28–31} In contrast, a 27 nm period lamellar pattern without apparent perforations can be observed along the (101) plane (see Figure 5c). The top view SEM images presented in Figures 5d,e show the layered structure inside the material skin layer at different magnifications. Figure 5e confirms the formation of a PL structure on the top surface layer since PS (bright) perforations are evident through the

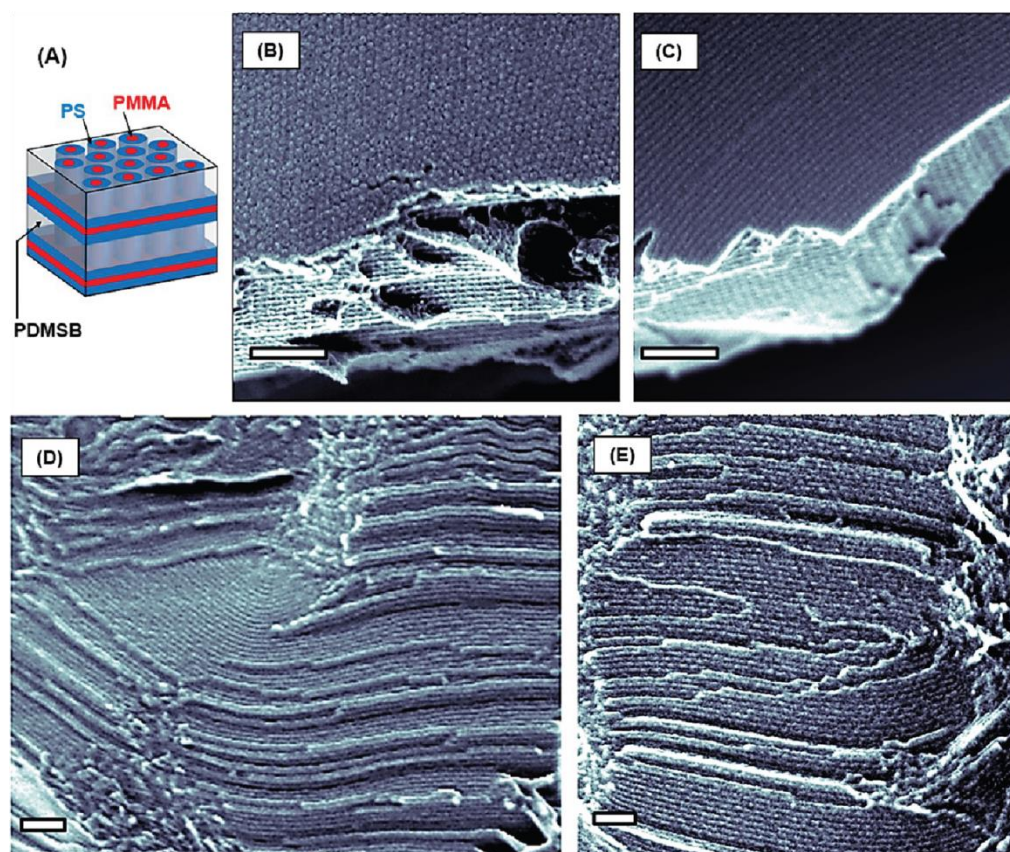


Figure 5. (a) Schematic representation of a bicontinuous PL structure having PMMA (red)/PS (blue) core–shell perforations. (b) and (c) Top view SEM images showing different PL planes oriented parallel to the air surface of a blended (35 wt %) PDMSB-*b*-PS-*b*-PMMA thick film generated by NIPS-SVA (3 h, CHCl₃). (d) and (e) Top view SEM images, at different magnifications, showing the PL phase inside the material skin layer. Scale bars: 200 nm.

PDMSB (dark) lamellae. A perforated lamellar structure with core–shell perforations arranged into a rhombic array has been recently achieved on the skin layer of solvent-annealed (CHCl₃) PDMSB-*b*-PS-*b*-P2VP thick films.³² For such PL structure having perforations stacked in ABAB... sequence, the (001) and (101) planes were also the most frequently observed at the material–air interface. Unfortunately, here the stacking sequence of the PMMA/PS perforations is unclear from the SEM images.

Bicontinuous network morphologies having an excellent long-range order were demonstrated on the skin layer of asymmetric and hydrophobic triblock terpolymer thick films manufactured by combining the conventional NIPS process with an SVA treatment used in advanced lithography application. Remarkably, an appealing triply periodic DA nanostructure of unprecedented complexity is achieved for the first time on a sponge-like microstructure. We believe this simple and scalable NIPS-SVA method, enabling the formation of appealing network nanostructures which differ from the common cylindrical morphology generated by SNIPS, can be viewed as a first step in the process of preparing newly designed membranes. Indeed, porous nanochannels are also mandatory to manufacture a permeable membrane. To avoid any additional challenging etching process to remove the PMMA nanopathways, pH-responsive P2VP-containing triblock terpolymer membranes, having either an open or closed

state of the pores depending on the pH value, are currently being studied in our laboratory.

METHODS

Fabrication of Asymmetric PDMSB-*b*-PS-*b*-PMMA-Based Thick Films. PDMSB-*b*-PS-*b*-PMMA (24 μm thick) films were drawn onto (1.5 × 2 cm²) silicon substrates by using a tape casting technique from a 18 wt % terpolymer solution in a mixture of 1,4-dioxane and tetrahydrofuran (DOX/THF: 80/20 by weight). To manufacture asymmetric materials with a sponge-like substructure, solvents were allowed to evaporate during 15 s to form a dense skin layer, and then the thick films were immersed into a water bath for 10 min to precipitate the PDMSB-*b*-PS-*b*-PMMA terpolymer. An SVA treatment was subsequently performed to transform the kinetically trapped morphology formed on the material top surface into a self-assembled nanostructure. As the neat PDMSB-*b*-PS-*b*-PMMA terpolymer self-assembles into a core–shell cylindrical morphology when exposed to a CHCl₃ vapor, the terpolymer solution was blended with either 25 wt % or 35 wt % of PDMSB-*b*-PS chains to achieve different bicontinuous network structures.

Self-Assembled PDMSB-*b*-PS-*b*-PMMA Thick Films. The self-assembly of unblended and blended PDMSB-*b*-PS-*b*-PMMA thick films was promoted by exposing the polymeric layers during different times to a continuous stream of CHCl₃ vapor produced by bubbling nitrogen gas through the liquid solvent as described previously.³³ This continuous flow system was used to control the CHCl₃ vapor pressure in the chamber having a lid made of quartz by dilution with a separate N₂ stream so that the solvent vapor consisted of 32 sccm CHCl₃ vapor and 8 sccm N₂ (total 40 sccm). As the in situ measurement of

the film thickness variation of an asymmetric thick film is not easy to achieve, the swelling ratio of a blended (25 wt %) PDMSB-*b*-PS-*b*-PMMA layer was estimated in thin configuration (initial thickness of ~95 nm), using a Filmetrics spectroscopic white light reflectometer apparatus (see Figure S8). The blended layer, spin-coated (2 krpm) from a 2 wt % BCP solution in a mixture of tetrahydrofuran and propylene glycol monomethyl ether acetate (THF/PGMEA: 2/1), reached a plateau for a 70% thickness variation.

SEM and AFM Characterizations. Scanning electron microscopy (SEM, JEOL 7800) was used in Gentle Beam mode (GBSH) at an accelerating voltage of 1 kV to take PDMSB-*b*-PS-*b*-PMMA film images. Atomic force microscopy (AFM Dimension FastScan, Bruker) was used in tapping mode to characterize the surface morphology of blended and unblended PDMSB-*b*-PS-*b*-PMMA thick films. Silicon cantilevers (Fastscan-A) with a typical tip radius of ~5 nm were used. The resonance frequency of the cantilevers was about 1.25 kHz. Prior to SEM and AFM measurements, PDMSB-*b*-PS-*b*-PMMA thick films were etched with a fluorine-rich plasma treatment in the PE-100 chamber (RIE, Plasma Etch) to remove partially and preferentially the PDMSB and PMMA phases (plasma conditions: 40 W, 17 sccm CF₄ and 3 sccm O₂, 180 mTorr, and 45 s).

Small-Angle X-ray Scattering (SAXS). SAXS experiments were performed on the D2AM French-CRG Beamline at the European Synchrotron Radiation Facility (ESRF) in Grenoble, France. A XPAD 2D pixel detector was used for recording the 2D scattering images, and a 2400 mm sample-to-detector distance was chosen. The energy of the X-ray beam was 11 keV. The 2D images were radially averaged around the center of the primary beam to obtain the isotropic SAXS intensity profiles. The scattering pattern from a specimen of silver behenate was used for the calibration of the wavevector scale of the scattering curves. Finally, the data were normalized to the intensity of the incident beam to correct for primary beam intensity fluctuations.

■ ASSOCIATED CONTENT

■ Supporting Information

The Supporting Information is available free of charge on the ACS Publications website at DOI: 10.1021/acsmacrolett.9b00403.

SEM images of a neat PDMSB-*b*-PS-*b*-PMMA thick film generated by NIPS-SVA (3 h, CHCl₃); SAXS profile of a thermally annealed (24 h, 180 °C) PDMSB-*b*-PS-*b*-PMMA sample; simulations for a cubic cell of the triply periodic bicontinuous D^A morphology and three different plane orientations; SEM images of a blended (25 wt %) PDMSB-*b*-PS-*b*-PMMA thick film generated by NIPS-SVA (3 h, CHCl₃); AFM topographic view and its associated 2D-FFT corresponding to the D^A (310) plane of a blended (25 wt %) PDMSB-*b*-PS-*b*-PMMA thick film (3 h, CHCl₃); AFM topographic views and an SEM image showing the D^A (311) plane oriented parallel to the air surface of a blended (25 wt %) PDMSB-*b*-PS-*b*-PMMA thick film (3 h, CHCl₃); panel of SEM images of a blended (25 wt %) PDMSB-*b*-PS-*b*-PMMA thick film; film thickness variation of a blended (25 wt %) PDMSB-*b*-PS-*b*-PMMA thin film plotted versus the swelling time in a CHCl₃ atmosphere (PDF)

■ AUTHOR INFORMATION

Corresponding Author

*E-mail: karim.aissou@umontpellier.fr.

ORCID

Karim Aissou: 0000-0002-9236-464X

Georges Hadziioannou: 0000-0002-7377-6040

Notes

The authors declare no competing financial interest.

■ ACKNOWLEDGMENTS

This work was performed within the framework of the Equipex ELORPrintTec ANR-10-EQPX-28-01 with the support of the ANR JCJC AFM_Ring project, grant ANR-18-CE09-00xx of the French Agence Nationale de la Recherche. The ESRF is acknowledged for allocating beamtime at the D2AM French Beamline for the SAXS experiments.

■ REFERENCES

- (1) Mehta, A.; Zydney, A. L. Permeability and Selectivity Analysis for Ultrafiltration Membranes. *J. Membr. Sci.* **2005**, *249* (1–2), 245–249.
- (2) Nunes, S. P. Block Copolymer Membranes for Aqueous Solution Applications. *Macromolecules* **2016**, *49*, 2905–2916.
- (3) Abetz, V. Isoporous Block Copolymer Membranes. *Macromol. Rapid Commun.* **2015**, *36* (1), 10–22.
- (4) Zhang, Y.; Sargent, J. L.; Boudouris, B. W.; Phillip, W. A. Nanoporous Membranes Generated from Self-Assembled Block Polymer Precursors: Quo Vadis? *J. Appl. Polym. Sci.* **2015**, DOI: 10.1002/app.41683.
- (5) Peinemann, K. V.; Abetz, V.; Simon, P. F. W. Asymmetric Superstructure Formed in a Block Copolymer via Phase Separation. *Nat. Mater.* **2007**, *6* (12), 992–996.
- (6) Marques, D. S.; Vainio, U.; Chaparro, N. M.; Calo, V. M.; Bezahd, A. R.; Pitera, J. W.; Peinemann, K.-V.; Nunes, S. P. Self-Assembly in Casting Solutions of Block Copolymer Membranes. *Soft Matter* **2013**, *9* (23), 5557.
- (7) Nunes, S. P.; Sougrat, R.; Hooghan, B.; Anjum, D. H.; Behzad, A. R.; Zhao, L.; Pradeep, N.; Pinnau, I.; Vainio, U.; Peinemann, K.-V. Ultraporos Films with Uniform Nanochannels by Block Copolymer Micelles Assembly. *Macromolecules* **2010**, *43* (19), 8079–8085.
- (8) Nunes, S. P.; Behzad, A. R.; Hooghan, B.; Sougrat, R.; Karunakaran, M.; Pradeep, N.; Vainio, U.; Peinemann, K.-V. Switchable pH-Responsive Polymeric Membranes Prepared via Block Copolymer Micelle Assembly. *ACS Nano* **2011**, *5* (5), 3516–3522.
- (9) Phillip, W. A.; Dorin, R. M.; Werner, J.; Hoek, E. M. V.; Wiesner, U.; Elimelech, M. Tuning Structure and Properties of Graded Triblock Terpolymer-Based Mesoporous and Hybrid Films. *Nano Lett.* **2011**, *11* (7), 2892–2900.
- (10) Qiu, X.; Yu, H.; Karunakaran, M.; Pradeep, N.; Nunes, S. P.; Peinemann, K. V. Selective Separation of Similarly Sized Proteins with Tunable Nanoporous Block Copolymer Membranes. *ACS Nano* **2013**, *7* (1), 768–776.
- (11) Gu, Y.; Wiesner, U. Tailoring Pore Size of Graded Mesoporous Block Copolymer Membranes: Moving from Ultrafiltration toward Nanofiltration. *Macromolecules* **2015**, *48* (17), 6153–6159.
- (12) Hahn, J.; Filiz, V.; Rangou, S.; Clodt, J.; Jung, A.; Buhr, K.; Abetz, C.; Abetz, V. Structure Formation of Integral-Asymmetric Membranes of Polystyrene-Block-Poly(ethylene Oxide). *J. Polym. Sci., Part B: Polym. Phys.* **2013**, *51* (4), 281–290.
- (13) Saleem, S.; Rangou, S.; Abetz, C.; Lademann, B.; Filiz, V.; Abetz, V. Block Copolymer Membranes from Polystyrene-*b*-Poly(solketal Methacrylate) (PS-*b*-PSMA) and Amphiphilic Polystyrene-*b*-Poly(glyceryl Methacrylate) (PS-*b*-PGMA). *Polymers (Basel)* **2017**, *9* (6), 216.
- (14) Schöttner, S.; Schaffrath, H.-J.; Gallei, M. Poly(2-Hydroxyethyl Methacrylate)-Based Amphiphilic Block Copolymers for High Water Flux Membranes and Ceramic Templates. *Macromolecules* **2016**, *49* (19), 7286–7295.
- (15) Clodt, J. I.; Filiz, V.; Rangou, S.; Buhr, K.; Abetz, C.; Höche, D.; Hahn, J.; Jung, A.; Abetz, V. Double Stimuli-Responsive Isoporous Membranes via Post-Modification of Ph-Sensitive Self-Assembled Diblock Copolymer Membranes. *Adv. Funct. Mater.* **2013**, *23* (6), 731–738.
- (16) Schacher, F.; Ulbricht, M.; Müller, A. H. E. Self-Supporting, Double Stimuli-Responsive Porous Membranes from Polystyrene-

Block-poly(N,N-Dimethylaminoethyl Methacrylate) Diblock Copolymers. *Adv. Funct. Mater.* **2009**, *19* (7), 1040–1045.

(17) Jung, A.; Filiz, V.; Rangou, S.; Buhr, K.; Merten, P.; Hahn, J.; Clodt, J.; Abetz, C.; Abetz, V. Formation of Integral Asymmetric Membranes of AB Diblock and ABC Triblock Copolymers by Phase Inversion. *Macromol. Rapid Commun.* **2013**, *34* (7), 610–615.

(18) Ju, X.-J.; Liu, Z.; Chu, L.-Y.; Xie, R.; Wang, W. Stimuli-Responsive Smart Gating Membranes. *Chem. Soc. Rev.* **2016**, *45* (3), 460–475.

(19) Yu, H.; Qiu, X.; Moreno, N.; Ma, Z.; Calo, V. M.; Nunes, S. P.; Peinemann, K. Self-Assembled Asymmetric Block Copolymer Membranes: Bridging the Gap from Ultra- to Nanofiltration. *Angew. Chem., Int. Ed.* **2015**, *54*, 13937–13941.

(20) Karunakaran, M.; Shevate, R.; Peinemann, K. V. Nanostructured Double Hydrophobic Poly(styrene-*b*-Methyl Methacrylate) Block Copolymer Membrane Manufactured via a Phase Inversion Technique. *RSC Adv.* **2016**, *6* (35), 29064–29071.

(21) Chisca, S.; Musteata, V.-E.; Sougrat, R.; Behzad, A. R.; Nunes, S. P. Artificial 3D Hierarchical and Isotropic Porous Polymeric Materials. *Sci. Adv.* **2018**, *4* (5), No. eaat0713.

(22) Aissou, K.; Mumtaz, M.; Marcasuzaa, P.; Brochon, C.; Cloutet, E.; Fleury, G.; Hadziioannou, G. Highly Ordered Nanoring Arrays Formed by Templated Si-Containing Triblock Terpolymer Thin Films. *Small* **2017**, *13* (12), 1603184.

(23) Bates, F. S. N. Etwork Phases in Block Copolymer Melts. *MRS Bull.* **2005**, *30* (JULY), 525–532.

(24) Aissou, K.; Mumtaz, M.; Fleury, G.; Portale, G.; Navarro, C.; Cloutet, E.; Brochon, C.; Ross, C. A.; Hadziioannou, G. Sub-10 Nm Features Obtained from Directed Self-Assembly of Semicrystalline Polycarbosilane-Based Block Copolymer Thin Films. *Adv. Mater.* **2015**, *27* (2), 261.

(25) Lee, S.; Cheng, L.-C.; Yager, K. G.; Mumtaz, M.; Aissou, K.; Ross, C. A. *In Situ* Study of ABC Triblock Terpolymer Self-Assembly under Solvent Vapor Annealing. *Macromolecules* **2019**, *52*, 1853.

(26) Asai, Y.; Suzuki, J.; Aoyama, Y.; Nishioka, H.; Takano, A.; Matsushita, Y. Tricontinuous Double Diamond Network Structure from Binary Blends of ABC Triblock Terpolymers. *Macromolecules* **2017**, *50* (14), 5402–5411.

(27) Aissou, K.; Mumtaz, M.; Portale, G.; Brochon, C.; Cloutet, E.; Fleury, G.; Hadziioannou, G. Templated Sub-100-nm-Thick Double-Gyroid Structure from Si-Containing Block Copolymer Thin Films. *Small* **2017**, *13* (20), 1603777.

(28) Hamley, I. W.; Koppi, K. A.; Rosedale, J. H.; Bates, F. S.; Almdal, K.; Mortensen, K. Hexagonal Mesophases between Lamellae and Cylinders in a Diblock Copolymer Melt. *Macromolecules* **1993**, *26* (22), 5959–5970.

(29) Hajduk, D. A.; Takenouchi, H.; Hillmyer, M. A.; Bates, F. S.; Vigild, M. E.; Almdal, K. Stability of the Perforated Layer (PL) Phase in Diblock Copolymer Melts. *Macromolecules* **1997**, *30* (13), 3788–3795.

(30) Zhu, L.; Huang, P.; Cheng, S.; Ge, Q.; Quirk, R.; Thomas, E.; Lotz, B.; Wittmann, J.-C.; Hsiao, B.; Yeh, F.; Liu, L. Dislocation-Controlled Perforated Layer Phase in a PEO-*b*-PS Diblock Copolymer. *Phys. Rev. Lett.* **2001**, *86* (26), 6030–6033.

(31) Ji, N.; Tang, P.; Qiu, F.; Shi, A.-C. C. Kinetic Pathways of Lamellae to Gyroid Transition in Weakly Segregated Diblock Copolymers. *Macromolecules* **2015**, *48* (23), 8681–8693.

(32) Aissou, K.; Mumtaz, M.; Bouzit, H.; Pécastaings, G.; Portale, G.; Fleury, G.; Hadziioannou, G. Bicontinuous Network Nanostructure with Tunable Thickness Formed on Asymmetric Triblock Terpolymer Thick Films. *Macromolecules* **2019**, DOI: [10.1021/acs.macromol.9b00572](https://doi.org/10.1021/acs.macromol.9b00572).

(33) Gotrik, K. W.; Hannon, A. F.; Son, J. G.; Keller, B.; Alexander-Katz, A.; Ross, C. A. Morphology Control in Block Copolymer Films Using Mixed Solvent Vapors. *ACS Nano* **2012**, *6* (9), 8052–8059.

3.F/ Lamellae stacking orientation

```

function LamellaeOrientation
% Created by Nils Demazy @ LCPO, Bordeaux
% Last update: April 30, 2020

%% INPUTS %%
T = 230; % Annealing temperature (°C)
gA = 42.1-0.072*T; % Surface tension of Block A (mJ/m²)
gB = 42.6-0.076*T; % Surface tension of Block B (mJ/m²)
gAB = 3.6-0.013*T; % Interfacial tension between A and B blocks (mJ/m²)
Chi = 0.028 + 3.9/(273+T); % Flory-Huggins parameter between A and B
N = 503; % Average Degree of polymerization
d = 1.09; % Average density between A and B (g/cm³)
Mn = 102; % Average monomer molar mass between A and B (g/mol)
L0 = 28; % Block copolymer pitch. If not known, please inform lK
lK = 1.5; % Average Kuhn length between A and B (nm). Only if L0 not known

topo = 1; % Surface topography (topo = 0 flat substrate, = 1 patterned substrate with L0 pitch wires)
h = 5; % Wires height of patterned substrate (nm) (if topo = 1)
r = 1; % Fraction of height that will be rounded: 0<r<1 (if topo = 1) (if r*h > L0/4, then r will be fixed at L0/4)

IH = 1; % Island/Hole simulation (IH = 0 not simulated, = 1 simulated)
radius = 100*L0; % Island or Hole radius (in nm) (if IH=1)
res = 2001; % Simulation Resolution (res = 101 low resolution, = 501 medium resolution, = 1001 high resolution, = 2001 ultra high resolution)

%% CHECKING %%
if ~exist('gA','var') || ~exist('gB','var') || ~exist('gAB','var')
    msgbox({'Surface Tension issue.'; 'Check your constants.'}, 'Error','error')
    return
elseif ~exist('Chi','var') || ~exist('N','var') || ~exist('d','var') || ~exist('Mn','var') || (~exist('L0','var') && ~exist('lK','var'))
    msgbox({'Block-Copolymer issue.'; 'Check your constants.'; 'If you don''t know L0, then put a value to lK'}, 'Error','error')
    return
elseif topo~=0 && topo~=1 || (topo==1 && (~exist('h','var') || ~exist('r','var')))
    msgbox({'Substrate topography issue.'; 'Use topo=0 for flat or topo=1 for patterned.'; 'Check your constants.'}, 'Error','error')
    return
elseif IH~=0 && IH~=1 || (IH==1 && ~exist('radius','var'))
    msgbox({'Island/Hole simulation issue.'; 'Use IH=0 for not simulating and IH=1 for simulating.'; 'Check your constants.'}, 'Error','error')
    return
elseif ~exist('res','var')
    msgbox({'Resolution issue.'; 'Use res=101 for Low resolution, 501 for Medium, 1001 for High, and 2001 for Ultra High'}, 'Error','error')
    return
end

%% INITIALIZATION
KbT = 1.38*10^-20*(273+T); % KbT constant at temperature T
Ncv = d*10^6/(N*Mn)*6.022*10^23; % Number of chain per volume

% Number of orientations
Nor = 13; % 13 basic orientations possible
lab =
{'\perp', '//BA', '//ABA', '//BABA', '//ABABA', '//BABABA', '//ABABABA', '//AB', '//BAB', '//ABAB', '//B
ABAB', '//ABABAB', '//BABABAB'}; % orientation labels
% If substrate patterned, 2 new orientations possible
if topo == 1
    Nor = Nor+2;
    lab{1} = '\perp\perp';
    lab{end+1} = '\perp//A';
    lab{end+1} = '\perp//B';
end
% If Island/Hole structures simulated, 4 new orientations
if IH == 1
    Nor = Nor+4;
    lab{end+1} = 'I/H//AA';
    lab{end+1} = 'I/H//BA';
    lab{end+1} = 'I/H//AB';
    lab{end+1} = 'I/H//BB';
end
end

```



```

fA = linspace(0,1,res); % A fraction in random A-B copolymer from 0 to 1
if exist('L0','var')==0 % If L0 not known
    L0 = 2*LK*(1/(2*pi^2*sqrt(6)))^(1/3)*Chi^(1/6)*N^(2/3); % Estimate L0 with LK
end
L = linspace(L0/2,3*L0,res); % Film thickness from L0/2 to 3L0

% Substrate initialization
Reso = res - 1;
X = linspace(0,L0,Reso+1);
Z = zeros(1,Reso+1);
if topo == 1 % Bump calculation
    for i = Reso/4+1:3/4*Reso
        Z(i) = h;
    end
    corner = round(r*h/(L0/Reso)); % Radius of round corner
    if corner>Reso/4
        corner = Reso/4;
        r = corner/h*L0/Reso;
    end
    % Crop right and left corners of step
    for i = 1:corner
        Z(Reso/4+i) = Z(Reso/4+i)-(h*r-sqrt((r*h)^2-((i-1)*L0/Reso-r*h)^2));
        Z(end-Reso/4-i) = Z(end-Reso/4-i)-(h*r-sqrt((r*h)^2-((i-1)*L0/Reso-r*h)^2));
    end
end
% Calculate bump surface area
S2 = 0;
for i = 1:Reso/2
    S2 = S2+sqrt((Z(i+1)-Z(i))^2+(X(i+1)-X(i))^2);
end
Zm = mean(Z); % Z mean to shift film thickness
Beta = (L0/2+S2)/(L0); % Beta != 1 for non-flat substrate

% Chain Stretching and Compressing
% x = R/Rg; R = L/n; Rmin = Req/Rg; L0 = 2*Req => x = 2*L*Rmin/n*L0
x = 0:0.01:10;
Estretch = zeros(length(x),1);
Echi = zeros(length(x),1);
for i=1:length(x)
    Estretch(i) = pi^2/12*(x(i)^2); % Stretching penalty
    Echi(i) = sqrt(Chi*N)/2./x(i); % Chi penalty
end
Echains = Estretch+Echi; % Total energy penalty
[~,ind] = min(Echains); % Find lower energy penalty
Rmin = x(ind); %Rmin = Req/Rg
Rmin2 = Rmin*mean([L0/2,S2])/(L0/2); % Rmin2 for stretched chains with bump

%% CALCULATION %%
WBv = 0;
WB = waitbar(WBv,'Simulating Orientations','Name','Please Wait');
EnergyMatrix = zeros(length(fA),length(L),Nor);
for k=1:Nor
    alpha = zeros(1,length(L)); % Initialize no Island/Hole extra interface
    Ec = zeros(1,length(L)); % Initialize chain energy cost

% Out-of-Plane
    if strcmp(lab{k}(1:2),'p')
        if strcmp(lab{k}(end),'A') % A on top of bump
            fAbottom = S2/(L0/2+S2); % Bottom composition rescaled by bump
            fAtop = 0.5; % Top composition
            for j=1:length(L)
                if 2*h<L(j) % Bump stretching height influence lower than thickness
                    Ec(j) = (2*h/L(j))*(pi^2/12*(Rmin2)^2+sqrt(Chi*N)/2*(1/Rmin2))
                        + (L(j)-2*h)/L(j)*(pi^2/12*(Rmin)^2+sqrt(Chi*N)/2*(1/Rmin));
                else % Bump stretching height influence higher than thickness
                    Ec(j) = pi^2/12*(Rmin2)^2 + sqrt(Chi*N)/2*(1/Rmin2);
                end
            end
        elseif strcmp(lab{k}(end),'B') % B on top of bump
            fAbottom = L0/2/(L0/2+S2); % Bottom composition rescaled by bump
            fAtop = 0.5; % Top composition
            for j=1:length(L)
                if 2*h<L(j) % Bump stretching height influence lower than thickness
                    Ec(j) = (2*h/L(j))*(pi^2/12*(Rmin2)^2+sqrt(Chi*N)/2*(1/Rmin2))
                        + (L(j)-2*h)/L(j)*(pi^2/12*(Rmin)^2+sqrt(Chi*N)/2*(1/Rmin));
                else % Bump stretching height influence higher than thickness
                    Ec(j) = pi^2/12*(Rmin2)^2 + sqrt(Chi*N)/2*(1/Rmin2);
                end
            end
        end
    end
end

```

```

        end
    end
    else % no bump or perpendicular to bump
        fAbottom = 0.5; % Bottom composition
        fAtop = 0.5; % Top composition
        for j=1:length(L)
            Ec(j) = pi^2/12*(Rmin)^2 + sqrt(Chi*N)/2*(1/Rmin);
        end
    end
end

% In-Plane
elseif strcmp(lab{k}(1:2), '//')
    if strcmp(lab{k}(3), 'A')
        fAbottom = 1; % Bottom composition
    else
        fAbottom = 0; % Bottom composition
    end
    if strcmp(lab{k}(end), 'A')
        fAtop = 1; % Top composition
    else
        fAtop = 0; % Top composition
    end
    n = length(lab{k})-3; % //AB gives n=1; //BAB gives n=2...
    for j=1:length(L)
        for l=1:length(Z)
            Ec(j) = Ec(j) + pi^2/12*(2*(L(j)-Z(l)+Zm)*Rmin/(n*L0))^2
                + sqrt(Chi*N)/2*(n*L0/(2*(L(j)-Z(l)+Zm)*Rmin));
        end
        Ec(j) = Ec(j)/length(Z); % Mean value over the whole pattern
    end
End

% In-Plane Island/Hole
elseif strcmp(lab{k}(1:3), 'I/H')
    fh1 = zeros(length(L),1); % area fraction of Island/Hole created
    n = zeros(length(L),1); % number of lamellae in hole
    prop = zeros(length(L)); % proportion between n and n+2 stacks
    if strcmp(lab{k}(end-1), 'A') && strcmp(lab{k}(end), 'A') % A wetting the substrate & A
on top
        fAbottom = 1; % Bottom composition
        fAtop = 1; % Top composition
        % fh1 and prop calculation
        for j=1:length(L)
            if L(j)<=L0 % Dewetting structure => not simulated
                fh1(j) = (L0-L(j))/L0;
                n(j) = NaN; % should be = 0; nothing holes, ABA islands
                prop(j)=NaN; % should be 1-L(j)/L0
            elseif L(j)<=1.5*L0 % ABA holes, ABABA islands, hole structure
                fh1(j) = (L(j)-L0)/L0;
                n(j) = 2;
                prop(j)=2-L(j)/L0;
            elseif L(j)<=2*L0 % ABA holes, ABABA islands, island structure
                fh1(j) = (2*L0-L(j))/L0;
                n(j) = 2;
                prop(j)=2-L(j)/L0;
            elseif L(j)<=2.5*L0 % ABABA holes, ABABABA islands, hole structure
                fh1(j) = (L(j)-2*L0)/L0;
                n(j) = 4;
                prop(j)=3-L(j)/L0;
            elseif L(j)<=3*L0 % ABABA holes, ABABABA islands, island structure
                fh1(j) = (3*L0-L(j))/L0;
                n(j) = 4;
                prop(j)=3-L(j)/L0;
            end
        end
    elseif strcmp(lab{k}(end-1), 'B') && strcmp(lab{k}(end), 'A') % B wetting the substrate
& A on top
        fAbottom = 0; % Bottom composition
        fAtop = 1; % Top composition
        % fh1 and prop calculation
        for j=1:length(L)
            if L(j)<=L0 %BA holes, BABA islands, hole structure
                fh1(j) = (L(j)-0.5*L0)/L0;
                n(j)=1;
                prop(j)=1.5-L(j)/L0;
            elseif L(j)<=1.5*L0 %BA holes, BABA islands, island structure
                fh1(j) = (1.5*L0-L(j))/L0;
                n(j)=1;

```

```

        prop(j)=1.5-L(j)/L0;
    elseif L(j)<=2*L0 %BABA holes, BABABA islands, hole structure
        fh1(j) = (L(j)-1.5*L0)/L0;
        n(j)=3;
        prop(j)=2.5-L(j)/L0;
    elseif L(j)<=2.5*L0 %BABA holes, BABABA islands, island structure
        fh1(j) = (2.5*L0-L(j))/L0;
        n(j)=3;
        prop(j)=2.5-L(j)/L0;
    elseif L(j)<=3*L0 %BABABA holes, BABABABA islands, hole structure
        fh1(j) = (L(j)-2.5*L0)/L0;
        n(j)=5;
        prop(j)=3.5-L(j)/L0;
    end
end
elseif strcmp(lab{k}(end-1),'A') && strcmp(lab{k}(end),'B') % A wetting the substrate
& B on top
    fAbottom = 1; % Bottom composition
    fAtop = 0; % Top composition
    % fh1 and prop calculation
    for j=1:length(L)
        if L(j)<=L0 %AB holes, ABAB islands, hole structure
            fh1(j) = (L(j)-0.5*L0)/L0;
            n(j)=1;
            prop(j)=1.5-L(j)/L0;
        elseif L(j)<=1.5*L0 %AB holes, ABAB islands, island structure
            fh1(j) = (1.5*L0-L(j))/L0;
            n(j)=1;
            prop(j)=1.5-L(j)/L0;
        elseif L(j)<=2*L0 %ABAB holes, ABABAB islands, hole structure
            fh1(j) = (L(j)-1.5*L0)/L0;
            n(j)=3;
            prop(j)=2.5-L(j)/L0;
        elseif L(j)<=2.5*L0 %ABAB holes, ABABAB islands, island structure
            fh1(j) = (2.5*L0-L(j))/L0;
            n(j)=3;
            prop(j)=2.5-L(j)/L0;
        elseif L(j)<=3*L0 %ABABAB holes, ABABABABA islands, hole structure
            fh1(j) = (L(j)-2.5*L0)/L0;
            n(j)=5;
            prop(j)=3.5-L(j)/L0;
        end
    end
elseif strcmp(lab{k}(end-1),'B') && strcmp(lab{k}(end),'B') % B wetting the substrate
& B on top
    fAbottom = 0; % Bottom composition
    fAtop = 0; % Top composition
    % fh1 and prop calculation
    for j=1:length(L)
        if L(j)<=L0 % Dewetting structure => not simulated
            fh1(j) = (L0-L(j))/L0;
            n(j) = NaN; % should be = 0; nothing holes, BAB islands
            prop(j)=NaN; % should be 1-L(j)/L0
        elseif L(j)<=1.5*L0 % BAB holes, BABAB islands, hole structure
            fh1(j) = (L(j)-L0)/L0;
            n(j) = 2;
            prop(j)=2-L(j)/L0;
        elseif L(j)<=2*L0 % BAB holes, BABAB islands, island structure
            fh1(j) = (2*L0-L(j))/L0;
            n(j) = 2;
            prop(j)=2-L(j)/L0;
        elseif L(j)<=2.5*L0 % BABAB holes, BABABAB islands, hole structure
            fh1(j) = (L(j)-2*L0)/L0;
            n(j) = 4;
            prop(j)=3-L(j)/L0;
        elseif L(j)<=3*L0 % BABAB holes, BABABAB islands, island structure
            fh1(j) = (3*L0-L(j))/L0;
            n(j) = 4;
            prop(j)=3-L(j)/L0;
        end
    end
end
end

alpha = 2*fh1*L0/radius; % alpha parameter
for j=1:length(L)
    for l=1:length(Z)
        Ec(j) = Ec(j) + prop(j)*pi^2/12*(Rmin*(1-2*(Z(l)-Zm)/(n(j)*L0)))^2
    end
end

```

```

        + (1-prop(j))*pi^2/12*(Rmin*(1-2*(Z(1)-Zm)/((n(j)+2)*L0)))^2
        + prop(j)*sqrt(Chi*N)/2*(1/(Rmin*(1-2*(Z(1)-Zm)/(n(j)*L0)))
        + (1-prop(j))*sqrt(Chi*N)/2*(1/(Rmin*(1-2*(Z(1)-Zm)/((n(j)+2)*L0))));
    end
    Ec(j) = Ec(j)/length(Z); % Mean value over the whole pattern
end
end

% Energy calculation for each orientation
Esf = gAB*abs(fAbottom*(1-fA)-(1-fAbottom)*fA); % Substrate-film interface energy
Efa = (gA*fAtop+gB*(1-fAtop)); % Film-air interface energy
Enewfa = alpha*(gA+gB)/2; % New film-air interface energy for Island/Holes
for i=1:length(fA)
    for j=1:length(L)
        EnergyMatrix(i,j,k) = (Esf(i)*Beta+Efa+Enewfa(j))/L(j)*10^9 + Ec(j)*KbT*Ncv;
    end
end
WBv = WBv+1/Nor;
waitbar(WBv,WB);
end
close(WB)

% Lower energy orientation
WB = waitbar(0,'Lowering Energy','Name','Please Wait');
I = zeros(res,res);
for i=1:res
    for j=1:res
        [~,I(i,j)] = min(squeeze(EnergyMatrix(i,j,:)));
    end

    waitbar(i/res,WB);
end
close(WB)

% Create a contour matrix for each orientation
cont = zeros(res,res,Nor);
for k=1:length(lab)
    for i=1:res
        for j=1:res
            if I(i,j)==k
                cont(i,j,k) = 1;
            else
                cont(i,j,k) = 0;
            end
        end
    end
end

%% PLOTS %%
% Bump Profile
figure
plot(X,Z,'LineWidth',2,'Color','red')
daspect([1 1 1])
xlim([X(1),X(end)])
ylim([min(Z),max(Z)+1])
xlabel('x (nm)')
ylabel('z (nm)')
title('Bump profile')

% Orientations diagram
figure
hold on
for k=1:length(lab)
    C=cont(:, :, k);
    if ~isempty(find(C==1,1))
        props = regionprops(logical(C), 'Centroid');
        contour(fA, L/L0, C', [0.5,0.5], 'LineColor','black','LineWidth',1);
        % Add name of each zone
        for i=1:length(props)
            text(fA(floor(props(i).Centroid(2))),L(floor(props(i).Centroid(1))/L0,
            lab{k}, 'HorizontalAlignment','center')
        end
    end
end
box('on')
xlim([0,1]);

```

```
ylim([L(1),L(end)]/L0);  
xlabel('f_{A}');  
ylabel('L/L_0');  
title('Lamellae forming Block-Copolymer Orientations')  
end
```

Chapter III/Figure 53 and Chapter IV/Figure 83 have been plotted using this function, with “*topo = 0*” and “*topo = 1*”, respectively.

3.G/ NanoScope AFM image viewer and processing

AFM images captured with NanoScope 9.4 software from Bruker can be directly analyzed with the embedded NanoScope Analysis software. However, this software has only limited tools for BCP self-assembly image analysis. Thus, a widely used alternative is the free software WSXM which proposes more advanced tools [12]. Unfortunately, this software seemed too complex and slow for routine BCP image analysis.

Within this Ph.D., a Matlab program has been developed to open, process and analyze NanoScope AFM image with tools specifically designed for BCP self-assembly. The software is divided in three parts (*Figure 126*). The top one has a loading button to import a NanoScope “.spm” image within the software and a list to choose an image channel (height, amplitude, phase, etc.). The raw data reading has been possible thanks to the “Open Nanoscope 6 AFM images” code developed on Matlab by Jaco de Groot, which were adapted for Nanoscope 9.4. The middle part consists in four different tabs with analyzing tools in each of them, which will be detailed in the following section. The bottom part is the “Export” panel, including tools for exporting a treated image and raw data.

3.G.i/ Tab 1: “Raw Image”

The first tab, correspond to the raw data without any modification (*Figure 126*). It also gives the roughness, calculated after flattening the image for removing any artifact due to the scanner tip (i.e. the same image observed during capturing which natively include this flattening). A “Restore Image” button allow to return to the initial state after having performed analysis with the other tabs.

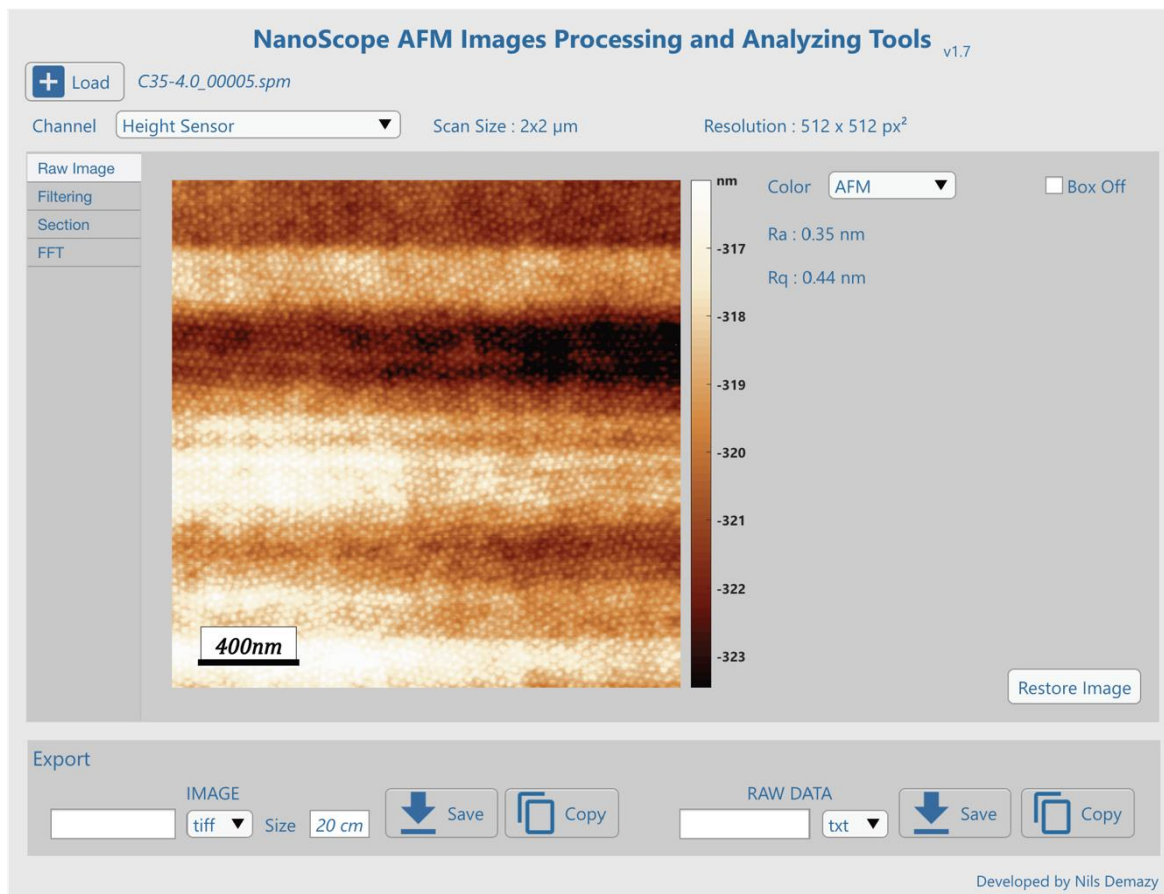


Figure 126. NanoScope AFM Images Processing and Analyzing Tools window showing the raw height AFM image of an PS-b-PMMA thin film forming out-of-plane cylinders.

3.G.ii/ Tab 2: “Filtering”

This tab is mandatory before performing any analysis of the image (Figure 127). It includes several filters to flatten the image, and remove noise:

- a X and Y direction flatten with offset, linear or quadratic functions. Two parameters (“High Aspect-Ratio and “Island/Hole Structure”) have been implemented to modify flattening calculations for overcoming artifact creation;
- a smoothing which applies a blur filter to the image;
- a remove background which subtracts to the image the same image with a high blur filter. It allows to programmatically remove non-flat background for better self-assembly structure analysis.

Also, several observation tools are available to embellish the image before exportation.

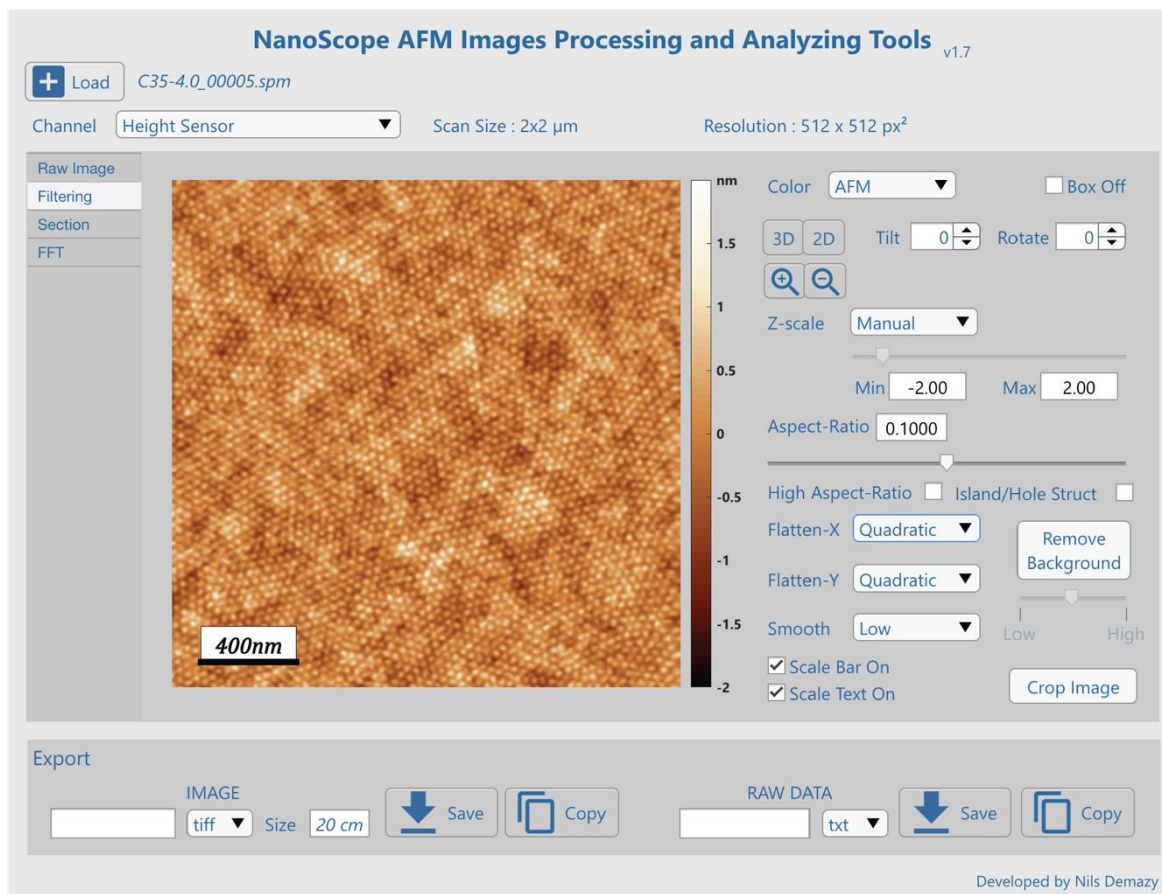


Figure 127. NanoScope AFM Images Processing and Analyzing Tools window showing the filtered height AFM image of the PS-*b*-PMMA cylinders.

3.G.iii/ Tab 3: “Section”

This tab is made to measure a profile section within the image (*Figure 128*). It is possible to observe horizontal or vertical sections of the whole image, or a manual profile along a chosen path. It also presents a step measurement tool which allows a very precise thickness measurement on a scratched thin film.

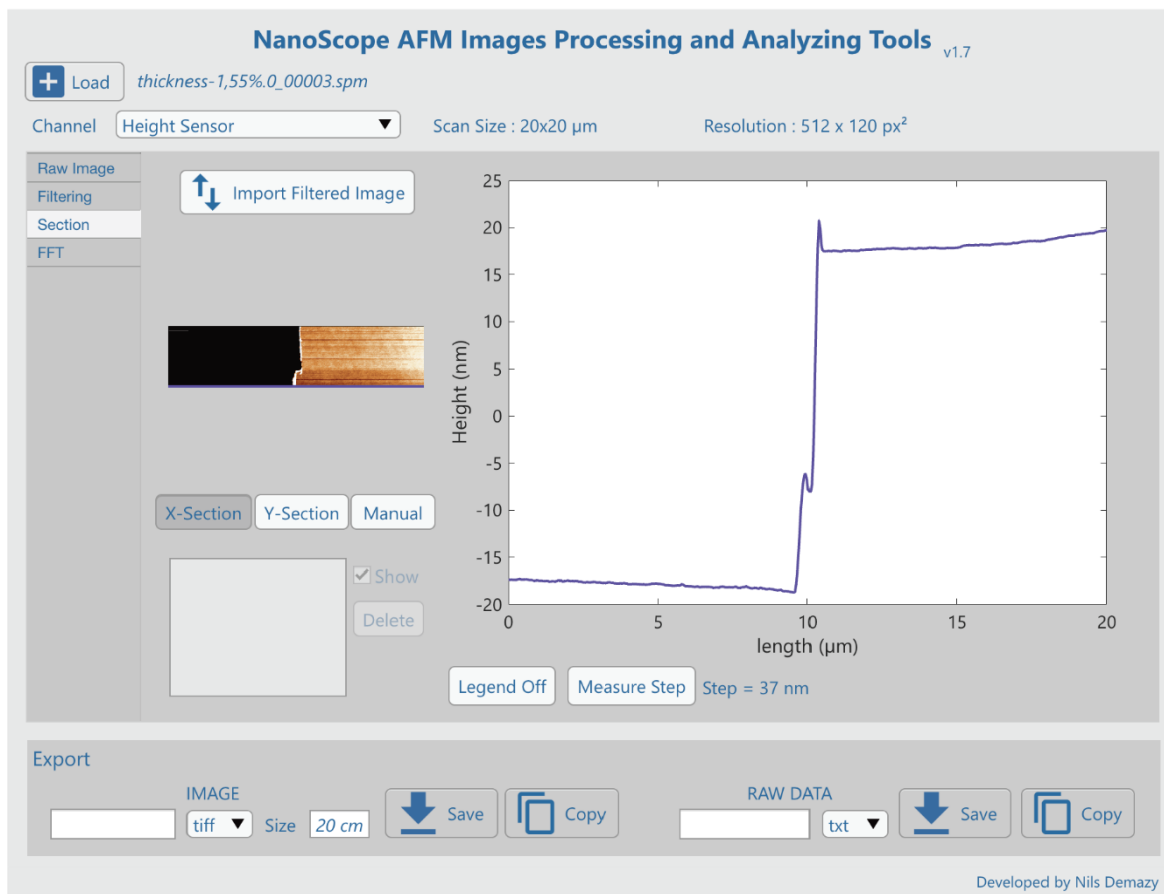


Figure 128. NanoScope AFM Images Processing and Analyzing Tools window showing the X-section of a scratched PS-b-PMMA thin film AFM image leading to a 37 nm step.

3.G.iv/ Tab 4: “FFT”

The last tab is dedicated to the Fast-Fourier Transform (FFT) (Figure 129). It gives two plots, the first one is the image FFT with the possibility to modify normalization and accentuate peak positions, and the second one is the Power Spectral Density (PSD), i.e. the radial average of the FFT with the possibility to measure the structure periodicity.

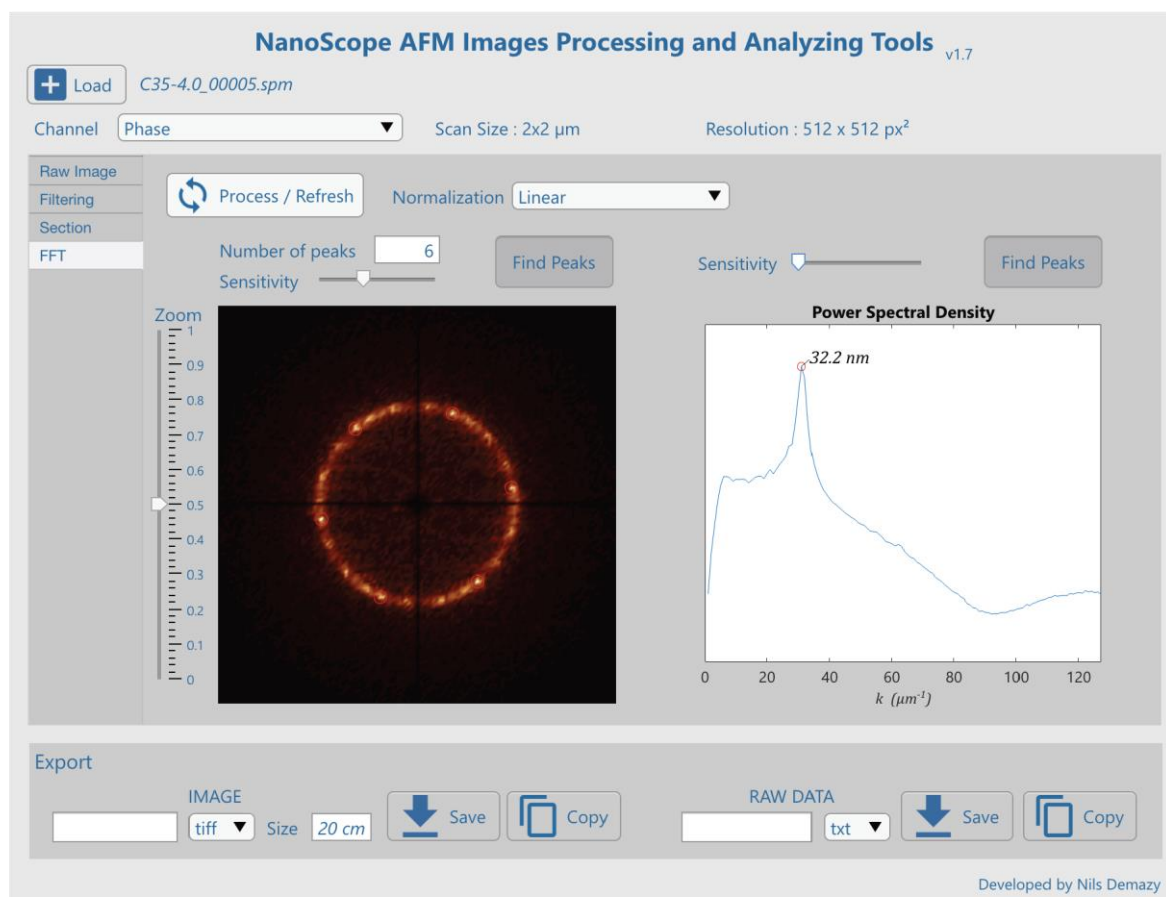


Figure 129. NanoScope AFM Images Processing and Analyzing Tools window showing the FFT and PSD of the PS-*b*-PMMA cylinders phase AFM image.

4/ 2D-structures large SEM images

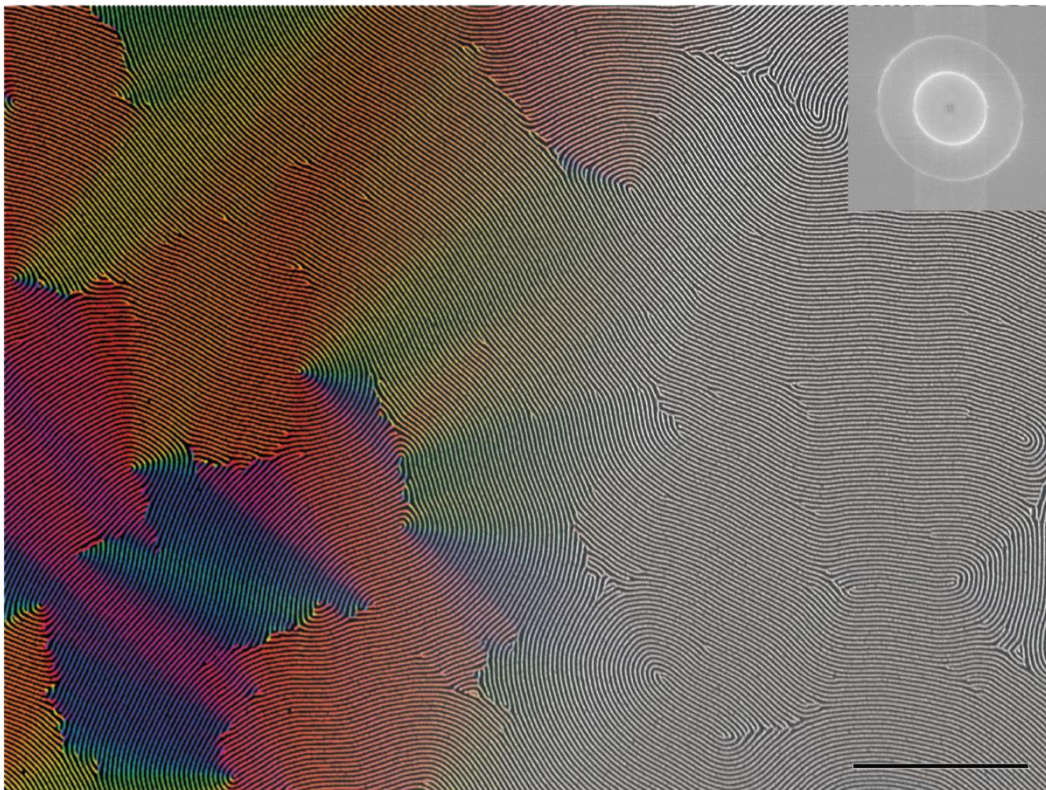


Figure 130. SEM image of L_{24} colorized with orientation. Top right inset is the FFT. Scale bar: 1 μm .

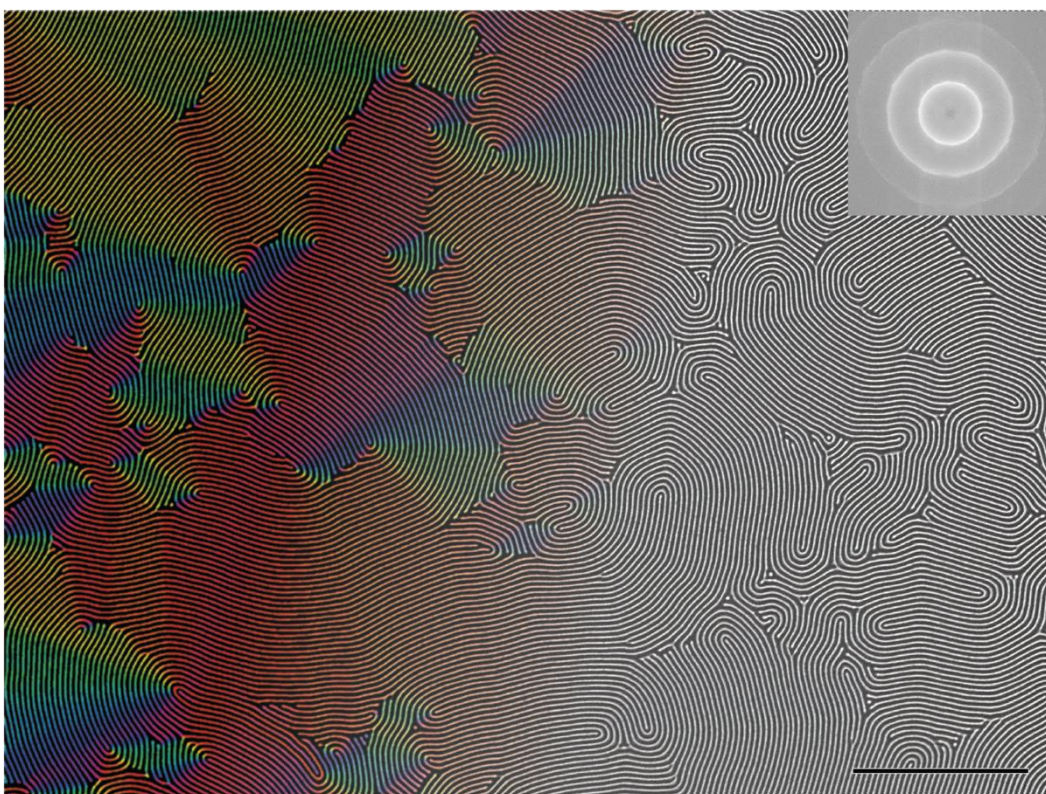


Figure 131. SEM image of L_{28} colorized with orientation. Top right inset is the FFT. Scale bar: 1 μm .

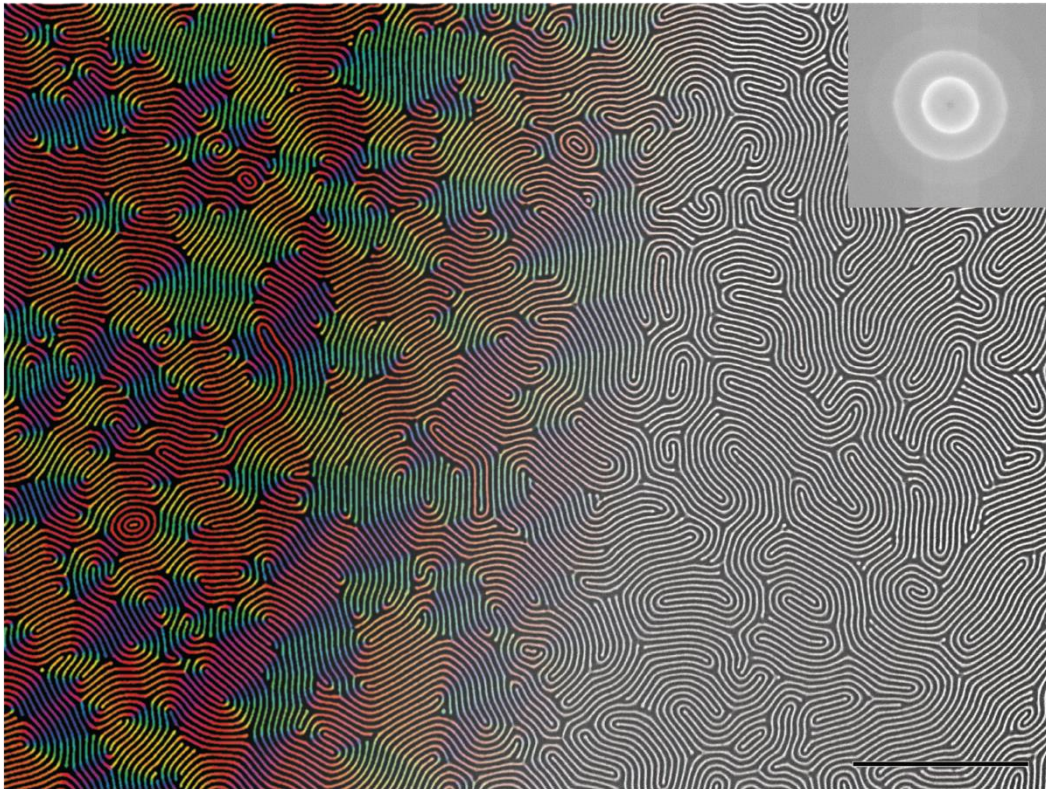


Figure 132. SEM image of L_{32} colored with orientation. Top right inset is the FFT. Scale bar: 1 μm .

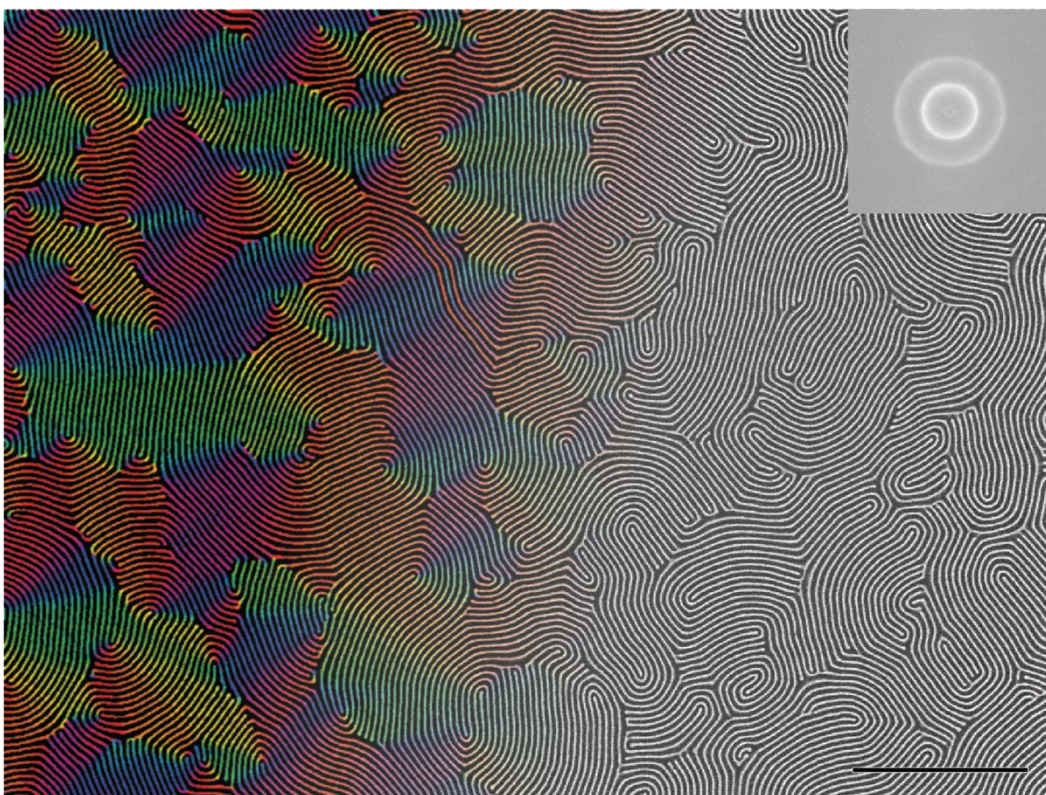


Figure 133. SEM image of L_{32-t} colored with orientation. Top right inset is the FFT. Scale bar: 1 μm .

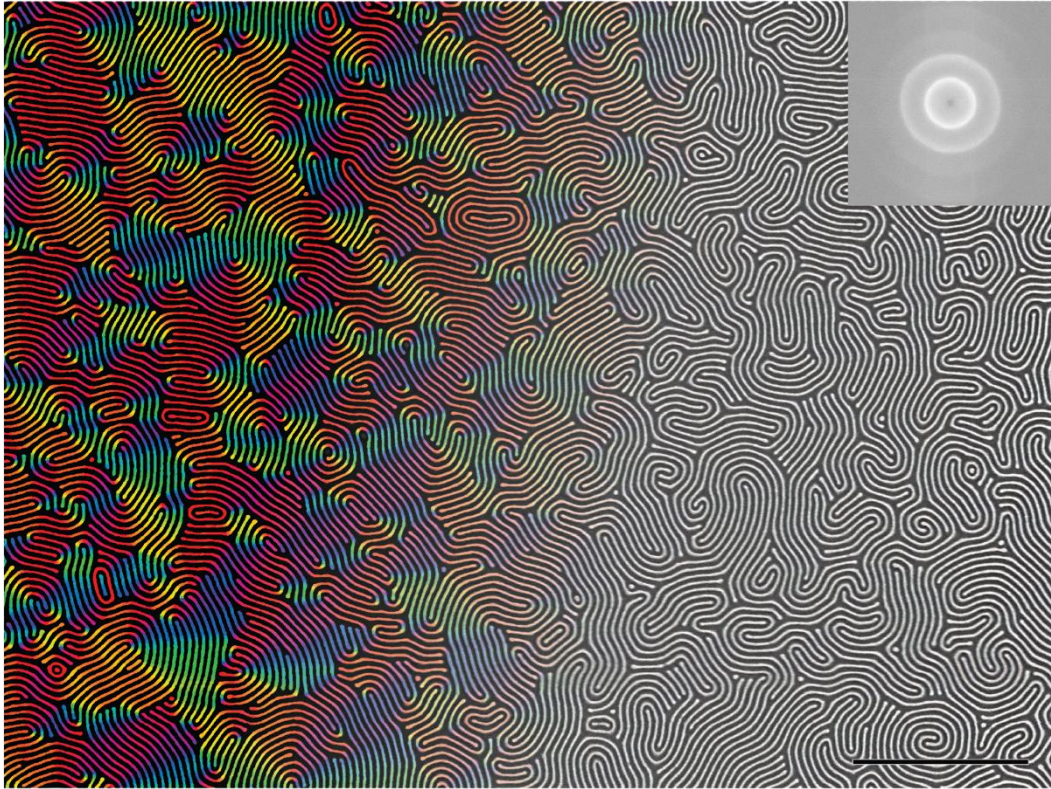


Figure 134. SEM image of L_{37} colorized with orientation. Top right inset is the FFT. Scale bar: $1\ \mu\text{m}$.

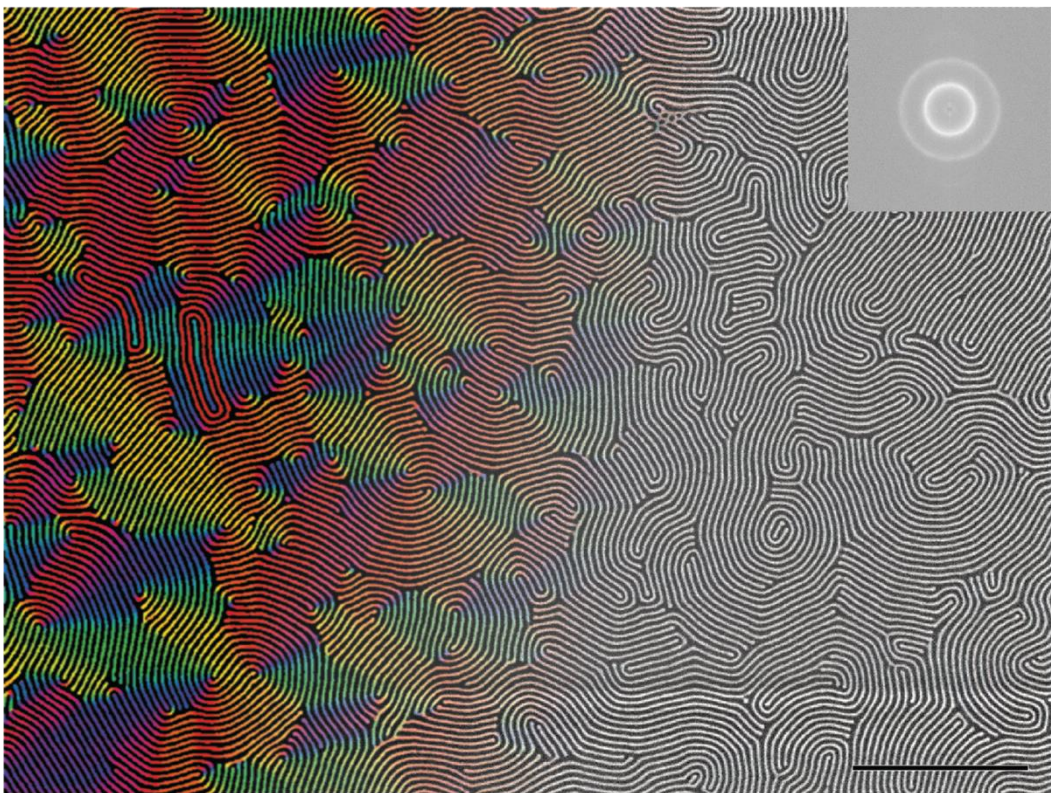


Figure 135. SEM image of L_{37-t} colorized with orientation. Top right inset is the FFT. Scale bar: $1\ \mu\text{m}$.

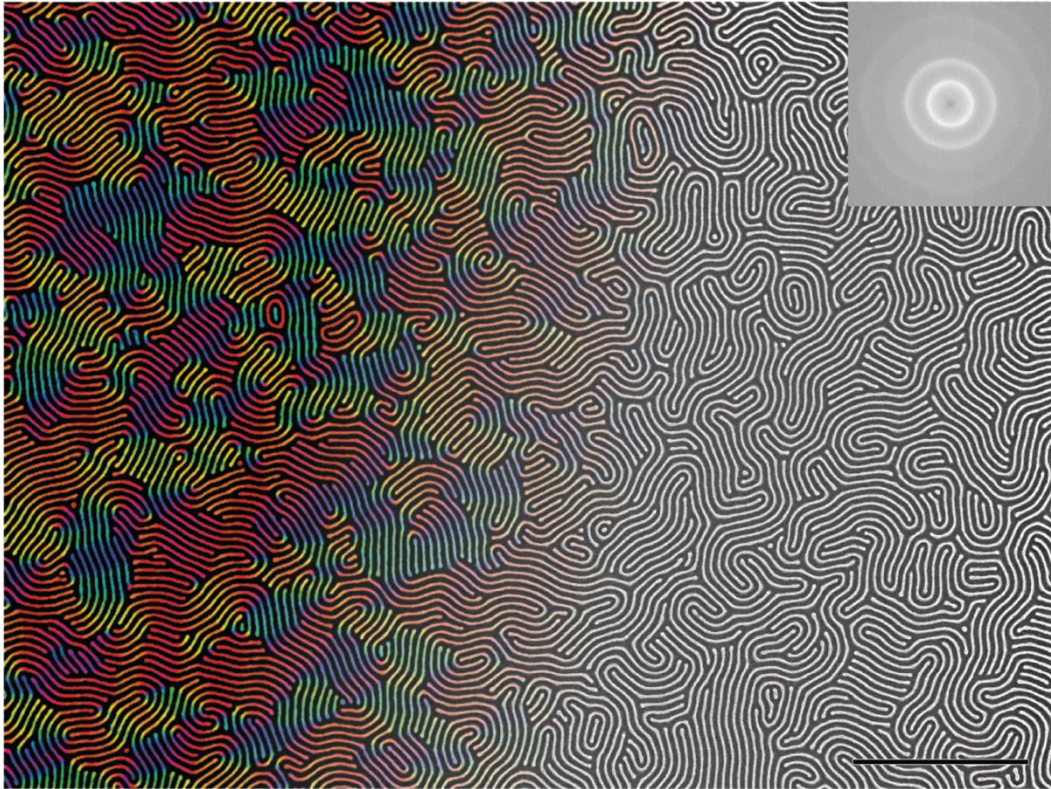


Figure 136. SEM image of L_{42} colored with orientation. Top right inset is the FFT. Scale bar: 1 μm .

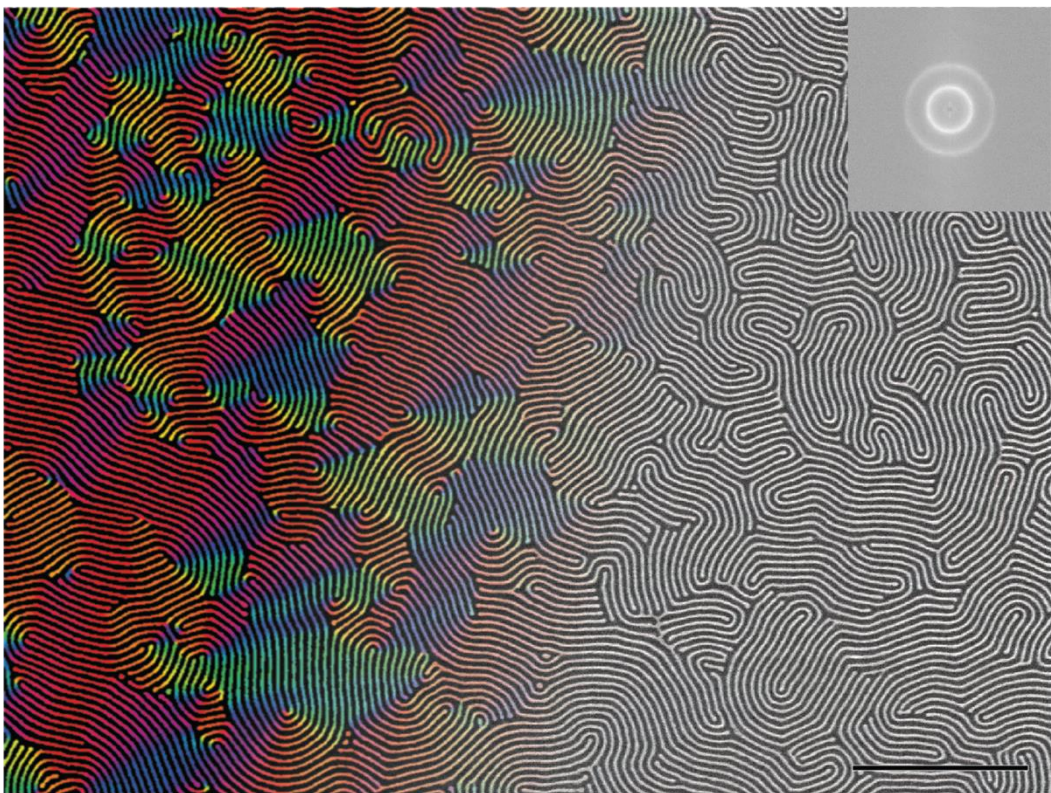


Figure 137. SEM image of L_{42-t} colored with orientation. Top right inset is the FFT. Scale bar: 1 μm .

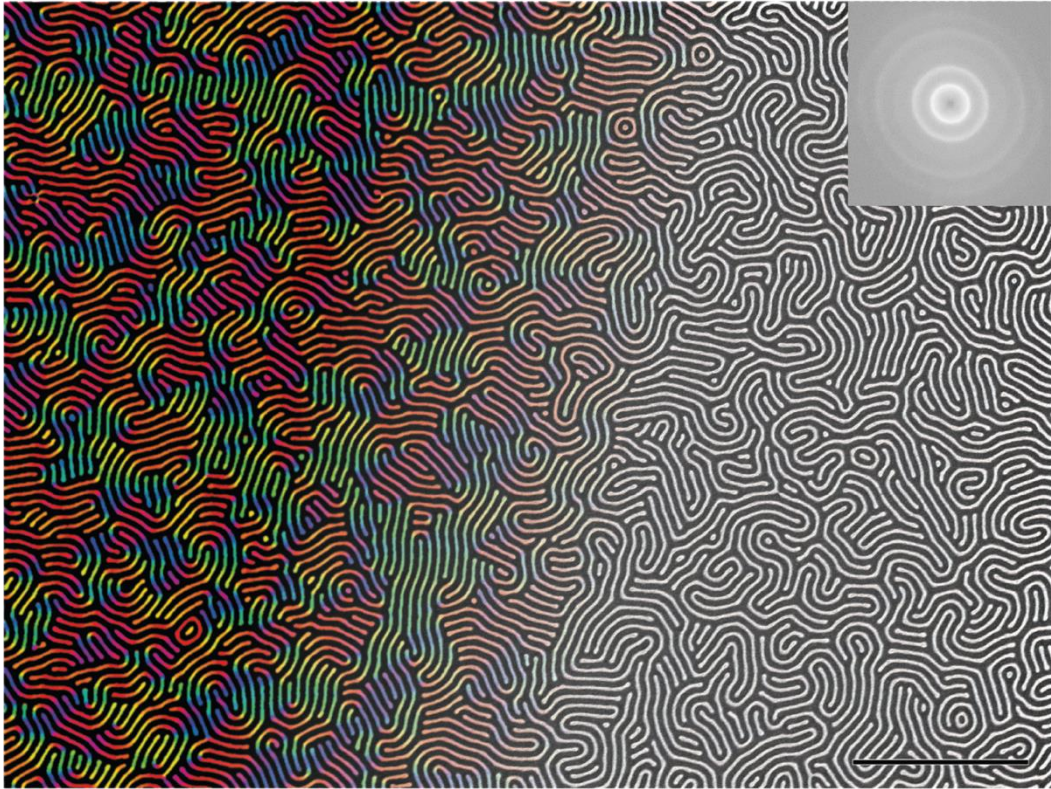


Figure 138. SEM image of L_{48} colored with orientation. Top right inset is the FFT. Scale bar: $1 \mu\text{m}$.

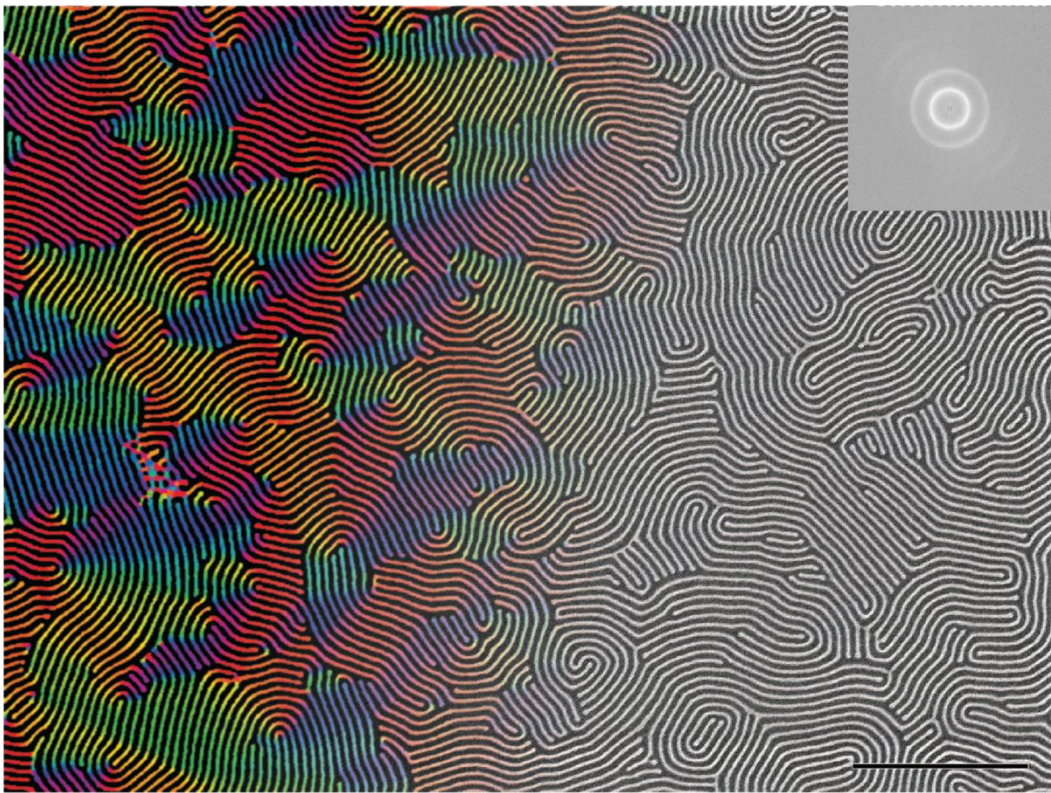


Figure 139. SEM image of L_{48-t} colored with orientation. Top right inset is the FFT. Scale bar: $1 \mu\text{m}$.

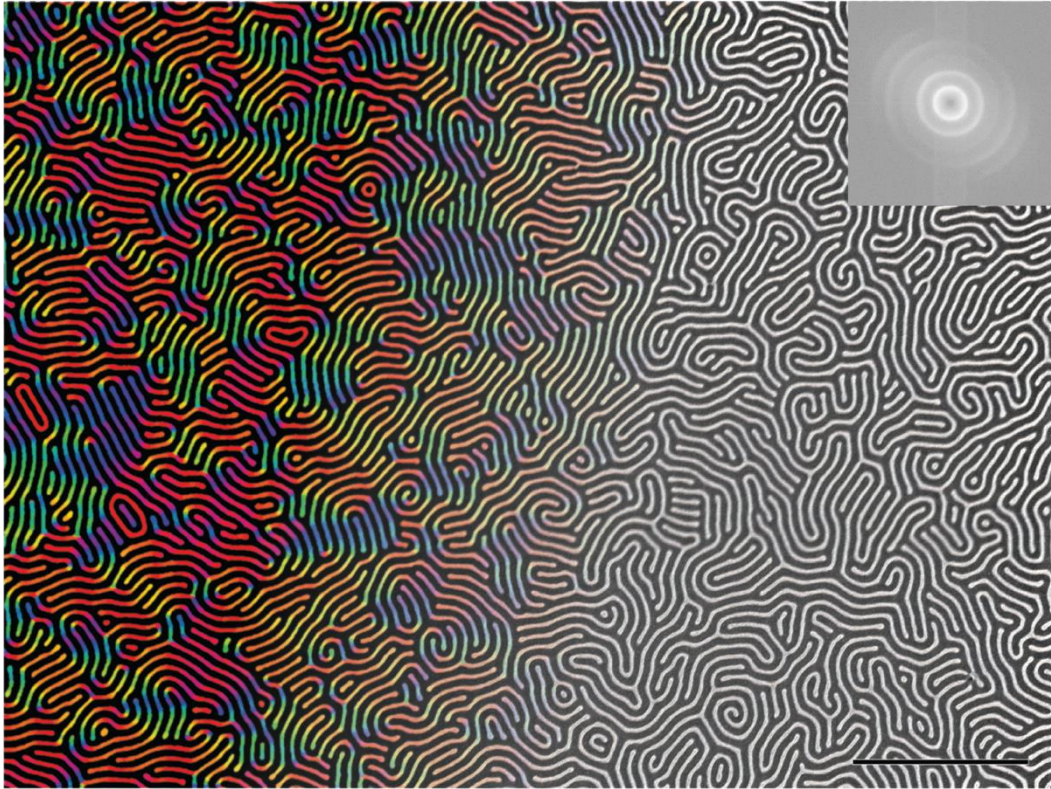


Figure 140. SEM image of L_{56} colorized with orientation. Top right inset is the FFT. Scale bar: $1\ \mu\text{m}$.

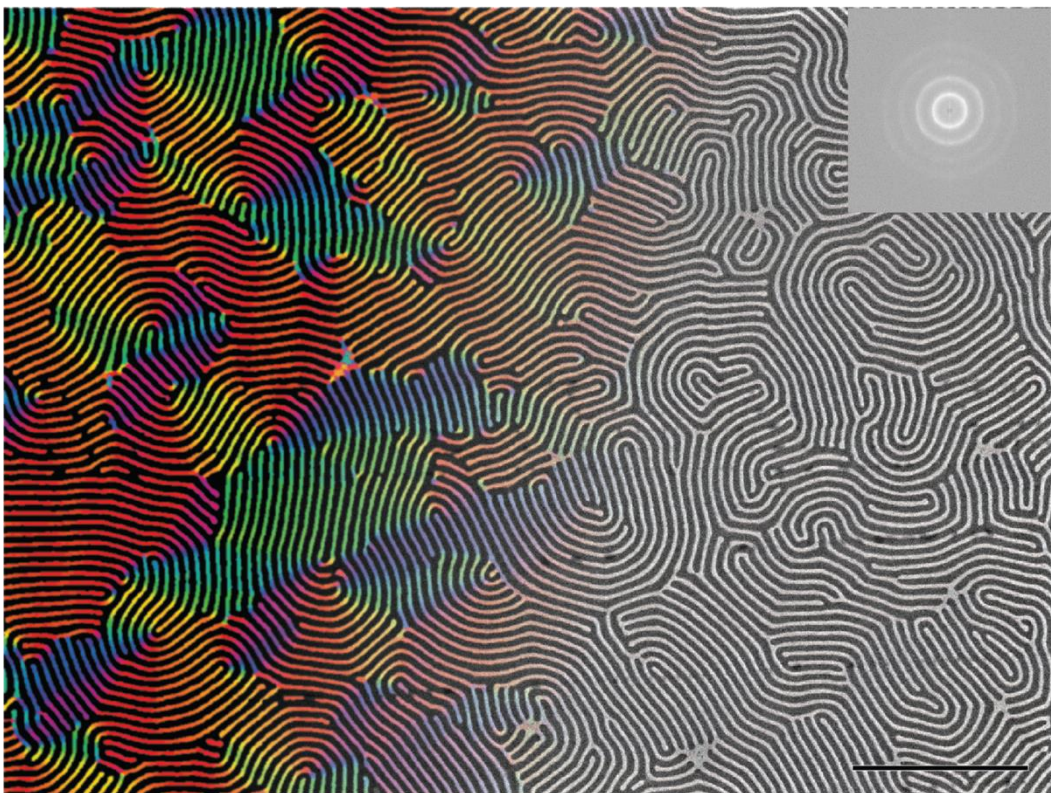


Figure 141. SEM image of L_{56-t} colorized with orientation. Top right inset is the FFT. Scale bar: $1\ \mu\text{m}$.

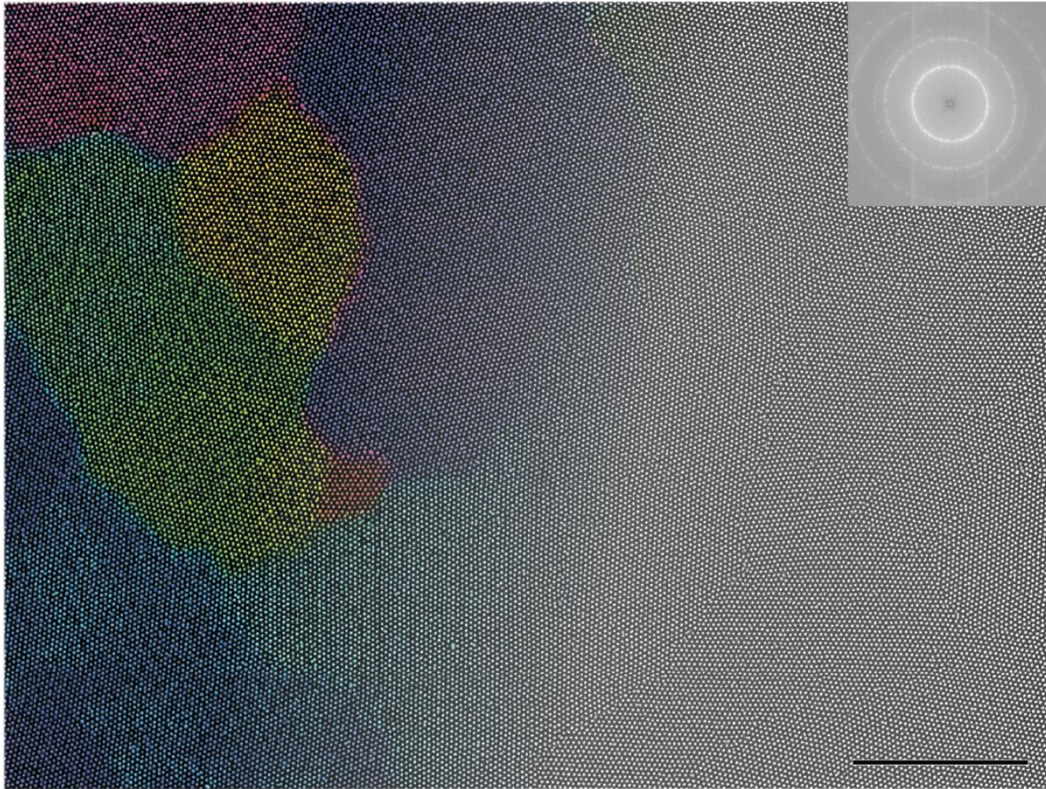


Figure 142. SEM image of D_{28} colored with orientation. Top right inset is the FFT. Scale bar: 1 μm .

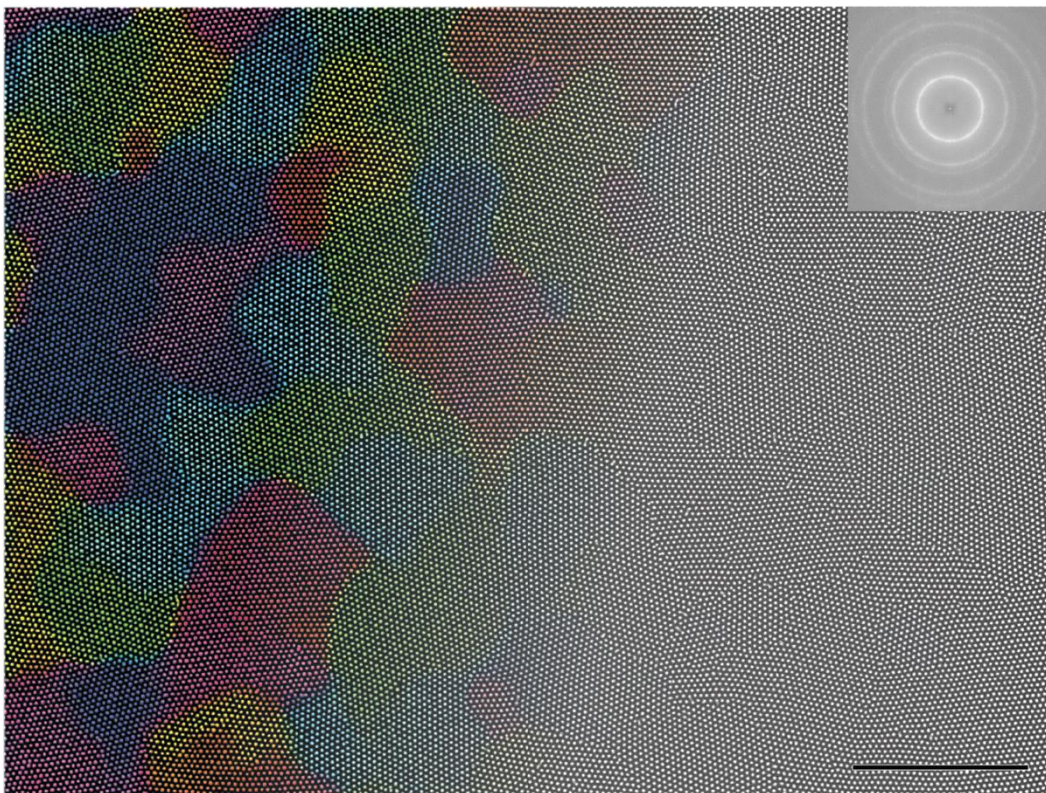


Figure 143. SEM image of D_{32} colored with orientation. Top right inset is the FFT. Scale bar: 1 μm .

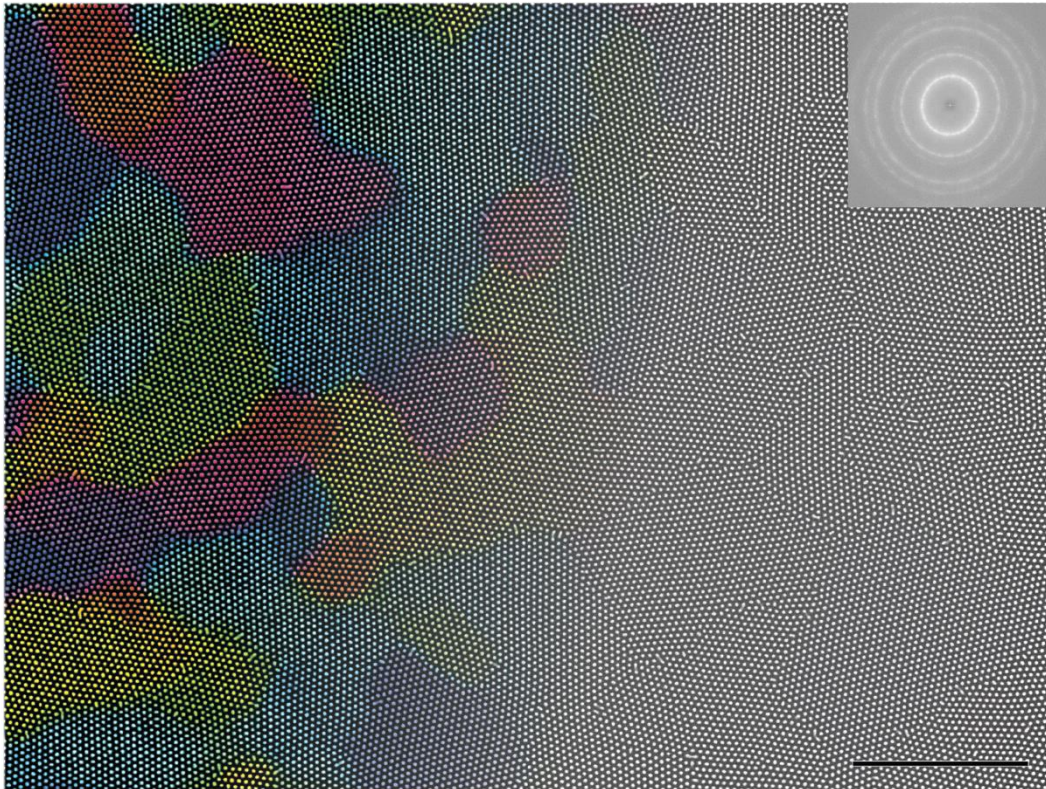


Figure 144. SEM image of D_{37} colored with orientation. Top right inset is the FFT. Scale bar: 1 μm .

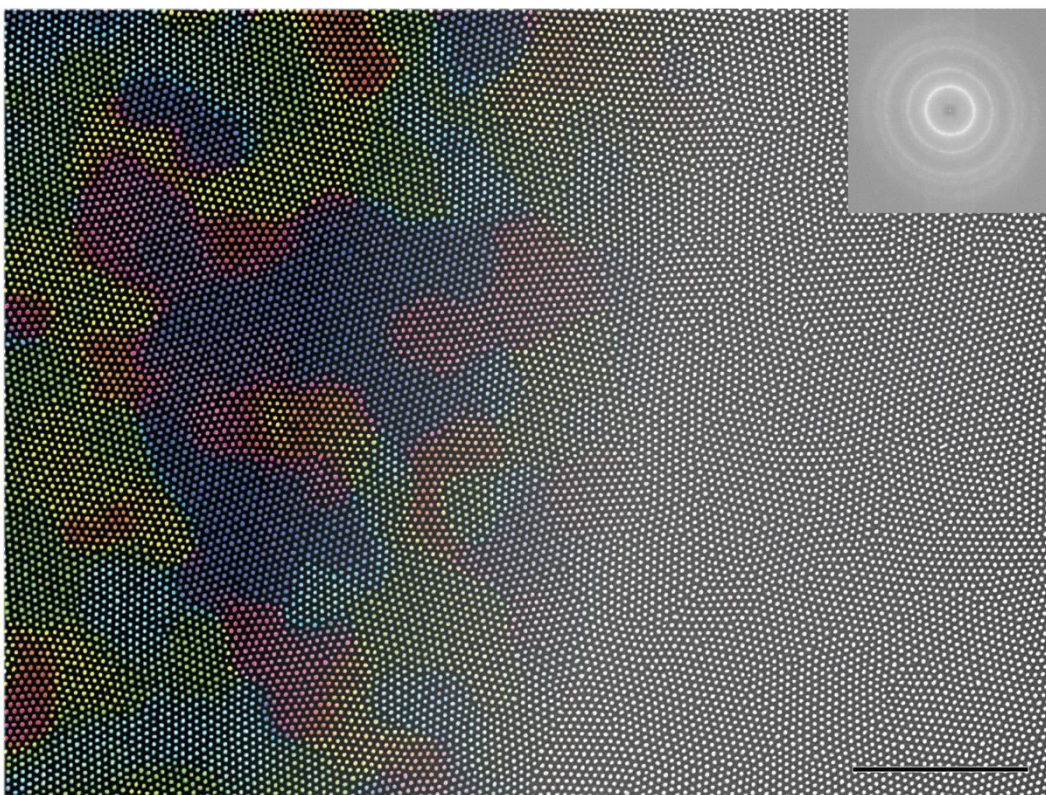


Figure 145. SEM image of D_{42} colored with orientation. Top right inset is the FFT. Scale bar: 1 μm .

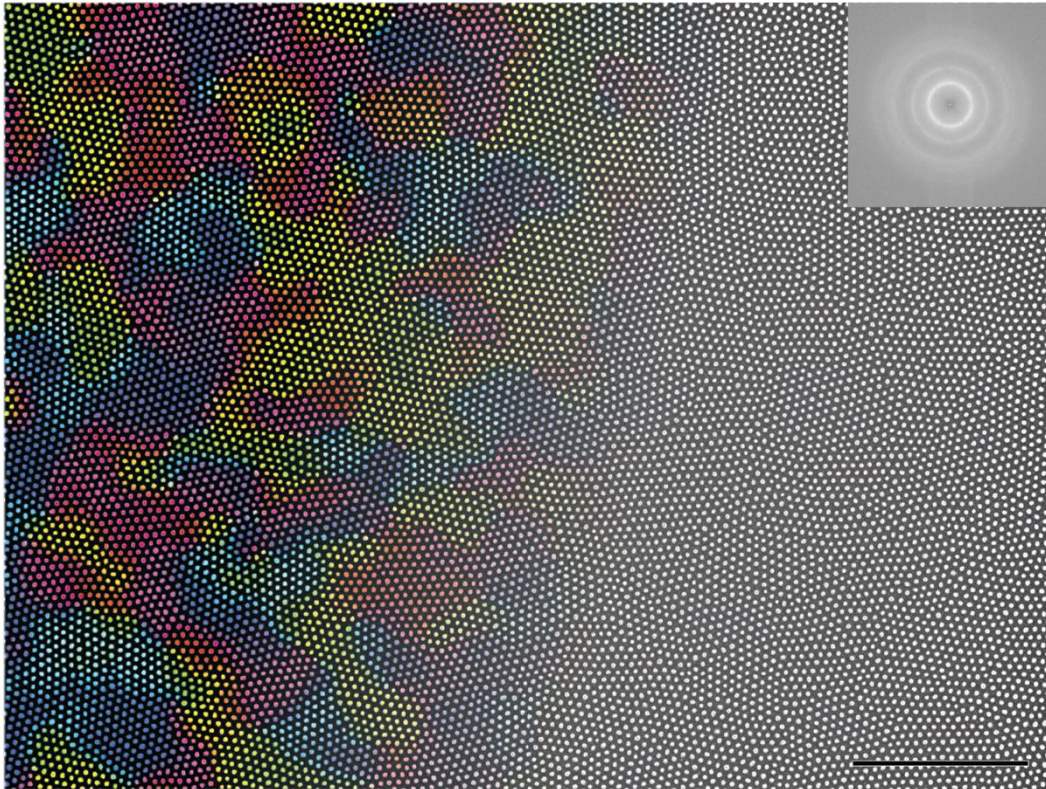


Figure 146. SEM image of D_{48} colorized with orientation. Top right inset is the FFT. Scale bar: 1 μm .

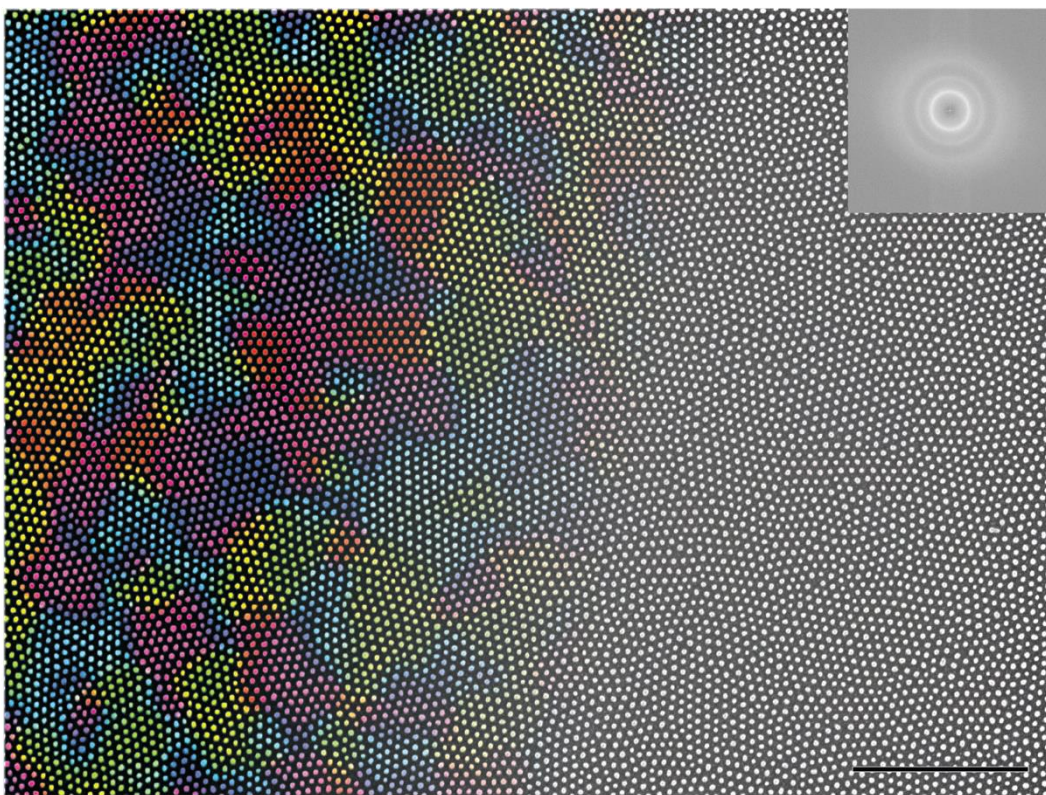


Figure 147. SEM image of D_{56} colorized with orientation. Top right inset is the FFT. Scale bar: 1 μm .

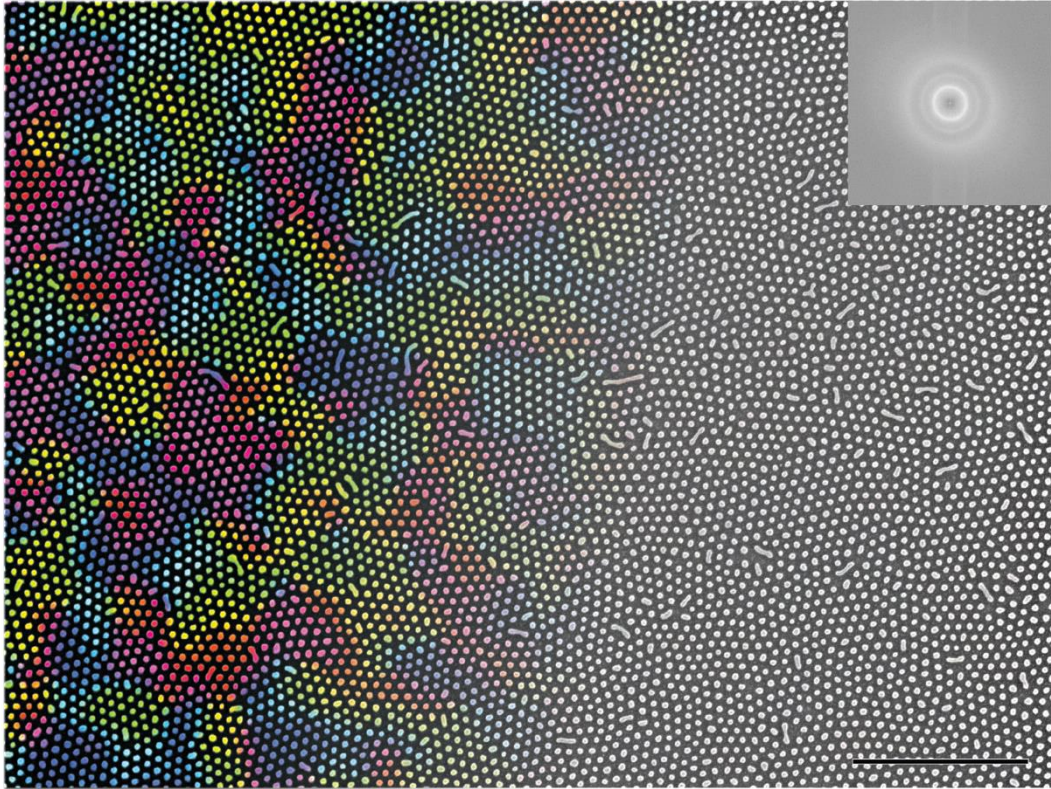


Figure 148. SEM image of D_{64} colorized with orientation. Top right inset is the FFT. Scale bar: 1 μm .

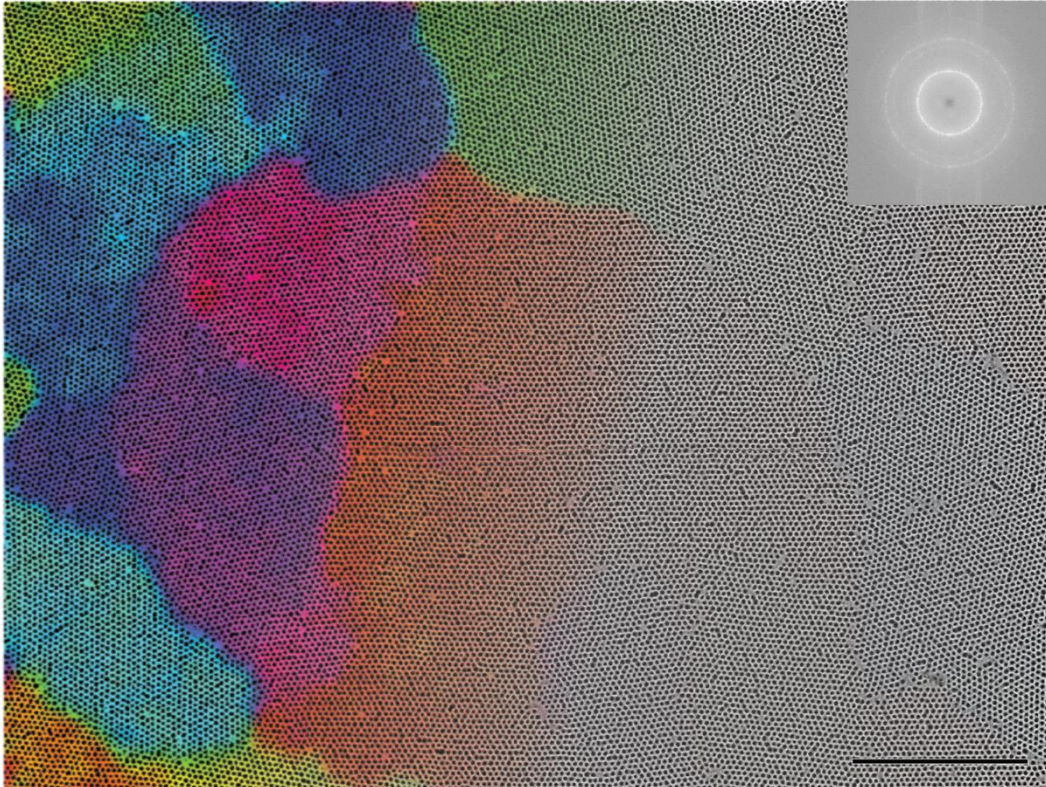


Figure 149. SEM image of H₃₂ colorized with orientation. Top right inset is the FFT. Scale bar: 1 μ m.

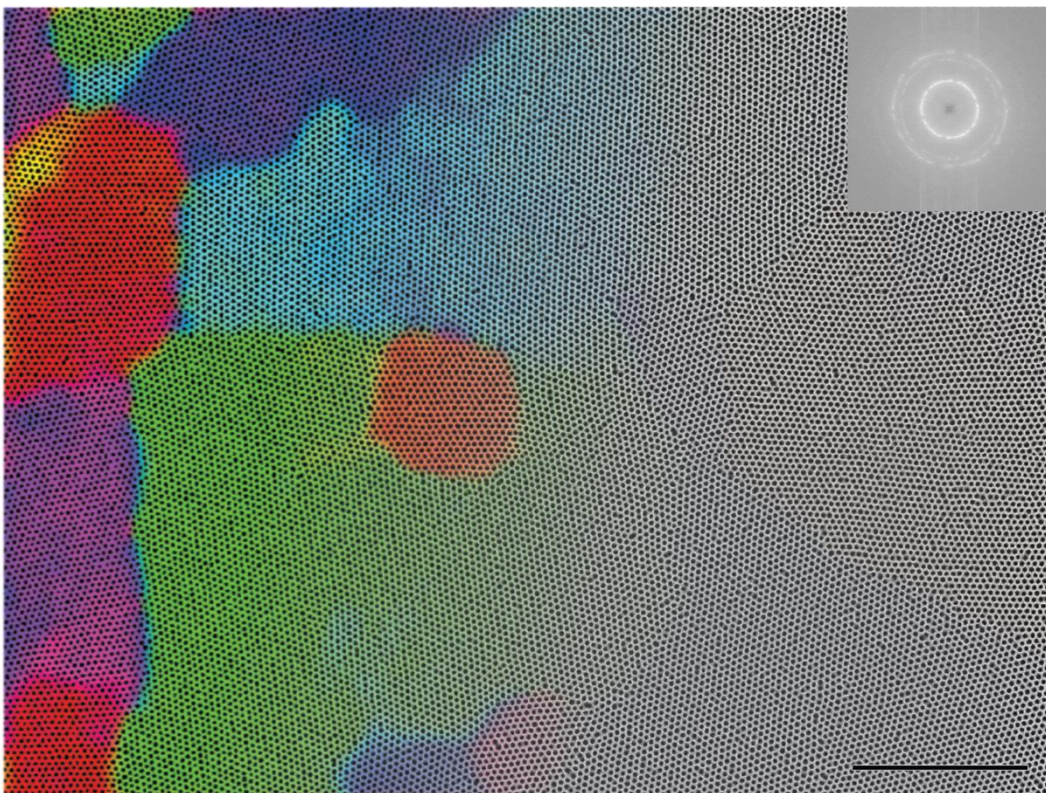


Figure 150. SEM image of H₃₇ colorized with orientation. Top right inset is the FFT. Scale bar: 1 μ m.

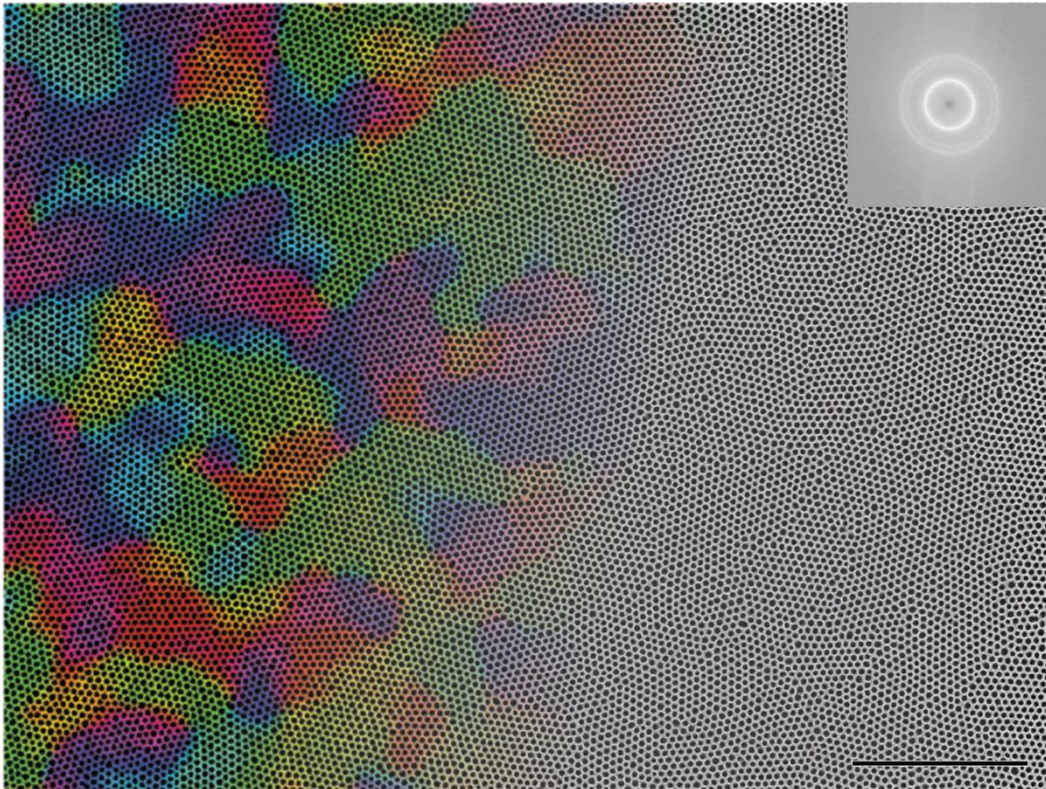


Figure 151. SEM image of H_{42} colored with orientation. Top right inset is the FFT. Scale bar: 1 μm .

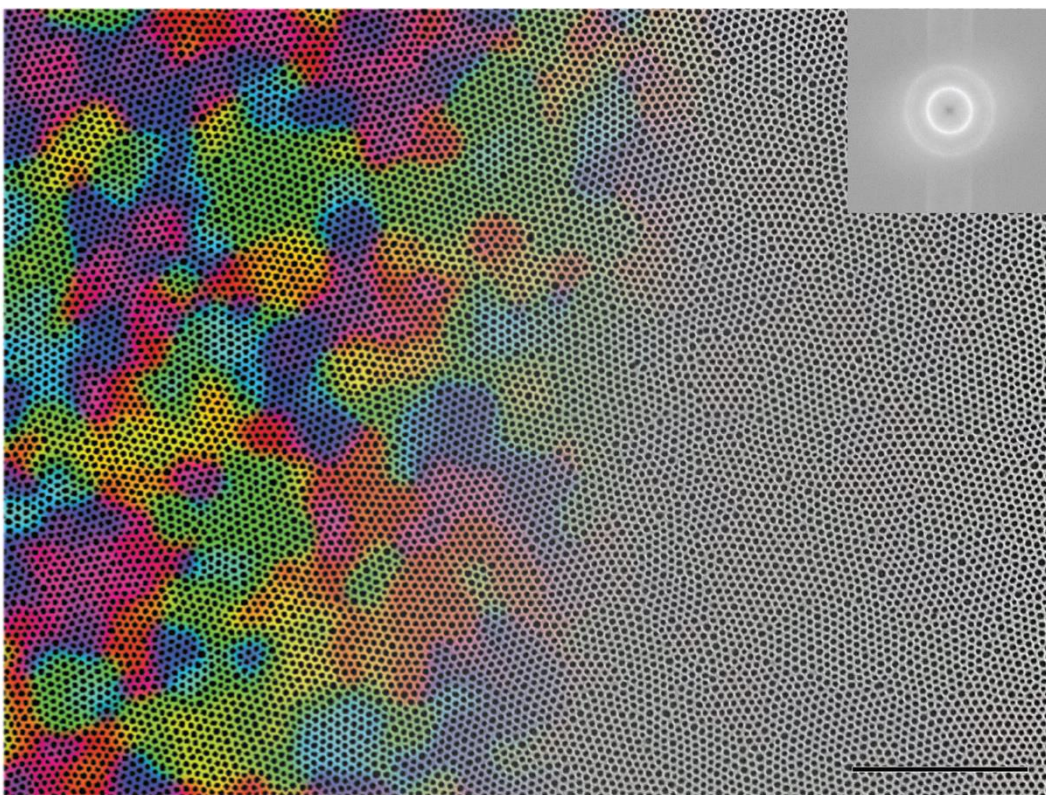


Figure 152. SEM image of H_{48} colored with orientation. Top right inset is the FFT. Scale bar: 1 μm .

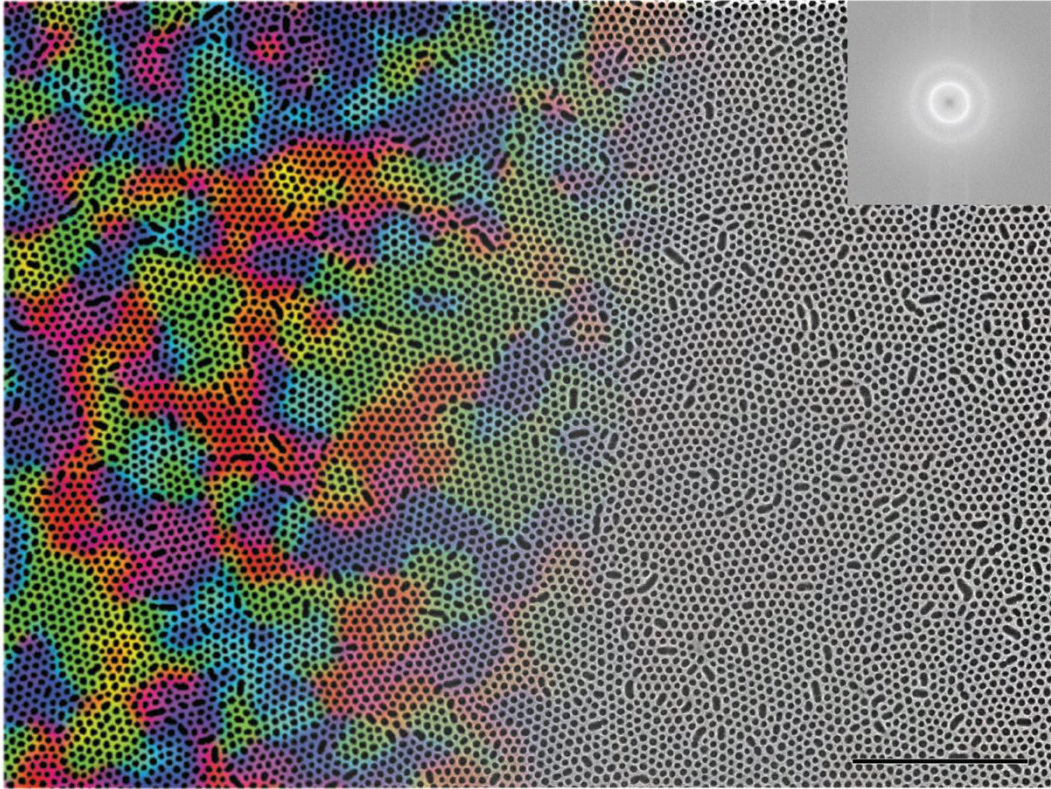


Figure 153. SEM image of H_{56} colored with orientation. Top right inset is the FFT. Scale bar: 1 μm .

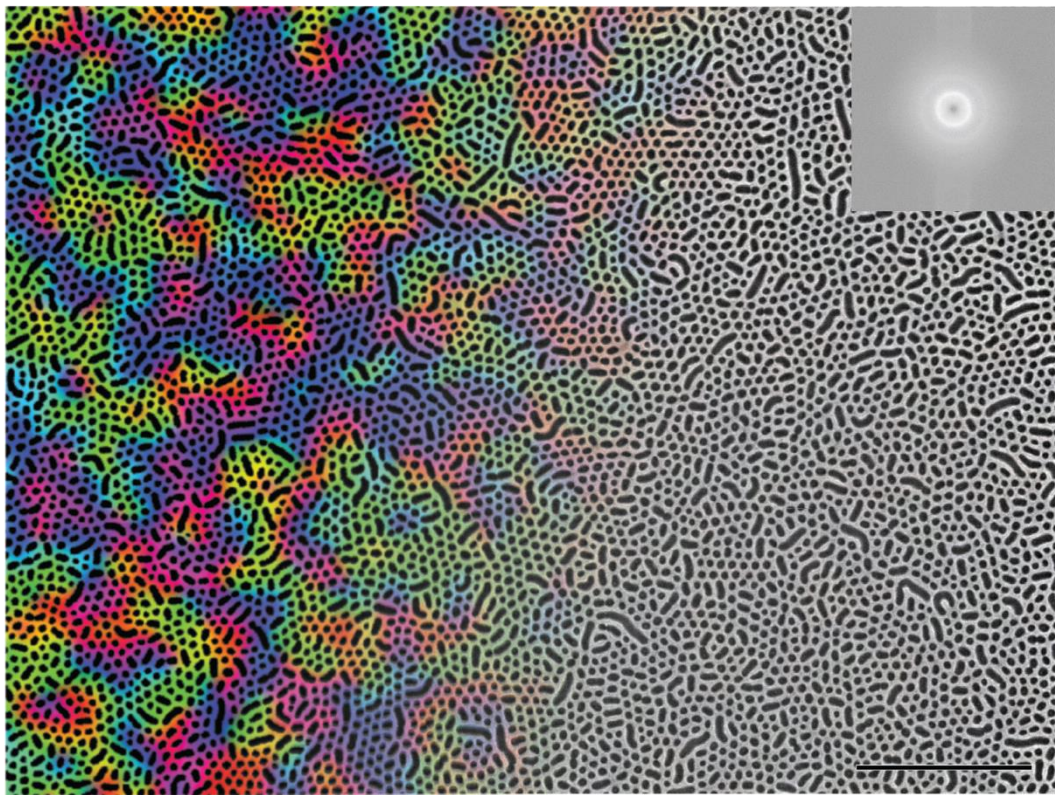


Figure 154. SEM image of H_{64} colored with orientation. Top right inset is the FFT. Scale bar: 1 μm .

5/ References

- [1] K. Sparnacci *et al.*, “High temperature surface neutralization process with random copolymers for block copolymer self-assembly,” *Polym. Int.*, vol. 66, no. 3, pp. 459–467, 2017, doi: 10.1002/pi.5285.
- [2] K. Sparnacci *et al.*, “Ultrathin Random Copolymer-Grafted Layers for Block Copolymer Self-Assembly,” *ACS Appl. Mater. Interfaces*, vol. 7, no. 20, pp. 10944–10951, 2015, doi: 10.1021/acsami.5b02201.
- [3] J. N. Murphy, K. D. Harris, and J. M. Buriak, “Automated defect and correlation length analysis of block copolymer thin film nanopatterns,” *PLoS One*, vol. 10, no. 7, pp. 1–32, 2015, doi: 10.1371/journal.pone.0133088.
- [4] M. W. Matsen and F. S. Bates, “Unifying weak- and strong-segregation block copolymer theories,” *Macromolecules*, vol. 29, no. 4, pp. 1091–1098, 1996, doi: 10.1021/ma951138i.
- [5] M. W. Matsen and F. S. Bates, “Conformationally asymmetric block copolymers,” *J. Polym. Sci. Part B Polym. Phys.*, vol. 35, no. 6, pp. 945–952, Apr. 1997, doi: 10.1002/(SICI)1099-0488(19970430)35:6<945::AID-POLB9>3.0.CO;2-G.
- [6] C. Sinturel, F. S. Bates, and M. A. Hillmyer, “High χ -Low N Block Polymers: How Far Can We Go?,” *ACS Macro Lett.*, vol. 4, no. 9, pp. 1044–1050, 2015, doi: 10.1021/acsmacrolett.5b00472.
- [7] C. Cummins *et al.*, “Rapid Self-Assembly and Sequential Infiltration Synthesis of High χ Fluorine-Containing Block Copolymers,” *Macromolecules*, vol. 53, no. 15, pp. 6246–6254, Aug. 2020, doi: 10.1021/acs.macromol.0c01148.
- [8] S. Park, Y. Kim, W. Lee, S. M. Hur, and D. Y. Ryu, “Gyroid Structures in Solvent Annealed PS-b-PMMA Films: Controlled Orientation by Substrate Interactions,” *Macromolecules*, vol. 50, no. 13, pp. 5033–5041, 2017, doi: 10.1021/acs.macromol.7b00898.
- [9] S. B. G. Blanquer *et al.*, “Surface curvature in triply-periodic minimal surface architectures as a distinct design parameter in preparing advanced tissue engineering scaffolds,” *Biofabrication*, vol. 9, no. 2, 2017, doi: 10.1088/1758-5090/aa6553.
- [10] L. Han and S. Che, “An Overview of Materials with Triply Periodic Minimal Surfaces and Related Geometry: From Biological Structures to Self-Assembled Systems,” *Adv. Mater.*, vol. 30, no. 17, pp. 1–22, 2018, doi: 10.1002/adma.201705708.
- [11] K. Aissou, M. Mumtaz, N. Demazy, G. Pécastaings, G. Fleury, and G. Hadziioannou, “Periodic Bicontinuous Structures Formed on the Top Surface of Asymmetric Triblock Terpolymer Thick Films,” *ACS Macro Lett.*, vol. 8, no. 8, pp. 923–930, 2019, doi: 10.1021/acsmacrolett.9b00403.
- [12] I. Horcas, R. Fernández, J. M. Gómez-Rodríguez, J. Colchero, J. Gómez-Herrero, and A. M. Baro, “WSXM: A software for scanning probe microscopy and a tool for nanotechnology,” *Rev. Sci. Instrum.*, vol. 78, no. 1, 2007, doi: 10.1063/1.2432410.

Titre : *Assemblage itératif de films nanostructurés de copolymères à blocs, vers le développement de structures tridimensionnelles fonctionnelles à périodicité nanométrique*

Résumé : Les copolymères à blocs ont la capacité de s'auto-assembler en une panoplie de structures périodiques à l'échelle nanométrique. L'objectif de ce travail a été de mettre en place un procédé itératif permettant l'empilement de films nanostructurés de copolymères à blocs, et de comprendre et contrôler les mécanismes d'orientation relatifs entre les couches. Pour cela, le système PS-*b*-PMMA a été choisi puisqu'il permet, après hybridation sélective des domaines de PMMA en alumine, de générer des nanostructures inorganiques permettant le couchage ultérieur d'une nouvelle couche de copolymères à blocs. Trois types de nanostructures bidimensionnelles ont plus particulièrement été étudiées : des lignes obtenues à partir d'une structure lamellaire des domaines de PMMA et PS, un réseau hexagonal de plots obtenu à partir de cylindres de PMMA dans une matrice de PS, et un réseau hexagonal de trous obtenu à partir de cylindres de PS dans une matrice de PMMA. En contrôlant la géométrie de chaque couche et sa périodicité par la modification des caractéristiques macromoléculaires des PS-*b*-PMMA, nous avons mis en évidence la possibilité de contrôler l'orientation relative de l'empilement de deux couches en faisant varier l'énergie interfaciale entre celles-ci. Ainsi, un grand nombre de nouvelles structures complexes de type bicouches formées à partir d'auto-assemblage de copolymères à blocs ont pu être observées pour la première fois. De plus, les observations expérimentales ont été rationalisées par la mise en place d'un modèle énergétique corroboré par des simulations avancées utilisant la dynamique des particules dissipatives. Finalement, il a été démontré que ce procédé d'empilement peut être extrapolé de deux couches à n couches de copolymères à blocs, ce qui permet d'imaginer la formation de nanostructures 3D fonctionnelles par ingénierie additive.

Mots clés : copolymères à blocs, auto-assemblage, nanostructure 3D, PS-*b*-PMMA

Title: *Iterative self-assembly of nanostructured block copolymer thin films, toward the development of functional three-dimensional structures with nanometric periodicity*

Abstract: Block copolymers have the potential to self-assemble in a variety of periodic structures at nanometric scale. The objective of this work was to explore the opportunity of iterative self-assembly of block copolymer thin films for the formation of three-dimensional structures. Particularly, a strong attention was devoted to the understanding of the stacking rules (i.e. relative orientation and alignment) between the different block copolymer layers. For this purpose, the PS-*b*-PMMA system was chosen as it allows the selective hybridization of the PMMA domains in alumina leading to the immobilization of the nanostructured layer for further stacking. Three types of bidimensional nanostructures obtained from block copolymer self-assembly were studied: lines obtained from PS-*b*-PMMA lamellae, a hexagonal array of dots from PMMA cylinders in a PS matrix, and a hexagonal array of holes from PS cylinders in a PMMA matrix. By controlling the geometry and periodicity of each layer through the PS-*b*-PMMA macromolecular characteristics, the possibility to control the relative orientation and alignment between the layers was demonstrated via the modification of the interfacial energy between the two block copolymer layers. Accordingly, novel bilayer structures obtained from block copolymer self-assembly were experimentally observed for the first time. Furthermore, an energetical mechanism corroborated by dissipative particles dynamics simulation allows predicting the stacking behavior observed experimentally. Finally, this stacking process was designed to be extrapolated from the two layers to n layers, enabling the generation of complex 3D nanostructures by additive manufacturing.

Keywords: block copolymers, self-assembly, 3D nanostructure, PS-*b*-PMMA

Unité de recherche

Laboratoire de Chimie des Polymères Organiques (LCPO), UMR 5629,
Bâtiment B8, Allée Geoffroy Saint Hilaire, 33615 Pessac Cedex, France